ACS SYMPOSIUM SERIES 1056

Advances in CO_2 Conversion and Utilization

EDITED BY
Yun Hang Hu

Downloaded by 89.163.34.136 on June 23, 2012 | http://pubs.acs.org
Publication Date (Web): December 3, 2010 | doi: 10.1021/bk-2010-1056.fw001

Advances in CO_2 Conversion and Utilization

In Advances in CO2 Conversion and Utilization; Hu, Y.;
ACS Symposium Series; American Chemical Society: Washington, DC, 2010.

Downloaded by 89.163.34.136 on June 23, 2012 | http://pubs.acs.org
Publication Date (Web): December 3, 2010 | doi: 10.1021/bk-2010-1056.fw001

ACS SYMPOSIUM SERIES **1056**

Advances in CO_2 Conversion and Utilization

Yun Hang Hu, Editor
Department of Materials Science and Engineering
Michigan Technological University

Downloaded by 89.163.34.136 on June 23, 2012 | http://pubs.acs.org
Publication Date (Web): December 3, 2010 | doi: 10.1021/bk-2010-1056.fw001

Sponsored by the
ACS Division of Fuel Chemistry

American Chemical Society, Washington, DC

Downloaded by 89.163.34.136 on June 23, 2012 | http://pubs.acs.org
Publication Date (Web): December 3, 2010 | doi: 10.1021/bk-2010-1056.fw001

Library of Congress Cataloging-in-Publication Data

Advances in CO2 conversion and utilization / Yun Hang Hu, editor ; sponsored by the ACS Division of Fuel Chemistry.
p. cm. -- (ACS symposium series ; 1056)
Includes bibliographical references and index.
ISBN 978-0-8412-2596-1 (alk. paper)
1. Carbon dioxide--Recycling--Congresses. 2. Carbon dioxide--Separation--Congresses. I. Hu, Yun Hang. II. American Chemical Society. Division of Fuel Chemistry.
QD181.C1A38 2010
628.5’32--dc22
2010046988

The paper used in this publication meets the minimum requirements of American National Standard for Information Sciences—Permanence of Paper for Printed Library Materials, ANSI Z39.48n1984.

Copyright © 2010 American Chemical Society

Distributed by Oxford University Press

All Rights Reserved. Reprographic copying beyond that permitted by Sections 107 or 108 of the U.S. Copyright Act is allowed for internal use only, provided that a per-chapter fee of $40.25 plus $0.75 per page is paid to the Copyright Clearance Center, Inc., 222 Rosewood Drive, Danvers, MA 01923, USA. Republication or reproduction for sale of pages in this book is permitted only under license from ACS. Direct these and other permission requests to ACS Copyright Office, Publications Division, 1155 16th Street, N.W., Washington, DC 20036.

The citation of trade names and/or names of manufacturers in this publication is not to be construed as an endorsement or as approval by ACS of the commercial products or services referenced herein; nor should the mere reference herein to any drawing, specification, chemical process, or other data be regarded as a license or as a conveyance of any right or permission to the holder, reader, or any other person or corporation, to manufacture, reproduce, use, or sell any patented invention or copyrighted work that may in any way be related thereto. Registered names, trademarks, etc., used in this publication, even without specific indication thereof, are not to be considered unprotected by law.

PRINTED IN THE UNITED STATES OF AMERICA

Downloaded by 89.163.34.136 on June 23, 2012 | http://pubs.acs.org
Publication Date (Web): December 3, 2010 | doi: 10.1021/bk-2010-1056.fw001

Foreword

The ACS Symposium Series was first published in 1974 to provide a mechanism for publishing symposia quickly in book form. The purpose of the series is to publish timely, comprehensive books developed from the ACS sponsored symposia based on current scientific research. Occasionally, books are developed from symposia sponsored by other organizations when the topic is of keen interest to the chemistry audience.

Before agreeing to publish a book, the proposed table of contents is reviewed for appropriate and comprehensive coverage and for interest to the audience. Some papers may be excluded to better focus the book; others may be added to provide comprehensiveness. When appropriate, overview or introductory chapters are added. Drafts of chapters are peer-reviewed prior to final acceptance or rejection, and manuscripts are prepared in camera-ready format.

As a rule, only original research papers and original review papers are included in the volumes. Verbatim reproductions of previous published papers are not accepted.

ACS Books Department

Downloaded by 89.163.34.136 on June 23, 2012 | http://pubs.acs.org
Publication Date (Web): December 3, 2010 | doi: 10.1021/bk-2010-1056.pr001

Preface

Carbon dioxide is a major greenhouse gas. There are several technological options for sequestration of CO_2 into one of the other global pools, including oceanic injection, geological injection, and scrubbing and mineral carbonation. The cost and leakage are principal issues of the geological sequestration which need to be resolved. For those reasons, the utilization of CO_2 is being considered as an attractive solution to solve CO_2 issues. To promote research and development in CO_2 areas, we organized a symposium on CO_2 conversion and utilization as a part of the 238th American Chemical Society (ACS) National Meeting, August 16-20, 2009, Washington, DC. This symposium was sponsored by the ACS Division of Fuel Chemistry. This book was developed on this ACS symposium.

This book contains 16 peer-reviewed chapters that cover various aspects of CO_2 conversion and utilization. This ACS book focuses on the following topics: application of solar energy for CO_2 conversion (Chapters 1-3), synthesis of organic compounds from CO_2 (Chapters 4-9), CO_2 reforming of methane into synthesis gas (Chapters 10-12), CO_2 adsorption and absorption (Chapters 13-15), and chemical lungs for CO_2 conversion into oxygen (Chapter 16). Most of those chapters were developed from ACS papers presented at the symposium and others were from invited contributors in the related research areas. All chapters were contributed by active research groups from universities, national laboratories, or industrial research organizations worldwide. All contributed manuscripts were sent to referees, and only those that passed through the peer review process became the chapters in the book.

I wish to thank all the authors of the chapters for their contributions to the ACS book and the ACS symposium. I would like to express my genuine appreciation to all the peer reviewers for their time and efforts in evaluating the manuscripts to improve the quality of most chapters in the book. I would like to thank the ACS Division of Fuel Chemistry and the ACS Books Department for the opportunities to organize the symposium and to publish this book, respectively. I also wish to thank Tim Marney, Bob Hauserman, and Tara Urban at the ACS Books Department for their great efforts in the peer-review process and production of this book.

Yun Hang Hu

Department of Materials Science and Engineering
Michigan Technological University
Houghton, Michigan 49931-1295

In Advances in CO2 Conversion and Utilization; Hu, Y.;
ACS Symposium Series; American Chemical Society: Washington, DC, 2010.

Downloaded by 89.163.34.136 on June 23, 2012 | http://pubs.acs.org
Publication Date (Web): December 3, 2010 | doi: 10.1021/bk-2010-1056.ch001

Chapter 1

Synthesis and Characterization of Ferrite Materials for Thermochemical CO_2 Splitting Using Concentrated Solar Energy

**Andrea Ambrosini,* Eric N. Coker, Mark A. Rodriguez,
Stephanie Livers, Lindsey R. Evans, James E. Miller,
and Ellen B. Stechel**

**Sandia National Laboratories, PO Box 5800 MS0734, Albuquerque,
New Mexico 87185, USA
*aambros@sandia.gov**

The Sunshine to Petrol effort at Sandia aims to convert carbon dioxide and water to precursors for liquid hydrocarbon fuels using concentrated solar power. Significant advances have been made in the field of solar thermochemical CO_2-splitting technologies utilizing yttria-stabilized zirconia (YSZ)-supported ferrite composites. Conceptually, such materials work via the basic redox reactions: $Fe_3O_4 \rightarrow 3FeO + 0.5O_2$ (Thermal reduction, >1350°C) and $3FeO + CO_2 \rightarrow Fe_3O_4 + CO$ (CO_2-splitting oxidation, <1200°C). There has been limited fundamental characterization of the ferrite-based materials at the high temperatures and conditions present in these cycles. A systematic study of these composites is underway in an effort to begin to elucidate microstructure, structure-property relationships, and the role of the support on redox behavior under high-temperature reducing and oxidizing environments. In this paper the synthesis, structural characterization (including scanning electron microscopy and room temperature and in-situ x-ray diffraction), and thermogravimetric analysis of YSZ-supported ferrites will be reported.

In Advances in CO2 Conversion and Utilization; Hu, Y.;
ACS Symposium Series; American Chemical Society: Washington, DC, 2010.

Downloaded by 89.163.34.136 on June 23, 2012 | http://pubs.acs.org
Publication Date (Web): December 3, 2010 | doi: 10.1021/bk-2010-1056.ch001

Introduction

The Sunshine to Petrol effort at Sandia National Laboratories aims to convert carbon dioxide and water to precursors for liquid hydrocarbon fuels using concentrating solar power (CSP). In doing so, the combustion process is "reversed" and transportation fuels can be synthesized from captured CO_2 that would otherwise be sequestered underground or released into the atmosphere. The use of thermal energy from concentrated solar to produce synthesis gas (H_2 and CO) from CO_2 and H_2O has potential advantages over other methods of syngas production (bio-, electrolysis, photovoltaic) because of its scalability and theoretical efficiency. Driving thermochemical processes via concentrating solar flux utilizes more of the solar spectrum and avoids the costly solar to electric conversion (*1*). At the heart of the S2P effort is the Counter-Rotating-Ring Receiver Reactor Recuperator (CR5), a heat engine designed to facilitate the splitting of CO_2 and H_2O using metal oxides as the reactive material. The design and concept of this device is described in detail elsewhere (*2*, *3*).

Significant advances have been made in the field of solar thermochemical H_2O- and CO_2- splitting technologies using redox-active metal oxides (*4*–*7*). Splitting technologies via thermochemical cycles are desirable because they divide what is normally an unfavorable reaction (direct thermolysis of H_2O or CO_2) into two or more steps that are thermodynamically more favorable. Metal oxide cycles are attractive as they are two-step reactions in which a solid oxide reacts with and produces gaseous products, resulting in facile isolation of the working solid material from the desired products. The reduction of the metal oxide occurs at temperatures lower than those required for thermolysis, yet still high enough to require substantial heating, such as that provided by concentrated solar. However, much of the materials development effort has been somewhat trial-and-error. This is due in part to a lack of fundamental understanding into the behavior of the metal oxides under development under the high temperature conditions present in these cycles. Basic questions such as oxygen transport, surface chemistry, structural changes vs. redox reactions, and the effects of synthesis methods and cycling on the material have not yet been answered.

One system that effectively demonstrates CSP-driven thermochemical splitting utilizes iron oxide as the redox active material. Conceptually, such materials work via the basic redox reactions:

$$Fe_3O_4 \rightarrow 3FeO + 0.5O_2 \qquad \text{(Thermal reduction, TR, >1350°C)}$$

$$3FeO + CO_2 \rightarrow Fe_3O_4 + CO \qquad \text{(}CO_2\text{-splitting oxidation, CDS, <1200°C)}$$

$$3FeO + H_2O \rightarrow Fe_3O_4 + H_2 \qquad \text{(}H_2O\text{-splitting oxidation, WS, <1200°C)}$$

However, it previously has been shown that the ferrite materials are not repeatably cyclable on their own; a support of some sort (e.g. ZrO_2, YSZ, HfO_2) is necessary (*8*). Effort has been expended in order to elucidate the poorly understood complex interaction between the ferrite and support (solid solubility, microstructure, reaction kinetics). The design and execution of in-situ experiments to elucidate the chemistry under operating conditions has been a main focus and will be discussed in this report. This includes simulating H_2O- and CO_2-splitting reactions in the

Downloaded by 89.163.34.136 on June 23, 2012 | http://pubs.acs.org
Publication Date (Web): December 3, 2010 | doi: 10.1021/bk-2010-1056.ch001

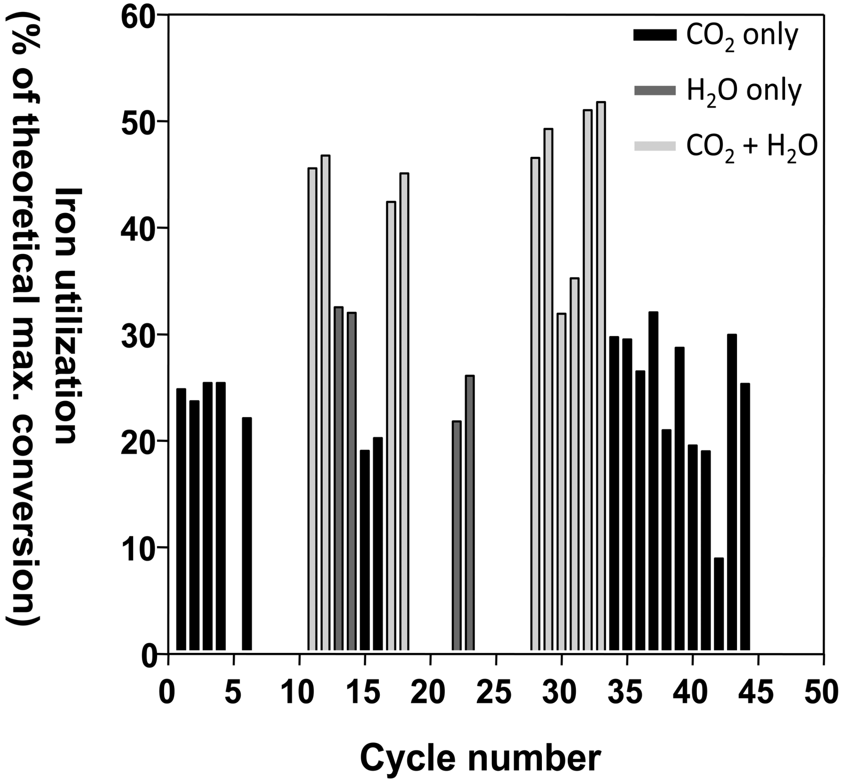

Figure 1. CO_2 and H_2O splitting cycles of 5 wt% Fe_2O_3 in 3YSZ. One cycle is equivalent to thermal reduction (under inert gas) followed by reoxidation by CO_2, H O, or a stream of both. The same sample was used over the course of the entire experiment, with the reactant gases varied from one cycle to another. Each bar represents the iron utilization in that specific cycle (i.e. not cumulative). The % max theoretical iron utilization assumes full conversion between Fe_3O_4 → FeO on a molar basis.

lab using temperature-programmed reduction and oxidation, thermogravimetric analysis (TGA), X-ray diffraction (XRD), and scanning electron microscopy (SEM). An understanding of the basic Fe_2O_3 system will be used as a basis to understand the more complex systems such as $CoFe_2O_4$ and other substituted ferrites currently under investigation.

Experimental

The iron oxide:yttria-stabilized zirconia (Fe_2O_3:YSZ) materials were made by SPEX milling Fe_2O_3 powder with cubic 8YSZ [$(ZrO_2)_{0.92}(Y_2O_3)_{0.08}$] powder in the desired proportions. (Poly)vinyl acetate (PVA) binder was then added, the dried powder was ground with an agate mortar and pestle, and the mixture uniaxially pressed into pellets. The samples were calcined at 1°C /min up to 1100°C to burn

Downloaded by 89.163.34.136 on June 23, 2012 | http://pubs.acs.org
Publication Date (Web): December 3, 2010 | doi: 10.1021/bk-2010-1056.ch001

out the binder, then sintered at 1375 °C /48 h, and finally 1500 °C/2h before cooling to room temperature at a rate of 10 °C /min .

Room temperature x-ray diffraction (XRD) was performed on a Bruker D8 Advance diffractometer in Bragg-Brentano geometry with Cu Kα radiation and analyzed with JADE 7.0+ analysis software (*9*). In situ XRD experiments utilized a Scintag PAD X diffractometer (Thermo Electron Inc.) and a controlled atmosphere, high temperature sample cell, described elsewhere (*10*). Scanning electron microscopy (SEM) and energy-dispersive spectroscopy (EDS) were performed on a in a Zeiss scanning electron microscope at 15 kV. Samples were sputtered with a thin layer of gold–palladium before analysis to prevent charging.

Thermogravimetric analysis (TGA) was performed on a TA Instruments SDT Q600 under TR and CDS conditions. Argon and CO_2 gas streams both passed through getters to remove traces of oxygen prior to entering the TGA. Samples for TGA analyses were generally sintered bars of reactive material (approx. 1.7 x 6 x 1 mm) placed atop a Pt crucible. Thermochemical cycling experiments in the TGA were conducted under heating and cooling rates of 20 °C/min, and gas flow rates of 100 ml/min. Generally, the sample was heated under Ar to 1400 °C, held at isotherm for 1 h (thermal reduction), cooled to 1100 °C, exposed to CO_2 and held at isotherm for 1 h (oxidation), heated back to 1400 °C, exposed to Ar, etc… This cycle was repeated 3-4 times per sample.

Bench reactor tests were carried out in a flow reactor consisting of a mullite tube situated in a high-temperature furnace (CSP surrogate) (*5*). Multiple cycles under various conditions were often run on the same sample during one experiment. After thermal reduction under inert gas, the oxidizing reactants (H_2O in argon, CO_2, or humidified CO_2) were flowed through the reactor and the effluent was monitored by gas chromatography.

Results and Discussion

Samples of Fe_2O_3:YSZ were tested on a bench-top apparatus to measure the amounts of H_2 and CO produced from the H_2O- and CO_2-splitting reaction, respectively. Figure 1 shows the results of multiple cycles for a sample of 5 weight% Fe_2O_3:YSZ. Several observations can be made:

- CO_2 and H_2O splitting was demonstrated over multiple temperature cycles ;
- % Fe utilization differed between single-source (CO_2 *or* H_2O) and mixed (CO_2 *plus* H_2O) feeds; and
- Material performance had not reached steady-state after multiple cycles. This was also observed in redox experiments on a TGA and tests performed on a solar furnace at the National Solar Thermal Test Facility at Sandia (*11*).

Downloaded by 89.163.34.136 on June 23, 2012 | http://pubs.acs.org
Publication Date (Web): December 3, 2010 | doi: 10.1021/bk-2010-1056.ch001

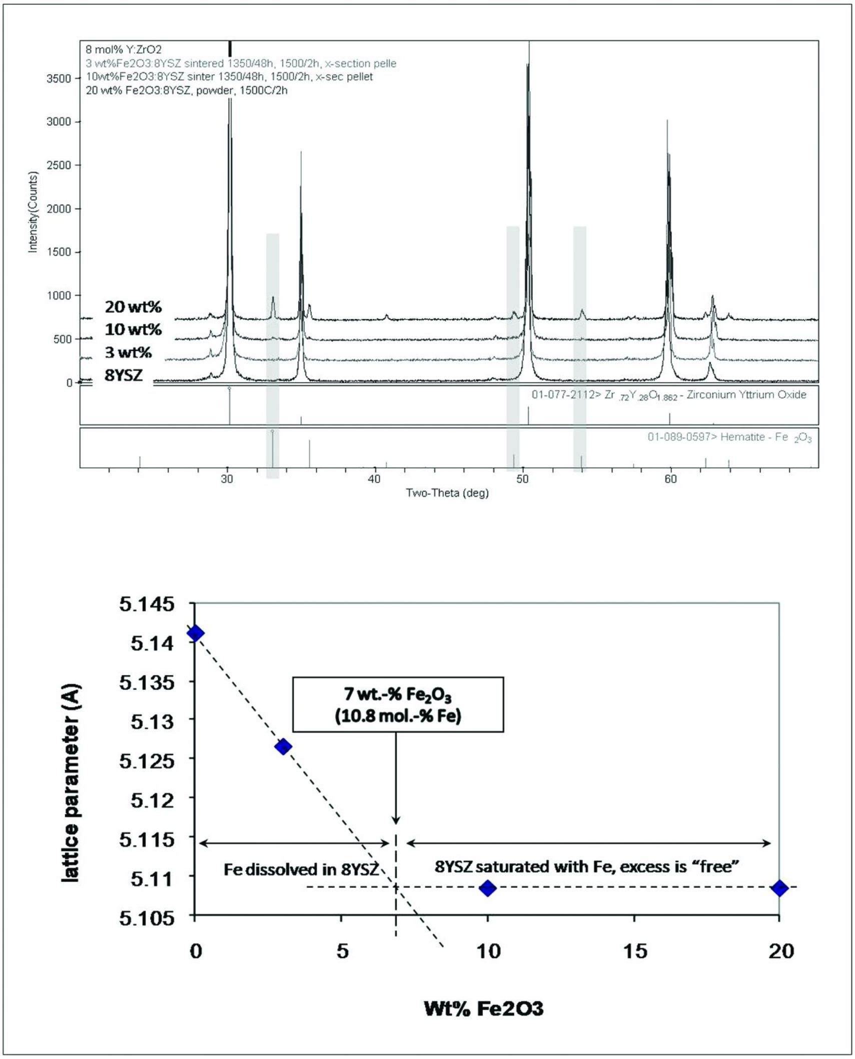

*Figure 2. **(top)** Room temperature XRD of Fe_2O_3 (wt %) in 8% yttria-stabilized zirconia (8YSZ). **(bottom)** Plot of YSZ cubic lattice parameter versus weight % of Fe_2O_3, showing regions of solid solubility and excess Fe_2O_3.*

In order to elucidate the reasons behind these observations, we have begun to structurally characterize these materials in-depth using XRD, TGA and SEM. An important question the current study has addressed is what exactly is the solid solubility of Fe_2O_3 in YSZ under pertinent conditions? There is not a straightforward answer, as the solubility seems to be influenced by a variety of factors, including synthesis conditions, temperature, atmosphere (redox state), and yttrium-content of the YSZ (*10*, *12–16*). The answer is important because preliminary evidence suggests that the redox properties of the composite are affected by the concentration of ferrite in solid solution.

Downloaded by 89.163.34.136 on June 23, 2012 | http://pubs.acs.org
Publication Date (Web): December 3, 2010 | doi: 10.1021/bk-2010-1056.ch001

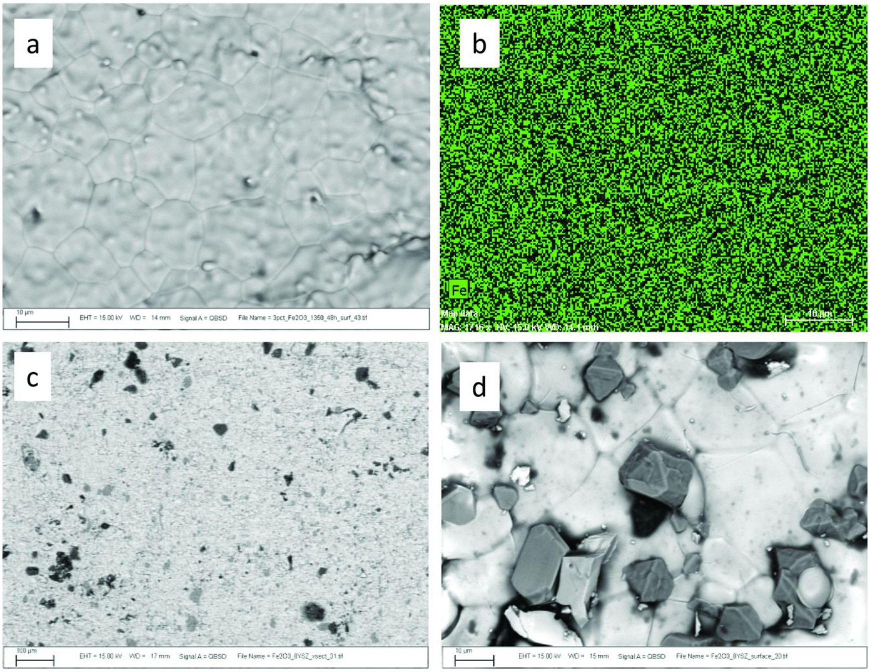

*Figure 3. **(a)** Electron backscattered (EBS) SEM image of 3 wt% Fe_2O_3:8YSZ. **(b)** Fe-EDS map of same are showing homogeneously-dispersed Fe (dark) in YSZ (light). **(c)** EBS-SEM image of 10 wt% Fe_2O_3:8YSZ cross-section showing crystallites (dark) of Fe_2O_3. **(d)** EBS-SEM of post-annealed surface of 10 wt% Fe_2O_3:8YSZ showing highly crystalline iron oxide presumably re-precipitated at the grain boundaries.*

An estimation of the solubility limit of iron in 8YSZ at room temperature was conducted by preparing samples of varying Fe_2O_3 / 8YSZ mass ratios (via the methods described in the Experimental section above) and measuring the lattice parameters of the resulting YSZ phase by XRD at ambient temperature (Figure 2a). Because Fe^{3+} has a smaller ionic radius than either Zr^{4+} or Y^{3+} (0.78 vs. 0.84 and 1.01 nm, respectively) (*17*), the dissolution of Fe^{3+} into YSZ should result in a decrease in the YSZ lattice parameter. When the solid solubility maximum is reached, there should be no further change in lattice parameter, as stated by Vegard's Law (*18*). Figure 2b shows a plot of lattice parameter versus weight percent of added Fe_2O_3. From the intersection of the two lines in this plot, a solid solubility of 7 wt% Fe_2O_3, corresponding to 10.8 mol% Fe, can be approximated. Thus, samples with iron loadings below 10.8 mol% that are synthesized under the above conditions should be complete solid solutions at room temperature, whereas those with higher loadings are composites consisting of both dissolved Fe plus "free" iron oxide.

SEM images of as-synthesized monoliths of Fe_2O_3:8YSZ revealed several interesting microstructural features. When doped with 3 wt% Fe_2O_3, the sample was homogeneous, supporting the formation of a complete solid solution. EDS analysis confirmed this observation (Figure 3a,b). However in samples

Downloaded by 89.163.34.136 on June 23, 2012 | http://pubs.acs.org
Publication Date (Web): December 3, 2010 | doi: 10.1021/bk-2010-1056.ch001

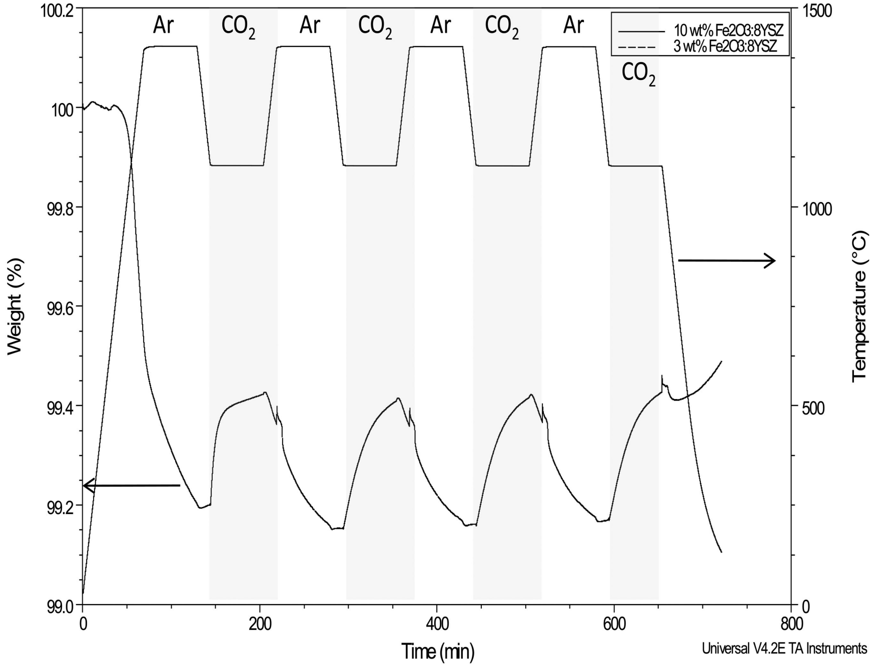

Figure 4. TGA plot of redox cycle of 10 wt.-% Fe_2O_3:8YSZ (bottom solid line) and 3 wt.-% Fe_2O_3:8YSZ (bottom dashed line) measured under identical conditions. The changes in shading indicate the change between Ar (thermal reducing) and CO_2 (oxidizing) regimes. The line on top corresponds to the reaction temperatures.

containing 10 wt% Fe_2O_3, un-reacted Fe_2O_3 remained heterogeneously distributed throughout the sample (Figure 3c). There was also evidence that migration of the iron oxide occurs during sample preparation, as evidenced by micron-sized iron oxide crystals present on the surface of the sintered pellet (Figure 3d). One possible mechanism to account for this is that the Fe_2O_3 became at least partially reduced at high temperatures, melted, migrated, and re-crystallized at the surface upon cooling. These findings have resulted in a rethinking of the materials fabrication process, which is currently being refined. In addition, substituted ferrites, such as $Co_xFe_{3-x}O_4$, are being considered due to their higher melting points (*19*).

Thermogravimetric analyses of the 3- and 10-wt% Fe_2O_3:8YSZ materials under reducing and oxidizing conditions simulating what might be experienced in the CR5 are shown in Figure 4. Two interesting results to point out are that (1) in both samples, the initial redox curve differs from successive cycles and (2) despite different iron loadings, the magnitude of reaction is similar (i.e. the TG curves of the 3% and 10% samples look almost identical), implying that in the 3% solid solution, a higher percentage of the iron is reacting, at least on the time scale of the TGA experiment. Compared to theoretical calculations, assuming all of the Fe is oxidized from 3+ to 2+, approximately 70% of the iron reacts in the 3% sample, but only 25% for the 10% sample; neither reacts completely. Complete

Downloaded by 89.163.34.136 on June 23, 2012 | http://pubs.acs.org
Publication Date (Web): December 3, 2010 | doi: 10.1021/bk-2010-1056.ch001

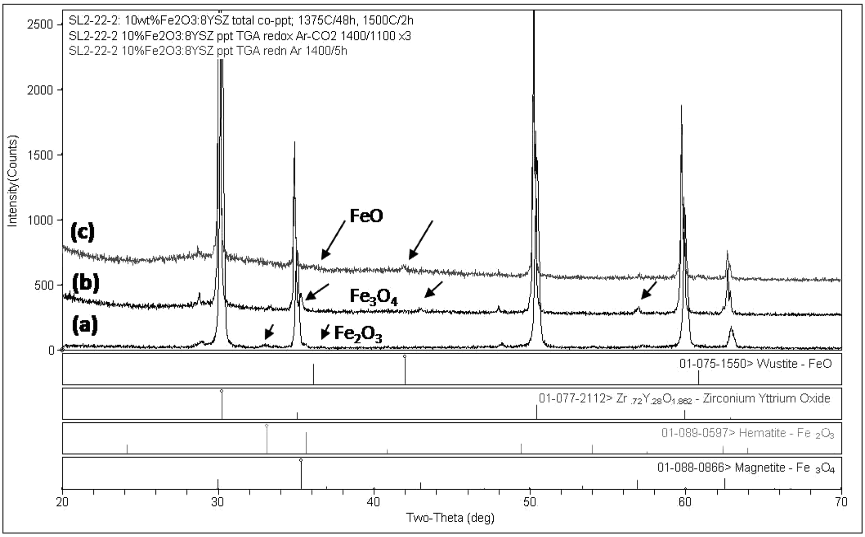

Figure 5. Room temperature XRD of 10 wt% Fe_2O_3:8YSZ ***(a)*** *as-synthesized,* ***(b)*** *after several TGA redox cycles, and* ***(c)*** *after reduction under Ar (1400 C/5h).*

reaction may not occur in either sample owing to limits in kinetics of transport in the bulk. A more detailed kinetic and thermodynamic study of these materials is underway and will be reported in a future publication.

There can be several possible reasons for the difference in behavior between the solid solution and the composite material. In the solid solution, one can assume redox reaction of the iron species is between $Fe^{3+}\leftrightarrow Fe^{2+}$, as it has been shown that in solid state reactions, the iron dissolves as Fe^{3+} (*20*). But for the composite containing "free" iron oxide (e.g., 10 wt% sample), the most likely reaction mechanism of the undissolved iron oxide is: $Fe_2O_3 \rightarrow Fe_3O_4 \leftrightarrow FeO$. After the initial reduction to FeO, it is unlikely that complete reoxidation to Fe_2O_3 occurs under the oxidation conditions; instead it shuttles between the FeO (Fe^{3+}) and Fe_3O_4 ($Fe^{\text{“}2.67\text{”}}$) phases. This hypothesis is supported by powder XRD taken of the materials post-TGA (Figure 5). While the solid solution sample shows no structural changes after reduction or reoxidation (not shown), the 10 wt% composite shows the presence of FeO after reduction and Fe_3O_4 after several redox cycles. Thus, only 2/3 of the Fe cations associated with the "free" iron oxide are redox active. This may partially (though not totally) account for the lower iron utilization compared to theoretical in the 10 wt% material. For example, if one expected all 10% of the Fe in the sample reduce from $Fe^{3+} \rightarrow Fe^{2+}$, the expected weight loss would be approximately 1% of the sample weight. If one were to assume that of the 10 wt% Fe_2O_3, 7% dissolved into the YSZ and 3% remained as "free" Fe_2O_3, then the expected weight loss would still be on the order of 0.9%--thus the weight loss observed in the TGA is still only approximately 30% of the theoretically calculated weight loss. Therefore, there must be an additional influence on the reactivity of the composite sample.

A second rationale that can account for the difference is that the iron is more accessible or mobile in the YSZ that in bulk iron oxides. In the solid solution, the

Downloaded by 89.163.34.136 on June 23, 2012 | http://pubs.acs.org
Publication Date (Web): December 3, 2010 | doi: 10.1021/bk-2010-1056.ch001

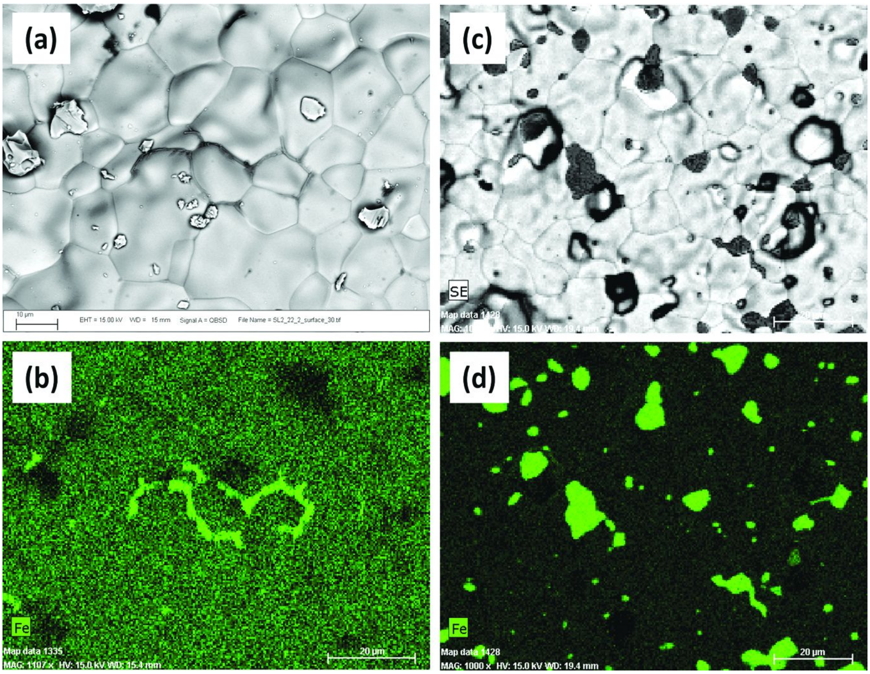
(a)
10 µm
EHT = 15.00 kV WD = 15 mm Signal A = QBSD File Name = SL2_22_2_surface_30.tif
(c)
SE
Map data 1428
(b)
Fe
Map data 1335
MAG: 1107 x HV: 15.0 kV WD: 15.4 mm
20 µm
(d)
Fe
Map data 1428
MAG: 1000 x HV: 15.0 kV WD: 19.4 mm
20 µm

Figure 6. Electron backscattered SEM (top) /EDS (bottom) map of the surface of a 10 wt% Fe_2O_3:8YSZ bar as-synthesized ***(a, b)*** *and after several TGA redox cycles* ***(c, d)****. Iron is represented by the dark images on the SEM and the light areas in the EDS.*

Fe cations are atomically and homogenously dispersed throughout the YSZ unit cell, which enables exposure of each iron atom to oxygen conducted through the YSZ lattice, facilitating the redox chemistry of the iron. However, the iron oxide that exists in excess in the composite material consists of iron oxide particles on the order of microns. Since iron oxide itself is not a facile oxygen conductive material (the diffusion coefficient of oxygen in YSZ at 1100 °C is on the order of 10^{-8} cm^2/s (*21*); for Fe_2O_3 it is closer to 10^{-12} cm^2/s) (*22*), reduction or oxidation of a particle is likely kinetically limited to the surface and not all of the iron is easily reactive. SEM/EDS were performed on the ceramics before and after TGA. As with the XRD, the 3 wt% sample shows neither appreciable change in microstructure nor any precipitation of iron oxide from the solid solution. However, SEM of the composite material (Figure 6) indicates that the free iron oxide species is mobile as it appears to melt, migrate along the grain boundaries, and re-precipitate at the surface of the YSZ monolith, probably during reduction step, since FeO has a lower melting point (1370 °C) than the other iron oxides. The dissolution and re-precipitation into larger particles on the surface of the composite monolith may also affect the kinetics and extent of reaction of the iron oxide. A final observation to consider is that the EDS map of the sample in Figure 6d qualitatively implies that there is less Fe in the solid solution than before. If the species in solid solution is assumed to be the more reactive, this will also affect the extent of reaction in the bulk composite.

Downloaded by 89.163.34.136 on June 23, 2012 | http://pubs.acs.org
Publication Date (Web): December 3, 2010 | doi: 10.1021/bk-2010-1056.ch001

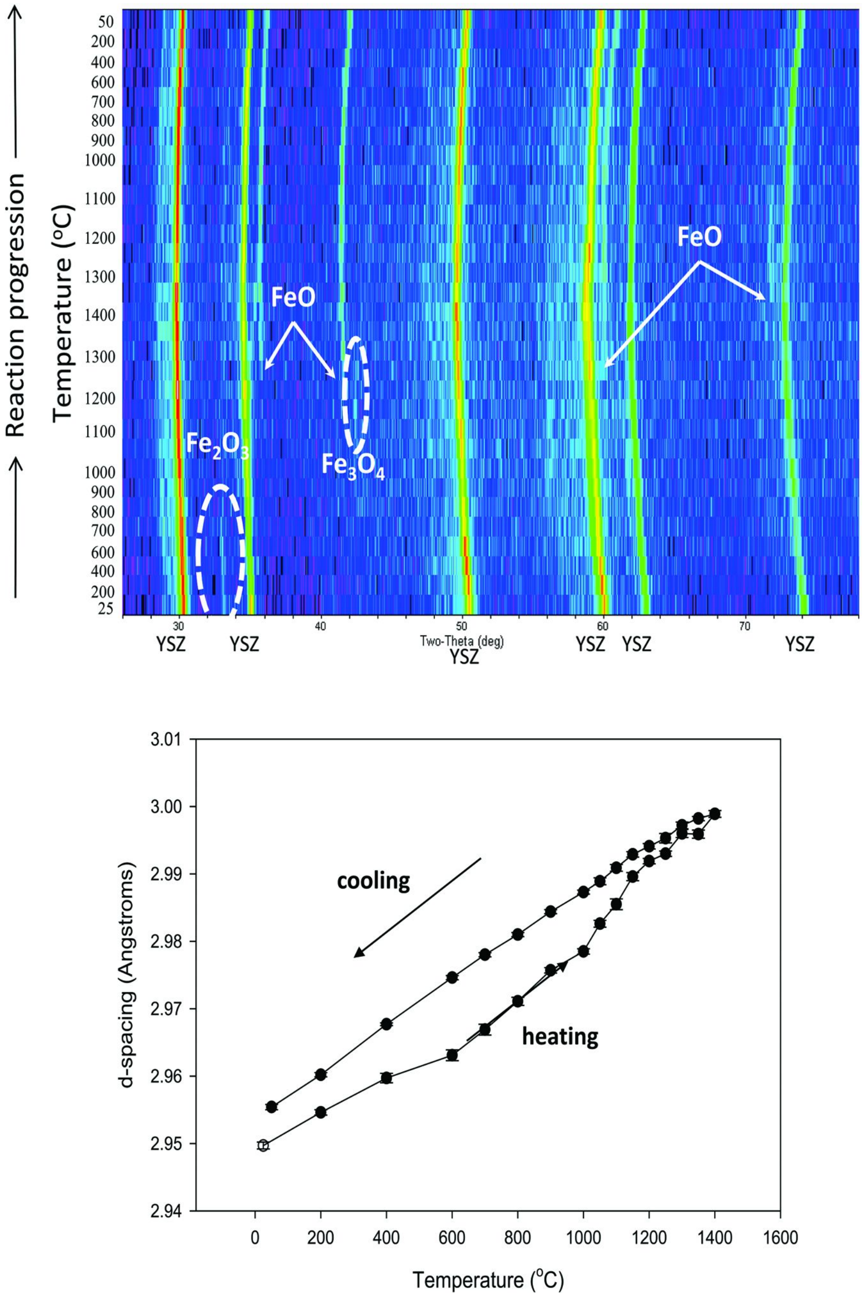

*Figure 7. **(Top)** HT-XRD intensity plot for 10 wt.-% Fe_2O_3:8YSZ, 25 °C → 1400 °C → 50 °C under helium. Intensities are plotted on a log scale. **(Bottom)** Variation in 8YSZ (111) peak position during heating and cooling cycles described in (a). (From Ref. (10))*

An ongoing series of in-situ X-ray diffraction (XRD) experiments has been designed to further investigate the solid solubility question as a function of temperature and atmosphere. They involve observing samples with varying Fe_2O_3 concentrations in YSZ as they are heated and cooled under air, CO_2, and He in order to mimic the synthesis and reaction conditions experienced by the reactive material. The full study will be reported in an upcoming paper (*10*). Figure 7a shows one experiment in which a composite of 10 wt% Fe_2O_3:8YSZ was heated and cooled under He gas. The initial XRD showed Fe_2O_3 plus a solid solution of Fe in YSZ (indexed to the cubic ZrO_2 phase). Upon heating, the loss of the Fe_2O_3 peak was observed around 800 °C and a faint signal for Fe_3O_4 formed at ~1150 °C. Then from ~1250 °C to 1400 °C, FeO formed at the expense of Fe_3O_4. At this point the sample was cooled, and the FeO persisted. Tracking the d-spacing for the YSZ (111) peak shows a non-linear increase of the d-spacing as the material is heated that does not appear upon cooling (Figure 7b). If the change in lattice parameter was due solely to thermal expansion of the unit cell as it was heated, one would expect a constant slope. The change in slope upon heating corresponds to the temperature at which the loss of the Fe_2O_3 peak was observed, implying that under those conditions, the solid solubility of Fe^{3+} in 8YSZ actually increases. The slope then increases around 1100 °C correlating with the appearance of Fe_3O_4 and then FeO, indicating Fe is expelled from the YSZ lattice. Therefore, this seems to be a dynamic behavior, with Fe shuttling between forms, during the heating process. In other words, the solubility of the iron is indeed changing with temperature. Upon cooling (still under He), the FeO remains stable, i.e., it does not dissolve back into the YSZ, as indicated by the persistence of FeO peaks in the XRD as well as a linear decrease of the (111) d-spacing. Once the FeO has formed, it shows stability in the absence of oxygen, and the YSZ lattice varies linearly with temperature during sample cooling. This implies that the Fe^{2+} cation is not as soluble as that of Fe^{3+}. If this is the case, it may be one of the causes of the apparent "leaching out" of iron oxide from the composite observed in the SEM/EDS images described above. Investigations are currently underway to more closely coordinate the in-situ XRD with the TGA experiments and observed behavior in the Fe_2O_3:YSZ system in order to elucidate a reaction mechanism.

Conclusions

We seek to develop a systematic understanding of the Fe_2O_3:YSZ composite materials used in CSP H_2O- and CO_2- splitting reactions, so as to optimize their redox performance and ultimately design new materials with improved efficiency and durability for thermochemical syn gas production. Preliminary investigations reveal the ferrites have H_2O- and CO_2-splitting capability, but require a support material for efficient long-term cyclability. However the ferrite-support interaction (solid solubility, microstructure, reaction kinetics) is not well-defined at high temperatures and under redox conditions. Measurements of redox cycles under various conditions revealed a material that had not reached steady-state and demonstrated varying levels of iron utilization depending on reactive gas and cycle number. The reasons behind such behavior are not completely understood.

Downloaded by 89.163.34.136 on June 23, 2012 | http://pubs.acs.org
Publication Date (Web): December 3, 2010 | doi: 10.1021/bk-2010-1056.ch001

Therefore, we have designed in-situ experiments to elucidate the chemistry of these materials under operating conditions. Preliminary results suggest that Fe^{3+} is soluble in 8YSZ up to approximately 11 mol% at room temperature. This "solubilized" iron is hypothesized to be more redox active than the iron oxide present as a second phase (i.e. not dissolved), which may account for the increased theoretical iron utilization in samples containing < 7 wt% Fe_2O_3, as seen in the TGA results. However, the scenario is complicated by the observation that the iron species appears mobile in YSZ vs. temperature and atmosphere, which affects the solid solubility of Fe and also the redox activity of the composite. Further analyses to better correlate the in-situ XRD, microscopy, and TGA results are underway in conjunction with theoretical modeling of the system and surface studies. These results will be reported in upcoming publications.

Acknowledgments

This work was supported by the Laboratory Directed Research and Development program at Sandia National Laboratories, in the form of a Grand Challenge project entitled Reimagining Liquid Transportation Fuels: Sunshine to Petrol. Sandia is a multiprogram laboratory operated by Sandia Corporation, a Lockheed Martin Company, for the United States Department of Energy's National Nuclear Security Administration under Contract DE-AC04-94AL85000. The authors would also like to thank Bonnie McKenzie (Sandia National Labs) for her aid obtaining the SEM/EDS images.

References

1. Miller, J. E.; Diver, R. B.; Siegel, N. P.; Coker, E. N.; Ambrosini, A.; Dedrick, D. E.; Allendorf, M. A.; McDaniel, A. H.; Kellogg, G. L.; Hogan, R. E.; Chen, K. S.; Stechel, E. B. Sunshine to Petrol: A Metal Oxide-Based Thermochemical Route to Solar Fuels. In *Energy Technology 2010*; Neelameggham, N. R., Reddy, R. G., Belt, C. K., Hagni, A. M., Das, S., Eds.; TMS (The Minerals, Metals & Materials Society: 2010.
2. Diver, R. B.; Miller, J. E.; Allendorf, M. D.; Siegel, N. P.; Hogan, R. E. Solar Thermochemical Water-Splitting Ferrite-Cycle Heat Engines. *Proceedings of the International Solar Energy Conference*; Denver, CO, Jul 8−13, 2006; American Society of Mechanical Engineers: New York, NY, 2007; p 301.
3. Diver, R. B.; Miller, J. E.; Allendorf, M. D.; Siegel, N. P.; Hogan, R. E. *J. Sol. Energy Eng., Trans. ASME* **2008**, *130*, 041001.
4. Kodama, T.; Gokon, N. *Chem. Rev.* **2007**, *107*, 4048.
5. Miller, J. E.; Allendorf, M. D.; Diver, R. B.; Evans, L. R.; Siegel, N. P.; Stuecker, J. N. *J. Mater. Sci.* **2007**, *43*, 4714.
6. Steinfeld, A. *Sol. Energy* **2005**, *78*, 603.
7. Abanades, S.; Flamant, G. *Sol. Energy* **2006**, *80*, 1611.
8. Kodama, T.; Nakamuro, Y.; Mizuno, T. *J. Sol. Energy Eng., Trans. ASME* **2006**, *128*, 3.
9. *Jade+*, version 9.1; Materials Data Inc.: Livermore, CA, 2009.

Downloaded by 89.163.34.136 on June 23, 2012 | http://pubs.acs.org
Publication Date (Web): December 3, 2010 | doi: 10.1021/bk-2010-1056.ch001

10. Coker, E. N.; Rodriguez, M. A.; Ambrosini, A.; Miller, J. E. *Chem. Mater.* **2009**, in preparation.
11. National Solar Thermal Test Facility, Sandia National Laboratories, http://www.sandia.gov/Renewable_Energy/solarthermal/nsttf.html.
12. Davison, S.; Kershaw, R.; Dwight, K.; Wold, A. *J. Solid State Chem.* **1988**, *73*, 47.
13. Garcia, F. L.; Resende, V. G. d.; De Grave, E.; Peigney, A.; Barnabé, A.; Laurent, C. *Mater. Res. Bull.* **2009**, *44*, 1301.
14. Gao, H. B.; Liu, J.; Chen, H. Y.; Li, S.; He, T. M.; Ji, Y.; Zhang, J. D. *Solid State Ionics.* **2008**, *179*, 1620.
15. Gokon, N.; Minno, T.; Nakamuro, Y.; Kodama, T. *J. Sol. Energy Eng., Trans. ASME* **2008**, *130*, 011018.
16. Nakajima, H.; Itoh, K.; Kaneko, H.; Tamaura, Y. *J. Phys. Chem. Solids* **2007**, *68*, 1946.
17. Shannon, R. D. *Acta Crystallogr. Sect. A: Cryst. Phys., Diffr., Theor. Gen. Crystallogr.* **1976**, *A32*, 751.
18. Vegard, L. *Z. Phys.* **1921**, *5*, 17.
19. Allendorf, M. D.; Diver, R. B.; Siegel, N. P.; Miller, J. E. *Energy Fuels* **2008**, *22*, 4115.
20. Argirusis, C.; Taylor, M. A.; Kilo, M.; Borchardt, G.; Jomard, F.; Lesage, B.; Kaitasov, O. *Phys. Chem. Chem. Phys.* **2004**, *6*, 3650.
21. Manning, P. S.; Sirman, J. D.; DeSouza, R. A.; Kilner, J. A. *Solid State Ionics* **1997**, *100*, 1.
22. Amami, B.; Addou, M.; Monty, C. *Defect Diffus. Forum* **2001**, *194-1*, 1051.

Downloaded by 89.163.34.136 on June 23, 2012 | http://pubs.acs.org
Publication Date (Web): December 3, 2010 | doi: 10.1021/bk-2010-1056.ch001

Downloaded by CORNELL UNIV on June 23, 2012 | http://pubs.acs.org
Publication Date (Web): December 3, 2010 | doi: 10.1021/bk-2010-1056.ch002

Chapter 2

Photocatalytic Reduction of CO_2 Using H_2 as Reductant over Solid Base Photocatalysts

Kentaro Teramura[1,*] and Tsunehiro Tanaka[2]

[1]Kyoto University Pioneering Research Unit for Next Generation, Kyoto University, Kyoto 615-8510, Japan
[2]Department of Molecular Engineering, Graduate School of Engineering, Kyoto University, Kyoto 615-8510, Japan
***teramura@moleng.kyoto-u.ac.jp**

We have found that CO is generated as a result of the photocatalytic reduction of CO_2 in the presence of H_2 or CH_4 over ZrO_2 in 1997, Rh/TiO_2 in 1999, MgO in 2001, and Ga_2O_3 in 2008. With the exception of Rh/TiO_2, these solid materials exhibit the properties of solid base catalysts; therefore, CO_2 can be adsorbed on the surface of these materials. We have insisted on the importance of CO_2 adsorption on the surface because this makes CO_2, which is a stable and linear molecular, into an active species which provides abundant reactivity for the photocatalytic reduction of CO_2. The determining factor for photocatalytic reduction is the adsorption of CO_2 on the surface. In the following section, we provide an overview of some solid base materials which exhibit the photocatalytic activity necessary for photocatalytic reduction of CO_2 in the presence of H_2.

Introduction

Recently, many countries that have approved the ratification of the Kyoto Protocol are enforcing strict regulations on carbon dioxide (CO_2) emission to meet international environmental standards. These countries are reducing CO_2 emission in many different ways, for example, by storage in the ground and sea, absorption into various functionalized materials, and large-scale forestation. In addition, the developed countries have established a framework for CO_2 emission trading to

Downloaded by CORNELL UNIV on June 23, 2012 | http://pubs.acs.org
Publication Date (Web): December 3, 2010 | doi: 10.1021/bk-2010-1056.ch002

achieve emissions targets. However, it is unlikely that the means described above will achieve substantial removal of excess CO_2. While large-scale forestation is a successful approach, it may not catch up with the increasing amount of CO_2. One potential way around this problem is to convert CO_2 into harmless compounds or other chemical products in the future.

Chemical fixation of CO_2 in the presence of a heterogeneous photocatalyst is a promising method for converting it into other carbon sources such as carbon monoxide (CO), formaldehyde (HCHO), formic acid (HCOOH), methanol (CH_3OH), and methane (CH_4) (*1*). The photocatalytic reduction of CO_2 using water as a reductant is desirable; therefore, it is important to replicate the same system as that used by plants. Halmann et al. (*2*) found that CO_2 could be reduced to HCOOH, HCHO, and CH_3OH using a p-type GaP electrode in an aqueous solution. Inoue et al. (*3*) reported some effective photocatalyst materials for the photocatalytic reduction of CO_2. In the 1980s, the effect of H_2O as a reductant on heterogeneous photocatalysts used for the photocatalytic reduction of CO_2 attracted considerable interest. Recently, there have been only a few reports on the photocatalytic reduction of CO_2 using H_2O as a reductant, as it is known that water splitting (decomposition of H_2O into H_2 and O_2) proceeds preferentially over photocatalytic reduction of CO_2 using H_2O. In addition, a few studies have been conducted on the photocatalytic reduction of CO_2 using other reductants such as hydrogen (H_2) (*4*) and hydrogen sulfide (H_2S) (*5*). We have been interested in the photocatalytic reduction of CO_2 in the presence of H_2 over the past decade. In the future, as large amounts of H_2 are likely to be produced by overall water splitting under sunlight irradiation, H_2 could become a conventional source of energy and chemicals (*6–9*).

We have found that CO is generated as a result of the photocatalytic reduction of CO_2 in the presence of H_2 or CH_4 over ZrO_2 in 1997, Rh/TiO_2 in 1999, MgO in 2001, and Ga_2O_3 in 2008. With the exception of Rh/TiO_2, these solid materials exhibit the properties of solid base catalysts; therefore, CO_2 can be adsorbed on the surface of these materials. We have insisted on the importance of CO_2 adsorption on the surface because this makes CO_2, which is a stable and linear molecular, into an active species which provides abundant reactivity for the photocatalytic reduction of CO_2. In the following section, we provide an overview of some solid base materials which exhibit the photocatalytic activity necessary for photocatalytic reduction of CO_2 in the presence of H_2.

Experimental Method

The reactants were purified before use in the following manner. H_2 was purified by passing it through a liquefied nitrogen and molecular sieve trap. CO_2 was purified by vacuum distillation at the temperature of liquid nitrogen. The photocatalytic reduction of CO_2 was carried out in a closed static or a gas circulation system connected to a vacuum line. Photocatalyst sample was placed at the flat bottom of a quartz reactor. Prior to photoreduction, the catalyst sample was heated and evacuated at 673 K and then treated with O_2 (80 kPa) for 60 min. After CO_2 and H_2 were introduced into the reactor, the catalyst sample was irradiated from the flat bottom of the reactor with a lamp. The reaction was analyzed using an online TCD gas chromatograph equipped with a column packed with active carbon and helium (He) as a carrier gas.

ZrO_2 in 1997

ZrO_2 was found to exhibit photocatalytic activity, whereas other metal oxides were inactive (*10–15*). After 6 h of photoirradiation, 1.0 μmol of CO was detected. When the photoirradiation time was extended to 40.5 h, 3.2 μmol of CO was formed. In addition, by heating the catalyst after the photocatalytic reduction of CO_2, 5.8 μmol of CO was evolved. Furthermore, we found that like H_2, CH_4 also functions as a reductant for the photocatalytic reduction of CO_2. CO was also generated as a main product in the presence of CH_4. When $^{13}CO_2$ was used instead of $^{12}CO_2$, only ^{13}CO was detected, indicating that the CO was produced from the introduced CO_2. TPD experiments indicated that photoadsorbed CO was desorbed at 630 K, while the maximum desorption of CO from the surface of ZrO_2 after the photocatalytic reduction was observed at 610 K. Accordingly, this suggests that intermediates may exist on the ZrO_2 surface under photoirradiation, and that the reaction proceeds via these intermediates to yield CO.

We attempted to detect and identify any surface intermediates by infrared spectroscopy in order to clarify reaction mechanisms. Absorption bands attributable to surface formates appeared when CO_2 and H_2 were contacted onto the surface of ZrO_2 under photoirradiation. However, the surface formate was not an intermediate. When formic acid alone was introduced onto ZrO_2, there was either no reaction at all, or no CO formation even under photoirradiation. On the other hand, when CO_2 was introduced together with formic acid and photoirradiation onto ZrO_2, the reaction proceeded and a significant amount of CO formed under photoirradiation. When $^{13}CO_2$ and $H^{12}CHO$ were used for the reaction, only ^{13}CO was observed. The surface formate acted as a reductant of CO_2 to yield CO under photoirradiation. It was produced by light with $\lambda >$ 330 nm even though ZrO_2 does not absorb light with $\lambda >$ 250 nm. This suggests that excitation of bulk ZrO_2 is not required for the photocatalytic reduction of CO_2. That is, the photoactive species is not simply ZrO_2, and another photoactive species must exist. The phosphorescent excitation spectra show that the increase in intensity above 300 nm caused by the introduction of CO_2 and H_2 onto ZrO_2 pre-adsorbed with CO decreases the intensity of the new peak at above 300 nm. Therefore, adsorption of CO_2 results in the formation of a new photoactive species, which is attacked by H_2 to generate the surface formate. We concluded that photocatalytic reduction of CO_2 in the presence of H_2 over ZrO_2 consists of the following two photoreactions: (i) formation of surface formate from CO_2 and H_2 and (ii) photocatalytic reduction of CO_2 to CO owing to the surface formate acting as a photoactive species.

As mentioned above, the photoactive species derived from CO_2 is generated on CO_2-adsorbed ZrO_2 under photoirradiation. What is this photoactive species? We measured the EPR spectra to examine the photoexcitation process of CO_2 during the photocatalytic reduction of CO_2 in the presence of H_2. The radical

Downloaded by CORNELL UNIV on June 23, 2012 | http://pubs.acs.org
Publication Date (Web): December 3, 2010 | doi: 10.1021/bk-2010-1056.ch002

species observed by EPR was assigned to the CO_2^- anion radical. H_2 was introduced in the dark onto ZrO_2 preirradiated for 60 min with adsorbed $^{13}CO_2$. We observed a clear decrease in the intensity of the signal assigned to the $^{13}CO_2^-$ anion radical after the introduction of H_2, and after 30 min, the signal disappeared completely. As the signal due to the CO_2^- anion radical was stable in the dark and kept its signal intensity almost constant for 60 min in vacuum, it is highly likely that contact with H_2 caused the disappearance of the CO_2^- anion radical. This suggests that the CO_2^- anion radical reacts with H_2 without photoirradiation, and that the reaction between the CO_2^- anion radical and H_2 yields the surface formate.

In conclusion, we propose the following reaction mechanism: (1) adsorbed CO_2 is photoexcited to a triplet state; part of the CO_2 in the triplet state is deactivated and returns to the ground state upon releasing an emission at 440 nm, while the rest is stabilized as a CO_2^- anion radical, (2) H_2 in the gas phase reacts with the CO_2^- anion radical, after which the surface formate is generated as a reductant, and (3) the surface formate reduces CO_2 in the gas phase to CO under photoirradiation.

Downloaded by CORNELL UNIV on June 23, 2012 | http://pubs.acs.org
Publication Date (Web): December 3, 2010 | doi: 10.1021/bk-2010-1056.ch002

Rh/TiO_2 in 1999

We found that the photocatalytic reduction of gaseous CO_2 to CO with H_2 proceeds over Rh/TiO_2 (*16*, *17*). As the reduction of CO_2 proceeded even in the dark but was enhanced under photoirradiation, the reaction should be considered as “photo-enhanced reduction of CO_2.” After 6 h of photoirradiation, 9.2 μmol of CO and a small amount (0.1 μmol) of CH_4 were produced. However this was not a photocatalytic reduction because a significant amount of CO was produced even when no irradiation was supplied with the reactor temperature slightly elevated in a water bath (323 K). The amount of CO evolution in the dark was larger than that with a glass filter cutting off light with $\lambda < 370$ nm or $\lambda < 450$ nm. This is not surprising considering that the temperature of the reactor was lower than 323 K under photoirradiation. On the basis of these results, it is our contention that CO_2 reduction using H_2 on Rh/TiO_2 is a photo-enhanced reaction similar to that suggested for Ru/TiO_2 by Thampi et al. (*4*). Other products such as hydrocarbons or oxygenates were not detected. When Rh in Rh/TiO_2 was strongly reduced to a fully metallic state, the activity was lowered and the main product changed from CO to CH_4. A similar effect was obtained by changing the loading amount of Rh: when it was raised, activity was lowered and the main product shifted form CO to CH_4. Rh/TiO_2 was characterized by means of infrared spectroscopy and X-ray absorption spectroscopy. Infrared spectroscopy revealed that CO was adsorbed even on strongly reduced samples showing low activity toward the reaction. Taking the X-ray absorption results into consideration, it was proposed that the mixture of Rh in metallic and oxidized states was effective in releasing the adsorbed CO into the gaseous phase. In the case of partially oxidized Rh/TiO_2, the desorption of CO from the surface to the gaseous phase proceeds as smoothly as the adsorption of CO.

Downloaded by CORNELL UNIV on June 23, 2012 | http://pubs.acs.org
Publication Date (Web): December 3, 2010 | doi: 10.1021/bk-2010-1056.ch002

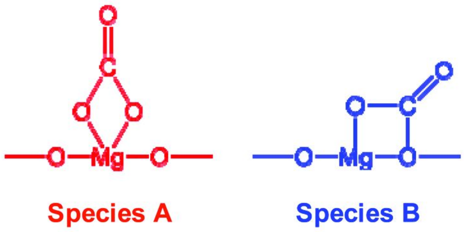

Chart 1. Two bidentate species on MgO after introduction of CO_2

MgO in 2001

MgO also exhibited high photocatalytic activity for the reduction of CO_2 to CO using H_2 as a reductant (*18*, *19*). After 40 h of photoirradiation, the amount of evolved CO reached 8.3 µmol. The heat treatment of MgO at 673 K in a vacuum after photoirradiation caused additional evolution of CO. As mentioned above, such a property of the surface intermediate has also been observed in the case of ZrO_2. When formaldehyde was also introduced onto MgO, no CO had evolved even after 6 h of photoirradiation. Neither was CO obtained when MgO was irradiated for 6 h in the presence of formaldehyde and H_2. However, whenCO evolved after 6 h of photoirradiation. These results indicate that the surface formate acts as a reductant and converts another CO_2 molecule to CO. On the other hand, in the absence of photoirradiation, no CO was detected even when CO_2 and formaldehyde were in contact with MgO. From this, we inferred that the evolution of CO from the surface formate ion with CO_2 on MgO was a photoreaction, much like the formation of the surface formate from CO_2 and H_2. When the carbon atom of the CO_2 molecule was labeled with ^{13}C and the reaction of $H^{12}CHO$ and $^{13}CO_2$ on Mg was carried out under photoirradiation, ^{13}CO was detected as a product. Therefore, the surface formate does not decompose to yield CO directly by itself, but acts as a reductant and converts another CO_2 molecule to gaseous CO under photoirradiation.

We investigated the dependence of the amount of CO evolved from the photocatalytic reduction and subsequent heat treatment on the initial amount of introduced CO_2. There was no CO evolution from the photocatalytic reaction until the amount of introduced CO_2 reached 66 µmol•g-MgO^{-1}. The CO evolution increased gradually and was constant after CO_2 reached 133 µmol•g-MgO^{-1}. On the other hand, the CO evolution due to heat treatment after the photocatalytic reaction was maximal when the amount of introduced CO_2 was 66 µmol•g-MgO^{-1}. The introduction of more than 133 µmol•g-MgO^{-1} of CO_2 did not have a marked influence on the amount of either mode of CO evolution. The amount of chemisorbed CO_2 was compatible with the minimum amount of introduced CO_2 in yielding the maximum CO evolution due to the photocatalytic reaction (133 µmol•g-MgO^{-1}). The introduction of 66 µmol•g-MgO^{-1} of CO_2 caused the most CO evolution due to heat treatment. In addition, the CO evolution due to the photocatalytic reaction could be detected in the gas phase after the amount of introduced CO_2 reached 66 µmol•g-MgO^{-1}. The CO evolutions due to the photocatalytic reaction and heat treatment were both constant after the amount of introduced CO_2 reached 133 μmol•g-MgO^{-1}. Interestingly, there were two different thresholds in the photocatalytic reduction of CO_2 over MgO. These results suggest that the species produced when the introduced CO_2 is under 66 μmol•g-MgO^{-1} is different from that produced when it is more than 66 μmol•g-MgO^{-1}.

We also monitored the absorbance behavior of two bidentate bands using FT-IR spectroscopy when the introduced CO_2 was increased gradually. Both species were detected when a small amount of CO_2 was introduced. The increase in the absorbance of the bidentate bands at 1660 and 1310 cm^{-1} (species A in Chart 1) ceased after the introduced CO_2 exceeded 66 μmol g-MgO^{-1}. On the other hand, the bidentate band at 1624 and 1346 cm^{-1} (species B in Chart 1) increased in absorbance when more than 66 μmol g-MgO^{-1} of CO_2 was introduced. Therefore, in this study, it was also confirmed that the bands at 1660 and 1310 cm^{-1} were stronger than those at 1624 and 1346 cm^{-1}. As mentioned above, the maximum amount of the chemisorbed CO_2 was 130 μmol•g-MgO^{-1}. The greatest amount of CO evolution due to heat treatment was achieved upon introducing 66 μmol•g-MgO^{-1} of CO_2. The CO evolution due to the photocatalytic reaction was confirmed in the gas phase when more than 66 μmol•g-MgO^{-1} of CO_2 was introduced to MgO. Also, the CO evolution due to the photocatalytic reaction and to heat treatment both became constant after the amount of introduced CO_2 reached 133 μmol•g-MgO^{-1}. The behavior obtained from the reaction is in agreement with that observed based on IR spectra. In conclusion, the stronger bidentate carbonate (species A) is reduced to a mere intermediate that is inactive for CO evolution. By introducing more than 66 μmol•g-MgO^{-1} of CO_2, the weaker bidentate carbonate (species B) is generated instead of species A. Species B is reduced to a surface-active intermediate that can produce CO in the gas phase from CO_2 using H_2 or CH_4 as a reductant. This is because the amount of H_2 or CH_4 consumption is compatible with that of species B evolution [66 μmol•g-MgO^{-1}].

Surface formate contributes to the evolution of CO under photoirradiation. Therefore, it is expected that the CO_2 adsorbed on MgO will be photoactivated under photoirradiation. When photoluminescence spectra were measured after the introduction of CO_2 to MgO, the excitation intensity at 250 nm was gradually quenched. Therefore, CO_2 interacts with the extrinsic lattice defects. As shown in Figure 1, it was found that absorption of the excitation wavelength at 320 nm increased in intensity when CO_2 was adsorbed on MgO. Thus, we obtained the same conclusion as in ZrO_2. This shows that new bands are formed between the valence and conduction bands of MgO. In addition, the broad peak observed at 350–600 nm was quenched after introducing H_2 or CH_4. This indicates that the photoactive species derived from the adsorbed CO_2 interacts with H_2 as a reductant. EPR spectra showed that the photoactivated species on MgO was highly stable in the dark after photoirradiation. On the other hand, the CO_2^- and CO_3^- radicals—the photoactivated species on MgO,—readily reacted with H_2 as a reductant. When H_2 was introduced to MgO in the dark, the signals derived from the CO_2^- and CO_3^- radicals disappeared in short order. In addition, the CO_2^- radical species vanished more quickly than the CO_3^- radical species. We

Downloaded by CORNELL UNIV on June 23, 2012 | http://pubs.acs.org
Publication Date (Web): December 3, 2010 | doi: 10.1021/bk-2010-1056.ch002

concluded that in this reaction, the CO_2^- radical is reduced by H_2 to the formate or the acetate rather than the CO_3^- radical.

We propose a mechanism of the CO_2 photocatalytic reduction in the presence of H_2 as a reductant. Two bidentate carbonates are generated on MgO in introducing CO_2. Species A is a stronger bidentate carbonate than species B. The bidentate carbonates are activated under photoirradiation and are converted to a CO_2^- or CO_3^- radical. The CO_3^- radical derived from species A is transformed to a bicarbonate, which is inactive for the CO_2 photocatalytic reduction. On the other hand, the CO_2^- radical species derived from species B is reduced to a surface bidentate formate in the presence of H_2. The surface bidentate formate is highly stable on MgO and reduces CO_2 in the gas phase to CO under photoirradiation.

Downloaded by CORNELL UNIV on June 23, 2012 | http://pubs.acs.org
Publication Date (Web): December 3, 2010 | doi: 10.1021/bk-2010-1056.ch002

Ga_2O_3 in 2008

β-Ga_2O_3 calcined at 1073 K showed good photocatalytic activity for the reduction of CO_2 (*20*). The rate of CO evolution gradually increased with photoirradiation time. After photoirradiation for 48 h, 10.96 μmol of CO gas evolved over Ga_2O_3 and the conversion rate of CO_2 was 7.3%. The amount of CO_2 chemisorbed on Ga_2O_3 saturated around 2.5 kPa of equilibrium pressure at 9.1 μmol•g-$Ga_2O_3^{-1}$. The amount of chemisorbed CO_2 was smaller than that of MgO or ZrO_2. Furthermore, the amount of evolved CO gas for the photocatalytic reduction of CO_2 in the presence of H_2 under photoirradiation increased with the initial pressure of introduced CO_2 gas, and depended on that of chemisorbed CO_2. This indicates that the chemisorbed CO_2 is reduced to CO under photoirradiation. It was reported that the Ga_2O_3 surface chemisorbs H_2 as well as CO_2, although H_2 is not adsorbed on MgO and ZrO_2. The adsorption isotherm of H_2 on Ga_2O_3 after the chemisorption of CO_2 could be fitted to a Langmuir isotherm with dissociation. Therefore, H_2 undergoes dissociation on the surface. The saturated amount of adsorbed H_2 was calculated to be 7.1 μmol•g-$Ga_2O_3^{-1}$. Ga_2O_3 is able to adsorb H_2 as well as CO_2; however, it is unclear whether the adsorption site of H_2 is the same as that of CO_2. The amount of H_2 adsorbed on Ga_2O_3 saturated around 2.5 kPa of equilibrium pressure at 1.2 μmol•g-$Ga_2O_3^{-1}$. The amount of adsorbed H_2 (1.2 μmol•g-$Ga_2O_3^{-1}$) markedly decreased after the chemisorption of CO_2 relative to that in pretreated Ga_2O_3 (7.1 μmol•g-$Ga_2O_3^{-1}$). This means that Ga_2O_3 possesses not only the sites where either CO_2 or H_2 is adsorbed but also the site where both CO_2 and H_2 can be adsorbed. Furthermore, as shown in Figure 2, the amount of evolved CO gas increased with the initial pressure of introduced H_2. The amount of evolved CO gas depended on that of H_2 adsorbed on Ga_2O_3 after CO_2 chemisorption, although the amount of introduced H_2 gas did not affect the photocatalytic activity in the case of ZrO_2 and MgO. Therefore, CO_2 is reduced to CO due to H_2 that is dissociatively adsorbed on the Ga_2O_3 surface. This implies that the photocatalytic reaction proceeds on the basis of a typical Langmuir-Hinshelwood mechanism. Therefore, we conclude that the reaction mechanism over Ga_2O_3 is different from that over MgO and ZrO_2, and that dissociatively adsorbed H_2 on Ga_2O_3 plays an important role in the photocatalytic reduction of CO_2.

Downloaded by CORNELL UNIV on June 23, 2012 | http://pubs.acs.org
Publication Date (Web): December 3, 2010 | doi: 10.1021/bk-2010-1056.ch002

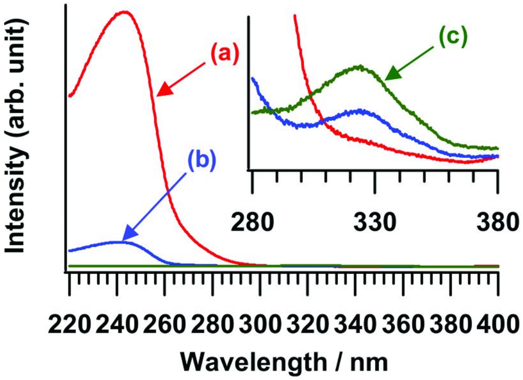

Figure 1. Phosphorescence excitation spectra of MgO (a) after pretreatment, (b) introduction of 33 μmol•g-MgO^{-1} of CO_2 and (c) 66 μmol•g-MgO^{-1} of CO_2

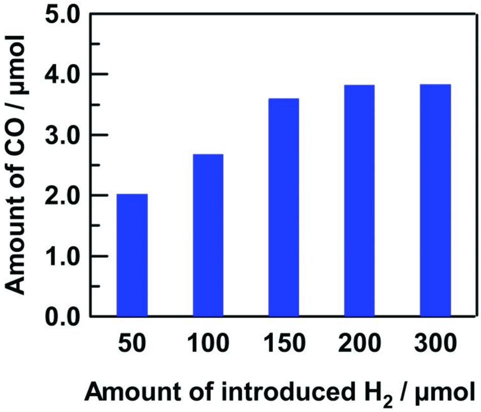

Figure 2. Dependence ot the CO formed over β-Ga_2O_3 under photoirradaition on verious amounts of introduced H_2 gas. CO_2: 150 μmol, photoirradiation time: 5 h

We propose a Langmuir-Hinshelwood type mechanism for the photocatalytic reduction of CO_2 over Ga_2O_3 in the presence of H_2. The FT-IR spectrum, which shows that the surface hydroxyl group remained on Ga_2O_3 after pretreatment, suggests that a monodentate bicarbonate species is formed in the presence of CO_2 on Ga_2O_3. H_2 is dissociatively adsorbed on Ga_2O_3, and Ga-H and Ga-OH species are formed via heterolytic adsorption. Under photoirradiation, the monodentate bicarbonate species is reduced to a bidentate formate species by the H_2 atom of the Ga-H species as a reductant. The bidentate formate species on Ga_2O_3 decomposes into CO and H_2O by photoirradiation. We found that the catalytic mechanisms over Ga_2O_3 are different from those over ZrO_2 and MgO.

In Advances in CO2 Conversion and Utilization; Hu, Y.;
ACS Symposium Series; American Chemical Society: Washington, DC, 2010.

Downloaded by CORNELL UNIV on June 23, 2012 | http://pubs.acs.org
Publication Date (Web): December 3, 2010 | doi: 10.1021/bk-2010-1056.ch002

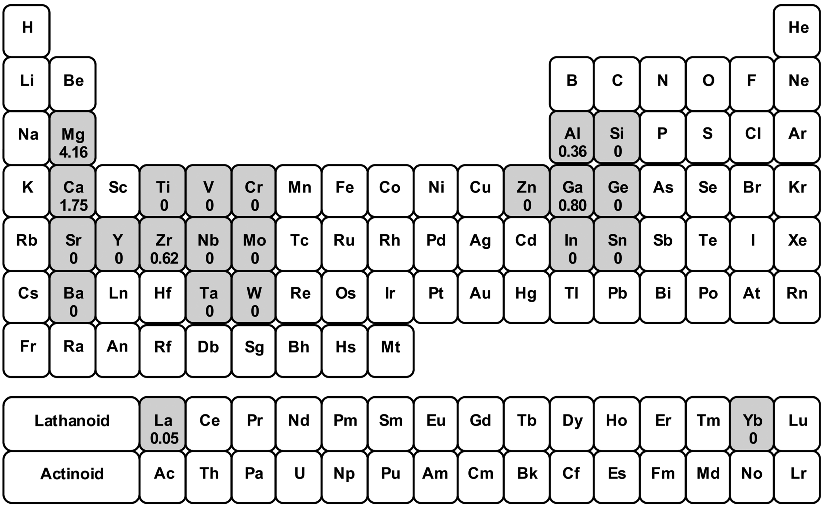

H																	He
Li	Be											B	C	N	O	F	Ne
Na	Mg 4.16											Al 0.36	Si 0	P	S	Cl	Ar
K	Ca 1.75	Sc	Ti 0	V 0	Cr 0	Mn	Fe	Co	Ni	Cu	Zn 0	Ga 0.80	Ge 0	As	Se	Br	Kr
Rb	Sr 0	Y 0	Zr 0.62	Nb 0	Mo 0	Tc	Ru	Rh	Pd	Ag	Cd	In 0	Sn 0	Sb	Te	I	Xe
Cs	Ba 0	Ln	Hf	Ta 0	W 0	Re	Os	Ir	Pt	Au	Hg	Tl	Pb	Bi	Po	At	Rn
Fr	Ra	An	Rf	Db	Sg	Bh	Hs	Mt									
Lathanoid			La 0.05	Ce	Pr	Nd	Pm	Sm	Eu	Gd	Tb	Dy	Ho	Er	Tm	Yb 0	Lu
Actinoid			Ac	Th	Pa	U	Np	Pu	Am	Cm	Bk	Cf	Es	Fm	Md	No	Lr

Figure 3. CO evolutions for the photoreduction of CO_2 in the presence of H_2 over various metal oxides under 5 h of photoirradiation.

Photocatalytic Reduction of CO_2 in the Future

We have shown that some photocatalysts such as ZrO_2, MgO, Rh/TiO_2, and Ga_2O_3 exhibit photocatalytic activity for the reduction of CO_2 in the presence of H_2. It is therefore important for candidate materials to have the basic site on the surface where CO_2 can be adsorbed. On the basis of this concept, we have also found suitable photocatalysts which exhibit photocatalytic activity as shown in Figure 3. The determining factor for photocatalytic reduction is the adsorption of CO_2 on the surface. On the other hand, the range of choices for reductants could be expanded. H_2 is a very strong reductant, and in the coming years, large amounts of H_2 will be produced by overall water splitting under sunlight irradiation; therefore, H_2 is likely to become a conventional source of energy and chemicals. However, the most desirable reductant for the chemical fixation of CO_2 is water (H_2O). We intend to establish a CO_2 fixation system that uses H_2O and solar light and resembles natural photosynthesis. We believe that solving these challenges persistently will reduce and immobilize CO_2 in the future.

References

1. Halmann, M. M. In *Chemical Fixation of Carbon Dioxide*; CRC Press, Inc.: United States of America, 1993.
2. Halmann, M. *Nature (London, United Kingdom)* **1978**, *275*, 115–6.
3. Inoue, T.; Fujishima, A.; Konishi, S.; Honda, K. *Nature (London, United Kingdom)* **1979**, *277*, 637–8.
4. Thampi, K. R.; Kiwi, J.; Graetzel, M. *Nature (London, United Kingdom)* **1987**, *327*, 506–8.
5. Aliwi, S. M.; Al-Jubori, K. F. *Solar Eng. Mater.* **1989**, *18*, 223–9.

6. Domen, K.; Kondo, J. N.; Hara, M.; Takata, T. *Bull. Chem. Soc. Jpn.* **2000**, *73*, 1307–1331.
7. Kudo, A. *Catal. Surv. Asia* **2003**, *7*, 31–38.
8. Maeda, K.; Teramura, K.; Saito, N.; Inoue, Y.; Kobayashi, H.; Domen, K. *Pure Appl. Chem.* **2006**, *78*, 2267–2276.
9. Maeda, K.; Teramura, K.; Domen, K. *Catal. Surv. Asia* **2007**, *11*, 145–157.
10. Kohno, Y.; Tanaka, T.; Funabiki, T.; Yoshida, S. *Chem. Commun.* **1997**, 841–842.
11. Kohno, Y.; Tanaka, T.; Funabiki, T.; Yoshida, S. *Chem. Lett.* **1997**, 993–994.
12. Kohno, Y.; Tanaka, T.; Funabiki, T.; Yoshida, S. *J. Chem. Soc., Faraday Trans.* **1998**, *94*, 1875–1880.
13. Kohno, Y.; Tanaka, T.; Funabiki, T.; Yoshida, S. *Phys. Chem. Chem. Phys.* **2000**, *2*, 2635–2639.
14. Kohno, Y.; Tanaka, T.; Funabiki, T.; Yoshida, S. *Phys. Chem. Chem. Phys.* **2000**, *2*, 5302–5307.
15. Yoshida, S.; Kohno, Y. *Catal. Surv. Jpn.* **2000**, *4*, 107–114.
16. Kohno, Y.; Hayashi, H.; Takenaka, S.; Tanaka, T.; Funabiki, T.; Yoshida, S. *J. Photochem. Photobiol. A* **1999**, *26*, 117–123.
17. Kohno, Y.; Yamamoto, T.; Tanaka, T.; Funabiki, T. *J. Mol. Catal. A: Chem.* **2001**, *175*, 173–178.
18. Kohno, Y.; Ishikawa, H.; Tanaka, T.; Funabiki, T.; Yoshida, S. *Phys. Chem. Chem. Phys.* **2001**, *3*, 1108–1113.
19. Teramura, K.; Tanaka, T.; Ishikawa, H.; Kohno, Y.; Funabiki, T. *J. Phys. Chem. B* **2004**, *108*, 346–354.
20. Teramura, K.; Tsuneoka, H.; Shishido, T.; Tanaka, T. *Chem. Phys. Lett.* **2008**, *467*, 191–194.

Downloaded by CORNELL UNIV on June 23, 2012 | http://pubs.acs.org
Publication Date (Web): December 3, 2010 | doi: 10.1021/bk-2010-1056.ch002

Downloaded by UNIV OF DELAWARE MORRIS LIB on June 23, 2012 | http://pubs.acs.org
Publication Date (Web): December 3, 2010 | doi: 10.1021/bk-2010-1056.ch003

Chapter 3

CO_2 Splitting via the Solar Thermochemical Cycle Based on Zn/ZnO Redox Reactions

**Peter G. Loutzenhiser,[1] Anton Meier,[2] Daniel Gstoehl,[2]
and Aldo Steinfeld[1,2,*]**

**[1]Department of Mechanical and Process Engineering, ETH Zurich, 8092
Zurich, Switzerland
[2]Solar Technology Laboratory, Paul Scherrer Institute, 5232 Villigen PSI,
Switzerland
*aldo.steinfeld@ethz.ch**

A two-step thermochemical cycle for splitting CO_2 and processing into solar fuels via ZnO/Zn redox reactions is considered. The first, solar step is the endothermic dissociation of ZnO to Zn and O_2. The second, non-solar step is the exothermic reduction of CO_2 with Zn to CO and ZnO; the latter is recycled to the solar step. The thermodynamics and kinetics of the pertinent reactions are examined and the reactor technology for both steps of the cycle is described and an outlook for the future is provided.

Introduction

A project currently underway that provides a promising and sustainable alternative to CO_2 sequestration is the splitting of CO_2 into separate streams of CO and O_2 using solar energy. CO can be either used as combustion gas or further processed to synthetic liquid fuels for transportation. The direct thermolysis of CO_2 at atmospheric pressure occurs at ultrahigh temperatures, i.e. 30% dissociation is theoretically obtained above 2700 K. Further complications arise from the need to separate the product gases at these high temperatures in order to avoid recombination upon cooling. The operating temperature can be reduced and the separation problem bypassed by making use of thermochemical cycles. Of special interest is the two-step thermochemical cycle based on ZnO/Zn redox reactions, shown schematically in Figure 1, comprising: 1) the solar endothermic

In Advances in CO2 Conversion and Utilization; Hu, Y.;
ACS Symposium Series; American Chemical Society: Washington, DC, 2010.

dissociation of ZnO(s) and 2) the non-solar exothermal reduction of CO_2 with Zn into CO and ZnO(s), and represented by:

1st solar step: $$\mathrm{ZnO} \rightarrow \mathrm{Zn} + \tfrac{1}{2}\mathrm{O_2} \quad \Delta H^{\circ}_{298K} = 350\ \mathrm{kJ\,mol^{-1}} \tag{1}$$

2nd non-solar step: $$\mathrm{Zn} + \mathrm{CO_2} \rightarrow \mathrm{ZnO} + \mathrm{CO} \quad \Delta H^{\circ}_{298K} = \text{-}65.5\ \mathrm{kJ\,mol^{-1}} \tag{2}$$

The net reaction is $CO_2 \rightarrow CO + \frac{1}{2} O_2$, with products formed in different steps, thereby eliminating the need for their high-temperature separation. A combination of theoretical and experimental work that includes thermodynamic and kinetic analyses and reactor technology is described to provide a project overview.

Previous work using Zn/ZnO redox reactions in a two-step solar thermochemical cycle has focused on splitting H_2O. A second law analysis indicates a maximum solar-to-chemical conversion efficiency of 29% (*1*). A comparison of the Zn/ZnO H_2O splitting cycle with other metal redox reaction cycles is given by (*2*). Kinetic analyses for determination of the rate law for reducing H_2O to H_2 with Zn were performed by (*3*, *4*). This reaction has been realized in aerosol reactors designed for *in-situ* Zn nanoparticle formation followed by a subsequent reaction with H_2O to produce H_2 and ZnO (*4–8*). A different type of reactor where steam was bubbled through molten Zn was designed by (*9*).

CO_2 splitting in two-step solar cycle has been examined for spinel ferrites (*10*, *11*) and splitting H_2O and CO_2 with ceria for synthesis gas production (*12*).

Thermodynamics and Kinetic Analyses

Thermodynamic equilibrium compositions were computed as a function of temperature and pressure. The thermal dissociation of ZnO, eq 1, proceeds endothermically and at reasonable rates at above 2000 K and 1 bar (*13*). A kinetic rate law was derived from experimental measurements in a solar-driven thermogravimeter for directly irradiated ZnO samples (*14*). Rapid quenching of the products was required to avoid product recombination (*15*). The reaction of CO_2 with Zn, eq 2, proceeds exothermically below 1000 K (*16*). Kinetic studies with thermogravimetry indicated an initial fast surface-controlled regime followed by a slow diffusion-controlled regime, described using a shell-core kinetic model (*17*). A second law thermodynamic analysis was performed for the CO_2 splitting flow diagram shown in Figure 2. The solar-to-chemical energy conversion efficiency is defined as the portion of solar energy that is converted into chemical energy, given by the Gibbs free energy of the products, i.e. the maximum possible amount of work that can be extracted from the products when transformed back to the reactants at 298 K in a reversible, ideal fuel cell:

$$\eta_{solar-to-chemical} = \frac{-\dot{n}\Delta G\big|_{CO+\frac{1}{2}O_2 \rightarrow CO_2 \text{ at } 298K}}{Q_{solar}} = \frac{W_{FC,ideal}}{Q_{solar}} \tag{3}$$

For the CO_2 splitting cycle with ZnO/Zn redox reaction operating at a solar concentration ratio of 5000 suns, $\eta_{solar-to-chemical}$= 39% (*16*). High efficiencies

In Advances in CO2 Conversion and Utilization; Hu, Y.;
ACS Symposium Series; American Chemical Society: Washington, DC, 2010.

Downloaded by UNIV OF DELAWARE MORRIS LIB on June 23, 2012 | http://pubs.acs.org
Publication Date (Web): December 3, 2010 | doi: 10.1021/bk-2010-1056.ch003

Downloaded by UNIV OF DELAWARE MORRIS LIB on June 23, 2012 | http://pubs.acs.org
Publication Date (Web): December 3, 2010 | doi: 10.1021/bk-2010-1056.ch003

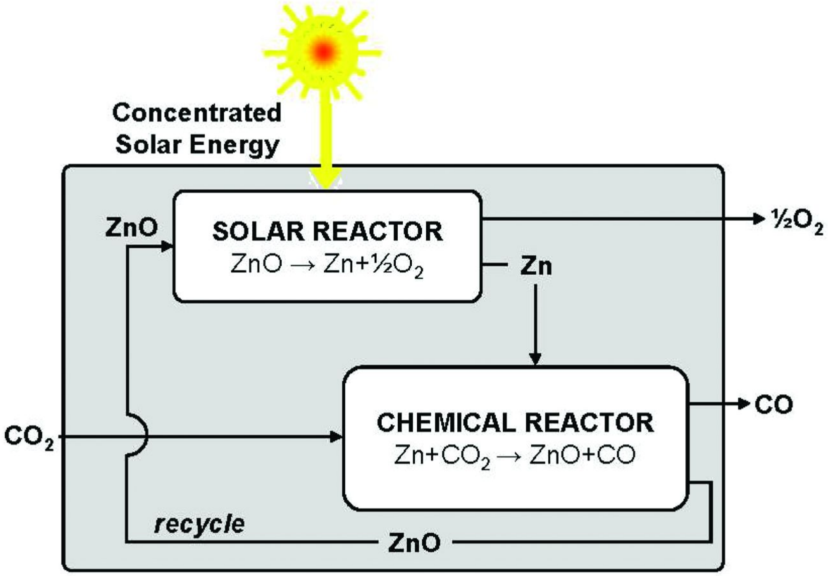
Concentrated Solar Energy
ZnO
SOLAR REACTOR
$ZnO \rightarrow Zn+½O_2$
½O_2
Zn
CO_2
CHEMICAL REACTOR
$Zn+CO_2 \rightarrow ZnO+CO$
CO
recycle
ZnO

Figure 1. Scheme of the two-step solar thermochemical cycle for CO_2 reduction via Zn/ZnO redox reactions.

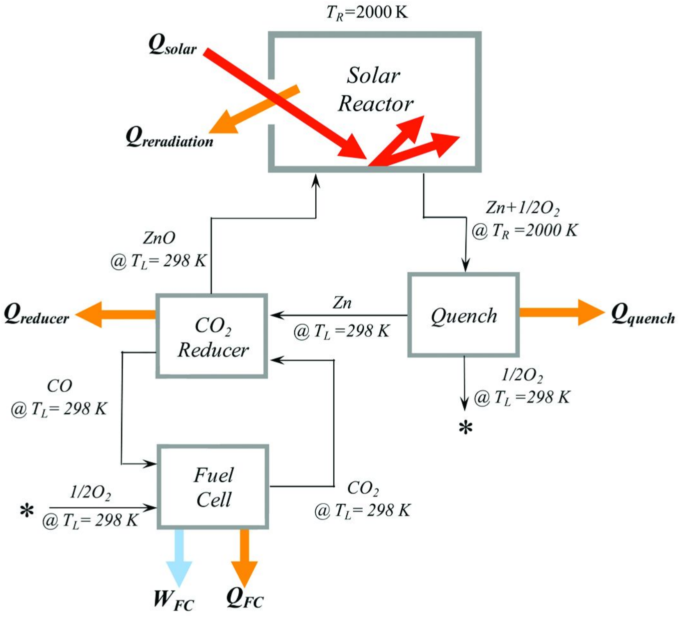
T_R=2000 K
Q_{solar}
$Q_{reradiation}$
Solar Reactor
ZnO @ T_L= 298 K
$Zn+1/2O_2$ @ T_R =2000 K
$Q_{reducer}$
CO_2 Reducer
Zn @ T_L =298 K
Quench
Q_{quench}
CO @ T_L= 298 K
$1/2O_2$ @ T_L =298 K
*
Fuel Cell
CO_2 @ T_L= 298 K
*
$1/2O_2$ @ T_L= 298 K
W_{FC}
Q_{FC}

Figure 2. Model flow diagram of the two-step CO_2-splitting solar thermochemical cycle applied for the Second-Law analysis.

Downloaded by UNIV OF DELAWARE MORRIS LIB on June 23, 2012 | http://pubs.acs.org
Publication Date (Web): December 3, 2010 | doi: 10.1021/bk-2010-1056.ch003

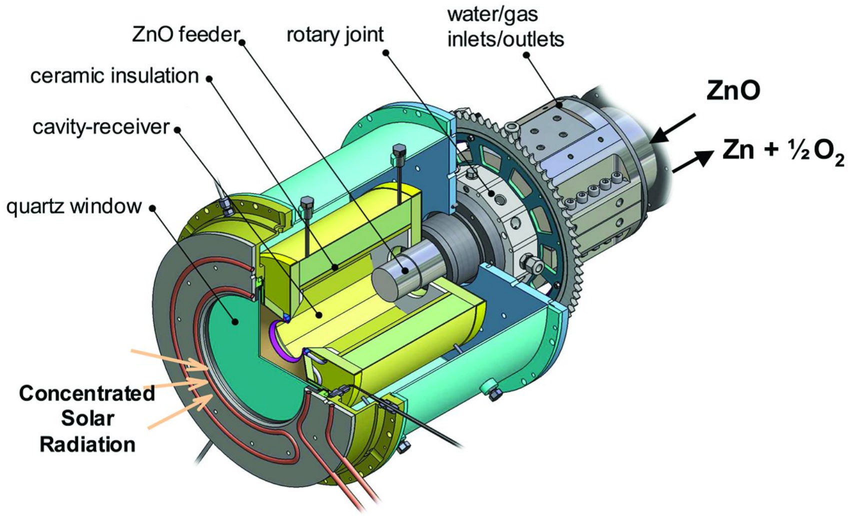

Figure 3. Scheme of the solar reactor configuration, featuring a rotating cavity-receiver lined with ZnO particles that are directly exposed to concentrated solar radiation and serve simultaneously the functions of radiant absorbers and chemical reactants (20).

directly translate to lower solar collection area and associated reduced costs of the heliostat field, which amount to about half of the capital cost for the entire solar CO_2 splitting plant.

Reactor Technology

A 10 kW solar reactor prototype for the thermal dissociation of ZnO has been designed, fabricated, and tested at the solar furnace at Paul Scherrer Institute (PSI) (*18*). Its configuration is shown in Figure 3. It features a rotating cavity-receiver lined with ZnO particles that are directly exposed to concentrated solar radiation and serve simultaneously the functions of radiant absorbers and chemical reactants. A transient heat transfer model was developed for analyzing the reactor thermal performance (*19*). This model couples radiation, convection, and conduction heat transfer to the reaction kinetics for a shrinking domain and simulates a transient ablation regime with semi-continuous feed cycles of ZnO particles.

The second step of the cycle was experimentally investigated in a hot-wall quartz aerosol flow reactor, shown in Figure 4 (*20*). It was designed for quenching of Zn(g), formation of Zn nanoparticles, and *in-situ* oxidation with CO_2. The effects of varying the reactants stoichiometry and reaction temperatures were investigated. Chemical conversions of Zn to ZnO of up to 88% were obtained for a residence time of ~3.0 s. For all experiments, high Zn conversions corresponded to large Zn depositions in the reaction zone thought to be a result of heterogeneous nucleation of the Zn of the reactor surfaces followed by a reaction with CO_2.

Downloaded by UNIV OF DELAWARE MORRIS LIB on June 23, 2012 | http://pubs.acs.org
Publication Date (Web): December 3, 2010 | doi: 10.1021/bk-2010-1056.ch003

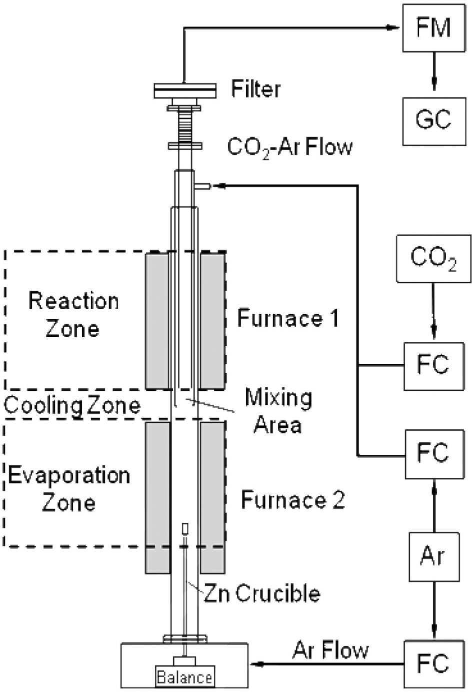

Figure 4. Scheme of the hot-wall aerosol flow reactor consisting of evaporation, cooling, and reaction zones for reducing CO_2 with Zn.

Summary and Outlook

A two-step thermochemical cycle for CO_2 splitting via Zn/ZnO redox reactions has been examined. In-depth descriptions are given in the cited references for the thermodynamics analysis, the reaction kinetics, and the reactor technology for both steps of the cycle. For the solar dissociation of ZnO, a scaleup of the reactor technology from 10 kW to 100 kW is currently underway. For the second non-solar step, a cycle that combines the CO_2 and H_2O splitting two-step cycles to produce synthesis gas into one cycles is being investigated. Preliminary thermodynamic and experimental works have demonstrated that reactions with mixtures of CO_2 and H_2O with Zn are possible (*21*). Kinetic modeling of the competitive reaction with varying concentrations of CO_2 and H_2O with Zn are being studied to optimize H_2/CO ratios for further processing to liquid fuels. A novel new fixed bed reactor concept is also being investigated aimed at immobilizing Zn particles on a substrate below the melting point to reduce particle sintering and increase the overall reaction extent.

Acknowledgments

This work is being financially supported by the Swiss Federal Office of Energy, the Swiss National Science Foundation, and the Baugarten Foundation. We acknowledge the assistance of our colleagues Alwin Frei, Markus Haenchen,

Lothar Schunk, Anastasia Stamatiou, and Daniel Wuillemin in performing the experimental campaigns at PSI's high-flux solar furnace/simulator and ETH's thermogravimetric system.

References

1. Steinfeld, A. *Int. J. Hydrogen Energy* **2002**, *27*, 611–619.
2. Perkins, C.; Weimer, A. *Int. J. Hydrogen Energy* **2004**, *29*, 1587–1599.
3. Ernst, F. O.; Steinfeld, A.; Pratsinis, S. E. *Int. J. Hydrogen Energy* **2009**, *34*, 1166–1175.
4. Funke, H. H.; Diaz, H.; Liang, X.; Carney, C. S.; Weimer, A. W.; Li, P. *Int. J. Hydrogen Energy* **2008**, *33*, 1127–1134.
5. Melchior, T.; Piatkowski, N.; Steinfeld, A. *Chem. Eng. Sci.* **2009**, *64*, 1095–1101.
6. Weiss, R. J.; Wegener, K.; Pratisinis, S. E.; Steinfeld, A. *AIChE J.* **2005**, *51*, 1966–1970.
7. Wegener, K.; Ly, H.; Weiss, R.; Pratisinis, S. E.; Steinfeld, A. *Int. J. Hydrogen Energy* **2005**, *31*, 55–61.
8. Ernst, F. O.; Tricoli, A.; Pratsinis, S. E.; Steinfeld, A. *AIChE J.* **2006**, *52*, 3297–3303.
9. Berman, A.; Epstein, M. *Int. J. Hydrogen Energy* **2000**, *20*, 957–967.
10. Siegel, N. P.; Diver, R. B.; Livers, S.; Garino, T.; Miller, J. E. *Proc. Solar PACES* **2009**.
11. Allendorf, M. D.; McDaniel, A. H.; Scheffe, J.; Weimer, A. W. *Proc. Solar PACES* **2009**.
12. Chueh, W. C.; Haile, S. M. *ChemSusChem* **2009**, *C88*, 735–739.
13. Palumbo, R.; Lede, J.; Boutin, O.; Elorza Ricart, E.; Steinfeld, A.; Möller, S.; Weidenkaff, A.; Fletcher, E. A.; Bielicki, J. *Chem. Eng. Sci.* **1998**, *53*, 2503–2517.
14. Schunk, L. O.; Steinfeld, A. *AIChE J.* **2009**, *55*, 1497–1504.
15. Gstoehl, D.; Brambilla, A.; Schunk, L. O.; Steinfeld, A. *J. Mater. Sci.* **2008**, *43*, 4729–4736.
16. Gálvez, M. E.; Loutzenhiser, P.; Hischier, I.; Steinfeld, A. *Energy Fuels* **2008**, *22*, 3544–3550.
17. Loutzenhiser, P.; Galvez, M. E.; Hischier, I.; Stamatiou, A.; Frei, A.; Steinfeld, A. *Energy Fuels* **2009**, *23*, 2832–2839.
18. Schunk, L. O.; Haeberling, P.; Wepf, S.; Wuillemin, D.; Meier, A.; Steinfeld, A. *J. Sol. Energy-T ASME* **2008**, *130*, 021009.
19. Schunk, L. O.; Lipinski, W.; Steinfeld, A. *Chem. Eng. J.* **2009**, *150*, 502–508.
20. Loutzenhiser, P. G.; Galvez, M. E.; Hischier, I.; Steinfeld, A. *Chem. Eng. Sci.* **2010**, *65*, 1855–1864.
21. Stamatiou, A.; Loutzenhiser, P. G.; Steinfeld, A. *Chem. Mater.* **2010**, *22*, 851–859.

Downloaded by UNIV OF DELAWARE MORRIS LIB on June 23, 2012 | http://pubs.acs.org
Publication Date (Web): December 3, 2010 | doi: 10.1021/bk-2010-1056.ch003

Downloaded by PENNSYLVANIA STATE UNIV on June 23, 2012 | http://pubs.acs.org
Publication Date (Web): December 3, 2010 | doi: 10.1021/bk-2010-1056.ch004

Chapter 4

Hydrothermal Conversion of CO_2 into Value-Added Products: A Potential Technology for Improving Global Carbon Cycle

Fangming Jin,[a,b,*] Zhibao Huo,[a] Xu Zeng,[a] and Heiji Enomoto[b]

**[a]State Key Laboratory of Pollution Control and Resources Reuse,
College of Environmental Science and Engineering, Tongji University,
Shanghai 200092, China
[b]Graduate School of Environmental Studies, Tohoku University,
Sendai 980-8579, Japan
[*]email: fmjin@tongji.edu.cn; jin@mail.kankyo.tohoku.ac.jp**

To reduce the amount of CO_2 being generated, processes for recirculating carbon are needed, especially those that do not require excessive energy and have high efficiencies. Hydrothermal reactions play an important role in the formation of fossil fuels, e.g., the conversion of dissolved CO_2 into hydrocarbons abiotically in the Earth's crust, and have shown excellent potential for the rapid conversion of a wide variety of biomass into value-added products. Thus, if the geologic formation of fossil fuels in nature could be combined with the hydrothermal methods being studied for material conversions, an efficient scheme could be realized to recycle carbon and produce chemicals. In this paper, we present some recent advances in our research on the hydrothermal conversion of CO_2 into chemicals with biomass or organic waste or metals as reductants. These results provide fundamental understanding that opens a new path for the use of CO_2 as chemical feedstock, thus speeding up the global carbon cycle.

Downloaded by PENNSYLVANIA STATE UNIV on June 23, 2012 | http://pubs.acs.org
Publication Date (Web): December 3, 2010 | doi: 10.1021/bk-2010-1056.ch004

1. Introduction

A global energy crisis and the increase in carbon dioxide at the atmosphere linked to global warming are threatening the earth. One of efficient methods for diminishing the imbalance of global carbon should involve rapid conversion of CO_2 into fuels and chemicals. However, low energy methods are also needed, especially those that do not require high-energy cost and have highly efficiency. Potential techniques that satisfy these needs have been studied extensively, including catalytic conversion involving hydrogen, photochemical or electrochemical conversions with precious metal catalysts (*1–6*). These processes, however, tend to be expensive and slow, have low yields and are relatively inefficient. To achieve CO_2 reduction with a low energy cost and high efficiency, we can learn from the natural carbon cycle. Figure 1 shows global-carbon-cycle pathways. CO_2 and water combine to form biomass with the help of solar energy in the earth's carbon cycle. Humans then use this biomass for survival while discharging a large amount of waste. Some waste is buried deeper and deeper under sediment. The enormous heat and pressure in the deep strata turns this waste and CO_2, such as dissolved CO_2, into petroleum, natural gas or coal. Humans consume these fuels in everyday life, again giving off CO_2 and waste. Thus, originally, there was a sustainable carbon cycle in the earth.

Realistically, however, the carbon balance is broken by anthropogenic activities because the imbalance of fossil-fuel formation from organic waste in the earth requires hundreds of millions of years, whereas humans use fossil fuels within 200 to 300 years and release a large amount of CO_2. The timelength requirement in fossil-fuel formation comes from the need for the sedimentation of organic wastes to reach the deep underground, where the conversion reaction from organic wastes to fuels occurs. Geochemists have experimentally proven that the conversion of organic wastes into oily materials can be sufficiently fast. High-temperature, high-pressure water plays an important role in the conversion reaction. Thus, by simulating these underground conditions, not only organic wastes or biomasses but also CO_2 could be quickly turned into fuels and chemicals artificially. Although geologic conversion of organic waste to fossil fuels is very well known, many researche have indicated that geologic conversion of CO_2 to fossil fuels is also present. For example, geochemical reduction-oxidation (redox) couples present in the mantle (*7*, *8*) and in hydrothermal vents via the H_2-CO_2 redox couple (*9*) have been shown to provide the necessary environment for organic compound formation, with striking evidence being reported for abiogenic hydrocarbon production via serpentinization in the Lost City Hydrothermal Field (*10*, *11*). CO_2 and H_2-bearing aqueous fluids in the presence of magnetite (*12*), cobalt-bearing magnetite (*13*), iron-chromium oxide (*14*), or formic acid aqueous solutions in the presence of pentlandite ($(Fe_2Ni_7)S_8$) (*15*), show that CO_2 can be reduced through a multitude of reaction pathways.

Downloaded by PENNSYLVANIA STATE UNIV on June 23, 2012 | http://pubs.acs.org
Publication Date (Web): December 3, 2010 | doi: 10.1021/bk-2010-1056.ch004

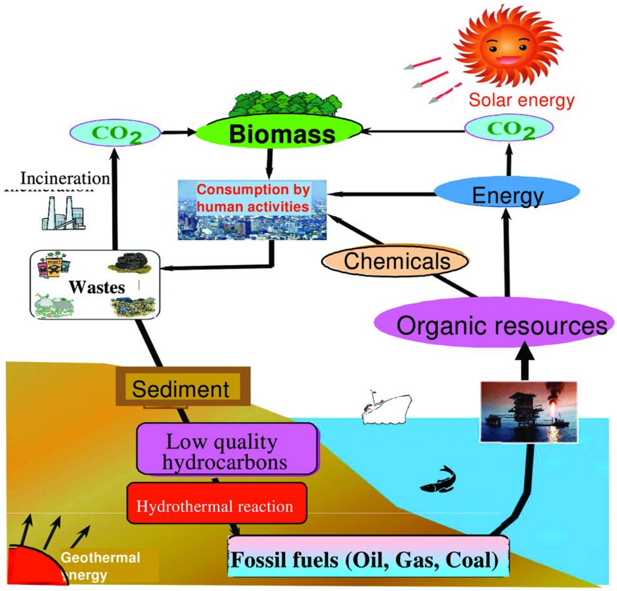

Figure 1. Globe-carbon-cycle pathways.

Based on the natural phenomena of fossil-fuel formation, we have investigated the application of hydrothermal reactions to the conversion of not only organic wastes and biomass but also CO_2 into fuel and chemicals. In research on the conversion of biomass and organic wastes, we found that hydrothermal reactions can convert various organic materials, particularly cellulose and lignocelluloses, efficiently and rapidly into useful chemicals (*16–24*), waste plastics into oil (*25*) and bitumen into light oil (*26*). Several researchers have also reported that the hydrothermal conversion of biomasses into chemicals is effective (*27–34*), most likely because high-temperature water (HTW) exhibits properties that are very different from those of ambient liquid water (*35–38*). Interesting, many reports, including our research, have demonstrated that HTW can supply hydrogen and oxygen in the hydrothermal reaction of some organic waste or biomass (*39–50*). For example Moriya and Enomoto have confirmed that the hydrogen from water exists in products in the oil samples and the oxygen in products containing oxygen, such as alcohols, aldehydes and ketones, are attributed to water in their study of supercritical-water upgradation of PE (*40*). One of the major challenges in CO_2 reduction is the development of economical hydrogen sources. Water is the most abundant hydrogen resource. Extensive attempts have been made to generate hydrogen from water; however, efficient and economical hydrogen production from water remains difficult. If hydrogen from water could be used to reduce CO_2 *in situ* in hydrothermal conversion of biomass or organic water, then an efficient scheme for CO_2 conversion and the use of biomass or organic waste could be realized. In this process, water acts not only as a hydrogen source but also as an environmentally benign solvent for CO_2 conversion. Additional benefits include the following. First, hydrogen from HTW could be active as a highly effective reductant, unlike generally stable H_2 (dry H_2), and would thus readily and directly react with CO_2 in mild conditions. Second, this proposed process requires neither high-purity CO_2 nor high-purity hydrogen, including pumps or storage, because hydrogen is derived from water and is reacted with CO_2 *in situ*. Third, this method would not require expensive catalysts. Finally, this process is expected to have a low energy cost because the input is biomass or organic waste. In this paper, we present some recent advances in research on the hydrothermal conversion of CO_2 into value-added chemicals with the use of biomass or organic waste or metals as reductants.

2. Hydrothermal Reduction of CO_2 in the Presence of Organic Wastes

As mentioned earlier, many researchers have shown that HTW can supply hydrogen in the hydrothermal reaction of some organic waste or biomass or can be split to produce hydrogen. Thus, we propose a process for converting CO_2 into organics under hydrothermal conditions in the presence of organics or biomass. Scheme 1 shows the rationale of the proposed process.

Hydrogen or its species split from water under hydrothermal conditions is used as a reactant to directly reduce CO_2 into organics *in situ*. At the same time, oxygen its species split from water oxidizes organic water or biomass into value-added products. The proposed process has many advantages over water-splitting cycles, including the following: (i) excess oxygen is not required because oxygen is used chemically and (ii) no hydrogen is required, including pumps or storage, because it is derived from water and reacted with CO_2 *in situ*.

2.1. Materials and Experimental Procedure

In this research, polyethylene (PE), representative of plastic waste, and the sulfur-containing EPDM (ethylene-propylene-dieneterpolymer), which is a common component in rubber used here as a model compound of sulfur-containing rubber, were used. PE and EPDM were selected because HTW can supply hydrogen to degrade PE and EPDM under hydrothermal conditions (*40*, *51*). Figure 2 shows the molecular structure of EPDM. Experiments were conducted in a bomb-type reactor with a Hastelloy-C-276 inner wall, an inner volume of 42 cm^3, a maximum working temperature of 773 K and a maximum working pressure of 50 MPa. The reactor was equipped with a high-pressure valve to allow pressure measurements, CO_2 input and gas sampling. The typical time required to raise the temperature of the reactor from 293 to 673 K was about 20 min. The reaction time was defined as the time period during which the reactor was kept in the induced heater. All experiments were performed with degassed water after purging the reactor with nitrogen.

Downloaded by PENNSYLVANIA STATE UNIV on June 23, 2012 | http://pubs.acs.org
Publication Date (Web): December 3, 2010 | doi: 10.1021/bk-2010-1056.ch004

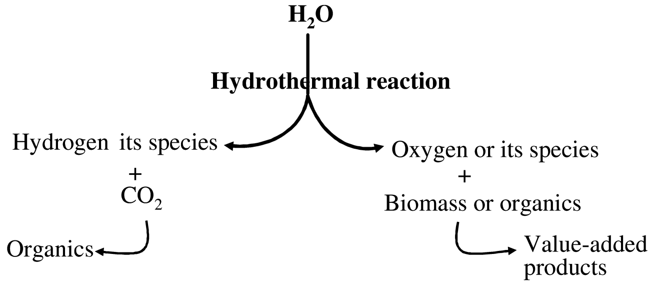

Scheme 1. The rationale for hydrothermal reduction of CO_2 into organics with biomass or organic waste.

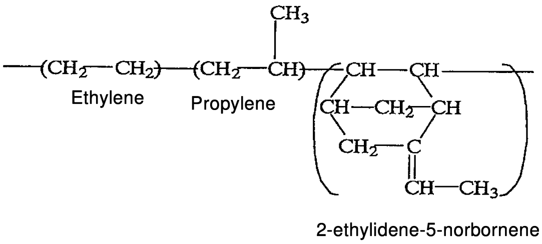

Figure 2. Molecular structure of EPDM.

The experimental setup has been described in detail elsewhere (*52*, *53*), and only a brief description is given below. The reactor was filled with the desired amounts of water and PE or EPDM, and a stirring ball was used to mix the material. Next, CO_2 was added into the reactor through the high-pressure valve. After adding CO_2, the sealed reactor with the high-pressure valve was placed into the induction oven for the reaction. After the desired time, the reactor was removed from the oven to cool. When the reactor temperature fell to room temperature, gases were collected in a saturated sodium chloride solution to prevent them from dissolving in the solution. After the gases were collected, the reactor was opened to recover the products. The liquid products were separated into both aqueous and oil phases. The oil phase was extracted with hexane. The aqueous phase was separated with a separation funnel. Anhydrous sodium sulfate was added to remove trace amounts of water remaining in the oil phase.

2.2. Results and Discussion

2.2.1. CO_2 Reduction in the Presence of PE

Experiments with PE were conducted at temperatures varying from 573 K to 723 K with and without CO_2. There is no significant difference in the amount of CO_2 before and after the hydrothermal reactions or in the products achieved in the absence of and presence of CO_2. These results suggest that CO_2 is rarely reduced into organics by the hydrothermal cracking of PE at temperatures from

Downloaded by PENNSYLVANIA STATE UNIV on June 23, 2012 | http://pubs.acs.org
Publication Date (Web): December 3, 2010 | doi: 10.1021/bk-2010-1056.ch004

300 to 450°C, although hydrogen can be produced from water by the hydrothermal cracking of PE, as mentioned before (*40*).

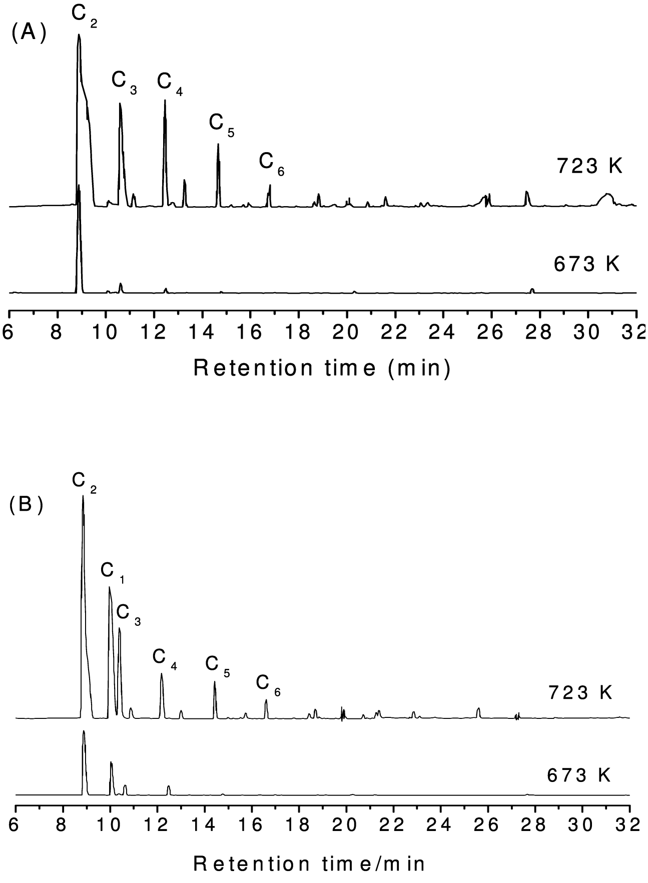

Figure 3. GC/MS chromatograms of water sample after reaction in the absence (A) and presence (B) of CO_2 (60 min) (C denote carboxylic acids, Arabic subscript numbers show the carbon number of carboxylic acids).

Downloaded by PENNSYLVANIA STATE UNIV on June 23, 2012 | http://pubs.acs.org
Publication Date (Web): December 3, 2010 | doi: 10.1021/bk-2010-1056.ch004

2.2.2. CO_2 Reduction in the Presence of EPDM

Similarly, experiments with EPDM were conducted at temperatures varying from 573 K to 723 K in the absence and presence of CO_2. Interestingly, significant CO_2 reduction was observed between 573 K and 723 K. Figure 3 shows the GC/MS chromatograms of water samples after reaction in the presence and absence of CO_2. In the absence of CO_2, no formic acid (C_1) was detected, and only carboxylic acids with 2 to 6 carbon atoms (C_2 to C_6) appeared. However, a large formic acid peak appeared in the presence of CO_2. Varying the initial pH from 4 to 13 in the absence of CO_2, testing whether the formic acid formation is due to the pH change in the presence of CO_2, showed that formic acid was not formed under all initial-pH conditions. These results suggest that formic acid is attributed to the reduction of CO_2. Analyses of gas samples show that the concentration of hydrocarbons with 2-4 carbon atoms was significantly higher in the presence of CO_2 than that in the absence of CO_2 (Table I). Quantitative analyses of the amount of CO_2 before and after the reactions showed that the amount of CO_2 after the reactions was much less than that before the reaction in the presence of CO_2. These results suggest that CO_2 is reduced into organics in the hydrothermal treatment of sulfur-containing rubber and that the main products of CO_2 reduction are formic acid and hydrocarbons having 2-4 carbon atoms. The highest efficiency for CO_2 reduction was about 20%, which occurred at 723 K and 60 min. The CO_2-reduction efficiency is defined as the ratio of the amount of CO_2 after the reaction to the initial amount of CO_2.

In previous research on the use of desulfurization in upgrading oil sand and bitumen in HTW, it was found that most of the sulfur from the desulfurization of oil sand or bitumen is most likely dissolved into water to form H_2S (*53*, *54*). Additionally, in recent research into hydrogen production from water with H_2S as reductant, we found that H_2S can reduce H_2O into hydrogen in HTW (*55*). Although we lack a clear understanding of how CO_2 reduces organics in supercritical-water cracking of EPDM, we are able to offer a probable explanation based on these results. EPDM undergoes desulfurization in supercritical water and forms dissolved H_2S, which then acts as a reductant of CO_2 into organics, such as formic acid and low-molecular-weight hydrocarbons.

Figure 4 shows the GC/MS results for the oil samples after the reactions. The major products are almost identical in the presence and the absence of CO_2, primarily featuring straight-chain n-alkanes with more than 9 carbon atoms. These results suggest that CO_2 reduction can be achieved and that EPDM can be converted into oils in the hydrothermal treatment of EPDM in the presence of CO_2.

At present, our results show that CO_2 reduction can be achieved using organic waste as a reductant and that organic waste can be simultaneously converted into oils.

Downloaded by PENNSYLVANIA STATE UNIV on June 23, 2012 | http://pubs.acs.org
Publication Date (Web): December 3, 2010 | doi: 10.1021/bk-2010-1056.ch004

Downloaded by PENNSYLVANIA STATE UNIV on June 23, 2012 | http://pubs.acs.org
Publication Date (Web): December 3, 2010 | doi: 10.1021/bk-2010-1056.ch004

Table I. Products in gas samples after reactions in the presence and absence of CO_2 at 673 K and 703 K for 60 min

Products	*673 K*		*723 K*	
	Without CO_2	*With CO_2*	*Without CO_2*	*With CO_2*
CO	0.77	9.81	135.73	171.69
H_2	10.75	37.92	170.10	97.39
N_2	12.25	89.60	35.85	35.45
CH_4	0.98	11.46	126.42	165.47
$CH_2{=}CH_2$	0.05	2.41	1.28	2.28
CH_3-CH_3	0.58	8.71	57.82	87.00
CH_3-$CH{=}CH_2$	0.43	6.74	8.04	7.44
CH_3-CH_2-CH_3	0.55	7.51	41.83	53.81
i-CH_3-CH_2-CH_2-CH_3	0.36	3.74	3.28	10.62
n-CH_3-CH_2-CH_2-CH_3	0.63	5.47	14.11	21.02

3. Hydrothermal Reduction of CO_2 in the Presence of Biomass

3.1. Materials and Experimental Procedure

In this study, $NaHCO_3$ was used as the CO_2 source for experimental convenience with respect to safety and handling. Glucose, as a model compound carbohydrate-biomass compound, was used to examine CO_2 reduction. Most of the experiments were conducted with the reactor system described in Section 2.1. In some cases, a batch reactor consisting of SUS 316 tubing (9.525-mm o.d., 1-mm wall thickness and 120-mm length) with two end fittings, giving an inner volume of 5.7 mL, was also used. Details of the apparatus have been described elsewhere (*17*, *20*, *24*). The typical reaction procedure used is as follows. A desired amount of $NaHCO_3$, glucose and deionized water was loaded into the reactor. After loading, the reactor was sealed and then immersed in a salt bath, which had been preheated to the desired temperature. The typical time required to raise the temperature of the reactor from 293 to 573 K was about 30 s. After the preset reaction time, the reactor was removed from the salt bath and immediately put into a cold-water bath. The reaction time is defined as the time period during which the reactor was kept in the salt bath.

Downloaded by PENNSYLVANIA STATE UNIV on June 23, 2012 | http://pubs.acs.org
Publication Date (Web): December 3, 2010 | doi: 10.1021/bk-2010-1056.ch004

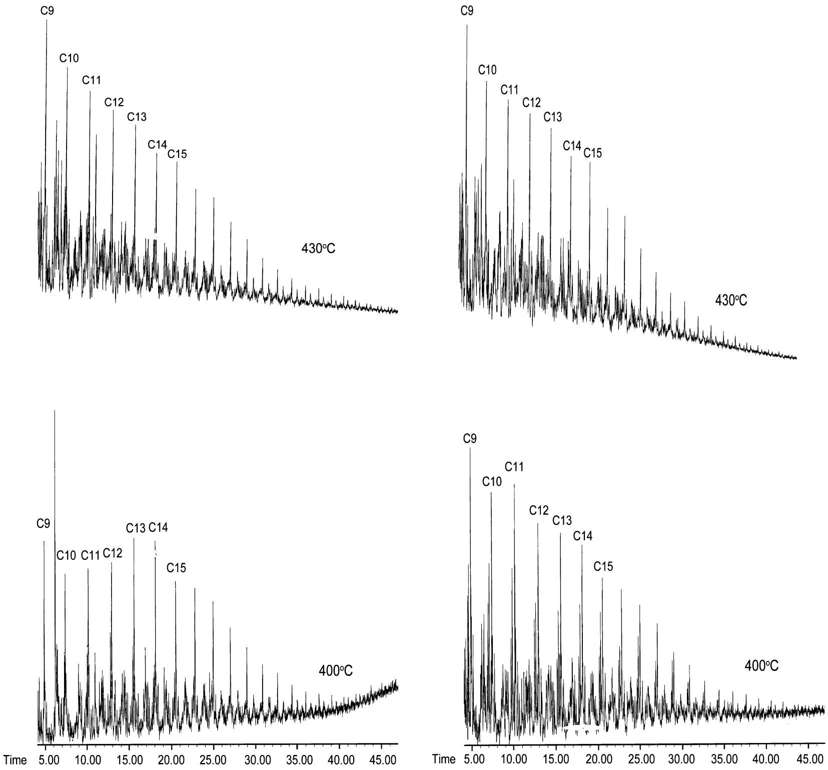

(A) In the absence of CO_2 *(B) In the presence of CO_2*

Figure 4. GC/MS chromatograms of oil sample after reaction in the absence (A) and presence (B) of CO_2 (60 min) (C denote alkanes, Arabic subscript numbers show the carbon number of alkanes).

3.2. Results and Discussion

3.2.1. Examination of Products from Glucose in the Absence and Presence CO_2

To compare the difference in products in the presence and absence of CO_2, thus aiding the examination of the effect of glucose on CO_2 reduction, the major products from glucose in the absence of CO_2 at 573 K were examined. This temperature was selected because it is better for carbohydrate conversion (*16*–*19*). The results show that lactic, acetic and formic acids are the major products. This observation agrees with previous research regarding the hydrothermal conversion of carbohydrate biomass (*18*, *21*, *23*, *28*).

Next, the major products from glucose in the presence of CO_2 were examined. As shown in Figure 5, a significant increase in formic acid is observed. The increase in formic acid may be attributed to the reduction of CO_2.

Downloaded by PENNSYLVANIA STATE UNIV on June 23, 2012 | http://pubs.acs.org
Publication Date (Web): December 3, 2010 | doi: 10.1021/bk-2010-1056.ch004

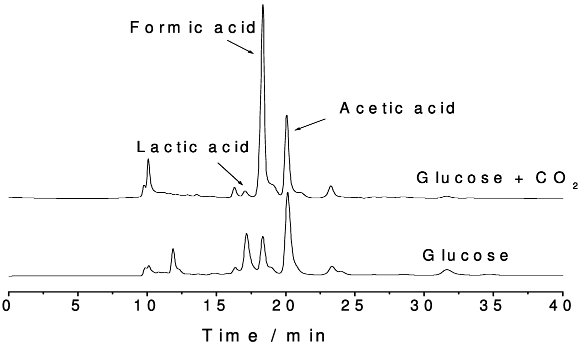

Figure 5. HPLC chromatograms of liquid samples after reaction of glucose in the presence and absence of NaHCO₃.

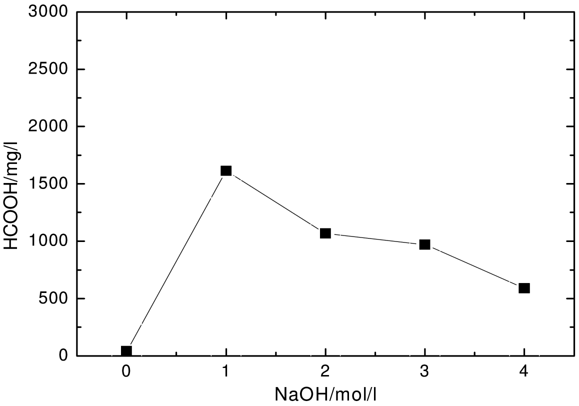

Figure 6. Effect of the initial NaOH concentration on formic acid from glucose (Glucose, 5 mmol; temperature, 573 K; time, 60 min; water fill rate, 50 %).

3.2.2. Examination of CO_2 Reduction into Formic Acid

Formic acid formation from glucose in the absence of CO_2 may be affected by the initial alkaline concentration; thus, the increase in formic acid may be attributed to the change in the initial pH caused by the presence of $NaHCO_3$. Thus, to examine whether the increase in formic acid in the presence of $NaHCO_3$ results from CO_2 reduction, the production of formic acid at different alkalinity without $NaHCO_3$ needs be investigated. The results are shown in Figure 6. As the alkalinity increases, the formic-acid concentration first increases and then decreases. The maximum formic-acid concentration of 1600 mg/L is achieved with a NaOH concentration of 1.0 mol/L. These results indicate that the hydrothermal conversion of glucose is greatly affected by the initial alkaline concentration; the highest formic-acid concentration is merely 1600 mg/L. Furthermore, an experiment with glucose in the presence of $NaHCO_3$ (2 M) under the same conditions was conducted. The results show that the formic-acid concentration was 7423 mg/L, which is much higher than the highest formic-acid concentration in the absence of $NaHCO_3$ (1600 mg/L).

Reduction of CO_2 into formic acid in the presence of glucose suggests that hydrogen is produced from glucose under hydrothermal conditions. To verify the production of hydrogen, gas products from glucose in alkaline hydrothermal reaction were analyzed. Results showed that hydrogen was detected in the gas products of hydrothermal reaction of glucose. Figure 7 gives the change of hydrogen amount with NaOH concentration. The amount of hydrogen increases with the increase in NaOH concentration.

Downloaded by PENNSYLVANIA STATE UNIV on June 23, 2012 | http://pubs.acs.org
Publication Date (Web): December 3, 2010 | doi: 10.1021/bk-2010-1056.ch004

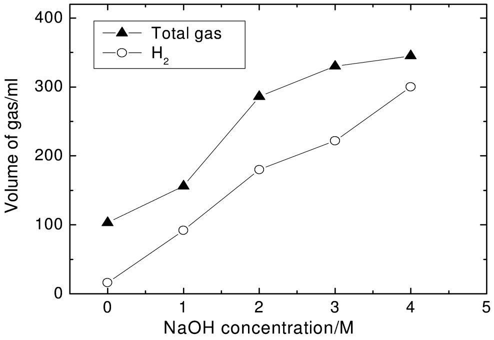

Figure 7. Effect of NaOH concentration on gases produced from glucose in the absence of $NaHCO_3$.

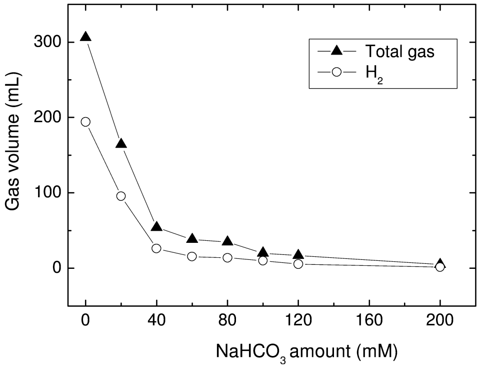

Figure 8. Effect of $NaHCO_3$ initial amount on gases in the presence of $NaHCO_3$. (Glucose 5 mM; NaOH 2 M; Temperature 573 K; Time 60 min; Water filling rate 50%)

In the coexistence system of CO_2 and glucose, gas products in hydrothermal reactions were also analyzed. The result is shown in Figure 8. The main component of the gas products is also hydrogen. With the increase of CO_2, the amount of hydrogen in the gas products gradually decreased. The decrease in hydrogen in the presence of CO_2 suggests that the production of hydrogen from hydrothermal conversion of glucose in the absence of CO_2 may involve the formation of formic acid from CO_2. Although further study is needed, these limited data suggest that some formic acids are attributed to CO_2 reduction when CO_2 and glucose coexist.

To further confirm whether CO_2 can be reduced into formic acid with glucose, a polyol, CO_2 reduction experiments with simple organic compounds containing an OH group, such as ethanol and glycerin, were conducted at 300 °C in the presence of NaOH. Results show that only formic acid and lactic acid were found in liquid samples when glycerin was used. Formic acid should be attributed to CO_2 reduction and lactic acid to glycerin because previous work has demonstrated that glycerin can be almost completely converted into lactic acid and hydrogen (*48*) and that about 50% of the hydrogen comes from water (*50*). Similarly, acetic acid is the only product and the ethanol concentration greatly decreases when ethanol is used, which suggests that CO_2 is reduced into formic acid and ethanol is oxidized into acetic acid. These observations should be further evidences that CO_2 can reduce formic acid in the presence of organics with the OH group. It should be noted that transition-metal catalysis is generally needed for CO_2 reduction. However, our results show that CO_2 can be reduced into formic acid without the addition of a catalyst, which suggests that organics like glucose, glycerin and ethanol, or HTW may act as catalysts in the hydrothermal reduction of CO_2. Work along these lines is now in progress.

Further, experiments with gaseous hydrogen and CO_2 with a 5:1 H_2/CO_2 ratio in the presence of a Ni catalyst were conducted at 573 K for 120 min, to examine whether CO_2 can be reduced into CO_2 under hydrothermal conditions. As a result, formic acid was formed with the yield of formic acid of about 26%. Ni was used because our research has shown that Ni can catalyze the reduction of CO_2 as discussed later. These results indicate that CO_2 can be reduced into formic acid with hydrogen in the presence of catalysts and that organics, like glucose, glycerin and ethanol, or HTW may play a catalytic role in the hydrothermal reduction of CO_2 into formic acid.

3.2.3. *Effect of Reaction Conditions on the Reduction of CO_2 into Formic Acid*

As mentioned earlier, some formic acid comes from glucose and the highest concentration of formic acid occurs with 1.0-M NaOH. Thus, in examination of the effect of reaction conditions on the reduction of CO_2 into formic acid, the highest concentration of formic acid from glucose with the addition of 1-M NaOH was selected as a background value. The yield of formic acid from CO_2 was determined by subtracting the background value from the total yield of formic acid when glucose and CO_2 coexist.

Downloaded by PENNSYLVANIA STATE UNIV on June 23, 2012 | http://pubs.acs.org
Publication Date (Web): December 3, 2010 | doi: 10.1021/bk-2010-1056.ch004

Downloaded by PENNSYLVANIA STATE UNIV on June 23, 2012 | http://pubs.acs.org
Publication Date (Web): December 3, 2010 | doi: 10.1021/bk-2010-1056.ch004

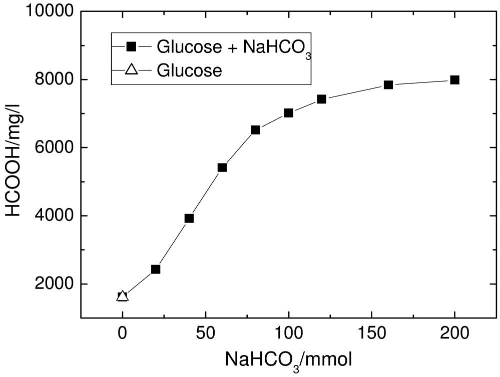

Figure 9. Effect of CO_2 initial amount on yield of formic acid (Glucose 5 mM; NaOH 2 M; temperature 573 K, time 60 min).

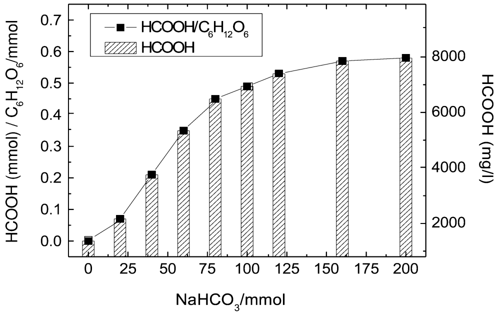

Figure 10. Effect of CO_2 initial addition on formic acid and the molar ratio of formic acid and the initial glucose.

Figure 9 shows the production of formic acid with different amounts of $NaHCO_3$. In comparison, the background value of formic acid from glucose (1600 mg/L) also is shown. The formic-acid concentration is much higher than that in the absence of CO_2 (background value). With an increase in the amount of CO_2, a rapid increase in formic acid is observed, which can be a further evidence that CO_2 is converted into formic acid.

To investigate the efficiency of glucose in reducing CO_2 into formic acid, we also examined the production of formic acid by unit glucose. As shown in Figure 10, an increase in the amount of $NaHCO_3$ leads to a rapid increase in the molar ratio of formic acid and the initial glucose. When the amount of $NaHCO_3$ increases to 120 mmol, the ratio of formic acid and the initial glucose reaches 0.53, and then with further increase in the amount of $NaHCO_3$, the increase in the ratio of formic acid and the initial glucose has no significant change.These results suggest that glucose has a better capability for reducing CO_2 into formic acid, and one mole of glucose can reduce 0.5 mole CO_2 into formic acid, which occurs at 120 mmol of $NaHCO_3$. Thus, in following studies, the initial concentration of $NaHCO_3$ was fixed at 120 mmol.

In Advances in CO2 Conversion and Utilization; Hu, Y.;
ACS Symposium Series; American Chemical Society: Washington, DC, 2010.

Downloaded by PENNSYLVANIA STATE UNIV on June 23, 2012 | http://pubs.acs.org
Publication Date (Web): December 3, 2010 | doi: 10.1021/bk-2010-1056.ch004

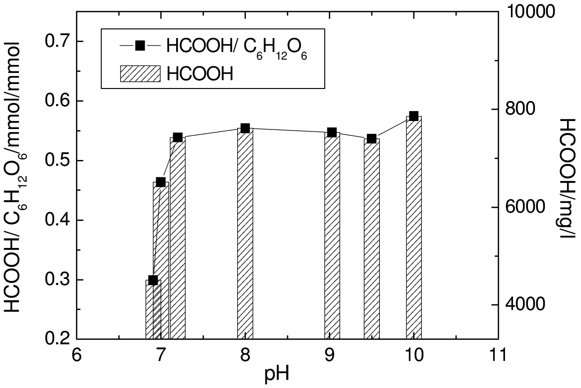

Figure 11. Effect of pH on formic acid and themolar ratio of formic acid and the initial glucose.

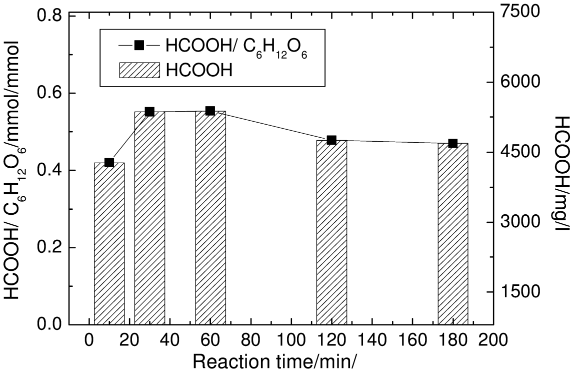

Figure 12. Effect of reaction time on formic acid and the molar ratio of formic acid and the initial glucose.

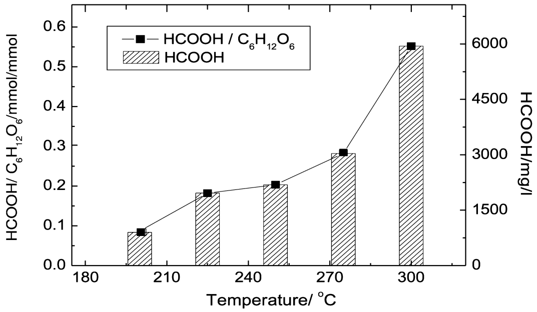

Figure 13. Effect of reaction temperature on the molar ratio of formic acid and the initial glucose.

Downloaded by PENNSYLVANIA STATE UNIV on June 23, 2012 | http://pubs.acs.org
Publication Date (Web): December 3, 2010 | doi: 10.1021/bk-2010-1056.ch004

Figure 11 shows the effect of the initial pH on formic acid and the molar ratio of formic acid and the initial glucose. When the pH is less than 7.2, formic acid and the ratio of formic acid to the initial glucose increase greatly with an increase in pH. When the pH is more than 7.2, the pH value has no significant effect on the formic acid and the ratio of formic acid to the initial glucose.

The effect of reaction time on formic acid and the ratio of formic acid and the initial glucose are shown in Figure 12. As shown in Figure 12, formic acid and the ratio of formic acid to the initial glucose first increase and then decrease. The highest formic acid and the ratio of formic acid to the initial glucose occur at 30 min.

From Figure 13, which is the effect of temperature on formic acid and the molar ratio of formic acid and the initial glucose, it can be seen that the higher temperature is favorable for the hydrothermal conversion of CO_2 to formic acid. At 573 K, the ratio of formic acid and the initial glucose reaches 0.55. However, owing to equipment limitations, these experiments could only be carried out at 573 K. If the experimental equipment limitations can be overcome, a higher conversion of CO_2 is likely to be obtained at higher temperature.

4. Hydrothermal Reduction of CO_2 with Metals as Reductants

Although CO_2 can be reduced into formic acid in the presence of biomass, such as glucose, and organic waste, like the EPDM polymer, mentioned earlier, the efficiency of CO_2 reduction and the selectivity of formic acid are low. Thus, we studied hydrothermal reduction of CO_2 with metals as reductants (*56*). In this study, transition metals Fe and Ni were chosen to be a reductant and a catalyst in the hydrothermal reactions, respectively, in consideration of their readily availability and low cost. It has been reported that Ni and Fe-Ni alloy play a catalytic role in CH_4 formation from dissolved CO_2 in hydrothermal reactions (*12–15*). Although Yamasaki et al. (*57*) reported that CO_2 can be converted into CH_4 in hydrothermal conditions with Fe as a reductant and Ni as a catalyst, they did not specify the formation and selectivity of formic acid from CO_2 and not investigate the role of CO_2 in the hydrothermal reduction.

4.1. Materials and Experimental Procedure

In this study, $NaHCO_3$ was used as the CO_2 source for experimental convenience with respect to safety and handling. The zero-valent metal iron was used in powder form with a particle size of 200 mesh. Most of the experiments were conducted using the same batch reactor as described in Section 3.1. The typical reaction procedure was similar to that described in Section 3.1. The desired amount of $NaHCO_3$ and metal powders and 2 mL of deionized water were loaded into the reactor and occupied about 35% of the total reaction volume. After loading, the reactor was sealed and immersed into a salt bath, which had been preheated to the desired temperature (523 to 573 K). After the preset reaction time, the reactor was removed from the salt bath and immediately put into a cold-water bath.

Teflon-lined stainless steel reactors with an inner volume of 22.8 mL were also used to examine possible catalytic effects of Ni existing in the stainless-steel reactor wall on the reaction. After loading the reactor with the desired starting material, the reactor was put in an oven, which had been preheated to the desired temperature of 523 K. During the reaction, the reactor was rotated to enhance mixing of the reactants. In the experiments using the Teflon-lined reactors, the temperature was limited to 523 K due to the maximum durable temperature of the Teflon material. After a given time, the reactor was taken out of the oven and cooled to room temperature with an electric fan.

After the reactors were cooled, the liquid, gaseous and solid samples were collected and treated by washing or diluting with water or ethanol when required for analysis. Liquid samples were analyzed by HPLC, GC/FID/MS, and a TOC analyzer. Solid samples were washed with deionized water several times, dried in air and characterized by X-ray diffraction (XRD) (D/MAX2550, Rigaku) using Ni-filtered Cu Kα radiation at an acceleration voltage of 40 kV and emission current of 100 mA.

Downloaded by PENNSYLVANIA STATE UNIV on June 23, 2012 | http://pubs.acs.org
Publication Date (Web): December 3, 2010 | doi: 10.1021/bk-2010-1056.ch004

4.2. Results and Discussion

4.2.1. Hydrogen Production and the Role of CO_2

At first, the formation of hydrogen from water under hydrothermal conditions with zero-valent metal Fe and Ni was studied. In the absence of CO_2, no hydrogen was produced when using Fe or Ni powder, as shown in Table II. Interestingly, in the presence of CO_2, hydrogen was produced in substantial quantities with the Fe, and the increase in the initial CO_2 amount leads to an increase in the hydrogen production. To understand the mechanism of hydrogen production, the solid residue after the reaction was analyzed by X-ray diffraction. No iron oxides except Fe were detected in the absence of CO_2, but Fe_3O_4 was detected in the presence of CO_2, clearly indicating that CO_2 contributes to the oxidation of Fe. Thus, it is reasonable to suggest that the hydrogen production mechanism using Fe could be explained as follows:

$$Fe + CO_2 + H_2O \rightarrow FeCO_3 + H_2 \quad (1)$$

$$3FeCO_3 + H_2O \rightarrow Fe_3O_4 + H_2 + 3CO_2 \quad (2)$$

Fe first reacts with CO_2 and H_2O to form $FeCO_3$, which then loses a CO_2 to form Fe_3O_4. However, no $FeCO_3$ was detected. An experiment with Fe within a very short reaction time of 5 min was conducted to test if $FeCO_3$ was decomposed at a longer reaction time of 2 h. There was no $FeCO_3$ detected in the solid residue by XRD. To further confirm whether $FeCO_3$ was produced, we conducted an experiment using a Fe and Mg mixture with a Fe:Mg molar ratio of 1:1 as reductants in the presence of CO_2. The reason for using a Fe and Mg mixture was that only $Mg(OH)_2$ was detected in the experiment using Mg as a reductant in the presence of CO_2. If $MgCO_3$ could be found in the experiment using the mixture

In Advances in CO2 Conversion and Utilization; Hu, Y.;
ACS Symposium Series; American Chemical Society: Washington, DC, 2010.

of Fe and Mg, then it should provide evidence for the formation of $FeCO_3$ in the experiment using Fe according to following reactions:

$$Mg+2H_2O \rightarrow Mg(OH)_2 + H_2 \quad (3)$$

$$Fe+CO_2+H_2O \rightarrow FeCO_3 + H_2 \quad (4)$$

$$Mg(OH)_2 + FeCO_3 \rightarrow MgCO_3+Fe(OH)_2 \quad (5)$$

As expected, $MgCO_3$ was detected in the experiment using the mixture of Fe and Mg. According to this mechanism, CO_2 clearly plays a catalytic role for improving hydrogen production from water. To our knowledge, the promotion effect of CO_2 in hydrogen production from water has not been reported.

According to the mechanism shown in Eq (1) and (2), CO_2 palys a catalytic role in hydrogen production from water with Fe as reductant. Thus, as shown in Table II, the increase in the initial CO_2 amount lead to the increase in hydrogen production.

Downloaded by PENNSYLVANIA STATE UNIV on June 23, 2012 | http://pubs.acs.org
Publication Date (Web): December 3, 2010 | doi: 10.1021/bk-2010-1056.ch004

4.2.2. Examination of Products from CO_2 Reduction in the Presence of Fe and Ni

CO_2 reduction in the presence of only Fe or both Fe and Ni under hydrothermal conditions was investigated, and formic acid formed in all cases. However, the yield of formic acid was very low in the presence of Fe and absence of Ni. For example, the yield of formic acid was only 1.8 at 573 K. A significant increase in formic acid was observed in the presence of both Fe and Ni, which indicates that Ni catalyzed the formation of formic acid from CO_2. To confirm the roles of Fe and Ni in the hydrothermal conversion of CO_2, the solid residue of the reaction with the addition of Fe and Ni powder was characterized by XRD. The results show that after the reaction, Ni still exists as a pure metal, while Fe is oxidized into Fe_3O_4. These results indicate that Fe is a reductant and Ni is a catalyst in the reduction of CO_2 into formic acid in the presence of Fe and Ni. In CO_2 hydrogenation with Ni as a catalyst in the absence of water, it is generally considered that CO_2 is probably activated and undergoes hydrogenation on Ni surfaces. The hydrothermal reduction of CO_2 may be CO_2 activation and hydrogenation on Ni surfaces. A detailed study of mechanism is needed.

4.2.3. Effect of the Major Reaction Conditions on the Yield of Formic Acid

To examine the efficiency of Fe for conversion of CO_2 into formic acid, the effect of the molar ratio of $Fe/NaHCO_3$ on the yield of formic acid was studied with a Fe:Ni ratio of 1:1. As shown in Table III, when the amount of Fe increases from 2 to 6, the formic acid yield, defined as the percentage of formic acid to the initial $NaHCO_3$ based on the carbon basis, increase approximately three fold. After that, no significant change in the yield of formic acid is observed with the increase in the ratio of $Fe/NaHCO_3$.

Downloaded by PENNSYLVANIA STATE UNIV on June 23, 2012 | http://pubs.acs.org
Publication Date (Web): December 3, 2010 | doi: 10.1021/bk-2010-1056.ch004

Table II. Hydrogen formation in the presence and absence of CO_2[a]

Entry	*Metal*	*$NaHCO_3$/mmol*	*Total gas[b]/ml*	*CO_2[b]/ml*	*H_2[b]/ml*
1	Ni	0	0	0	0
2	Ni	1	0	0	0
3	Fe	0	0	0	0
4	Fe	1	50	2	48
5	Fe	2	80	2	75
6	Fe	3	100	4	90

[a] Reaction conditions: 573 K, 120 min, Fe, Ni = 6 mmol. [b] Gas volumes corrected to 298 K and 1 atm.

Table III. Formic acid yield at different molar ratio of Fe/$NaHCO_3$ and Fe/Ni[a]

Entry	*Fe/$NaHCO_3$*	*Fe/Ni*	*Formic acid yield /%*
1	2:1	1:1	5.4
2	4:1	1:1	9.4
3	6:1	1:1	15.6
4	8:1	1:1	16.3
5	10:1	1:1	15.7
6	6:1	1:2	14.5
7	6:1	3:4	15.0
8	6:1	1:1	15.6
9	6:1	4:3	13.0
10	6:1	2:1	9.1

[a] Temp.: 573 K; reaction time: 120 min; filling rate: 35%; $NaHCO_3$: 1 mmol; Fe: 6 mmol.

Subsequently, the effect of the Fe/Ni ratio was studied by fixing the ratio of Fe/$NaHCO_3$ of 6:1, while varying Fe/Ni ratio between 1/2 and 2/1 with the addition of 1 mmol $NaHCO_3$ at the temperature of 573 K and the reaction time of 120 min. As shown in Table III, formic acid yield reaches its peak level at the Fe/Ni ratio of 1:1. The results indicate that there is an optimal ratio of reductant Fe to catalyst Ni for the hydrothermal conversion of CO_2 into formic acid. When the Fe/Ni ratio increased further, that is, reduced the amount of catalyst, the yield of formic acid decreased gradually may be due to the insufficient catalyst. On the other hand, when the Fe/Ni ratio is less than 1:1, a decrease in Fe/Ni ratio (or increase of catalyst amount) resulted in a slowly decline of formic acid yield. This may be caused by the further decomposition or conversion of formic acid under excess amount of catalyst Ni.

Table IV. Formic acid yield at different reaction temperature and time[a]

Formic acid yield /%	*Temp./K (60 min)*	*Formic acid yield /%*	*Time/min (573 K)*
4.0	523	3.9	30
9.0	548	8.0	60
15.6	573	12.5	90
15.3	600	15.6	120

[a] Water filling rate: 35%; Fe:NaHCO3: 1:6; Fe/Ni: 6:6/mmol/mmol.

Downloaded by PENNSYLVANIA STATE UNIV on June 23, 2012 | http://pubs.acs.org
Publication Date (Web): December 3, 2010 | doi: 10.1021/bk-2010-1056.ch004

One exciting result to be noted is that the selectivity of formic acid from CO_2 conversion, defined as the percentage of carbon contained in formic acid to the total organic carbon in the liquid phase, was always larger that 98%. This result means that formic acid was almost the only product in the liquid phase, which is favorable to the concentration or separation of formic acid from its aqueous solution in future.

Since the reactor was made of SUS 316, which is an alloy containing Ni, the effect of the reactor material was studied by using a reactor with Teflon liner. It was found that almost no formic acid was formed in reactions without the addition of catalyst Ni into the Teflon-lined reactor. This result suggests that Ni existing in the SUS 316 reactor material may take part in the catalysis of the hydrothermal conversion of CO_2. However, due to the temperature limit of the Teflon material and the structural limit of the reactor (no gas collection apparatus), all reactions in the Teflon-lined reactors had to be set at not more than 523 K and no gas samples could be collected. Therefore, in the following hydrothermal reactions, we still use the SUS 316 reactor unless otherwise stated. Additionally, if only Ni and not Fe was used, no formic acid was formed in the liquid sample.

The effect of temperature on hydrothermal conversion of CO_2 was studied by varying it between 523 and 598 K. As shown in Table IV, the formic acid yield increases with the reaction temperature, and does not increase further with temperature when the temperature exceeds 573 K. This result could possibly be caused by the decomposition of the formic acid under the catalysis by Ni or the some inhibition effect on the catalysis Ni itself under too much high temperatures. On the other hand, the high temperature is not favorable to the energy saving; therefore, we set the hydrothermal reaction at a milder temperature of 573 K in the following studies.

To further study the effect of reaction time on the formic acid yield, the yields of formic acid after different reaction times were examined at 573 K with Fe/Ni ratio of 1:1. As shown in Table IV, an optimal yield of formic acid is obtained with reaction time of 120 min. The increase in the yield of formic acid during the first 120 min can be attributed to more formic acids being produced compared to those decomposing. On the other hand, after 120 min the decomposition of formic acid may be in the ascendant; consequently, the yield of formic acid decreases with further increasing reaction time.

In studies of the influence of alkalinity on the yield of formic acid, it was found that alkalinity has a great influence on the formation of formic acid. In the

Downloaded by PENNSYLVANIA STATE UNIV on June 23, 2012 | http://pubs.acs.org
Publication Date (Web): December 3, 2010 | doi: 10.1021/bk-2010-1056.ch004

case of only Fe, the yield of formic acid increases with NaOH concentration until 0.1 mmol/L to attain an optimal formic acid yield of 12.5% and then decreases gradually with a further increase of NaOH concentration. These results suggest that, although proper alkalinity can stabilize formic acid in the solution, excessive alkalinity is not favorable to the formation of formic acid. This result was not reported by Takahashi et al. (*57*), although they found that CO_2 was converted to formic acid in alkaline solution under hydrothermal conditions. In the presence of both Fe and Ni, the yield of formic acid decreased gradually with the increase of NaOH concentration.

In addition, a difference in the solution pH values before and after reactions was not observed at initial NaOH concentration of 0, 0.1 and 0.3 mmol/L. While in the case of 0.5-mmol/L NaOH initial concentration, a significant increase in alkalinity was observed after reaction. This result suggests that excessive alkali was responsible for the decrease of the yield of formic acid. Thereby, no additional alkali is used throughout the present study.

Finally, we also made a simple energy assessment for the hydrothermal conversion of CO_2 into formic acid. The energy needed to produce one ton of formic acid from the hydrothermal reduction of CO_2 is less than that from conventional method with fossil fuels as substrates (sodium formiate acidification method).

5. Conclusions and Prospects

The hydrothermal process can efficiently and directly convert CO_2 into value-added products. The proposed hydrothermal reduction of CO_2 into organics possesses several benefits:

(1) Water acts not only as a hydrogen source but also as an environmentally benign solvent.
(2) Hydrogen from high-temperature water or biomass can be a highly effective reductant, unlike the generally stable H_2 (dry H_2), and thus readily and directly reacts with CO_2 in mild conditions.
(3) This process does not require elaborately prepared catalysts, expensive reagents, or high-purity CO_2.
(4) This method does not require hydrogen, including pumps or storage, because hydrogen is derived from water and biomass and is reacted with CO_2 *in situ*.
(5) CO_2 promotes *in situ* hydrogen production. The mechanism can be explained as the shift of the reaction of water reduction into hydrogen to the right due to consumption of hydrogen (CO_2 hydrogenation) in the presence of CO_2.

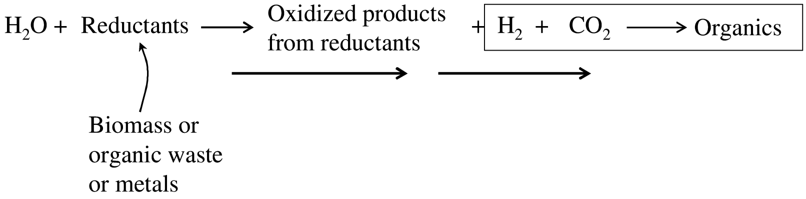
H_2O + Reductants
Oxidized products from reductants
+ H_2 + CO_2
Organics
Biomass or organic waste or metals

Thus, the proposed hydrothermal reduction of CO_2 is expected to convert CO_2, e.g., CO_2 captured from large-scale industry plants with high-energy use, in large scale. Although challenges remain for the industry-scale conversion of CO_2 into organics, our research opens a new path for the use of CO_2 as chemical feedstock, thus improving the global carbon cycle.

Acknowledgments

We gratefully acknowledge financial support from the Natural Science Foundation of China (Grant No. 20777054), and the National High Technology Research and Development Program ("863" Program) of China (No. 2009AA05Z405).

References

1. Jessop, P. G.; Joó, F.; Tai, C. C. *Coord. Chem. Rev.* **2004**, *248*, 2425–2442.
2. Jessop, P. G.; Ikariya, T.; Noyori, R. *Chem. Rev.* **1995**, *95*, 259–272.
3. Hara, K.; Kudo, A.; Sakata, T. *J. Electroanal. Chem.* **1995**, *391*, 141–147.
4. Barton, E. E.; Rampulla, D. M.; Bocarsly, A. B. *J. Am. Chem. Soc.* **2008**, *130*, 6342–6344.
5. Parkinson, B. A.; Weaver, P. F. *Nature* **1984**, *309*, 148–149.
6. Inui, T.; Yamamoto, T.; Inoue, M.; Hara, H.; Takeguchi, T.; Kim, J. B. *Appl. Catal., A* **1999**, *186*, 395–406.
7. Frost, D. J.; McCammon, C. A. *Annu. Rev. Earth Planet. Sci.* **2008**, *36*, 389–420.
8. McCammon, C. *Science* **2005**, *308*, 807–808.
9. Martin, W.; Baross, J.; Kelley, D.Russell, J. *Nat. Rev. Microbiol.* **2008**, *6*, 805–814.
10. Proskurowski, G.; Lilley, M. D.; Seewald, J. S.; Fruh-Green, G. L.; Olson, E. J.; Lupton, J. E.; Sylva, S. P.; Kelley, D. S. *Science* **2008**, *319*, 604–607.
11. Proskurowski, G.; Lilley, M. D.; Seewald, J. S.; Fruh-Green, G. L.; Olson, E. J.; Lupton, J. E.; Sylva, S. P.; Kelley, D. S. *Geochim. Cosmochim. Acta* **2008**, *72*, A764.
12. Fu, Q.; Lollar, B. S.; Horita, J.; Lacrampe-Couloume, G.; Seyfried, W. E. *Geochim. Cosmochim. Acta* **2007**, *71*, 1982–1998.
13. Ji, F. W.; Zhou, H. Y.; Yang, Q. H. *Origins Life Evol. Biospheres* **2008**, *38*, 117–125.
14. Foustoukos, D. I.; Seyfried, W. E. *Science* **2004**, *304*, 1002–1005.

Downloaded by PENNSYLVANIA STATE UNIV on June 23, 2012 | http://pubs.acs.org
Publication Date (Web): December 3, 2010 | doi: 10.1021/bk-2010-1056.ch004

15. Fu, Q.; Foustoukos, D. I.; Seyfried, W. E. *Geophys. Res. Lett.* **2008**, *35*, L07612-1–L07612-5.
16. Jin, F.; Kishita, A.; Moriya, T.; Enomoto, H.; Sato, N. *Chem. Lett.* **2002**, *31* (1), 88–89.
17. Jin, F.; Moriya, T.; Enomoto, H. *Environ. Sci. Technol.* **2003**, *37* (14), 3220–3231.
18. Jin, F.; Zhou, Z.; Moriya, T.; Kishida, H.; Higashijima, H.; Enomoto, H. *Environ. Sci. Technol.* **2005**, *39* (6), 1893–1902.
19. Jin, F.; Zhou, Z.; Kishita, A.; Enomoto, H.; Kishida, H.; Moriya, T. *IChemE* **2007**, *85* (2), 201–206.
20. Jin, F.; Cao, J.; Enomoto, H.; Moriya, T. *J. Supercrit. Fluids* **2006**, *39*, 80–88.
21. Kishita, H.; Jin, F.; Zhou, Z.; Moriya, T.; Enomoto, H. *Chem. Lett.* **2005**, *34* (11), 1560–1561.
22. Jin, F.; Yun, J.; Li, G.; Kishita, A.; Tohji, K.; Enomoto, H. *Green Chem.* **2008**, *10*, 612–615.
23. Jin, F.; Cao, J.; Kishida, H.; Moriya, T.; Enomoto, H. *Carbohydr. Res.* **2007**, *342*, 1129–1132.
24. Jin, F.; Kishita, A.; Moriya, T.; Enomoto, H. *J. Supercrit. Fluids* **2000**, *19*, 251–262.
25. Moriya, T.; Enomoto, H. *Polym. Degrad. Stab.* **1999**, *65*, 373–386.
26. Kishita, A.; Takahashi, S.; Kamimura, H.; Miki, M.; Moriya, T.; Enomoto, H. *J. Jpn. Petrol. Inst.* **2003**, *46*, 215–221.
27. Matsumura, Y.; Sasaki, M.; Okuda, K.; Takami, S.; Ohara, S.; Umetsu, M.; Adschiri, T. *Combust. Sci. Technol.* **2006**, *178* (1-3), 509–536.
28. Fang, Z.; Fang, C. *AIChE J.* **2008**, *54* (10), 2751–2758.
29. Akiya, N.; Savage, P. E. *Chem. Rev.* **2002**, *102*, 2725–2750.
30. An, J.; Bagnell, L.; Cablewski, T.; Strauss, C. R.; Trainor, R. W. *J. Org. Chem.* **1997**, *62*, 2505–2511.
31. Ikushima, Y.; Hatakeda, K.; Sato, O.; Yokoyama, T.; Arai, M. *Angew. Chem., Int. Ed.* **2000**, *38*, 2910–2914.
32. Fukuoka, A.; Dhepe, P. L. *Angew. Chem., Int. Ed.* **2006**, *45*, 5161–5163.
33. Watanabe, M.; Sato, T.; Inomata, H.; Smith, R. L.; Arai, K.; Kruse, A.; Dinjus, E. *Chem. Rev.* **2004**, *104*, 5803–5821.
34. Peterson, A. A.; Vogel, F.; Lachance, R. P.; Fröling, M.; Antal, M. J.; Tester, J. W. *Energy Environ. Sci.* **2008**, *1*, 32–65.
35. Akiya, N.; Savage, P. E. *Chem. Rev.* **2002**, *102*, 2725–2750.
36. Shaw, R. W.; Brill, Y. B.; Clifford, A. A.; Eckert, C. A.; Franck, E. U. *Chem. Eng. News* **1991**, *69*, 26–39.
37. Marshall, W. L.; Frank, E. U. *J. Phys. Chem. Ref. Data.* **1981**, *10*, 295–304.
38. Franck, E. U. *Fluid Phase Equilib.* **1983**, *10*, 211–222.
39. Jin, F.; Zhou, Z.; Moriya, T.; Kishida, H.; Higashijima, H.; Enomoto, H. *Environ. Sci. Technol.* **2005**, *39*, 1893–1902.
40. Moriya, T.; Enomoto, H. *Polym. Degrad. Stabil.* **1999**, *65*, 373–386.
41. Tenou, S. Ph.D Thesis, Tohoku University, Japan, 1997, in Japanese.
42. Takahashi, H.; Hisaoka, S.; Nitta, T. *Chem. Phys. Lett.* **2002**, *363*, 80–86.
43. Nakahara, M.; Tennoh, T.; Wakai, C.; Fujita, E.; Enomoto, H. *Chem. Lett.* **1997**, *2*, 163–164.

Downloaded by PENNSYLVANIA STATE UNIV on June 23, 2012 | http://pubs.acs.org
Publication Date (Web): December 3, 2010 | doi: 10.1021/bk-2010-1056.ch004

44. Kuhlmann, B.; Arnett, E. M.; Siskin, M. J. *J. Org. Chem.* **1994**, *59*, 3098–3101.
45. Kuhlmann, B.; Arnett, E. M.; Siskin, M. J. *J. Org. Chem.* **1994**, *59*, 5377–5380.
46. Akiya, N.; Savage, P. E. *Chem. Rev.* **2002**, *102*, 2725–2750.
47. Watanabe, M.; Sato, T.; Inomata, H.; Smith, R. L.; Arai, K.; Kruse, A.; Dinjus, E. *Chem. Rev.* **2004**, *104*, 5803–5822.
48. Toshihiko, A.; Nakahara, K.; Nagami, K.; Kajimo, O. *Tetrahedron Lett.* **2003**, *44*, 1081–1086.
49. Wang, P.; Kojima, H.; Kobiro, K.; Nakahara, K.; Arita, T.; Kajimoto, O. *Bull. Chem. Soc. Jpn.* **2007**, *80*, 1828–1832.
50. Shen. Z. Ph.D Thesis, Tongji University, China, 2009, in Chinese.
51. Tenou, S. Ph.D Thesis, Tohoku University, Japan, 1997, in Japanese.
52. Kishita, H.; Jin, F.; Zhou, Z.; Moriya, T.; Enomoto, H. *Chem. Lett.* **2005**, *34*, 1560–1561.
53. Kishita, A.; Takahashi, S.; Jin, F.; Yamasaki, Y.; Moriya, T.; Enomoto, H. *J. Jpn. Petrol. Inst.* **2005**, *48*, 272–280.
54. Kishita, A.; Takahashi, S.; Yamasaki, Y.; Jin, F.; Moriya, T.; Enomoto, H. *J. Jpn. Petrol. Inst.* **2006**, *49*, 177–185.
55. Jin, F.; Ma, C.; Mogi, T.; Kishita, A.; Enomoto, H. *Prepr. Pap. - Am. Chem. Soc., Div. Fuel Chem.* **2008**, *53*, 689–690.
56. Wu, B.; Gao, Y.; Jin, F.; Cao, J.; Du, Y.; Zhang, Y. *Catal. Today* **2009**, *148*, 405–410.
57. Takahashi, H.; Liu, L. H.; Yashiro, Y.; Ioku, K.; Bignall, G.; Yamasaki, N. *J. Mater. Sci.* **2006**, *41*, 1585–1589.

Downloaded by PENNSYLVANIA STATE UNIV on June 23, 2012 | http://pubs.acs.org
Publication Date (Web): December 3, 2010 | doi: 10.1021/bk-2010-1056.ch004

Downloaded by OHIO STATE UNIV LIBRARIES on June 23, 2012 | http://pubs.acs.org
Publication Date (Web): December 3, 2010 | doi: 10.1021/bk-2010-1056.ch005

Chapter 5

Electrocatalytic Reduction of CO_2 to Small Organic Molecule Fuels on Metal Catalysts

Wenzhen Li[*]

Department of Chemical Engineering, Michigan Technological University,
Houghton, MI 49931, USA.
[*]Email: wzli@mtu.edu. Tel: 906-487-2298. Fax: 906-487-3213.

The electrocatalytic reduction of carbon dioxide (CO_2) to liquid fuels has tremendous positive impacts on atomospheric carbon balance and help to reduce global warming issues. This paper reviewed current knowledge of electrochemical CO_2 reduction to small organic molecule fuels on metal catalysts and gas-phase CO_2 reduction techniques based on gas diffusion electrode and solid polymer electrolyte. Future research and development needs in this area were also discussed.

Keywords: carbon dioxide; electrocatytic reduction; synthetic fuels; electrochemistry; electro-driven conversion; catalysis; gas diffusion electrode; electrolysis; photoelectrochemical reactor

1. Introduction

The increase of carbon dioxide (CO_2) in the atmosphere is claimed to be one of the major contributors to the greenhouse effect and will result in serious global warming issues (*1–3*). The electrocatalytic reduction of CO_2 to liquid fuels is a critical goal that would positively impact the global carbon balance by recycling CO_2 into usable fuels (*4–8*). However, CO_2 is an extremely stable molecule generally produced by fossil fuel combustion and respiration, returning CO_2 to a useful chemical state on the same scale as its current production rates is beyond our current scientific and technology ability (*4*). No commercially available processes exist for the conversion of CO_2 to fuels and chemicals yet. The challenges presented are great, but the potential rewards are

In Advances in CO2 Conversion and Utilization; Hu, Y.;
ACS Symposium Series; American Chemical Society: Washington, DC, 2010.

enormous. To address this challenging scientific problem, we need to advance our fundamental understanding of the chemistry of CO_2 activation and develop novel multifunctional catalysts that could use electricity to efficiently break C-O bond and form C-H and C-C bonds (*4*). Appropriate energy input and reasonable productivity of fuels are also important considerations for practical industrial processes.

The CO_2 electrocatalytic reductions to usable fuels are 'reverse' electrochemical processes compared to the anode reactions occurred in fuel cells. CO_2 reduction converts electrical energy back to chemical energy stored in the chemical bonds of fuels. In thermodynamics, the Gibbs free energy of CO_2 reduction is always positive at medium and high pH range, and the theoretical potentials are negative. Thus, CO_2 reduction is an electrolysis process that requires electrical energy input. In kinetics, the overpotential needed to electrochemically reduce CO_2 is always > 1.0 V, to get reasonable amounts of fuels, such as methane, ethylene, etc. In an aqueous electrolyte, the water reduction always occurs, and H_2 is a major by-product accompanied with CO_2 reduction. High hydrogen overvoltage metals, such as Hg, can suppress H_2 evolution, but it leads to formation of formate ions ($HCOO^-$) at very high overpotentials (high energy cost).

A milestone work is that Hori group found the CO_2 reduction on copper (Cu) behaves very different from the other metals. Cu can directly reduce CO_2 to hydrocarbons (mainly methane and ethylene) with reasonable current density (i.e. 5-10 mA/cm^2) and current efficiency (i.e. > 69% at 0°C) in aqueous electrolyte (*6*, *9*). Cu-based catalysts (Cu single crystals, adatom Cu electrode, and Cu alloys electrodes) have been extensively studied from both fundamental and applied perspectives (*9–17*). Although the process has not been commercialized to produce hydrocarbon products yet, gas mixtures of hydrogen, methane, ethylene and CO would form 'hythane' that can be promoted as alternative fuel for existing vehicles (*18*).

CO_2 reduction in gas phase based on gas diffusion electrode (GDE) and solid polymer electrolyte (SPE) can greatly improve CO_2 transport, thus facilitating CO_2 reduction (*19–23*). Taking the advantages of established electrolysis cell and fuel cell technologies, electrocatalytic recycling of CO_2 and small organic molecule fuels appears to be a promising means to achieving sustainable, carbon neutral energy conversions. Recently, surprising long carbon chain organic molecules, such as iso-propanol and $C_{\geq 4}$ oxygenates, were found in the GDE based electrocatalytic reduction of CO_2 based on CNT-encapsulate metal catalysts (*24*, *25*), although in very small amounts, they might open new avenues to CO_2 electrocatalytic conversion to liquid fuels.

Some excellent review articles are already available in this field. Frese reviews CO_2 electrocatalytic reduction on solid electrodes (*5*), Gattrell focused on fundamental mechanisms of electrochemical reduction of CO_2 to hydrocarbons on copper electrode in aqueous electrolyte solution (*6*), and Hori recently gave a comprehensive review on CO_2 reduction on metal electrodes based on his pioneer work in this area (*7*). This paper will introduce current knowledge of electrochemical CO_2 reduction on heterogeneous metal catalysts, review present CO_2 reduction techniques based on GDE and SPE, and discuss future research and

Downloaded by OHIO STATE UNIV LIBRARIES on June 23, 2012 | http://pubs.acs.org
Publication Date (Web): December 3, 2010 | doi: 10.1021/bk-2010-1056.ch005

development needs in this area. Although homogeneous catalysis is an efficient approach to CO_2 reduction (*8*), it is out of the scope of this paper.

2. Review

2.1. Fundamental Challenges for Electrochemical Reduction of CO_2

The products of CO_2 reduction vary from liquid fuels (i.e. formic acid and isopropanol), hydrocarbons (i.e. methane and ethylene) to fuel precursors (i.e. CO). The reactivity of CO_2 reduction is very low, however, the equilibrium potentials of CO_2 reduction are not very negative (equation 123456), compared to hydrogen evolution reaction (HER) in aqueous electrolyte solutions (equation 7). The primary reactions that occurred on electrode in aqueous solution at pH 7.0 at 25°C, versus standard hydrogen electrode (SHE) are shown below (*7*, *26*):

$$CO_2 + H_2O + 2e^- = HCOO^- + OH^- \quad (-0.43V) \qquad (1)$$

$$CO_2 + H_2O + 2e^- = CO + 2OH^- \quad (-0.52\ V) \qquad (2)$$

$$CO_2 + 6H_2O + 8e^- = CH_4 + 8OH^- \quad (-0.25\ V) \qquad (3)$$

$$2CO_2 + 8H_2O + 12e^- = C_2H_4 + 12OH^- \quad (-0.34\ V) \qquad (4)$$

$$2CO_2 + 9H_2O + 12e^- = C_2H_5OH + 12OH^- \quad (-0.33\ V) \qquad (5)$$

$$3CO_2 + 13H_2O + 18e^- = C_3H_7OH + 18OH^- \quad (-0.32\ V) \qquad (6)$$

$$2H_2O + 2e^- = 2OH^- + H_2 \quad (-0.41\ V) \qquad (7)$$

CO_2 reduction does not occur easily and the real applied electrolysis potentials for CO_2 reduction are more negative than the equilibrium values. This is mainly because the single electron reduction of CO_2 to $CO_2^{\cdot-}$ (equation 8), which has been well recognized as the first step to activate CO_2 for subsequent reduction steps, occurs at -1.90 V, due to a large reorganizational energy between linear molecule and bent radical anion. This step has also been determined as the rate determining step (RDS) for CO_2 reduction.

$$CO_2 + e^- = CO_2^{\cdot-} \quad (-1.90\ V) \qquad (8)$$

It should be noted that the theoretical equilibrium potentials decrease with pH increasing, governed by the Nernst equation (*6*). For example, the equilibrium

Downloaded by OHIO STATE UNIV LIBRARIES on June 23, 2012 | http://pubs.acs.org
Publication Date (Web): December 3, 2010 | doi: 10.1021/bk-2010-1056.ch005

potential is +0.17 V for CO_2 reduction to methane at pH 0 (Equation 9). The equilibrium potentials over the range of pH values around where the reactions are typically carried out are shown in Fig. 1.

$$CO_2 + 8H^+ + 8e^- = CH_4 + 2H_2O \qquad (+0.17V) \qquad (9)$$

The key problem of the conversion of CO_2 to liquid fuels is the assembly of the nuclei and formation of chemical bonds to convert the relatively simple CO_2 molecule into more complex and energetic molecules. The CO_2 reduction is greatly limited by reaction kinetics. Considering their low equilibrium potentials as shown in Fig. 1, thermodynamically, the products of methane and ethylene should occur at a less cathodic potential than hydrogen, however, kinetically this does not happen.

The products distribution for CO_2 reduction on Cu electrode as a function of potential is plotted in Fig. 2. Initially, CO_2 reduction produces CO and formate until below -1.12V, where hydrocarbons begin to form, with first ethylene (C_2H_4), then methane (CH_4) appearing. The methane production shows the stronger potential dependence, and these reactions accelerate, dominating over CO and formate at around -1.35V. Therefore, the fundamental challenges for CO_2 reduction come from both thermodynamics and kinetics.

In addition, hydrogen evolution reaction (HER) takes place in aqueous electrolytes by cathodic polarization, competing with CO_2 reduction, HER is prevalent in acidic solutions, while CO_2 does not exist in a basic solution. Therefore, most CO_2 reduction study was conducted in close neutral electrolyte solutions (i.e. 0.05 – 0.5 M $NaHCO_3$).

2.2. Classification of Electrocatalytic Metals and Reaction Selectivity

The product selectivity in CO_2 reduction depends on many factors, such as concentration of the reactants, electrode potential, temperature, electrocatalyst material and electrolyte solution (i.e. aqueous or non-aqueous electrolyte). As widely accepted by most researchers, the electrocatalyst materials govern the selectivity of CO_2 reduction, when the other conditions are identical. Hori's group has carried out a series of elegant research on CO_2 reduction (*9–13*), and found electrocatalytic metals can be generally divided into four groups based on product selectivity, as shown in Table 1.

The 1st group metals include Pb, Hg, In, Sn, Cd, TI, Bi, etc. They have high hydrogen overvoltages, negligible CO adsorption properties, and high overvoltages for CO_2 to $CO_2^{\cdot-}$, and hence weak stabilization of $CO_2^{\cdot-}$. The major product is formate ion ($HCOO^-$).

The 2nd group metals include Au, Ag, Zn, etc. They have medium hydrogen overvoltages and weak CO adsorption properties, and the major product is carbon monoxide (CO). Because they can catalyze the breakage of the C-O bond in CO_2 but allow the CO desorb, thus, the major product is CO.

The 3rd group metals include Ni, Fe, Pt, Ti, etc. They have low hydrogen overvoltages and strong CO adsorption properties and the major product is H_2, because the main reaction is water reduction to H_2.

Downloaded by OHIO STATE UNIV LIBRARIES on June 23, 2012 | http://pubs.acs.org
Publication Date (Web): December 3, 2010 | doi: 10.1021/bk-2010-1056.ch005

Downloaded by OHIO STATE UNIV LIBRARIES on June 23, 2012 | http://pubs.acs.org
Publication Date (Web): December 3, 2010 | doi: 10.1021/bk-2010-1056.ch005

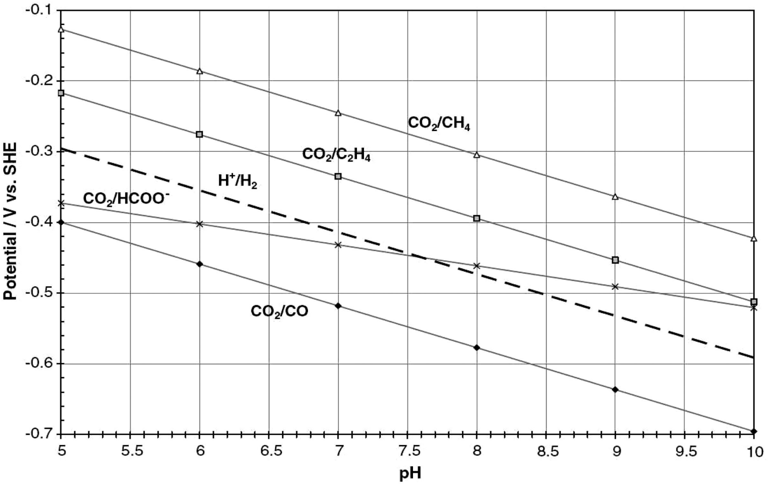

Figure 1. The equilibrium potentials as a function of pH for the principal CO_2 reduction reaction at 25°C (Ref. (7)). Copyright (2007) with permission from Elsevier.

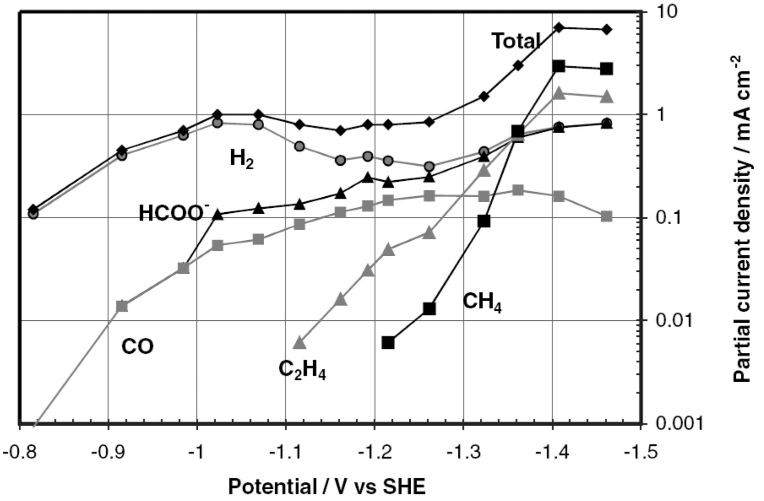

Figure 2. Partial current data obtained from high-purity Cu electrode from Ref (7), conditions: 0.1 M $KHCO_3$, 19°C, CO_2 bubbled, $[H^+]=1.55\times10^{-7}$ M, $[CO_2]=3.41\times10^{-2}$ M. Copyright (2007) with permission from Elsevier.

The 4th group: Cu. Cu is unique for CO_2 reduction, because it is able to further react CO to more reduced species, such as CH_4 and C_2H_4 with significant amounts. The detailed mechanisms are discussed in section 2.3.

Azuma et al. applied 32 metals to CO_2 reduction at similar conditions (-2.2 V vs. SCE, 0.05M $KHCO_3$) and confirmed these results given in Table 1 (from Hori's group). They showed that Cu is the unique metal that can reduce CO_2 to appreciable amounts of hydrocarbons CH_4 and C_2H_4, while Ni and Pt catalysts

Downloaded by OHIO STATE UNIV LIBRARIES on June 23, 2012 | http://pubs.acs.org
Publication Date (Web): December 3, 2010 | doi: 10.1021/bk-2010-1056.ch005

scarcely give products in CO_2 reduction at ambient temperature and pressure, but can reduce CO_2 to CO or formic acid under elevated pressure (i.e. 60 atm). They also provided a classical roadmap for CO_2 electrocatalytic reduction on metal catalysts (*16*), which can be found in Ref (*16*).

It is interesting that the presence of small amount of foreign atoms on the electrode surface could greatly change the reaction selectivity of CO_2 reduction (*6*, *27*). These adatom modified electrodes were prepared by under potential deposition or overpotential deposition techniques. For example, at -1.44 V vs SHE, the CO selectivity of pure Cu is 69%, while that of Cd and Pd adatom modified Cu is 82% and 0, respectively.

2.3. Reaction Mechanisms

The CO_2 reduction on various metal electrodes has been extensively studied, but knowledge about CO2 reduction is still limited, the reaction mechanisms were mainly obtained base on observed charge transfer coefficients and reaction orders acquired from macroscopic electrochemical testing. The partially understood reaction mechanisms are discussed as follows.

a. Formation of $CO_2^{\cdot-}$ Is the Rate-Determining Step (RDS)

The CO_2 can be chemisorbed as a bent $CO_2^{\delta-}$ molecule, which is promoted by surface defects, alkali metal promoted surfaces, and possibly through X-rays or photoelectrons during measurements. The exact geometry of $CO_2^{\delta-}$ metal is unclear, and the possible structures for adsorbed $CO_2^{\delta-}$ are shown in Fig. 3. CO_2 is an 'amphoteric' molecule possessing both acid and basic properties. The adsorption and stabilization of $CO_2^{\delta-}$ are dominantly governed by the electrode metals. The electrode metals interact with carbon or oxygen or both in CO_2 to form carbon coordination or oxygen coordination, or mixed coordination adsorption mode, respectively. The $CO_2^{\delta-}$ species is most easily produced at surface defects or in the presence of sublyer coverage of an alkali metal. It is generally agreed that the formation of $CO_2^{\cdot-}$ is the rate-determining step at medium and high overpotential regions. Jordan and Smith firstly proposed the formation of $CO_2^{\cdot-}$ anion radical by one electron transfer to CO_2 is the initial step for subsequent reduction of CO_2, as shown in Fig. 4 (a) (*28*). Pacansky et al. studied scf ab initio molecular orbital energies and atomic population analysis of $CO_2^{\cdot-}$ at the minimum energy geometry and found the unpaired electron density at the highest occupied orbital is localized at C atom at 84% (*29*). This result suggests that $CO_2^{\cdot-}$ is ready to react as a nucleophilic reactant at the carbon atom. The standard potential of $CO_2^{\cdot-}$ formation is -1.90 V or -1.85 V vs SHE, -2.21 V vs. SCE in aqueous media (*30–32*). The transfer coefficient of RDS in the lower overvoltage region was found to be 0.67 (*33*). The $CO_2.^-$ is mostly present freely in both aqueous and non-aqueous electrolyte solutions, and has been captured by ultraviolet spectroscopy (*34*).

Downloaded by OHIO STATE UNIV LIBRARIES on June 23, 2012 | http://pubs.acs.org
Publication Date (Web): December 3, 2010 | doi: 10.1021/bk-2010-1056.ch005

Table 1. Faradaic efficiencies of products in CO_2 reduction at various metal electrodes. Electrolyte: 0.1 M $KHCO_3$ (T = 18.5 ± 0.5°C, Ref. (*12*)). Copyright (1995) with permission from Elsevier.

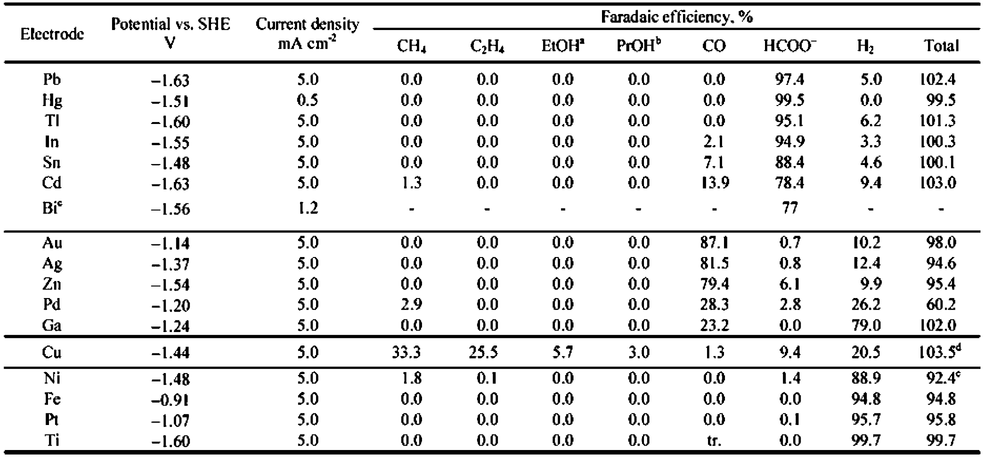

Electrode	Potential vs. SHE V	Current density mA cm^{-2}	Faradaic efficiency, %							
			CH_4	C_2H_4	EtOH[a]	PrOH[b]	CO	$HCOO^-$	H_2	Total
Pb	−1.63	5.0	0.0	0.0	0.0	0.0	0.0	97.4	5.0	102.4
Hg	−1.51	0.5	0.0	0.0	0.0	0.0	0.0	99.5	0.0	99.5
Tl	−1.60	5.0	0.0	0.0	0.0	0.0	0.0	95.1	6.2	101.3
In	−1.55	5.0	0.0	0.0	0.0	0.0	2.1	94.9	3.3	100.3
Sn	−1.48	5.0	0.0	0.0	0.0	0.0	7.1	88.4	4.6	100.1
Cd	−1.63	5.0	1.3	0.0	0.0	0.0	13.9	78.4	9.4	103.0
Bi[c]	−1.56	1.2	-	-	-	-	-	77	-	-
Au	−1.14	5.0	0.0	0.0	0.0	0.0	87.1	0.7	10.2	98.0
Ag	−1.37	5.0	0.0	0.0	0.0	0.0	81.5	0.8	12.4	94.6
Zn	−1.54	5.0	0.0	0.0	0.0	0.0	79.4	6.1	9.9	95.4
Pd	−1.20	5.0	2.9	0.0	0.0	0.0	28.3	2.8	26.2	60.2
Ga	−1.24	5.0	0.0	0.0	0.0	0.0	23.2	0.0	79.0	102.0
Cu	−1.44	5.0	33.3	25.5	5.7	3.0	1.3	9.4	20.5	103.5[d]
Ni	−1.48	5.0	1.8	0.1	0.0	0.0	0.0	1.4	88.9	92.4[e]
Fe	−0.91	5.0	0.0	0.0	0.0	0.0	0.0	0.0	94.8	94.8
Pt	−1.07	5.0	0.0	0.0	0.0	0.0	0.0	0.1	95.7	95.8
Ti	−1.60	5.0	0.0	0.0	0.0	0.0	tr.	0.0	99.7	99.7

Downloaded by OHIO STATE UNIV LIBRARIES on June 23, 2012 | http://pubs.acs.org
Publication Date (Web): December 3, 2010 | doi: 10.1021/bk-2010-1056.ch005

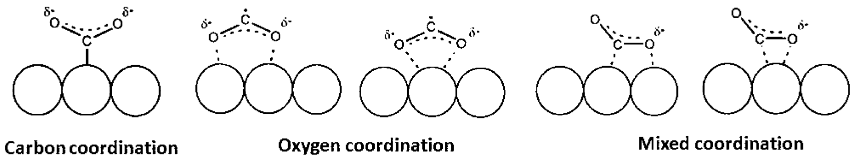
Carbon coordination
Oxygen coordination
Mixed coordination

Figure 3. Possible structure for adsorbed $CO_2^{\delta-}$ on metals (Ref (7)). Copyright (2007) with permission from Elsevier.

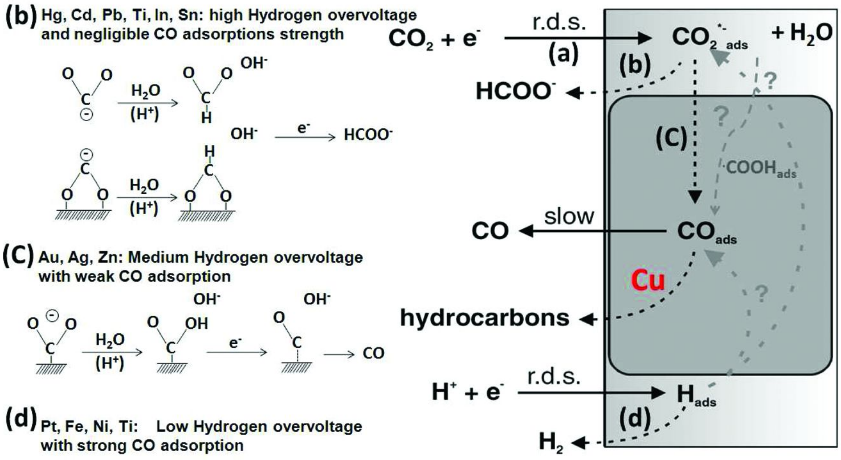
(b) Hg, Cd, Pb, Ti, In, Sn: high Hydrogen overvoltage and negligible CO adsorptions strength
H2O
(H+)
OH-
e-
HCOO-
(C) Au, Ag, Zn: Medium Hydrogen overvoltage with weak CO adsorption
CO
(d) Pt, Fe, Ni, Ti: Low Hydrogen overvoltage with strong CO adsorption
CO2 + e-
r.d.s.
(a)
CO2·- ads
+ H2O
(b)
?
HCOO-
(C)
COOHads
slow
CO
COads
Cu
hydrocarbons
H+ + e-
r.d.s.
Hads
(d)
H2

Figure 4. The main reaction pathways at the electrode surface, with adsorbed blocking the majority of the surface and hydrocarbon products being formed by the further reduction of adsorbed CO. (Ref (6, 7). Copyright (2007) with permission from Elsevier. (see color insert)

There are two main pathways for further reduction of adsorbed $CO_2^{\cdot-}$ to respective final product of CO, and formate ion ($HCOO^-$), which is governed by the properties of metal electrocatalysts.

b. Formation of Adsorbed $CO_2^{\cdot-}$Leading to Further Reduction to $HCOO^-$

Erring et al. studied CO_2 reduction polarization data at Hg electrode in aqueous electrolyte with HCO_3^-, and obtained a major product of $HCOO^-$ (*35*). On Hg, CO_2 reduction is initiated by one electron transfer to form $CO_2^{\cdot-}$ at the potential negative of −1.6 V vs. SHE. The $CO_2^{\cdot-}$ will take a proton from a H_2O molecule at the nucleophilic carbon atom, forming $HCOO^{\cdot}$. H^+ will not be bonded to the O atom of $CO_2^{\cdot-}$, since p*K*a value of the acid-base couple ($CO_2^{\cdot-}/CO_2H$) is low of 1.4 (*36*). Hori et al found that the electrode potential is constant as the current density for $HCOO^-$ formation at a pH range of 2-8, thus, H_2O is believed to be the proton donor in the formate formation from $CO_2^{\cdot-}$. $HCOO^{\cdot}$ is subsequently reduced to $HCOO^-$ at the electrode in aqueous media. The reaction steps are:

$$CO_2^{\cdot -}{}_{ads} + H_2O \longrightarrow HCOO^{\cdot}{}_{ads} + OH^- \quad (10)$$

$$HCOO^{\cdot}{}_{\mathbf{ads}} + e^- \longrightarrow HCOO^- \quad (11)$$

Formate could also be produced directly by reaction with adsorbed hydrogen, which would be present as an intermediate in the hydrogen evolution reaction:

$$CO_2^{\cdot -}{}_{\mathbf{ads}} + H_{ads} \longrightarrow HCOO^- \quad (12)$$

Such a reaction mechanism would appear to be favored by $CO_2^{\cdot -}$ being adsorbed with oxygen coordination or being just close to the electrode. Other high hydrogen overvoltage electrodes, including Cd, Pb, Tl, In, and Sn, with weak adsorption of hydrogen, have high overvoltage for CO_2 reduction to $CO_2^{\cdot -}$, and hence weak stabilization of $CO_2^{\cdot -}$. The CO_2 reduction on these metals follows a similar mechanism as shown in Fig. 4 (b). In non-aqueous electrolyte, CO_2 electrolysis on Pb leads to formation of oxalic acid, due to formation of $(CO_2)_2^{\cdot -}$ (*6*).

c. *Formation of Adsorbed $CO_2^{\cdot -}$ Leading to Further Reduction to CO*

The other pathway also involves first protonation then reduction, which is similar to step b), however, the hydrogen appears to be added on oxygen not carbon in $CO_2^{\cdot -}$. The steps will occur more favorably on carbon coordination adsorption mode.

$$CO_2^{\cdot -}{}_{ads} + H_2O \longrightarrow {}^{\cdot}COOH_{ads} + OH^- \quad (13)$$

$${}^{\cdot}COOH_{ads} + e^- \longrightarrow CO_{ads} + OH^- \quad (14)$$

CO could be formed by a direct reaction with adsorbed hydrogen:

$$CO_2^{\cdot -}{}_{ads} + H_{ads} \longrightarrow CO_{ads} + OH^- \quad (15)$$

In these reactions, the electrophilic reagents, H_2O in aqueous solution, react with the O atom of adsorbed $CO_2^{\cdot -}$, forming CO_{ads} and OH^- as depicted in Fig. 4(c). Sasaki et al used an ab initio molecular orbital approach to study the configuration of $NiF(NH_3)_4(CO_2)$ as a model for CO_2 reduction and showed that C atom of CO_2 molecule is favorably coordinated with the transition metal atom in a complex and can be stabilized by a strong charge transfer due to back donation from Ni to CO_2, which indicates carbon coordination can facilitate protonation of oxygen (Eq.13), leading to formation of ${}^{\cdot}COOH$ not $HCOO^{\cdot}$.

At Au electrode, H^+ will not take part in the CO formation, since the partial current of CO formation is independent of pH. The CO_{ads} is readily desorbed from

In Advances in CO2 Conversion and Utilization; Hu, Y.;
ACS Symposium Series; American Chemical Society: Washington, DC, 2010.

Downloaded by OHIO STATE UNIV LIBRARIES on June 23, 2012 | http://pubs.acs.org
Publication Date (Web): December 3, 2010 | doi: 10.1021/bk-2010-1056.ch005

Downloaded by OHIO STATE UNIV LIBRARIES on June 23, 2012 | http://pubs.acs.org
Publication Date (Web): December 3, 2010 | doi: 10.1021/bk-2010-1056.ch005

the electrode as a gaseous molecule. The reaction scheme is suitable to other metal electrodes, such as Ag, Cu and Zn in aqueous media. The sequence of CO selectivity roughly agrees with that of the electrode potentials. This agreement verifies the hypothesis that CO is favorably produced from the electrode metals which stabilize $CO_2^{\cdot -}$ effectively. Because the CO adsorption on Au, Ag and Zn surface is weak, CO is the major product, as shown in Fig. 4 c. In comparasion, CO will be further reduced to hydrocarbon products on Cu electrode (as discussed in section 2.4).

d. Hydrogen Evolution Reaction (HER)

HER is a major side reaction that accompanies CO_2 reduction in an aqueous electrolyte. It has been found that the reaction kinetics of HER are pH dependent in the acid region and pH independent in the alkaline region. The HER can be written as

$$H^+ + e^- \longrightarrow H_{ads} \qquad (16)$$

$$2H_{ads} \longrightarrow H_2 \qquad (17)$$

$$\text{or} \qquad H_{ads} + H^+ + e^- \longrightarrow H_2 \qquad (18)$$

Adsorbed hydrogen H_{ads} and/or H^+ are the hydrogen source for hydrogenation in CO_2 reduction. Because CO is strongly adsorbed on Pt/Fe/Ni/Ti surface, in an applied potential range, the major product is H_2, rather than CO, as shown in Fig. 4 d.

2.4. Cu-Based Electrocatalysts

Cu is a unique metal that can reduce CO_2 to CH_4 and C_2H_4 and alcohols in aqueous electrolyte at low temperature (*6*). Some known mechanisms are reviewed as below.

a. Formation of CO_{ads} as Reaction Intermediate

From Fig. 2, at low overpotential, i.e. -0.9 V, the faradic yields of CO and $HCOO^-$ are both appreciable, while C_2H_4 begins to increase at -1.1V, CH_4 starts at -1.2V, these data indicate that CO and $HCOO^-$ may be precursors to hydrocarbons and alcohols. However, FTIR and Raman spectrum show CO is linearly adsorbed on Cu polycrystal electrode at -0.6V, which suggests that CO is the reaction intermediate formed at Cu electrode, serving as a precursor for further reduction to hydrocarbons and alcohols (*37*, *38*). The surface of the Cu electrode is covered by CO with coverage >90% as estimated from the current at -1.0V with and without CO, this could severely suppress hydrogen evolution reaction. The heat of adsorption of CO on Cu is appropriate (-17.7 kcal/mol), which is higher than Au, but lower than Ni and Pt, as listed in Table 2 (*39*). Therefore, Cu allows efficiently subsequent reduction of CO to produce hydrocarbons and alcohols.

b. From CO_{ads} to Hydrocarbons

Since CO has been identified as a primary reaction intermediate for formation of hydrocarbons, CO was used to investigate mechanisms of CO_2 reduction on Cu. Fig. 2 suggests that CH_4 formation starts at a more negative potential than C_2H_4 (-1.22 vs -1.12 V), but C_2H_4 formation is more favorable in high pH media. In addition, the Tafel slope for the two reactions are very different. All these strongly indicate that formation of CH_4 and C_2H_4 is through different reaction pathways from common starting substance CO. Interestingly, the evidence of lack of formation of methanol implies that the C-O bond of CO is broken early and consistently in the mechanism.

For the case of formation of CH_4, the transfer efficient of > 1 suggests that there is an initial electron transfer in equilibrium before RDS, this could result in a CO anion radical, as shown in Fig. 5 (a). Ab initio calculations were used to evaluate the state of the adsorbed CO anion radical, a slight decrease of the Cu-C bond and an increase of the C-O bond to about 1.25 Å were found, this predicts a mostly double bond character (*40*).

There are two possible reaction paths after formation of CO anion radicals. The first path is shown in Fig. 5 (b). This path involves a proton in the reaction, which must occur reversibly before the second electron transfer for RDS to yield the observed transfer coefficient. This is an acid-base reaction at the oxygen. The formation of four C-H bond would be not reversible, leading to production of CH_4. The second path involves reaction of C-O anion radical with an adsorbed hydrogen. Once the adsorbed CO has been electrochemically split, the hydrogen will add on carbon to form C-H radical and result in formation of CH_4, as shown in Fig. 5(c).

For the case of C_2H_4 formation, ethylene formation begins at a lower potential without a pH dependence and with first electron transfer as the RDS. As the first electron transfer begins a reaction pathway that subsequently results in a two carbon product, it is reasonable to assume that some type of bond formation occurs in this reaction step. A reaction is proposed that involves a “prior association” of two adsorbed CO (see Fig. 6). The postulation of a starting “associated pair” of adsorbed CO also would be consistent with the lower activation potential vs. the formation of CO (and hence methane).

The other possible reaction path is through the step of $–CH_2$ (ads) with CO. Since C(ads) is readily reduce to $–CH_2$ as shown in Fig. 5 b, two $–CH_2$ can dimerize to form C_2H_4, or alternatively, CO inserts into $–CH_2$ to form $–COCH_2$ which is further reduced to C_2H_4, as shown in Fig. 6.

So far, we still lack convinced experimental data i.e. FT-IR / Raman spectrum under real reaction conditions, to clearly elucidate the elementary steps for the complex CO_2 reduction to hydrocarbons. It is still not very clear how H species

Downloaded by OHIO STATE UNIV LIBRARIES on June 23, 2012 | http://pubs.acs.org
Publication Date (Web): December 3, 2010 | doi: 10.1021/bk-2010-1056.ch005

Downloaded by OHIO STATE UNIV LIBRARIES on June 23, 2012 | http://pubs.acs.org
Publication Date (Web): December 3, 2010 | doi: 10.1021/bk-2010-1056.ch005

Table 2. CO reduction in 0.1 M $KHCO_3$ at various metal electrodes (Ref (*11*)). Copyright (1987) with permission from Japan Chemical Society.

Electrode	Potential V vs.SHE	Faradaic efficiency/ %				CO heat of adsorption kcal mol^{-1} [c]
		CH_4	C_2H_4	Other HCs and alcohols[b]	H_2	
Au	−1.49	0.0	0.0	0.0	101.6	9.2
Cu	−1.40	16.3	21.2	12.5	45.5	17.7
Ni	−1.46	2.6	0.3	0.7	94.2	40.8
Pt	−1.29	0.1	0.0	0.0	96.8	46.6

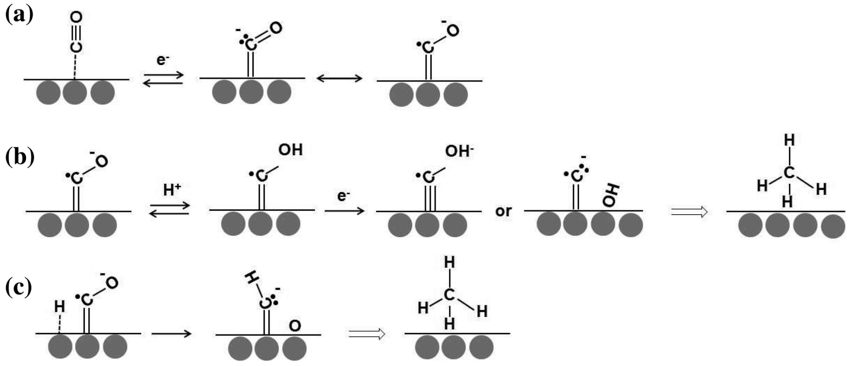

Figure 5. (a) the expected mechanism for initial electron transfer to adsorbed CO, (b) (c) the reaction mechanisms that could lead to the observed transfer coefficient and reaction order with pH. Grey particle: Cu atom, (Redrawn based on Ref (7)). Copyright (2007) with permission from Elsevier.

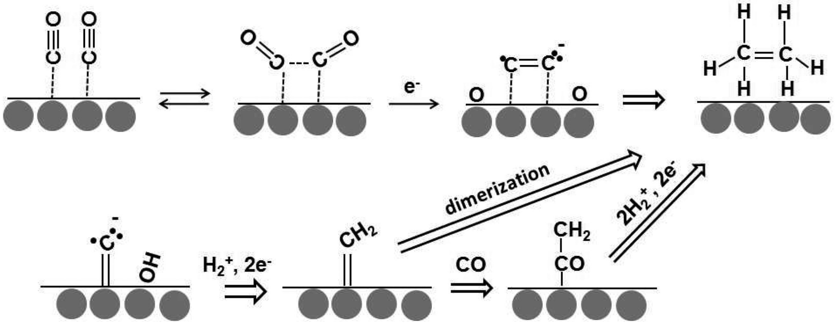

Figure 6. The proposed reaction mechanisms for producing a two carbon product. Grey particle: Cu atom, (Redrawn based on Refs. (6, 7)). Copyright (2007) with permission from Elsevier.

react with $CO_2^{\cdot-}$ or CO to generate hydrocarbons on Cu electrodes, the detailed reaction steps are question marks, as shown in Fig. 4.

Downloaded by OHIO STATE UNIV LIBRARIES on June 23, 2012 | http://pubs.acs.org
Publication Date (Web): December 3, 2010 | doi: 10.1021/bk-2010-1056.ch005

The crystal faces dominated by Cu(100) tend to result in a significant current efficiency for ethylene at relatively low overpotentials (*41*), one possible reason might be related to the hypothesized rate determining step in Fig. 7. Such step would require the π orbitals of the adsorbed CO to interact simultaneously with vibrational motions bringing the two oxygens close to Cu surface atoms. Such an intermediate state would be more likely with a right arrangement of surface atoms, preferably with wide Cu (100) terrace surfaces (see Fig. 7, ref (*7*, *41*)).

The crystal faces dominated by Cu(111) tend to be polarised to more negative potentials and favor methane production. The Cu(110) type surfaces polarise to the most negative potentials and result in other 2 carbon and 3 carbon product, such as acetic acid (*42*). The product partial currents for methane and ethylene at polycrystalline Cu, Cu(100), Cu(110) and Cu(111) electrodes generally followed the same trends (*7*).

The overall CO_2 reduction required a higher overpotential, and a greater difference in overpotentials was found between the different crystal faces. The results of single crystal studies show why the electrode preparation could have a strong influence on the results obtained. Metallic nanostructures will be expected to provide more opportunities in deliberately produce more advantageous crystalline (*43*, *44*), i.e. nanocube is rich in (100), thus, improving the productivity of long-carbon chain organic molecules from CO_2 reduction. In addition, it was found that no simple choice of rate determining steps from among reactions fit the data, it implies that shifting and/or parallel mechanisms operate, varying electrode preparation and possibly electrolyte compositions might change the mechanisms.

c. Surface Treatment and Cu Alloy Electrocatalysts

Surface treatments affect the activity and selectivity of CO_2 reduction on Cu catalysts (*45–47*). Formation of CH_3OH was reported at intentionally preoxidized Cu electrodes, and the maximum partial current of CH_3OH production reached 15 mA/cm^2 (*48*). However, other researchers did not detect CH_3OH from Cu electrodes oxidized in various manners (*46*). Steady formation of CH_3OH from Cu electrodes at a high current density has not yet been confirmed by other researchers to date (*6*).

Cu-based alloys have been investigated for CO_2 reduction. The modifications can be due to a combination of changes in the electronic structure and changes in the surface crystallographic characteristics, including the introduction of dislocations and vacancies, leading to major changes in the products distributions and reaction rates. Cu-Ni and Cu-Fe alloys, formed by in-situ deposition during CO_2 reduction, gradually lose CH_4 and C_2H_4 yields simultaneously with increased H_2 evolution with the increase of Ni or Fe coverage on the Cu surface (*49*). A Cu-Cd electrode produced CH_4 and C_2H_4. The yields gradually dropped with the increase of Cd coverage, but the CO formation increased (*47*). Watanabe et al. studied various Cu based alloys; Cu-Ni, Cu-Sn, Cu-Pb, Cu-Zn, Cu-Cd, and found that the major products are CO and $HCOO^-$. Surface Cu-Au alloy electrodes showed that the surface alloying severely suppresses the formation of hydrocarbons and alcohols, leading to the increase of CO formation (*14*).

Downloaded by OHIO STATE UNIV LIBRARIES on June 23, 2012 | http://pubs.acs.org
Publication Date (Web): December 3, 2010 | doi: 10.1021/bk-2010-1056.ch005

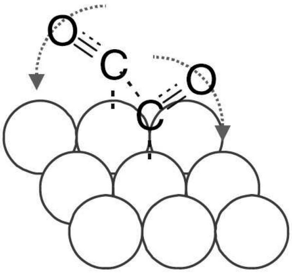

Figure 7. One possible mechanism for the catalysis of C_2H_4 formation on Cu (100) crystal (Ref. (7)). Copyright (2007) with permission from Elsevier.

2.5. Major Issues Associated with Aqueous CO_2 Reduction

Numerous researches have been carried out to investigate electrocatalytic reduction of CO_2 in aqueous phase and advanced the understanding of the reaction mechanisms. However, liquid phase CO_2 electrocatalytic reduction suffers from serious problems which are difficult to overcome:

1) Sluggish reaction kinetics: this leads to >1.0 V overpotential, which greatly increases the energy cost for electrolysis process.
2) Low selectivity of CO_2 reduction. CO_2 reduction and hydrogen evolution are two competitive reactions, hydrogen is inevitably a by-product accompanying with CO_2 reduction in aqueous electrolyte.
3) Formation of various by-products: they mainly remain in electrolyte solution and separation and recovery are high energy-cost.
4) Low solubility of CO_2 in aqueous electrolyte (≈ 0.08M): high pressures are normally needed to improve CO_2 transport.
5) Deactivation: the electrode catalysts loose their high initial selectivity and reactivity after a short period of operation.
6) Low tolerance to impurities and contaminations: The surface contamination and non-pure electrolyte will often lead to low productivity and selectivity of hydrocarbon products.

2.6. Gas Phase CO_2 Reduction Based on Gas Diffusion Electrode (GDE) and Solid Polymer Electrolyte (SPE)

An excellent alternative to CO_2 reduction in aqueous electrolyte is the use of GDEs and SPE (including cation exchange membrane (CEM) and anion exchange membrane (AEM)) for a continuous CO_2 reduction system which could enable considerable enhancements of mass transfer of CO_2 (*19–23*, *49–69*). GDE is a porous composite electrode developed for fuel cell technology, usually composed of Teflon bonded catalyst particles and carbon black. SPE membrane with GDE can provide gas phase electrolysis of CO_2. The acquired knowledge for CO_2 reduction over metal electrodes in aqueous electrolyte has been used to investigate the GDE/SPE-based electrolysis cells to convert CO_2 into usable fuels or syngas

H_2/CO, with reasonably good energy efficiencies. The main advances in this area are summarized as follow.

a. From CO_2 to Fuel Precursors (CO and H_2)

It is relatively easy to electrocatalytic reduce CO_2 to CO using the 2nd group metals (Table 1), such as Au, Ag, etc, or to reduce H_2O to H_2 (HER) using the 3rd group metals (Table 1), such as Ni, etc.

Yamamoto et al conducted CO_2 reduction and water oxidation in a CO_2-reducing electrolysis cell with Ni catalyst, 1/1 CO/H_2 gas ratio at a current density of 10 mA/cm^2 at a cell voltage of 3.05V was obtained, the overall energy efficiency is 44.6% (*49*).

Newman group has demonstrated a method for CO_2 and water reduction for making syngas (CO+H_2) operated at room temperature by employing GDEs embedded with an aqueous $KHCO_3$ (pH buffer) layer between the Au/Ag based cathode catalyst layer and the Nafion membrane (*4*, *55*). The schematic representation of the electrolysis cell is shown in Fig. 8. The cathode catalyst is Au or Ag, and the gas products are CO and H_2. Each catalyst was shown very selective for CO_2 reduction to CO at an overall current density of 20 mA/cm^2 for Ag and Au, respectively with the balance corresponding to H_2. A lower overpotential of 200 mV was observed on Au catalyst than Ag catalyst. As the overall current density efficiency increases, a decrease in CO current efficiency was observed, likely related to CO mass-transport limitation. Energy efficiency for the overall cell (with Pt-Ir as anode catalyst) is ca. 47% at 20 mA/cm^2 and decrease to ca. 32% at 100 mA/cm^2 for both catalysts, which is mostly due to joule heating losses. Their recent investigation show the CO partial current densities as high as 135 mA/cm^2 could be obtained for a short period based on supported Au catalyst (*4*). A CO/H_2 ratio of 1/2 was obtained, especially suitable for methanol synthesis, at a potential of ca. -0.2V vs SCE with a total current density of 80 mA/cm^2. Unfortunately, a decrease of catalyst selectivity for CO evolution with time has been identified as a critical technical issue (*55*).

b. From CO_2 to C_1-C_2 Fuels (Formic Acid, Methane and Ethylene)

An alternative possibility is to convert CO_2 to formic acid, that can be used as both fuels and chemicals. The ‘Formic Acid Economy’ was advocated by the UK government to promote sustainable energy development. Mahmood et al. demonstrated high rates of reduction of CO_2 to formic acid at Pb impregnated GDEs operated at 115 mA/cm^2 in aqueous acidic electrolytes (pH of 2) with a current efficiency of nearly 100% at an IR-corrected potential of 1.8 V (vs SCE) (*19*). Furuya et al. showed a current efficiency of 90% for the formation of formic acid at a GDE impregnated with Ru–Pd catalysts that can be obtained at the current density of 80 mAcm^2 (*22*).

The research efforts on CO_2 reduction to $C_{\leq 2}$ hydrocarbons (mainly methane and ethylene) using SPE cells were also studied. Hara et al. observed high

Downloaded by OHIO STATE UNIV LIBRARIES on June 23, 2012 | http://pubs.acs.org
Publication Date (Web): December 3, 2010 | doi: 10.1021/bk-2010-1056.ch005

Downloaded by OHIO STATE UNIV LIBRARIES on June 23, 2012 | http://pubs.acs.org
Publication Date (Web): December 3, 2010 | doi: 10.1021/bk-2010-1056.ch005

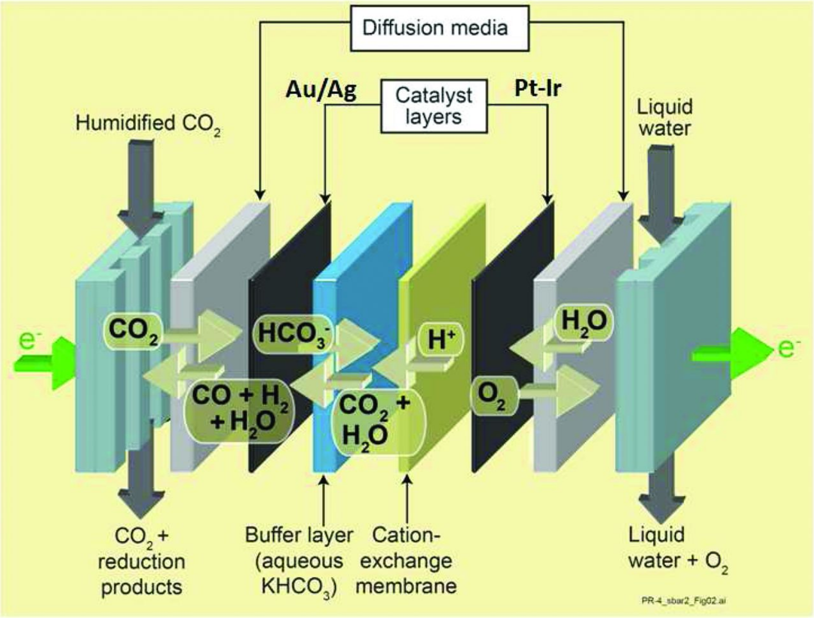
Diffusion media
Au/Ag
Catalyst layers
Pt-Ir
Humidified CO_2
Liquid water
e⁻
CO_2
HCO_3^-
H^+
H_2O
e⁻
CO + H_2 + H_2O
CO_2 + H_2O
O_2
CO_2 + reduction products
Buffer layer (aqueous $KHCO_3$)
Cation-exchange membrane
Liquid water + O_2
PR-4_sbar2_Fig02.ai

Figure 8. Schematic representation of an electrolysis cell for producing synthesis gas (CO + H_2) by reduction of CO_2 and H_2O. (Ref. (4)). (see color insert)

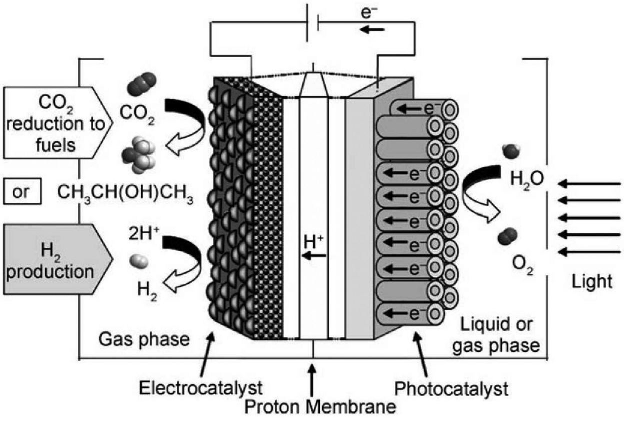
e⁻
CO_2 reduction to fuels
CO_2
or
$CH_3CH(OH)CH_3$
H_2 production
$2H^+$
H_2
H^+
e⁻
H_2O
O_2
Light
Gas phase
Liquid or gas phase
Electrocatalyst
Proton Membrane
Photocatalyst

Figure 9. A proposed photoelectrochemical (PEC) device for the CO_2 reduction to fuels and the H_2 production using solar energy. (Ref (70)) Copyright (2010) with permission from Wieley.

current density attainment up to 900 mA/cm_2 and 46% faradaic efficiency during the reduction of CO_2 with the formation of methane on the GDE using Pt electrocatalysts at increased CO_2 pressures of 50 atm (*21*). DeWulf et al. applied an SPE with Cu as the catalyst layer on a Nafion 115. CH_4 and C_2H_4 were produced, but the current density for CO_2 reduction dropped below 1 mA/cm^2 after 70 min electrolysis, which indicates a durability issue (*56*). Sammells et al.

prepared a Cu coated SPE electrode using a CEM Nafion 117, and they found CO_2 was reduced to C_2H_4 and C_2H_6 with the current density of 10 to 30 mA/cm^2 with the terminal voltage 1.5 to 3.5 V. The faradaic efficiency for CO_2 reduction remained < 10% (*57–59*). Kamatsu et al studied Cu deposited on cation exchange membrane (CEM, Nafion) and anion exchange membrane (AEM, Selemion) and found the total efficicencies for CO_2 reduction has maximum values of 19% and 27%, respectively. The use of CEM gave C_2H_4 as the major product, while, with use of AEM, the HCOOH and CO were obtained. It is also interesting to find that NO has no influence on the CO_2 reduction, but the removal of SO_2 is needed to obtain C_2H_4 on high current densities (*61*). The best results in term of hydrocarbon formation were reported using immobilized CuCl on Cu mesh electrodes, a Faradic efficiency of about 70% for ethylene was obtained, even if the presence of a fast deactivation (*60*).

Downloaded by OHIO STATE UNIV LIBRARIES on June 23, 2012 | http://pubs.acs.org
Publication Date (Web): December 3, 2010 | doi: 10.1021/bk-2010-1056.ch005

c. From CO_2 to Long-Chain Carbon Fuels

An ultimate goal for CO_2 cycling is direct reduction of CO_2 to liquid long-chain carbon fuels. It is still very challenging to achieve direct reduction CO_2 to such fuels based on current science and technology ability. Both the selectivity and productivity are very low and they are far from real applications.

It was reported that very small amount of parraffins and olefins up to C_6 hydrocarbons can be obtained in CO_2 electroreduction at room temperature and atmospheric pressure through commercially available Cu-electrode. Certain Cu-electrodes produce products in CO_2 electroreduction with a distribution as typically obtained in the Fischer–Tropsch reaction of syn-gas over heterogeneous Co- or Fe-based catalysts. The paraffin products fit to Schultz-Flory product distribution with an exception of olefins C_2H_4, which suggests that C_2H_4 is produced via another reaction path than chain propagation (*70*).

A new concept of photoelectrocatalytic (PEC) reactor was proposed in Fig. 9. At the anode, the water is photooxidized to oxygen and produce electrons and protons, which electrocatalytic reduce CO_2 to liquid fuels at the cathode (*71*). This concept was originally proposed by Hitachi Green Center researchers (*72*, *73*). Centi group reported Fe and Pt nanoparticles / carbon nanotubes (CNTs) exhibit encouraging electrocatalytic selectivity to CO reduction, the isopropanol can be the major product at a formation rate of 0.06 μmol.h^{-1}.cm^{-2} , besides CO and H_2 (Fig. 10 a). Other long carbon-chain hydrocarbons were detected in trace amounts.

It has been reported that the selectivity of CO_2 reduction to $C_{<2}$ hydrocarbons with the micropores of activated carbon fibers could be significantly enhanced, due to a special nanospace effect, which gives rise to a similar high-pressure-like effect at ambient pressure (*52*). As a unique support material, CNTs-based catalysts have demonstrated high activity and superior durability in low temperature fuel cell applications (*76–79*). The Bao group recently revealed that CNTs channels could provide an intriguing confinement environmental for Fisher-Tropsch synthesis (*80*, *81*). The strategy of design and preparation of catalysts could be widely applied to other gas-liquid reaction systems, such as CO_2 reduction to liquid fuels. As what Centi group demonstrated in their recent publications, the CNTs encapsulated Fe

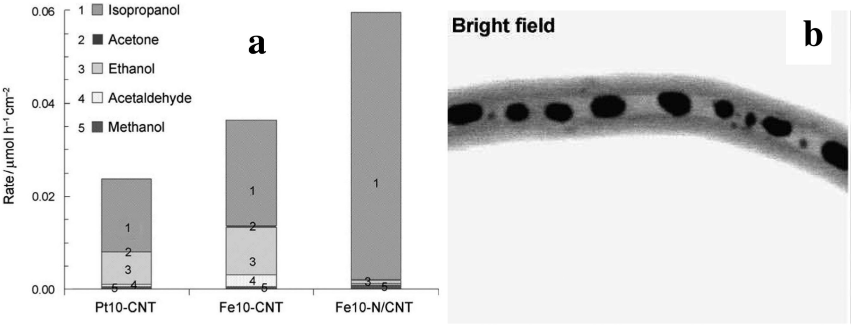

Figure 10. (a) Products distribution at 60°C in CO_2 reduction in gas phase over Nafion 117 cation exchange membrane /carbon cloth GDM electrode, (b) Fe encapsulated in CNTs. (Ref (24)) Copyright (2009) with permission from Elsevier.

nanoparticles (Fig. 10 b) can effectively promote long-carbon chain oxygenates, due to 'space-restriction' effect (*24*, *25*, *74*, *75*).

3. Conclusions and Future Directions

CO_2 is an extremely stable molecule generally produced by fossil fuel combustion and respiration, electrocatalytic approaches have potentials to direct convert CO_2 to small carbon chain fuels. The energy-efficient CO_2 reduction demand catalysts that can operate near thermodynamic potentials with high rate of electrochemical reaction. However, our current understanding on the reaction mechanisms is still very limited, and controllably returning CO_2 to useful carbon-fuels on the same scale as their current production rates is beyond our current scientific and technology ability. Conversion of CO_2 to liquid fuels and useful chemicals will require new methods and approaches for activating the CO_2 molecule. Novel complex catalysts and catalyst assemblies including hybrid catalysts, hierarchal nanostructured catalytic systems, and multi-site catalysts, that can work in concert, should be studied to achieve the overall efficient CO_2 reduction process.

It is imperative to advance our understanding of the reaction mechanisms of C-O bond cleavage and C-C and C-H bonds formation (especially for >2 carbon-chain molecules). Multi-step, multi-electron chemical transformations, coupled charge and atom transfer reactions are needed to be thoroughly investigated. At the mean time, developing advanced *in-situ* / *on-site* characterization tools under 'real' electrochemical operations is demanded to identify the key reaction intermediates and elucidate reaction pathways. The 'space-restriction effects' were discovered to change the reaction pathways, investigations on the interplay between various catalytic sites and catalyst environments in multifunctional catalysts are required. Extensive study on the model catalysts, including single crystal, atatom, and electro-deposited catalysts for CO_2 reduction have been carried out, bridging the gap between model catalysts and '*real-word'* nanostructured catalysts is highly demanded. Nano-techniques

Downloaded by OHIO STATE UNIV LIBRARIES on June 23, 2012 | http://pubs.acs.org
Publication Date (Web): December 3, 2010 | doi: 10.1021/bk-2010-1056.ch005

provide exciting opportunities in this area by precisely controlling the surface facets, morphologies and structures of multi-metal nanoparticles.

In the future, research efforts should also be focused on addressing the engineering issues related with design and construction of electrolysis cells and photoelectrocatalytic reactors, fabrication of electrodes, assembly of membrane electrode and solid electrolyte, etc. The efforts will help realize efficient CO_2 recycling processes and devices.

Acknowledgments

I acknowledge fruitful discussions with Drs. Overbury, Steve and Wu, Zili of Oak Ridge National Laboratory (ORNL). I also thank Michigan Technological University start-up fund (D90925) and research excellence fund – research seeds (RES-RS, E49236) for supporting this work.

References

1. Halmann, M. M.; Steinberg, M. *Green Gas CO_2 Mitigation*; CRC Press: Boca Raton, FL, 1999.
2. Socolow, R.; Pacala, S. *Science* **2004**, *305*, 968.
3. Song, C. S. *Catal. Today* **2006**, *115*, 2.
4. Bell, A. T. Basic Research Needs: Catalysis for Energy; Report from the U.S. Department of Energy, Basic Energy Sciences Workshop; 2007, p 69.
5. Frese, K. W., Jr. In *Electrochemical and Electrocatalytic Reactions of Carbon Dioxide*; Sullivan, B. P., Krist, K., Guard, H. E., Eds.; Elsevier: Amsterdam, 1993; p 145.
6. Hori, Y. Electrochemical CO_2 Reduction on Metal Electrodes. In *Modern Aspects of Electrochemistry*; Springer: New York, 2008; pp 89−189.
7. Gattrell, M.; Gupta, N.; Co, A. *J. Electroanal. Chem.* **2006**, *594*, 1.
8. Benson, E. E.; Kubiak, C. P.; Sathrum, A. J.; Smieja, J. M. *Chem. Soc. Rev.* **2009**, *38*, 89–99.
9. Hori, Y.; Kikuchi, K.; Suzuki, S. *Chem. Lett.* **1985**, 1695.
10. Hori, Y.; Kikuchi, K.; Murata, A.; Suzuki, S. *Chem. Lett.* **1986**, 897.
11. Hori, Y.; Murata, A.; Takahashi, R.; Suzuki, S. *Chem. Lett.* **1987**, 1665.
12. Hori, Y.; Wakebe, H.; Tsukamoto, T.; Koga, O. *Electrochim. Acta* **1994**, *39*, 1833.
13. Hori, Y.; Takahashi, R.; Koga, O.; Hoshi, N. *J. Phys. Chem. B.* **2002**, *106*, 15.
14. Watanabe, M.; Shibata, M.; Kato, Azuma, M.; Sakata, T. *J. Electrochem. Soc.* **1991**, *138*, 3382.
15. Katoh, A.; Uchida, H.; Shibata, M.; Watanabe, M. *J. Electrochem. Soc.* **1991**, *141*, 2054.
16. Azuma, M.; Hashimoto, K.; Hiramoto, M.; Watanabe, M.; Sakata *J. Electrochem. Soc.* **1990**, *137*, 1772.
17. Cook, R.; MacDuff, R. C.; Sammells, A. F. *J. Electrochem. Soc.* **1988**, 1320.
18. Lynch, F. E.; Marmaro, R. W. U.S. Patent 5,139,002, 1992.

Downloaded by OHIO STATE UNIV LIBRARIES on June 23, 2012 | http://pubs.acs.org
Publication Date (Web): December 3, 2010 | doi: 10.1021/bk-2010-1056.ch005

Downloaded by OHIO STATE UNIV LIBRARIES on June 23, 2012 | http://pubs.acs.org
Publication Date (Web): December 3, 2010 | doi: 10.1021/bk-2010-1056.ch005

19. Mahood, M. N.; Masheder, D.; Harty, C. J. *J. Appl. Electrochem.* **1987**, *17*, 1159.
20. Hara, K.; Kudo, A.; Sakata *J. Electroanal. Chem.* **1995**, *391*, 141.
21. Hara, K.; Kudo, A.; Sakata; Watanabe, M. *J. Electroanal. Chem.* **1995**, *342*, L57.
22. Furuya, N.; Yamazaki, T.; Shibata, M. *J. Electroanal. Chem.* **1997**, *431*, 39.
23. Lee, J.; Kwon, Y.; Machunda, R. L.; Lee, H. J. *Chem.-- Asian J.* **2009**, *4*, 1516.
24. Gangeri, M.; Perathoner, S.; Caudo, S.; Centi, G.; Amadou, J.; Begin, D.; Pham-Huu, C.; Ledoux, M. J.; Tessonnier, J. P.; Su, D. S.; Schlogl, R. *Catal. Today* **2009**, *143*, 57.
25. Venti, G.; Perathoner, S.; Wine, G.; Gangeri, M. *Green Chem.* **2007**, *9*, 671.
26. Dean, A. J. *Lange's Handbook of Chemistry*, 13th ed.; McGraw-Hill: New York, 1985; Vol. 6-2, pp 9-4−9-107.
27. Hori, Y.; Wakebe, T.; Tsukamoto, T.; Koga, O. *Electrochim. Acta* **1994**, *39*, 1833.
28. Jordan, J.; Smith, P. T. *Proc. Chem. Soc.* **1960**, 246.
29. Pacansky, J.; Wahlgren, U.; Bagus, P. S. *J. Chem. Phys.* **1975**, *62*, 2740.
30. Lamy, E.; Nadjo, L.; Savéant, J.-M. *J. Electroanal. Chem.* **1977**, *78*, 403.
31. Schwarz, H. A.; Dodson, R. W. *J. Phys. Chem.* **1989**, *93*, 409.
32. Surdhar, P. S.; Mezyk, S. P.; Armstrong, D. A. *J. Phys. Chem.* **1989**, *93*, 3360.
33. Hori, Y.; Suzuki, S. *Bull. Chem. Soc. Jpn.* **1982**, *55*, 660.
34. Aylmer-Kelly, A. W. B.; Bewick, A.; Cantrill, P. R.; Tuxford, A. M. *Faraday Discuss. Chem. Soc.* **1973**, *56*, 96.
35. Paik, W.; Andersen, T. N.; Eyring, H. *Electrochim. Acta* **1969**, *14*, 1217.
36. Buxton, G. V.; Sellers, R. M. *J. Chem. Soc., Faraday Trans. I* **1973**, *69*, 555.
37. Hori, Y.; Koga, O.; Yamazaki, H.; Matsuo, T. *Electrochim. Acta* **1995**, *40*, 2617.
38. Oda, I.; Ogasawara, H.; Ito, M. *Langmuir* **1996**, *12*, 1094.
39. Hori, Y.; Murata, A.; Takahashi, R.; Suzuki, S. *Chem. Commun.* **1988**, 17.
40. Watanabe, K.; Nagashima, U.; Hosoya, H. *Appl. Surf. Sci.* **1994**, *75*, 121.
41. Hori, Y.; Takahashi, I.; Koga, O.; Hoshi, N. *J. Mol. Catal. A: Chem.* **2003**, *199*, 39.
42. Takahashi, I.; Koga, O.; Hoshi, N.; Hori, Y. *J. Electroanal. Chem.* **2002**, *533*, 135.
43. Astruc, D. In *Transition-Metal Nanoparticles in Catalysis*; Astruc, D., Ed.; Wiley-VCH: Weinheim, Germany, 2007; Vol. 1, p 1.
44. Somorjai, G. A.; Tao, F.; Park, J. Y. *Top. Catal.* **2008**, *47*, 1.
45. Kim, J. J.; Summers, D. P.; Frese, K. W., Jr. *J. Electroanal. Chem.* **1988**, *245*, 223.
46. Koga, O.; Nakama, K.; Murata, A.; Hori, Y. *Denki Kagaku* **1989**, *57*, 1137.
47. Kyriacou, G.; Anagnostopoulos, A. *J. Electroanal. Chem.* **1992**, *322*, 233.
48. Frese, K. W., Jr. *J. Electrochem. Soc.* **1991**, *138*, 3338.
49. Yamamoto, T.; Tryk, D. A.; Fujishima, A.; Phata, H. *Electrochim. Acta* **2002**, *47*, 3327.

50. Sanchez-Sanchez, C. M.; Montiel, V.; Tryk, D. A.; Aldaz, A.; Fujishima, A. *Pure Appl. Chem.* **2001**, *12*, 1917.
51. Tryk, D. A.; Yamamoto, T.; Kokubun, M.; Hirota, K.; Hashimoto, K.; Okawa, M.; Fujishima, A. *Appl. Organomet. Chem.* **2001**, *15*, 113.
52. Yamamoto, M.; Tryk, D. A.; Hashimoto, K.; Fujishima, A.; Okawa, M. *J. Electrochem. Soc.* **2000**, *147*, 3393.
53. Yamamoto, T.; Hirota, K.; Tryk, D. A.; Hashimoto, K.; Fujishima, A.; Okawa, M. *Chem. Lett.* **1998**, 825.
54. Magdesieva, T. V.; Yamamoto, T.; Tryk, D. A.; Fujishima, A. *J. Electrochem. Soc.* **2002**, *149*, D89.
55. Dealacout, C.; Ridgway, P. L.; Kerr, J. B.; Newman, J. *J. Electrochem. Soc.* **2008**, *155*, 42.
56. DeWulf, D. W.; Bard, A. J. *Catal. Lett.* **1988**, *1*, 73.
57. Cook, R. L.; MacDuff, R. C.; Sammells, A. F. *J. Electrochem. Soc.* **1990**, *137*, 607.
58. Cook, R. L.; MacDuff, R. C.; Sammells, A. F. *J. Electrochem. Soc.* **1988**, *135*, 1470.
59. Cook, R. L.; MacDuff, R. C.; Sammells, A. F. *J. Electrochem. Soc.* **1990**, *137*, 187.
60. Hori, Y.; Konishi, H.; Futamura, T.; Murata, A.; Koga, O.; Sakurai, T.; Ohta, K *Electrochim. Acta* **2005**, *50*, 5354.
61. Komatsu, S.; Tanaka, M.; Okumura, A.; Kunugi, A. *Electrochim. Act.* **1995**, *40*, 745.
62. Hara, K.; Sakata, T. *Anal. Sci. Technol.* **1995**, *8*, 683.
63. Hara, K.; Sakata, T. *Bull. Chem. Soc. Jpn.* **1997**, *70*, 571.
64. Hori, Y.; Ito, H.; Okano, K.; Nagasu, K.; Sato, S. *Electrochim. Act.* **2003**, *48*, 2651.
65. Hori, Y.; Murata, A.; Ito, S.; Yoshinami, Y.; Koga, O. *Chem. Lett.* **1989**, 1567.
66. Shibata, M.; Yoshida, K.; Furuya, N. *J. Electrochem. Soc.* **1998**, *145*, 595.
67. Shibata, M.; Furuya, N. *J. Electroanal. Chem.* **2001**, *507*, 177.
68. Shibata, M.; Furuya, N. *Electrochim. Act.* **2003**, *48*, 3953.
69. Ikeda, S.; Ito, T.; Azuma, K.; Ito, K.; Noda, H. *Denki Kagaku* **1995**, *65*, 303.
70. Shibata, H.; Moulijn, J.; Mul, G. *Catal. Lett.* **2008**, *123*, 186.
71. Centi, G.; Perathoner, S. *ChemSusChem* **2010**, *3*, 195.
72. Doi, R.; Ichikawa, S.; Hida, H. Patent JP P08296077, 1995.
73. Ichikawa, S.; Doi, R. *Catal. Today* **1996**, *27*, 271.
74. Centi, G.; Perathoner, S. *Catal. Today* **2009**, *148*, 191.
75. Centi, G.; Perathoner, S. *Catal. Today* **2010**, *150*, 151.
76. Li, W.; Liang, C.; Qiu, J.; Zhou, W.; Han, H.; Wei, Z.; Sun, G.; Xin, Q. *Carbon* **2002**, *40*, 791–794.
77. Li, W.; Liang, C.; Zhou, W.; Qiu, J.; Zhou, Z.; Sun, G.; Xin, Q. *J. Phys. Chem. B* **2003**, *107*, 6292–6299.
78. Li, W.; Wang, X.; Chen, Z.; Waje, M.; Yan, Y. *J. Phys. Chem. B* **2006**, *110*, 15353–15358.
79. Wang, X.; Li, W.; Chen, Z.; Waje, M.; Yan, Y. *J. Power Sources* **2006**, *158*, 154–159.

Downloaded by OHIO STATE UNIV LIBRARIES on June 23, 2012 | http://pubs.acs.org
Publication Date (Web): December 3, 2010 | doi: 10.1021/bk-2010-1056.ch005

80. Pan, X.; Fan, Z.; Chen, W.; Ding, Y.; Luo, H.; Bao, X. *Nat. Mater.* **2008**, *6*, 507.
81. Pan, X.; Bao, X. *Chem. Commun.* **2008**, 6271.

Downloaded by OHIO STATE UNIV LIBRARIES on June 23, 2012 | http://pubs.acs.org
Publication Date (Web): December 3, 2010 | doi: 10.1021/bk-2010-1056.ch005

Downloaded by DUKE UNIV on June 23, 2012 | http://pubs.acs.org
Publication Date (Web): December 3, 2010 | doi: 10.1021/bk-2010-1056.ch006

Chapter 6

CO_2 Chemistry at Nankai Group: Catalytic Conversion of CO_2 into Value-Added Chemicals

Liang-Nian He,* Zhen-Zhen Yang, An-Hua Liu, and Jian Gao

Institute of Elemento-Organic Chemistry, Nankai University, Weijin Rd. 94,
Tianjin 300071, P. R. China
***Email:heln@nankai.edu.cn**

Carbon dioxide is very attractive as a typical renewable feedstock for manufacturing commodity chemicals, fuels and materials since it is an abundant, nontoxic, nonflammable and easily available carbon resource. In this context, development of catalytic methodologies for chemical transformation of CO_2 into useful compounds is of paramount importance from a standpoint of C1 chemistry and green chemistry. Great efforts have been directed towards constructing C-C, C-O and C-N bond on the basis of CO_2 activation through molecular catalysis owing to its kinetic and thermodynamic stability. The aim of this chapter is to demonstrate the versatile use of CO_2 in organic synthesis, with the main focus on utilization of CO_2 as a building block for synthesis of industrial useful compounds such as cyclic carbonates, oxazolidinones, lactones, quinazolines, etc. The potential use of dense CO_2 as an alternative solvent and otherwise specific roles in organic synthesis are also evaluated. The most results presented herein could be based on our recent research work on CO_2 chemistry.

Carbon Dioxide Chemistry

CO_2 as an abundant, typical renewable C1 source as well as an important "greenhouse" gas has been drawing more and more attention. And chemists may often think what we can do with CO_2 from a scientific and engineering point of view? Obviously, CO_2 capture and storage looks particularly effective for temporarily preserving large volumes of CO_2 (*1*). To our delight, a great progress

In Advances in CO2 Conversion and Utilization; Hu, Y.;
ACS Symposium Series; American Chemical Society: Washington, DC, 2010.

has been seen on chemical utilization of CO_2 as an alternative to phosgene and/or carbon monooxide in organic synthesis. In general, potential uses of CO_2 as a raw material, as a sound green solvent, or as a Lewis acid catalyst or tunable reagent could offer profound advantages for both green chemistry and improved economics in terms of creating novel chemistry, reaction control, product separation, and operation simplification. CO_2 can be regarded as an abundant and readily accessed atmospheric gas that could, in principle, be useful synthon for organic compounds. However, its inherent thermodynamic stability and kinetic inertness hinder the development of metal catalysts that achieve CO_2 activation and functionalization. In this regards, the formation of a transition metal-CO_2 complex via direct coordination is one of the most powerful ways to induce the inert CO_2 molecule to undergo chemical reactions. However, only weak interactions between CO_2 and the active catalytic centre are sufficient to bring about catalytic reactions involving the insertion of CO_2. Accordingly, only if we understand the underlying principles of CO_2 activation can the goal of using CO_2 as an environmentally friendly and economically feasible source of carbon be achieved. In this chapter, we would like to illustrate potential applications of CO_2 in the synthesis of heterocyclic compounds and industrial useful chemicals, mainly based on our recent work performed at Nankai University. Those findings summarized herein would open synthetic pathways for the selective synthesis of heterocycles such as cyclic carbonates and oxazolidinones as well as industrial important compounds from CO_2 and demonstrate that such CO_2 functionalization with high energy starting material like epoxides is easily operative. CO_2 chemistry disclosed herein will stimulate further interest in research that may lead to the development of CO_2 as a new source for a wide set of value-added organic compounds like solvents, fuels, fine/bulk chemicals, pharmaceuticals and ploymers.

Downloaded by DUKE UNIV on June 23, 2012 | http://pubs.acs.org
Publication Date (Web): December 3, 2010 | doi: 10.1021/bk-2010-1056.ch006

Synthesis of Cyclic Carbonates from Epoxides and CO_2

Currently, organic carbonates and oxazolidinones are valuable products with wide applications in industry. In particular, five-membered cyclic carbonates, as one of the most important classes of heterocycles starting from CO_2, have found extensive applications such as polar aprotic solvents, intermediates for organic and polymeric synthesis, chemical ingredients for pharmaceutical/fine chemicals in biomedical applications, and electrolytic elements of lithium secondary batteries (*2*). The carboxylation of epoxides/aziridine with CO_2 is one of the most promising and eco-friendly methods for chemical conversion of CO_2 into cyclic carbonates and oxazolidinones or corresponding polymers. During the past several years, great efforts have been devoted to producing cyclic carbonate by using CO_2 as a replacement of the conventional phosgene route. The significance of this research topic could also be embodied by the recent emerged reviews on preparation and applications of five-membered cyclic carbonates (*3*, *4*). Herein, the synthetic pathways to five-membered cyclic carbonates from CO_2 are classified according to the initial substrates as summarized in Scheme 1.

Downloaded by DUKE UNIV on June 23, 2012 | http://pubs.acs.org
Publication Date (Web): December 3, 2010 | doi: 10.1021/bk-2010-1056.ch006

The ring expansion of epoxides with CO_2 to produce five-membered cyclic carbonates, which has been industrialized since the 1950s, represents one of the most promising methodologies for chemical fixation of CO_2 with high selectivity, high yield, and full atom-efficiency. Various kinds of catalysts have been developed to achieve higher catalyst performance at lower CO_2 pressure, recover and reuse the catalyst, and perform asymmetric reactions. On the basis of understanding and insight into the reaction mechanism at molecule level, the ideal catalysts would be a kind of bifunctional ones with both Lewis acid and Lewis base group in one molecule. Homogeneous catalysts, mainly including onium salts, metal complexes, ionic liquids (ILs), and multi-component bifunctional catalysts (*5*–*9*), generally show high catalyst performance.

In general, an additive is commonly required to achieve high efficiency by employing metal(salen) catalysts for the reaction. To our delight, we have recently found a bifunctional cobalt-salen complex containing a Lewis acidic metal center and a quaternary phosphonium salt unit anchored on the ligand that effectively catalyzes the synthesis of cyclic carbonates from CO_2 and epoxides under mild conditions without the utilization of additional organic solvents or co-catalysts/additives (Scheme 2) (*10*). The effects of various reaction variables on the catalytic performance were studied in detail, indicating an optimized reaction temperature of about 100 °C and CO_2 pressure of around 4 MPa. Furthermore, the reaction proceeds smoothly even at pressures as low as 2 MPa. The catalyst is applicable to a variety of epoxides, producing the corresponding cyclic carbonates in good yields in most cases. In addition, the catalyst can be easily recovered and reused several times without significant loss of its catalytic activity. This process thus represents a greener pathway for the environmentally benign chemical fixation of CO_2 to produce cyclic carbonates. Recently, the cyclic carbonates can be synthesized under atmospheric pressure of CO_2 and room temperature catalyzed by one-component catalysts based on metal(salen) complexes (*11*).

It is practical using chiral metal-salen catalysts for producing optically active cyclic carbonates from the racemic epoxides and CO_2. Following the first report by Lu and co-workers of a convenient route to optically active cyclic carbonates through a catalytic kinetic resolution process catalyzed by simple and highly efficient chiral salenCo-(III)/quaternary ammonium halide systems under solvent-free and extremely mild conditions (*12*), there are only a few reports available in this area (*13*). Very recently, a novel catalytic system comprising salen-Co(OAc)/CIL (CIL: chiral ionic liquid) has been developed for the asymmetric cycloaddition of CO_2 to epoxide under very mild conditions (Scheme 3) (*14*). Several chiral ionic liquids of TBAX (X = amino acidic anions, tartaric acidic anions, lactic acidic anion) have been synthesized and tested for the reaction. Moreover, it has been found that the chiral catalyst salen-Co(OAc) and chiral co-catalyst of CIL work together in an additive or a synergistic manner. The same absolute configurations would induce a higher *ee* of chiral propylene carbonate (PC); whereas the opposite absolute configurations result in a lower *ee* of chiral PC.

In current processes employed by industry and in academia, a homogeneous catalyst is undesirably dissolved in a phase containing cyclic carbonate. Thus, it is required to separate the catalyst from the product through a purification process such as distillation after completion of the reaction, thus resulting in complicated production processes, and possible decomposition of the catalyst or formation of by-products during the separation step. In order to facilitate the separation of the catalyst, several efficient recycling concepts have been successfully applied to the cycloaddition reaction.

One strategy would be heterogenization of homogeneous catalysts. Supporting chemically or physically ammonium salts or ionic liquids onto a polymer, silica, MCM-41, and MOF-5 (metal-organic frameworks) (*15–21*) is regarded as an effective methodology to prepare solid catalysts for the cycloaddition reaction. It is noteworthy that using silica-supported onium salts or imidazolium-based ionic liquids not only provide ease of catalyst separation but also offer improved catalytic activity. Binding onium salts with silica *via* covalent bonds is more effective than physically mixing both the catalytic species and the support. The synergistic effect stemming from the silanol group of silica would presumably account for the catalytic activity enhancement of the heterogenized catalysts in terms of the reaction mechanistic consideration at molecule level (*22*).

Our previous work shows that one type of polystyryl supported catalysts containing ammonium salt or amino group (*17*), and silica supported ammonium salts and silica supported imidazolium-based ionic liquids (*19*) as well as a functionalized biopolymer chitosan-supported quaternary ammonium salt (abbreviated as CS-N^+R_3X) (*16*), are efficient and reusable heterogeneous catalysts for the synthesis of PC from propylene oxide (PO) and CO_2 under supercritical CO_2 ($scCO_2$) conditions without any additional organic solvent (Scheme 4). The almost quantitative yield together with excellent selectivity is obtained. The purity of product directly separated out by filtration from the reaction mixture in a batch reactor, reaches more than 99.3%. The catalyst is then recovered and reused in subsequent cycles. The process represents a simple, ecologically safer, cost-effective approach to cyclic carbonates from epoxides and CO_2.

Very recently, Cheng and co-workers (*23*) disclosed an impressive method for catalyst separation by magnetic force. The magnetic nanoparticle supported ionic liquid catalysts demonstrated high activity at lower CO_2 pressure, which is comparable with that of the ionic liquids itself. Furthermore, the catalysts could be easily recycled using a magnetic force and reused for up to 11 times with essentially no loss of activity. In general, heterogeneous catalyst possesses the merit of easy separation, but the catalyst performance dropped off in most cases. To preserve the benefits of a homogeneous catalyst while co-opting the primary benefits of a heterogeneous catalyst, an appealing methodology so-called "homogeneous reaction, heterogeneous separation" process has been employed for the cycloaddition reaction.

Sakakura and coworkers (*24*) developed an efficient procedure for recycling homogeneous catalyst. The $scCO_2$-soluble polyfluoroalkyl phosphonium iodides Rf_3RPI (Rf = $C_4F_9C_2H_4$, $C_6F_{13}C_2H_4$, $C_8F_{17}C_2H_4$; R = Me, Rf)-catalyzed PC synthesis from PO and CO_2 under $scCO_2$ conditions, where PC is spontaneously separated out of the $scCO_2$ phase. The Rf_3RPI catalyst could be recycled with maintaining a high CO_2 pressure and temperature by separating the PC from the

Downloaded by DUKE UNIV on June 23, 2012 | http://pubs.acs.org
Publication Date (Web): December 3, 2010 | doi: 10.1021/bk-2010-1056.ch006

Downloaded by DUKE UNIV on June 23, 2012 | http://pubs.acs.org
Publication Date (Web): December 3, 2010 | doi: 10.1021/bk-2010-1056.ch006

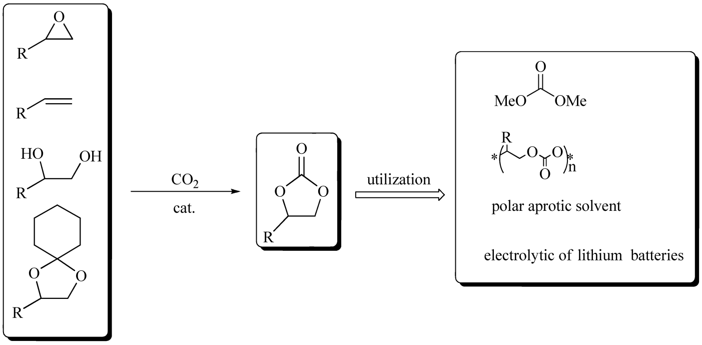

Scheme 1. Various routes to cyclic carbonates.

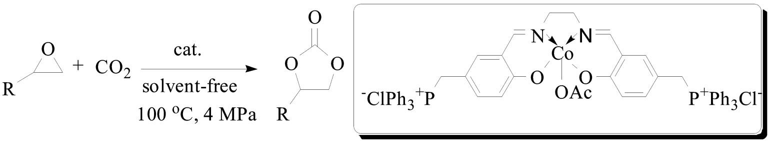

Scheme 2. A Co catalyst with no co-catalyst for the cycloaddition reaction of CO_2 and epoxide.

bottom of the reactor followed by supplying PO and CO_2 to the upper $scCO_2$ phase in which the Rf_3RPI remained as depicted in Figure 1.

We adopted a CO_2-philic polymer as a support to design the CO_2-expandable polymer supported catalysts such that the supported catalyst could be dissolved partially or expanded during the reaction in $scCO_2$, subsequently could be separated by filtration completely (*9*, *10*, *15*). PEG and its derivatives are known to be inexpensive, thermally stable, recoverable, have almost negligible vapor pressure, toxicologically innocuous and environmentally benign media for chemical reactions. In this context, they are regarded as good candidates of CO_2-philic supports. Several kinds of onium or guanidinium bromide functionalized-PEG are synthesized and proved to be a highly effective homogeneous catalyst for the eco-friendly synthesis of cyclic carbonates from CO_2 and epoxides under mild conditions (Scheme 5), which requires no additional organic solvents or co-catalyst. Notably, it has been found that there is a pronounced cooperative effect between the catalyst part and the support. The enhancement of catalyst performance by grafting active molecular catalyst on soluble PEG is presumably attributed to the benefits from changes in the physical properties of the reaction mixture, such as lower melting points, lower viscosity, high diffusion rates, and increased solubility for PO and CO_2 through 'CO_2-expansion of a liquid' effect. Indeed, as judged by visual inspection through a window-equipped high-pressure reactor, PEG and its derivatives are shown to be expandable with CO_2. Moreover, the catalyst is able to be reused with retention of high catalytic activity and selectivity. This process looks promising as a strategy for homogeneous catalyst recycling.

Downloaded by DUKE UNIV on June 23, 2012 | http://pubs.acs.org
Publication Date (Web): December 3, 2010 | doi: 10.1021/bk-2010-1056.ch006

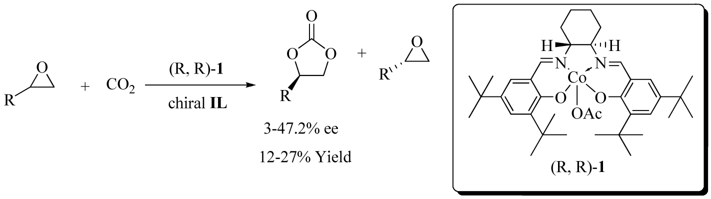
(R, R)-1
chiral IL
3-47.2% ee
12-27% Yield
(R, R)-1

Scheme 3. Chiral Co-salen induced asymmetric version of the cycloaddition.

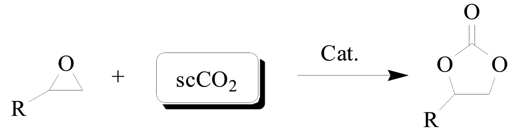

Cat.: R_4NX/SiO_2; ILs/SiO_2; $R_3N^+X^-$polystyrene; CS-$N^+R_3X^-$

Scheme 4. Cyclic carbonate synthesis catalyzed by the supported catalsyt.

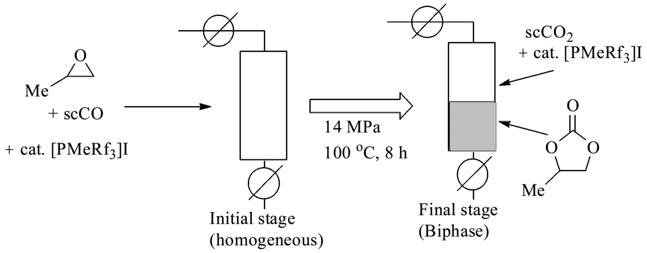
+ scCO
+ cat. [PMeRf3]I
14 MPa
100 °C, 8 h
scCO2
+ cat. [PMeRf3]I
Initial stage
(homogeneous)
Final stage
(Biphase)

Figure 1. Homogeneous catalyst recycling by using CO2-soluble catalyst.

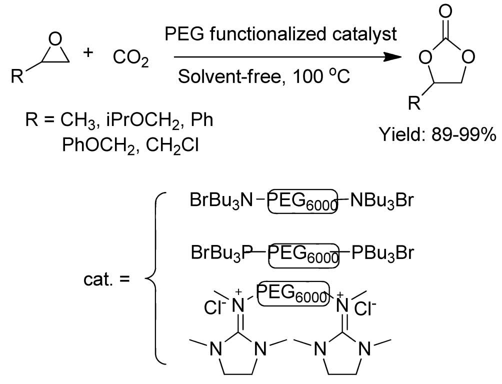
PEG functionalized catalyst
Solvent-free, 100 °C
R = CH3, iPrOCH2, Ph
PhOCH2, CH2Cl
Yield: 89-99%
cat. =
BrBu3N-PEG6000-NBu3Br
BrBu3P-PEG6000-PBu3Br
PEG6000

Scheme 5. Synthesis of cyclic carbonates catalyzed by the functionalized-PEG.

Synthesis of Cyclic Carbonates from Olefins and CO_2

As described above, the cycloaddition of epoxide with CO_2 is one of the most promising methodologies for CO_2 incorporation to synthesize the five-membered cyclic carbonates. However, such a cycloaddition generally requires the initial synthesis of an epoxide, which involves toxic or costly reagents and needs tedious

Downloaded by DUKE UNIV on June 23, 2012 | http://pubs.acs.org
Publication Date (Web): December 3, 2010 | doi: 10.1021/bk-2010-1056.ch006

workup for separation. Therefore, a more promising approach would be direct synthesis of cyclic carbonates from olefins instead of epoxides, a so-called one-pot "oxidative carboxylation" of olefin utilizing CO_2 as a building block. Generally, there are three accesses to cyclic carbonate via direct carboxylation of olefins with CO_2 (*25–27*) as illustrated in Scheme 6.

Based on the advancement in this field and inspired by the biomimetic oxybromination, a binary catalyst system composed of sodium phosphotungstate and *n*-Bu_4NBr was developed for facile synthesis of styrene carbonate in a single operation from styrene and CO_2 using 30 % H_2O_2 as an oxidant with an aid of an inorganic base as a "CO_2-activator" or "deprotonation reagent" (*28*). Notably, the presence of a base like $NaHCO_3$ markedly improves the formation of styrene carbonate. Interestingly, an oxidized product *i.e.* phenacyl benzoate could be obtained exclusively in good yield directly from styrene in the absence of CO_2 under the appropriate reaction conditions (Scheme 7). This methodology is easily found to be applicable to several styrene derivatives, producing the corresponding cyclic carbonates. It is worth mentioning that the catalyst system can be recovered and reused with excellent activity. On the other hand, this finding represents a simpler and cost-effective pathway for the environmentally benign chemical fixation of CO_2 to produce cyclic carbonates and also offers a practical methodology to the synthesis of benzoate derivatives.

Cyclic Carbonates from 1,2-Diols and CO_2

Dibutyltin oxide (Bu_2SnO) or dibutyltin dimethoxide ($Bu_2Sn(OMe)_2$) can be used as a remarkable selective catalyst for the synthesis of PC from propylene glycol (PG) and CO_2 in supercritical conditions using N,N-dimethylformamide (DMF) as solvent. Under the optimized conditions, the amount of PC was nearly proportional to PG concentration. The use of DMF as a co-solvent in this study significantly enhanced the catalytic activity, and the ketals as dehydrating agents greatly improved the yield of PC. As for mechanistic consideration, CO_2 is likely to insert into the metal-oxygen bond. As shown in Scheme 8, the possible mechanism for Bu_2SnO catalyzed PC synthesis from PG and CO_2 is proposed. The key intermediates **a**, **b** or analog of **b** in the catalytic cycle are successfully characterized by IR and Solid State Cross-Polarization Magic Angle Spinning ^{13}C NMR analysis. Furthermore, low toxic magnesium and its oxide are also proved to be a catalyst for highly selective synthesis of PC through the carbonylation of PG with CO_2 without any organic solvents or additives. Interestingly, the catalyst is demonstrated to be applicable to a variety of 1, 2-diols such as glycol, phenyl glycol, and methanol, forming the corresponding carbonates in 100% selectivity (*29*, *30*). As a result, employing a low toxic and cheap catalyst could make PC synthesis much environmentally friendlier.

Organic bases, such as 1,5,7-triazabicyclo[4.4.0]dec-5-ene (TBD), DBU (1,8-diazabicyclo[5.4.0]undec-7-ene) and triethylamine (TEA) can be also used as effective catalysts for the synthesis of PC from PG and CO_2 in the presence of acetonitrile. Acetonitrile in the reaction would act as not only the solvent but also the dehydrating reagent to remove the water produced from the reaction. With

In Advances in CO2 Conversion and Utilization; Hu, Y.;
ACS Symposium Series; American Chemical Society: Washington, DC, 2010.

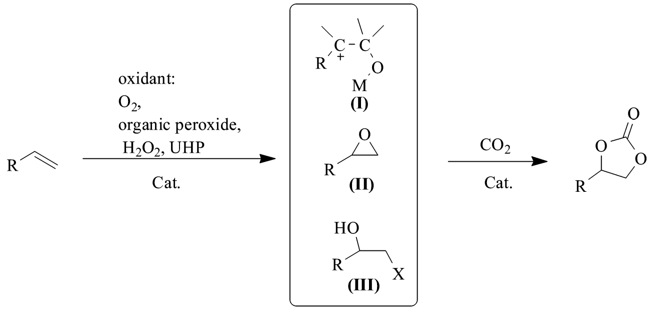
oxidant:
O_2,
organic peroxide,
H_2O_2, UHP
Cat.
(I)
(II)
(III)
CO_2
Cat.

Scheme 6. Direct synthesis of cyclic carbonate from alkenes and CO_2.

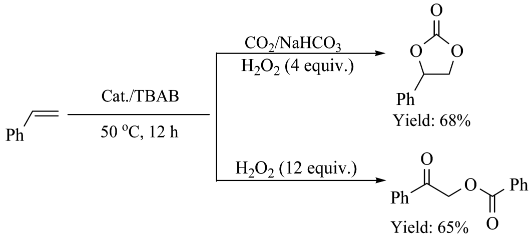
Cat./TBAB
50 °C, 12 h
CO_2/$NaHCO_3$
H_2O_2 (4 equiv.)
Yield: 68%
H_2O_2 (12 equiv.)
Yield: 65%

Scheme 7. The CO_2/H_2O_2-tunable reaction.

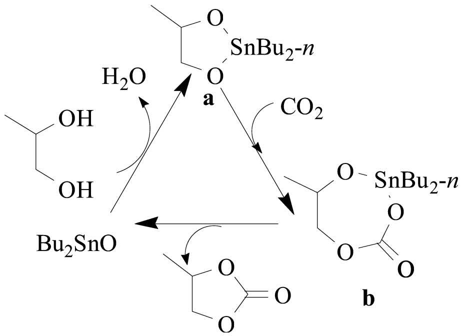
H_2O
a
CO_2
Bu_2SnO
b

Scheme 8. A postulated mechanism for the Bu_2SnO-catalyzed reaction.

TBD as the catalyst, the yield of PC could reach 15.3% with the selectivity of 100% under the optimal conditions.

Cyclic Carbonate from Vicinal Halohydrin and CO_2

With increasing regulatory pressure on using organic solvents, the development of environmentally benign process is so desirable that various kinds of alternative solvents such as $scCO_2$, fluorous media, ionic liquid, and water have been explored as well as solvent-free processes (*31*). Furthermore, one of the key areas of Green Chemistry is the elimination of solvents in chemical processes or the replacement of hazardous solvent with environmentally benign one.

Downloaded by DUKE UNIV on June 23, 2012 | http://pubs.acs.org
Publication Date (Web): December 3, 2010 | doi: 10.1021/bk-2010-1056.ch006

Downloaded by DUKE UNIV on June 23, 2012 | http://pubs.acs.org
Publication Date (Web): December 3, 2010 | doi: 10.1021/bk-2010-1056.ch006

Recently, we have reported an environmentally benign synthesis of styrene carbonate directly from styrene and CO_2 catalyzed by a binary system composed of sodium phosphotungstate and *n*-Bu_4NBr using 30% H_2O_2 as an oxidant (*28*). In terms of mechanistic consideration, a bromohydrin is assumed to be an intermediate in the single operation, thereby leading to the formation of cyclic carbonate with the aid of a base. We envisaged that there would be an alternative route to cyclic carbonate through the coupling of halohydrin and CO_2, whereby avoiding the pre-preparation of epoxides. Indeed, Venturello et al. found that the reaction of halohydrin with tetramethylammonium hydrogen carbonate in acetonitrile was preferentially carried out under a CO_2 atmosphere.

Very recently, Kawanami and Ikushima (*32b*) published the results on such a subject that organic carbonates were successfully prepared from vicinal halohydrins and CO_2 in the presence of sodium hydroxide using the ionic liquids as the reaction media at 120 °C and CO_2 pressure of 20 MPa. In continuation of our work on the development of practical synthetic methodologies and green process for organic carbonates and their derivatives using CO_2 as a synthon through molecular activation (*16*), PEG in this work proved to be an efficient reaction medium for the reaction of vicinal halohydrin with CO_2 in the presence of a base to synthesize cyclic carbonates as shown in Scheme 9. Notably, PEG-400 as an environmentally friendly solvent exhibits a unique character on the reactivity compared with conventional organic solvents. And various cyclic carbonates in high yields were prepared employing this protocol. This process presented here could show much potential application in industrial production of cyclic carbonates due to its simplicity, cost benefit, readily available starting materials, and mild reaction conditions.

In summary, the advantages of using PEG-400 as the reaction medium in the present study could be outlined as follows besides its environmentally benign characters. Firstly, it is assumed that PEG-400 can form complexes through coordinating the potassium cation as the crown ether does, thus resulting in increasing basicity of K_2CO_3 (*33*). Secondly, the "CO_2-expansion of PEG" effect (*34*) leads to the changes in the physical properties of the reaction mixture, such as lowered viscosity, increased gas/liquid diffusion rates and solubility for the reactants, thereby improving the synthetic process. Thirdly, another merit of using PEG as a reaction media would be especially beneficial for product separation. In a typical experiment, cyclic carbonates were separated by extraction. We have developed a viable alternative protocol for cyclic carbonates synthesis from vicinal halohydrins and CO_2 employing PEG-400 as a promising reaction medium. High yield of cyclic carbonates together with excellent selectivity was achieved under mild reaction conditions. Moreover, the product can be easily separated by extraction. We feel that this would be a cost effective route to cyclic carbonate in an environmentally friendly manner.

Synthesis of Oxazolidinones from Aziridines and CO_2

Aziridines, as a nitrogen analogue of epoxides, could react with CO_2 to afford the corresponding oxazolidinones (Scheme 10). Numerous catalyst systems like iodine, metal halide, Lewis acid/base dual component system, (salen)-Cr(III)/DMAP, quaternary ammonium salt have been developed for the coupling of aziridines and CO_2. Based on the conception of Lewis acid/base catalyzed mechanism, many catalysts for the cycloaddition of epoxides and CO_2 can also be developed for this reaction. For example, phenol/DMAP, (salen)-Cr(III)/DMAP and ammonium salt (*35*) are active for the carboxylation of aziridines with CO_2. The electrochemical approch involving nickel-catalyzed CO_2 incorporation into aziridines can work well under mild reaction conditions (CO_2 pressure of 1 atm, 20 °C) (*36*).

Although various catalysts have been found for this process, the development of high efficiency, eco-friendly single component catalyst is still very attractive. Meanwhile, catalyst recovery is also an important issue to be addressed. We developed an efficient and recyclable PEG supported ammonium bromide as a catalyst for high selective synthesis of 5-substituted oxazolidinones from CO_2 and various aziridines without any added organic solvents or co-catalysts (Scheme 9, (1)) (*35*). It is also found that selective formation of 5-substituted oxazolidinone or 4-substituted isomer relies on substituent at the carbon of the substrate. One of the salient features of this protocol would be that the catalyst can be readily recovered by centrifugation and reused with retention of high catalytic activity and both chemo- and regioselectivities.

Zirconyl chloride as an efficient, simple, and environmentally friendly solid catalyst has been evaluated for the synthesis of 5-aryl-2-oxazolidinones without any solvent and additive (*35c*). Furthermore, the catalyst could be easily separated by filtration and reused for at least five times. The catalytic system offers salient advantages and features: (1) it requires no organic solvent; (2) the catalyst is very effective under mild conditions; (3) the catalyst is moisture-stable, cheap and has low toxicity, is easily handled, and readily available; (4) excellent yields, regio-, and stereoselectivities toward the target products are attained; (5) simple workup procedure; (6) the utility of this method is proven as evidenced from synthesizing various 5-aryl-2-oxazolidinones.

Downloaded by DUKE UNIV on June 23, 2012 | http://pubs.acs.org
Publication Date (Web): December 3, 2010 | doi: 10.1021/bk-2010-1056.ch006

Synthesis of Oxazolidinones from Propargylamines and CO_2

Synthesis of α-alkylidene oxazolidinones through the cyclization of propargylamines and CO_2 has attracted much attention recently (scheme 9, (2)). Transition-metal catalysts including ruthenium and palladium complexes and organic bases, e.g. TBD, DBU, alkylguanidines and phosphazene bases (*37*) have been developed as the active species for the reaction of propargylamines with CO_2 to give α-alkylidene oxazolidinones. In order to facilitate the product-catalyst separation and catalyst recycling process, commercially available basic alumina is developed as an efficient catalyst for the reaction of propargylamines with CO_2 under supercritical conditions (*38*).

It has been reported that propargylic amines could react smoothly with CO_2 under supercritical conditions in the absence of any catalyst, which is considered to be a self-catalyzed process (*39*). (Z)-configuration of product is confirmed by

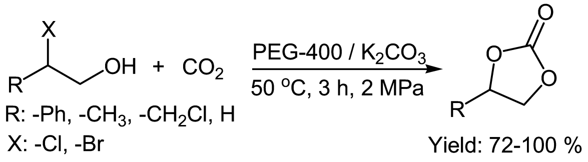

Scheme 9. Cyclic carbonate from halohydrin with CO_2.

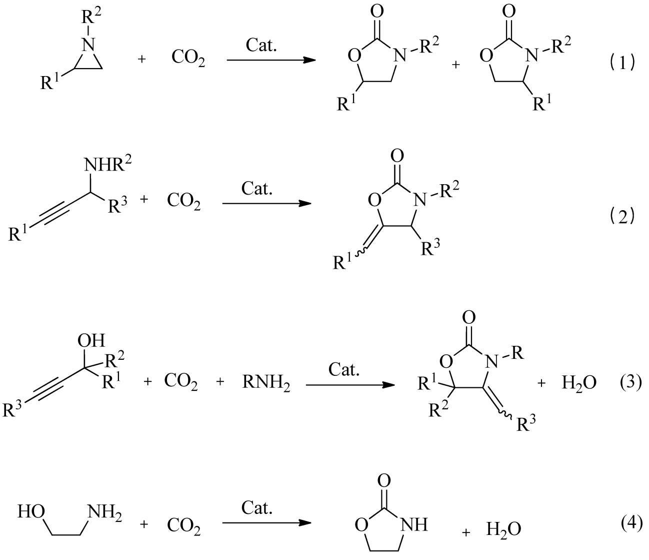

Scheme 10. Various routes to oxazolidinones from CO_2.

NMR spectroscopy and X-ray crystallography and the self-catalyzed mechanism is proposed as shown in Scheme 11.

Very recently, we (*40*) found that basic ion-exchange resins, one kind of polystyryl supported tertiary amines such as D301R (a Trade name for the ion-exchange resin supplied by the Chemical Plant of Nankai University, Tianjin, China; bead diameter: 0.3–1.25 mm, maximum operating temperature: 120 °C; Exchange capacity: 4.8 mmol g^{-1}, crosslinking degree of bead: 1 %, true density: 1.03-1.07 g/mL), were proved to be highly efficient and recyclable catalysts for the fixation of CO_2 with aziridines under mild conditions, leading to formation of 5-aryl-2-oxazolidinone with excellent regio-selectivities (Scheme 12). Notably, neither solvent nor any additives were required, and the catalyst can be recovered by simply filtration and directly reused at least five times without significant loss of catalytic activity and selectivity. To be delighted, the present protocol was successfully applied to reactions of epoxides/propargyl amines with CO_2/CS_2 (Scheme 12). In general, this solvent-free process thus represents environmentally friendly catalytic conversion of CO_2 into value-added chemicals and has great potential to be applied in various continuous flow reactors in industry.

Downloaded by DUKE UNIV on June 23, 2012 | http://pubs.acs.org
Publication Date (Web): December 3, 2010 | doi: 10.1021/bk-2010-1056.ch006

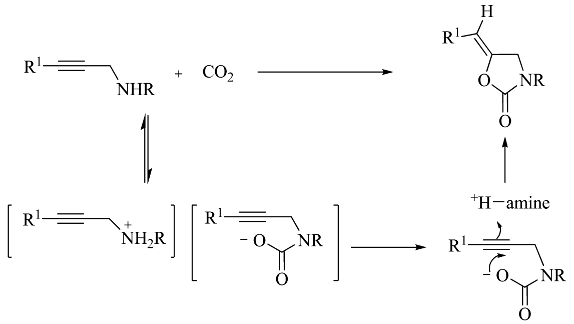

Scheme 11. Possible mechansim for the catalyst-free process.

Downloaded by DUKE UNIV on June 23, 2012 | http://pubs.acs.org
Publication Date (Web): December 3, 2010 | doi: 10.1021/bk-2010-1056.ch006

Quinazoline Synthesis from Aminobenzonitrile and CO_2

In recent years, quinazoline-2, 4-(1H, 3H)-diones and their derivatives have drawn high attention and interests due to their wide range of biological and pharmacological activities. For example, 7-chloroquinazoline-2, 4(1H, 3H)-dione is an important intermediate for the synthesis of FK 366 (Zenarestat®) and KF31327. FK 366 (Zenarestat®) functions as an aldose reductase inhibitor and a remedy for complications of diabetes mellitus; and KF31327 has also been developed as s an important medicine to treat heart disease (*41*) (Scheme 13).

Due to the important and diverse biological and pharmacological activities, the development of synthetic methodologies for quinazoline-2, 4-(1H, 3H)-diones has also drawn much attention in the past decades. The traditional synthetic methods involve the use of anthranilic acid with urea, anthranilamide with phosgene, and anthranilic acid with potassium cyanate or chlorosulfonyl isocyanate (*42*). An environmental benign pathway such as solid phase synthetic approach for the construction of quinazolinedione template from anthranilic acid could be promissing, in order to build structurally diverse molecular libraries with a frame structure of quinazolinedione for drugs screening (*43*). In addition, the microwave-assisted synthesis of quinazoline-2, 4-(1H, 3H)-diones is also found in the literature. However, owing to its high toxic reagents or harsh conditions, stringent restrictions have been imposed on the use of those methods mentioned above. Recently, a greener synthetic method from CO_2 and 2-aminobenzonitrile has been developed for the synthesis of quinazoline-2, 4-(1H, 3H)-diones and their derivatives. A promising strategy for the synthesis of quinazoline-2, 4-(1H, 3H)-diones from CO_2 was firstly reported by Mizuno et al (*44a*, *44b*), in which stoichiometric organic base DBU is required.

Besides the progress made in homogeneous catalysis, heterogeneous catalysis systems have also been developed in order to facilitate the product separation and catalyst recovery. Catalytic amounts of inorganic base Cs_2CO_3 has been used for synthesizing quinazoline-2, 4-(1H, 3H)-diones using DMF as solvent (*44c*) (Scheme 14).

Organic guanidines, which are categorized as organic superbases with ease of structural modification, are efficient organic catalysts for the types of base induced reactions in organic synthesis (*45*). Particularly, guanidines could interact with CO_2 through a kinetically reversible way, leading to CO_2 fixation (*46*). We

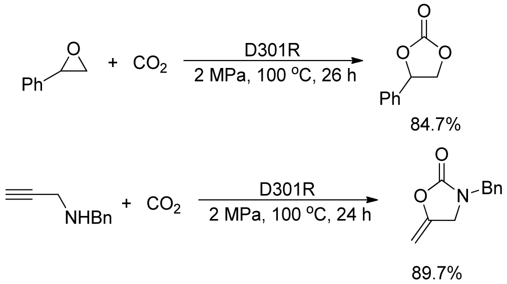

Scheme 12. *Carboxylation of epoxide/propargyl amine with CO_2.*

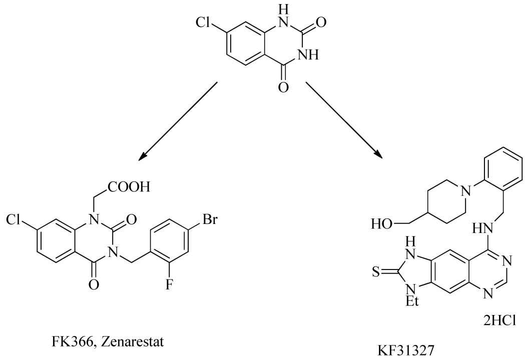

Scheme 13. *FK 366 and KF31327 from 7-chloroquinazoline-2, 4(1H, 3H)-dione.*

developed a greener process for the synthesis of several quinazoline-2, 4-(1H, 3H)-diones via a chemical fixation of CO_2 to 2-aminobenzonitriles in high isolated yield by utilizing guanidines (Scheme 15) as efficient catalysts under solvent-free conditions (*47*). Notably, the reaction could work well even at 2 mol% of catalyst loading or under CO_2 pressure as low as 0.5 MPa. This approach would be more promising from the viewpoint of Green Chemistry and Sustainable Society.

Lactone Synthesis from CO_2

As mentioned above, one of the most effective methods to activate CO_2 is its incorporation with high energy compounds under certain conditions. From 1970s, there have been a large number of publications focused on the reactions of CO_2 with unsaturated compounds such as alkynes, diynes, alkene, dienes, allenes and benzynes (*48*), in the presence of transition metal to afford pyrones, lactones, esters, and acids, respectively. And much advancement has been documented in the recent couple of decades (*49*). Generally speaking, low valent metal complexes (Ni (0) and Pd (0)) are able to react with CO_2 and unsaturated compounds giving the five-membered metallalactones (*50*), in which the Ni (η_2-CO_2)(Pcy_3)$_2$ was first isolated and characterized by the X-ray diffraction. Following the insertion of aforementioned unsaturated compounds into the five-membered metallalactones, a reductive elimination procedure led to the target lactones. Accordingly, there

Downloaded by DUKE UNIV on June 23, 2012 | http://pubs.acs.org
Publication Date (Web): December 3, 2010 | doi: 10.1021/bk-2010-1056.ch006

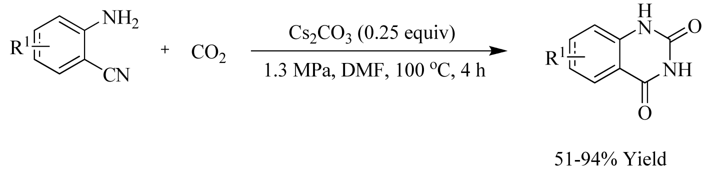

Scheme 14. Synthesis of quinazoline-2,4-(1H, 3H)-dione.

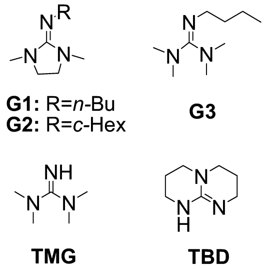

Scheme 15. Guanidines used in this study.

are more reports on construction of six-membered lactones starting from CO2 compared with the five-membered lactones.

The formation of lactones through the reactions of CO2 with arynes was reported three decades ago (*50*). In this context, the reaction of two dialkyl-substituted alkynes with CO2 catalyzed by Ni (0) complexes could give lactones with moderate yield (*51*) (Scheme 16). In particular, an intramolecular reaction of diynes with CO2 under high pressure is found to furnish the fused pyranone derivatives subsequently (*52*) (Scheme 17). A series of poly (2-pyrones) are also obtained by Nickel (0)-catalyzed cyclic copolymerization of diynes with CO2 as shown in Scheme 18 (*53*).

Dimethyl Carbonate Synthesis from CO2

Dimethyl carbonate (DMC) has been drawing much attention as a safe, non-corrosive, and environmentally friendly building block for the production of polycarbonate and other chemicals. Most promisingly, DMC is of interest as an additive to fuel oil owing to a high octane number, reducing particulate emission from diesel engines (*54*). In addition, it has been used as an electrolyte in lithium batteries due to its high dielectric constant. Therefore, the development of green and efficient DMC production technology and its fuel properties has attracted much more attention in oil and chemical industries. From the viewpoint of green chemistry, the two-step transesterification process utilizing CO2 as a raw material, as illustrated in Scheme 19, is more attractive compared with other commercial processes (*55*) including methanolysis of phosgene, carbon monoxide-nitrite process, and gas-phase oxidative carbonylation of methanol using toxic, corrosive, flammable and explosive gases.

In the past decades, numerous heterogeneous catalysts have been proposed for the transesterification of alkylene carbonate with methanol, such as molecular

Downloaded by DUKE UNIV on June 23, 2012 | http://pubs.acs.org
Publication Date (Web): December 3, 2010 | doi: 10.1021/bk-2010-1056.ch006

Downloaded by DUKE UNIV on June 23, 2012 | http://pubs.acs.org
Publication Date (Web): December 3, 2010 | doi: 10.1021/bk-2010-1056.ch006

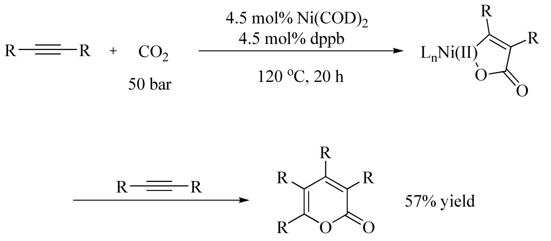
4.5 mol% Ni(COD)$_2$
4.5 mol% dppb
120 °C, 20 h
CO$_2$
50 bar
L$_n$Ni(II)
57% yield

Scheme 16. Lactones from arynes and CO₂.

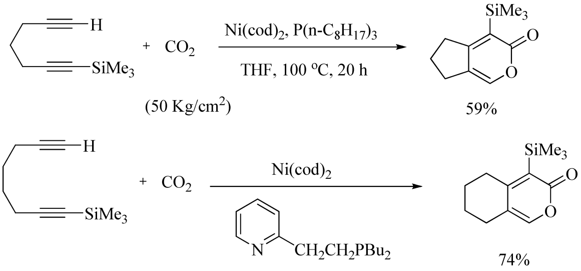
Ni(cod)$_2$, P(n-C$_8$H$_{17}$)$_3$
THF, 100 °C, 20 h
(50 Kg/cm^2)
59%
Ni(cod)$_2$
CH$_2$CH$_2$PBu$_2$
74%

Scheme 17. Lactones from diynes and CO₂.

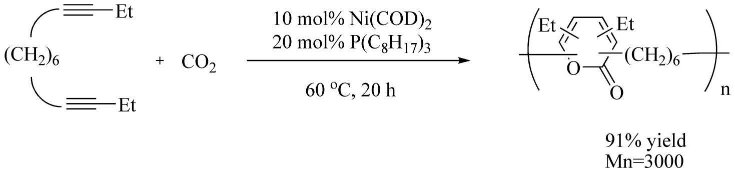
10 mol% Ni(COD)$_2$
20 mol% P(C$_8$H$_{17}$)$_3$
60 °C, 20 h
(CH$_2$)$_6$
91% yield
Mn=3000

Scheme 18. Cyclic polymerization of diacetylene with CO₂.

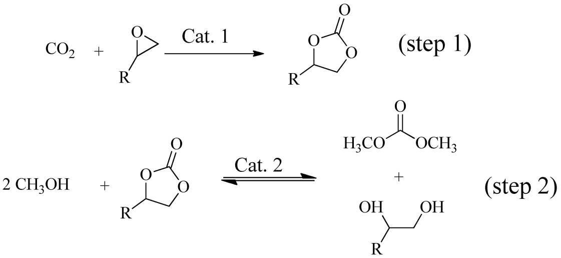
Cat. 1
(step 1)
2 CH$_3$OH
Cat. 2
(step 2)

Scheme 19. Two-step process for DMC production from CO₂.

sieves, basic metal oxides, metal cyanides, basic salts, dawsonites hydrotalcites, smectites, basic anion-exchange resin, functionalized chitosan and silica. In addition, the transesterification reaction also proceeded very efficiently by using homogeneous catalysts including alkali metals, quaternary ammonium salts and ILs. Although great advances have been seen (*56*), most catalytic processes suffer from low catalytic activity, and high CO_2 pressure, high reaction temperature and/or the use of expensive metallic compounds are often required.

So development of more efficient, easily prepared, low cost, and single component catalyst for DMC synthesis is still highly desired.

We (*57*) found that a kind of DABCO-based basic ionic liquids, e.g. [C_4DABCO]OH was a highly efficient and recyclable catalyst for DMC synthesis through the transesterification reaction of ethylene glycol with methanol under mild reaction conditions (Scheme 20). The ionic liquids used in this study represent as air stable, easily synthesized, cheap, extremely robust and environmentally benign catalysts, which can effectively activate methanol through tertiary nitrogen in the cation part of the IL in combination with hydroxide anion. The catalyst could be recycled for four times without loss of yield and selectivity. Therefore, this green process could show much potential application in industry.

It is worth mentioning that 2-hydroxyethyl methyl carbonate (HEMC) being regarded as the intermediate for DMC formation (Scheme 21), was identified by GC and NMR. Specifically, HEMC was indeed found to be the sole product when using [C_8DABCO]BF_4 as the catalyst for the transesterification reaction.

Downloaded by DUKE UNIV on June 23, 2012 | http://pubs.acs.org
Publication Date (Web): December 3, 2010 | doi: 10.1021/bk-2010-1056.ch006

Synthesis of Urea Derivatives from CO_2

Urea derivatives are an important class of carbonyl compounds and useful chemical intermediates in the synthesis of pharmaceuticals, agricultural chemicals, dyes; and they have been also used as antioxidants in gasoline and additives in plastics. On the other hand, conventionally preparative methodologies of urea derivatives are based on the use of dangerous reagents such as phosgene and isocyanates (*58*). Nowadays, replacement of these hazardous reagents in chemical processes would be one of the main goals of green chemistry. Therefore, the synthesis of ureas starting from CO_2 has been drawing much attention because CO_2 is a renewable, abundant, cheap, and non-toxic source of functional carbon unit. In this regard, successful routes to urea derivatives directly from CO_2 and amines have also been reported (*59*); however, the stoichiometric or excessive dehydrating agents such as diorganophosphites, carbodiimides, propargyl alcohols and P_4S_{10} are required to reach significant product yields. Accordingly, it is desirable to develop simple and environmentally benign processes for the synthesis of substituted ureas from amines and CO_2 in the absence of dehydrating agent (*60*).

We (*61*) developed a simple process for synthesis of symmetrical ureas from amines and CO_2 without using any dehydrating agents (Scheme 22). Notably inorganic base/PEG1000 was proved to be an efficient and recyclable catalyst and PEG1000 as support could enhance the reaction. Interestingly, the catalyst can be recovered after a simple separation procedure, and reused over 5 times with retention of high activity. This process presented here could show much potential application in industry due to its simplicity and ease of catalyst recycling. and PEG was found to improve the reaction. The reaction involves two steps, i.e. formation of the ammonium carbamate (exothermic step) and dehydration to the urea (endothermic step).

In this reaction, PEG could form $[R_2NH_2\cdot PEG]^+$ $[R_2NCO_2]^-$, and thus could increase the thermodynamic stability of $[R_2NH_2]^+$ (*62*). In deed, ^{1}H NMR

Downloaded by DUKE UNIV on June 23, 2012 | http://pubs.acs.org
Publication Date (Web): December 3, 2010 | doi: 10.1021/bk-2010-1056.ch006

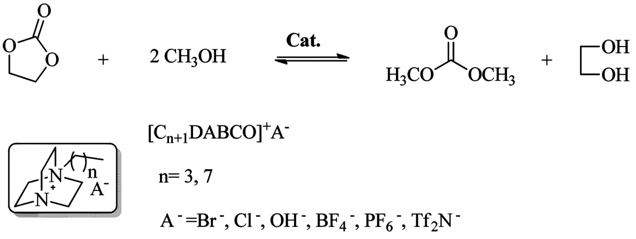

Scheme 20. Lewis basic ionic liquids-catalyzed synthesis of DMC via transesterification of EC with methanol.

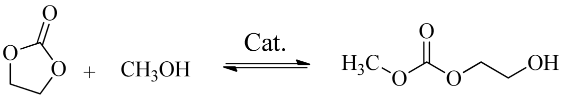

Scheme 21. The formation of 2-hydroxyethyl methyl carbonate.

measurement also supports the complexation of PEG with ammonium cation. Increasing in basicity of the base in aid of PEG could also facilitate formation of the ammonium carbamate salt (*63*). On the other hand, PEG can act as a physical dehydrating agent since PEG is strongly hygroscopic.

One-Pot Synthesis of Oxazolidinone from Olefin and CO_2

Currently, there are four main synthetic strategies for 2-oxazolidinones starting from CO_2 as C1 resources: (i) direct addition of CO_2 to 1, 2-aminoalcohols; (ii) reaction of propargylamines with CO_2; (iii) reaction of amine/aminoalcohol with cyclic carbonate from CO_2 and (iv) insertion of CO_2 into the aziridines. Among them, cycloaddition of CO_2 with aziridines is one of the most promising methods for synthesis of oxazolidinones. Several catalyst systems have been explored for this reaction (*37a*, *64*). However, such a cycloaddition generally involves the initial synthesis of aziridine from olefin and a nitrogen source (*65*), which requires a tedious workup for separation and involves metal catalysts in most cases. In other words, this two-step manipulation is one of the main drawbacks of this process. So it is more desirable to synthesize an oxazolidinone directly from olefin, a nitrogen source and CO_2.

We (*66*) developed a simple and effective process catalyzed by n-Bu_4NBr_3/n-Bu_4NBr in a single operation for the synthesis of 5-substituted 2-oxazolidinones with perfect regioselectivity directly from olefins, chloramine-T, and CO_2 (Scheme 23). The choice of efficient binary catalysts for two steps, i.e. aziridination and cycloaddition, and the optimization of reaction condition are keys to the one-pot synthesis of 5-substituted 2-oxazolidinones. The present protocol could show an additional example for efficiently utilizing CO_2 as a carbon source in the field of green chemistry and catalysis.

Downloaded by DUKE UNIV on June 23, 2012 | http://pubs.acs.org
Publication Date (Web): December 3, 2010 | doi: 10.1021/bk-2010-1056.ch006

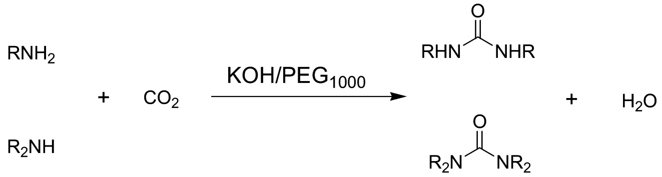

Scheme 22. KOH/PEG-catalyzed synthesis of urea from amine and CO₂

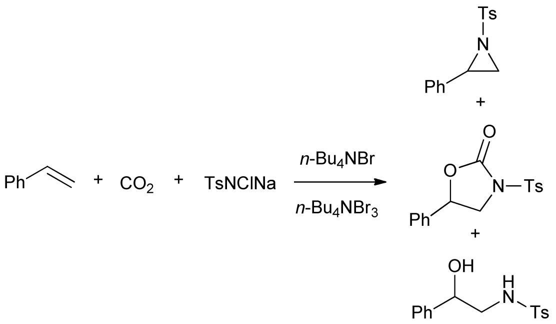

Scheme 23. One-pot synthesis of 5-phenyl-2-oxazolidinone via the three-component coupling of styrene, chloramine-T and CO₂.

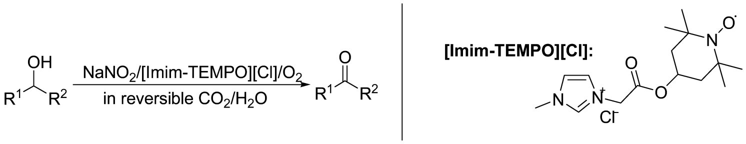

Scheme 24. Aerobic oxidation of alcohols catalyzed by NaNO₂/[Imim-TEMPO][Cl]/CO₂/H₂O.

Aerobic Oxidation of Alcohols in Self-Neutralizing *in Situ* Acidic CO_2/H_2O System

Acids are the most common industrial catalysts but have the disadvantage of requiring post-reaction neutralization and salt disposal. In this context, the reversible reaction of CO_2 with water to form carbonic acid is well-known, resulting in low pH values of about 3. This provides *in situ* formation of the acid catalyst. Indeed, self-neutralizing *in situ* acid catalysis from CO_2 has shown great applications, e.g. decarboxylation, diazotization, cyclization, with profound advantages for both green chemistry and improved economics (*67*). Particularly, the CO_2/H_2O system provides *in situ* acid formation for catalysis which can be readily neutralized by the removal of CO_2. In other words, the acid formation is reversible upon the removal of CO_2. Thus carbonic acid offers simple neutralization and does not require any waste disposal.

The selective oxidation of primary and secondary alcohols into the corresponding aldehydes and ketones is undoubtedly one of the most important and challenging transformations in organic chemistry. In our previous work (*68*), recyclable acidic imidazolium salts were developed to replace those conventional acids used in the TEMPO-catalyzed oxidation of alcohols. A self-neutralizing *in situ* acidic catalyst system from CO_2 comprised of a recyclable TEMPO functionalized imidazolium salt/$NaNO_2$/CO_2/H_2O (*69*) was developed for the selective oxidation of a series of aliphatic, allylic, heterocyclic and benzylic alcohols to the respective carbonyl compounds in order to avoid the tedious synthesis of above recyclable acid (Scheme 24). The present protocol offers simple neutralization which does not require any waste disposal with advantages of improved reaction, facilitated seperation of the catalyst and products, safe operation for aerobic oxidation.

Downloaded by DUKE UNIV on June 23, 2012 | http://pubs.acs.org
Publication Date (Web): December 3, 2010 | doi: 10.1021/bk-2010-1056.ch006

PEG Radical Chemistry in Dense CO_2: Oxidation Reaction in Biphasic PEG/CO_2 System

Compressed CO_2 has been touted as a suitable solvent for organic synthesis, offering economical and environmental benefits due to its favorable properties and readily tunable solvent parameters (*70*). In particular, dense CO_2 appears to be an ideal solvent for use in oxidation. Unlike almost any organic solvent, CO_2 will not be oxidized further, and hence the use of CO_2 as a reaction medium eliminates by-products originating from solvents. At the same time, dense CO_2 provides a safe reaction environment with excellent mass and heat transfer for aerobic oxidations. As a consequence, novel chemistry relevant to enhancing selectivity toward desired products, improving reactivity and ease of product separation could be created when utilizing dense CO_2 as a reaction medium.

The thermal/oxidative degradation of PEG is known to occur under oxygen atmosphere at elevated temperature. The utility of this concept of practically utilizable free-radical chemistry of PEG induced by molecule oxygen in dense CO_2 is demonstrated to be successfully applied to important and fundamental organic reactions with enormous synthetic potentials. Current applications include selective formylation of primary and secondary aliphatic alcohols, and oxidation of benzylic alcohols, and benzylic C=C cleavage reactions, and benzylic sp^3 C-H oxidation. We find that both PEG and molecule oxygen are prerequisite to performing those reactions smoothly. Given that dense CO_2 is immune to free radical chemistry; it is an ideal solvent for such free radical reactions. As a result, dense CO_2 in this study allows such reactions initiated by PEG radical able to be tuned by subtly adjusting reaction parameter like CO_2 pressure, thus leading to enhancing the product selectivity. Attaining high selectivity towards the desired product makes this methodology more practical in organic synthesis. These scrutinous findings inspired with a serendipity in the course of continuing effort devoted to developing efficient sustainable process for the oxidation of organic substrates like alcohols and olefins in PEG/dense CO_2 biphasic system lead to creating a novel concept of utilizable free-radical chemistry of PEG, and would whereby offer an environmentally friendly, metal-free, cost-efficient and viable access to a diverse set of synthetic useful transformations without any additional free radical initiator nor a catalyst as depicted in Scheme 25 (*71*).

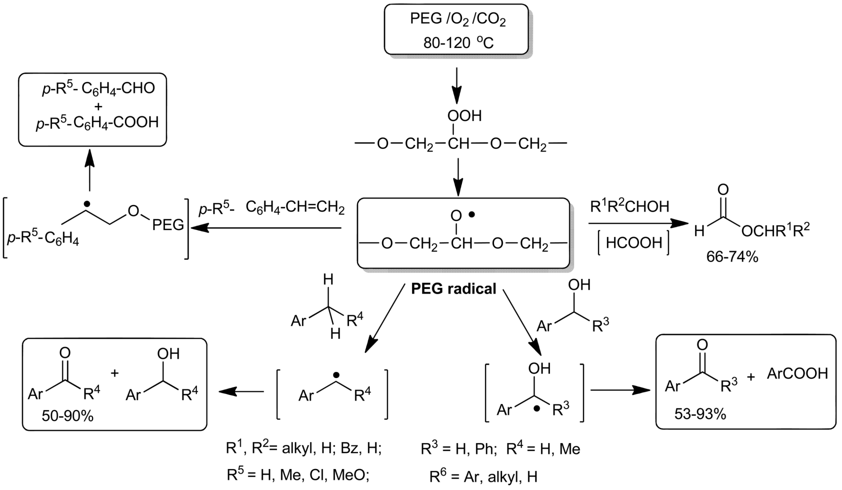

Scheme 25. The spectra and proposed pathways of organic reactions initiated by PEG radical arising from PEG thermal oxidative degradation.

The reaction of PEG with oxygen is prone to generating PEG radical (*72*), which is supposed to further formation of acetic acid or initiating substrates to generate relatively stable radicals relying on the substrate structure. As anticipated, benzylic or allylic substrates could be favorable for forming benzylic or allylic radical and thus predominately undergo oxidation such as oxidation of benzylic alcohols, benzylic C=C cleavage reactions, and benzylic/allylic sp^3 C-H oxidation; whereas aliphatic alcohols could preferentially go through formylating pathway. The proposed free radical mechanism was also supported as evidenced by following facts. Those cover producing trace amounts of formylated products of the degraded PEG, broadening PEG molecule weight distribution, generating a peroxide intermediate as detected by a KI/starch text, and suppressing effect of TEMPO (2, 2, 6, 6-tetramethyl-piperidine-1-oxyl) on the reactions. Given more time for in-depth investigation, free-radical chemistry of PEG thermal degradation will surely become an even more powerful tool for organic synthesis and find its place in many more industrial applications to establish sustainable and economically competitive process.

Conclusions

Carbon dioxide plays a crucial role not only in biological chemistry as a C1 building block in nature but also in synthetic chemistry as an environmentally friendly feedstock for making bulk chemicals, fuels, and materials. As a renewable feedstock, the transformation of CO_2 into useful chemicals is particularly promissing and deserves worldwide research efforts. In this context, CO_2 chemistry is undoubtedly going to be of ever-increasing importance in heterocyclic synthesis because of real advantages with current environmental benefits in terms of natural resource utilization, novel chemistry creation and

Downloaded by DUKE UNIV on June 23, 2012 | http://pubs.acs.org
Publication Date (Web): December 3, 2010 | doi: 10.1021/bk-2010-1056.ch006

engineering improvement such as reaction control, reactivity enhancement, and product purification. Many routes have been developed for utilization of CO_2 in organic synthesis, some of which are of great commercial interest with respect to the synthesis of specialized/commodity chemicals. There remain many opportunities to be explored further on the topic of CO_2 in organic synthesis, particularly in terms of functionalization of CO_2 through CO_2 activation by using metal catalysts, smartly utilizing dense CO_2 as an environmentally benign solvent, using CO_2 as a catalyst or tunable ragent. We hope this presentation will stimulate further interest in academic research and industrial development that may lead to the development of CO_2 as a synthon for organic synthesis.

Downloaded by DUKE UNIV on June 23, 2012 | http://pubs.acs.org
Publication Date (Web): December 3, 2010 | doi: 10.1021/bk-2010-1056.ch006

Acknowledgments

Our work on CO_2 chemistry presented in this chapter is the fruit derived from the exceptional talented students whose names appear in the references, Dr. Ya Du, Dr. Jing-Quan Wang, Dr. Jing-Lun Wang, Dr. Cheng-Xia Miao, Dr. De-Lin Kong, Mr. Xiao-Yong Dou, Mr. Jie-Sheng Tian, Miss Ying Wu, Dr. Yuan Zhao, Miss Fang Wu, to whom we give warm thanks for their devotion, sincerity and contribution. We are grateful to the National Natural Science Foundation of China (Grant Nos. 20672054, 20872073), and Research Fellowship for International Young Scientists from NSFC(20950110325), the 111 project (B06005), and the Committee of Science and Technology of Tianjin for financial support. Special thanks are extended to Professor Toshiyasu Sakakura (AIST, Japan) for introducing us to the intriguing field of chemical transformation of CO_2 and green chemistry.

References

1. Chen, C.; Yang, S.-T.; Ahn, W.-S.; Ryoo, R. *Chem. Commun.* **2009**, 3627.
2. Sakakura, T.; Kohno, K. *Chem. Commun.* **2009**, 1312.
3. Sakakura, T.; Choi, J.-C.; Yasuda, H. *Chem. Rev.* **2007**, *107*, 2365.
4. Aresta, M.; Dibenedetto, A. *Dalton Trans.* **2007**, *28*, 2975.
5. Caló, V.; Nacci, A.; Monopoli, A.; Fanizzi, A. *Org. Lett.* **2002**, *4*, 2561.
6. Sit, W. N.; Ng, S. M.; Kwong, K. Y.; Lau, P. L. *J. Org. Chem.* **2005**, *70*, 8583.
7. Wang, J.-Q.; Yue, X.-D.; Cai, F.; He, L.-N. *Catal. Commun.* **2007**, *8*, 167.
8. Tian, J.-S.; Miao, C.-X.; Wang, J.-Q.; Cai, F.; Du, Y.; Zhao, Y.; He, L.-N. *Green Chem.* **2007**, *9*, 566.
9. Du, Y.; Wang, J.-Q.; Chen, J.-Y.; Cai, F.; Tian, J.-S.; Kong, D.-L.; He, L.-N. *Tetrahedron Lett.* **2006**, *47*, 1271.
10. Miao, C.-X.; Wang, J.-Q.; Wu, Y.; Du, Y.; He, L.-N. *ChemSusChem* **2008**, *1*, 236.
11. Mélendez, J.; North, M.; Villuendas, P. *Chem. Commun.* **2009**, 2577.
12. Lu, X.-B.; Liang, B.; Zhang, Y.-J.; Tian, Y.-Z.; Wang, Y.-M.; Bai, C.-X.; Wang, H.; Zhang, R. *J. Am. Chem. Soc.* **2004**, *126*, 3732.
13. Berkessel, A.; Brandenburg, M. *Org. Lett.* **2006**, *8*, 4401.

Downloaded by DUKE UNIV on June 23, 2012 | http://pubs.acs.org
Publication Date (Web): December 3, 2010 | doi: 10.1021/bk-2010-1056.ch006

14. Zhang, S.-L.; Huang, Y.-Z.; Jing, H.-W.; Yao, W.-X.; Yan, P. *Green Chem.* **2009**, *11*, 935.
15. (a) Dou, X.-Y.; Wang, J.-Q.; Du, Y.; Wang, E.; He, L.-N. *Synlett* **2007**, *19*, 3058. (b) Tian, J.-S.; Cai, F.; Wang, J.-Q.; Du, Y.; He, L.-N. *Phosphorus, Sulfur, Silicon* **2008**, *183*, 494.
16. (a) Zhao, Y.; Tian, J.-S.; Qi, X.-H.; Han, Z.-N.; Zhuang, Y.-Y.; He, L.-N. *J. Mol. Catal. A: Chem.* **2007**, *271*, 284. (b) He, L.-N.; Wang, J.-Q.; Wang, J.-L. *Pure Appl. Chem.* **2009**, *81*, 2069. (c) He, L.-N.; Du, Y.; Miao, C.-X.; Wang, J.-Q.; Dou, X.-Y.; Wu, Y. *Front. Chem. Eng. China* **2009**, *3*, 224. (d) Gao, J.; Miao, C.-X.; Wang, J.-L.; He, L.-N. *Pet. Technol.* **2010**, *39*, 465. (e) Wang, J.-L.; He, L.-N.; Wang, J.-Q.; Du, Y.; Miao, C.-X.; Dou, X.-Y.; Wu, Y.; Gao, J. *Fine Chem. Intermediate* **2009**, *39*, 1. (f) Wang, J.-L.; He, L.-N.; Miao, C.-X.; Li, Y.-N. *Green Chem.* **2009**, *11*, 1317.
17. Du, Y.; Cai, F.; Kong, D.-L.; He, L.-N. *Green Chem.* **2005**, *7*, 518.
18. Sakai, T.; Tsutsumi, Y.; Ema, T. *Green Chem.* **2008**, *10*, 337.
19. Wang, J.-Q.; Kong, D.-L.; Chen, J.-Y.; Cai, F.; He, L.-N. *J. Mol.Catal. A: Chem.* **2006**, *249*, 143.
20. Song, J.-L.; Zhang, Z.-F.; Hu, S.-Q.; Wu, T.-B.; Jiang, T.; Han, B.-X. *Green Chem.* **2009**, *11*, 1031.
21. Srivastava, R.; Srinivas, D.; Ratnasamy, P. *Tetrahedron Lett.* **2006**, *47*, 4213.
22. Takahashi, T.; Watahiki, T.; Kitazume, S.; Yasuda, H.; Sakakura, T. *Chem. Commun.* **2006**, 1664.
23. Zheng, X.-X.; Luo, S.-Z.; Zhang, L.; Cheng, J.-P. *Green Chem.* **2009**, *11*, 455.
24. He, L.-N.; Yasuda, H.; Sakakura, T. *Green Chem.* **2003**, *5*, 92.
25. Eghbali, N.; Li, C. J. *Green Chem.* **2007**, *9*, 213.
26. Aresta, M.; Dibenedetto, A. *J. Mol. Catal. A: Chem.* **2002**, *182-183*, 399.
27. Sun, J.; Fujika, S.-I.; Arai, M. *J. Organomet. Chem.* **2005**, *690*, 3490.
28. Wang, J.-L.; Wang, J. -Q.; He, L.-N.; Dou, X.-Y.; Wu, F. *Green Chem.* **2008**, *10*, 1218.
29. Du, Y.; Kong, D.-L.; Wang, H.-Y.; Cai, F.; Tian, J- S.; Wang, J.-Q.; He, L.-N. *J. Mol. Catal. A: Chem.* **2005**, *241*, 233.
30. Du, Y.; He, L.-N.; Kong, D.-L. *Catal. Commun.* **2008**, *9*, 1754.
31. (a) Horváth, I. T.; Anastas, P T. *Chem. Rev.* **2007**, *107*, 2169. (b) Tanaka, K.; Toda, F. *Chem. Rev.* **2000**, *100*, 1025. (c) Curran, D. P. *Pure Appl. Chem.* **2000**, *72*, 1649. (d) Li, C.-J. *Tetrahedron* **1996**, *52*, 5643. (e) Welton, T. *Chem. Rev.* **1999**, *99*, 2071.
32. (a) Venturello, C.; D'Aloisio, R. *Synthesis* **1985**, 33. (b) Kawanami, H.; Ikushima, Y. J. P. Patent 2007022976A, 2007.
33. Wang, M.; Chang, K. R. *Ind. Eng. Chem. Res.* **1990**, *29*, 40.
34. (a) Gourgouillon, D.; Avelino, H. M. N. T.; Fareleira, J. M. N. A.; Nunes da Ponte, M. *J. Supercrit. Fluids* **1998**, *13*, 177. (b) Heldebrant, D. J.; Jessop, P. G. *J. Am. Chem. Soc.* **2003**, *125*, 5600.
35. (a) Shen, Y.-M.; Duan, W.-L.; Shi, M. *Eur. J. Org. Chem.* **2004**, *14*, 3080. (b) Miller, A. W.; Nguyen, S. T. *Org. Lett.* **2004**, *6*, 2301. (c) Du, Y.; Wu, Y.; Liu, A-H.; He, L.-N. *J. Org. Chem.* **2008**, *73*, 4709. (d) Wu, Y.; He, L.-N.; Du, Y.; Wang, J.-Q.; Miao, C.-X. *Tetrahedron* **2009**, *65*, 6204.

36. Tascedda, P.; Dunach, E. *Chem. Commun.* **2000**, *6*, 449.
37. (a) Mitsudo, T.; Hori, Y.; Yamakawa, Y.; Watanabe, Y. *Tetrahedron Lett.* **1987**, *28*, 4417. (b) Shi, M.; Shen, Y.-M. *J. Org. Chem.* **2002**, *67*, 16. (c) Costa, M.; Chiusoli, G. P.; Rizzardi, M. *Chem. Commun.* **1996**, *14*, 1699.
38. Maggi, R.; Bertolotti, C.; Orlandini, E.; Oro, C.; Sartoria, G.; Selvab, M. *Tetrahedron Lett.* **2007**, *48*, 2131.
39. Kayaki, Y.; Yamamoto, M.; Suzuki, T.; Ikariya, T. *Green Chem.* **2006**, *8*, 1019.
40. Liu, A.-H.; He, L.-N.; Peng, S.-Y.; Pan, Z.-D.; Wang, J.-L.; Gao, J. *Sci. China, Ser. B: Chem.* **2010**, *53*, 1578.
41. Mohri, S. J. *Synth. Org. Chem. Jpn.* **2001**, *59*, 514.
42. (a) Pastor, G. J.; Blanchard, C.; Montginoul, C.; Torreilles, E.; Giral, L.; Texier, A. *Bull. Soc. Chim. Fr.* **1975**, 1331. (b) Vorbrueggen, H.; Krolikiewicz, K. *Tetrahedron* **1994**, *50*, 6549.
43. Gordeev, M. F.; Hui, H. C.; Gordon, E. M.; Patel, D. V. *Tetrahedron Lett.* **1997**, *38*, 1729.
44. (a) Mizuno, T.; Okamoto, N.; Ito, T.; Miyata, T. *Tetrahedron Lett.* **2000**, *41*, 1051. (b) Mizuno, T.; Okamoto, N.; Ito, T.; Miyata, T. *Heteroat. Chem.* **2000**, *11*, 428. (c) Patil, Y. P.; Tambade, P. J; Jagtap, S. R; Bhanage, B. M. *Green Chem. Lett. Rev.* **2008**, *1*, 127.
45. (a) Kovacevic, B.; Maksic, Z. B. *Org. Lett.* **2001**, *3*, 1523. (b) Ishikawa, T.; Kumamoto, T. *Synthesis* **2006**, *8*, 737.
46. Pereira, F. S.; deAzevedo, E. R.; da Silva, E. F.; Bonagamba, T. J.; da Silva Agostíni, D. L.; Magalhães, A.; Eloizo Job, A.; Pérez Gonzaález, E. R. *Tetrahedron* **2008**, *64*, 10097.
47. Gao, J.; He, L.-N.; Miao, C.-X.; Chanfreau, S. *Tetrahedron* **2010**, *66*, 4063.
48. (a) Yoshida, H.; Fukushima, H.; Ohshita, J.; Kunai, A. *J. Am. Chem. Soc.* **2006**, *128*, 11040. (b) Hoberg, H.; Peres, Y.; Kruger, C.; Tsay, Y. H. *Angew. Chem., Int. Ed.* **1987**, *26*, 771. (c) Tsuda, T.; Chujo, Y.; Saegusa, T. *Synth. Commun.* **1979**, *9*, 427.
49. Louie, J. *Curr. Org. Chem.* **2005**, *9*, 605.
50. (a) Behr, A. *Angew. Chem., Int. Ed.* **1988**, *27*, 661. (b) Aresta, M.; Nobile, C. F.; Albano, V. G.; Forni, E.; Manassero, M. *J. Chem. Soc., Chem. Commun.* **1975**, *15*, 636.
51. Hoberg, H.; Schaefer, D.; Burkhart, G.; Krüger, C.; Romão, M. J. *J. Organomet. Chem.* **1984**, *266*, 203.
52. Tsuda, T.; Morikawa, S.; Hasegawa, N.; Saegusa, T. *J. Org. Chem.* **1990**, *55*, 2978.
53. Oi, S. C.; Fukue, Y.; Nemoto, K.; Inoue, Y. *Macromolecules* **1996**, *29*, 2694.
54. (a) Pacheco, M. A.; Marshall, C. L. *Energy Fuels* **1997**, *11*, 2. (b) Wei, T.; Sun, Y. *Green Chem.* **2003**, *5*, 343.
55. (a) Aresta, M.; Quaranta, E. *Chem. Tech.* **1997**, *27*, 32. (b) Zhao, Y.; He, L.-N.; Wang, J.-Q. *Chin. Chem. Lett.* **2008**, *19*, 286. (c) Choi, J.-C.; He, L.-N.; Yasuda, H.; Sakakura, T. *Green Chem.* **2002**, *4*, 230.
56. (a) Wang, H.; Sun, Y. H. *Catal. Today* **2006**, *115*, 107. (b) Srivastava, R.; Srinivas, D.; Ratnasamy, P. *J. Catal.* **2006**, *241*, 34. (c) Stoica, G.; Abelló, S.; Pérez-Ramírez, J. *ChemSusChem* **2009**, *2*, 301. (d) Bhanage, B. M.; Arai,

Downloaded by DUKE UNIV on June 23, 2012 | http://pubs.acs.org
Publication Date (Web): December 3, 2010 | doi: 10.1021/bk-2010-1056.ch006

M. *Green Chem.* **2003**, *5*, 71. (e) Ju, H. Y.; Manju, M. D.; Park, D. W. *React. Kinet. Catal. Lett.* **2007**, *90*, 3.

57. Yang, Z.-Z.; He, L.-N.; Dou, X.-Y.; Chanfreau, S. *Tetrahedron Lett.* **2010**, *51*, 2931.
58. (a) Shriner, R. L.; Horne, W. H.; Cox, R. F. B. *Org. Synth.* **1943**, *2*, 453. (b) Nowick, J. S.; Powell, N. A.; Nguyen, T. M.; Noronha, G. *J. Org. Chem.* **1992**, *57*, 7364.
59. (a) Yamazaki, N.; Higashi, F.; Iguchi, T. *Tetrahedron Lett.* **1974**, *13*, 1191. (b) Ogura, H.; Takeda, K.; Tokue, R.; Kobayashi, T. *Synthesis* **1978**, 394. (c) Nomura, R.; Yamamoto, M.; Matsuda, H. *Ind. Eng. Chem. Res.* **1987**, *26*, 1056. (d) Fournier, J.; Bruneau, C.; Dixneuf, P. H.; Lgcolier, S. *J. Org. Chem.* **1991**, *56*, 4456. (e) Nomura, R.; Hasegawa, Y.; Ishimoto, M.; Toyosaki, T.; Matsuda, H. *J. Org. Chem.* **1992**, *57*, 7339. (f) Tai, C.-C.; Huck, M. J.; McKoon, E. P.; Woo, T.; Jessop, P. G. *J. Org. Chem.* **2002**, *67*, 9070. (g) Porwanski, S.; Menuel, S.; Marsura, X.; Marsura, A. *Tetrahedron Lett.* **2004**, *45*, 5027.
60. (a) Shi, F.; Deng, Y.; SiMa, T.; Peng, J.; Gu, Y.; Qiao, B. *Angew. Chem., Int. Ed.* **2003**, *42*, 3257. (b) Munshi, P.; Heldebrant, D. J.; McKoon, E. P.; Kelly, P. A.; Tai. C.-C.; Jessop, P. G. *Tetrahedron Lett.* **2003**, *44*, 2725. (c) Shi, F.; Zhang, Q.; Ma, Y.; He, Y.; Deng, Y. *J. Am. Chem. Soc.* **2005**, *127*, 4182. (d) Ion, A.; Parvulescu, V.; Jacobs, P.; Vos, D. D. *Green Chem.* **2007**, *9*, 158. (e) Jiang, T.; Ma, X.; Zhou, Y.; Liang, S.; Zhang, J.; Han, B. *Green Chem.* **2008**, *10*, 465.
61. Kong, D.-L.; He, L.-N.; Wang, J.-Q. *Synlett* **2010**, 1276.
62. Aresta, M.; Quaranta, E. *Tetrahedron* **1992**, *48*, 1515.
63. Abribat, B.; Bigot, Y. L.; Gaset, A. *Synth. Commun.* **1994**, *24*, 2091.
64. (a) Dinsmore C. J.; Mercer, S. P. *Org. Lett.* **2004**, *6*, 2885. (b) Feroci, M.; Orsini, M.; Sotgiu, G.; Rossi, L.; Inesi, A. *J. Org. Chem.* **2005**, *70*, 7795. (c) Yoshida, M.; Komatsuzaki, Y.; Ihara, M. *Org. Lett.* **2008**, *10*, 2083. (d) Ihata, O.; Kayaki, Y.; Ikariya, T. *Angew. Chem., Int. Ed.* **2004**, *43*, 717. (e) Ihata, O.; Kayaki, Y. *Macromolecules* **2005**, *38*, 6429.
65. (a) Evans, D. A.; Faul, M. M.; Bilodeau, M. T. *J. Am. Chem. Soc.* **1994**, *116*, 2742. (b) Jeong, J. U.; Tao, B.; Sagasser, I.; Henniges, H.; Sharpless, K. B. *J. Am. Chem. Soc.* **1998**, *120*, 6844. (c) Cui, Y.; He, C. *J. Am. Chem. Soc.* **2003**, *125*, 16202. (d) Ney, J. E.; Wolfe, J. P. *J. Am. Chem. Soc.* **2006**, *128*, 15415. (e) Varszegi, C.; Ernst, M.; van Laar, F.; Sels, B. F.; Schwab, E.; De Vos, D. E. *Angew. Chem., Int. Ed.* **2008**, *47*, 1477.
66. Kong, D.-L.; He, L.-N.; Wang, J.-Q. *Catal. Commun.* **2010**, *11*, 992.
67. (a) Hallett, J. P.; Pollet, P.; Liotta, C. L.; Eckert, C. A. *Acc. Chem. Res.* **2008**, *41* (3), 458. (b) Eckert, C. A.; Liotta, C. L.; Bush, D.; Brown, J. S.; Hallett, J. P. *J. Phys. Chem. B* **2004**, *108*, 18108. (c) Roosen, C.; Ansorge-Schumacher, M.; Mang, T.; Leitner, W.; Greiner, L. *Green Chem.* **2007**, *9*, 455. (d) Hunter, S. E.; Ehrenberger, C. E.; Savage, P. E. *J. Org. Chem.* **2006**, *71*, 6229. (e) Tundo, P. Loris, A.; Selva, M. *Green Chem.* **2007**, *9*, 777. (f) Yamaguchi, A.; Hiyoshi, N.; Sato, O.; Bando, K. K.; Shirai, M. *Green Chem.* **2009**, *11*, 48.

Downloaded by DUKE UNIV on June 23, 2012 | http://pubs.acs.org
Publication Date (Web): December 3, 2010 | doi: 10.1021/bk-2010-1056.ch006

68. (a) Miao, C.-X.; He, L.-N.; Wang, J.-Q.; Wang, J.-L. *Adv. Synth. Catal.* **2009**, *351*, 2209. (b) Miao, C.-X.; He, L.-N.; Wang, J.-Q.; Gao, J. *Synlett* **2009**, 3291.
69. Miao, C.-X.; He, L.-N.; Wang, J.-L.; Wu, F. *J. Org. Chem.* **2010**, *75*, 257.
70. (a) Beckman, E. J. *J. Supercrit. Fluids* **2004**, *28*, 121. (b) A. Baiker, *Chem. Rev.* **1999**, *99*, 453. (c) Musie, G.; Wei, M.; Subramaniam, B.; Busch, D. H. *Coord. Chem. Rev.* **2001**, *219−221*, 789. (d) Leitner, W. *Acc. Chem. Res.* **2002**, *35*, 746.
71. (a) Wang, J.-Q.; He, L.-N. *New J. Chem.* **2009**, *33*, 1637. (b) Wang, J.-Q.; He, L.-N.; Miao, C.-X.; Gao, J. *ChemSusChem* **2009**, *2*, 755. (c) Wang, J.-Q.; He, L.-N.; Miao, C.-X. *Green Chem.* **2009**, *11*, 1013.
72. (a) Bortel, E.; Hodorowicz, S.; Lamot, R. *Makromol. Chem.* **1979**, *180*, 2491. (b) Han, S.; Kim, C.; Kwon, D. *Polymer* **1997**, *38*, 317. (c) Riecke, A. *Angew. Chem.* **1958**, *709*, 251. (d) Glastrup, J. *Polym. Degrad. Stab.* **1996**, *52*, 217. (e) Conder, J. R.; Fruitwala, N. A.; Shingari, M. K. *J. Chromatogr.* **1983**, *269*, 171. (f) Altwicker, E. A. *Chem. Rev.* **1967**, *67*, 475.

Downloaded by DUKE UNIV on June 23, 2012 | http://pubs.acs.org
Publication Date (Web): December 3, 2010 | doi: 10.1021/bk-2010-1056.ch006

Chapter 7

Oxidative Dehydrogenation of Ethane to Ethylene with CO_2 as Oxidant over CoO_x Supported on $MgAl_2O_4$ Spinel: Preparation, Characterization and Catalytic Performance

X. Zhang*

Department of Chemical Engineering, School of Chemical Engineering,
Northwest University, Xi'an 710069, P R China
***E-mail: zhangxinzhangcn@yahoo.com.cn**

Downloaded by STANFORD UNIV GREEN LIBR on June 23, 2012 | http://pubs.acs.org
Publication Date (Web): December 3, 2010 | doi: 10.1021/bk-2010-1056.ch007

$CoO_x/MgAl_2O_4$ catalysts with the different Co-loading and support $MgAl_2O_4$ were prepared for oxidative dehydrogenation of ethane with CO_2. CoO_x species (Co_3O_4, Co^{n+} and $Co^{\delta+}$) might be close relative to the catalytic activity of these catalysts. The loading of Co modified the reducibility of $CoO_x/MgAl_2O_4$ catalysts, which in turn affected the catalytic reactivity of these catalysts. The support $MgAl_2O_4$ prepared by the hydrothermal method ($MgAl_2O_4$-HT) was high-surface-area porous nanocrystallite $MgAl_2O_4$ spinel, which improved the dispersion of active sites and the diffusion of reactants and products on $CoO_x/MgAl_2O_4$-HT catalysts. 5-$CoO_x/MgAl_2O_4$-HT catalyst exhibited the higher apparent formation rate of ethylene (γ_{C2H4}) in the reaction than any other investigated catalysts because it had the proper amount of active Co species, the appropriate reducibility and $MgAl_2O_4$-HT as support.

Introduction

Nowadays, ethylene mainly produces from steam cracking of naphtha. Nevertheless, the production of ethylene from steam cracking is not sufficient to meet the market demands. The catalytic transformation of ethane to ethylene by

In Advances in CO2 Conversion and Utilization; Hu, Y.;
ACS Symposium Series; American Chemical Society: Washington, DC, 2010.

direct dehydrogenation or oxidative dehydrogenation has attracted great attention, because it is supplement for the shortage of ethylene.

Direct dehydrogenation of ethane (DDE) to ethylene is a strong endothermic reaction. In order to obtain the high conversion of ethane, DDE is often operated at the high temperature (800-900 °C). Hence, DDE inevitably causes the formation of coke and consumes a large amount of energy.

Comparing with DDE, oxidative dehydrogenation of ethane (ODE) to ethylene by O_2 can take place at low temperature and avoid the formation of coke. However, the easily further oxidation of ethylene drastically reduces the selectivity of ethylene in the reaction, which becomes major hardship for the real application of ODE with O_2.

ODE with CO_2 provides an alternative rout for achieving the high selectivity of ethylene. CO_2 as oxidant has many advantages because it is (i) to reduce drastic over-oxidation reaction, (ii) to remove coke on catalysts, (iii) to eliminate the flammability of reactants, (iv) to possibly make good use of the carbon-containing products by the existing technology, (v) to be inexpensive and available in great amount, etc.

Up to the present, a lot of catalysts have been developed for ODE with CO_2, such as, Mn-based oxide catalysts, Cr-based oxide catalysts, Ga-based oxide catalysts, Ce-based oxide catalysts, Na_2WO_4-Mn/SiO_2 catalysts and Mo_2C/SiO_2 catalysts, etc. In the following part of this section, we shortly review the recent R&D of these catalysts for ODE with CO_2.

1.1. Mn-Based Oxide Catalysts

Krylov and co-workers found that 1.5%K-5.5%Cr-17%Mn-O/SiO_2 catalyst showed 82.6% conversion of ethane and 55.7% conversion of CO_2 as well as 76.8% selectivity of ethylene at 830°C, 3600 h^{-1} and $CO_2/C_2H_6=1.5$ (*1*). Both chromium oxide and manganese oxide were involved in the redox cycle by CO_2; therefore, the redox properties of manganese carbonate decomposing on the phase boundary of MnO-CrO played an important role on the catalytic reactivity of the catalyst (*1*, *2*). They considered that moderate basic sites were necessary for CO_2 absorption and Cr^{3+} reoxidation (*1*, *2*).

68.6% conversion of ethane and 92.3% selectivity of C_2H_4 were obtained on Fe-Mn/silicalite-2 zeolite catalyst at 800 °C, 1000 h^{-1} and $CO_2/C_2H_6=1$ (*3*). The component Mn prohibited the formation of coke and enhanced the catalytic reactivity of the catalyst greatly (*3*–*5*).

1.2. Cr-Based Oxide Catalysts

The supported Cr oxide catalysts were prepared for ODE with CO_2. Effects of supports and Cr species on the catalytic reactivity of these catalysts were investigated. Wang et al. (*6*) found that the catalytic reactivity order of these catalysts in ODE with CO_2 followed $Cr_2O_3/SiO_2 > Cr_2O_3/ZrO_2 > Cr_2O_3/Al_2O_3 > Cr_2O_3/TiO_2$. 8 wt.% Cr_2O_3/SiO_2 catalysts appeared 55.5% yield of ethylene and 61% of conversion ethane at 650 °C and $CO_2/C_2H_6=1$ (*6*). The doping of sulfate to Cr_2O_3/SiO_2 catalyst further improved the activity and stability of the catalyst

Downloaded by STANFORD UNIV GREEN LIBR on June 23, 2012 | http://pubs.acs.org
Publication Date (Web): December 3, 2010 | doi: 10.1021/bk-2010-1056.ch007

(*7*). The acidity and redox properties of support and the Cr-loading affected the distribution and the structure of chromium species on the catalyst surface, which determined the catalytic reactivity of the catalyst (*6*, *7*).

Mimura et al. (*8*, *9*) reported that Cr/H-ZSM-5 ($SiO_2/Al_2O_3 \geq 190$) catalyst exhibited the maximum formation rate of ethylene 0.516 mmol/(g.min) and >90% selectivity of ethylene at 923 K, $CO_2/C_2H_6=9$ and W/F=2480 g.min/mol. In addition, Cr/TS-1 (Si/Ti=30) catalyst gave 47.4% yield of ethylene and 90.0% selectivity of ethylene under the reaction conditions of 650 °C, SV=9000 mL/(g.h), $V(C_2H_6)/V(CO_2)=1/4$ (*10*). Bi et al. (*11*, *12*) prepared Cr-MCM-41 catalyst by hydrothermal synthesis for ODE with CO_2 and the catalyst showed ca. 60% conversion of ethane with ca. 95% selectivity of ethylene at 1000 K, $CO_2/C_2H_6=2$ and total flow of 6 L/h. The catalytic activity of Cr-MCM-41 was stable for at least 25 h on stream at 873 K, but decreased to one half upon operation at 1000 K. The authors thought that this deactivation might be due either to carbonaceous deposits on the catalyst or to over-reduction of ethylene at the high temperature (*11*, *12*).

There are some debates about the active Cr species on these catalysts for ODE with CO_2. Wang et al. (*6*, *7*) considered that Cr^{3+} species and Cr^{6+}/Cr^{3+} couples were active sites for ODE with CO_2 on Cr_2O_3/SiO_2 catalyst. Mimura et al. (*8*, *9*) believed that $Cr^{6+}=O$ or $Cr^{5+}=O$ was the catalytic species on Cr/H-ZSM-5 ($SiO_2/Al_2O_3 \geq 190$) catalyst for the reaction. During ODE with CO_2 on Cr/H-ZSM-5 catalyst, Cr^{6+} (or Cr^{5+}) species were reduced to an octahedral Cr^{3+} species by ethane at 773 K, and the reduced Cr species were reoxidized to the Cr^{6+} (or Cr^{5+}) species by CO_2 at 673-773 K (*8*). Zhao et al. (*10*) thought that the existence of reducible chromium species on Cr/TS-1 catalyst might be active species for the reaction. By means of the results of ESR and UV-DRS characterization, Ge et al. proposed that Cr^{5+} and/or Cr^{6+} species were important for ODE with CO_2 on Cr/SiO_2 catalyst (*13*).

1.3. Ga-Based Oxide Catalysts

Nakagawa et al. (*14*) studied the catalytic reactivity of a series of oxides, such as, MgO, Al_2O_3, SiO_2, CaO, TiO_2, V_2O_5, Cr_2O_3, Mn_3O_4, Fe_3O_4, ZnO, Ga_2O_3, Y_2O_3, ZrO_2, Nb_2O_5, MoO_3, In_2O_3, SnO_2, La_2O_3, CeO_2, Ta_2O_5, and Tl_2O_3, in ODE with CO_2. Ga_2O_3 was found to be an effective catalyst for the reaction at 650 °C, giving 18.6% yield of ethylene with 94.5% selectivity of ethylene. The adsorption of CO_2 on Ga_2O_3 improved the acidity of Ga_2O_3 and promoted the desorption of ethylene on the catalyst surface (*15*). Ga_2O_3 with proper acidity might be active species for ODE with CO_2 (*15*).

In order to further improve the yield of ethylene, supported Ga_2O_3 catalysts were developed for ODE with CO_2. For example, Ga_2O_3/TiO_2 catalyst showed the high conversion of ethane and the high yield of ethylene comparing with Ga_2O_3 (*15*, *16*). In addition, 15% conversion of ethane and 94% selectivity of ethylene without any observable deactivation in 70 h were obtained on Ga_2O_3/HZSM-5(97) catalyst, which was much better activity and stability than β-Ga_2O_3 (*17*). Support HZSM-5 with high Si/Al ratio decreased the acidity of the catalysts and suppressed

Downloaded by STANFORD UNIV GREEN LIBR on June 23, 2012 | http://pubs.acs.org
Publication Date (Web): December 3, 2010 | doi: 10.1021/bk-2010-1056.ch007

the side reactions (*17*). Therefore, the properties of support determined the activity and stability of these catalysts in ODE with CO_2.

1.4. Ce-Based Oxide Catalysts

Both nanometer crystalline CeO_2 and CaO-CeO_2 were catalytic activity in ODE with CO_2 (*13*, *18–20*). The incorporation of Ca into the ceria framework (the formation of CaO-CeO_2 solid solution) reduced the activity but markedly improved the selectivity of ethylene and the efficiency of CO_2. CaO-CeO_2 catalyst showed 22% yields of ethylene with 91% selectivity of ethylene at 750 °C, 12000 mL/(h.g) and $CO_2/C_2H_6=2$ (*19*). The redox couple Ce^{4+}/Ce^{3+} activated CO_2 to produce active oxygen species for the reaction (*20*). The catalyst sintering and a change in the proportion of selective and unselective active sites induced the deactivation of the catalyst (*20*).

Downloaded by STANFORD UNIV GREEN LIBR on June 23, 2012 | http://pubs.acs.org
Publication Date (Web): December 3, 2010 | doi: 10.1021/bk-2010-1056.ch007

1.5. Other Catalysts

$Na_2WO_4/Mn/SiO_2$ catalyst exhibited excellent catalytic performance in the oxidative coupling of methane (*21*, *22*). Liu et al. (*23*) further studied the catalytic performance of the catalyst for ODE with CO_2. 90% selectivity of C_2H_4 with 69.5% conversion of C_2H_6 was obtained on $Na_2WO_4/Mn/SiO_2$ catalyst at 800 °C, $CO_2/C_2H_6=1$ and GHSV=3600 h^{-1} (*23*).

Recently, Zhu et al. (*24*) investigated the simultaneous production of ethylene and synthesis gas ($C_2H_4/CO/H_2=1/1/1$) over Co-doped $Na_2WO_4/Mn/SiO_2$ catalyst in ODE with CO_2. These products with $C_2H_4/CO/H_2=1/1/1$ (molar ratio) can be directly used as feedstock for hydroformylation to propanal, leading to use 100% of the carbon-containing products. The synthesis gas and ethylene with the molar ratio of $C_2H_4/CO/H_2=1/1/1$ were obtained on Na_2WO_4/Co(12)-Mn/SiO_2 (12 wt.% Co-doping) catalyst under the optimal conditions of $C_2H_6/CO_2=1/5$, F=60 mL/min, 750 °C and 0.3 g catalyst (*24*). The Co doping improved the catalytic performance moderately by enhancing the reforming of ethane with CO_2. The Co species reduced into metal Co might act as the active phase for CO production.

Mo_2C/SiO_2 catalyst exhibited 90-95% selectivity of ethylene and 8-30% conversion of ethane in ODE with CO_2 at 850-923 K and $CO_2/C_2H_6=1\text{-}2.7$ (*25*). Active oxygen and Mo oxycarbide formed in the reaction between CO_2 and Mo_2C (*25*). Ethane reacted with the activated oxygen attached to Mo to produce ethylene and water (*25*).

In summary, since the intrinsic complexity of ODE with CO_2, the selectivity of ethylene is dependent on many factors, such as, the composition of catalyst, the properties of active sites, the preparation of catalysts and the interaction of reactants with catalyst, etc. Moreover, it is not certain what species on these catalysts are responsible for ODE with CO_2. Without the deep understanding the properties-function relationship of these catalysts, it is difficult to improve the catalytic performance of the catalyst by the preparation and component modification. Therefore, in view of both practical and academic interest, it is highly desirable to further explore the properties-catalytic function relation of the catalyst in ODE with CO_2 to guide the development of an effective catalyst.

Recently, Zhu et al. (*25*) found that the addition of Co into Na_2WO_4/Mn/SiO_2 catalyst enhanced ethane conversion in ODE with CO_2. Kabouss et al. (*26*) reported that CoO_x/CaO catalysts showed high reactivity in ODE with O_2. The role of cobalt was to favor the reactivity of the bridging oxygen (formation/replenishing of the vacancies) whereas calcium ions brought the basicity in CoO_x/CaO catalysts, promoting ethane activation and hydrogen abstraction (*26*). Zhang et al. (*27*) observed that 7 wt% Co–$BaCO_3$ catalysts exhibited the maximal formation rate of ethylene 0.264 mmol/(min.g) at 650 °C, C_2H_6/CO_2=1/3 and 6000 ml.(g.h)$^{-1}$. Co^{4+} species might be main active sites on 7 wt% Co–$BaCO_3$ catalyst and the co-operation of $BaCO_3$ and $BaCoO_3$ was one of possible reasons for the high catalytic activity of the catalyst (*27*).

It is found that $MgAl_2O_4$ has high melting temperature (2135 °C), high resistance to chemical attack, good mechanical strength, low dielectric constant and acid-base properties, etc. (*28*, *29*). $MgAl_2O_4$ has been used as catalyst support for alkane dehydrogenation (*30–34*), methane oxidation (*35*), alkane reforming (*36–39*) and ammonia decomposition (*40*). As catalyst support, it is desirable that $MgAl_2O_4$ is high surface area. However, the conventional preparation method, for example, solid-state reaction method, is rather difficult to synthesize high-surface-area $MgAl_2O_4$ at low temperature (<1450 °C). In order to extend the catalytic application of $MgAl_2O_4$, we should explore an available route to prepare high-surface-area $MgAl_2O_4$. Up to date, several methods, such as, co-precipitation method (*36*, *37*, *41*), sol-gel process (*42–44*), spray-drying (*45*, *46*), freeze-drying (*47*), modified Pechini process (*48*) and combustion synthesis (*49*) etc., have been used to prepare high-surface-area $MgAl_2O_4$. Hydrothermal synthesis is considered to be an alternative method for preparing high-surface-area material with the controlled stoichiometric composition. However, to our knowledge, few works on the hydrothermal synthesis of $MgAl_2O_4$ have been reported.

In this present work, high-surface-area $MgAl_2O_4$ was synthesized by hydrothermal method and co-precipitation method. In addition, $CoO_x/MgAl_2O_4$ catalysts with the different Co-loading and $MgAl_2O_4$ were used for ODE with CO_2. Effects of the Co-loading and the support $MgAl_2O_4$ on the catalytic performance of $CoO_x/MgAl_2O_4$ catalysts were investigated. The physicochemical properties of these catalysts were comparatively characterized by x-ray diffraction (XRD), X-ray florescence (XRF), infrared spectroscopy (IR), N_2 isothermal adsorption-desorption, transmission electron microscopy (TEM) and H_2 temperature-programmed reduction (H_2-TPR) techniques. The catalytic function-properties relations of these catalysts are discussed.

Experimental

2.1. Preparation of $MgAl_2O_4$

$MgAl_2O_4$ was prepared by hydrothermal synthesis and co-precipitation method, respectively. The typical hydrothermal synthesis process of $MgAl_2O_4$ is described as following steps, (1) 6.4 g $Mg(NO_3)_2{\cdot}6H_2O$ (Guoyao Jituan Co., A.R.) and 18.8 g $Al(NO_3)_3{\cdot}9H_2O$ (Beijing Chem. Co., A.R.) were solved in 50 mL deionized water to form the solution A. (2) 1.2 g cetyltrimethylammonium

Downloaded by STANFORD UNIV GREEN LIBR on June 23, 2012 | http://pubs.acs.org
Publication Date (Web): December 3, 2010 | doi: 10.1021/bk-2010-1056.ch007

Downloaded by STANFORD UNIV GREEN LIBR on June 23, 2012 | http://pubs.acs.org
Publication Date (Web): December 3, 2010 | doi: 10.1021/bk-2010-1056.ch007

bromide (CTBA, Beijing Chem. Co., A.R.) was added into the solution A to form the mixture B. (3) With quick stirring, 25 mL ammonia aqueous solution (25 wt.%, Tianjing Chem. Co.) was added drop by drop into the mixture B to produce the viscous liquid mixture C (pH=11). The composition of the mixture C was about Al: Mg: OH^-: CTBA: H_2O= 2: 1: 15: 0.1:150 (mol ratio). (4) The mixture C was transferred to an autoclave (100 mL, Toflon-lined stainless steel autoclave) and heated at 180 °C for 24 h in the carefully sealed autoclave. After the hydrothermal treatment was completed, the autoclave was quenched with cool water. The solid product was filtered and washed thoroughly by deionized water until wash water was pH=7. (5) The solid product was dried at 110 °C for 4 h and then calcined at 600 °C for 3 h. The sample prepared by hydrothermal method is donated as $MgAl_2O_4$-HT.

For reference, $MgAl_2O_4$ was prepared by the co-precipitation method. 100 mL alumina sulphate aqueous solution (0.5 mol/L, $Al_2(SO_4)_3{\cdot}16H_2O$, Beijing Shiji Co., A.R.) and 100 mL magnesium sulphate aqueous solution (0.5 mol/L, $MgSO_4{\cdot}7H_2O$, Tianjing Shiji Co., A.R.) were mixed well to form mixture D. Under fast stirring, ammonia aqueous solution (25 wt.%, Tianjing Chem. Co.) was added drop by drop into the mixture D to produce white precipitation (pH=11). The precipitation was aged for 4 h at room temperature (r.t.). Subsequently, the precipitation was filtered and washed thoroughly by deionized water until wash water was pH=7. The precipitation was dried at 110 °C for 8 h and then calcined at 1000 °C for 10 h in flowing air. The resultant $MgAl_2O_4$ is remarked as $MgAl_2O_4$-CP.

2.2. Catalysts Preparation

$CoO_x/MgAl_2O_4$-HT and $CoO_x/MgAl_2O_4$-CP catalysts were prepared by impregnation method. Under quick stirring, $MgAl_2O_4$-HT or $MgAl_2O_4$-CP powder was introduced to $Co(NO_3)_2$ ($Co(NO_3)_2 \cdot 6H_2O$, Beijing Shuanghuan Chemical, A.R.) aqueous solution with a certain concentration (wt.%) to give the different Co-loading on the catalyst. The volume of the aqueous solution was ca. 1.5 times more than that of the support. The mixture was evaporated at 90 °C under reduced pressure (90 kPa) for 4 h. Subsequently; it was calcined at 350 °C for 3 h and 600 °C for 4 h in air. The catalyst is denoted as n-$CoO_x/MgAl_2O_4$-HT or n-$CoO_x/MgAl_2O_4$-CP, in which n approximately expresses the Co-loading on the catalyst.

2.3. Characterization

XRD patterns were collected by Rogaku Rotflex D/Max-C powder X-ray diffractometer with Cu *K*α radiation (λ=0.15046 nm) operated at 40 kV and 30 mA to identify the structure of the sample.

XRF measurement was made by Rogaku 3013 XRF instrument to indentify the Co-loading on these catalysts.

IR spectra of the catalyst (ca. 12 mg) dispersed in KBr pellet were recorded by Bruker IF113V FT-IR spectrometer in the range of 400-1100 cm^{-1}. The resolution of IR spectra was ca. 4 cm^{-1}.

In Advances in CO2 Conversion and Utilization; Hu, Y.;
ACS Symposium Series; American Chemical Society: Washington, DC, 2010.

Downloaded by STANFORD UNIV GREEN LIBR on June 23, 2012 | http://pubs.acs.org
Publication Date (Web): December 3, 2010 | doi: 10.1021/bk-2010-1056.ch007

N_2 isothermal adsorption-desoprtion characterization of the sample was performed by Micromeritics ASAP400 adsorptionmeter at the liquid nitrogen temperature. The sample (ca. 240 mg) was degassed at 200 °C and 1.3×10^{-3} Pa for 4 h before the measurement of data. The specific surface area was calculated according to BET method. The volume of pores was evaluated by *t*-plot analysis of the adsorption isotherm.

TEM images were recorded on PHILPS TECNAI G2-F20 operating at 200 kV to observe the morphology and the particle size of the sample.

H_2-TPR experiment of these catalysts was carried out by a home-built fixed-bed TPR apparatus. The catalyst (ca. 200 mg) was pretreated by 30 mL/min air flow at 600 °C for 1 h, and then purged with 20 mL/min He flow. In H_2-TPR experiment, the catalyst was exposed to 20 mL/min 5 %v H_2/N_2 flow, and heated from r.t. to 850 °C with a rate of 10 °C/min. Water was removed from the outlet gas with a cold trap (at -85 °C) to avoid its interference with TCD detector.

2.4. Catalytic Test

ODE with CO_2 was carried out in a continuous-flow fixed-bed quartz reactor (i.d.=10 mm) mounted inside a tube furnace. In order to suppress the gas-phase homogenous ODE with CO_2, the space up and down the catalyst bed (0.5 g, 20-40 mesh) in the reactor was filled with quartz wool. The catalyst was firstly heated to reaction temperature in CO_2 flow, and then exposed to the feed (C_2H_6/CO_2=1/3; C_2H_6: 99.99%; CO_2: 99.995%; Huayuan Gas). The feed and products were analyzed by an on-line gas chromatograph (Angilent 1490GC) with TDX-01 column (TCD, Ar carrier, 99.999%) for the separation of H_2, CH_4, CO, CO_2, C_2H_4 and C_2H_6. The experimental data were corrected after the reaction ran for 1 h. Water in the outlet gas was collected by a cold trap (-55 °C).

The conversion of reactants and the selectivity of product are calculated as,

$$\mathbf{C_2H_6\ Conversion\ (mol\%) = (2nC_2H_4+nCH_4)/(2nC_2H_6+2nC_2H_4+nCH_4)}$$

$$\mathbf{CO_2\ Conversion\ (mol\%) = nCO/(nCO_2+nCO)}$$

$$\mathbf{C_2H_4\ Selectivity\ (mol\%) = 2nC_2H_4/(2nC_2H_4+nCH_4)}$$

$$\mathbf{CH_4\ Selectivity\ (mol\%) = nCH_4/(2nC_2H_4+nCH_4)}$$

The conversion of ethane to coke is neglected because the instantaneous formation of coke is dependent on the reaction time and difficult to estimate.

In order to further evaluate the catalytic reactivity of these catalysts, the apparent formation rate of ethylene (γ_{C2H4}) is identified in terms of the amount of ethylene produced on the unit mass of the catalyst and on the reaction time (mol/(g.h)) as following,

$$\gamma_{C2H4}\ (\text{mol./(g.h)}) = W_{C2H4}\times F_{total}$$

Where W_{C2H4} is the concentration of C_2H_4 in outlet gas obtained by GC analysis (mol%), F_{total} is space velocity of feed gas (mol/(g.h)).

Downloaded by STANFORD UNIV GREEN LIBR on June 23, 2012 | http://pubs.acs.org
Publication Date (Web): December 3, 2010 | doi: 10.1021/bk-2010-1056.ch007

Table 1. Catalytic performance of these catalysts in ODE with CO_2 [a]

		Conv. (mol%)		*Sele. (mol%)*			
Catalysts	*Co%* [c]	*C_2H_6*	*CO_2*	*C_2H_4*	*CH_4*	*CO/H_2* [d]	*γ_{C2H4}* [e]
Blank Reactor [b]	-	2.4	-	97.2	2.8	-	0.5
Quartz wool [b]	-	1.1	-	99.5	0.5	-	0.2
$MgAl_2O_4$-HT	-	17.0	4.0	80.2	19.8	1.0	1.8
$MgAl_2O_4$-CP	-	11.5	2.5	75.5	24.5	1.1	1.2
1-CoO_x/ $MgAl_2O_4$-HT	0.9	32.5	18.5	99.0	1.0	1.0	6.5
3-CoO_x/ $MgAl_2O_4$-HT	3.2	38.2	20.5	98.8	1.2	1.0	7.6
5-CoO_x/ $MgAl_2O_4$-HT	5.3	47.5	25.2	98.4	1.6	1.1	9.4
8-CoO_x/ $MgAl_2O_4$-HT	8.0	54.5	31.8	85.5	14.5	1.2	9.3
10-CoO_x/ $MgAl_2O_4$-HT	10.0	62.6	35.8	62.5	37.5	1.3	7.8
5-CoO_x/ $MgAl_2O_4$-CP	5.4	39.2	19.9	92.0	8.0	1.2	7.2

[a] Reaction conditions: 600 °C, 6000 mL/(g.h), $C_2H_6/CO_2=1/3$. [b] Reaction conditions: 650 °C, 6000 mL/(g.h), $C_2H_6/CO_2=1/3$. [c] The Co-loading (wt.%) was identified by XRF. [d] Mol ratio. [e] The unit is ($\times 10^{-2}$, mol/(g.h)).

Results

3.1. Catalytic Performance

3.1.1. Effects of the Co-Loading

Table 1 shows the catalytic reactivity of $CoO_x/MgAl_2O_4$ catalysts with the different Co-loading. Ethane conversion was 2.4% and CO_2 conversion was nearly zero in the blank reactor at 650 °C, 6000 ml/(g.h) and $C_2H_6/CO_2=1/3$. When quartz wool was filled in the reactor, ethane conversion further decreased to 1.1% under the reaction conditions. These results indicate that homogenous gas-phase reaction of ethane could be negligible at the temperature $\leq$ 650 °C. The distinct conversion of ethane and CO_2 with products ethylene, CH_4, CO, H_2 and water was detected on these catalysts in ODE with CO_2. The observed activity is mainly due to the present of these catalysts in the reaction.

$CoO_x/MgAl_2O_4$-HT catalysts exhibited the higher conversion of ethane and the higher γ_{C2H4} than the support $MgAl_2O_4$-HT. Similarly, 5-$CoO_x/MgAl_2O_4$-CP catalyst showed the higher catalytic reactivity than $MgAl_2O_4$-CP. These results indicate that the loading of Co enhances the oxidative dehydrogenation of ethane to ethylene with CO_2 on $CoO_x/MgAl_2O_4$ catalysts. With increasing the Co-loading, ethane conversion and CO_2 conversion gradually increased while ethylene selectivity decreased on $CoO_x/MgAl_2O_4$-HT. CO/H_2 ratio slightly increased with the increase of the Co-loading. γ_{C2H4} varied as the Co-loading on $CoO_x/MgAl_2O_4$-HT and the maximal γ_{C2H4} was obtained on 5-$CoO_x/MgAl_2O_4$-HT. Hence, the Co-loading greatly affected the catalytic reactivity of $CoO_x/MgAl_2O_4$-HT catalysts in ODE with CO_2.

3.1.2. *Effects of Support $MgAl_2O_4$*

As can be seen in Table 1, $MgAl_2O_4$-HT shows the higher catalytic reactivity than $MgAl_2O_4$-CP in ODE with CO_2. It is remarkable that 5-$CoO_x/MgAl_2O_4$-HT exhibited the higher ethane conversion and the higher selectivity of ethylene than 5-$CoO_x/MgAl_2O_4$-CP under the reaction conditions. In addition, 5-$CoO_x/MgAl_2O_4$-HT had the higher γ_{C2H4} than 5-$CoO_x/MgAl_2O_4$-CP. These results suggest that the support $MgAl_2O_4$ prepared by different method plays important influences on the catalytic performance of $CoO_x/MgAl_2O_4$.

In order to further evaluate the effect of support $MgAl_2O_4$ on the catalytic reactivity of these catalysts, the apparent activation energy (E_a) of ODE with CO_2 on 5-$CoO_x/MgAl_2O_4$-HT and 5-$CoO_x/MgAl_2O_4$-CP was respectively estimated in terms of Arrhenius equation $\gamma = A\exp(-E_a/RT)$ (*50*). γ is the apparent formation rate of ethylene (γ_{C2H4}) in the reaction, A is preexponential and T is reaction temperature (K). The lineal plot of $\ln(\gamma_{C2H4})$ versus 1/T was obtained by lineal regression method (*50*). The apparent active energy of the reaction on 5-$CoO_x/MgAl_2O_4$-HT is ca. 163 KJ/mol and that on $CoO_x/MgAl_2O_4$-CP is ca. 176 KJ/mol, which is consistent with 5-$CoO_x/MgAl_2O_4$-HT exhibiting the higher reactivity in the reaction than 5-$CoO_x/MgAl_2O_4$-CP (*50*). These results further indicate that support $MgAl_2O_4$ prepared by different method has great influences on the catalytic reactivity of these catalysts. Comparing with $MgAl_2O_4$-CP, $MgAl_2O_4$-HT is much propitious to be as support of 5-$CoO_x/MgAl_2O_4$ for ODE with CO_2.

3.1.3. *Effects of Reaction Temperature*

Figure 1 presents effects of reaction temperature on the catalytic reactivity of 5-$CoO_x/MgAl_2O_4$-HT catalyst in ODE with CO_2. With the increase of reaction temperature, both ethane conversion and CO_2 conversion monotonously increased. These results indicate that the high reaction temperature enhances the transformation of ethane and CO_2 on the catalyst. When the reaction temperature rose, the selectivity of ethylene gradually decreased while the selectivity of CH_4 increased. CO/H_2 ratio slightly increased with the increase of the reaction temperature (not shown in Figure 1). γ_{C2H4} increased on 5-$CoO_x/MgAl_2O_4$-HT catalyst with increasing the reaction temperature. The result indicates that the high reaction temperature favors the yield of ethylene in ODE with CO_2 on the catalyst. Therefore, the catalytic reactivity of 5-$CoO_xMgAl_2O_4$-HT is strongly depended on the reaction temperature.

Downloaded by STANFORD UNIV GREEN LIBR on June 23, 2012 | http://pubs.acs.org
Publication Date (Web): December 3, 2010 | doi: 10.1021/bk-2010-1056.ch007

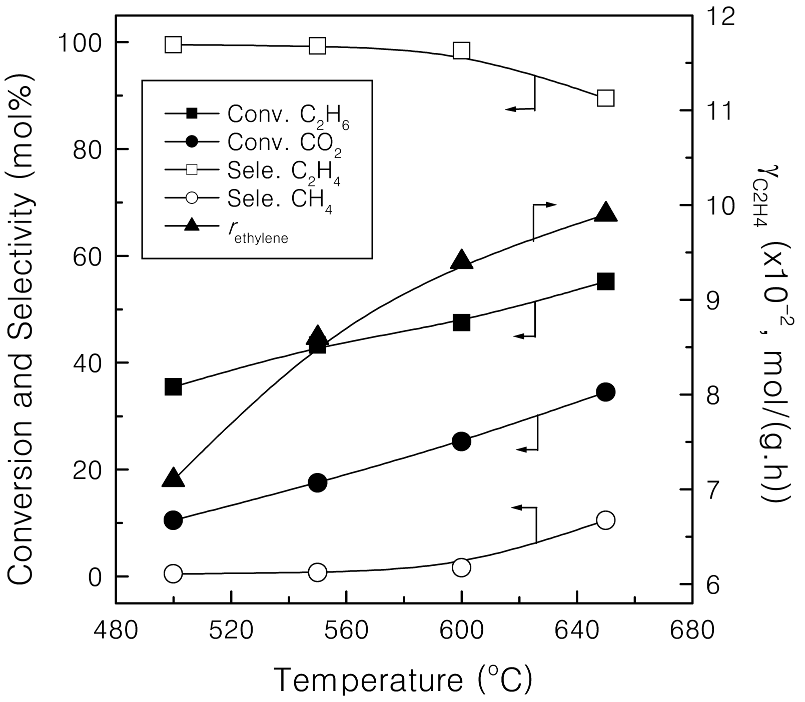

Figure 1. Effects of reaction temperature on the catalytic reactivity of 5-$CoO_x/MgAl_2O_4$-HT in ODE with CO_2. Reaction conditions: $C_2H_6/CO_2=1/3$, 6000 mL/(g.h.)

3.2. Characterization

3.2.1. XRD Characterization

Figure 2 shows XRD patterns of these supports and catalysts. $MgAl_2O_4$-HT and $MgAl_2O_4$-CP appear XRD peaks at 2θ=19.0, 31.3, 36.8, 44.7, 55.8, 59.1, 65.2 and 77.2°, relative to (111), (220), (533), (311), (400), (422), (440) and (511) diffraction of spinel $MgAl_2O_4$ (*51*). Although XRD peaks of γ-Al_2O_3 are not observed in the patterns of the as-prepared $MgAl_2O_4$, it is possible that γ-Al_2O_3-$MgAl_2O_4$ solid solution formed during the preparation. The previous works revealed that the intensity ratio of (400) with (311) reflection (χ=I(400)/I(311)) could determine whether the solid solution was formed or not (*52*). A pure $MgAl_2O_4$ is $\chi=0.65$, while γ-Al_2O_3-$MgAl_2O_4$ solid solution is $\chi>0.65$ (*51*, *52*). In case of this work, the χ value of $MgAl_2O_4$-HT and $MgAl_2O_4$-CP is 0.70 and 1.1, respectively. Therefore, $MgAl_2O_4$-HT almost is impurity spinel $MgAl_2O_4$, while $MgAl_2O_4$-CP may contain γ-Al_2O_3-$MgAl_2O_4$ solid solution.

As can be seen in Figure 2, $CoO_x/MgAl_2O_4$-HT and $CoO_x/MgAl_2O_4$-CP presents XRD patterns as similar as the corresponding supports $MgAl_2O_4$-HT and $MgAl_2O_4$-CP. The result suggests that the loading of Co onto these supports can not significantly change the structure of these supports. On the other hand, the XRD peaks belonging to cobalt oxide were not detected on $CoO_x/MgAl_2O_4$-HT

In Advances in CO2 Conversion and Utilization; Hu, Y.;
ACS Symposium Series; American Chemical Society: Washington, DC, 2010.

Downloaded by STANFORD UNIV GREEN LIBR on June 23, 2012 | http://pubs.acs.org
Publication Date (Web): December 3, 2010 | doi: 10.1021/bk-2010-1056.ch007

and $CoO_x/MgAl_2O_4$-CP catalysts. The result implies that there are high dispersed small Co-O species on these catalysts.

3.2.2. FT-IR Characterization

Figure 3 gives FT-IR spectra of $MgAl_2O_4$-HT, $MgAl_2O_4$-CP and γ-Al_2O_3. The three samples present IR bands corresponding to the vibration of CO_3^{2-} (1100 and 1378 cm^{-1}), H_2O (1630 cm^{-1}), and OH group (3342 cm^{-1}) (*53–55*). $MgAl_2O_4$-HT and $MgAl_2O_4$-CP appear two additional IR bands at 527 and 696 cm^{-1} comparing with γ-Al_2O_3. These additional bands are characteristic IR bands of AlO_6 groups, which constitute the inorganic network of spinel $MgAl_2O_4$ (*37*, *48*, *53*). These results indicate that spinel $MgAl_2O_4$ forms in $MgAl_2O_4$-HT and $MgAl_2O_4$-CP. On the other hand, IR bands at 606 and 791 cm^{-1} with respective to the vibration of Al-O in γ-Al_2O_3 were observed in $MgAl_2O_4$-CP but were not clearly detected in $MgAl_2O_4$-HT. These results suggest that $MgAl_2O_4$-HT is spinel $MgAl_2O_4$ and $MgAl_2O_4$-CP is γ-Al_2O_3-$MgAl_2O_4$ solid solution. These results are agreement with those of XRD studies.

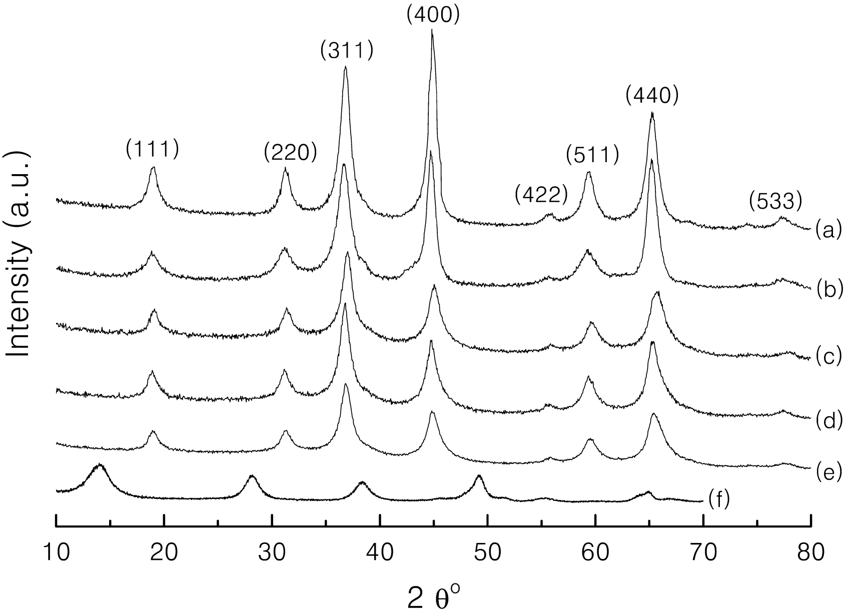

Figure 2. XRD patterns of these samples, (a) $MgAl_2O_4$-CP, (b) 5-$CoO_x/MgAl_2O_4$-CP, (c) $MgAl_2O_4$-HT, (d) 5-$CoO_x/MgAl_2O_4$-HT, (e) 10-$CoO_x/MgAl_2O_4$-HT, (f) γ-Al_2O_3

Downloaded by STANFORD UNIV GREEN LIBR on June 23, 2012 | http://pubs.acs.org
Publication Date (Web): December 3, 2010 | doi: 10.1021/bk-2010-1056.ch007

Downloaded by STANFORD UNIV GREEN LIBR on June 23, 2012 | http://pubs.acs.org
Publication Date (Web): December 3, 2010 | doi: 10.1021/bk-2010-1056.ch007

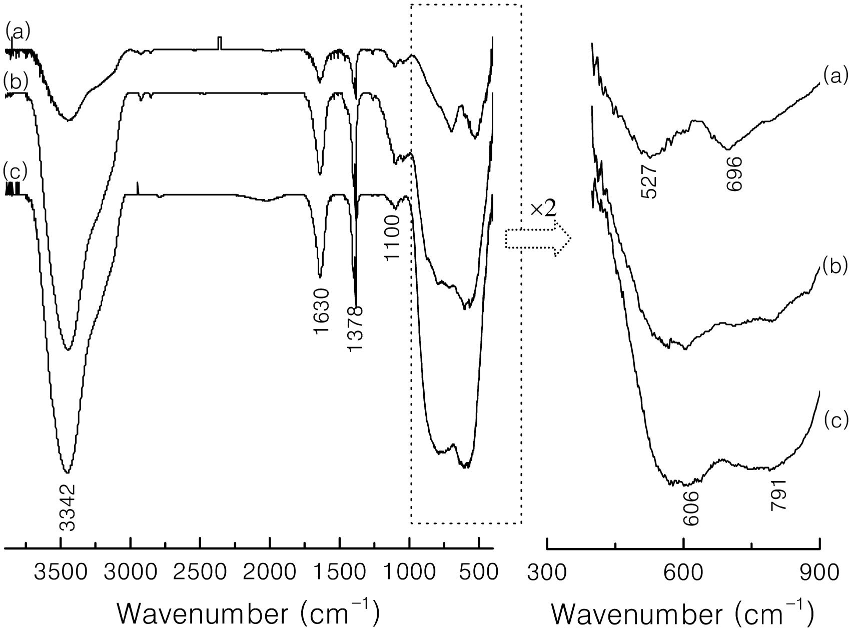

Figure 3. FT-IR spectra of these samples (a) $MgAl_2O_4$-HT, (b) $MgAl_2O_4$-CP, (c) γ-Al_2O_3.

3.2.3. N_2 Isothermal Adsorption-Desorption Characterization

Table 2 shows the specific surface area (S_{BET}) and the pore volume (V_{pore}) of these catalysts. The S_{BET} of $MgAl_2O_4$-HT is 230.6 m^2/g, which is much higher than that of $MgAl_2O_4$-CP (37.0 m^2/g). Hence, the high-surface-area spinel $MgAl_2O_4$ can be synthesized by the present hydrothermal method. The V_{pore} of $MgAl_2O_4$-HT is ca. 0.29 cm^3/g and that of $MgAl_2O_4$-CP is ca. 0.11 cm^3/g. The loading of Co on the support $MgAl_2O_4$ reduced the S_{BET} and V_{pore} of $CoO_x/MgAl_2O_4$ catalysts. With the increase of the Co-loading, both S_{BET} and V_{pore} of $CoO_x/MgAl_2O_4$-HT constantly decreased.

3.2.4. TEM Characterization

The morphology of $MgAl_2O_4$-HT, $MgAl_2O_4$-CP, 5-$CoO_x/MgAl_2O_4$-HT and 5-$CoO_x/MgAl_2O_4$-CP catalysts was examined by TEM. Figure 4 demonstrates TEM images of these catalysts. It is clearly observed from the TEM images that $MgAl_2O_4$-HT and 5-$CoO_x/MgAl_2O_4$-HT particles are little agglomeration and narrow size distribution. $MgAl_2O_4$-HT and 5-$CoO_x/MgAl_2O_4$-HT show small particles. A mean particle size of $MgAl_2O_4$-HT and 5-$CoO_x/MgAl_2O_4$-HT by the measurement of thirty particles is about 15 nm. On the other hand, $MgAl_2O_4$-CP and 5-$CoO_x/MgAl_2O_4$-CP appear to be composed of superposed platelet and

In Advances in CO2 Conversion and Utilization; Hu, Y.;
ACS Symposium Series; American Chemical Society: Washington, DC, 2010.

Table 2. Specific surface area and pore volume of these catalysts

Catalysts	*S_{BET} (m^2/g)*	*V_{pore} (cm^3/g)*	*Catalysts*	*S_{BET} (m^2/g)*	*V_{pore} (cm^3/g)*
$MgAl_2O_4$-HT	230.6	0.29	$MgAl_2O_4$-CP	37.0	0.11
3-CoO_x/ $MgAl_2O_4$-HT	230.0	0.29	5-CoO_x/ $MgAl_2O_4$-HT	222.5	0.28
10-CoO_x/ $MgAl_2O_4$-HT	199.2	0.27	5-$CoO_xMgAl_2O_4$-CP	29.5	0.10

needle-like particles. The observed superposed platelets with the size of ca. 100 nm are $MgAl_2O_4$ and the needle-like particles are γ-Al_2O_3 (*32*). These results further confirm that the γ-Al_2O_3-$MgAl_2O_4$ solid solution forms in $MgAl_2O_4$-CP. $MgAl_2O_4$-HT and 5-CoO_x/$MgAl_2O_4$-HT appear the small particle size and different morphology comparing with $MgAl_2O_4$-CP and 5-CoO_x/$MgAl_2O_4$-CP.

3.2.5. H_2-TPR Characterization

Figure 5 displays H_2-TPR plots of CoO_x/$MgAl_2O_4$ catalysts with the different Co-loading and the results are summarized in Table 3. A lot of works on H_2-TPR of the supported cobalt oxide catalysts have been reported. The previous works revealed that the H_2 reduction process of Co-O species was much complicated (*56*, *57*). Rodrigues and Bueno (*56*) considered that three types of cobalt species existed on Co/SiO_2 catalysts, viz. the bulk-like Co_3O_4 phase, Co^{n+} and $Co^{\delta+}$ species. Both the Co^{n+} and $Co^{\delta+}$ species were the surface Co species, which had intermediate or strong interaction with the support SiO_2, respectively. In addition, they assigned the H_2 consumption peaks at 300 and 360 °C to the reduction of bulk-like Co_3O_4 phase (a two-step reduction process of $Co_3O_4 \rightarrow Co^{2+} \rightarrow Co^0$), the H_2 consumption peak at 430 °C to the reduction of the Co^{n+} species and the H_2 consumption peak at 550–800 °C to the reduction of the $Co^{\delta+}$ species (*56*). Huang et al. (*57*) observed that there were three kinds of Co species on the supported cobalt catalysts. They thought that H_2-TPR peaks at 290, 330, 390 and 625 °C were respectively relative to the reduction of Co_3O_4 (290 and 330 °C), Co^{n+} (390 °C) and $Co^{\delta+}$ species (625 °C).

In case of these work, $MgAl_2O_4$ did not presented any H_2 reduction peaks under the used H_2-TPR conditions. It is found that CoO_x/$MgAl_2O_4$ catalysts show four H_2 consumption peaks at ca. 220-240, 320-350, 420-450 and 560-600 °C (Figure 5 and Table 3). For example, H_2-TPR plots of 5-CoO_x/$MgAl_2O_4$-HT and 5-CoO_x/$MgAl_2O_4$-CP could be divided to four peaks at ca. 220-245, 300-315, 400-420 and 560-575 °C by using Lorentz multi-fit method (Figure 5). According to the previous works (*56*, *57*), we tentatively assign the H_2 consumption peaks at 220-240 and 320-350 °C to the stepwise reduction of bulk-like $Co_3O_4 \rightarrow Co^{2+} \rightarrow Co^0$. The H_2 consumption peaks at 420-450 and 560-600 °C are respectively attributed to the reduction of Co^{n+} and $Co^{\delta+}$ species on these catalysts (*56*, *57*).

Downloaded by STANFORD UNIV GREEN LIBR on June 23, 2012 | http://pubs.acs.org
Publication Date (Web): December 3, 2010 | doi: 10.1021/bk-2010-1056.ch007

Downloaded by STANFORD UNIV GREEN LIBR on June 23, 2012 | http://pubs.acs.org
Publication Date (Web): December 3, 2010 | doi: 10.1021/bk-2010-1056.ch007

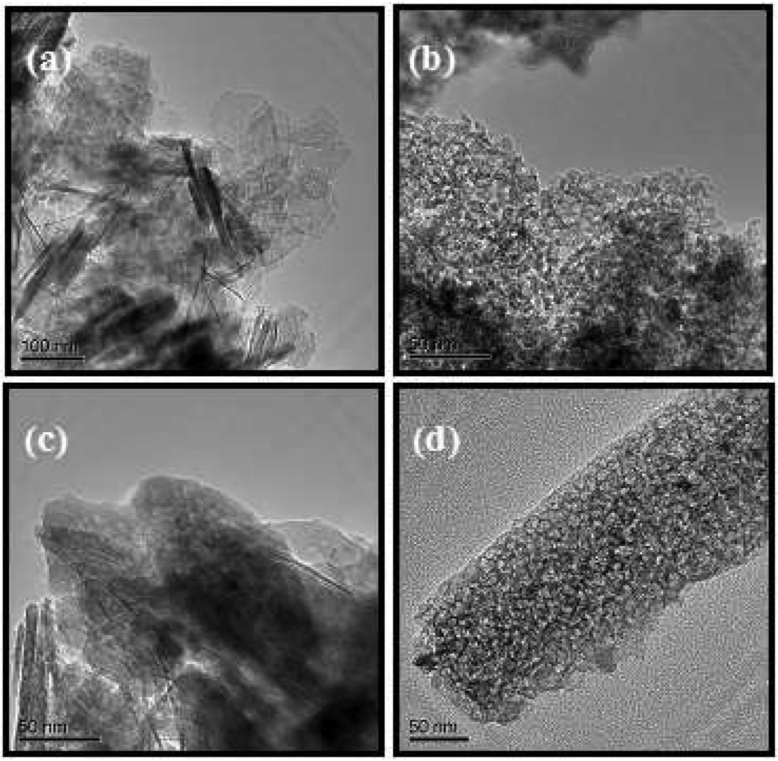

Figure 4. TEM images of these catalysts (a) $MgAl_2O_4$-CP, (b) $MgAl_2O_4$-HT, (c) 5-CoO_x/ $MgAl_2O_4$-CP and (d) 5-CoO_x/ $MgAl_2O_4$-HT.

With the increase of Co-loading, the initial reduction temperature of Co species on CoO_x/$MgAl_2O_4$-HT shifted to the low temperature. H_2 consumption of these catalyst is roughly estimated by the intergration of the H_2 reduction peaks area. The total H_2 consumption of CoO_x/$MgAl_2O_4$-HT gradually increased with the Co-loading increasing (Table 3). These results indicate that the reducibility of CoO_x/$MgAl_2O_4$-HT becomes stronger and stronger as the increase of the Co-loading.

As can be seen in Table 3, the reduction peaks of 5-CoO_x/$MgAl_2O_4$-HT shift toward the low temperature comparing with the corresponding reduction peaks of 5-CoO_x/$MgAl_2O_4$-CP. Moreover, 5-CoO_x/$MgAl_2O_4$-HT has the more total H_2 consumption than 5-CoO_x/$MgAl_2O_4$-CP. These results suggest that 5-CoO_x/$MgAl_2O_4$-HT has the stronger reducibility than 5-CoO_x/$MgAl_2O_4$-CP.

Downloaded by STANFORD UNIV GREEN LIBR on June 23, 2012 | http://pubs.acs.org
Publication Date (Web): December 3, 2010 | doi: 10.1021/bk-2010-1056.ch007

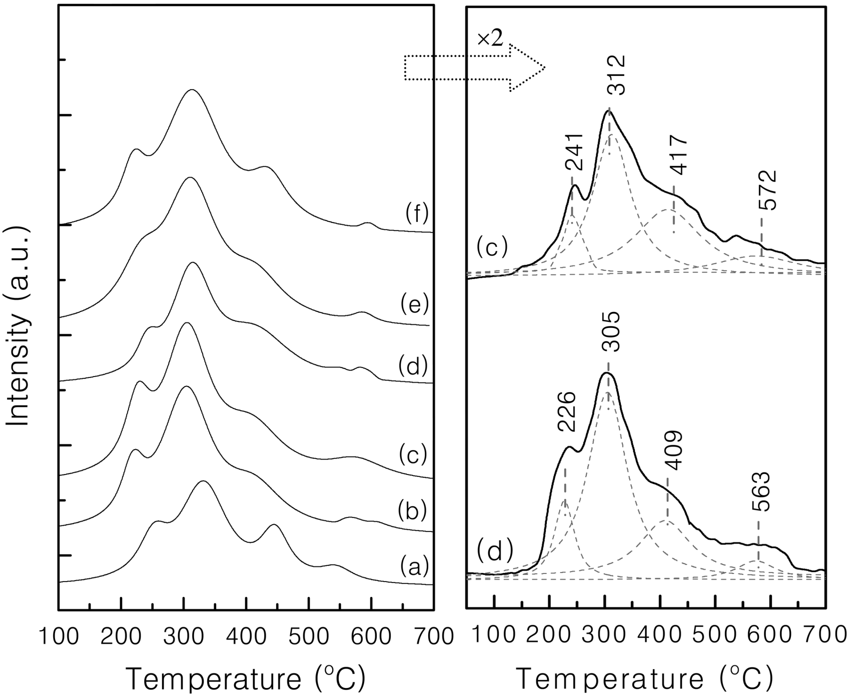

Figure 5. H_2-TPR plots of these catalysts (a) 1-$CoO_x/MgAl_2O_4$-HT, (b) 3-$CoO_x/MgAl_2O_4$-HT, (c) 5-$CoO_x/MgAl_2O_4$-HT, (d) 5-$CoO_x/MgAl_2O_4$-CP, (e) 8-$CoO_x/MgAl_2O_4$-HT, (f) 10-$CoO_x/MgAl_2O_4$-HT

Discussion

4.1. Effects of the Co-Loading and Reducibility on the Catalytic Reactivity of $CoO_x/MgAl_2O_4$

The above results reveal that the loading of Co onto $CoO_x/MgAl_2O_4$-HT catalysts not only modifies the reducibility of these catalysts, but also enhances the catalytic reactivity of these catalysts in ODE with CO_2. The catalytic reactivity and reducibility of these catalysts are close relative to the Co-loading on these catalysts. 5-$CoO_x/MgAl_2O_4$-HT exhibites the highest selectivity of ethylene and the highest γ_{C2H4} among the investigated catalysts under the reaction conditions.

In order to explain the effects of the reducibility and the Co-loading on the catalytic performance of of $CoO_x/MgAl_2O_4$-HT catalysts, we correlate the relation of the Co-loading with H_2 consumption of the Co species and γ_{C2H4} on these catalysts by multinomial regression method (Figure 6). With the increase of the Co-loading, γ_{C2H4} shows the shape-peak tendency while the total H_2 consumption of these catalysts monotonously increases. In other words, γ_{C2H4} appears the maximal value with the increase of total H_2 consumption of these catalyst. These phenomena imply that the reducibility of the Co species (Co_3O_4, Co^{n+} and $Co^{\delta+}$) and the Co-loading are closely relative to the catalytic performance of these catalysts in ODE with CO_2. The loading of Co onto the catalyst modifies the

Downloaded by STANFORD UNIV GREEN LIBR on June 23, 2012 | http://pubs.acs.org
Publication Date (Web): December 3, 2010 | doi: 10.1021/bk-2010-1056.ch007

Table 3. H_2-TPR results of $CoO_x/MgAl_2O_4$-HT with the different Co-loading and 5-$CoO_x/MgAl_2O_4$-CP

	H_2-TPR		
Sample	*Temp. (°C)*	*Assign.*	*H_2 uptake (a.u./g)*
1-$CoO_x/MgAl_2O_4$-HT	252	$Co_3O_4 \rightarrow Co^{2+}$	14.7
	331	$Co^{2+} \rightarrow Co^0$	66.2
	446	Co^{n+}	18.2
	543	$Co^{\delta+}$	6.6
			ΣH_2 uptake =105.7
3-$CoO_x/MgAl_2O_4$-HT	226	$Co_3O_4 \rightarrow Co^{2+}$	14.1
	305	$Co^{2+} \rightarrow Co^0$	95.1
	413	Co^{n+}	22.4
	597	$Co^{\delta+}$	4.3
			ΣH_2 uptake =135.9
5-$CoO_x/MgAl_2O_4$-HT	226	$Co_3O_4 \rightarrow Co^{2+}$	17.8
	305	$Co^{2+} \rightarrow Co^0$	80.3
	409	Co^{n+}	38.5
	563	$Co^{\delta+}$	10.7
			ΣH_2 uptake =147.3
8-$CoO_x/MgAl_2O_4$-HT	221	$Co_3O_4 \rightarrow Co^{2+}$	13.7
	313	$Co^{2+} \rightarrow Co^0$	117.3
	436	Co^{n+}	22.3
	595	$Co^{\delta+}$	13.4
			ΣH_2 uptake =166.7
10-$CoO_x/MgAl_2O_4$-HT	221	$Co_3O_4 \rightarrow Co^{2+}$	26.3
	313	$Co^{2+} \rightarrow Co^0$	98.1
	417	Co^{n+}	29.5
	595	$Co^{\delta+}$	27.2
			ΣH_2 uptake =181.1
5-$CoO_x/MgAl_2O_4$-CP	241	$Co_3O_4 \rightarrow Co^{2+}$	12.5
	312	$Co^{2+} \rightarrow Co^0$	50.5
	417	Co^{n+}	40.5
	572	$Co^{\delta+}$	10.2
			ΣH_2 uptake =113.7

redox properties of the catalyst, which in turn affects the catalytic reactivity of the catalyst.

The redox mechanism is believed to play important roles in ODE with CO_2 on $CoO_x/MgAl_2O_4$ catalysts. Ethane reacts with the active oxygen species attached to the surface Co species to produce ethylene and the Co species are reduced. Subsequently, CO_2 oxidizes the reduced Co species and forms CO. CO_2 takes part in the redox cycle in ODE with CO_2 on $CoO_x/MgAl_2O_4$-HT catalyst. Dehydrogenation of ethane and the oxidative dehydrogenation of ethane with CO_2 simutaneously occur on $CoO_x/MgAl_2O_4$-HT through the parallel reaction pathways. On the other hand, products CO, H_2 and water were detected on the catalyst in ODE with CO_2. It can be deduced that the reforming of ethane with CO_2 and/or the reverse water gas shift reaction take place. CH_4 may produce from the cracking of ethane. Therefore, the possible reaction pathways on $CoO_x/MgAl_2O_4$-HT are proposed as following:

$$C_2H_6 + CoO_x \Leftrightarrow C_2H_4 + CoO_{x-1} + H_2O \tag{i}$$

$$CO_2 + CoO_{x-1} \Leftrightarrow CoO_x + CO \tag{ii}$$

$$C_2H_6 \Leftrightarrow C_2H_4 + H_2 \tag{iii}$$

$$CO_2 + H_2 \Leftrightarrow CO + H_2O \tag{iv}$$

$$CO_2 + C_2H_6 \Leftrightarrow CO + H_2 \tag{v}$$

$$C_2H_6 + H_2 \Leftrightarrow 2CH_4 \tag{vi}$$

The increase of Co-loading may increase the amount of active Co species. The more active Co species the catalyst has, the higher the reducibility of the catalyst is. The improvement of the amount of active Co species and the reducibility of these catalysts enhances the activation of ethane and CO_2. Hence, the high conversion of ethane and CO_2 was obtained on the catalysts with the high Co-loading. Nevertheless, the large number of active Co species and the high reducibility may cause the over-oxidation of ethylene on the catalyst. On the other hand, Zhu et al. (*24*) observed that the addition of Co into $Na_2WO_4/Mn/SiO_2$ catalyst improved the CO_2 reforming of ethane on the catalyst during ODE with CO_2. Wang et al. (*58*) reported that the Co/SiO_2 catalysts showed high catalytic reactivity in CO_2 reforming of methane with the Co-loading increasing from 8% to 36%. San-José-Alonso et al. (*59*) found that alumina supported Ni, Co and bimetallic Ni–Co catalysts with the high Co-loading were most active and stable among these investigated catalysts in CO_2 reformaing of methane. In this work, CO/H_2 ratio gradually increased on $CoO_x/MgAl_2O_4$-HT catalyst with the increase of the Co-loading. In view of these points, $CoO_x/MgAl_2O_4$-HT catalyst with the high Co-loading might enhance the CO_2 reforming of ethane. Therefore, it is necessary that $CoO_x/MgAl_2O_4$-HT catalyst has the proper amount of active Co species and appropriate reducibility to achieve the high selectivity and yield of ethylene in ODE with CO_2.

Downloaded by STANFORD UNIV GREEN LIBR on June 23, 2012 | http://pubs.acs.org
Publication Date (Web): December 3, 2010 | doi: 10.1021/bk-2010-1056.ch007

Downloaded by STANFORD UNIV GREEN LIBR on June 23, 2012 | http://pubs.acs.org
Publication Date (Web): December 3, 2010 | doi: 10.1021/bk-2010-1056.ch007

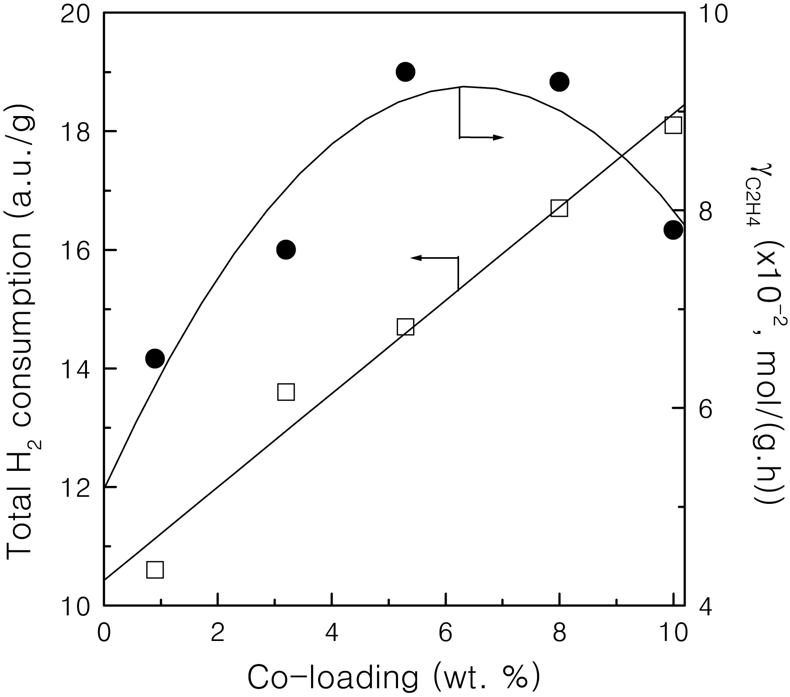

Figure 6. Relation of the Co-loading with the total H_2 consumption and catalytic reactivity of $CoO_x/MgAl_2O_4$-HT catalysts in ODE with CO_2. Reaction condition: 600 °C, 6000 mL/(g.h), $C_2H_6/CO_2=1/3$.

4.2. Effects of Support $MgAl_2O_4$ on the Catalytic Reactivity of $CoO_x/MgAl_2O_4$

Generally speaking, $MgAl_2O_4$ forms through the reaction of Mg oxide (Mg hydroxide) with Al oxide (Al hydroxide) particles. It is well known that metal oxide and metal hydroxide particles are easily to form the long chains of particle by hydrogen bond in the wet-chemical preparation. Such phenomena cause the growth of oxide particle when the oxide calcines at the high-temperature. The addition of CTBA and the hydrothermal treatment of the oxide at low temperature can prevent from the formation of the long chains of the oxide particles. Hence, Mg oxide (Mg hydroxide) and Al oxide (Al hydroxide) particles are small and little agglomeration. Small Mg oxide (Mg hydroxide) and small Al oxide (Al hydroxide) particles can easily react to form nanocrystallite $MgAl_2O_4$ at relative low temperature because they have high reactivity (*53*). In addition, CTBA can give off gas and heat energy during the heated process. The release of heat energy can further reduce the formation temperature of $MgAl_2O_4$. The low formation temperature favors the formation of high-surface-area nanocrystallite $MgAl_2O_4$. The release of gas during the heated process enhances the formation of pores in the as-synthesized $MgAl_2O_4$. Therefore, the addition of CTBA and

In Advances in CO2 Conversion and Utilization; Hu, Y.;
ACS Symposium Series; American Chemical Society: Washington, DC, 2010.

the hydrothermal treatment favor the formation of high-surface-area porous nanocrystallite $MgAl_2O_4$.

High-surface-area porous nanometer spinel $MgAl_2O_4$ was prepared by the present hydrothermal method. The hydrothermally prepared $MgAl_2O_4$ ($MgAl_2O_4$-HT) has the higher S_{BET} and the larger V_{pore} as well as the smaller particle size than the co-precipitation prepared $MgAl_2O_4$ ($MgAl_2O_4$-CP).

The support $MgAl_2O_4$-HT has the higher surface area and the larger pore volume than $MgAl_2O_4$-CP. High-surface-area porous nanocrystallite $MgAl_2O_4$-HT can enhance the high dispersion of active sites and improve the diffusion of reactants and products. Therefore, 5-CoO_x/$MgAl_2O_4$-HT exhibited the lower activity energy (Ea) and the higher catalytic reactivity than 5-CoO_x/$MgAl_2O_4$-CP in ODE with CO_2. $MgAl_2O_4$-HT is better support of the supported Co-based catalyst for ODE with CO_2 than $MgAl_2O_4$-CP.

Evans et al. (*30*) reported that VO_x/$MgAl_2O_4$ presented high catalytic performance in oxidative dehydrogenation of propane, due to high-surface-area mesoporous $MgAl_2O_4$ as support. The high-surface-area mesoporous $MgAl_2O_4$ increased the dispersion of VO_x species and enhanced the formation of the active VO_x species (*30*). Bocanegra et al. (*32*) found that Pt/$MgAl_2O_4^{mec}$ showed a better catalytic performance in dehydrogenation of n-butane than Pt/$MgAl_2O_4^{cer}$ and Pt/$MgAl_2O_4^{cop}$ because $MgAl_2O_4^{mec}$ prepared by mechanochemical synthesis had the higher surface area than $MgAl_2O_4^{cer}$ prepared by ceramic method and $MgAl_2O_4^{cop}$ prepared by co-precipitation method. $MgAl_2O_4^{mec}$ improved the metallic dispersion and H_2 chemisorption capacity on Pt/$MgAl_2O_4^{mec}$, which resulted in the high catalytic performance of Pt/$MgAl_2O_4^{mec}$ in the dehydrogenation of n-butane. Waston et al. (*39*) developed high performance and stability Rh/Mg-stabilized alumina layer/substrate catalyst for methane steam reforming. The characteristic configuration of the catalyst determined the excellent performance of the catalyst in the reaction. Mg-stabilized alumina layer was $MgAl_2O_4$ spinel and coated over the substrate with high surface area and large pore, which provided high surface area for good metal dispersion and high metal loading and provided the excellent stability of the catalyst in methane steam reforming.

Conclusions

5-CoO_x/$MgAl_2O_4$-HT catalyst is an effective catalyst for ODE with CO_2. The loading of Co modifies the reducibility and CO_2 reforming of ethane on CoO_x/$MgAl_2O_4$ catalysts, which in turn affects the catalytic reactiviy of these catalysts in ODE with CO_2. The surface CoO_x (Co_3O_4, Co^{n+} and $Co^{\delta+}$) species are close relative to the catalytic reactivity of CoO_x/$MgAl_2O_4$-HT catalyst in ODE with CO_2. It is necessary that the catalyst possesses the proper amount of active Co species and the appropriate reducibility to achieve the high selectivity and yield of ethylene in the reaction.

High-surface-area porous nanometer spinel $MgAl_2O_4$ ($MgAl_2O_4$-HT) can be synthesized by the present hydrothermal method. $MgAl_2O_4$-HT can highly disperse active sites on the catalyst and improve the diffusion of

Downloaded by STANFORD UNIV GREEN LIBR on June 23, 2012 | http://pubs.acs.org
Publication Date (Web): December 3, 2010 | doi: 10.1021/bk-2010-1056.ch007

reactants and products in the reaction, which is one of possible reasons that 5-CoO_x/$MgAl_2O_4$-HT showed high catalytic reactivity than 5-CoO_x/$MgAl_2O_4$-CP. $MgAl_2O_4$-HT is a kind of promising catalyst support.

Acknowledgments

We gratefully acknowledged the finical support of the work by National Ministry of Education (20096101120018, NCET-10-878, scientific research foundation for returned Chinese scholars-2009-37th), Shaanxi "13115" Innovation Project (2009ZDKJ-70), Science Research Project of Shaanxi Education Department (09JK793), Northwest University (No: PR09005) and State Key Lab for Physical Chemistry of Solid Surfaces (2009).

Downloaded by STANFORD UNIV GREEN LIBR on June 23, 2012 | http://pubs.acs.org
Publication Date (Web): December 3, 2010 | doi: 10.1021/bk-2010-1056.ch007

References

1. Krylov, O. V.; Mamedov, A. K.; Mirzabekova, S. R. *Stud. Surf. Sci. Catal.* **1994**, *82*, 159–166.
2. Krylov, A. K.; Mamedov, S. R.; Mirzabekov, S. R. *Catal. Today* **1995**, *24*, 371–375.
3. Xu, L.; Lin, L.; Wang, Q.; Li, Y.; Wang, D.; Liu, W. *Stud. Surf. Sci. Catal.* **1998**, *119*, 605–610.
4. Xu, L.; Liu, J.; Yang, H.; Xu, Y.; Wang, Q.; Lin, L. *Catal. Lett.* **1999**, *62*, 185–189.
5. Xu, L.; Liu, J.; Xu, Y.; Yang, H.; Wang, Q.; Lin, L. *Appl. Catal., A* **2000**, *193*, 95–101.
6. Wang, S.; Murata, K.; Hayakawa, T.; Hamakawa, S.; Suzuki, K. *Appl. Catal., A* **2000**, *196*, 1–8.
7. Wang, S.; Murata, K.; Hayakawa, T.; Hamakawa, S.; Suzuki, K. *Catal. Lett.* **1999**, *63*, 59–64.
8. Mimura, N.; Takahara, I.; Inaba, M.; Okamoto, M.; Murata, K. *Catal. Commun.* **2002**, *3*, 257–262.
9. Mimura, N.; Okamoto, M.; Yamashita, H.; Oyama, S. T.; Murata, K. *J. Phys. Chem. B* **2006**, *110*, 21764–21770.
10. Zhao, X.; Wang, X. *Catal. Commun.* **2006**, *7*, 633–638.
11. Bi, Y. L.; Cortes Corberan, V.; Zhuang, H.; Zhen, K. J. *Stud. Surf. Sci. Catal.* **2004**, *153*, 343–347.
12. Cortes Corberan, V. *Catal. Today* **2005**, *99*, 33–41.
13. Ge, X.; Zhu, M.; Shen, J. *React. Kinet. Catal. Lett.* **2002**, *77*, 103–108.
14. Nakagawa, K.; Okamura, M.; Ikenaga, N.; Suzuki, T.; Kobayashic, T. *Chem. Commun.* **1998**, 1025–1026.
15. Nakagawa, K.; Kajita, C.; Okumura, K.; Ikenaga, N.; Nishitani-Gamo, M.; Ando, T.; Kobayashi, T.; Suzuki, T. *J. Catal.* **2001**, *203*, 87–93.
16. Nakagawa, K.; Kajita, C.; Ide, Y.; Okamura, M.; Kato, S.; Kasuya, H.; Ikenaga, N.; Kobayashi, T.; Suzuki, T. *Catal. Lett.* **2000**, *64*, 215–221.
17. Shen, Z.; Liu, J.; Xu, H.; Yue, Y.; Hua, W.; Shen, W. *Appl. Catal., A* **2009**, *356*, 148–153.

18. Valenzuela, R. X.; Bueno, G; Solbes, A.; Sapiña, F.; Martínez, E.; Cortés Corberán, V. *Top. Catal.* **2001**, *15*, 2–4.
19. Valenzuela, R. X.; Bueno, G.; Cortes Corberan, V.; Xu, Y.; Chen, C. *Catal. Today* **2000**, *61*, 43–48.
20. Guıo, M.; Prieto, J.; Cortes Corberan, V. *Catal. Today* **2006**, *112*, 148–152.
21. Fang, X. P.; Li, S. B.; Lin, J. Z.; Gu, J. F.; Yang, D. X. *China J. Mol. Catal.* **1992**, *6*, 255–261.
22. Fang, X. P.; Li, S. B.; Lin, J. Z.; Chu, Y. L. *China J. Mol. Catal.* **1992**, *6*, 427–432.
23. Liu, Y.; Xue, J.; Liu, X.; Li, S. B. *Stud. Surf. Sci. Catal.* **1998**, *119*, 593–598.
24. Zhu, J.; Qin, S.; Ren, S.; Peng, X.; Tong, D.; Hu, C. *Catal. Today* **2009**, *148*, 310–315.
25. Solymosi, F.; Nemeth, R. *Catal. Lett.* **1999**, *62*, 197–200.
26. Kabouss, K. E.; Kacimi, M.; Ziyad, M.; Ammar, S.; Ensuque, A.; Piquemal, J.; Bozon-Verduraz, F. *J. Mater. Chem.* **2006**, *16*, 2453–2463.
27. Zhang, X.; Ye, Q.; Xu, B.; He, D. *Catal. Lett.* **2007**, *117*, 140–145.
28. Kingdom, A. I.; Davis, R. F.; Thackery, M. M. *Introduction to Glasses and Ceramics*, Vol.4; ASM International: New York, 1999.
29. Baudin, G.; Martinez, R.; Pena, P. *J. Am. Ceram. Soc.* **1995**, *80*, 1857–1862.
30. Evans, W.; Bell, A. T.; Tilley, T. D. *J. Catal.* **2004**, *226*, 292–300.
31. Bocanegra, S.; Cuerrero-Ruiz, A.; de Miguel, S.; Scelza, O. *Appl. Catal., A* **2004**, *277*, 11–22.
32. Bocanegra, S.; Ballarini, A. D.; Scelza, O. A.; de Miguel, S. R. *Mater. Chem. Phys.* **2008**, *111*, 534–541.
33. Bocanegra, S.; de Miguel, S. R.; Castro, A. A.; Scelza, O. A. *Catal. Lett.* **2004**, *96*, 129–134.
34. Armendariz, H.; Guzman, A.; Toledo, J.; Llanos, M.; Vazquez, A.; Aguilar-Rios, G. *Appl. Catal., A* **2001**, *211*, 69–80.
35. Basile, F.; Fornasari, G.; Rosetti, V.; Trifiro, F.; Vaccari, A. *Catal. Today* **2004**, *91/92*, 293–297.
36. Guo, J.; Luo, H.; Zhao, H.; Chai, D.; Zheng, X. *Appl. Catal., A* **2004**, *273*, 75–82.
37. Guo, J.; Liu, H.; Zhang, H.; Wang, X.; Zheng, X. *Mater. Lett.* **2004**, *58*, 1920–1923.
38. Sehested, J.; Carlsson, A.; Janssens, T.; Hansen, P.; Datye, A. *J. Catal.* **2001**, *197*, 200–209.
39. Waston, J. M.; Daly, F. P.; Wang, Y.; Tonkovich, A. L.; Fitzgerald, S. P.; Perry, S. T.; Silva, L. T.; Taha, R.; de Alba, E. A.; Chin, Y.; Rozmicrek, R.; Li, X. U.S. Patent US2004/0266615 A1, 2004.
40. Szmigel, D.; Rarog-Pilecka, W.; Miskiewicz, E.; Kaszkur, Z.; Kowalczyk, Z. *Appl. Catal., A* **2004**, *264*, 59–63.
41. Shiono, T.; Shiono, K.; Miyamoto, K. *J. Am. Ceram. Soc.* **2000**, *83*, 235–237.
42. Zhang, H.; Jia, X.; Liu, Z.; Li, Z. *Mater. Lett.* **2004**, *58*, 1625–1628.
43. Li, J. G.; Ikegami, T.; Lee, J. H. *J. Eur. Ceram. Soc.* **2001**, *21*, 139–247.
44. Li, G.; Sun, Z.; Chen, C.; Cui, X.; Ren, R. *Mater. Lett.* **2007**, *61*, 3585–3588.

Downloaded by STANFORD UNIV GREEN LIBR on June 23, 2012 | http://pubs.acs.org
Publication Date (Web): December 3, 2010 | doi: 10.1021/bk-2010-1056.ch007

45. Bickmore, C. R.; Walder, K. F.; Treadwell, D. R. *J. Am. Ceram. Soc.* **1996**, *79*, 1419–1423.
46. Montouillout, V.; Massiot, D.; Douy, A.; Coutres, J. P. *J. Am. Ceram. Soc.* **1999**, *82*, 3299–3304.
47. Wang, C. T.; Lin, L. S.; Yang, S. J. *J. Am. Ceram. Soc.* **1992**, *75*, 2240–2243.
48. Adak, A. K.; Saha, S. K.; Pramanik, P. *J. Mater. Sci. Lett.* **1997**, *16*, 234–235.
49. Bhaduri, S.; Bhaduri, S. B.; Prisbrey, K. A. *J. Mater. Res.* **1999**, *14*, 3571–3578.
50. Zhang, X. *Mater. Chem. Phys.* **2009**, *116*, 415–420.
51. JCPDS Card No. 21-1152
52. Pasquier, J. F.; Komarneni, S.; Roy, R. *J. Mater. Sci.* **1991**, *26*, 3797–3802.
53. Parmentier, J.; Richard-Plouet, M.; Vilminot, S. *Mater. Res. Bull.* **1998**, *33*, 1717–1724.
54. Zic, M.; Ristic, M.; Music, S. *J. Mol. Struct.* **2007**, *141*, 834–836.
55. Nagaraju, P.; Srilakshmi, C.; Pasha, N.; Lingaiah, N.; Suryanarayana, I.; Sai Prasad, P. S. *Appl. Catal., A* **2008**, *334*, 10–19.
56. Rodrigues, E. L.; Bueno, J. M. C. *Appl. Catal., A* **2002**, *232*, 147–158.
57. Huang, L.; Zhu, Y.; Zheng, H.; Du, M.; Li, Y. *Appl. Catal., A* **2008**, *349*, 204–211.
58. Wang, H. Y; Ruckenstein, E. *Appl. Catal., A* **2001**, *209*, 207–215.
59. San-José-Alonso, D.; Juan-Juan, J.; Illán-Gómez, M. J.; Román-Martínez, M. C. *Appl. Catal., A* **2009**, *371*, 54–55.

Downloaded by STANFORD UNIV GREEN LIBR on June 23, 2012 | http://pubs.acs.org
Publication Date (Web): December 3, 2010 | doi: 10.1021/bk-2010-1056.ch007

Downloaded by UNIV OF GUELPH LIBRARY on June 23, 2012 | http://pubs.acs.org
Publication Date (Web): December 3, 2010 | doi: 10.1021/bk-2010-1056.ch008

Chapter 8

Catalytic CO_2 Hydrogenation to Feedstock Chemicals for Jet Fuel Synthesis Using Multi-Walled Carbon Nanotubes as Support

Robert W. Dorner,§ Dennis R. Hardy, Frederick W. Williams, and Heather D. Willauer*

Naval Research Laboratory, Code 6180, Navy Technology Center for Safety and Survivability Branch, 4555 Overlook Avenue, SW, Washington, DC, 20375
***Corresponding Author; heather.willauer@nrl.navy.mil**
§Presenting Author

Hydrogenation of CO_2 to hydrocarbons is investigated over a K/Mn/Fe catalyst dispersed over multi-walled carbon nanotubes (MWCNT). Higher conversion yields were observed, but the catalyst favors methane formation and yields a lower olefin/paraffin ratio than an analogue catalyst dispersed on alumina reported previously. Both phenomena are ascribed to differences in the catalyst's active phase and particle size, leading to a shift in concentrations of carbonaceous surface intermediates.

Introduction

The U.S. Department of Defense (DOD) is the single largest buyer and consumer of fuel using approximately 12.6 million gal per day in 2008 (*1*). At that time the Department of Defense was paying \$4/gal, amounting to a cost of \$18 billion/year. With the introduction of the cap-and-trade system, which is aimed at reducing the amount of CO_2 a company can emit, one can expect costs for energy in general to rise in the foreseeable future (*2*). The bill (H.R. 2454) furthermore serves to reduce carbon dioxide emissions from major U.S. sources by 17% by 2020 and 83% by 2050 (based on 2005 levels). The variable price of fuel, the dependence on foreign sources of oil, and environmental concerns surrounding CO_2 emissions has encouraged DOD to invest in finding alternative routes to

In Advances in CO2 Conversion and Utilization; Hu, Y.;
ACS Symposium Series; American Chemical Society: Washington, DC, 2010.

Downloaded by UNIV OF GUELPH LIBRARY on June 23, 2012 | http://pubs.acs.org
Publication Date (Web): December 3, 2010 | doi: 10.1021/bk-2010-1056.ch008

attain fuel, specifically synthetic fuel (synfuel) and biofuel. Keeping in mind the idea of reducing CO_2 emissions, an interesting route to obtaining fuel would be to convert CO_2 with the use of hydrogen to fuel over a heterogeneous catalyst.

Due to the increased awareness of the environmental impact of CO_2, R&D efforts to bind CO_2 have increased over the last few years. Proposals range from CO_2 capture from the atmosphere by binding it in CaO using solar energy (*3*), to converting CO_2 to hydrocarbons over catalysts, either photocatalytically, electrocatalytically or thermochemically. Electrochemical and photochemical CO_2 conversion is still in its research infancy and has major drawbacks at present. Photocatalysts tend to need a sacrificial electron donor (*4*, *5*) and neither photocatalytic or electrocatalytic conversion show very high yields nor do they produce long chain hydrocarbons (HC) (*6*). Thermochemical CO_2 conversion has been known for several decades (*7*) and is presently the most proven and successful approach in producing a greater yield of HC products above methane. Riedel et al. reported a calculated equilibrium conversion of 72% at 573 K over a K-promoted Fe catalyst, with direct hydrogenation of CO_2 only playing a minor role (*8*). They proposed a conversion of CO_2 to CO via the reverse water-gas shift reaction (RWGS) followed by chain propagation. The following enthalpies describe (a) the RWGS followed by (b) the conversion of CO to hydrocarbons via a Fischer-Tropsch mechanism:

$$\text{(a)}\ CO_2 + H_2 \rightarrow CO + H_2O \qquad \Delta_R H_{573K} = +38\ \text{kJ/mol}$$

$$\text{(b)}\ CO + 2H_2 \rightarrow \text{-}(CH_2)\text{-} + H_2O \qquad \Delta_R H_{573K} = -166\ \text{kJ/mol}$$

A rather low activation energy was reported for the CO_2 shift reaction, with the overall reaction being exothermic and thus a feasible route to converting CO_2 to hydrocarbons (*8*). Furthermore, the endothermic nature of the RWGS is helpful as it lowers the temperature in the Continuously Stirred Tank Reactor (CSTR) and thus cooling of the reactor to avoid sintering plays a less prominent role. It must be noted though that methane is thermodynamically the most favored HC product (*8*).

Previous work by our group has shown the advantage to using iron-based catalysts over Co-based ones (*9*) in the hydrogenation of CO_2 to more valuable products such as olefinic compounds (*10*). The K/Mn/Fe CO_2 hydrogenation catalyst supported on alumina showed an overall CO_2 conversion of 41.4%, with 26.1% selectivity towards methane, 62.4% towards the C_2-C_{5+} fraction with the remainder being CO (11.5%). Within the C_2-C_{5+} fraction the products were comprised of a 4.2 ratio of olefins to paraffins. It was shown that Mn acted as a structural promoter by reducing the catalyst's particle sizes, leading to an increased CO_2 conversion, as well as an electronic promoter as evidenced by the shift in product distribution towards longer chain hydrocarbons (HC) (*10*). The addition of K to the catalyst leads to a significant change in olefin/paraffin ratio in comparison to the K-free catalyst (almost 4-fold), with the support (γ-alumina) reported to play a pivotal role in the formation of part of the catalyst's active phase (*10*). It has furthermore been reported that potassium increases the iron's

Downloaded by UNIV OF GUELPH LIBRARY on June 23, 2012 | http://pubs.acs.org
Publication Date (Web): December 3, 2010 | doi: 10.1021/bk-2010-1056.ch008

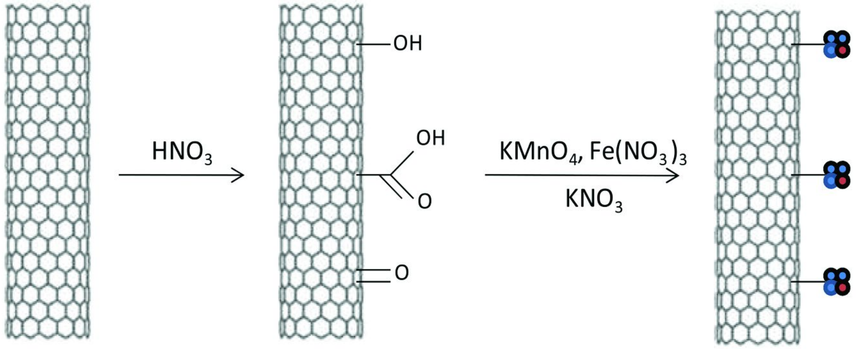

Figure 1. Schematic representation of MWCNT pre-treatment followed by catalyst impregnation.

surface basicity, leading to an increase in the dissociative adsorption of CO and lowering the H_2 adsorption ability (*11*).

Carbon nanotubes (CNT) have drawn a lot of attention as supports for heterogeneous catalysts in recent years (*12–15*), especially in the field of Fischer-Tropsch synthesis (FTS) (*16*, *17*). Besides having a large surface area, CNT increase the catalyst's dispersion and do not deactivate the catalyst by forming inactive metal-oxide species during synthesis or catalyst testing as seen on supports such as SiO_2 (*18*) It was thus of interest to test and characterize the same catalyst (K 8 wt%/Mn 12 wt%/Fe 17 wt%) dispersed on multi-walled carbon nanotubes (MWCNT) and elucidate the role the support plays in the formation of the catalyst's active phase and how that active phase changes and effects product distribution.

This work describes CO_2 hydrogenation over iron based catalysts dispersed on MWCNT. Spectroscopic and diffraction techniques are used to analyze and interpret how the support affects the surface characteristics and dispersion of the catalyst and thus the overall catalyst's performance.

Experimental Methods

Catalyst Preparation

MWCNT Pre-Treatment

The as-purchased (Helix Material Solutions) short MWCNT (Length: 1-2 μm, Specific Surface Area: 40 ~ 300 m^2/g) were cleaned and activated via refluxing in a 35 vol% HNO_3 solution at 383 K for 20 hours. During the reflux step, oxygen-containing surface groups are introduced (*19*), which have been proven to be most effective in obtaining high metal dispersions (*20*). The acid treatment also removes the nanotubes' caps. Subsequently the treated MWCNT are collected via standard vacuum procedures, thoroughly washed with distilled water and dried at 333 K for 30 min.

Downloaded by UNIV OF GUELPH LIBRARY on June 23, 2012 | http://pubs.acs.org
Publication Date (Web): December 3, 2010 | doi: 10.1021/bk-2010-1056.ch008

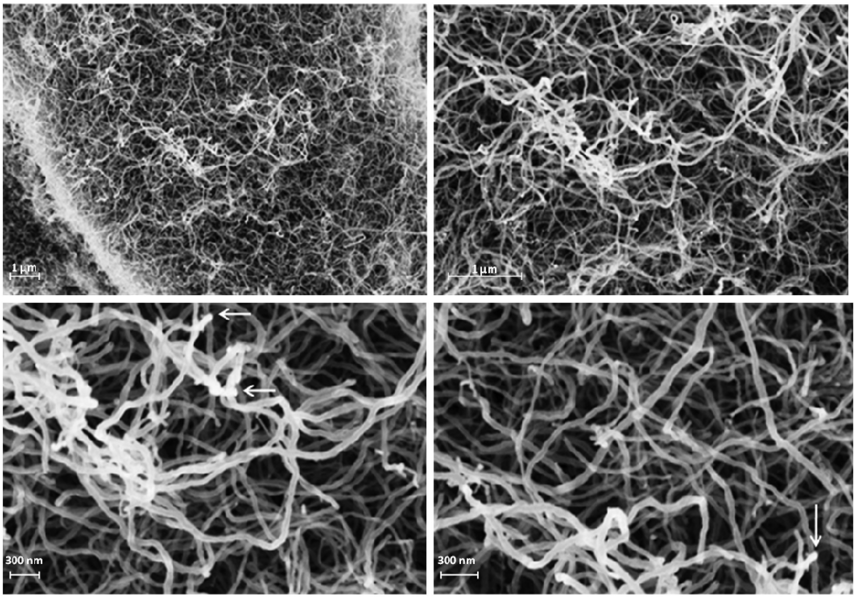

Figure 2. SEM images taken of the MWCNT as received at different magnifications. Caps on the tubes are highlighted by arrows. The scale is given on the images.

Metal Impregnation onto MWCNT

A co-incipient wetness impregnation (IWI) method was used for catalyst preparation. The same loading as was determined in previous studies was chosen (*20*), as both supports had comparable surface areas. $Fe(NO_3)_3 \cdot 6H_2O$ (Aldrich), $KMnO_4$ (Aldrich), and KNO_3 (Aldrich) were added to a flask, containing the pre-treated MWCNT dispersed in deionized water at the concentrations required to obtain the desired K/Mn/Fe weight ratio (see Figure 1 for schematic MWCNT treatment). The impregnated sample was then dried at 393 K in ambient air for 16 hours. Finally, the catalyst was calcined at 623 K for 3 hours, under static air conditions.

Catalyst Testing and Characterization

All CO_2 hydrogenation reactions with the catalyst described within were conducted in a 1 L Parr three-phase slurry Continuously Stirred Tank Reactor (CSTR). All runs were repeated to corroborate the results. Upon completion of the hydrogenation reactions, the catalyst properties were characterized by a series of spectroscopic and diffraction techniques (XRD, XPS and SEM) described below.

Downloaded by UNIV OF GUELPH LIBRARY on June 23, 2012 | http://pubs.acs.org
Publication Date (Web): December 3, 2010 | doi: 10.1021/bk-2010-1056.ch008

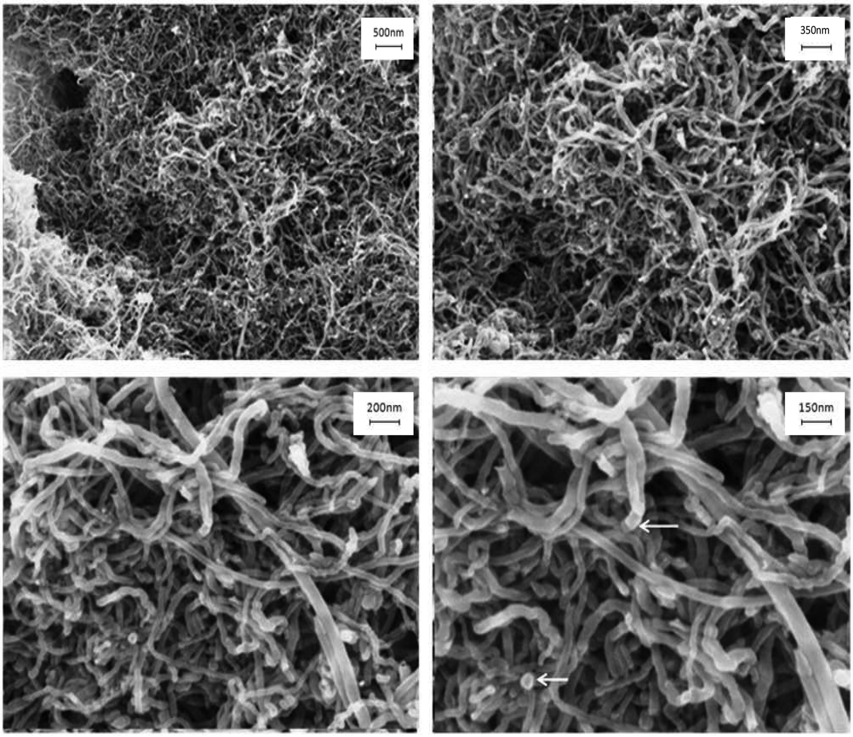

Figure 3. SEM images taken of the MWCNT after HNO_3 treatment at different magnifications. No clear physical difference is detected after the acid treatment, i.e. MWCNT's diameter, size and bundling. However, open tubes can be observed after the removal of the caps by the acid treatment (indicated by arrows). The scale is given on the images.

Continuously Stirred Tank Reactor (CSTR) Set-Up

10g of calcined catalyst were dispersed in approximately 400 ml of mineral oil (Aldrich) in the CSTR and subsequently reduced *in-situ* using CO at 563 K for 48 h. Hydrogenation of CO_2 was conducted at 563 K, 200 psig and a gas hourly space velocity (GHSV) of 0.0015 L g^{-1} s^{-1} at a H_2:CO_2 ratio of 3:1. The reactor and gas chromatograph (GC) set-up were described elsewhere (*10*). Time-on-stream (TOS) for the catalyst was 72 hours.

Powder X-Ray Diffraction (XRD)

Powder XRD measurements were performed on all materials. The catalyst was dissolved in heptane before XRD measurements were taken, to remove the mineral oil from the solid. The catalyst was subsequently recovered by conventional filtering procedures. The data were collected on a D8 Siemens

Table 1. Product selectivity, olefin/paraffin (O/P) ratio and CO_2 conversion over K/Mn/Fe catalysts, impregnated on Al_2O_3 and MWCNT supports

Catalyst	***Selectivity (%, carbon base)***			***O/P***	***CO_2 Conv. (%)***
	C_1	***C_2-C_{5+}***	***CO***		
Mn12/Fe17/Al_2O_3	34.0	55.3	10.7	1.2	37.7
K8/Mn12/Fe17/ Al_2O_3	26.0	62.4	11.5	4.2	41.4
K8/Mn12/Fe17/MWCNT	30.0	54.3	16.3	3.1	44.6

Bruker diffractometer with a general area detector employing the Bragg-Brentano geometry and the $CuK_{\alpha}1$ wavelength. The data were collected in the 10-50° 2θ range with a step increment of 0.01° and the time for each step was 2s. The data were visualized using the celref3 software (*21*).

X-ray Photoelectron Spectroscopy (XPS)

XPS measurements were performed on all spent catalyst materials and were used to assess the surface species and quantities present on the powder particles. The XPS studies were carried out using a K-Alpha machine (Thermo Scientific, UK) and the Unifit software (*22*) for data analysis. The system's base pressure was less than 5×10^{-9} mbar, however the pressure in the analysis chamber during data collection and analysis was 2×10^{-7} mbar due to the use of the low-energy electron flood gun for charge neutralization. A monochromated Al K_{α} (hν = 1486.6 eV) was used as the x-ray source. The instrument is regularly calibrated to the binding energies (BE) of Au, Cu and Ag peaks. The C 1s and O 1s BE are used as internal standards. All atomic percentages obtained by XPS in this work are converted to weight percentages for comparability sake.

Scanning Electron Microscope (SEM)

Structural and chemical characterization was performed with a field emission scanning electron microscope (FESEM) - Model LEO DSM 982, LEO. The SEM was operated at an accelerating voltage of 5 kV and the working distance varied from 3 to 8mm. The powder was placed under the SEM detector as a loosely scattered powder stuck to conducting tape. All particle sizes quoted in this paper are average particle sizes representative of the total sample.

Results and Discussion

Previous work on a K/Mn/Fe CO_2 hydrogenation catalyst impregnated on γ-alumina has shown great promise in CO_2 conversion yield as well as desirable product distribution (*10*). The results indicated that the support contributed to the formation of the catalyst's active phase, by forming an alanate structure during

Downloaded by UNIV OF GUELPH LIBRARY on June 23, 2012 | http://pubs.acs.org
Publication Date (Web): December 3, 2010 | doi: 10.1021/bk-2010-1056.ch008

Downloaded by UNIV OF GUELPH LIBRARY on June 23, 2012 | http://pubs.acs.org
Publication Date (Web): December 3, 2010 | doi: 10.1021/bk-2010-1056.ch008

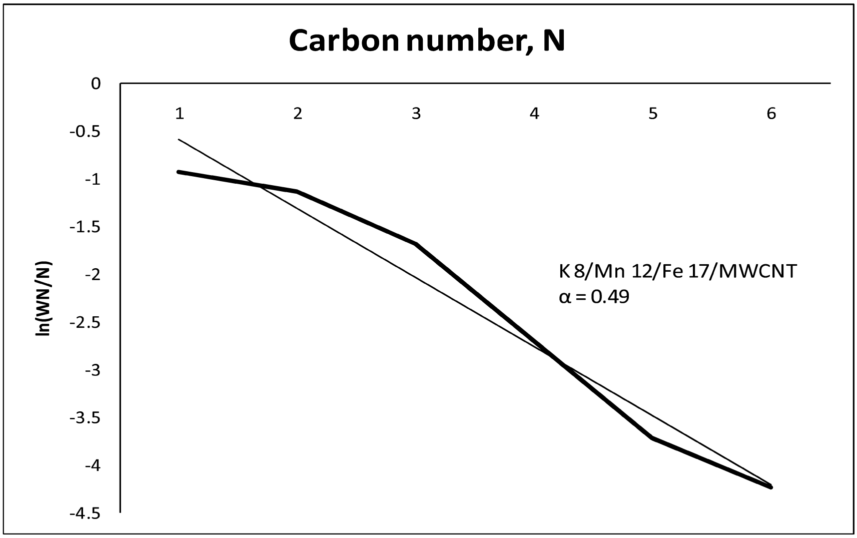

Figure 4. Anderson-Schulz-Flory distribution over the K 8 wt% Mn 12 wt % Fe 17 w% / MWCNT catalyst, showing a chain growth probability of 0.49.

catalyst testing. It would thus suggest that a different catalyst support would affect product distribution and yield in CO_2 hydrogenation. Carbon based supports have been widely reported as excellent supports for Co-based Fischer-Tropsch (FT) catalysts (*23–25*), and to a lesser extent for Fe-based FT catalysts (*26*), because they promote the catalyst's dispersion and have remarkable stability. Thus it was of interest to investigate how changing the support from γ-alumina to MWCNT, while keeping all other experimental conditions constant would affect the conversion yield and the product distribution.

Figures 2 and 3 are SEM images of the MWCNT support before and after pre-treatment with HNO_3. The images show that no significant change in MWCNT size and diameter occurred after exposure to the acid. However, the images indicate that the acid treatment successfully resulted in cap opening of the initially closed MWCNT (compare Figure 2 and Figure 3). MWCNT of 10-30 nm diameter were observed under the microscope with the fibers intertwined and forming a mesh.

Having reached steady-state conditions within 24 hours, the catalyst on the MWCNT support (K 8% Mn 12% Fe 17%/MWCNT – referred to from here onwards as KMFM) showed a CO_2 conversion yield of 44.6% (see Table 1), which is higher than was reported on the same catalyst dispersed over alumina (K 8% Mn 12% Fe 17%/Al_2O_3- referred to from here onwards as KMFA).

Interestingly however, the product distribution over the catalyst impregnated on MWCNT differs considerably from the previously reported one. Methane and CO selectivity is considerably higher on KMFM in comparison to KMFA; however the C_2-C_{5+} fraction is markedly reduced (~13%) (see Table 1). Similar results were reported on an Fe/Ru/Cu/K FT catalyst dispersed over MWCNT (*26*) in comparison to a comparable alumina supported catalyst (*27*) used in FTS, with the former showing a considerably higher methane selectivity. Interestingly the

Downloaded by UNIV OF GUELPH LIBRARY on June 23, 2012 | http://pubs.acs.org
Publication Date (Web): December 3, 2010 | doi: 10.1021/bk-2010-1056.ch008

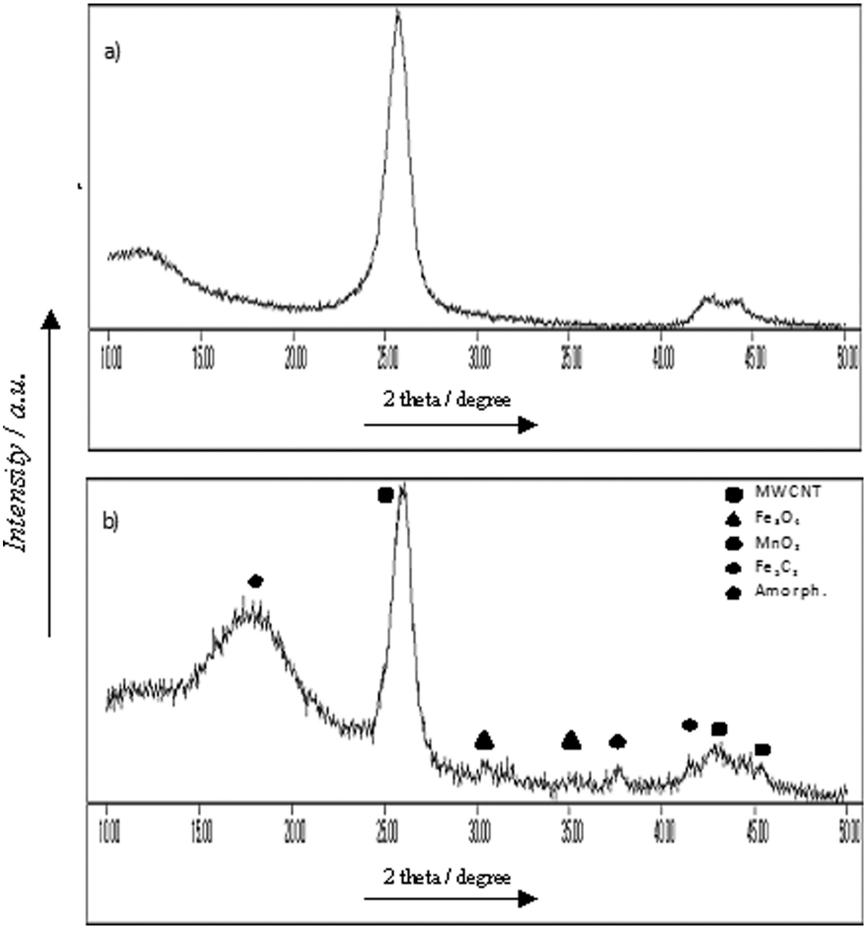

Figure 5. XRD of the a) MWCNT support and b) K/Mn/Fe used catalyst supported on the MWCNT. Besides the diffraction peak arising from the support, there are no distinct diffraction peaks associated with the catalyst's phases, indicating a very well dispersed catalyst (all minor peaks are assigned to their phases – MnO_2, Fe_3O_4, Fe_5C_2 and amorphous species – see caption in Figure).

product distribution over KMFM is more comparable to the K-free Mn/Fe catalyst impregnated on alumina than the potassium containing one (see Table 1), with the chain growth probability (α) also comparable between these two catalysts (α = 0.47 and 0.49 respectively) (see Figure 4). Furthermore, while the addition of potassium clearly has an effect on olefin selectivity even when the catalyst is dispersed on MWCNT, the effect is much more pronounced on the KMFA catalyst with olefin/paraffin ratios being 4.2 compared to 3.1, while the potassium-free alumina based catalyst merely shows a ratio of 1.16 (*10*). Potassium is known to considerably lower methane selectivity, increase chain growth probability, and increase conversion levels both in FTS as well as CO_2 hydrogenation (*10*, *28*). Thus it is surprising to see comparable chain growth probabilities and methane selectivities in the KMFM and the K-free Mn/Fe alumina catalysts.

Downloaded by UNIV OF GUELPH LIBRARY on June 23, 2012 | http://pubs.acs.org
Publication Date (Web): December 3, 2010 | doi: 10.1021/bk-2010-1056.ch008

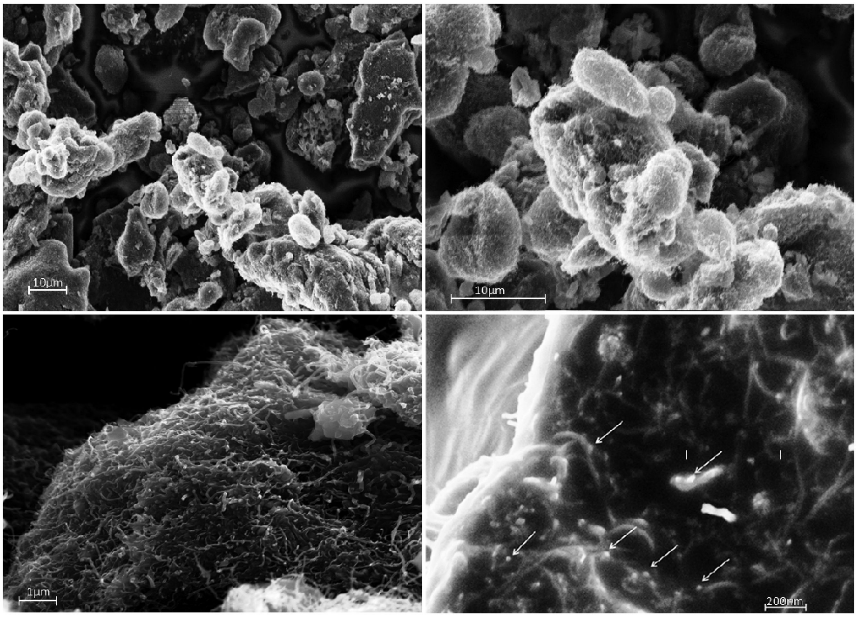

Figure 6. SEM images taken of the catalyst dispersed on the MWCNT after the catalytic run at different magnifications. Well dispersed nano-particles are visible ranging up to around 20 nm. The scale is given on the images.

The XRD pattern of the used KMFM catalyst (see Figure 5) does not show any distinct and well defined diffraction peaks besides the ones arising from the MWCNT (un-treated MWCNT pattern shown for reference in Figure 5a). Only minor peaks are observed which can be assigned to the Fe_3O_4, MnO_2 and Fe_2C_5 phases. A possible shoulder at 24.5° 2θ on the MWCNT peak may be assigned to the K_2O phase, but is purely speculative (*10*). The absence of any distinct diffraction peaks indicates a well dispersed catalyst in the low nm range over the MWCNT. Indeed SEM images of the used catalyst (see Figure 6), show catalyst particles ranging up to 20 nm spread over the MWCNT surface. This is much smaller than observed in the KMFA sample, with particles ranging up to 70 nm (*10*). This reduction in particle size is most likely the underlying cause behind the increased CO_2 conversion over the KMFM sample in relationship to the KMFA catalyst.

XPS spectra of the used catalyst were taken to investigate the surface species distribution of the KMFM sample. Unlike the KMFA sample where the support was detectable by XPS, it was not possible to de-convolute the C 1s signal into the different carbon species as the peak at 284.7 eV is fairly symmetric. This is attributed to solvent residue, product residue and iron carbide on the MWCNT support. Thus it was decided to only look at the metal species present on the support. For comparison reasons, the XPS intensities from the KMFA sample were adjusted accordingly and are listed in Table 2. Interestingly, the KMFM catalyst shows a slightly lower K surface coverage than the KMFA one, with surface Fe and

Downloaded by UNIV OF GUELPH LIBRARY on June 23, 2012 | http://pubs.acs.org
Publication Date (Web): December 3, 2010 | doi: 10.1021/bk-2010-1056.ch008

Table 2. XPS data, showing peak assignment, area under the curve (measured in at. %) and correlated weight %

Catalyst	*Peak*	*BE (eV)*	*Area*	*w %*	*Expected*
K8/Mn12/Fe17/MWCNT	Fe 2p	709-712.5	3.1	12.8%	45.9%
	Mn2p	641	4.4	17.8%	32.4%
	K 2p	293	24.4	69.4%	21.6%
	SUM		32.0	100%	100%
K8/Mn12/Fe17/Al_2O_3	Fe 2p	709-712.5	4.0	10.9%	45.9%
	Mn 2p	641	6.0	14.6%	32.4%
	K 2p	293	43.0	74.4%	21.6%
	SUM		53.0	100%	100%

Mn concentrations consequently being higher. This difference in intensities most likely arises from the better dispersion of the Fe/Mn particles on this support, rather than certain species being deposited on the inside of the MWCNT. The preparation method of the catalyst, i.e. the MWCNT dispersed in water prior to IWI, leads to flooding of the inner void of the MWCNT by water, resulting in the metal particles being primarily deposited on the outer walls of the MWCNT (*29*).

Particle size has been reported to be of importance in FTS using Co-based catalysts, with particles below a certain size being deactivated by CO irreversibly binding to its surface (*25*). Such a phenomena has however, to our knowledge not been reported for Fe-based catalysts. It is thus unlikely that this is the underlying reason for the difference in product distribution between iron based catalysts, supported on MWCNT and alumina respectively, especially when considering the higher CO_2 conversion of the MWCNT supported catalyst.

The role potassium plays in FTS using iron based catalysts is still not clearly understood, but it is thought to primarily act as a base. Dry et al. proposed that potassium lowers the metal work function by donating electron density to the vacant d-orbital of the iron, enhancing the dissociative adsorption of CO while lowering the H_2 adsorption ability and thus leading to an increase in olefins being formed – with potassium either present as K_2O or KOH (*11*). In previous work we reported the presence of $KAlH_4$ as part of the active phase in a K/Mn/Fe catalyst supported on alumina in addition to K_2O (*10*). Even though the overall CO_2 conversion was lower over the KMFA catalyst in comparison to the KMFM one, which can be explained by the larger particle size, its olefin selectivity is about a third higher. Interestingly, while the KMFM does show a clear improvement in olefin production over the potassium-free KMFA catalyst (close to 3-fold), its olefin/paraffin ratio is not equal to the KMFA catalyst. The lower olefin production over the KMFM in relations to the KMFA catalyst may be explained by the lack of the $KAlH_4$ phase present in the MWCNT-based catalyst. It is postulated that the potassium alanate binds H_2 in its structure, thus reducing the availability of hydrogen needed to fully hydrogenate the alkenes bound to the surface (*10*). While the presence of K_2O obviously plays a large role in the suppression of alkene hydrogenation, this finding suggests that $KAlH_4$ seems to indeed have a role to play in olefin selectivity during CO_2 hydrogenation.

Besides having a lower olefin/paraffin ratio, KMFM also yields a higher fraction of methane and a lower fraction of the C_2-C_{5+} product fraction in comparison to the KMFA catalyst. This occurrence can also be attributed to the absence of $KAlH_4$. Hydrogenation of CO_2 to methane is suppressed over the KMFA catalyst, as the alanate-phase reduces the hydrogen available for hydrogenation. However, as this phase is not present in the KMFM catalyst, the methane selectivity increases within the products. Govender et al. reported a mechanistic pathway for methane formation over an iron-based FTS catalyst, using steady state isotopic transient kinetic analysis (SSITKA) (*30*). They concluded, that a mechanism involving C_α and C_β C_1-intermediates describes the methanation as well as the overall Fischer-Tropsch process best over iron carbide surfaces. Their model shows that both intermediates are active for methanation and higher HC formation. However, C_β is not only more abundantly present on the catalyst's surface (amounting to 92% of the total C_1 coverage), it is also less active towards methanation than C_α. C-C coupling is proposed to occur via the combination of C_α and C_β to form C_2-surface intermediates. It is thus hypothesized that based on abundance and role the intermediates play, C_α and C_β are CH_3 and CH_2 (methylene) intermediates respectively. This assumption is in good agreement with a previously stated Fischer-Tropsch mechanism over iron catalysts, where chain growth via $–CH_2$- propagation has been proposed (*31*, *32*), with CH_3- playing a role in chain growth initiation (*33*).

Taking the model proposed by Govender et al. for methanation and chain growth into consideration over iron based FTS catalysts and applying it to CO_2 hydrogenation over the KMFM and KMFA catalysts, it might be possible to explain the shift in product distribution towards C_1 over KMFM. As mentioned earlier, the KMFM catalyst does not have the potassium alanate present as part of its structure. Correlated to this is an increased amount of hydrogen available for hydrogenation of carbonaceous surface species. Thus with the absence of the $KAlH_4$ phase, the C_α surface species would increase on the KMFM as opposed to the KMFA catalyst, resulting in a higher proportion of CH_3 intermediates and consequently methane being formed. Assuming C_β is indeed the methylene intermediate, this would also explain the reduction in olefin/paraffin ratio for the KMFM catalyst. As the concentration of CH_3-species increases for KMFM, the products formed are more likely to be saturated hydrocarbons, while an increase in concentration of CH_2 intermediates would indicate more olefins being formed (as seen for KMFA) (see Figure 7 for detailed mechanism). Taking the mechanism proposed by Govender et al. and the presence of $KAlH_4$ as part of the catalytic phase into consideration, we can explain the change in product distribution over the KMFM compared to the KMFA catalyst by a shift in distribution of C_1 surface intermediates. Furthermore, the XPS data showed lower potassium coverage on the KMFM in comparison to the KMFA catalyst, which can be attributed to the smaller particle being formed as stated earlier. This subsequently leads to a higher hydrogenation ability, which contributes to the lower olefin/paraffin ratio as well as the higher methane selectivity. However, the increase in iron and manganese surface species cannot by itself explain the total difference observed between

Downloaded by UNIV OF GUELPH LIBRARY on June 23, 2012 | http://pubs.acs.org
Publication Date (Web): December 3, 2010 | doi: 10.1021/bk-2010-1056.ch008

KMFM and KMFA, and thus also corroborates the proposed role $KAlH_4$ plays as part of the KMFA catalyst's active phase.

While MWCNT and other carbon-based supports seem to be highly favorable supports in many applications, especially in Co-based FT regimes, they seem to be less beneficial when used as supports for iron-based CO_2 hydrogenation catalysts.

Conclusion

Having shown the possibility of an iron-based catalyst hydrogenating CO_2 with an efficiency of 41.4%, giving a high olefin/paraffin ratio, further research was conducted to improve upon previously reported catalyst (*10*). MWCNT have been shown to be very advantageous as supports for FT based catalysts, as they lead to higher dispersions of the catalytic phase resulting in a higher yield of desirable products. It was thus decided to investigate a K/Mn/Fe based catalyst dispersed on MWCNT.

It was possible to increase the CO_2 conversion from 41.4% to 44.6% when changing the support from alumina to MWCNT, but concurrently the product distribution was moved away from the desirable, high energy density C_2-C_{5+} and olefin fraction and towards methane and CO. Chain growth probability was also reduced when MWCNT were applied as support as was the olefin/paraffin ratio. We previously reported the potassium alanate phase to be part of the active phase in the KMFA catalyst, acting as a hydrogenation suppressant by binding H_2 in its structure, resulting in a high olefin/paraffin ratio (*10*). This phase is not able to form when using MWCNT as a support, resulting in a lower olefin but higher methane fraction in the product effluent. The higher CO_2 conversion can be ascribed to the much smaller particles that are formed over the MWCNT in comparison to alumina support.

This work highlights the significant role the catalyst support plays in CO_2 hydrogenation. By altering the support, changes in conversion yield and product distribution (most likely through a shift in distribution of surface methylene intermediates) were observed. The higher methane selectivity over the catalyst supported on MWCNT instead of alumina can be explained by the change in catalytically active species that result from the metal interacting with the support and thus leading to a change in carbonaceous surface intermediates. Having demonstrated the importance of the choice in support, further catalyst development will be pursued to improve both the olefin/paraffin ratio and CO_2 conversion efficiencies in efforts to produce a catalyst for commercial CO_2 conversion to valuable fossil fuel free HC.

Downloaded by UNIV OF GUELPH LIBRARY on June 23, 2012 | http://pubs.acs.org
Publication Date (Web): December 3, 2010 | doi: 10.1021/bk-2010-1056.ch008

Downloaded by UNIV OF GUELPH LIBRARY on June 23, 2012 | http://pubs.acs.org
Publication Date (Web): December 3, 2010 | doi: 10.1021/bk-2010-1056.ch008

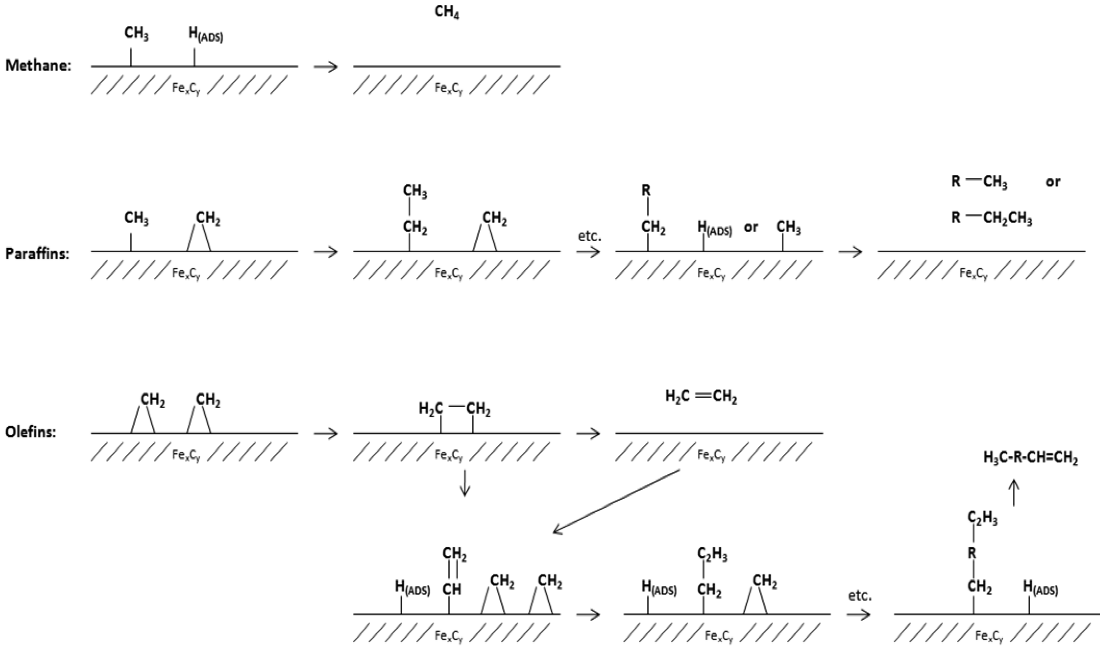
Methane:
CH3
H(ADS)
CH4
FexCy
Paraffins:
CH3
CH2
CH3
CH2
CH2
etc.
R
CH2
H(ADS)
or
CH3
R —CH3
or
R —CH2CH3
Olefins:
CH2
CH2
H2C —CH2
H2C =CH2
H3C-R-CH=CH2
C2H3
R
CH2
H(ADS)
CH2
CH
CH2
CH2
C2H3
CH2
etc.

Figure 7. Proposed reaction mechanism over the Fe_xC_y surface. Methane and paraffin chain growth is initiated by CH_3 intermediates, while olefins are predominantly grown by CH_2 building blocks, with re-adsorption of olefins possible. Based on this mechanism, a decrease in CH_3 intermediates would explain the shift of products towards olefins and away from methane and paraffins when the alanate is present. The occurrence of the alanate, by suppressing hydrogenation leads to a higher concentration of CH_2 intermediates on the surface.

Downloaded by UNIV OF GUELPH LIBRARY on June 23, 2012 | http://pubs.acs.org
Publication Date (Web): December 3, 2010 | doi: 10.1021/bk-2010-1056.ch008

Acknowledgments

This work was supported by the Office of Naval Research both directly and through the Naval Research Laboratory. The research was performed while RWD held a National Research Council Research Associateship Award at the Naval Research Laboratory.

References

1. *Petroleum Quality Information System Report*; Defense Energy Support Center -DESC-BP; Fort Belvoir, VA, 2008.
2. *H.R 2454 American Clean Energy and Security Act*; 2009.
3. Nikulshina, V.; Gebald, C.; Steinfeld, A. *Chem. Eng. J.* **2009**, *146*, 244–248.
4. Collin, J. P.; Sauvage, J. P. *Coord. Chem. Rev.* **1989**, *93*, 245–268.
5. Fujita, E.; Hayashi, Y.; Kita, S.; Brunschwig, B. S. Carbon Dioxide Utilization for Global Sustainability. *Stud. Surf. Sci. Catal.* **2004**, *153*, 271–276.
6. Noda, H.; Ikeda, S.; Oda, Y.; Imai, K.; Maeda, M.; Ito, K. *Bull. Chem. Soc. Jpn.* **1990**, *63*, 2459–2462.
7. Russell, W. W.; Miller, G. H. *J. Am. Chem. Soc.* **1950**, *72*, 2446–2454.
8. Riedel, T.; Schaub, G.; Jun, K. W.; Lee, K. W. *Ind. Eng. Chem. Res.* **2001**, *40*, 1355–1363.
9. Dorner, R. W.; Hardy, D. R.; Williams, F. W.; Davis, B. H.; Willauer, H. D. *Energy Fuels* **2009**, *23*, 4190–4195.
10. Dorner, R. W.; Hardy, D. R.; Williams, F. W.; Willauer, H. D. *Appl. Catal., A* **2010**, *373*, 112–121.
11. Dry, M. E.; Shingles, T.; Boshoff, L. J.; Oosthuiz, G. J. *J. Catal.* **1969**, *15*, 190.
12. Garcia, J.; Gomes, H. T.; Serf, P.; Kalck, P.; Figueiredo, J. L.; Faria, J. L. *Carbon* **2006**, *44*, 2384–2391.
13. Tian, Z. Q.; Jiang, S. P.; Liang, Y. M.; Shen, P. K. *J. Phys. Chem. B* **2006**, *110*, 5343–5350.
14. Shaijumon, M. M.; Ramaprabhu, S.; Rajalakshmi, N. *Appl. Phys. Lett.* **2006**, *88*, 253105.
15. Zhang, A. M.; Dong, J. L.; Xu, Q. H.; Rhee, H. K.; Li, X. L. *Catal. Today* **2004**, *93−5*, 347–352.
16. Tavasoli, A.; Sadagiani, K.; Khorashe, F.; Seifkordi, A. A.; Rohaniab, A. A.; Nakhaeipour, A. *Fuel Process. Technol.* **2008**, *89*, 491–498.
17. van Steen, E.; Prinsloo, F. F. *Catal. Today* **2002**, *71*, 327–334.
18. Kiss, G.; Kliewer, C. E.; DeMartin, G. J.; Culross, C. C.; Baumgartner, J. E. *J. Catal.* **2003**, *217*, 127–140.
19. Kundu, S.; Wang, Y. M.; Xia, W.; Muhler, M. *J. Phys. Chem. C* **2008**, *112*, 16869–16878.
20. van der Lee, M. K.; van Dillen, A. J.; Bitter, J. H.; de Jong, K. P. *J. Am. Chem. Soc.* **2005**, *127*, 13573–13582.
21. Laugier, J.; Bochu, B. *Celref*; 2003.

22. Hesse, R.; Chasse, T.; Szargan, R. *Anal. Bioanal. Chem.* **2003**, *375*, 856–863.
23. Bezemer, G. L.; van Laak, A.; van Dillen, A. J.; de Jong, K. P. *Proc. Natural Gas Conversion VII* **2004**, *147*, 259–264.
24. Bezemer, G. L.; Radstake, P. B.; Koot, V.; van Dillen, A. J.; Geus, J. W.; de Jong, K. P. *J. Catal.* **2006**, *237*, 291–302.
25. den Breejen, J. P.; Radstake, P. B.; Bezemer, G. L.; Bitter, J. H.; Froseth, V.; Holmen, A.; de Jong, K. P. *J. Am. Chem. Soc.* **2009**, *131*, 7197–7203.
26. Bahome, M. C.; Jewell, L. L.; Padayachy, K.; Hildebrandt, D.; Glasser, D.; Datye, A. K.; Coville, N. J. *Appl. Catal., A* **2007**, *328*, 243–251.
27. Bukur, D. B.; Sivaraj, C. *Appl. Catal., A* **2002**, *231*, 201–214.
28. Yang, Y.; Xiang, H. W.; Xu, Y. Y.; Bai, L.; Li, Y. W. *Appl. Catal., A* **2004**, *266*, 181–194.
29. Malek Abbaslou, R. M.; Tavasoli, A.; Soltan, J.; Dalai, A. K. *Appl. Catal., A* **2009**, *355*, 33–41.
30. Govender, N. S.; Botes, F. G.; de Croon, M.; Schouten, J. C. *J. Catal.* **2008**, *260*, 254–261.
31. Biloen, P.; Helle, J. N.; Sachtler, W. M. H. *J. Catal.* **1979**, *58*, 95–107.
32. Schulz, H.; Riedel, T.; Schaub, G. *Top. Catal.* **2005**, *32*, 117–124.
33. Brady, R. C.; Pettit, R. *J. Am. Chem. Soc.* **1981**, *103*, 1287–1289.

Downloaded by UNIV OF GUELPH LIBRARY on June 23, 2012 | http://pubs.acs.org
Publication Date (Web): December 3, 2010 | doi: 10.1021/bk-2010-1056.ch008

Downloaded by UNIV OF GUELPH LIBRARY on June 23, 2012 | http://pubs.acs.org
Publication Date (Web): December 3, 2010 | doi: 10.1021/bk-2010-1056.ch009

Chapter 9

Utilization of Carbon Dioxide as a Hydrogen Storage Material: Hydrogenation of Carbon Dioxide and Decomposition of Formic Acid Using Iridium Complex Catalysts

Yuichiro Himeda*

National Institute of Advanced Industrial Science and Technology,
1-1-1 Higashi, Tsukuba, Ibaraki 305-8565, Japan
***himeda.y@aist.go.jp**

We demonstrate the utilization of carbon dioxide (CO_2) as a hydrogen storage material using organometallic complex catalysts that strongly catalyze hydrogenation of CO_2 under basic conditions and decomposition of formic acid under acidic conditions. For this purpose, a sophisticated catalyst was designed, in which a phenolic hydroxyl group was introduced to a ligand. This led to pronounced catalytic activation, and control of the catalytic activity and solubility. As a first step of the hydrogen storage system, CO_2 hydrogenation was achieved by increasing the catalytic activity and recycling the catalyst without waste generation—a result of automatically tuning the activity and water solubility of the catalyst via the acid-base equilibrium of its ligand. The strong electron-donating ability of the oxyanion generated from the hydroxyl group resulted in remarkably high catalytic activity—greater than 1300 times that of the unsubstituted bipyridine complex. The catalyst design concept and excellent ligand properties are expected to have broad implications for designing new homogeneous catalysts. As a second step, decomposition of formic acid using the same catalyst provides an efficient evolution of CO-free hydrogen under acidic conditions. High catalytic activity and complete consumption of formic acid were realized in water, and pressurized hydrogen was also generated. The proposed system using the iridium catalyst is promising for practical applications in terms of both the hydrogenation of CO_2 and the decomposition of formic acid.

Introduction

Massive emissions of carbon dioxide (CO_2) from the combustion of fossil fuels to supply energy are the most important cause of global warming. Plants utilize CO_2 as recipients of the abundant energy generated by photosynthesis, during which CO_2 is reduced. Unfortunately, a suitable method of storing energy (i.e., hydrogen) based on this the concept is currently unavailable. The development of technologies for efficiently storing hydrogen in a safe and reversible manner is an important challenge for realizing a hydrogen economy. At the present time, particularly intensive efforts are being devoted to low-cost, large-scale production of CO-free hydrogen for fuel cell applications.

Formic acid, which contains 4.4 wt% and 53 g/L of hydrogen, is one of the promising hydrogen storage materials, because it has low toxicity and can be easily handled and stored. Therefore, both catalytic hydrogenation of CO_2 and catalytic decomposition of formic acid have recently received renewed attention for use in a hydrogen storage system (Figure 1) (*1*, *2*). However, since the catalysts for each reaction were independently developed, to our knowledge there is no known catalyst that shows high activity for both reactions (*3*–*5*).

Herein we demonstrate the utilization of CO_2 as a hydrogen storage material by combining hydrogenation of CO_2 and decomposition of formic acid in water. One of the remarkable features of the system is that either of the two reactions can be selected by the pH of the solution, using the same iridium catalyst that hydrogenates CO_2 under basic conditions and decomposes formic acid under acidic conditions. Using a sophisticated catalyst design, we achieve hydrogenation of CO_2 by high catalytic activity and recycling of the catalyst without waste generation in water. Decomposition of formic acid provides efficient CO-free hydrogen evolution with complete conversion of formic acid. The system lays out many of the elements necessary for practical application.

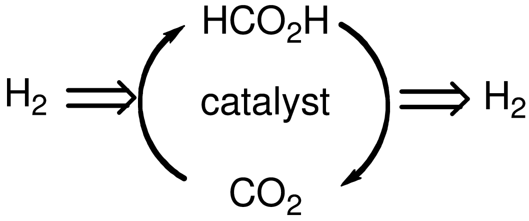

Figure 1. Hydrogen storage system based on interconversion between CO_2 and formic acid.

Downloaded by UNIV OF GUELPH LIBRARY on June 23, 2012 | http://pubs.acs.org
Publication Date (Web): December 3, 2010 | doi: 10.1021/bk-2010-1056.ch009

Downloaded by UNIV OF GUELPH LIBRARY on June 23, 2012 | http://pubs.acs.org
Publication Date (Web): December 3, 2010 | doi: 10.1021/bk-2010-1056.ch009

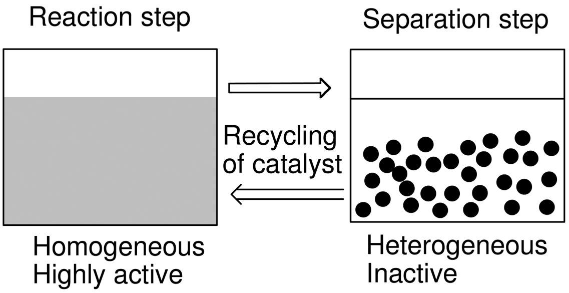

Figure 2. Ideal homogeneous catalytic process

Hydrogenation of CO_2

As a first step, the homogeneous hydrogenation of CO_2 or bicarbonate is well studied, and several highly efficient catalysts have been reported. Detailed reviews of studies up to 2006 have been published (*6–9*). Recently, Nozaki reported a highly active catalyst for hydrogenation of CO_2 in KOH/H_2O/THF solution at 5 MPa and 200 °C (*10*). Peris reported an interesting study on transfer hydrogenation of CO_2 to formate using iPrOH as a hydrogen donor catalyzed by iridium complexes (*11*).

However, several critical problems for practical application remain to be solved. These include the following: (1) activation of the catalyst, because the high energy demand for converting thermodynamically stable CO_2 generally lowers the overall energy balance; (2) recycling of catalysts which generally contain noble metals; (3) control of catalytic activity in both the reaction and separation steps to avoid potential reverse reactions; and (4) prevention of waste generation (generally an organic solvent and additive) during the reaction. The strategic goal to overcome these problems will be to design a catalyst that is homogeneous and active during the reaction step but is heterogeneous and inactive during the separation step (Figure 2).

Catalyst Design

A half-sandwich bipyridine rhodium complex $[Cp^*Rh(bpy)Cl]^+$ (**1**), which serves as an efficient catalyst for transfer hydrogenation using formate as a hydrogen source in water (*12*, *13*), was chosen as the prototype catalyst (Figure 3). Preliminary studies showed that **1** interconverted between CO_2/H_2 and formic acid (eqs. 1 and 2) (*14*). However, the abovementioned problems remained unresolved.

Before designing the catalyst, it was first considered that CO_2 reaches an equilibrium with bicarbonate and carbonate—one that is strongly dependent on the pH, temperature, and CO_2 pressure (eq. 3). In addition, changes in the pH of the solution during the reaction (i.e., from basic to acidic) due to the consumption of bicarbonate and production of formic acid were considered.

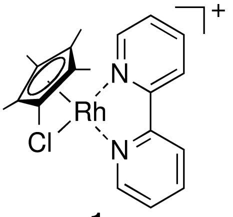

1

Figure 3. Prototype catalyst for hydrogenation of CO_2 and decomposition of formic acid in water.

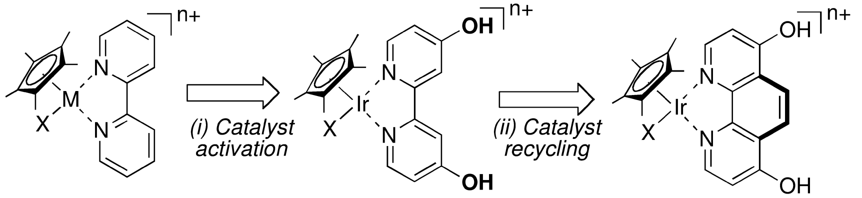

Prototype catalyst DHBP catalyst **2** DHPT catalyst **3**

Scheme 1. Design of the catalyst for hydrogenation of CO_2 in water.

In light of these considerations, the design of the catalyst for hydrogenation of CO_2 was elaborated via the route shown in Scheme 1. Namely, (i) *catalyst activation* was achieved by the introduction of a hydroxyl group to the bipyridine ligand, during which a strong electron-donating oxyanion generated by its deprotonation plays a significant role; and (ii) *catalyst recycling* was achieved by replacement of the bipyridine ligand with the phenanthroline analog, which shows negligible water solubility under weakly acidic conditions.

$$CO_2 + H_2 + OH^- \xrightarrow[\substack{\text{4 MPa, 80 °C}\\ \text{pH - 8}}]{\substack{\mathbf{1}\\ \text{TOF} = 20\ \text{h}^{-1}}} HCO_2^- + H_2O \qquad (1)$$

$$HCO_2H \xrightarrow[\substack{\text{40 °C}\\ \text{pH} = 3.5}]{\substack{\mathbf{1}\\ \text{TOF} = 238\ \text{h}^{-1}}} CO_2 + H_2 \qquad (2)$$

$$CO_2 + H_2O \rightleftharpoons H_2CO_3 + H_2O \overset{\text{p}K_1 = 6.35}{\rightleftharpoons} HCO_3^- + H^+ \overset{\text{p}K_1 = 10.33}{\rightleftharpoons} CO_3^{2-} + 2H^+ \qquad (3)$$

Downloaded by UNIV OF GUELPH LIBRARY on June 23, 2012 | http://pubs.acs.org
Publication Date (Web): December 3, 2010 | doi: 10.1021/bk-2010-1056.ch009

Downloaded by UNIV OF GUELPH LIBRARY on June 23, 2012 | http://pubs.acs.org
Publication Date (Web): December 3, 2010 | doi: 10.1021/bk-2010-1056.ch009

Catalyst Activation

The first focus of the catalyst design is on the enhancement and control of the catalytic activity. The most important development in this regard is based on the acid-base equilibrium of the phenolic hydroxyl group in a bipyridine ligand (Figure 4). Namely, the hydroxyl group shows moderate electron-donating ability and polarity, while its deprotonated oxyanion shows strong electron-donating ability and polarity. Therefore, 4,4'-dihydroxy-2,2'-bipyridine (DHBP) is devised from bipyridine as a ligand. The acid-base equilibrium of DHBP leads to simultaneous changes in both the electronic and polar properties of the catalyst, which are attributed to the properties of the hydroxyl and oxyanion groups. In fact, the oxyanion at the beginning of the reaction will be protonated to generate the hydroxyl group at the end of the reaction, since the basic reaction solution changes to a weakly acidic one. Thus, the strong electron-donating ability of the oxyanion should lead to the activation of the catalyst, and the significant differences in electronic properties between the hydroxyl and the oxyanion groups should lead to the control over the catalytic properties.

We examined the acid–base equilibrium of **2** (X = H_2O), which has two types of proton-donating groups (i.e., two phenolic hydroxyl groups and an aqua ligand). Figure 5 shows the absorption spectra of **2** (X = H_2O) as a function of pH (adjusted by H_2SO_4/KOH) (*15*). The percentage change in the optical density of **2** (X = H_2O) at 265 nm plotted against the pH is shown in Figure 6. From our previous studies, the change from pH 3 to 6 can be attributed to the acid–base equilibrium of the hydroxyl groups in the bipyridine ligand. The change from pH 8 to 10 may be attributed to that of the aqua ligand. Thus, the complex appears to exist in a hydroxyl form at pH 2.6, in an oxyanion form at pH 7.3, and as a hydroxo complex at pH values above 10.

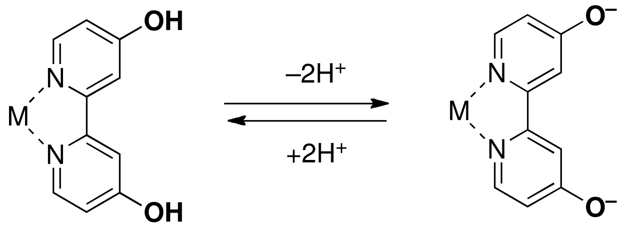

Hydroxyl form		Oxyanion form
Moderate	Electron donation Polarity	Strong

Figure 4. Acid-base equilibrium between hydroxyl and oxyanion forms.

Downloaded by UNIV OF GUELPH LIBRARY on June 23, 2012 | http://pubs.acs.org
Publication Date (Web): December 3, 2010 | doi: 10.1021/bk-2010-1056.ch009

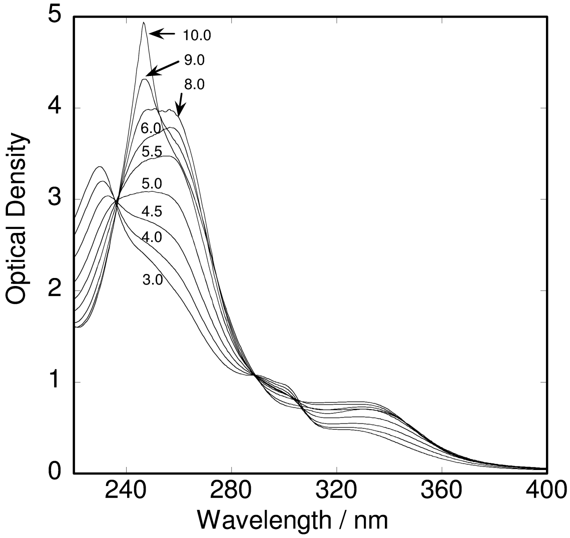

*Figure 5. Absorption spectra of **2** (X = H_2O) (0.1 μM) in an aqueous solution as a function of pH. The values indicate the value of pH.*

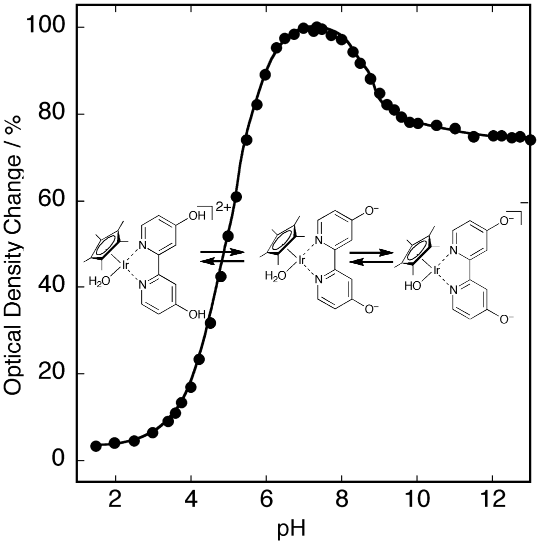

*Figure 6. Absorbance change of **2** (X = H_2O) at 265 nm as a function of pH.*

The electronic effect of the substituent on the hydrogenation of CO_2 was then investigated using a series of iridium complexes (**2** and **4a-d**). The good correlation between the substituent (-R) and the initial TOF can be explained on the basis of Hammett's rule (Figure 7). Note that the phenolic hydroxyl group

(σ_p^+ = –0.92) and the carboxyl group (+0.42) are deprotonated to generate the oxyanion (–2.30) and carboxylate (–0.02) under basic reaction conditions (*16*). The large σ_p^+ value of –2.30 and the ρ value of –1.3 resulted in a remarkably high initial TOF for **2**, which was over 1300 times greater than that of the unsubstituted complex **4a**. It is clear that enhancement of catalytic activity is achieved by the strong electron-donating effect of the oxyanion generated by the deprotonation of the hydroxyl group (*17*).

Table 1 summarizes the results for the iridium DHBP catalyst **2**. High activity was obtained at 6 MPa and 120 °C (entry 1). Compared to the previously reported catalyst $[RuCl_2(tppms)_2]_2$ (TOF = 30–50 h^{-1} at 1 MPa and 50 °C) (*18*), **2** showed far superior catalytic activity under the same conditions (entry 2). Furthermore, the hydrogenation of CO_2 proceeded at atmospheric pressure (entry 3). The result shows that the corresponding hydride complexes can easily be generated as active species at atmospheric pressure. This is presumed by the observation that the color of the solution changed immediately from pale yellow to deep yellow when H_2 was admitted (*8*).

In addition, the control of the catalytic activity, which is attributed to the acid-base equilibrium, resulted in activation of the catalyst in the reaction step and its deactivation in the separation step, because of a change in the pH of the solution. Therefore, the undesirable reverse reaction, i.e., the decomposition of formic acid, was prevented in the separation step.

Downloaded by UNIV OF GUELPH LIBRARY on June 23, 2012 | http://pubs.acs.org
Publication Date (Web): December 3, 2010 | doi: 10.1021/bk-2010-1056.ch009

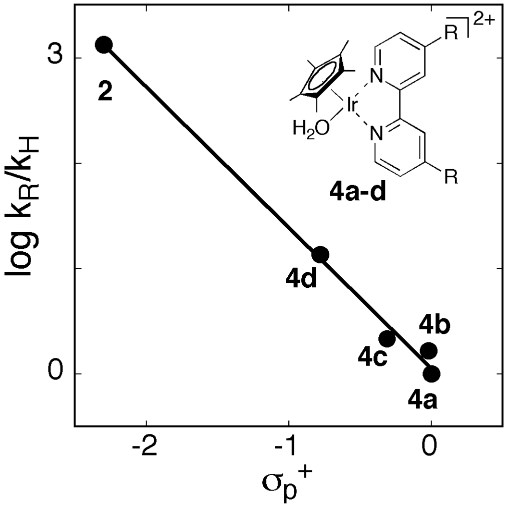

*Figure 7. Hammett plot of initial TOF vs. σ_p^+ value of substituent (R) in the catalyst (0.02–0.2 mM) at 80 °C in 1 M aqueous KOH solution at 4 MPa. **4a** (R = H: σ_p^+ = 0.0), **4b** (R = CO_2H: see text), **4c** (R = Me: σ_p^+ = –0.31), **4d** (R = OMe: σ_p^+ = –0.78)*

Downloaded by UNIV OF GUELPH LIBRARY on June 23, 2012 | http://pubs.acs.org
Publication Date (Web): December 3, 2010 | doi: 10.1021/bk-2010-1056.ch009

Table 1. Hydrogenation of CO_2 using iridium-DHBP catalyst 2[a]

Entry	*Conc. of **2** / μM*	*Temp. / °C*	*Time / h*	*P / MPa*	*Initial TOF / h^{-1}*	*TON*
1	0.5	120	57	6	42,000	190,000
2	20	50	30	1	820	9,500
3	200[b]	60	50	0.1	33	376

[a] The reaction was carried out in an aqueous KOH solution (1 M) at the desired CO_2/H_2 (1:1) pressure. [b] The reaction was carried out in an aqueous K_2CO_3 solution (0.1 M).

Table 2. Batch-wise catalyst recycling in the conversion of CO_2 into formate using iridium-DHPT catalyst 3[a]

Cycle	*Loaded/recovered iridium / ppm*	*Recovery Efficiency / %*	*Leaching iridium / ppm[b]*	*Final conc. of formate / M[c]*
1	9.0		0.11	0.105
2	8.4	93	0.22	0.104
3	7.7	92	0.42	0.103
4	7.0	91	0.61	0.103

[a] The reaction was carried out using catalyst **3** (2.5 μmol) under 6 MPa of H_2:CO_2 (1:1) in 0.1 M KOH solution (50 mL) at 60 °C for 20 h. [b] The Ir concentration was measured by ICP-MS analysis. [c] No bicarbonate was detected in any of the four cycles.

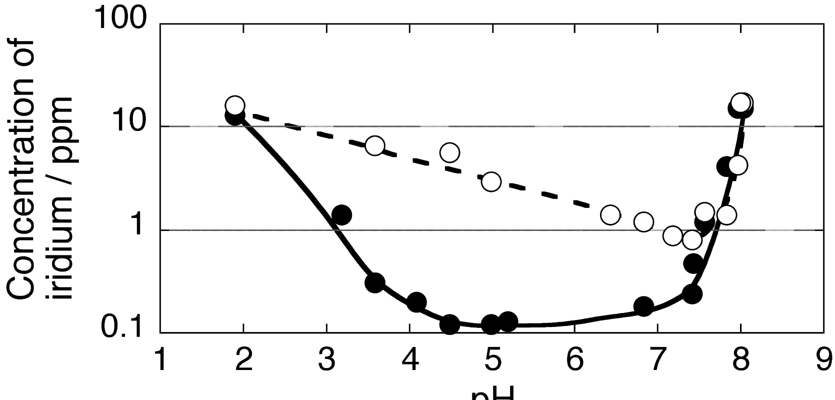

*Figure 8. Solubilities of **2** (open circles/dotted line) and **3** (filled circles/solid line) in a 1 M aqueous formate solution.*

Downloaded by UNIV OF GUELPH LIBRARY on June 23, 2012 | http://pubs.acs.org
Publication Date (Web): December 3, 2010 | doi: 10.1021/bk-2010-1056.ch009

Catalyst Recycling

The final goal in designing the catalyst is to recover and recycle it efficiently. The abovementioned acid-base equilibrium leads to changes not only in the electronic properties of the catalyst but also in its polarity, thus enabling tuning of its water-solubility. Figure 8 shows the solubilities of the complexes at various pH values in a 1 M formate solution. The DHBP complex **2** is soluble (albeit slightly, ca. 1 ppm) under neutral conditions. For satisfactory catalyst recovery, the ligand was changed from DHBP to the less water-soluble phenanthroline analog 4,7-dihydroxy-1,10-phenanthroline (DHPT) (Scheme 1). The negligible water solubility of **3** (ca. 100 ppb) under weakly acidic conditions can lead to efficient recovery of the catalyst by simple filtration.

Recycling of the catalyst **3** was examined in a batch-wise cycle (Table 2) (*19*). When the reaction was carried out under optimized conditions, the catalyst precursor spontaneously precipitated and the added KOH was completely consumed. The catalyst was recovered by filtration, and the iridium leaching into the filtrate was found to be 0.11 ppm (<2% of the loaded Ir). In addition, it was possible to isolate the pure product by simply evaporating the filtrate since the catalytic performance was high and the reverse reaction was prevented. The recovered catalyst retained high catalytic activity across the four cycles.

We thus show that the three components (catalyst, product, and solvent) can be separated easily without waste generation. We also demonstrate the functions to which the oxyanion generated from the hydroxyl group on the catalyst ligand significantly contributes: catalyst recovery by acid-base equilibrium, and catalyst activation by its electron-donating ability. These results suggest that, by carefully considering reaction profiles and the use of an innovative homogeneous catalyst, a tailor-made catalyst system can overcome the disadvantages of homogeneous catalysis.

Decomposition of Formic Acid

The second step is the reproduction of hydrogen by catalytic decomposition of formic acid. A number of heterogeneous and homogeneous catalysts for hydrogen production by decomposition of formic acid have been reported in the past five decades (*20–22*). Recently, remarkable developments in homogeneous catalyst systems have been reported. We found that H_2 and CO_2 evolved during transfer hydrogenation using formate catalyzed by the rhodium catalyst **1** in water (*12*, *13*). The evolved volumes of H_2 and CO_2 increased linearly with time, and the TOFs for each were 238 h^{-1} at 40 °C and a pH of 3.5 (*14*). Since 2008, a number of highly active catalytic systems under milder reaction conditions have been reported. Beller (*23–25*) and Wills (*26*, *27*) independently published a series of reports on the use of ruthenium-based systems in the presence of amines. Laurenczy independently reported ruthenium catalysts in aqueous systems (*28*, *29*).

As described above, we have reported a remarkable improvement of catalytic activity by introducing hydroxyl groups to bipyridine ligands. Thus, the increasing demand for a hydrogen economy prompted us to reinvestigate the decomposition of formic acid by the DHBP catalyst **2** (*30*).

The decomposition of formic acid was investigated using ruthenium-, rhodium-, and iridium-DHBP catalysts in an aqueous formic acid solution at 60 °C (Table 3). The rhodium catalyst $[Cp^*Rh(DHBP)(H_2O)]^{2+}$ (**5**) and ruthenium catalyst $[(C_6Me_6)Ru(DHBP)(H_2O)]^{2+}$ (**6**) showed moderate to low TOFs (entries 1–2). On the other hand, the iridium catalyst **2** showed a TOF of 2800 h^{-1}(entry 3). The highest TOF (14000 h^{-1}) was obtained at 90 °C (entry 5). It should be noted that formic acid was almost completely decomposed by the end of the reaction. The activity of the iridium catalyst was strongly dependent on the pH of the reaction solution. An increase in the pH caused the TOF and conversion to decrease (entries 3, 6, 7). Moreover, a negligible amount of gas evolution was observed above a pH of 4.5. The catalytic activity was dependent on the concentration of the formic acid: the highest TOF at 60 °C (3100 h^{-1}) was obtained in a 4 M formic acid solution (entries 3, 8, 9). However, the catalytic activity in 99% formic acid was significantly reduced (TOF = 760 h^{-1}). For efficient gas evolution, it is necessary to use formic acid diluted with H_2O in the reaction. During these reactions, no CO (<10 ppm) was detected by GC using a flame ionization detector equipped with a methanizer.

The catalytic activity was also affected by the electronic effect of the substituents in the bipyridine ligand. The TOF of **2** was approximately 90 and 2 times those of the unsubstituted analogue **4a** and the methoxy analogue **4d**, respectively. Similar to previous studies, the TOF values for a series of iridium complexes showed a good correlation with the Hammett substituent constants (σ_p^+) (Figure 9), in which the substituent in **2** behaved as a hydroxyl group ($\sigma_p^+ = -0.91$) under acidic conditions.

Table 3. Decomposition of formic acid in water[a]

Entry	*Catalyst*	*Temp. / °C*	*Solution*	*Initial TOF / h^{-1}*	*Conversion / %*
1	**5**·SO_4[b]	60	2 M HCO_2H	510	-
2	**6**·SO_4[b]	60	2 M HCO_2H	40	-
3	**2**·SO_4	60	2 M HCO_2H	2800	> 99
4	**2**·SO_4	40	2 M HCO_2H	450	> 99
5	**2**·SO_4	90	2 M HCO_2H	14000	> 99
6	**2**·SO_4	60	1 M pH 3.0	750	46
7	**2**·SO_4	60	1 M pH 4.0	111	16
8	**2**·SO_4	60	4 M HCO_2H	3100	> 99
9	**2**·SO_4	60	8 M HCO_2H	3000	> 99

[a] The reaction was carried out using the catalyst (2 μmol) in an aqueous formate solution (10 ml). [b] catalyst (5 μmol).

Downloaded by UNIV OF GUELPH LIBRARY on June 23, 2012 | http://pubs.acs.org
Publication Date (Web): December 3, 2010 | doi: 10.1021/bk-2010-1056.ch009

Downloaded by UNIV OF GUELPH LIBRARY on June 23, 2012 | http://pubs.acs.org
Publication Date (Web): December 3, 2010 | doi: 10.1021/bk-2010-1056.ch009

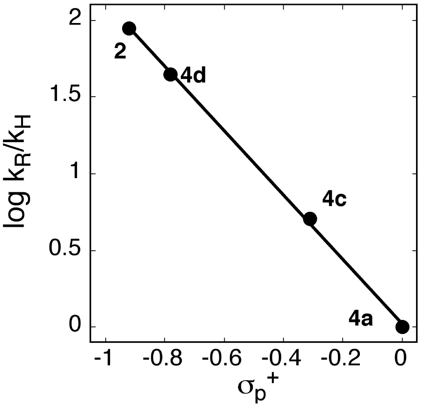

Figure 9. Hammett plot of initial TOF vs. σ_p^+ value of substituent (R) in the catalyst (2.0–20 μmol) at 60 °C in 1 M aqueous formic acid solution (10 mL).

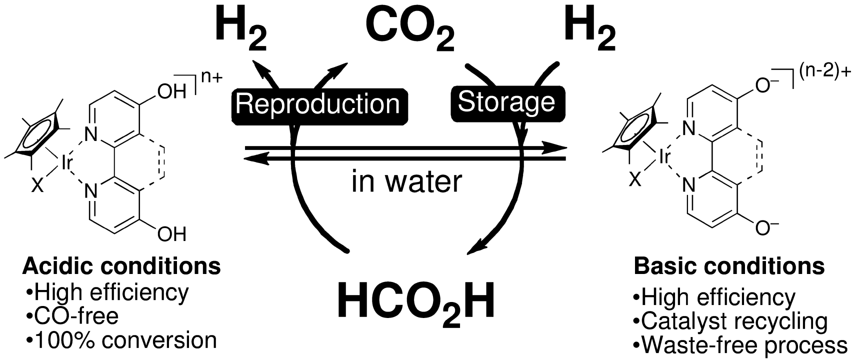
H_2
CO_2
H_2
Reproduction
Storage
in water
HCO_2H
OH
n+
N
Ir
X
N
OH
O⁻
(n-2)+
N
Ir
X
N
O⁻
Acidic conditions
•High efficiency
•CO-free
•100% conversion
Basic conditions
•High efficiency
•Catalyst recycling
•Waste-free process

Figure 10. Utilization of CO_2 using a combination of the preparation and decomposition of formic acid catalyzed by iridium catalyst.

Catalytic decomposition of formic acid proceeded in a closed system. The gas smoothly evolved in an autoclave and the pressure exceeded 4 MPa. It was possible to control the rate of gas evolution by the reaction temperature. These results indicated that the catalytic system could provide the desired amount of CO-free hydrogen gas for an extended period of time.

We have achieved the highest catalytic activity for the decomposition of formic acid in water, in which CO-free and pressurized hydrogen could be evolved. These results suggest that a procedure for producing CO-free hydrogen from formic acid can serve as the basis for generating electricity by fuel cells. In the near future, formic acid obtained from biomass may be of importance as hydrogen source (*31*).

Downloaded by UNIV OF GUELPH LIBRARY on June 23, 2012 | http://pubs.acs.org
Publication Date (Web): December 3, 2010 | doi: 10.1021/bk-2010-1056.ch009

Summary

We have demonstrated a hydrogen-storage system using a combination of the preparation and decomposition of formic acid under mild conditions in water (Figure 10). One of two reactions can be selected by the pH of the solution using the same iridium catalyst, which hydrogenates CO_2 *in a basic solution* and decomposes formic acid *in an acidic solution*. Overall, the system should be environmentally benign and highly efficient. More importantly, the acid-base equilibrium of the hydroxyl group on the catalyst ligand offers a novel tool for simultaneous control over the activity and water solubility of the catalyst. The remarkable catalytic activity is due to the strong electron-donating oxyanion generated from the hydroxyl group.

Acknowledgments

Financial support from the Ministry of Economy, Trade, and Industry is gratefully acknowledged.

References

1. Enthaler, S. *ChemSusChem* **2008**, *1*, 801–804.
2. Joó, F. *ChemSusChem* **2008**, *1*, 805–808.
3. Preti, D.; Squarcialupi, S.; Fachinetti, G. *Angew. Chem., Int. Ed.* **2010**, *49*, 2581–2584.
4. Man, M. L.; Zhou, Z. Y.; Ng, S. M.; Lau, C. P. *Dalton Trans.* **2003**, 3727–3735.
5. Gao, Y.; Kuncheria, J. K.; Jenkins, H. A.; Puddephatt, R. J.; Yap, G. P. A. *J. Chem. Soc., Dalton Trans.* **2000**, 3212–3217.
6. Jessop, P. G.; Joó, F.; Tai, C. C. *Coord. Chem. Rev.* **2004**, *248*, 2425–2442.
7. Jessop, P. G. In *Handbook of Homogeneous Hydrogenation*; De Vries, J. G., Elsevier, C. J., Eds.; Wiley-VCH: Weinheim, Germany, 2007; Vol. 1, pp 489–511.
8. Himeda, Y. *Eur. J. Inorg. Chem.* **2007**, 3927–3941.
9. Walther, D. *Nachr. Chem.* **2007**, *55*, 1188–1194.
10. Tanaka, R.; Yamashita, M.; Nozaki, K. *J. Am. Chem. Soc.* **2009**, *131*, 14168–14169.
11. Sanz, S.; Benitez, M.; Peris, E. *Organometallics* **2010**, *29*, 275–277.
12. Himeda, Y.; Onozawa-Komatsuzaki, N.; Sugihara, H.; Arakawa, H.; Kasuga, K. *J. Mol. Catal. A: Chem.* **2003**, *195*, 95–100.
13. Himeda, Y.; Onozawa-Komatsuzaki, N.; Sugihara, H.; Arakawa, H.; Kasuga, K. In *The 50th Symposium on Coordination Chemistry of Japan*; Japan Society of Coordination Chemistry: Kusatsu, 2000; 1P3K01.
14. Himeda, Y.; Onozawa-Komatsuzaki, N.; Sugihara, H.; Arakawa, H.; Kasuga, K. *Organometallics* **2004**, *23*, 1480–1483.
15. Himeda, Y.; Onozawa-Komatsuzaki, N.; Miyazawa, S.; Sugihara, H.; Hirose, T.; Kasuga, K. *Chem. Eur. J.* **2008**, *14*, 11076–11081.
16. Hansch, C.; Leo, A.; Taft, R. W. *Chem. Rev.* **1991**, *91*, 165–195.

17. Himeda, Y.; Onozawa-Komatsuzaki, N.; Sugihara, H.; Kasuga, K. *J. Photochem. Photobiol., A* **2006**, *182*, 306–309.
18. Elek, J.; Nadasdi, L.; Papp, G.; Laurenczy, G.; Joó, F. *Appl. Catal., A: General* **2003**, *255*, 59–67.
19. Himeda, Y.; Onozawa-Komatsuzaki, N.; Sugihara, H.; Kasuga, K. *J. Am. Chem. Soc.* **2005**, *127*, 13118–13119.
20. Johnson, T. C.; Morris, D. J.; Wills, M. *Chem. Soc. Rev.* **2010**, *39*, 81–88.
21. Makowski, P.; Thomas, A.; Kuhn, P.; Goettmann, F. *Energy Environ. Sci.* **2009**, *2*, 480–490.
22. Loges, B.; Boddien, A.; Gartner, F.; Junge, H.; Beller, M. *Top. Catal.* **2010**, *53*, 902–914.
23. Boddien, A.; Loges, B.; Junge, H.; Beller, M. *ChemSusChem* **2008**, *1*, 751–758.
24. Boddien, A.; Loges, B.; Junge, H.; Gartner, F.; Noyes, J. R.; Beller, M. *Adv. Synth. Catal.* **2009**, *351*, 2517–2520.
25. Loges, B.; Boddien, A.; Junge, H.; Beller, M. *Angew. Chem., Int. Ed.* **2008**, *47*, 3962–3965.
26. Majewski, A.; Morris, D. J.; Kendall, K.; Wills, M. *ChemSusChem* **2010**, *3*, 431–434.
27. Morris, D. J.; Clarkson, G. J.; Wills, M. *Organometallics* **2009**, *28*, 4133–4140.
28. Fellay, C.; Yan, N.; Dyson, P. J.; Laurenczy, G. *Chem. Eur. J.* **2009**, *15*, 3752–3760.
29. Fellay, C.; Dyson, P. J.; Laurenczy, G. *Angew. Chem., Int. Ed.* **2008**, *47*, 3966–3968.
30. Himeda, Y. *Green Chem.* **2009**, *11*, 2018–2022.
31. Taccardi, N.; Assenbaum, D.; Berger, M. E. M.; Bosmann, A.; Enzenberger, F.; Wolfel, R.; Neuendorf, S.; Goeke, V.; Schodel, N.; Maass, H.-J.; Kistenmacherc, H.; Wasserscheid, P. *Green Chem.* **2010**, *12*, 1150–1156.

Downloaded by UNIV OF GUELPH LIBRARY on June 23, 2012 | http://pubs.acs.org
Publication Date (Web): December 3, 2010 | doi: 10.1021/bk-2010-1056.ch009

Downloaded by STANFORD UNIV GREEN LIBR on June 23, 2012 | http://pubs.acs.org
Publication Date (Web): December 3, 2010 | doi: 10.1021/bk-2010-1056.ch010

Chapter 10

Advances in Catalysts for CO_2 Reforming of Methane

Yun Hang Hu*

Department of Materials Science and Engineering, Michigan Technological University, 1400 Townsend Drive, Houghton, MI 49931-1295, USA
***Email: yunhangh@mtu.edu**

CO_2 reforming of methane is attractive, because it can convert two greenhouse gases into synthesis gas (H_2/CO), which is an important feedstock for many industrial processes. So far, there is no commercial process for the reforming due to several issues, such as high energy cost and unavailability of effective catalysts. In the past 20 years, the research for CO_2 reforming of methane has been focused on the development of catalysts. This chapter provides a critical assessment of the literature regarding catalysts for CO_2 reforming of methane.

Although noble metal catalysts, such as Rh, have excellent activity and selectivity as well as stability, the high cost limits their industrial application for CO_2 reforming of methane. On the other hand, non-noble metal catalysts (particularly Ni-based catalysts) exhibit excellent catalytic activity and selectivity at low cost. However, their stability is poor due to carbon deposition. Therefore, the inhibition of carbon deposition for non-noble metal catalysts became the most important topic for CO_2 reforming of methane. The strategies, which were exploited to inhibit carbon deposition, are to control particle sizes of active components and to increase the surface basicity of catalysts. Several approaches were developed to control the metal particle sizes, including the enhancement of metal-support interaction, the formation of solid solutions, and plasma-treatments. To increase the surface basicity of catalysts, basic metal oxides were employed as support or promoter.

In Advances in CO2 Conversion and Utilization; Hu, Y.;
ACS Symposium Series; American Chemical Society: Washington, DC, 2010.

Downloaded by STANFORD UNIV GREEN LIBR on June 23, 2012 | http://pubs.acs.org
Publication Date (Web): December 3, 2010 | doi: 10.1021/bk-2010-1056.ch010

1. Introduction

There are several technological options for sequestration of atmospheric CO_2 into one of the other global pools (*1*), including oceanic injection, geological injection, and scrubbing and mineral carbonation. Injection of a pure CO_2 stream deep in the ocean has been widely considered by engineers for about three decades. However, CO_2 injection may have some adverse effects on deep sea biota (*2*). Industrial CO_2 can also be injected into deep geological strata (*3*). The cost and leakage are principal issues of the geological sequestration which need to be resolved. Industrial strength CO_2 emission can be transformed into $CaCO_3$, $MgCO_3$ and other minerals in the form of geologically and thermodynamically stable mineral carbonates. However, this is not only a slow mineral reaction process, but also an expensive disposal approach. For those reasons, the utilization of CO_2 is being considered as a more attractive solution to solve CO_2 issues.

In recent years, carbon dioxide has found a growing application as a fluid in dry-cleaning, refrigerators, air conditioners, fire-extinguishers, separation techniques, water treatment, and food-industry. Furthermore, supercritical CO_2 fluid technology has made tremendous strides in the past decade (*4*). This happened because supercritical fluids have the best of two worlds: they can have gas-like diffusivities that have important implications for reaction kinetics, while having liquid-like densities that allow for salvation of many compounds (*5*). Application of supercritical CO_2 fluid as solvent can improve the separation of the polymer from starting materials and catalysts and the polymer molecular weight fractionation. However, solubility is a key factor that affects the application of supercritical CO_2 fluid for the synthesis of polymers. Although CO_2 is a good solvent for the most nonpolar and some polar molecules of low molar mass (*6*), it is a poor solvent for most high molar mass polymers under mild conditions (<100°C, <350bar). Nevertheless, the solubility of CO_2 can enhance with the increasing content of polar groups in polymer (*7*). It was found that specific interaction between CO_2 and the dipoles of C-F bonds (*8*) or fluorine (*9*) led to the increased solubility of CO_2 in fluorine-containing polymers. As a result, a supercritical carbon dioxide-based solvent was successfully applied to the DuPont industrial production of fluoropolymers (*10*). On the other hand, the capabilities of CO_2 as a solvent can also be increased by using suitable additives, such as surfactants, that exhibit favorable thermodynamic interactions with CO_2 (*11*, *12*). However, in those processes, CO_2 is not converted into other chemicals, and is recovered as such at the end of the application.

The conversion of CO_2 into useful products is very attractive. However, it still remains a challenging subject, because CO_2 is the lowest in energy of all carbon-containing binary neutral compounds. In nature, an enormous amount of CO_2 is transformed into carbohydrate in enzymatic systems. In contrast, the industrial application of CO_2 as a feedstock for chemical processes is limited. Currently, the largest industrial conversion of CO_2 is production of Urea (H_2NCONH_2), which is 95Mt per year, via the reaction of CO_2 and ammonia (*13*):

$$2NH_3+CO_2 \rightarrow H_2NCONH_2+H_2O \qquad (1)$$

Production of inorganic carbonates and pigments consumes about 30 Mt CO_2 per year. Furthermore, CO_2 (6Mt per year) is used as an additive to CO for the synthesis of methanol. Other chemicals produced from CO_2 have a minor share of the market.

CO_2 reforming of methane to synthesis gas was investigated as early as 1888:

$$CH_4 + CO_2 \rightarrow 2CO + 2H_2, \quad \Delta H^0_{298} = 247 kJmol^{-1} \qquad (2)$$

Although this process is endothermic, it produces synthesis gas with a lower H_2/CO ratio than steam reforming, and is therefore suitable for the Fischer-Tropsch synthesis of long-chain hydrocarbons (*14*). Furthermore, it can be carried out with natural gas from fields containing large amounts of CO_2, without the pre-separation of CO_2 from the feed. Because CO_2 is a greenhouse gas that causes warming of the earth and climate change, there are incentives for reducing its concentration in the atmosphere (*15*). Methane should be also considered as a greenhouse gas, because it can absorb 20 times more heat than CO_2. The CO_2 reforming of methane may provide a practical method for consumption of those two greenhouse gases. So far, there is no commercial process for the CO_2 reforming of methane due to several issues, such as high energy cost and ineffective catalysts. In the past 20 years, the research and development of catalysts for the CO_2 reforming have attracted much attention. The purpose of this chapter is to provide a critical assessment of the literature regarding catalyst compositions, structures, and performances with emphasis on enhancing stability of catalysts.

2. Thermodynamic Consideration

The reaction equilibrium of CH_4 and CO_2 to syngas (CO/H_2) (Eq. 2) is influenced by the reverse water-gas shift reaction (RWGS)

$$CO_2 + H_2 \rightarrow CO + H_2O, \Delta H^o_{298} = 41 \text{ kJ/mol} \qquad (3)$$

As shown in Fig.1, the equilibrium composition indicates the formation of water (*16*, *17*). At 1 atm, water effectively disappears above about 900°C. The formation of water leads to lower hydrogen concentrations than CO due to the RWGS reaction, which is the main water formation route. Compared to the product composition at 1atm, the presence of water at 10 atm is much more pronounced, extending well beyond 900°C. When pressure increases from 1 to 10 atm, the equilibrium conversion of CH_4 decreases from 97 to 90% at 900°C. This occurs because the CO_2 reforming of methane is a volume-enlargement process.

Furthermore, the CO_2/CH_4 reforming is likely to suffer carbon formation via reactions:

$$CH_4 \rightarrow C + 2H_2, \Delta H^o_{298} = 75 \text{ kJ/mol} \qquad (4)$$

$$2CO \rightarrow C + CO_2, \Delta H^o_{298} = -171 \text{ kJ/mol} \qquad (5)$$

Thermodynamic considerations suggest operation at high CO_2/CH_4 ratios (>1) and high temperatures to minimize carbon formation in the CO_2 reforming of methane

Downloaded by STANFORD UNIV GREEN LIBR on June 23, 2012 | http://pubs.acs.org
Publication Date (Web): December 3, 2010 | doi: 10.1021/bk-2010-1056.ch010

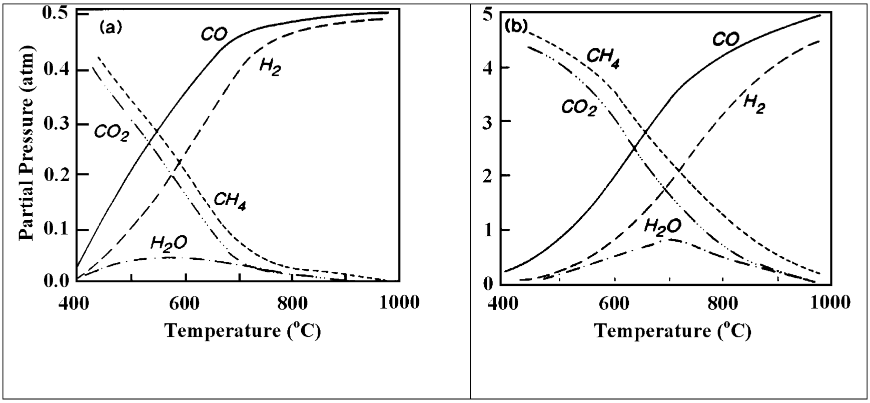

Figure 1. Equilibrium gas composition calculated for the reforming reaction at temperature range 400-1000°C using a CO_2/CH_4 feed ratio of 1/1 at (a) pressures of 1 atm and (b) pressures of 10 atm (16).

(*14*, *18*, *19*). However, from an industrial viewpoint, it is desirable to operate at lower temperatures and with a CO_2/CH_4 (or H_2O/CH_4) ratio near unity. Such an operation requires a catalyst that kinetically inhibits the carbon formation under conditions that are thermodynamically favorable for carbon deposition. In other words, the role of suitable catalysts would be not only to speed up the overall reaction but also to adjust the appropriate elementary steps in a way which prevents net carbon deposition.

3. Developments of Catalysts

There are three critical properties that must be considered for catalyst development: activity, selectivity, and stability. So far, almost all transition metals were evaluated as catalysts for the CO_2 reforming (*20*, *21*). It was found that Ni, Co, Ru, Rh, Pd, Ir, and Pt constitute effective catalytic components. Fe may be only one inactive element in Group VIII. Various sequences of activities for those transition metals catalyzing CO_2 reforming of methane are reported (*22–24*). For example, the activity sequences are Ru>Rh & Ni >Ir>Pt>Pd from Rostrup-Nielsen and Hansen (*23*), Ni>Ru>Rh>Pt>Pd from Takayasu *et al.* (*24*), and Ni>Pd & Ir >Rh > Ru (supported on Al_2O_3) from Ashcroft *et al.* (*22*). Nevertheless, it is a general recognition that both supported noble-metals and Ni catalysts have high activity and selectivity. However, the stabilities of noble-metal catalysts and non-noble metal catalysts are very different. The deactivation of non-noble metal catalysts by carbon deposition is a critical issue hindering the application of the CO_2 reforming of methane. It was reported that the amount of carbon deposited on metal catalysts decreases in the order Ni >> Rh > Ir = Ru > Pt ≅ Pd at 773 K and Ni > Pd = Rh > Ir > Pt >> Ru at 923 K (*25*, *26*). Thus, the noble metals exhibit higher selectivities for a carbon-free operation than nickel (*25–30*). Nevertheless, most of the reported research for CO_2 reforming has been focused on non-noble metal catalysts, particularly nickel, because nickel has activity and selectivity comparable to those of noble metals at much less cost. Without doubt,

In Advances in CO2 Conversion and Utilization; Hu, Y.;
ACS Symposium Series; American Chemical Society: Washington, DC, 2010.

Downloaded by STANFORD UNIV GREEN LIBR on June 23, 2012 | http://pubs.acs.org
Publication Date (Web): December 3, 2010 | doi: 10.1021/bk-2010-1056.ch010

the inhibition of carbon deposition for CO_2 reforming of methane over non-noble metal catalysts is one of important topics.

3.1. Strategies for Developing Effective Catalysts

In the CO_2 reforming of methane, carbon formation can occur via two possible pathways: CH_4 decomposition (Eq.4) and CO disproportionation (the Boudouard reaction) (Eq.5). It was found that carbon formation by CH_4 decomposition is a structure-sensitive reaction (*31*, *32*). For example, the Ni(100) and Ni(110) surfaces are more active in the decomposition of CH_4 to carbon than the Ni(111) surface (*31*). Furthermore, the carbon adsorbed on the smaller metal particles diffuses with more difficulty than that on the larger particles (*33*). The structure-sensitivity of carbon formation provides the possibility for inhibition of the carbon deposition by modification of the catalyst surface structure. On the other hand, adsorption of CO_2 in the CO_2 reforming of methane is strongly dependent on the acidity of catalysts. The high Lewis basicity of the support increases the ability of the catalyst to chemisorb CO_2 in the CO_2 reforming of methane and the species react with carbon to form CO, resulting in decreased net carbon formation. Therefore, the modifications of surface structure and acidity constitute an effective strategy to inhibit carbon deposition on catalysts:

- *To inhibit carbon deposition, one can control the size of the ensembles of metal atoms on the surface, because the ensembles necessary for carbon formation are larger than those needed for CH_4 reforming (34). So far, the several approaches have been applied to control particle sizes: sulfur passivation (35, 36), increasing metal-support interaction (21), solid solution formation (21, 37–40), and plasma treatments (41, 42).*
- *It has also been noted that carbon deposition can be attenuated or even suppressed when the metal is supported on a metal oxide with a strong Lewis basicity (43–46). Therefore, an effective approach is to exploit basic metal oxide as support or promoter for catalysts.*

3.2. Role of Supports

For heterogeneous catalysts, supports play important roles, including dispersing active components, stabilizing and promoting active sites, and even becoming part of active sites. In CO_2 reforming of methane, supports were mainly exploited to enhance the resistance to carbon deposition via tuning metal-support interaction and thus controlling particle sizes of active components.

Alumina is widely used as a support for nickel catalysts (*46*–*57*). Ni/Al_2O_3 exhibits carbon deposition (*58*) that depends on the catalyst structure, composition, and preparation conditions. It was observed that the carbon deposition was markedly suppressed when $NiAl_2O_4$ was formed during high temperature pretreatment (*59*). This suppression might be the result of a strengthening of the Ni-O bond in $NiAl_2O_4$ when compared to that in the NiO crystal (*60*). The stronger Ni-O bond increases the difficulty of reduction of Ni^{2+} to Ni^{o}, resulting in smaller nickel crystallites on the catalyst surface. These nickel crystallites, which

Downloaded by STANFORD UNIV GREEN LIBR on June 23, 2012 | http://pubs.acs.org
Publication Date (Web): December 3, 2010 | doi: 10.1021/bk-2010-1056.ch010

Downloaded by STANFORD UNIV GREEN LIBR on June 23, 2012 | http://pubs.acs.org
Publication Date (Web): December 3, 2010 | doi: 10.1021/bk-2010-1056.ch010

are smaller than the size necessary for carbon deposition, decrease the carbon formation (*48*). Furthermore, Kim *et al.* (*47*, *61*) noted that, in comparison with the alumina-supported nickel catalyst prepared by the conventional impregnation method, Ni/Al_2O_3 catalysts prepared from aerogel alumina exhibited markedly low coking rates probably due to the high dispersion of the metal particles. A similar observation was obtained by Osaki *et al.* (*62*) and Hayashi *et al.* (*63*).

The deactivation of Ni/SiO_2 catalysts during the CO_2 reforming of methane was examined as a function of various operating parameters (*50*, *64*, *65*). The two principal causes of catalyst deactivation, nickel sintering and carbon deposition, were shown to depend strongly on the pretreatment conditions. Kroll *et al.* (*65*) noted that for the Ni/SiO_2 catalyst, nickel carbide-like layers, formed during the very initial period of the run, provided the active phase for CO_2 reforming. However, when the carbon formation, which takes place at equilibrium with gaseous CH_4, became faster than the oxidation of the carbon with the oxygen adspecies formed by carbon dioxide activation, carbon deposition occurred. The carbon deposition depended strongly on the nickel loading (*50*). It was found that a 13.6 wt% Ni/SiO_2 catalyst exhibited a greater carbon deposition than a 1 wt% Ni/SiO_2.

It was reported that a Ni/La_2O_3 catalyst exhibited a higher activity and higher long-term stability for CO_2 reforming of methane to synthesis gas than Ni/Al_2O_3 and Ni/CaO catalysts (*66*). Although the initial rate of reaction on Ni/γ-Al_2O_3 was higher than that on Ni/CaO (probably as a consequence of the higher dispersion of nickel in the former catalyst), the deactivation rate of Ni/γ-Al_2O_3 was higher than that of Ni/CaO (Fig.2). In contrast, the rate of reaction on a Ni/La_2O_3 catalyst increased significantly with time on stream during the initial 2-5 h of reaction, and then remained unchanged with time on stream for 100 operating hours. In these experiments, low conversions of CH_4 and CO_2 were observed at a very high space velocity (*66*, *67*). However, when higher CH_4 and CO_2 conversions (about 75 and 80%, respectively) were obtained by reducing the space velocity, the Ni/La_2O_3 catalyst exhibited deactivation (Fig. 3) (*67*). The higher stability of the catalyst at low reactant conversions occurred probably because high concentrations of unreacted CO_2 inhibited carbon deposition by the reaction $CO_2 + C = 2CO$. The preparation method also affects the Ni/La_2O_3 catalysts (*68*). The conversions of CH_4 and CO_2 in the CO_2 reforming of CH_4 catalyzed by Ni/La_2O_3 prepared by a sol-gel technique were significantly higher than those catalyzed by Ni/La_2O_3 prepared by wet impregnation. The amount of carbon deposited in the former case was smaller than in the latter case. The difference might be due to the uniform dispersion of nanoscale nickel particles in the sol gel-generated Ni/La_2O_3 catalyst.

Zirconia-supported nickel catalysts were investigated for the CO_2 reforming reaction with emphasis on the stability of the catalysts under conditions favorable for carbon formation (*69–73*). It was found that at temperatures between 993 and 1053 K, the ZrO_2-supported catalysts with lower nickel loadings (< 2 wt%) were more stable than those with higher nickel loadings for a stoichiometric CO_2/CH_4 ratio. Furthermore, two forms of deposited carbon were observed in the less stable catalysts, and only one form was observed in the more stable ones. Carbon deposits were formed on the reduced catalyst at a very high rate during the temperature-programmed surface reaction (TPSR) (*70*). The amount of deposited

Downloaded by STANFORD UNIV GREEN LIBR on June 23, 2012 | http://pubs.acs.org
Publication Date (Web): December 3, 2010 | doi: 10.1021/bk-2010-1056.ch010

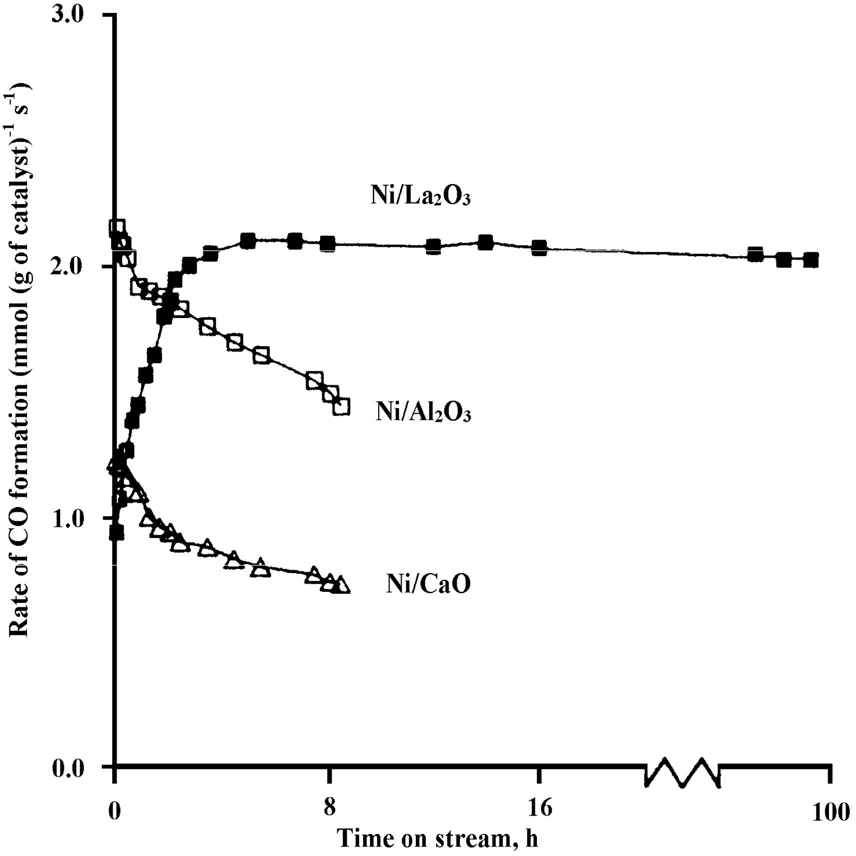

Figure 2. CO formation rates determined from reactant conversions and product selectivities in a fixed-bed flow reactor for CO_2 reforming of CH_4. The catalysts were nickel supported on La_2O_3, γ-Al_2O_3, or CaO. Each catalyst contained 17 wt% Ni. Before reaction, the catalyst was reduced in flowing H_2 at 773 K for at least 5 h and then at 1023 K for 2 h. Reaction conditions: Pressure, 1.0 atm; temperature, 1023 K; feed gas molar ratio, $CH_4/CO_2/He = 2/2/6$; GHSV, 1800,000 mL (g of catalyst)$^{-1}$ h^{-1}. Reproduced with permission from (66). Copyright 1995, the Royal Society of Chemistry.

carbon remained constant on the catalyst during reaction at 973 K (*70*), consistent with the inference that the initially formed carbon acted as a reaction intermediate that transformed CO_2 into CO. Even with catalysts having high nickel loadings, catalyst lives without significant deactivation were achieved for 30 h at 1023 K and for 20 h at 1123 K (*71*). The stabilities of Ni/ZrO_2 catalysts were also dependent on the preparation method. It was found that the Ni/ZrO_2 catalyst prepared from large $Zr(OH)_4$ particles deactivated rapidly (*73*). In contrast, a catalyst with a high metal loading of nickel (27 wt%), obtained by impregnating ultra-fine $Zr(OH)_4$ particles (6 nm) with nickel nitrate, exhibited a high and stable activity for CO_2 reforming without deactivation by carbon deposition.

Downloaded by STANFORD UNIV GREEN LIBR on June 23, 2012 | http://pubs.acs.org
Publication Date (Web): December 3, 2010 | doi: 10.1021/bk-2010-1056.ch010

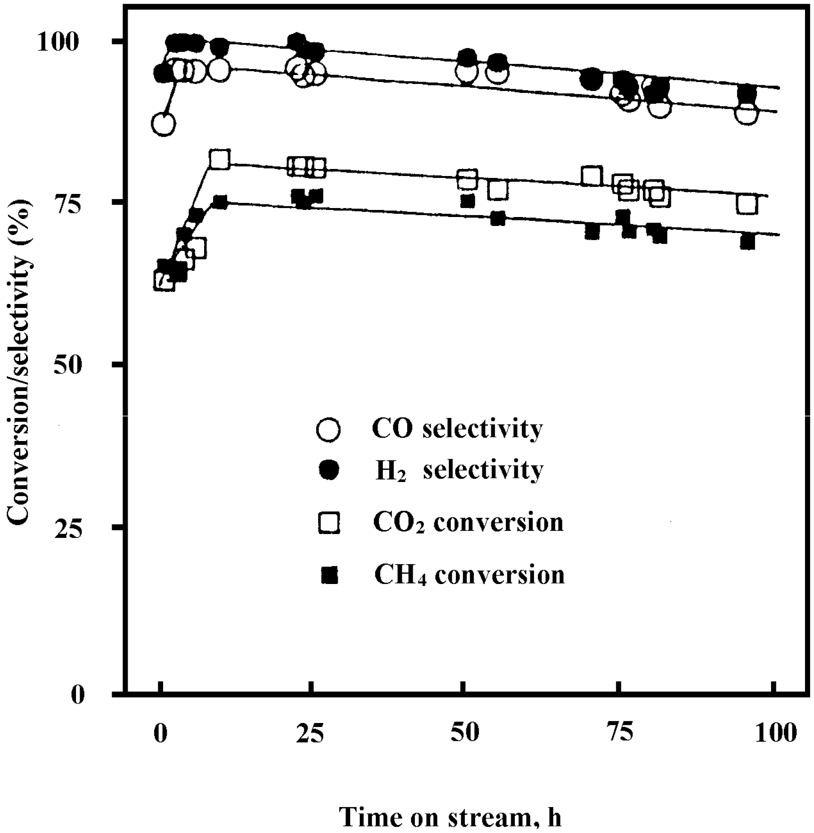

Figure 3. Conversions of CH_4 and CO_2 and selectivities for formation of CO and H_2 as a function of time on stream for CO_2 reforming of CH_4 catalyzed by 17 wt% Ni/La_2O_3. Before reaction, the catalyst was reduced in flowing H_2 at 773 K for at least 5 h and then at 1023 K for 2 h. Reaction conditions: Pressure, 1 atm; temperature, 1023 K; feed gas molar ratio, $CH_4/CO_2 = 1/1$; GHSV is unknown (67). Reproduced with permission from (67). Copyright 1996, Elsevier.

Supports can also play an important role in CO_2 reforming of methane over noble metal catalysts. It was found that platinum supported on ZrO_2 has a lower rate of carbon formation than supported on other supports (*74–79*). For example, the rate of carbon formation decreased in the sequence Pt/Al_2O_3 >> Pt/TiO_2 > Pt/ZrO_2 (*77*). The low rate of carbon deposition on the zirconia-based catalysts is probably associated with the strong Pt-Zr^{n+} interactions, which reduce the carbon formation during reaction by promoting the CO_2 dissociation (*78*). The effect of supports on Rh was also observed for CO_2 reforming of methane. It was showed that the conversions of CO_2 and methane are dependent on supports (*75*). Among various supports (CeO_2, Nb_2O_5, Ta_2O_5, TiO_2, ZrO_2, γ-Al_2O_3, La_2O_3, MgO, SiO_2, and Y_2O_3), MgO and Al_2O_3 are the most promising supports for Rh (*80*). However, the role of supports for Rh catalyst is to increase number of active Rh sites instead of inhibiting carbon deposition.

So far, many other types of supports were also employed to develop catalysts for the CO_2 reforming of methane (*20*, *21*), including perovskite (*81*), Y zeolite (*82*, *83*), 5A zeolite (*84*), high-silica ZSM-5 zeolite (*85*), $AlPO_4$ (tridymite) (*86*), and MCM-41 (*87*, *88*).

3.3. Promoting Effects

Many promoters have been used to improve the performance of Ni/Al_2O_3 catalysts. The effect of the basic oxides of Na, K, Mg, and Ca on Ni/Al_2O_3 was examined by a number of groups (*44*, *56*, *89–92*). They found that these added oxides markedly decrease carbon deposition. The kinetics results showed that the added metal oxides changed the reaction order in CH_4 from negative to positive and that in CO_2 from positive to negative. This observation implies that the surface of a nickel catalyst incorporating basic metal oxides is abundant in adsorbed CO_2, whereas the surfaces devoid of these oxides are abundant in adsorbed CH_4 (*44*). The coverage of nickel with CO_2 is most likely unfavorable to CH_4 decomposition and, as a result, the carbon deposition is decreased.

Choi *et al.* (*93*) examined the effect of Co, Cu, Zr, and Mn as promoters of Ni/Al_2O_3 catalysts. They found that, in comparison with the unmodified Ni/Al_2O_3 catalysts, those modified with Co, Cu, and Zr exhibited slightly improved activities, whereas other promoters reduced the activity. The Mn-promoted catalyst provided a remarkable reduction in coke deposition with only a small reduction in catalytic activity. Furthermore, Seok *et al.* (*94*) noted that the manganese addition to Ni/Al_2O_3 led to a partial coverage of the surface of nickel by patches of MnO_x, which promoted the adsorption of CO_2. Both the partial coverage of the nickel surface with MnO_x and the promoted CO_2 adsorption appear to be responsible for the decreased carbon deposition on $Ni/MnO\text{-}Al_2O_3$ catalysts. Mo can also improve the stability of Ni/Al_2O_3 via reducing the carbon deposition (*95*). The introduction of noble metal (Ru or Pd) into supported nickel catalysts can markedly improve both activity and stability (*96*, *97*).

Rare earth metals have also been used to promote Ni/Al_2O_3 catalysts. Slagten *et al.* (*98*) tested $Ni/Ln/Al_2O_3$ (Ln = rare earth mixture) catalysts containing 0.15 wt% Ni for their lifetimes (60-600 h) in a fluidized-bed reactor at 1073 K and 1 atm. The catalyst with a rare earth content of 1.7 wt% Ln was more active and stable than the unpromoted catalyst, and more active than a catalyst containing 8.5 wt% Ln. Neodymium can also promote Ni/Al_2O_3 catalysts, by reducing the carbon deposition (*99*). Although CeO_2 is not a suitable support for nickel because of the strong metal-support interaction, which reduces the catalytic activity, it can have a positive effect on the catalytic activity, stability, and suppression of carbon deposition when used as a promoter for Ni/Al_2O_3 catalysts (*100*, *101*). A loading of 1-5 wt% CeO_2 was found to be the optimum. The stability and reduced coking characteristic of CeO_2-promoted Ni/Al_2O_3 catalysts can be attributed to the redox properties of CeO_2, which can react directly with carbon-containing species to generate CO and CeO_x, followed by the reoxidation of CeO_x by CO_2 back to CeO_2 (*100*).

Promoters for noble metals have also a significant effect on carbon deposition. It was found that the bimetallic $Pt\text{-}Au/SiO_2$, $Pt\text{-}Sn/SiO_2$, and $Pt\text{-}Sn/ZrO_2$ catalysts

Downloaded by STANFORD UNIV GREEN LIBR on June 23, 2012 | http://pubs.acs.org
Publication Date (Web): December 3, 2010 | doi: 10.1021/bk-2010-1056.ch010

exhibited less carbon deposition during CO_2 reforming of CH_4 than the respective monometallic platinum catalysts (*102*), probably because of the formation of alloys. Vanadium oxide also plays a promoting role in the Rh/SiO_2 catalyst at temperatures of 723-773 K (*103*). Vanadium oxide enhances the catalytic activity of Rh/SiO_2 and decreases the carbon deposition. This benefit was attributed to the formation of a partial VO_x overlayer on the rhodium surface, which decreases the sizes of the accessible ensembles of Rh atoms, making some of them too small for coke formation; new sites at the Rh-VO_x interface that are considered to activate CO_2 dissociation were also created. The addition of cerium or lanthanum resulted in a significant improvement in the stability of Pt/ZrO_2, with no decrease in either CH_4 or CO_2 conversion (*104*). Temperature-programmed oxidation (TPO) data showed that although the total amount of carbon deposited on the Ce-promoted Pt/ZrO_2 catalyst was not less than that on the unpromoted catalyst, these deposits were eliminated at much lower temperatures, indicating the ability of the catalyst to self-clean its active sites.

Downloaded by STANFORD UNIV GREEN LIBR on June 23, 2012 | http://pubs.acs.org
Publication Date (Web): December 3, 2010 | doi: 10.1021/bk-2010-1056.ch010

3.4. Solid Solution Formation

The most important role of solid solution formation is to control particle sizes of active components, which contribute to inhibiting carbon deposition.

MgO is widely selected as a catalyst support due to its high thermal stability and low cost. MgO has a very high melting point (2850°C), which can allow MgO to maintain a relatively large surface area at high temperatures compared to most oxides used as catalyst supports. Furthermore, MgO, NiO, and CoO have a face centered cubic structure with almost the same lattice parameters: 4.2112Å for MgO, 4.1684Å for NiO, and 4.2667Å for CoO. As a result, the combination of MgO and NiO (or CoO) leads to the formation of solid-solution (NiO-MgO or CoO-MgO). The NiO-MgO (or CoO-MgO) solid solution provides a unique approach to inhibit carbon deposition. MgO is a strong Lewis base, which has a strong adsorption for CO_2 to reduce or inhibit carbon deposition. Furthermore, it was observed that the reduction of NiO or (CoO) in NiO-MgO (or CoO-MgO) solid solution was much more difficult than that of pure NiO (or pure CoO), leading to small nickel particles formed on the surface (*105–107*). The combination of the surface basicity and the small metal particle size constitutes the ability of MgO-based solid solution catalysts to inhibit carbon inhibition.

Several groups reported the excellent results of CO_2 reforming of methane in the presence of NiO-MgO and CoO-MgO solid solution catalysts (*37–40, 105–113*). As shown in Fig.4, a 20wt% NiO/MgO solid-solution catalyst for CO_2 reforming of methane, which was prepared by impregnation and was calcined at 1073 K, was reported (*38*). The reduced solid solution catalyst exhibited almost 100% conversion of CO_2, >91% conversion of CH_4, and >95% selectivities to CO and H_2 at 1063 K, atmospheric pressure, and the very high space velocity of 60,000 ml (g of catalyst)$^{-1}$ h^{-1} for a CH_4/CO_2 (1/1) feed (Fig. 4). The conversion and selectivity remained unchanged during the entire reaction time employed (120 h), indicating that the reduced NiO/MgO catalyst had a high stability. In contrast to MgO, the other alkaline-earth oxides, such as CaO, SrO, and BaO, were found to be poor supports for NiO, as they provided catalysts with low

In Advances in CO2 Conversion and Utilization; Hu, Y.;
ACS Symposium Series; American Chemical Society: Washington, DC, 2010.

activities, selectivities, or stabilities (*38*). Furthermore, although the reduced NiO/Al_2O_3 catalyst provided high initial conversions (CH_4, 91%; CO_2, 98%) and selectivities (>95% for both CO and H_2), it suffered a rapid carbon deposition, resulting in the complete plugging of the reactor after 6 hours of reaction (*106a*). It is reasonable to conclude that the excellent catalytic performance of NiO/MgO should be attributed to the formation of a solid solution (*106*). The performance of NiO/MgO solid-solution catalysts is dependent on their composition, preparation conditions, and even the properties of the MgO (*105*, *106*). High and constant H_2 and CO yields (> 95%) occurred with NiO/MgO catalysts having NiO contents between 9.2 and 28.6 wt% (*106b*). No activity was observed, however, for a NiO content of 4.8 wt%. At the high NiO content of 50 wt%, the CO yield decreased from 91 to 53% after 40 h due to carbon deposition. This indicates that too small amounts of NiO in the NiO/MgO catalysts provided too-small numbers of Ni sites, and too-large amounts supplied numerous nickel metal particles that could easily sinter and generate large particles, which facilitated carbon deposition. Furthermore, the MgO surface area, pore size distribution, and lattice parameters exhibited significant effects on the performance of NiO/MgO solid-solution catalysts (*106c*).

It was reported that the addition of a noble metal could promote both the activity and the stability of NiO/MgO solid solution catalysts (*107e*). The resistance of the $Ni_{0.03}Mg_{0.97}O$ solid-solution catalyst to carbon deposition was retained by the bimetallic catalysts (*107e*). The improved stability of the catalyst was attributed to the increased catalyst reducibility caused by noble metal promotion. Furthermore, the water treatment of the $Ni_{0.03}Mg_{0.97}O$ solid-solution catalyst increased the catalytic activity and stability for CO_2 reforming of CH_4 (*107g*). This promoting effect was inferred to be the consequence of a structural rearrangement of the solid solution by the formation of nickel and magnesium hydroxides (*107g*). Very recently, Liu and Ge *et al.* revealed the effect of water on CO_2 adsorption on γ-Al_2O_3 by using Density Functional Theory (DFT) calculations (*114*). Their interesting results would be useful for ones to explain the effect of water on CO_2 reforming of methane.

The catalytic performance of NiO/MgO solid solution catalysts for CO_2 reforming of methane is also affected by reactor type (*112*). It was found that the methane and CO_2 conversion in the fluidized bed reactor was higher than those in the fixed bed reactor over $Ni_{0.15}Mg_{0.85}O$ catalyst at a pressure of 1.0 MPa. It was suggested that the promoting effect of catalyst fluidization on the activity is related to the catalyst reducibility. The oxidized and deactivated catalyst can be reduced with the produced syngas and the reforming activity can be regenerated in the fluidized bed reactor during the catalyst fluidization.

CoO/MgO solid solution catalysts exhibited similar catalytic performance to those of NiO/MgO (*108*, *113*). However, activities of CoO/MgO solid-solution catalysts for CO_2 reforming of methane are lower than those of NiO/MgO solid solution catalysts (*105*, *108*, *113*).

It is worth noting that the high stability of NiO/MgO solid solution catalyst for CO_2 reforming of methane at the atmospheric pressure was not maintained in the initial period of the reaction at a high pressure of 1.5MPa (Fig. 5) (*109a*). However, after the initial period, the catalyst got stabilized again at the high

Downloaded by STANFORD UNIV GREEN LIBR on June 23, 2012 | http://pubs.acs.org
Publication Date (Web): December 3, 2010 | doi: 10.1021/bk-2010-1056.ch010

Downloaded by STANFORD UNIV GREEN LIBR on June 23, 2012 | http://pubs.acs.org
Publication Date (Web): December 3, 2010 | doi: 10.1021/bk-2010-1056.ch010

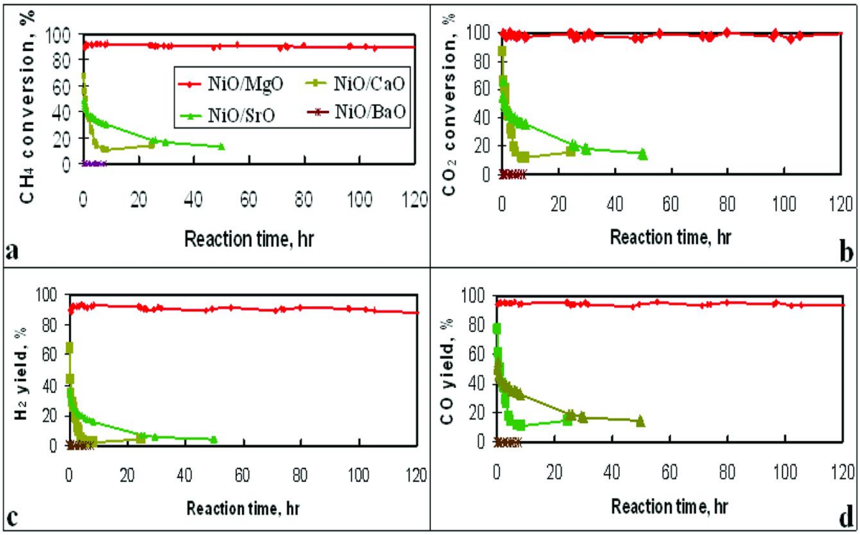

Figure 4. CH_4 conversion (a), CO_2 conversion (b), H_2 yield (c), and CO yield (d) in the CO_2 reforming of CH_4 catalyzed by reduced 20wt% NiO/alkaline earth metal oxides. Before reaction, each catalyst was reduced in flowing H_2 at 773 K for 14 h. Reaction conditions: Pressure=1 atm, T=1063 K, CH_4/CO_2 = 1/1, GHSV= 60,000 ml (g of catalyst)$^{-1}$ h^{-1} (38). Reproduced with permission from (38). Copyright 1995, Elsevier.

pressure (Fig.5b). It was found that the amount of carbon deposits first increased with the reaction time at the high-pressure reaction and then remained unchanged. This indicates that the decrease in stability of the catalyst in the initial period is due to the carbon deposition. The carbon deposition did not continue after 12 h, leading to the re-stabilization of the catalyst. The re-stabilization was explained as the presence of two types of active sites for the reaction at the high pressure, namely, when the sites responsible for the carbon deposition become blocked, the formation of carbon deposits would stop to increase with the reaction time. Then, the other type of the metallic sites would function to give a stable activity for the reaction. The carbon deposition on NiO/MgO catalysts at high pressures can also be inhibited by fluidizing catalysts in the presence of O_2 (*115*). This happened because the deposited carbon was formed on the catalyst in oxygen-free reforming zone, and it was gasified in oxygen-rich zone by catalyst fluidization.

As shown above, the difficult reduction of NiO (or CoO) in NiO-MgO (or CoO-MgO) solid solution contributes to its excellent performance for CO_2 reforming of methane. However, it is unknown why the formation of solid solution creates a difficulty for the reduction of NiO (or CoO). Very recently, we proposed that the difficult reduction of NiO (or CoO) in NiO-MgO(or CoO-MgO) could be due to isolation effect (*116*), which is briefly described as follows:

Downloaded by STANFORD UNIV GREEN LIBR on June 23, 2012 | http://pubs.acs.org
Publication Date (Web): December 3, 2010 | doi: 10.1021/bk-2010-1056.ch010

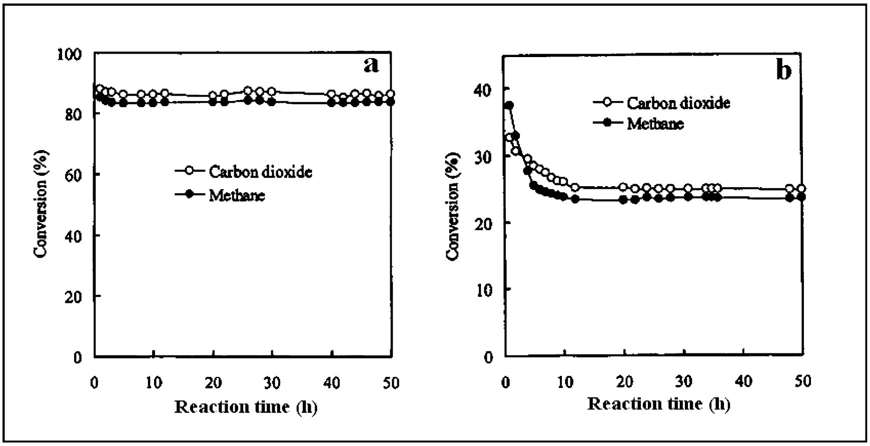

Figure 5. CH_4 and CO_2 Conversions versus reaction time over 8.8wt%NiO/MgO catalyst at (a)atmospheric pressure and (b)high pressure of 1.5MPa . Reaction condition: T=1123K, $CH_4/CO_2=1$, GHSV=16,000 ml (g of catalyst)$^{-1}$ h^{-1} (109a). Reproduced with permission from (109a). Copyright 2005, Springer.

The reduction process of metal oxide (MO) can be expressed as:

$$MO + H_2 = M + H_2O \tag{6}$$

It is generally accepted that the reduction of a metal oxide was controlled by the strength of M-O bond: the stronger the M-O bond, the more difficult the reduction is. However, as shown in Table 1, one can see that the M-O bond strength of PtO is the largest among 5 metal oxides, but its reduction takes place at the lowest temperature. Although MgO occupies the second lowest M-O bond strength, it cannot be reduced even at a very high temperature. This indicates that the reduction of a metal oxide is not simply controlled by the strength of M-O bond. Actually, the energy change in the reduction of a metal oxide includes the break of the M-O bond (of metal oxide) and the H-H bond (of H_2) and the formation of the M-M (of solid metal) and the H-O bond (of H_2O). Because the break of the H-H bond and the formation of the H-O bond are the same for the reduction of all metal oxides, the difference in the reduction of various metal oxides is essentially dependent on the strengths of M-M and M-O bonds. The energy is required to break M-O bond of metal oxide, and the formation of the M-M bond of solid-metal product releases energy. It is reasonable to expect that the reduction should be proportional to the energy difference between M-O and M-M bonds instead of only the strength of M-O bond. Indeed, as shown in Table 1, the reduction temperature of metal oxides increases with the strength difference between M-O and M-M bonds. The bond strength of Mg-O (363kJ/mol) is slightly lower than those of Ni-O (382kJ/mol) and Co-O (384kJ/mol), but the strength of Mg-Mg bond is only 9kJ/mol, which is much lower than those of Ni-Ni (200kJ/mol) and Co-Co (167kJ/mol), indicating that no reduction of MgO is mainly due to its too-low Mg-Mg bond strength. In other words, Ni-Ni (or Co-Co) bond formation plays a critical role in the reduction of NiO (or CoO),

In Advances in CO2 Conversion and Utilization; Hu, Y.;
ACS Symposium Series; American Chemical Society: Washington, DC, 2010.

Table 1. Reduction temperatures of metal oxides and bond energies of metal oxides and metals (*116*)

Reduction	***T* *(°C)***	***$E_{M\text{-}O}$* *(kJ/mol)***	***$E_{M\text{-}M}$* *(kJ/mol)***	***ΔE* *(kJ/mol)*[a]**
PtO→Pt	-23	395	307	88
CuO→Cu	227	269	176	93
NiO→Ni	327	382	200	182
CoO→Co	377	384	167	217
MgO→Mg	No reduction	363	9	354

[a] Strength difference between M-O and M-M bonds, i.e., $\Delta E = E_{M-O} - E_{M-M}$.

namely, the reduction of NiO (or CoO) cannot take place without the formation of Ni-Ni (or Co-Co) bonds. This was confirmed by Gibbs free energy changes (*116*). This principle allows ones to explain why the formation of NiO-MgO solid solution creates a difficulty for the reduction of NiO as follows (*116*). In the NiO-MgO solid solution, there are two possible types of NiO species: (1) NiO surrounded by MgO and (2) NiO surrounded by NiO. The first type of NiO cannot be reduced, because NiO is isolated by MgO, leading to impossibility to form Ni-Ni bond during removing O atom by hydrogen. In contrast, the reduction of the second type of NiO can take place, because the NiO is not isolated by MgO and therefore Ni-Ni bond can be formed during removing O by hydrogen. When NiO content is too low in NiO-MgO solid solution, NiO is mainly the first type that the NiO is surrounded by MgO. As a result, the NiO cannot be reduced. This is consistent with the experimental result that the 4.8wt% NiO/MgO solid solution catalyst had a negligible activity for CO_2 reforming of methane, even after it was reduced by H_2 at a high temperature (*106b*). In contrast, if NiO content is high, it has a high chance to form the second type that NiO is surrounded by NiO. Therefore, a large amount of NiO can be reduced to generate large Ni particles, which can cause carbon deposition. This would be the reason why the NiO/MgO solid solution catalyst with a high content of NiO had a low stability (*106b*). If the NiO content is neither too low nor too high in the solid solution, most of NiO should be the first type (NiO isolated by MgO) and the small part of NiO constitutes the second type (NiO surrounded by NiO), leading to the reduction of small amount of NiO to generate very small particles, which contribute to the inhibition of carbon deposition. As a result, such a NiO-MgO solid solution with a suitable NiO content had an excellent stability with a high activity (*106b*). Similarly, the isolation effect of solid solution can also be employed to explain the excellent catalytic performance of CoO/MgO solid solution catalysts for CO_2 reforming of methane.

3.5. Plasma Treatments

Recently, Liu's group developed an effective approach, "plasma treatment", to modify catalysts for the CO_2 reforming of methane (*41*, *42*). Ni/Al_2O_3 catalyst was first treated by argon glow discharge plasma followed by calcination in air (*41*).

Downloaded by STANFORD UNIV GREEN LIBR on June 23, 2012 | http://pubs.acs.org
Publication Date (Web): December 3, 2010 | doi: 10.1021/bk-2010-1056.ch010

The obtained catalyst exhibited an improved low-temperature activity for carbon dioxide reforming of methane, compared to the catalyst prepared without plasma treatment. This occurred because the plasma treatment followed by calcination thermally induced the generation of specific nickel species on the support. This kind of "plasma" metal species is highly dispersed on the support and can remain stable during the CO_2 reforming. The plasma treatment can also enhance the anti-carbon deposition performance of the catalyst. As a result, the formation of carbon species, which is responsible for catalyst deactivation, can be inhibited, leading to a higher stability of the catalyst. This occurred because the "plasma" metal species contain high concentration of close packed plane, resulting in the improved Ni dispersion and enhanced Ni-alumina interaction, which contribute to its high catalytic activity and excellent resistance to formations of filamentous carbon and encapsulating carbon (*42*). Similar to Ni/Al_2O_3 catalysts, Ni/SiO_2 catalyst can also be improved by plasma treatment (*117*).

The effect of plasma treatment on noble metal catalysts for CO_2 reforming was also evaluated by Liu's group (*118*, *119*). They found that argon glow discharge plasma can effectively reduce H_2IrCl_6/Al_2O_3 catalyst into Ir/Al_2O_3 without the use of any conventional reducing chemicals. Such plasma-reduced Ir/Al_2O_3 catalyst showed a significantly enhanced dispersion, leading to a high conversions of methane and CO_2 in the CO_2 reforming of methane (*118*). An argon glow discharge plasma was also exploited to reduce $RhCl_3$ impregnated Al_2O_3 powder at room temperature (*119*). The characterizations of XRD and EDX showed that Rh ions were reduced into metallic Rh during the plasma treatment. Furthermore, TEM analysis revealed that the argon plasma reduction induced a high dispersion of Rh nano-particles with average size of 1.2 nm. Such plasma-reduced Rh/Al_2O_3 exhibited comparable activity to a conventional hydrogen-reduced catalyst for the CO_2 reforming of methane (*119*). This indicates that the regular pre-reduction by H_2 is not necessary for plasma-treated Rh/Al_2O_3 catalysts for the CO_2 reforming of methane.

Downloaded by STANFORD UNIV GREEN LIBR on June 23, 2012 | http://pubs.acs.org
Publication Date (Web): December 3, 2010 | doi: 10.1021/bk-2010-1056.ch010

4. Conclusions

CO_2 reforming of methane is an attractive technology because it converts two greenhouse gases into useful chemicals. Both noble and non-noble metals have excellent activity and selectivity for the CO_2 reforming of methane. However, the deactivation of the catalyst, caused by carbon deposition, constitutes a greatest challenge for non-noble metal catalysts. Although noble metal catalysts are less subjected to carbon deposition, nickel-containing catalysts have attracted the most research interest, in part because of the relatively low cost of nickel. In the past 20 years, several approaches have been developed to enhance resistance of non-noble metal catalysts (particularly Ni-based catalysts), resulting in several types of effective nickel-containing catalysts with high activities and stabilities.

References

1. Lal, R. *Philos. Trans. R. Soc. B* **2008**, *363*, 815.

In Advances in CO2 Conversion and Utilization; Hu, Y.;
ACS Symposium Series; American Chemical Society: Washington, DC, 2010.

2. Auerbach, D. I.; Caulfield, J. A.; Adams, E. E.; Herzog, H. J. *Environ. Model. Assess.* **1997**, *2*, 333.
3. Kintisch, E. *Science* **2007**, *315*, 1481.
4. Tomasko, D. L.; Li, H.; Liu, D.; Han, X.; Wingert, M. J.; Lee, L. J.; Koelling, K. W. *Ind. Eng. Chem. Res.* **2003**, *42*, 6431.
5. Kendall, J. L.; Canelas, D. A.; Young, J. L.; DeSimone, J. M. *Chem. Rev.* **1999**, *99*, 543.
6. Hyatt, J. A. *J. Org. Chem.* **1984**, *49*, 5097.
7. (a) Tomasko, L.; Li, H.; Liu, D.; Han, X.; Wingert, M. J.; Lee, L. J.; Koelling, K. W. *Ind. Eng. Chem. Res.* **2003**, *42*, 6431. (b) Shieh, Y. T.; Lin, Y. G. *Polymer* **2002**, *43*, 1849.
8. Tuminello, W. H.; Dee, G. T.; McHugh, M. A. *Macromolecules* **1995**, *28*, 1506.
9. Shah, V. M.; Hardy, B. J.; Stern, S. A. *J. Polym. Sci., Part B: Polym. Phys.* **1993**, *31*, 313.
10. Kendall, J. L.; Canelas, D. A.; Young, J. L.; DeSimone, J. M. *Chem. Rev.* **1999**, *99*, 543.
11. Fan, X.; Potluri, V. K.; McLeod, M. C.; Wang, Y.; Liu, J.; Enick, R. M.; Hamilton, A. D.; Roberts, C. B.; Johnson, J. K.; Beckman, E. J. *J. Am. Chem. Soc.* **2005**, *127*, 11754.
12. Kilic, S.; Michalik, S.; Wang, Y.; Johnson, J. K.; Enick, R. M.; Beckman, E. *Macromolecules* **2007**, *40*, 1332.
13. Ricci, M. In *Recovery and utilization of carbon dioxide*; Aresta, M., Ed.; Kluwer Academic Publishers, Amsterdam, The Netherlands, 2003; p 395.
14. Gadalla, A. M.; Bower, B. *Chem. Eng. Sci.* **1988**, *43*, 3049.
15. Dyrssen, D.; Turner, D. R. In *Carbon Dioxide Chemistry: Environmental Issues*; Paul, J., Pradier, C. M., Eds.; Athenaeum Press: Cambridge, 1994; p 317.
16. Fraenkel, D.; Levitan, R.; Levy, M. *Int. J. Hydrogen Energy* **1986**, *11*, 267.
17. Edward, J. H.; Maitra, A. M. *Fuel Process. Technol.* **1995**, *42*, 269.
18. Reitmeier, R. E.; Atwood, K.; Bennet, H. A., Jr.; Baugh, H. M. *Ind. Eng. Chem.* **1948**, *40*, 620.
19. White, G. A.; Roszkowski, T. R.; Stanbridge, D. W. *Hydrocarbon Process.* **1975**, *54*, 130.
20. Hu, Y. H.; Ruckenstein, E. *Adv. Catal.* **2004**, *48*, 298.
21. Bradford, M. C. J.; Vannice, M. A. *Catal. Rev.* **1999**, *41*, 1.
22. (a) Solymosi, F.; Kutsan, G.; Erdohelyi, A. *Catal. Lett.* **1991**, *11*, 149. (b) Ashcroft, A. T.; Cheetham, A. K.; Green, M. L. H.; Vernon, P. D. F. *Nature* **1991**, *352*, 225. (c) Vernon, P. D. F.;Green, M. L. H.; Cheetham, A. K.; Ashcroft, A. T. *Catal. Today* **1992**, *13*, 417.
23. Rostrup-Nielsen, J. R.; Hansen, J. H. B. *J. Catal.* **1993**, *144*, 38.
24. Takayasu, O.; Hirose, E.; Matsuda, N.; Matsuura, I. *Chem. Express* **1991**, *6*, 447.
25. Rostrup-Nielsen, J. R.; Hansen, J. H. B. *J. Catal.* **1993**, *144*, 38.
26. Inui, T. *Catalysis*; The Royal Society of Chemistry: 2002, Vol. 16, p133.
27. Perera, J. S. H.; Couves, J. W.; Sankar, G.; Thomas, J. M. *Catal. Lett.* **1991**, *11*, 219.

Downloaded by STANFORD UNIV GREEN LIBR on June 23, 2012 | http://pubs.acs.org
Publication Date (Web): December 3, 2010 | doi: 10.1021/bk-2010-1056.ch010

28. Qin, D.; Lapszewicz, J. *Catal. Today* **1994**, *21*, 551.
29. Solymosi, F.; Kustan, Gy.; Erohelyi, A. *Catal. Lett.* **1991**, *11*, 149.
30. Erdohelyi, A.; Fodor, K.; Solymosi, F. *Stud. Surf. Sci. Catal.* **1997**, *107*, 525.
31. Schouten, S. C.; Gijzeman, O. L. J.; Bootsma, G. A. *Bull. Soc. Chim. Belg.* **1979**, *88*, 541.
32. Bartholomew, C. H. *Catal. Rev. - Sci. Eng.* **1982**, *24*, 67.
33. Eizenberg, M.; Blakely, J. M. *Surf. Sci.* **1979**, *82*, 228.
34. Rostrup-Nielsen, J. R. *Stud. Surf. Sci. Catal.* **1991**, *68*, 85.
35. Udengaar, N. R.; Hansen, J.-H. B.; Hanson, D. C.; Stal, J. A. *Oil Gas J.* **1992**, *90*, 62.
36. Dibbern, H. C.; Olesen, P.; Rostrup-Nielsen, J. R.; Totrrup, P. B.; Udengaard, N. R. *Hydrocarbon Process.* **1986**, *65*, 71.
37. Hu, Y. H.; Ruckenstein, E. *Catal. Rev.* **2002**, *44*, 423.
38. Ruckenstein, E.; Hu, Y. H. *Appl. Catal. A* **1995**, *133*, 149.
39. Hu, Y. H.; Ruckenstein, E. *J. Catal.* **1999**, *184*, 298.
40. Hu, Y. H.; Ruckenstein, E. *Langmuir* **1997**, *13*, 2055.
41. Cheng, D. G.; Zhu, X. L.; Ben, Y. H.; He, F.; Cui, L.; Liu, C. J. *Catal. Today* **2006**, *115*, 205.
42. Zhu, X. L.; Huo, P. P.; Zhang, Y. P.; Cheng, D. G.; Liu, C. J. *Appl. Catal. B* **2008**, *81*, 132.
43. (a)Yamazaki, O.; Nozaki, T.; Omata, K.; Fujimoto, K. *Chem. Lett.* **1992**, 1953. (b) Zhang, Z. L.; Verykios, X. E. *Catal. Today* **1994**, *21*, 589.
44. Horiuchi, T.; Sakuma, K.; Fukui, T.; Kubo, Y.; Osaki, T.; Mori, T. *Appl. Catal., A* **1996**, *144*, 111.
45. Kim, G. J.; Cho, D.-S.; Kim, K.-H.; Kim, J.-H. *Catal. Lett.* **1994**, *28*, 41.
46. Tsipouriari, V. A.; Zhang, Z.; Verykios, X. E. *J. Catal.* **1998**, *179*, 283.
47. Kim, J. H.; Suh, D. J.; Park, T. J.; Kim, K. L. *Appl. Catal., A* **2000**, *197*, 191.
48. Bhattacharyya, A.; Chang, V. W. *Stud. Surf. Sci. Catal.* **1994**, *88*, 207.
49. Halliche, D.; Bouarab, R.; Cherifi, O.; Bettahar, M. M. *Catal. Today* **1996**, *29*, 373.
50. (a) Ruckenstein, E.; Hu, Y. H. *J. Catal.* **1996**, *162*, 230. (b) Hu, Y. H.; Ruckenstein, E. *J. Phys. Chem. B* **1999**, *101*, 7563.
51. Wang, S.; Lu, G. O. M. *Appl. Catal., B* **1998**, *16*, 269.
52. Yan, Z.-F.; Ding, R.-G.; Song, L.-H.; Qian, L. *Energy Fuels* **1998**, *12*, 1114.
53. Wang, S.; Lu, G. Q. *Appl. Catal., A* **1998**, *169*, 271.
54. Wang, S.; Lu, G. Q. *Ind. Eng. Chem. Res.* **1999**, *38*, 2615.
55. Ito, M.; Tagawa, T.; Goto, S. *Appl. Catal., A* **1999**, *177*, 15.
56. Xu, Z.; Li, Y. M.; Zhang, J. Y.; Chang, L.; Zhou, R. Q.; Duan, Z. T. *Appl. Catal., A* **2001**, *210*, 45.
57. Wang, S. B.; Lu, G. Q. *Energy Fuels* **1998**, *12*, 1235.
58. Perera, J. S. H.; Couves, J. W.; Sankar, G.; Thomas, J. M. *Catal. Lett.* **1991**, *11*, 219.
59. Chen, Y. G.; Ren, J. *Catal. Lett.* **1994**, *29*, 39.
60. Sridhar, S.; Sichen, D.; Seetharaman, S. *Z. Metallkd.* **1994**, *85*, 9.
61. Kim, J. H.; Suh, D. J.; Park, T. J.; Kim, K . L. Natural Gas Conversion V. *Stud. Surf. Sci. Catal.* **1998**, *119*, 771.

Downloaded by STANFORD UNIV GREEN LIBR on June 23, 2012 | http://pubs.acs.org
Publication Date (Web): December 3, 2010 | doi: 10.1021/bk-2010-1056.ch010

62. Osaki, T.; Horiuchi, T.; Sugiyama, T.; Suzuki, K.; Mori, T. *Catal. Lett.* **1998**, *52*, 171.
63. Hayashi, H.; Murata, S.; Tago, T.; Kishida, M.; Wakabayashi, K. *Sekiyu Gakkaishi-J. Jpn. Pet. Inst.* **2001**, *44*, 334.
64. Kroll, V. C. H.; Swaan, H. M.; Mirodatos, C. *J. Catal.* **1996**, *161*, 409.
65. Kroll, V. C. H.; Delichure, P.; Mirodatos, C. *Kinet. Catal.* **1996**, *37*, 698.
66. Zhang, Z. L.; Verykios, X. E. *J. Chem. Soc., Chem. Commun.* **1995**, 71.
67. Zhang, Z.; Verykios, X. E. *Appl. Catal., A* **1996**, *138*, 109.
68. Liu, B. S.; Au, C. T. *Catal. Lett.* **2003**, *85*, 165.
69. Hally, W.; Bitter, J. H.; Seshan, K.; Lercher, J. A.; Ross, J. R. H. Catalyst Deactivation 1994. *Stud. Surf. Sci. Catal.* **1994**, *88*, 167.
70. Li, X. S.; Chang, J. S.; Lee, F. K.; Park, S. E. *React. Kinet. Catal. Lett.* **1999**, *67*, 383.
71. Li, X. S.; Chang, J. S.; Park, S. E. *React. Kinet. Catal. Lett.* **1999**, *67*, 375.
72. Lercher, J. A.; Bitter, J. H.; Hally, W.; Niessen, W.; Seshan, K. In *Proceedings of the 11th International Congress on Catalysis*; Studies in Surface Science and Catalysis; Hightower, J. W., Delgass, W. N., Iglesia, E., Bell, A. T., Eds.; Elsevier: Amsterdam, 1996; Vol. 101, p 463.
73. Wei, J. M.; Xu, B. Q.; Li, J. L.; Cheng, Z. X.; Zhu, Q. M. *Appl. Catal., A* **2000**, *196*, L167.
74. Bitter, J. H.; Hally, W.; Seshan, K.; van Ommen, J. G.; Lercher, J. A. *Catal. Today* **1996**, *29*, 349.
75. Bitter, J. H.; Seshan, K.; Lercher, J. A. *J. Catal.* **1998**, *176*, 93.
76. O'Connor, A. M.; Ross, J. R. H. *Catal. Today* **1998**, *46*, 203.
77. Bitter, J. H.; Seshan, K.; Lercher, J. A. *J. Catal.* **1999**, *183*, 336.
78. Souza, M. M. V. M.; Aranda, D. A. G.; Schmal, M. *Ind. Eng. Chem. Res.* **2002**, *41*, 4681.
79. Chen, Y. Z.; Liaw, B. J.; Lai, W. H. *Appl. Catal., A* **2002**, *230*, 73.
80. Wang, H. Y.; Ruckenstein, E. *Appl. Catal., A* **2000**, *204*, 143.
81. Hayakawa, T.; Suzuki, S.; Nakamura, J.; Uchijima, T.; Hamakawa, S.; Suzuki, K.; Shishido, T.; Takehira, K. *Appl. Catal., A* **1999**, *183*, 273.
82. Chang, J. S.; Park, S. E.; Lee, K. W. *Stud. Surf. Sci. Catal.* **1994**, *84*, 1587.
83. Park, S. E.; Nam, S. S.; Choi, M. J.; Lee, K. W. *Energy Convers. Manage.* **1995**, *36*, 573.
84. Luo, J. Z.; Gao, L. Z.; Ng, C. F.; Au, C. T. *Catal. Lett.* **1999**, *62*, 153.
85. Chang, J. S.; Park, S.-E.; Chon, H. *Appl. Catal., A* **1996**, *145*, 111.
86. Choudhary, V. R.; Uphade, B. S.; Mamman, A. S. *Microporous Mesoporous Mater.* **1998**, *23*, 61.
87. Liu, D. P.; Lau, R.; Borgna, A.; Yang, Y. H. *Appl. Catal. A* **2009**, *358*, 110.
88. Qu, Y.; Sutherland, A. M.; Guo, T. *Energy Fuels* **2008**, *22*, 2183.
89. Mori, T.; Osaki, T.; Horiuchi, T.; Sugiyama, T.; Suzuki, K. Catalyst Deactivation 1999. *Stud. Surf. Sci. Catal.* **1999**, *126*, 365.
90. Lemonidou, A. A.; Goula, M. A.; Vasalos, I. A. *Catal. Today* **1998**, *46*, 175.
91. Osaki, T.; Mori, T. *J. Catal.* **2001**, *204*, 89.
92. Wang, S. B.; Lu, G. Q. M. *J. Chem. Technol. Biotechnol.* **2000**, *75*, 589.
93. Choi, J. S.; Moon, K. I.; Kim, Y. G.; Lee, J. S.; Kim, C. H.; Trimm, D. L. *Catal. Lett.* **1998**, *52*, 43.

Downloaded by STANFORD UNIV GREEN LIBR on June 23, 2012 | http://pubs.acs.org
Publication Date (Web): December 3, 2010 | doi: 10.1021/bk-2010-1056.ch010

94. Seok, S. H.; Han, S. H.; Lee, J. S. *Appl. Catal., A* **2001**, *215*, 31.
95. Quincoces, C. E.; de Vargas, S. P.; Grange, P.; Gonzalez, M. G. *Mater. Lett.* **2002**, *56*, 698.
96. Crisafulli, C.; Scire, S.; Maggiore, R.; Minico, S.; Galvagno, S. *Catal. Lett.* **1999**, *59*, 21.
97. Damyanova, S.; Pawelec, B.; Arishtirova, K.; Fierro, J. L. G.; Sener, C.; Dogu, T. *Appl. Catal. B* **2009**, *92*, 250.
98. Slagtern, A.; Olsbye, U.; Blom, R.; Dahl, I. M.; Fjellvag, H. *Appl. Catal., A* **1997**, *165*, 379.
99. Li, W. Y.; Feng, J.; Xie, K. C. *React. Kinet. Catal. Lett.* **1998**, *64*, 381.
100. Wang, S. B.; Lu, G. Q. *Appl. Catal., B* **1998**, *19*, 267.
101. Xu, G. L.; Shi, K. Y.; Gao, Y.; Xu, H. Y.; Wei, Y. D. *J. Mol. Catal. A: Chem.* **1999**, *147*, 47.
102. Stagg, S. M.; Resaco, D. E. *Stud. Surf. Sci. Catal.* **1997**, *111*, 543.
103. Sigl, M.; Bradford, M. C. J.; Knözinger, H.; Vannice, M. A. *Top. Catal.* **1999**, *8*, 211.
104. Stagg-Williams, S. M.; Noronha, F. B.; Fendley, G.; Resasco, D. E. *J. Catal.* **2000**, *194*, 240.
105. (a) Hu, Y. H.; Ruckenstein, E. *J. Phys. Chem. B* **1999**, *101*, 7563 (b) Ruckenstein, E.; Hu, Y. H. *Catal. Lett.* **1998**, *51*, 183. (c) Hu, Y. H.; Ruckenstein, E. *Catal. Lett.* **1997**, *43*, 71.
106. (a) Ruckenstein, E.; Hu, Y. H. *J. Catal.* **1996**, *162*, 230. (b) Hu, Y. H.; Ruckenstein, E. *Catal. Lett.* **1996**, *36*, 145. (c) Ruckenstein, E.; Hu, Y. H. *Appl. Catal. A* **1997**, *154*, 185. (d) Hu, Y. H.; Ruckenstein, E. *J. Catal.* **1996**, *163*, 306.
107. (a) Tomishige, K.; Himeno, Y., Matsuo, Y., Yoshinaga, Y.; Fujimoto, K. *Ind. Eng. Chem. Res.* **2000**, *39*, 1891. (b) Chen, Y. G.; Tomishige, K.; Yokoyama, K.; Fujimoto, K. *J. Catal.* **1999**, *184*, 479. (c) Tomishige, K.; Yamazaki, O.; Chen, Y.; Yokoyama, K.; Li, X.; Fujimoto, K. *Catal. Today* **1998**, *45*, 35. (d) Chen, Y.; Tomishige, K.; Fujimoto, K. *Chem. Lett.* **1997**, 999. (e) Chen, Y.; Tomishige, K.; Yokoyama, K.; Fujimoto, K. *Appl. Catal. A* **1997**, *165*, 335. (f) Chen, Y. G.; Tomishige, K.; Fujimoto, K. *Appl. Catal. A* **1997**, *161*, L11. (g) Yamazaki, O.; Nozaki, T.; Omata, K.; Fujimoto, K. *Chem. Lett.* **1992**, 1953.
108. (a) Ruckenstein, E.; Wang, H. Y. *J. Catal.* **2002**, *205*, 289. (b) Ruckenstein, E.; Wang, H. Y. *Catal. Lett.* **2001**, *73*, 99. (c) Ruckenstein, E.; Wang, H. Y. *Appl. Catal. A* **2000**, *204*, 257.
109. (a) Wang, Y. H.; Xu, B. Q. *Catal. Lett.* **2005**, *99*, 89. (b) Wang, Y. H.; Liu, H. M.; Xu; B. Q. *J. Mol. Catal. A* **2009**, *299*, 44.
110. Djaidja, A.; Libs, S.; Kiennemann, A.; Barama, A. *Catal. Today* **2006**, *113*, 194.
111. Song, C. S.; Wei, P. *Catal. Today* **2004**, *98*, 463.
112. Tomishige, K. *Catal. Today* **2004**, *89*, 405.
113. (a) Choudhary, V. R.; Mamman, A. S. *Appl. Energy* **2000**, *66*, 161. (b) Choudhary, V. R.; Mamman, A. S. *J. Chem. Technol. Biotechnol.* **1998**, *73*, 345. (c) Mondal, K. C.; Choudhary, V. R.; Joshi, U. A. *Appl. Catal., A* **2007**, *316*, 47.

Downloaded by STANFORD UNIV GREEN LIBR on June 23, 2012 | http://pubs.acs.org
Publication Date (Web): December 3, 2010 | doi: 10.1021/bk-2010-1056.ch010

114. Pan, Y.; Liu, C. J.; Ge, Q. *Langmuir* **2008**, *24*, 12410.
115. Tomishige, K.; Matsuo, Y.; Yoshinaga, Y.; Sekine, Y.; Asadullah, M.; Fujimoto, K. *Appl. Catal., A* **2002**, *223*, 225.
116. Hu, Y. H. *Catal. Today* **2009**, *148*, 206.
117. Shi, P.; Liu, C. J. *Catal. Lett.* **2009**, *133*, 112.
118. Zhao, Y.; Pan, Y. X.; Xie, Y. B.; Liu, C. J. *Catal. Commun.* **2008**, *9*, 1558.
119. Wang, Z. J.; Zhao, Y.; Cui, L.; Du, H.; Yao, P.; Liu, C. J. *Green Chem.* **2007**, *9*, 554.

Downloaded by STANFORD UNIV GREEN LIBR on June 23, 2012 | http://pubs.acs.org
Publication Date (Web): December 3, 2010 | doi: 10.1021/bk-2010-1056.ch010

Downloaded by OHIO STATE UNIV LIBRARIES on June 23, 2012 | http://pubs.acs.org
Publication Date (Web): December 3, 2010 | doi: 10.1021/bk-2010-1056.ch011

Chapter 11

Development of Coke Resistant Ni Catalysts for CO_2 Reforming of Methane via Glow Discharge Plasma Treatment

**Chang-jun Liu,[1],* Peng Shi,[1] Jiaojun Jiang,[1] Pingyu Kuai,[1] Xinli Zhu,[1]
Yunxiang Pan,[1] and Yueping Zhang[2]**

**[1]Key Laboratory for Green Chemical Technology of Ministry of Education,
School of Chemical Engineering, Tianjin University, Tianjin 300072, China
[2]Department of Chemistry, Tianjin University, Tianjin 300072, China
*ughg_cjl@yahoo.com**

We have previously reported a novel preparation of Ni catalysts for CO_2 reforming of methane using glow discharge plasma treatment. Smaller particle size and flat metal-support interface obtained lead to a significantly enhanced coke resistant property with a significantly improved activity. However, the mechanism for how the plasma treatment enhances the coke resistance is still unclear. In this work, we attempt to summarize the present understanding regarding the mechanism. From the infred image, the plasma treatment is operated at room temperature. The thermal effect can be ignored. The energetic electron in the plasmas is the controlling influence factor on the catalyst treatment. It was observed the plasma treatment improves the hydrophilic property of the support. And, the negative charge of the supporting materials under the influence of plasmas changes the reactivity of the surface and the interaction between the nickel and the support. All these changes induce the formation of nano particles with samller size, narrow size distribution and flat morphology, which significantly enhance the coke resistant property of the catalyst.

In Advances in CO2 Conversion and Utilization; Hu, Y.;
ACS Symposium Series; American Chemical Society: Washington, DC, 2010.

Downloaded by OHIO STATE UNIV LIBRARIES on June 23, 2012 | http://pubs.acs.org
Publication Date (Web): December 3, 2010 | doi: 10.1021/bk-2010-1056.ch011

Introduction

CO_2 reforming of methane has attracted a great attention recently (*1*–*8*). One of the reasons for it is that this reaction has a potential to be used for utilization of carbon dioxide in a large scale. It can be used together with steam reforming that is be applied extensively for syngas or hydrogen production. It is also very potential to use it for the utilization of natural gas or biogas containing carbon dioxide. Supported Ni catalysts are the mostly investigated catalysts for the CO_2 reforming (*1*, *2*). However, the serious coke formation limits the further application of the nickel catalysts. Several ways have been exploited to improve the coke resistance, including the use of promoters and modification of the supporting materials (*4*). Recently, several groups demonstrated that the plasma treatment of nickel catalysts shows a significant improvement in the coke resistance (*5*, *8*). It has shown that the plasma treatment leads to a formation of smaller particle size and direct metal-support interface (*8*, *9*) that lead to an enhanced coke resistant property. It is very potential to develop a practical catalyst prepration using plasmas not only for CO_2 reforming but many others (*10*–*15*). However, the mechanism for how the plasma treatment enhances the coke resistance of Ni catalysts is still unclear. In this work, we attempt to summarize the present understanding of the glow discharge plasma treatment. A mechanism was proposed for further investigations.

Catalyst Preparation with the Glow Discharge Plasma Treatment

We have previously reported the procedures of the plasma treatment for the preparation of the supported Ni catalysts using glow discharges (*8*, *16*, *17*). The supported Ni catalysts was previously prepared by starting to use incipient wetness impregnation method. An aqueous solution of nickel nitrate was normally applied for the impregnation. After that, the obtained sample was treated by the plasma before further thermally calcination at elevated temperatures. No drying applied between the plasma treatment and calcination thermally. Exactly, the plasma treatment used here replace the drying. Compared to the conventional drying, the plasma treatment is rapid. The plasma treatment apparatus is shown in Figure 1. The sample was loaded in a quartz boat and placed in the ‘positive column’ region of the glow discharge. In this region, a plentiful of energetic electrons exists. When the pressure in the discharge tube was about 100 Pa, the glow discharge plasma was generated by applying around 900 V to the electrode using a high voltage amplifier. DC or low frequency AC was previously applied. Argon or air has been used as the plasma-forming gas. The discharge was initiated at room temperature without external heating or cooling. According to the infrared (IR) temperature measurements (Icron 100PHT), the heating effect of the glow discharge could be ignored and the temperature of the catalyst powder was close to room temperature. Figure 2 shows an image of the glow discharge during the plasma catalyst treatment. Specific striations have been observed. The striations normally show up after one to several minutes. We believe the striations hide some information of the formation of plasma crystal. Further investigation will be conducted.

Downloaded by OHIO STATE UNIV LIBRARIES on June 23, 2012 | http://pubs.acs.org
Publication Date (Web): December 3, 2010 | doi: 10.1021/bk-2010-1056.ch011

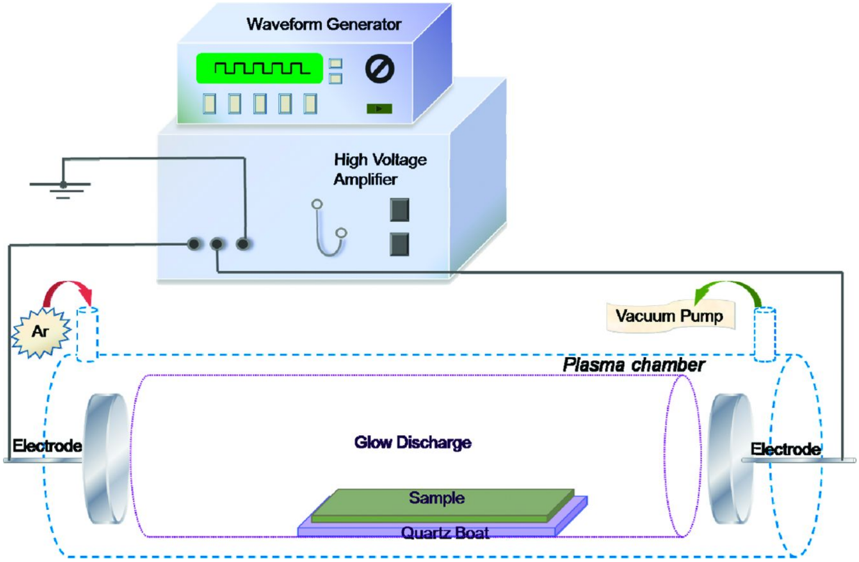

Figure 1. The schematical representative of glow discharge plasma treatment

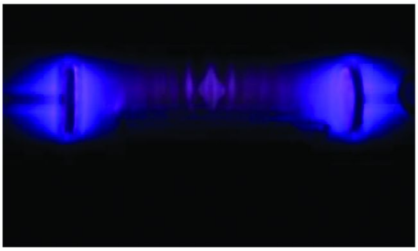

Figure 2. Image of the glow discharge during the plasma catalyst treatment

Figure 3 presents an infrared image to confirm the room temperature operation of the glow discharge plasma treatment. From the image, the highest temperature is 8.7 °C higher than the room temperature (20.2 °C). Obviously, the thermal effect can be ignored during the plasma catalyst treatment. Regarding the characteristics of the glow discharge, the effect of electrons within the glow discharge has the principal effect on the plasma catalyst treatment.

During the glow discharge plasma treatment, the electrons will attach to the powder samples and make the powder negatively charged. This will change the reactivity of the powder surfaces totally. The hydrophilic property of the powders has been also enhanced remarkably. Both changes should be responsible for the reduced size and flat morphology of nickel nano particles obtained from the glow discharge plasma treatment. We exactly observed the color change of impregnated nickel nitrate on the supports, as shown in Fugure 4. The color change shown in Figure 4 indicates chemical reactions during the glow discharge plasma treatment. However, the color of plasma treated sample will be changed back to the color before the plasma treatment when the plasma treated sample has been exposed to the air for about an hour. Partial decomposition of nickel nitrate

Downloaded by OHIO STATE UNIV LIBRARIES on June 23, 2012 | http://pubs.acs.org
Publication Date (Web): December 3, 2010 | doi: 10.1021/bk-2010-1056.ch011

hydrate was proposed during the glow discharge plasma treatment. Specific plasma nano crystal would be therefore generated. It is very necessary to explore the plasma reactions *in situ* or *on site*. However, it is still difficult to do so because of the non-equilibrium characteristics of the glow discharge. We are trying to use the thermal anaylyses to study it and will report the results in the future works.

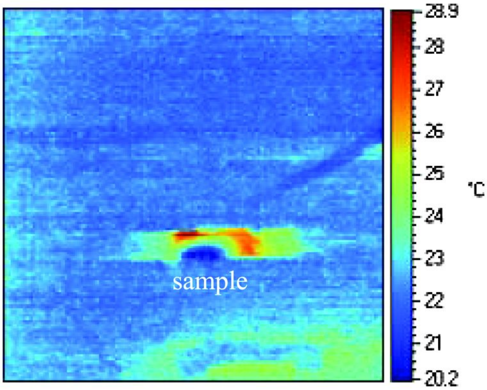

Figure 3. The IR image of the glow discharge plasma in the presence of Al_2O_3 powder impregnated by Ni nitrate

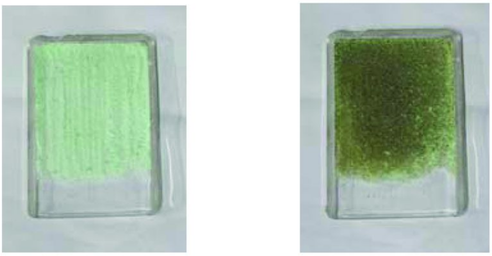

(a) before the plasma treatment (b) after the plasma treatment

Figure 4. Images of SiO_2 powder impregnated by nickel nitrate

Effect of the Supporting Material

We have tested Al_2O_3 and SiO_2 as the catalyst supports for the glow discharge plasma treatment. Both of them showed a significantly enhanced coke resistance after the plasma treatment (*8*, *16*, *17*). To further study the effect of the supporting materials, MgO and MCM-41 mesoporous material was also applied for the catalyst support. All the supports tested show the similar results for tests of CO_2 reforming and related methane decomposition. However, there are still a lot needs to be further investigated to understand clearly, esp., the functional groups and defect sites on the supporting materials. The difficulty, as mentioned above, is the lack of the *in situ* or *on site* characterization or diagnosis technologies. The podwer size has an obvious influence. We attempted to measure the charge

Downloaded by OHIO STATE UNIV LIBRARIES on June 23, 2012 | http://pubs.acs.org
Publication Date (Web): December 3, 2010 | doi: 10.1021/bk-2010-1056.ch011

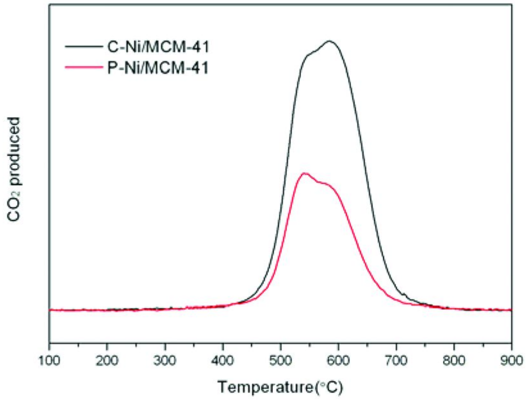

Figure 5. TPO curves of the used Ni/MCM-41 catalysts for one-hour methane decomposition at 750 °C

amount of the podwer under the plasmas by Faraday Cup test that was normally used for the electrostatic measurement. There is a big negative effect of the plasma (probably the electric-magnetic fields of the plasma) on the accuracy of the test.

We previously reported that the plasma treated nickel catalyst shows a lower rate of methane decomposition rate and also a lower carbon yield, compared to the catalyst prepared thermally (*18*). The lower methane decomposition rate is very helpful to a good balance between methane decomposition (to carbon and hydrogen) and the reaction of the formed carbon with carbon dioxide (to carbon monoxide) for carbon dioxide reforming of methane. By this way, the carbon accumulation can be inhibited and the reforming reaction can be sustained. We previously reported too that the carbon nanofiber growth pathway shifts from a mixture of tip and base growth for the non-plasma treated sample to base growth from the plasma treated sample. Very diiferent from the carbon nanofibers obtained over the non-plasma treated catalyst, the tips of about 80% carbon nanofibers obtained over the plasma treated sample are open (*18*). This suggests that the plasma treatment has a remarkable effect on the catalyst structure.

As an example of the effect of the supporting materials, Figure 5 shows the temperature programming oxidation (TPO) results of used Ni/MCM-41 catalysts for methane decomposition. The procedure for this TPO measurement is similar to that previously reported (*17*). The TPO results with the Ni/MCM-41 is also similar to the results obtained over Ni/SiO_2 (*17*). The plasma treated Ni catalyst (P-Ni/MCM-41) shows a much lower carbon formation compared to the catalyst prepared thermally (C-Ni/MCM-41). This plasma treated Ni/MCM-41 catalyst presents a good activity for CO_2 reforming too. We will report the details in our future works.

Conclusions

The catalyst preparation with the glow discharge plasma treatment has shown a great potential to solve the carbon deposition problem of Ni catalysts for

CO_2 reforming. The samller size, narrow size distribution and flat morphology obtained from the plasma treatment have been considered as the reasons for the significantly enhanced coke resistance property. The thermal effect can be ignored for the plasma treatment. The electronic effect is significant to the plasma catalyst treatment. However, the mechanism for the plasma treatment is still unclear. In order to put the plasma treatment technology for the practical uses, further investigations are being performed experimentally and theoretically and will be reported in our future works.

Downloaded by OHIO STATE UNIV LIBRARIES on June 23, 2012 | http://pubs.acs.org
Publication Date (Web): December 3, 2010 | doi: 10.1021/bk-2010-1056.ch011

Acknowledgments

The support from the National Natural Science Foundation of China (#20990223) and the instruments supplied by ABB Switzerland are greatly appreciated.

References

1. Hu, Y. H. *Catal. Today* **2009**, *148*, 206–211.
2. Centi, G.; Perathoner, S. *Catal. Today* **2009**, *148*, 191–205.
3. Pan, Y. X.; Liu, C. J.; Ge, Q. F. *Langmuir* **2008**, *24*, 12410–12419.
4. Hu, Y. H.; Ruckenstein, E. *Adv. Catal.* **2004**, *48*, 297–345.
5. Shang, S.; Liu, G.; Chai, X.; Tao, X.; Li, X.; Bai, M.; Chu, W.; Dai, X.; Zhao, Y.; Yin, Y. *Catal. Today* **2009**, *148*, 268–274.
6. Pan, W.; Song, C. *Catal. Today* **2009**, *148*, 232–242.
7. Wang, L. S.; Murata, K.; Inaba, M. *ACS Symp. Series* **2003**, *852*, 57–68.
8. Zhu, X. L.; Huo, P. P.; Zhang, Y. P.; Cheng, D. G.; Liu, C. J. *Appl. Catal. B* **2008**, *81*, 132–140.
9. Zou, J.-J.; Liu, C.-J.; Zhang, Y. P. *Langmuir* **2006**, *22*, 2334–2339.
10. Vissokov, G. P.; Pirgov, P. S. *Appl. Catal. A* **1998**, *168*, 229–233.
11. Lee, H. M.; Juan, L. K.; Yeh, F. M.; Li, H. Y.; Chen, H. L.; Chang, M. B.; Chen, S. H.; Tzeng, C. C. *IEEE Trans. Plasma Sci.* **2009**, *37*, 2213–2220.
12. Phillips, J.; Luhrs, C. C.; Richard, M. *IEEE Trans. Plasma Sci.* **2009**, *37*, 726–739.
13. Jang, B.; Helleson, M.; Shi, C.; Rondinone, A.; Schwartz, V.; Liang, C. D.; Overbury, S. *Top. Catal.* **2008**, *49*, 145–152.
14. Li, Y.; Yang, R. T.; Liu, C.-J.; Wang, Z. *Ind. Eng. Chem. Res.* **2007**, *46*, 8277–8281.
15. Wang, Z.-J.; Liu, Y.; Shi, P.; Liu, C.-J.; Liu, Y. *Appl. Catal. B* **2009**, *90*, 570–577.
16. Pan, Y.-X.; Liu, C.-J.; Shi, P. *J. Power Sources* **2008**, *176*, 46–53.
17. Pan, Y.-X.; Liu, C.-J.; Cui, L. *Catal. Lett.* **2008**, *123*, 96–101.
18. Zhu, X. L.; Cheng, D. G.; Kuai, P. Y. *Energy Fuels* **2008**, *22*, 1480–1484.

Downloaded by PENNSYLVANIA STATE UNIV on June 23, 2012 | http://pubs.acs.org
Publication Date (Web): December 3, 2010 | doi: 10.1021/bk-2010-1056.ch012

Chapter 12

A Carbide Catalyst Effective for the Dry Reforming of Methane at Atmospheric Pressure

**Jun Guo,[a] An-Jie Zhang,[a] Ai-Min Zhu,[a] Yong Xu,[a] C. T. Au,[c]
and Chuan Shi*,[a,b]**

**[a]Laboratory of Plasma Physical Chemistry, Dalian University of Technology,
Dalian, PR China
[b]State Key Laboratory of the Fine Chemicals,
Dalian University of Technology, Dalian, PR China
[c]Department of Chemistry, Hong Kong Baptist University,
Kowloon Tong, Hong Kong
*E-mail: chuanshi@dlut.edu.cn. Fax: +86-411-84708548-808.
Tel: +86-411- 84708548.**

A catalyst composed of metallic nickel and molybdenum carbide has been fabricated for CO_2 reforming of CH_4. Aspects concerning the formation of Ni and Mo_2C, their synergistic effects for CH_4 and CO_2 activation, and the establishment of a redox cycle were studied. Due to the catalytic oxidation-recarburization cycle, the Ni-Mo_2C catalyst is superior to the traditional metal carbide catalysts as verified by its stable activity in the dry reforming of CH_4 at atomspheric pressure.

1. Introduction

Methane is the major component of natural gas. It can be converted to liquid fuels and valuable chemicals such as synthesis gas (syngas; H_2 + CO). In the past decades, there are many reports on the catalytic conversion of methane to syngas through reforming as well as oxidation methods (*1–5*). In recent years, attention has been paid to the dry reforming of methane (DRM). It is considered sensible to capture and utilize CH_4 and CO_2 (greenhouse gases) before their emission into the atmosphere (*6–12*). Unlike methane partial oxidation, the reforming of CH_4 using CO_2 is heat-consuming and has to be conducted at high temperatures. Nonetheless, the DRM produces syngas with CO/H_2 molar ratio suitable for Fisher–Tropsch (F-T), methanol, and acetic acid synthesis (*13–17*). The catalysts for CO_2 reforming of CH_4 are usually based on Group VIII metals such as Ni, Rh and Pt (*18–24*). Among them, the nickel-based ones are commercially preferred due to the inherent availability and low costs of nickel. However, the problem of the nickel-based catalysts is coke formation that leads to the deactivation of catalyst.

It is known that transition metal carbides show chemical properties similar to those of noble metals (*25–27*). This kind of catalysts were investigated for reactions such as methane conversion (*28*, *29*), hydrotreating of oil fractions (*30*, *31*), hydrocarbon isomerization (*32*, *33*), as well as hydrogenation of carbon oxides and F-T synthesis (*34*, *35*). According to Claridge et al. (*28*), stable activity (72 h) at 1120 K could be achieved in CO_2 reforming of CH_4 over Mo_2C and WC catalysts at high pressure (8.3 bar) using a feed of CH_4:CO_2=1:1 molar ratio. On the other hand, stable catalytic activity (100 h) was observed by Shao et al. (*36*) over bimetallic Co-W carbides at 1123 K and 3.4 bar. LaMont and Thomson pointed out that at atmospheric pressure (*37*), rapid deactivation of transition metal carbides occurs due to oxidation by CO_2, and such kind of deactivation could be partially prevented by adding CO into the feeds.

Herein, we report the results of our recent study on the catalytic performance of Ni-Mo_2C for DRM at atmospheric pressure, with attention given to the synergistic effect of Ni and Mo_2C. This is the first report on a carbide catalyst that stable DRM activity can be achieved at atmospheric pressure without the need of adding a reductant into the feed.

2. Experimental

2.1. Catalyst Preparation

We synthesized the $NiMoO_x$ precursor by stirring an aqueous solution of $(NH_4)_6Mo_7O_{24}{\cdot}4H_2O$ and $Ni(NiO_3)_2{\cdot}6H_2O$ (Ni:Mo = 2:3) at 353 K for 4 h. The as-obtained $NiMoO_x$ was filtered out and dried at 393 K for 12 h and calcined at 773 K for 4 h. Then $NiMoO_x$ was carburized in CH_4/H_2 (20vol% CH_4) to Ni-Mo_2C following a series of temperature-programmed processes: temperature was raised from room temperature (RT) to 573 K in a span of 1 h, then from 573 to a desired temperature (i.e. 873, 923, or 973 K) at a rate of 1 K/min, and subsequently kept at the desired temperature for 2 h. The as-obtained material was cooled down to RT in flowing CH_4/H_2 and passivated in a mixture of 1%O_2/Ar for 12 h. In a similar manner, MoO_3 powder purchased from Tianjin Kermel Chemical Reagent was carburized as well.

2.2. Catalyst Characterization

X-ray powder diffraction (XRD) analysis was conducted using a XRD-6000 (Shimadzu, Kyoto, Japan) equipment with Cu Kα radiation (λ = 0.1542 nm), operating at 40 kV and 30 mA and at a scanning rate of 2°/min; phase identification was achieved through comparison of XRD patterns to those of "Joint Committee on Powder Diffraction Standards (JCPDS)".

Downloaded by PENNSYLVANIA STATE UNIV on June 23, 2012 | http://pubs.acs.org
Publication Date (Web): December 3, 2010 | doi: 10.1021/bk-2010-1056.ch012

Methane temperature-programmed reduction (CH_4-TPR) studies were performed using a mass spectrometer (OmniStar™ Pfeiffer Vacuum, Germany) interfaced with a computer. With the sample (0.050 g) securely placed in a quartz tubular reactor, CH_4-TPR profile was obtained by heating the sample from RT to 1250 K at a rate of 10 K/min in a flow of 10% CH_4/Ar (30 ml/min). The signal intensity of CH_4 (m/e = 15), H_2 (m/e = 2), H_2O (m/e = 18), CO (m/e = 28), and CO_2 (m/e = 44) were detected. Temperature-programmed oxidation using CO_2 (CO_2-TPO) was carried out by introducing 10%CO_2/Ar with a total flow rate of 30 ml/min into the same system while the sample temperature was raised from RT to 1250 K at a rate of 10 K/min. The signal intensity of CO (m/e = 28) and CO_2 (m/e = 44) were monitored. Prior to the CH_4-TPR and CO_2-TPO experiments, the sample was treated in situ in a flow of Ar and H_2 separately at 773 K for 2 h.

Downloaded by PENNSYLVANIA STATE UNIV on June 23, 2012 | http://pubs.acs.org
Publication Date (Web): December 3, 2010 | doi: 10.1021/bk-2010-1056.ch012

2.3. Catalyst Evaluation

Catalyst performance and stability were evaluated using a continuous down-flow quartz fixed-bed reactor (i.d. = 6 mm). Prior to the test, the catalyst (1 cm) was treated in situ at 773 K for 2 h in a flow of H_2, and purged with a flow of Ar for 0.5 h. The reaction was conducted at atmospheric pressure with a feed stream showing a constant volume ratio of CH_4/CO_2 (1:1). The gas hourly space velocity (GHSV) of the reactant feed was fixed at 14000 h^{-1}. For the test of catalyst stability, reaction temperature was kept constant at 1073 K during time on stream. The exit gas was analyzed using an on-line gas chromatograph (GC112A) equipped with a thermal conductivity detector. The conversion of CH_4 and CO_2, and the selectivity to H_2 and CO were calculated according to the following equations:

$$CH_{4\,conv} = \frac{[CH_4]_{in} - [CH_4]_{out}}{[CH_4]_{in}} \times 100\%$$

$$CO_{2\,conv} = \frac{[CO_2]_{in} - [CO_2]_{out}}{[CO_2]_{in}} \times 100\%$$

$$H_{2\,sele} = \frac{[H_2]_{out}}{2 \times CH_{4\,conv} \times [CH_4]_{in}} \times 100\%$$

$$CO_{sele} = \frac{[CO]_{out}}{CH_{4\,conv} \times [CH_4]_{in} + CO_{2\,conv} \times [CO_2]_{in}} \times 100\%$$

In: concentration in feed gas before reaction
Out: concentration in effluent gas after reaction

Downloaded by PENNSYLVANIA STATE UNIV on June 23, 2012 | http://pubs.acs.org
Publication Date (Web): December 3, 2010 | doi: 10.1021/bk-2010-1056.ch012

3. Results

3.1. Effect of Nickel Presence on Carbide Formation

Depicted in Figure 1a are the XRD patterns of Mo_2C generated from MoO_3 after carburization at 923, 943 and 973 K. The diffraction peaks at 34.4 °, 38.0 °, 39.4 °, 52.1 °, 61.5 °, 69.6 °, 74.6 °, 75.6 ° can be assigned to Mo_2C, while those at 26.0 °, 37.12 °, 53.47 °, 60.7 °, 66.6 ° to MoO_2. The results indicate that for complete carburization of MoO_3 to Mo_2C, a temperature as high as 973 K is required. Figure 1b shows the XRD patterns of Ni-Mo_2C generated after the carburization of $NiMoO_x$ at 873, 923, and 973 K. Besides the peaks of Mo_2C and MoO_2, there are peaks at 44.37 ° and 51.59 ° ascribable to metallic Ni. With the presence of nickel, carburization at 923 K would bring about the complete conversion of MoO_x to Mo_2C, a lowering of 50 K in comparison with the case of MoO_3 carburization (Figure 1a). It is apparent that the presence of nickel promotes the carburization process. Similar phenomenon was observed by Zhang et al. (*38*) in the synthesis of Ni-WC catalyst that was used in the direct conversion of cellulose to ethylene glycol.

In the CO_2 reforming of CH_4 over the carbide, it is important to ensure the regeneration of the carbide once it is oxidized to MoO_x by CO_2. The establishment of such a catalytic redox cycle is a key issue for catalyst stability. In the cases of having Mo_2C and Ni-Mo_2C first exposed to CO_2 and then to CH_4 at 1073 K, we observed Mo_2C regeneration in the latter but not in the former (Figure 2). It is obviouos that only in the presence of Ni, MoO_x can be carburized to Mo_2C under the adopted conditions. The results provide clear evidence that a unique oxidation and carburization cycle could be established in the case of Ni-Mo_2C.

3.2. Catalyst Evaluation

As shown in Figure 3, catalytic activity at 1073 K over Ni-Mo_2C is high, and there is no decline of activity in a run of over 35 h. On the other hand, rapid decline of performance is observed over the Mo_2C catalyst. A sample of used Mo_2C displays strong XRD peaks of MoO_2, whereas that of used Ni-Mo_2C shows peaks of Mo_2C and metallic Ni (Figure 4). The results indicate that the deactivation of Mo_2C is a result of Mo_2C bulk oxidation by CO_2, in agreement with the report of LaMont and Thomson (*37*) . It is obvious that Mo_2C can be retained during the DRM reaction when Ni is distributed among the Mo_2C catalyst.

Downloaded by PENNSYLVANIA STATE UNIV on June 23, 2012 | http://pubs.acs.org
Publication Date (Web): December 3, 2010 | doi: 10.1021/bk-2010-1056.ch012

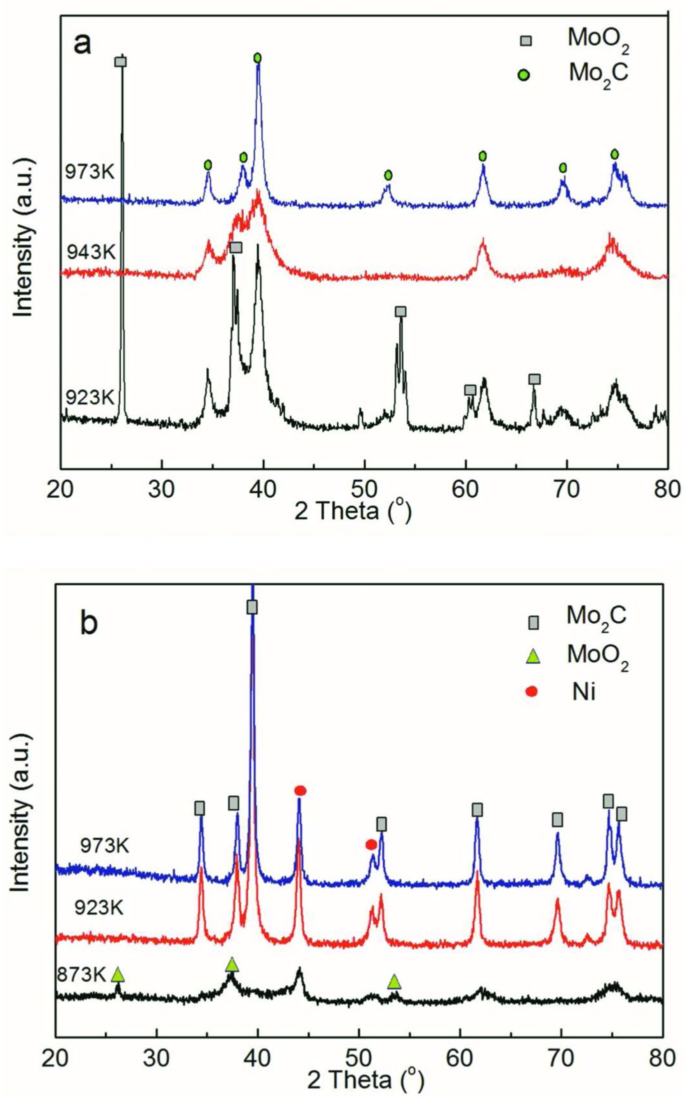

Figure 1. XRD patterns of (a) Mo_2C and (b) Ni-Mo_2C catalysts prepared at different carburizing temperatures

Downloaded by PENNSYLVANIA STATE UNIV on June 23, 2012 | http://pubs.acs.org
Publication Date (Web): December 3, 2010 | doi: 10.1021/bk-2010-1056.ch012

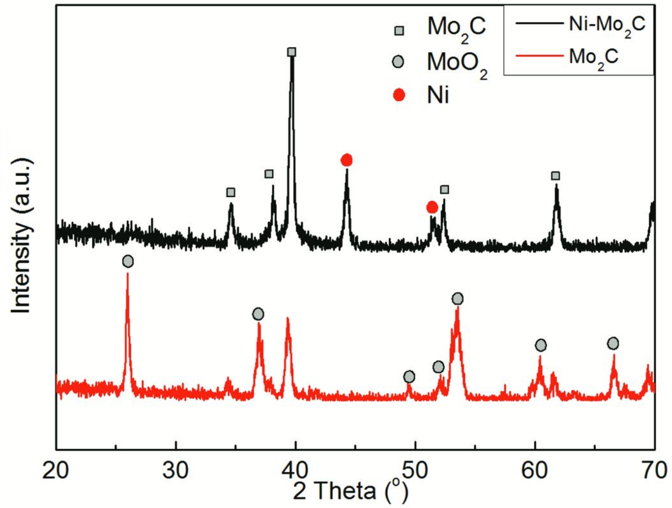

Figure 2. XRD patterns of Mo_2C and Ni-Mo_2C after exposure to CO_2 and then to CH_4 at 1073 K

3.3. Surface Reactions of CH_4 and CO_2 over Mo_2C and Ni-Mo_2C

Figure 5 displays the results of CH_4-TPR obtained over Mo_2C and Ni-Mo_2C in a gas stream of 10%CH_4/Ar. Over Mo_2C, parallel to the consumption of CH_4 (m/e = 15), there is obvious evolution of H_2 (m/e = 2), H_2O (m/e = 18), CO (m/e = 28), and CO_2 (m/e = 44) at around 943 K (Figure 5(a)). Above 1123 K, there is a weak signal of CH_4 consumption along with a weak signal of H_2 formation. The CH_4-TPR profiles obtained over Ni-Mo_2C (Figure 5(b)) are distinctly different from those obtained over Mo_2C. Below 973 K, there are two peaks of CH_4 consumption accompanied by peaks of H_2, CO and CO_2 evolution. Above 973 K, there are obvious CH_4 consumption and H_2 formation. The generation of H_2 is ascribed to CH_4 dissociation on the catalysts. The H_2O, CO and CO_2 peaks observed below 973 K can be a result of CH_4 interaction with the oxygen species that left behind due to incomplete carburization (*39*). Over Mo_2C, CH_4 dissociation occurs above 1123 K, but remains insignificant even at 1200 K. Based on the CH_4-TPR profiles recorded over Mo_2C and Ni-Mo_2C, we deduce that the decomposition of CH_4 above 1000 K is significantly promoted by the presence nickel.

Downloaded by PENNSYLVANIA STATE UNIV on June 23, 2012 | http://pubs.acs.org
Publication Date (Web): December 3, 2010 | doi: 10.1021/bk-2010-1056.ch012

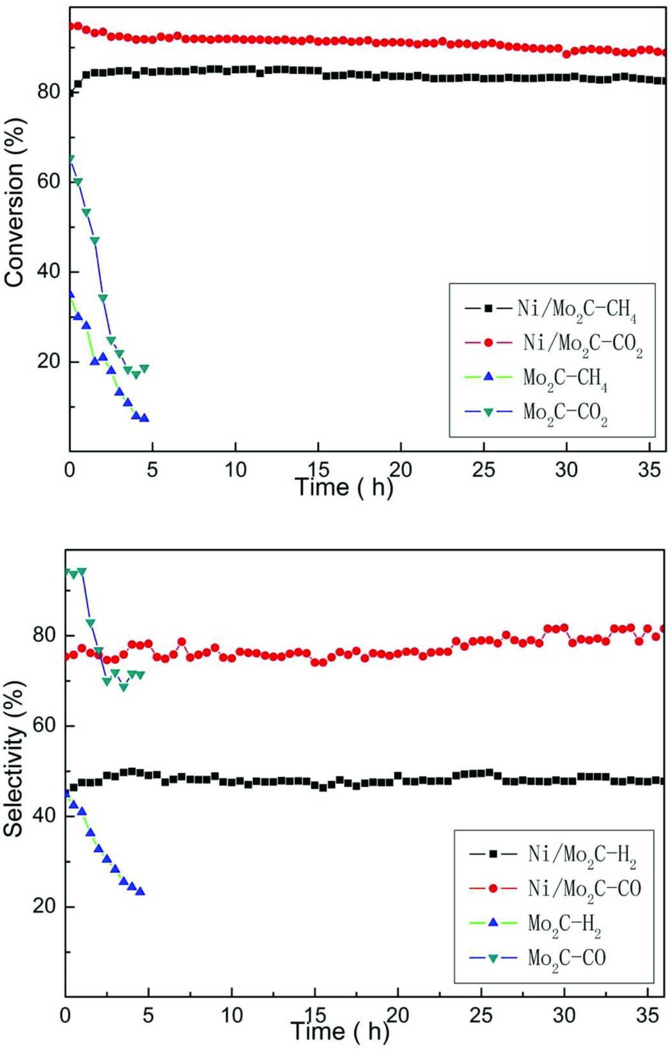

Figure 3. Lifetime study of Mo_2C and Ni-Mo_2C catalysts in CH_4/CO_2 dry reforming at 1073 K (atmospheric pressure, GHSV =14000 h^{-1}, CH_4/CO_2 =1:1)

Downloaded by PENNSYLVANIA STATE UNIV on June 23, 2012 | http://pubs.acs.org
Publication Date (Web): December 3, 2010 | doi: 10.1021/bk-2010-1056.ch012

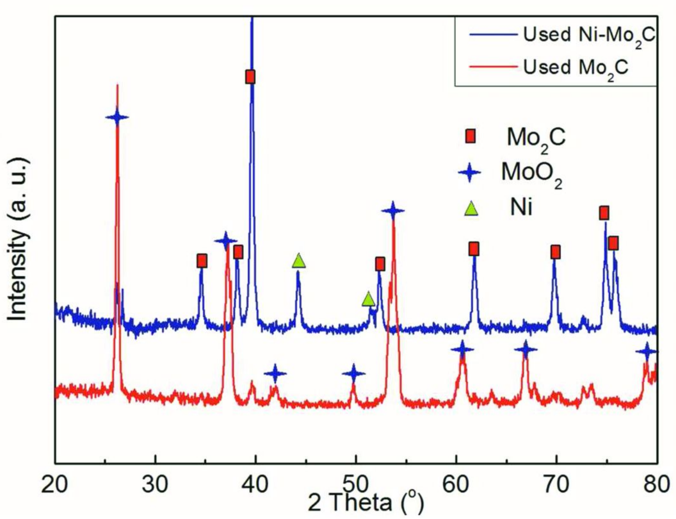

Figure 4. XRD patterns of Mo_2C and Ni-Mo_2C catalysts recorded after CH_4/CO_2 dry reforming at 1073 K (atmospheric pressure, GHSV =14000 h^{-1}, CH_4/CO_2 =1:1)

Figure 6 displays the results of CO_2-TPO investigation. The insets of Figure 6 show the XRD patterns of Mo_2C and Ni-Mo_2C after 10-min exposure to CO_2 at a specified temperature. There are two CO_2 consumption peaks observed over Mo_2C, one at 933 K and the other at 1013 K (Figure 6a). In the case of Ni-Mo_2C, two peaks are observed at 933 and 1098 K (Figure 6b). According to the XRD patterns (inset of Figure 6a), Mo_2C was partially converted to MoO_2 (2θ = 26.0°, 37.1 ° and 53.5 °) after exposure to CO_2 at 933 K. It is not the case with Ni-Mo_2C (inset of Figure 6b); it is only after exposure of Ni-Mo_2C to CO_2 at 1098 K that signals of MoO_2 (together with that of NiO) are detected. In other words, bulk oxidation of Ni-Mo_2C does not occur at 933 K, and oxidation activity due to CO_2 decomposition at 933 K is restricted to the surface of Mo_2C. At or above 1098 K, the consumption of CO_2 should be associated with bulk oxidation of Mo_2C. It is apparent that the presence of Ni prevents the bulk of Mo_2C from being oxidized.

In Advances in CO2 Conversion and Utilization; Hu, Y.;
ACS Symposium Series; American Chemical Society: Washington, DC, 2010.

Downloaded by PENNSYLVANIA STATE UNIV on June 23, 2012 | http://pubs.acs.org
Publication Date (Web): December 3, 2010 | doi: 10.1021/bk-2010-1056.ch012

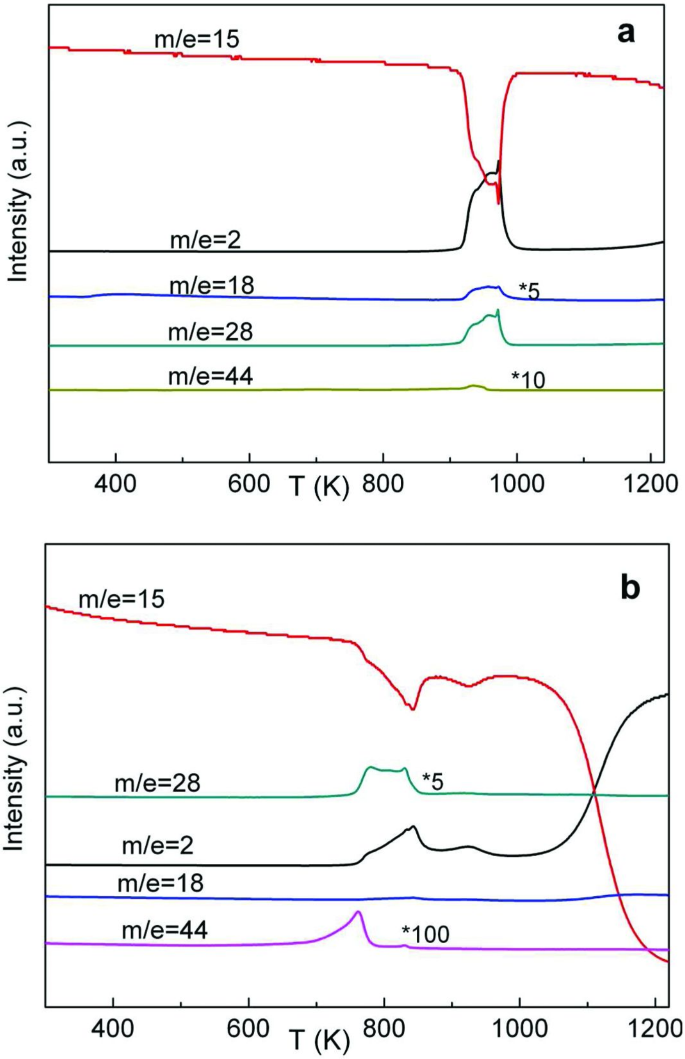

Figure 5. CH_4–TPR profiles of (a) Mo_2C and (b) Ni-Mo_2C

Downloaded by PENNSYLVANIA STATE UNIV on June 23, 2012 | http://pubs.acs.org
Publication Date (Web): December 3, 2010 | doi: 10.1021/bk-2010-1056.ch012

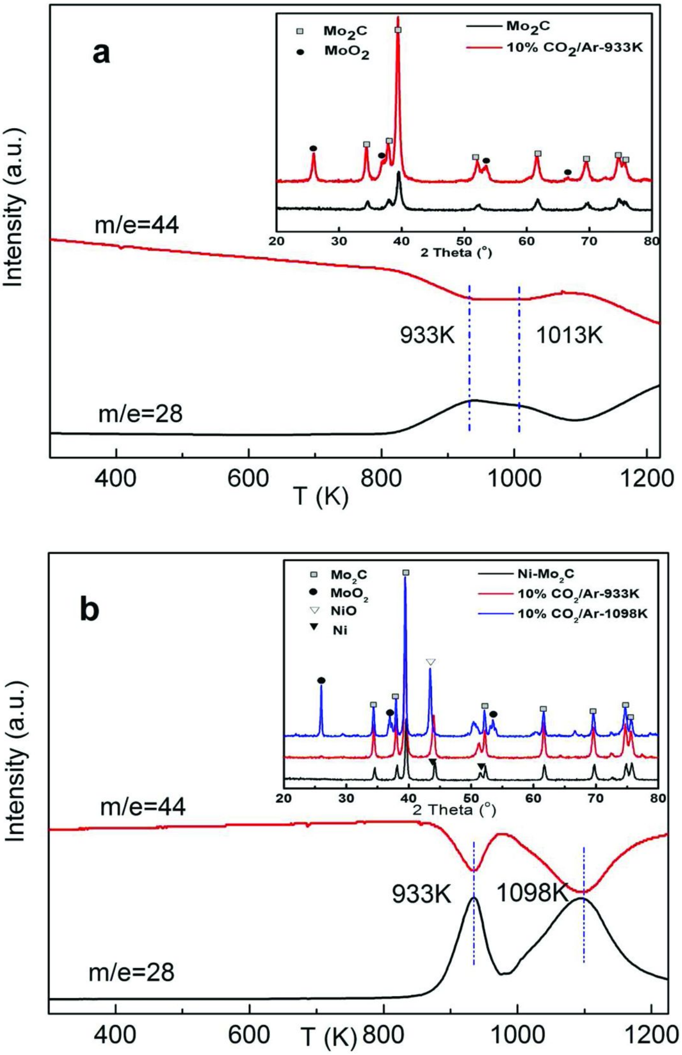

Figure 6. CO_2–TPO profiles of (a) Mo_2C and (b) Ni-Mo_2C

Downloaded by PENNSYLVANIA STATE UNIV on June 23, 2012 | http://pubs.acs.org
Publication Date (Web): December 3, 2010 | doi: 10.1021/bk-2010-1056.ch012

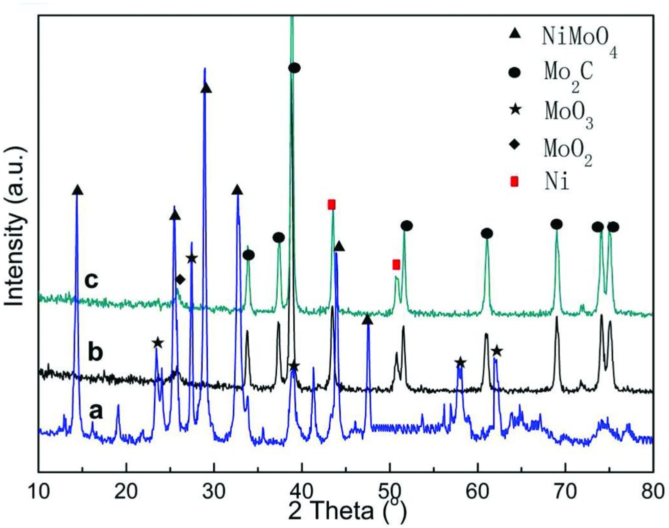

Figure 7. XRD patterns of (a) NiMoO$_x$, and those obtained after in situ carburization of NiMoO$_x$ for a on stream time of (b) 2 h, and (c) 4 h

3.4. Ni and Mo_2C Generation during DRM

It was found that Ni and Mo_2C could be in-situ generated from $NiMoO_x$ in the CO_2 reforming of CH_4. As shown in Figure 7, the XRD peaks of $NiMoO_4$ disappear and those of Mo_2C and metallic Ni appear after exposing $NiMoO_x$ to CH_4-CO_2 gas (30 ml/min) at 1073 K for 4 h. When $NiMoO_x$ was first treated in an Ar atmosphere at 773 K for 2 h and then exposed to CH_4-CO_2 gas, and temperature-programmed to 1073 K, CH_4 conversion declines from an initial value of around 98% to 80% in the first 5 h (Figure 8) and stays unchange afterwards. It is obvious that certain amount of the CH_4 consumed in the initial 5-h period is for $NiMoO_x$ carburization. Once $NiMoO_x$ carburization is done, CH_4 conversion stays around 80%. One can come to similar deduction based on the trend of CO selectivity. The selectivity to CO is around 68% initially and rises to 78% within the first 5 h, reflecting the consumption of carbon for $NiMoO_x$ carburization. As for CO_2 conversion and H_2 selectivity, there is no significant change within the initial period of 5 h.

Downloaded by PENNSYLVANIA STATE UNIV on June 23, 2012 | http://pubs.acs.org
Publication Date (Web): December 3, 2010 | doi: 10.1021/bk-2010-1056.ch012

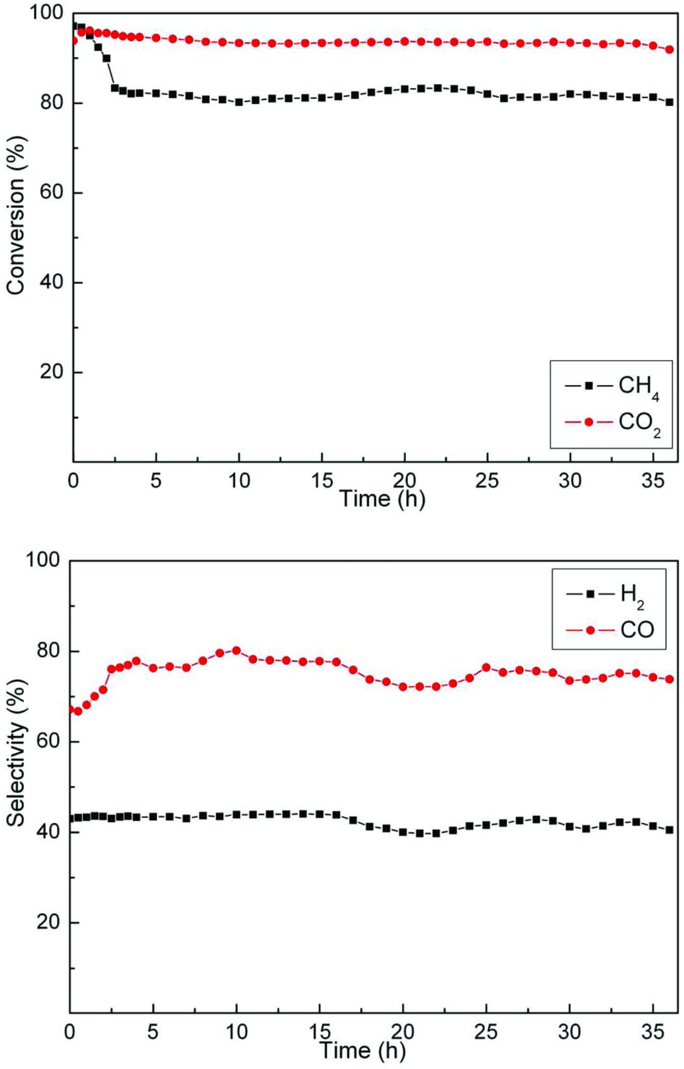

Figure 8. Lifetime study of Ni-Mo_2C in situ generated from $NiMoO_x$ for CH_4/CO_2 dry reforming at 1073 K (atmospheric pressure, GHSV =14000 h^{-1}, CH_4/CO_2 =1:1)

4. Discussion

For DRM, the Ni-based catalysts are commercially more desirable than the catalysts that are based on noble metals, but the drawback of using the former is catalyst deactivation due to coke formation. Despite efforts of modifying nickel catalysts through the use of a support or the adding of a second metal (*41–43*), catalyst lifetime remains poor. As for the catalysts of transition metal carbides, stable activity could only be achieved under elevated pressure of 5-8 bar (*28*).

At atmospheric pressure (*37*), there is facile oxidation of catalysts by CO_2, and catalyst lifetime is far from being acceptable.

It is believe that carbon accumulation on Ni-based catalysts (*43*, *44*) in DRM is a result of CH_4 dissociation or CO boudouard reaction. At temperatures higher than 1073 K, the former is believed to be the main cause of surface coking (*40*, *44*). The decomposition of CH_4 would generate surface carbon (denoted hereinafter as C*) that can be oxidized to CO by surface oxygen (denoted hereinafter as O*) originated from CO_2 decomposition. In cases that there is surface coking in DRM reaction, the rate of CH_4 dissociation should be higher than that of CO_2 decomposition.

Unlike the Ni-based catalysts, the catalysts of transition metal carbides deactivate mainly due to bulk oxidation. It has been suggested (*45*) that the transition metal carbides follow a redox mechanism in CH_4 reforming .Using Mo_2C as an example, the catalysis follows an oxidation-reduction cycle:

$$Mo_2C + 5CO_2 \rightarrow 2MoO_2 + 6CO$$
$$2MoO_2 + 5CH_4 \rightarrow Mo_2C + 4CO + 10H_2$$

It is envisaged that the reaction of a carbon atom of Mo_2C with an O* originated from the dissociation of adsorbed CO_2 would result in the creation of a vacancy, making the Mo_2C more vulnerable to oxidation. The filling of the vacancy with a C* is hence desirable to avoid bulk oxidation. In other words, if the rate of CH_4 dissociation is lower than that of CO_2 decomposition, the catalyst would likely be oxidized and lose its activity.

In order to fabricate a Mo_2C catalyst that is active and stable, we introduced Ni into Mo_2C. The strategy is to have simultaneous activation of CH_4 and CO_2 using Ni and Mo_2C, respectively. By regulating the molar ratio of Ni and Mo_2C, one can establish a catalytic redox cycle in which the deactivation of the two active components (i.e. Ni and Mo_2C) could be avoided. In other words, we match the rate of CH_4 dissociation with that of CO_2 activation to avoid carbon accumulation and Mo_2C bulk oxidation.

According to the results of CH_4-TPR and CO_2-TPO investigations (Figure. 5 and 6), the dissociation of CH_4 and CO_2 occur almost simultaneously over the Ni-Mo_2C catalyst at around 1000 K. It is clear that a catalytic redox cycle could hence be established over Ni-Mo_2C as verified by the stable activity of Ni-Mo_2C (Figure 3) and its regeneration after oxidation by CO_2 (Figure 2). Over Mo_2C, however, there is a mismatch of bulk oxidation and CH_4 dissociation; the former occurs around 933 K while the latter around 1123 K. Consequently, there is the deactivation of the Mo_2C catalyst. The catalytic oxidation–reduction cycle is illustrated in Scheme 1. Without the presence of Ni, the oxidized Mo cannot be recarburized by CH_4 and the oxidation–reduction cycle cannot be established. With the presence of Ni, the dissociation of CH_4 is promoted to cause timely carburization of MoO_2 for the completion of the oxidation–reduction cycle. It is worth pointing out that there is no need to prepare the Ni-Mo_2C before hand. For DRM, the $NiMoO_x$ precursor can be carburized in situ to produce Ni and Mo_2C. This can be considered as an advantage in industrial application.

Downloaded by PENNSYLVANIA STATE UNIV on June 23, 2012 | http://pubs.acs.org
Publication Date (Web): December 3, 2010 | doi: 10.1021/bk-2010-1056.ch012

Downloaded by PENNSYLVANIA STATE UNIV on June 23, 2012 | http://pubs.acs.org
Publication Date (Web): December 3, 2010 | doi: 10.1021/bk-2010-1056.ch012

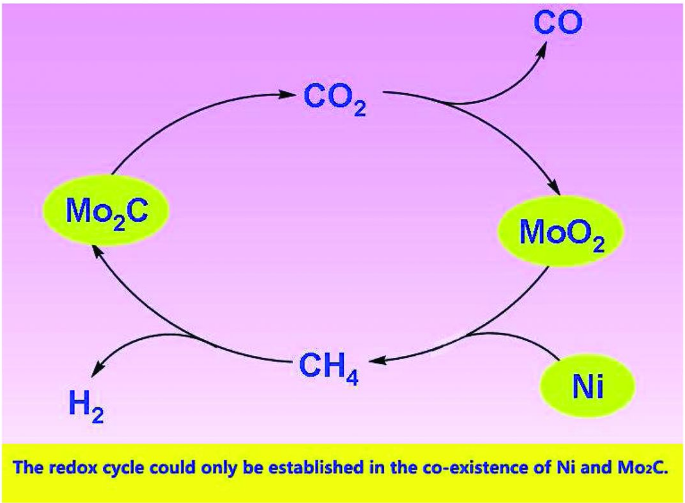
CO
CO_2
Mo_2C
MoO_2
CH_4
Ni
H_2
The redox cycle could only be established in the co-existence of Ni and Mo2C.

Scheme 1. Catalytic oxidation–reduction cycle over Mo_2C promoted by Ni

5. Conclusions

We have demonstrated that the Ni-Mo_2C catalyst performs well in CH_4/CO_2 reforming. The advantage of Ni-Mo_2C over Mo_2C or other traditional carbide catalysts is its stable performance at atmospheric pressure. This is the first report that a carbide catalyst can show stable activity at atmospheric pressure without the need of adding a reductant into the CH_4-CO_2 feed. The role of Ni is to enhance the dissociation of CH_4 for the regeneration of Mo_2C. In such a catalytic oxidation–reduction cycle, MoO_2 can be carburized back to Mo_2C in a timely manner.

Acknowledgments

The work was supported by the National Natural Science Foundation of China (Nos. 20573014 and 20673016) and by the Program for New Century Excellent Talents in University (NCET-07-0136).

References

1. Hohn, K. L.; Schmidt, L. D. *Appl. Catal. A: Gen.* **2001**, *211*, 53–68.
2. Jin, W.; Gu, X.; Li, S.; Huang, P.; Xu, N.; Shi, J. *Chem. Eng. Sci.* **2000**, *55*, 2617–2625.
3. Choudhary, V. R.; Rane, V. H.; Rajput, A. M. *Appl. Catal., A* **1997**, *162*, 235–238.
4. Choudhary, V. R.; Rajput, A. M.; Prabhakar, B.; , A. S. *Fuel* **1998**, *77*, 1803–1807.
5. Bharadwaj, S. S.; Schmidt, L. D. *Fuel Process. Technol.* **1995**, *42*, 109–127.

6. Zhang, A. J.; Zhu, A. M.; Guo, J.; Xu, Y.; Shi, C. *Chem. Eng. J.* **2010**, *156*, 601–606.
7. Zhang, J. G.; Wang, H.; Dalai, A. K. *Ind. Eng. Chem. Res.* **2009**, *48*, 677–684.
8. Lima, S. M.; Assaf, J. M.; Peña, M. A.; Fierro, J. L. G. *Appl. Catal., A* **2006**, *311*, 94–104.
9. Schulz, P. G.; Gonzalez, M. G.; Quincoces, C. E.; Gigola, C. E. *Ind. Eng. Chem. Res.* **2005**, *44*, 9020–9029.
10. Hou, Z. Y.; Yashima, T. *Appl. Catal., A.* **2004**, *261*, 205–209.
11. Iyer, M. V.; Norcio, L. P.; Kugler, E. L.; Dadyburjor, D. B. *Ind. Eng. Chem. Res.* **2003**, *42*, 2712–2721.
12. Zhang, K.; Kogelschatz, U.; Eliasson, B. *Energy Fuels* **2001**, *15*, 395–402.
13. Subramani, V.; Gangwal, S. K. *Energy Fuels* **2008**, *22*, 814–839.
14. Olah, G. A.; Goeppert, A.; Prakash, G. K. S. *J. Org. Chem.* **2009**, *74*, 487–498.
15. Khodakov, A. Y.; Chu, W.; Fongarland, P. *Chem. Rev.* **2007**, *107*, 1692–1744.
16. Xu, B. Q.; Sachtler, W. M. H. *J. Catal.* **1998**, *180*, 194–206.
17. Tjatjopoulos, G. J.; Vasalos, I. A. *Ind. Eng. Chem. Res.* **1998**, *37*, 1410–1421.
18. Bradford, M. C. J.; Vannice, M. A. *Appl. Catal., A* **1996**, *142*, 73–96.
19. Zhang, Z. L; Verykios, X. E. *Catal. Lett.* **1996**, *38*, 175–179.
20. Chen, Y. G.; Tomishige, K.; Fujimoto, K. *Appl. Catal., A* **1997**, *161*, L11–L17.
21. Gronchi, P.; Centola, P.; Rosso, R. D. *Appl. Catal., A* **1997**, *152*, 83–92.
22. Portugal, U. L.; Santos, A. C. S. F.; Damyanova, S.; Marques, C. M. P.; Bueno, J. M. C. *J. Mol. Catal. A: Chem.* **2002**, *184*, 311–322.
23. Yang, M; Papp, H *Catal. Today* **2006**, *115*, 199–204.
24. Damyanova, S; Pawelec, B.; Arishtirova, K.; Fierro, J. L. G.; Sener, C.; Dogu, T. *Appl. Catal., B* **2009**, *92*, 250–261.
25. Levy, R. B.; Boudart, M. *Science* **1973**, *181*, 547–549.
26. Hwu, H. H.; Chen, J. G. *Chem. Rev.* **2005**, *105*, 185–212.
27. York, A. P. E.; Claridge, J. B.; Brungs, A. J.; Tsang, S. C.; Green, M. L. H. *Chem. Commun.* **1997**, 39–40.
28. Claridge, J. B.; York, A. P. E.; Brungs, A. J.; Marquez-Alvarez, C.; Sloan, J.; Tsang, S. C.; Green, M. L. H. *J. Catal.* **1998**, *180*, 85–100.
29. Sehested, J.; Jacobsen, C. J. H.; Rokni, S.; Rostrup-Nielsen, J. R. *J. Catal.* **2001**, *201*, 206–212.
30. Aegerter, P. A.; Quigley, W. W. C.; Simpson, G. J.; Ziegler, D. D.; Logan, J. W.; McCrea, K. R.; Glazier, S.; Bussell, M. E. *J. Catal.* **1996**, *164*, 109–121.
31. Schlatter, J. C.; Oyama, S. T.; Metcalfe, J. E.; Lambert, J. M. *Ind. Eng. Chem. Res.* **1988**, *27*, 1648–1653.
32. Delgallo, P.; Meunier, F.; Pham-Huu, C.; Crouzet, C.; Ledoux, M. J. *Ind. Eng. Chem. Res.* **1997**, *36*, 4166–4175.
33. Hemming, F.; Wehrer, P.; Katrib, A.; Maire, G. *J. Mol. Catal. A: Chem.* **1997**, *124*, 39–56.
34. Nagai, M.; Kurakami, T.; Omi, S. *Catal. Today* **1998**, *45*, 235–239.

Downloaded by PENNSYLVANIA STATE UNIV on June 23, 2012 | http://pubs.acs.org
Publication Date (Web): December 3, 2010 | doi: 10.1021/bk-2010-1056.ch012

35. Ranhotra, G. S.; Bell, A. T.; Reimer, J. A. *J. Catal.* **1987**, *108*, 40–49.
36. Shao, H.; Kugler, E.; Ma, W.; Dadyburjor, D. *Ind. Eng. Chem. Res.* **2005**, *44*, 4914–4921.
37. LaMont, D. C.; Thomson, W. J. *Chem. Eng. Sci.* **2005**, *60*, 3553–3559.
38. Ji, N.; Zhang, T.; Zheng, M. Y.; Wang, A. Q.; Wang, H.; Wang, X. D.; Chen, J. G. *Angew. Chem., Int. Ed.* **2008**, *47*, 8510–8513.
39. LaMont, D. C.; Gilligan, A. J.; Darujati, A. R. S.; Chellappa, A. S.; Thomson, W. J. *Appl. Catal., A* **2003**, *255*, 239–253.
40. Ferreira-Aparicio, P.; Benito, M; Kouachi, K.; Menad, S. *J. Catal.* **2005**, *231*, 331–343.
41. Guo, J. Z.; Gao, J.; Chen, B. H.; Hou, Z. Y.; Fei, J. H.; Lou, H.; Zheng, X. M. *Int. J. Hydrogen Energy* **2009**, *34*, 8905–8911.
42. Tsyganok, A. I.; Inaba, M.; Tsunoda, T.; Uchida, K.; Suzuki, K.; Takehira, K.; Hayakawa, T. *Appl. Catal., A* **2005**, *292*, 328–343.
43. Al-Fatish, A. S. A.; Ibrahim, A. A.; Fakeeha, A. H.; Soliman, M. A.; Siddiqui, M. R. H.; Abasaeed, A. E. *Appl. Catal., A* **2009**, *364*, 150–155.
44. Guo, J. J.; Lou, H.; Zheng, X. M. *Carbon* **2007**, *45*, 1314–1321.
45. Brungs, A. J.; York, A. P. E.; Green, M. L. H. *Catal. Lett.* **1999**, *57*, 65–69.

Downloaded by PENNSYLVANIA STATE UNIV on June 23, 2012 | http://pubs.acs.org
Publication Date (Web): December 3, 2010 | doi: 10.1021/bk-2010-1056.ch012

Chapter 13

A DFT Investigation of the γ-Al_2O_3 Supported Fe_3Zn and Fe_4 Clusters as Catalysts for CO_2 Adsorption and Activation

Shuxia Yin, Yun-xiang Pan, and Qingfeng Ge*

Department of Chemistry and Biochemistry, Southern Illinois University, Carbondale, IL 62901
***qge@chem.siu.edu**

Downloaded by CORNELL UNIV on June 23, 2012 | http://pubs.acs.org
Publication Date (Web): December 3, 2010 | doi: 10.1021/bk-2010-1056.ch013

The synergy between different components in a multicomponent catalyst has been exploited in many important catalytic processes, including CO_2 conversion and utilization. In the present work, the clusters Fe_4 and Fe_3Zn supported on γ-Al_2O_3 have been studied for CO_2 adsorption and activation using density functional theory slab calculations. Our results indicated that γ-Al_2O_3 induces charge redistribution in the supported clusters, resulting in $Fe^{\delta+}$ and $Fe^{\delta-}$ sites. This charge redistribution is believed to be the origin of the experimentally observed promotion effect of γ-Al_2O_3 toward CO_2 conversion. Furthermore, we found that the tetrahedral configuration of Fe_4 and F_3Zn is stabilized by the strong metal-support interaction to a larger degree than the planar configuration. Upon CO_2 adsorption and activation, the metal atoms of the supported cluster are all oxidized as indicated by the electron transfer from cluster to the adsorbed CO_2. Our study showed that the incorporation of Zn in the cluster modified both the geometrical and electronic properties of the Fe-based catalyst.

Introduction

The anthropogenic emission of green house gases, mainly CO_2, has been accelerated by the rapid growth of carbon-based energy consumption over the past half century (*1*, *2*). Catalytic processes that convert or fix CO_2 in the form of useful liquid fuel or other value-added chemicals help to mitigate the CO_2 emission. In fact, CO_2 utilization and conversion have been identified as one of the strategic directions in a recent US. Department of Energy report (*3*).

Chemically, CO_2 is very stable and is in a deep free energy well (*2*, *4*, *5*). by reacting with more reactive molecules, such as CH_4 and H_2, the overall reaction becomes less endothermic, making the conversion of CO_2 to hydrocarbon thermodynamically feasible. Direct hydrogenation and natural gas reforming of CO_2 have been widely studied. In these CO_2 conversion processes, transition metal catalysts allow the reactions to operate at relatively mild conditions. Extensive efforts have been made to search for catalysts with high activity and selectivity toward the desired products.

Catalysts composed of multiple active components are widely studied and used in CO_2 conversions. In these catalysts, promoter(s) may be used to modify the physical and chemical properties of the supported metal catalyst and improve the overall catalytic performance (*6*, *7*). The activity and the selectivity of the reaction can be optimized by changing the promoter and/or tuning the composition. For example, highly dispersed Cu/ZnO catalysts supported on oxides, including Al_2O_3, ZrO_2, SiO_2 and TiO_2, are active for CO_2 hydrogenation to methanol (*8–11*). ZnO is thought to be an active component of the catalyst, not only acting as a support. Different models, including active site model on Cu (*11*) and Cu-Zn alloying (*12*), have been proposed to explain the observed activity. The oxide supports were also found to play important roles in CO_2 conversion. For example, ZrO_2 supported Cu/ZnO catalyst had a higher methanol selectivity whereas the Cu/ZnO/Al_2O_3 catalyst exhibited a poorer catalytic (*9*, *10*).

Fe-based catalysts, which have been used in Fischer-Tropsch (F-T) synthesis to produce hydrocarbons from syngas (*13*, *14*), were found to be active for hydrocarbon production from CO_2-containing feeds (*15–18*). The production of hydrocarbons was believed to happen in two steps, namely the reverse water-gas shift and the F-T synthesis. However, the process suffers from the high selectivity toward methane. Potassium-promoted Fe catalysts on γ-Al_2O_3 were found to enhance the CO_2 uptake and the selectivity to the long-chain hydrocarbons (*18*). Among many promoters tested, Zn was shown to offer the highest selectivity toward C2-C4 alkene. The effect of Zn has been attributed to the more basic Fe sites being stabilized by the addition of Zn (*18*).

In supported multi-component catalysts, the metal-metal interaction and metal-support interaction will affect the interaction of the reactive species and the catalytic sites. Understanding the underlying mechanism at the atomic level is a challenging while significant task in heterogeneous catalysis. Experimentally, the catalytic reactivity is measured as an ensemble average. In a few cases, it has been shown that surface reaction steps can be followed. On the other hand, theoretical modeling has been shown to be a powerful tool in exploring individual features by building appropriate models. There have been a number of theoretical studies on CO_2 adsorption and activation (*19–22*), including the recent work from our group (*23*). In the present communication, we report our density functional theory (DFT) study on CO_2 adsorption and activation on γ-Al_2O_3 supported Fe_4 and Fe_3Zn clusters.

We chose the γ-Al_2O_3(110) surface as the model of the support and focused on the effect of the introduction of a second metal, Zn, on the catalyst structure

Downloaded by CORNELL UNIV on June 23, 2012 | http://pubs.acs.org
Publication Date (Web): December 3, 2010 | doi: 10.1021/bk-2010-1056.ch013

and on its reactivity toward CO_2. The structural model of the γ-Al_2O_3 has been established previously (*24*), and we used this model to build the support surfaces in a number of our previous studies (*23*). We found that substituting Fe by Zn changes the morphology of the cluster from tetrahedral to planar. The adsorption of CO_2 further stabilizes this transition, and this, in turn, enhances CO_2 activation. The role of metal-metal and metal-support interaction in modifying the structural and electronic properties has been clearly demonstrated.

Computational Details

Density functional theory periodic slab calculations were carried out using the Vienna ab-initio simulation package (VASP) (*25–27*). The projector augmented wave method was employed to describe the interactions between ions and electrons (*28*). The exchange and correlation potential was determined by Purdew-Burke-Ernzehof generalized gradient approximation (GGA) (*29*). The cutoff energy for the plane wave basis set was set to 400eV. Monkhorst–Pack grid with a 2x2x1 k-point mesh was used to perform the Brillouin zone integrations for both the geometry and energy calculations (*30*). The atomic structures were optimized using the conjugated gradient algorithm and/or the quasi-Newton scheme until the forces on the atoms were less than 0.03 eV/Å. The spin polarization was included in all calculations.

The hydroxylated (110) surface model of nonspinel γ-Al_2O_3 was built from our previous work (*23*). A supercell with a dimension of 8.404 Å x 8.018 Å x 19.182 Å was used, which includes twelve Al_2O_3 units distributed in six layers and a 12 Å vacuum to separate slabs. Isolated Fe_4 and Fe_3Zn clusters in both planar rhombic and tetrahedral configurations were first optimized separately. The adsorption of Fe_4 and Fe_3Zn clusters on the above hydroxylated surface was explored at different surface sites. CO_2 was then introduced around the supported metal cluster. In all calculations, the bottom two layers of the slab were fixed in their bulk position, while the top four layers as well as the adsorbed clusters and CO_2 were allowed to relax. Bader-charge analysis was used to further characterize the nature of the stable structural configurations (*31*, *32*). The stability of the free and supported metal cluster was evaluated by the binding energy

$$E_{bind\text{-}iso}=E_{cluster}-4E_M$$
$$E_{bind\text{-}ad}=E_{M4\text{-}\gamma\text{-}Al2O3}-E_{\gamma\text{-}Al2O3}-4E_M$$

where $E_{cluster}$ and E_M are the total energy of the free (isolated) cluster, and free metal atom (four Fe atoms in Fe_4 and three Fe atoms and one Zn atom in Fe_3Zn), respectively. $E_{M4\text{-}\gamma\text{-}Al2O3}$ is the total energy of the metal cluster supported on the substrate and $E_{\gamma\text{-}Al2O3}$ is the total energy of the γ-Al_2O_3 surface. The binding energy of CO_2 on the metal cluster was defined as,

$$E_{bind}=E_{CO2\text{-}M4\text{-}\gamma\text{-}Al2O3}-E_{\gamma\text{-}Al2O3}-4E_M-E_{CO2}$$

where $E_{CO2\text{-}M4\text{-}\gamma\text{-}Al2O3}$ is the total energy of adsorbed CO_2 on the supported cluster and E_{CO2} is the total energy of the free CO_2 molecule.

Downloaded by CORNELL UNIV on June 23, 2012 | http://pubs.acs.org
Publication Date (Web): December 3, 2010 | doi: 10.1021/bk-2010-1056.ch013

Downloaded by CORNELL UNIV on June 23, 2012 | http://pubs.acs.org
Publication Date (Web): December 3, 2010 | doi: 10.1021/bk-2010-1056.ch013

Results and Discussion

A. Adsorption of Metal Clusters

Fig.1 shows the isolated Fe_4 and Fe_3Zn clusters along with the bond lengths. Table 1 lists the binding energies of both the isolated and the adsorbed state of the clusters. Using the tetrahedral structure as the corresponding reference, the relative stability of different configurations is characterized by E_{rel}. The isolated tetrahedral Fe_4 cluster has four Fe-Fe bonds of 2.23 Å and two Fe-Fe bonds of 2.60 Å. The planar cluster has four Fe-Fe bonds of 2.24 Å and one Fe-Fe bond of 2.38 Å with a rhombic shape. The two types of clusters show very different stability. The tetrahedral cluster is energetically more favorable, by 0.17 eV, than the planar one. The atomic charges for these configurations by Bader analysis are provided in Table 2. The results show that the charges on all Fe atoms in the tetrahedral cluster are close to zero. On the other hand, there is charge redistribution in the planar cluster, i.e. the atoms at the acute protrusion are more negative whereas those at the obtuse positive. The charge redistribution resulted in polarization in the cluster.

We then examined the adsorption of the clusters on the hydroxylated γ-Al_2O_3(110) surface by initially placing the cluster on a number of surface sites, including Al_{4c} and O_{2c} and O_{3c} sites. These sites were explored for transition metal dimer adsorptions and were found to result in stable adsorption configurations in our previous work (*24*). The adsorbed tetrahedral cluster lies on the surface, forming Fe-O_{2c}, two Fe-O_{3c} and three Fe-Al_{4c} bonds, whereas the planar cluster adsorbed edgewise to the surface, forming Fe-O_{2c}, Fe-O_{3c} and two Fe-Al_{4c} bonds, as shown in Fig.2. The adsorption energy of the tetrahedral Fe_4 is -2.30 eV, according to $E_{ad}=E_{M4\text{-}\gamma\text{-}Al2O3}-E_{\gamma\text{-}Al2O3}-E_{M4}$, indicating a strong surface-cluster interaction. The strong interaction is accompanied by the strong surface-cluster electron transfer shown in Table 2. The adsorbed tetrahedral Fe_4 is positively charged by 0.29 e, larger than that of the planar Fe_4 (0.20 e). Considerable charge redistribution among the atoms in the adsorbed Fe_4 clusters was induced by the adsorption. The top Fe atom not directly in contact with the surface and the Fe atom binding the Al_{4c} site are negatively charged (being reduced) whereas the Fe atoms binding the O_{2c} and O_{3c} sites are positively charged (being oxidized), by as much as ~0.30 e. The charge redistribution creates $Fe^{\delta+}$ and $Fe^{\delta-}$ sites in the adsorbed Fe_4 cluster. In the adsorbed planar cluster, the electron transfer between the surface and cluster and the charge redistribution in the adsorbed cluster also occur but to a lesser extent, i.e., generated less $Fe^{\delta-}$ sites. Overall, the tetrahedral Fe_4 is stabilized more by the supporting surface than the planar cluster. These results demonstrate that the multiple bonds formed between cluster atoms and surface acidic/basic sites contribute to the strong cluster-surface interaction. These newly generated $Fe^{\delta-}$ sites are expected to have a stronger affinity than Fe^0 toward the acidic CO_2. Consequently, the formation of the $Fe^{\delta+}$ and $Fe^{\delta-}$ sites on the γ-Al_2O_3 supported Fe catalyst is expected to enhance the reactivity toward CO_2 adsorption and activation.

Downloaded by CORNELL UNIV on June 23, 2012 | http://pubs.acs.org
Publication Date (Web): December 3, 2010 | doi: 10.1021/bk-2010-1056.ch013

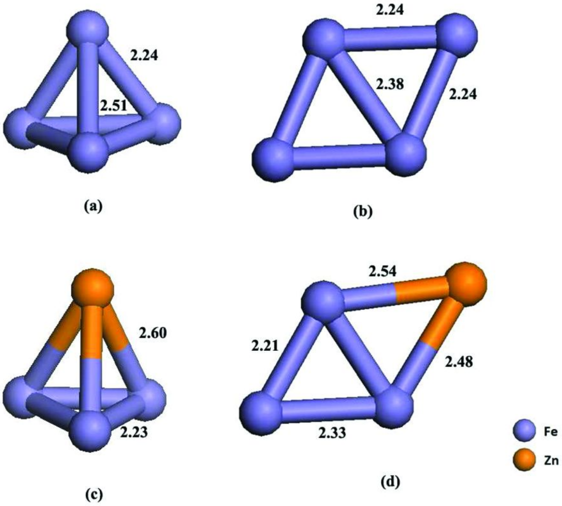

Figure 1. Isolated Fe_4 (a, b) and Fe_3Zn clusters (c, d) in tetrahedral and planar configurations.

Table 1. Binding energy and relative energy of the isolated and adsorbed clusters in different configurations. (The energy unit is in eV)

	Fe_4			
	$E_{bind\text{-}iso}$	E_{rel}	$E_{bind\text{-}ad}$	E_{rel}
tetrahedral	-8.51	0.0	-10.81	0.0
planar	-8.34	0.17	-10.09	0.72
	Fe_3Zn			
tetrahedral	-5.97	0.0	-8.09	0.0
planar	-6.50	-0.53	-8.22	-0.13

As shown in Fig. 1 (c) and (d), both the tetrahedral and planar Fe_3Zn clusters were deformed from their Fe_4 counterparts due to the substitution of Fe by Zn. In contrast to the Fe_4 cluster, the planar Fe_3Zn cluster is energetically more favorable, by 0.53 eV, than the tetrahedral cluster. The atomic charges in Table 2 indicate that the tetrahedral cluster has a larger redistribution of electronic charges than that in the planar cluster. Combined with the results of the Fe_4 clusters, we conclude that the free metal clusters energetically favor the structure with smaller charge redistribution, and therefore, less polarization in the cluster, as manifested in tetrahedral Fe_4 and planar Fe_3Zn.

The substitution also resulted in significant differences in the adsorbed clusters. Upon adsorption on the hydroxylated γ-Al_2O_3(110) surface, the Fe_3Zn cluster binds at surface acidic/basic sites with the Zn site staying away from the surface (Fig. 2). The adsorption energy of Fe_3Zn in tetrahedral adsorbed configuration is -2.11 eV, according to $E_{ad}=E_{M4\text{-}\gamma\text{-}Al2O3}-E_{\gamma\text{-}Al2O3}-E_{M4}$. The tetrahedral Fe_3Zn cluster in the adsorbed state is more positively charged (0.25

e) than the planar one (0.20 e). The electron transfer is accompanied by a significant redistribution of charges within the adsorbed cluster, as shown in Table 2. Although the adsorbed planar cluster is still energetically more favorable than the tetrahedral one, the tetrahedral cluster is stabilized further upon adsorption. The energy difference between the tetrahedral and planar structures is reduced from -0.53 eV for free clusters to -0.13 eV for adsorbed clusters. For both Fe_4 and Fe_3Zn clusters, adsorption stabilizes the clusters and causes charge redistribution within the clusters.

Our results indicate that both metal-metal and metal-support interactions have a significant effect on the cluster stability and the electronic structures. The free cluster prefers the configuration with a relatively uniform charge distribution whereas the supported cluster is stabilized by charge transfer between cluster and surface as well as charge redistribution within the cluster, resulting in a strong metal-support interaction. In the following section, we will explore the effect of these changes in cluster properties on CO_2 adsorption and activation.

Downloaded by CORNELL UNIV on June 23, 2012 | http://pubs.acs.org
Publication Date (Web): December 3, 2010 | doi: 10.1021/bk-2010-1056.ch013

B. Adsorption of CO_2 on the Supported Fe_4 and Fe_3Zn

The stable adsorbed configurations of the Fe_4 and Fe_3Zn clusters in both tetrahedral and planar arrangement were selected as the substrate for CO_2 adsorption. Different adsorption configurations have been explored and three types were found to be stable. The schematics of CO_2 adsorption structures are presented in Fig. 3. To distinguish adsorption on two different types of clusters, we use T to represent the adsorption configuration on the tetrahedral cluster and P the one on planar cluster. In the T type of adsorption, there are two stable adsorption configurations: CO_2 adsorbs on the bridge of the top Fe atom and the Fe atom binding the surface Al_{4c}, denoted as T1; and CO_2 adsorbs at the interfacial bridge Fe atoms bound with the surface O_{3c} and Al_{4c}, labeled as T2. In the P1 structure, CO_2 is bound on the bridge site of the Fe_4 cluster and also interacts with the Fe atom of the neighboring image. Effectively, the Fe_4 clusters in P1 are connected by the adsorbed CO_2, forming a chain–like structure due to the periodic condition. Table 3 summarizes the binding energies and the structural parameters of the adsorbed CO_2. Using T1 as the reference, the relative stability of different configurations is also given in Table 3.

For CO_2 adsorption on Fe_4/Al_2O_3, the configuration T1 is the most favorable. This configuration is 0.21 eV more stable than P1. In all adsorbed configurations, CO_2 is activated, indicated by stretched C-O bonds (1.24~1.30 Å) and bent O-C-O (ÐOCO is in the range of 125~140°). CO_2 is activated to the greatest extent in the P1 configuration, as indicated by the largest deformation. Bader charge in Table 4 revealed that CO_2 is negatively charged whereas the metal cluster becomes more positive, indicating electron transfer from cluster to CO_2 and the surface. The adsorption of CO_2 caused all metal atoms in the cluster to be positively charged. This is a direct consequence of the oxidative nature of CO_2. The activated adsorption of CO_2 contributed to the stabilization of P1 significantly, resulting in a smaller energy difference between the tetrahedral and planar configurations on the supported Fe_4 clusters. These results show that CO_2 and the oxide support have a similar effect on relative stability of the clusters.

In Advances in CO2 Conversion and Utilization; Hu, Y.;
ACS Symposium Series; American Chemical Society: Washington, DC, 2010.

Downloaded by CORNELL UNIV on June 23, 2012 | http://pubs.acs.org
Publication Date (Web): December 3, 2010 | doi: 10.1021/bk-2010-1056.ch013

Table 2. Atomic charges for Fe_4/γ-Al_2O_3, Fe_3Zn/γ-Al_2O_3 system

		Fe_4		Fe_3Zn	
		isolated	Ads.	isolated	Ads.
tetrahedral	Fe (-O3c)	0.00	0.30	0.00	0.25
	Fe (-Al4c)	0.03	-0.11	0.06	-0.14
	Fe (-O2c)	-0.01	0.18	0.04	0.23
	Fe or Zn (top)	-0.02	-0.09	-0.10	-0.09
	total		*0.29*		*0.25*
planar	Fe	-0.09	0.32	0.01	0.06
	Fe (top)	0.08	0.05	0.03	-0.01
	Fe	0.11	0.00	0.02	0.16
	Fe or Zn (top)	-0.10	-0.16	-0.06	-0.01
	total		*0.20*		*0.20*

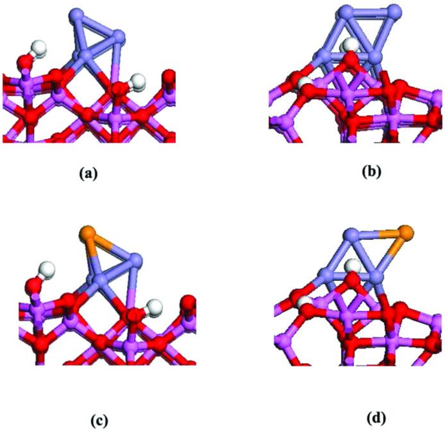

Figure 2. Side view of adsorbed cluster on γ-Al_2O_3(110). Tetrahedral (a) and planar (b) structure for Fe_4, (c) and (d) for Fe_3Zn

For CO_2 adsorption on Fe_3Zn/Al_2O_3, the planar configuration P1 is more favorable than the tetrahedral configurations T1 and T2, by -0.89 and -0.25 eV, respectively. The Fe_3Zn cluster in T2 is no longer tetrahedral. The cluster is distorted dramatically. The deformation of CO_2 and electron transfer in P1 is also the most significant. Similar to CO_2 adsorption on Fe_4/Al_2O_3, the CO_2 adsorption on Fe_3Zn/Al_2O_3 enhances the stability of P1. As shown in Tables 1 and 3, the stability difference of tetrahedral and planar configuration varies according to contribution from the CO_2-metal and metal-support interaction, which correlates with the electron transfer and the charge redistribution in the clusters. For cluster adsorption, the tetrahedral configuration is stabilized more,

Downloaded by CORNELL UNIV on June 23, 2012 | http://pubs.acs.org
Publication Date (Web): December 3, 2010 | doi: 10.1021/bk-2010-1056.ch013

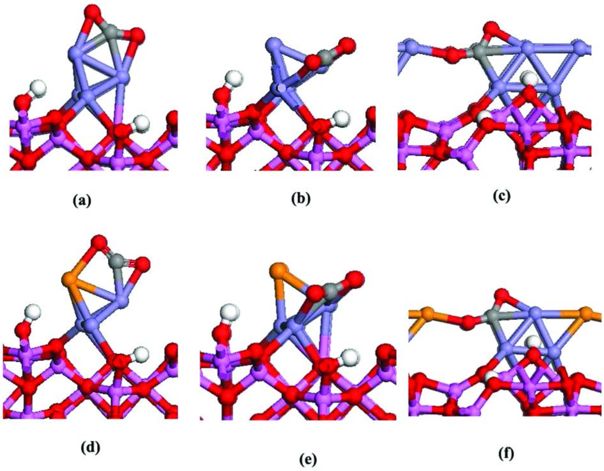

Figure 3. CO_2 adsorption configurations on γ-Al_2O_3(110) supported Fe_4 and Fe_3Zn. (a) T1,(b) T2 and (c) P1 for Fe_4; (d) , (e) , and (f) correspond the structures for Fe_3Zn.

Table 3. Energies (eV) and structural parameters (bond distance in Å and angles in °) for CO_2 adsorbed on Fe_4/γ-Al_2O_3, Fe_3Zn/γ-Al_2O_3 system

	Model	E_{bind}	E_{rel}	ΔE_{ad}	$C\text{-}O_a$	$C\text{-}O_b$	$O_a\text{-}C\text{-}O_b$
Fe_4/Al_2O_3	T1	-11.97	0	-1.16	1.26	1.26	139.2
	T2	-11.53	0.44		1.26	1.24	139.7
	P1	-11.76	0.21		1.28	1.30	125.0
Fe_3Zn/Al_2O_3	T1	-8.85	0.0	-0.76	1.24	1.26	140.4
	T2	-9.10	-0.25		1.26	1.26	138.5
	P1	-9.74	-0.89		1.27	1.30	129.4

due to multiple interactions between cluster and surface acidic and basic sites, than the planar configuration. On the other hand, CO_2 adsorption stabilizes the planar configuration to a greater extent than the tetrahedral cluster.

C. The Synergetic Effect

The adsorption and activation of CO_2 are determined by the properties of the metal and support surfaces. In the present study, we used the same support surface and examined the effect of a second metal component on the cluster stability as well as its activity toward CO_2 adsorption and activation. Our results indicate that the cluster may adopt different configurations as the composition varies. For example, the supported Fe_4 will be in a tetrahedral form whereas the Fe_3Zn prefers a planar configuration. The γ-Al_2O_3 support increases the energy difference between tetrahedral and planar Fe_4 clusters but reduces the difference for Fe_3Zn. We point out the tetrahedral is the more stable one for Fe_4 whereas the planer is more stable in the case of Fe_3Zn.

The strong support-metal interaction causes significant charge redistribution in the supported metal clusters, changing from Fe^0 in the free cluster to $Fe^{\delta+}$ and $Fe^{\delta-}$ sites in the supported cluster. The multiple $Fe^{\delta+}$ and $Fe^{\delta-}$ sites, derived from the strong metal-support interaction, led to high activity toward CO_2 adsorption. Furthermore, CO_2 adsorption led to oxidation of all Fe atoms in the cluster. The synergy of the metal-metal, metal-support interaction and CO_2-metal interaction is clearly observed by following the change of catalyst morphology and charge states of metal atoms.

In the isolated metal cluster, a uniform and low polarized configuration is energetically favored. This is shown in the isolated tetrahedral Fe_4 cluster. When Zn is introduced and substitutes one of the Fe atoms, the cluster favors the planar rhombic structure. In this case, metal-metal interaction plays a key role in determining the cluster structure.

When the cluster adsorbs on the surface, the metal-support interaction becomes important. In this case, the nature of the Al_2O_3 surface plays an important role. As both acidic and basic sites coexist on the surface, the cluster can form multiple bonds with available surface sites. A strong binding energy of the cluster is generally accompanied by a significant electron transfer from cluster to surface. The positively charged cluster will then undergo a redistribution of charges, generating $Fe^{\delta+}$ and $Fe^{\delta-}$ sites. These $Fe^{\delta+}$ and $Fe^{\delta-}$ sites not only stabilize the charged cluster but also promote CO_2 adsorption and activation.

The stability difference, indicated by the binding energy difference between the tetrahedral configuration and the planar configuration (i.e., the relative energy E_{rel} in Tables 1 and 3), is plotted in Fig. 4 for all the structures. These energy differences are referenced to the corresponding tetrahedral structure. The positive one corresponds to the case where the tetrahedral is favorable and negative that the planar structure is more stable. We divided the differences into three contributions. The first contribution is the intrinsic difference, determined by the metal-metal interaction in the free clusters, as shown in Table 1. The second contribution originates from the cluster-support binding strength and the third from CO_2 adsorption. Each contribution has different effects on the cluster stability and charge property in different situations. For example, the strong cluster-surface interaction enhances the stability of the tetrahedral Fe_4 configuration and generates the $Fe^{\delta+}$ and $Fe^{\delta-}$ sites within the cluster. This effect is reflected by the peak values in the energy difference plots in Fig. 4. On the other hand, the CO_2-cluster-surface interaction stabilizes the planar cluster configuration and contributes to the oxidation of the Fe atoms in the cluster. As shown in Fig. 4, the stability differences for Fe_4 related configurations are all above zero, indicating that the tetrahedral configurations are energetically

Downloaded by CORNELL UNIV on June 23, 2012 | http://pubs.acs.org
Publication Date (Web): December 3, 2010 | doi: 10.1021/bk-2010-1056.ch013

Downloaded by CORNELL UNIV on June 23, 2012 | http://pubs.acs.org
Publication Date (Web): December 3, 2010 | doi: 10.1021/bk-2010-1056.ch013

Table 4. Atomic charges for CO_2 adsorbed on $Fe_4/\gamma\text{-}Al_2O_3$ and $Fe_3Zn/\gamma\text{-}Al_2O_3$

	Tetrahedral (T1)			Planar (P1)	
	Fe_4	Fe_3Zn		Fe_4	Fe_3Zn
Fe (-O3c)	0.24	0.16	Fe	0.24	0.04
Fe (-Al4c)	0.14	0.26	Fe (top)	0.24	0.40
Fe (-O2c)	0.30	0.25	Fe	0.48	0.43
Fe or Zn (top)	0.30	0.21	Fe or Zn (top)	0.32	0.33
Cluster total	0.99	0.88		1.28	1.20
CO_2 total	-0.73	-0.68		-1.04	-1.02

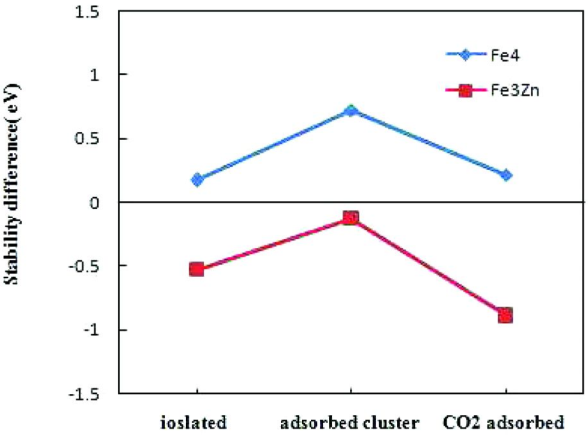

Figure 4. Binding energy difference between the tetrahedral configuration and the planar configuration of Fe_4 and Fe_3Zn clusters.

favorable over the planar structures in the isolated state, the adsorbed state and the CO_2 adsorbed state. For Fe_3Zn, the stability differences are all negative, implying the planar configuration is more favorable.

We would point out that Zn substitution in the Fe cluster changes its morphology in both the isolated state and the adsorbed state at the interface. The morphological change of the supported cluster in turn modifies the electronic structure and activity of the supported catalyst. These modifications can be exploited to improve the catalyst performance by tuning the composition of the metal catalyst and the surface properties of the support.

Conclusions

Periodic DFT slab calculations were carried out to study the Fe_4 and Fe_3Zn clusters supported on hydroxylated $\gamma\text{-}Al_2O_3(110)$ surface as well as CO_2 adsorption on these clusters. We showed that incorporation of Zn changes the cluster morphology and electronic structures. In the isolated state, the cluster prefers the least polarized structure. The strong interaction with the support induces a strong electron transfer from cluster to the support, accompanied by a significant redistribution of charge within the cluster. Consequently, active $Fe^{\delta+}$ and $Fe^{\delta-}$ sites are created for CO_2 adsorption. The Fe_4 cluster favors the tetrahedral configuration in both the isolated and the supported form as well as when CO_2 is adsorbed. In contrast, the Fe_3Zn cluster prefers a planar configuration in both isolated and adsorbed states as well as CO_2 adsorbed state. The metal-metal, metal-support and CO_2-metal-support interactions all contribute to the stability of the adsorption system. We showed that the strength of these interactions can be controlled by tuning the composition of the catalyst, providing a promising means to improve catalyst performance.

Downloaded by CORNELL UNIV on June 23, 2012 | http://pubs.acs.org
Publication Date (Web): December 3, 2010 | doi: 10.1021/bk-2010-1056.ch013

Acknowledgments

This work is supported in part by the Illinois Clean Coal Institute. We acknowledge the support of the Molecular Science Computing Facility in the William R. Wiley Environmental Molecular Science Laboratory (EMSL), located at Pacific Northwest National Laboratory (PNNL).

References

1. Halmann, M. M.; Steinberg, M. *Greenhouse Gas Carbon Dioxide Mitigation: Science and Technology*; CRC Press: Boca Raton, FL, 1999.
2. Song, C. S. *Catal. Today* **2006**, *115*, 2.
3. Bell, T.; Gates, B. C.; Ray, D. Basic Research Needs: Catalysis for Energy; PNNL-17214; U.S. Department of Energy: Washington, DC, 2007. http://www.sc.doe.gov/bes/reports/files/CAT_rpt.pdf.
4. Dorner, R. W.; Hardy, D. R.; William, F. W.; Davis, B. H.; Willauer, H. D. *Energy Fuels* **2009**, *23*, 4190.
5. Zhang, Y.; Jacobs, G.; Sparks, D. E.; Dry, M. E.; Davis, B. H. *Catal. Today* **2002**, *71*, 411.
6. Kim, H. S.; Kim, T. W.; Koh, H. L.; Lee, S. H.; Min, BR *Appl. Catal., A* **2005**, *280*, 125.
7. Sathiro, M.; Takeuchi, M.; Watanabe, T. *Pergamon* **1997**, *38*, S403.
8. (a) Tang, Q. L.; Hong, Q. J.; Liu, Z. P. *J. Catal.* **2009**, *263*, 114. (b) Arena, F.; Italiano, G; Barbera, K.; Bonura, G.; Spadaro, L.; Frusteri, F. *Catal. Today* **2009**, *143*, 80.
9. Arena, F.; Barbera, K.; Italiano, G; Bonura, G.; Spadaro, L.; Frusteri, F. *J. Catal.* **2007**, *249*, 185.
10. Guo, X.; Mao, D.; Lu, G.; Wang, S.; Wu, G. *J. Catal.* **2010**, *271*, 178.
11. Choi, Y.; Futagami, K.; Fujitani, T.; Nakamura, J. *Appl. Catal., A* **2001**, *208*, 163.
12. (a) Ovesen, C. V.; Clausen, B. S.; Schiøtz, J.; Stoltze, P.; Topsøe, H.; Nørskov, J. K. *J. Catal.* **1997**, *168*, 133. (b) Hadden, R. A.; Sakakini, B.; Tabatabaei, J.; Waugh, K. C. *Catal. Lett.* **1997**, *44*, 145. (c) Topsøe, N. Y.; Topsøe, H. *J. Mol. Catal. A: Chem.* **1999**, *141*, 95.

13. Anderson, J. R.; Boudart, M. *Catalyst: Science and Technology*, Vol. 1; Springer-Verlag: Berlin, Heidelberg, 1984.
14. Wang, J.; Funk, S.; Burghaus, U. *Catal. Lett.* **2005**, *103*, 219.
15. Krishnamoorthy, S.; Li, A. W.; Iglesia, E. *Catal. Lett.* **2002**, *80*, 77.
16. Li, S. Z.; Li, A. W.; Krishnamoorthy, S.; Iglesia, E. *Catal. Lett.* **2001**, *77*, 197.
17. Kishan, G.; Lee, M. W.; Nam, S. S.; Choi, M. J.; Lee, K. W. *Catal. Lett.* **1998**, *56*, 215.
18. Sai Prasad, P. S.; Bae, J. W.; Jun, K. W.; Lee, K. W. *Catal. Surv. Asia* **2008**, *12*, 170.
19. Freund, H. J.; Messmer, R. P. *Surf. Sci.* **1986**, *172*, 1.
20. Ding, X.; De Rogatis, L.; Vesselli, E.; Baraldi, A.; Comelli, G.; Rosei, R.; Savio, L.; Vattuone, L.; Rocca, M.; Fornasiero, P.; Ancilotto, F.; Baldereschi, A.; Peressi, M. *Phys. Rev. B* **2007**, *76*, 195425.
21. Rodriguez, J. A. *Langmuir* **1988**, *4*, 1006.
22. Kakumoto, T.; Watanabe, T. *Catal. Today* **1997**, *36*, 39.
23. (a) Pan, Y.-x.; Liu, C.-j.; Ge, Q. *Langmuir* **2008**, *24*, 12410. (b) Pan, Y.-x.; Liu, C.-j.; Wiltowski, T. S.; Ge, Q. *Catal. Today* **2009**, *24*, 68. (c) Pan, Y.-x.; Liu, C.-j.; Ge, Q. *J. Catal.* **2010**, in press.
24. Digne, M.; Sautet, P.; Raybaud, P.; Euzen, P.; Toulhoat, H. *J. Catal.* **2004**, *226*, 54.
25. Kresse, G.; Hafner, J. *Phys. Rev. B* **1993**, *48*, 13115.
26. Kresse, G.; Furthmueller, J. *Phys. Rev. B* **1996**, *54*, 11169.
27. Kresse, G.; Joubert, D. *Phys. Rev. B* **1999**, *59*, 1758.
28. Blöchl, P. E. *Phys. Rev. B* **1994**, *50*, 17953.
29. Perdew, J. P.; Burke, K.; Ernzerhof, M. *Phys. Rev. Lett.* **1996**, *77*, 3865.
30. Monkhorst, H. J.; Pack, J. D. *Phys. Rev. B* **1976**, *13*, 5188.
31. Bader, R. F. W. *Acc. Chem. Res.* **1985**, *18*, 9.
32. Henkelman, G.; Arnaldsson, A.; Jonsson, H. *Comput. Mater. Sci.* **2006**, *36*, 354.

Downloaded by CORNELL UNIV on June 23, 2012 | http://pubs.acs.org
Publication Date (Web): December 3, 2010 | doi: 10.1021/bk-2010-1056.ch013

Downloaded by UNIV OF GUELPH LIBRARY on June 23, 2012 | http://pubs.acs.org
Publication Date (Web): December 3, 2010 | doi: 10.1021/bk-2010-1056.ch014

Chapter 14

CO_2 Adsorption on Porous Materials: Experimental and Simulation Study

Jun Hu and Honglai Liu*

State Key Laboratory of Chemical Engineering and Department of Chemistry, East China University of Science and Technology, Shanghai 200237, China
***hlliu@ecust.edu.cn**

Removal and sequestration of CO_2 from flue gas has been proposed as one of the most reliable solutions to mitigate globe greenhouse emissions. Adsorption technology based on porous adsorbent is known to be one of the most efficient processes for the CO_2 capture from flue gas. The key issue of this technology is to find the adsorbent with high adsorption capacity and selectivity for CO_2. In this chapter, both the experimental and the computer simulation works about the CO_2 adsorption behavior on porous materials in our laboratory were introduced. In the experimental works, the mesoporous materials such as MCM-41 and SBA-15 were selected as the fundamental adsorbent. After surface modification by aminosilane, the amine groups became active centers and the CO_2 adsorption capacity was obviously increased due to the chemisorption. It is shown that the dual amine groups of AEAPMDS had better effect on CO_2 adsorption than the single amine group of APTS. The best CO_2 adsorption capacity of MCM-41-AEAPMDS was 2.20 $mmol \cdot g^{-1}$ at room temperature. Another effective way was incorporation metal Mg into the mesoporous materials. By various impregnating or doping methods, such as the co-condensation, the dispersion with the enhancement of Al^{3+} or amine, and the ionic exchange, a suitable amount of Mg^{2+} can be successfully introduced into MCM-41 and SBA-15, which effectively increased the CO_2 adsorption capacity. Different pore structures had their corresponding optimized methods, the real reason behind was the highly dispersed MgO state in the channels. The best CO_2 adsorption capacities of Mg-Al-SBA-15-D1 and Mg-EDA-MCM-41-D10 were about 1.35 mmol·g^{-1}. In the simulation works, some novel porous materials such as the micro/mesoporous composite, the covalent organic frameworks, the metal organic framework and the zeolitic imidazolate frameworks were selected as the potential adsorbents for the CO_2 capture. The CO_2 adsorption behavior of the zeoilte of MFI, the mesoporous MCM-41 and the micro/mesoporous composite of MFI/MCM-41 were simulated and compared. It is revealed that the micro/mesoporous composite had better performances on the CO_2 adsorption capacity and selectivity at high pressure, as well as the diffusion performance.

Downloaded by UNIV OF GUELPH LIBRARY on June 23, 2012 | http://pubs.acs.org
Publication Date (Web): December 3, 2010 | doi: 10.1021/bk-2010-1056.ch014

Introduction

The concentration of the greenhouse gas CO_2 has increased by 30% in the atmosphere since the late 19th century. This has caused a number of severe environmental impacts. The rapidly increasing of the CO_2 concentration is largely due to the emission of vast amounts of flue gases by industrial and utility power generation plants using carbon-based fossil fuels. The goal of stabilization of the CO_2 concentration below 450 ppmv, the limitation of maintaining the normal climate, demands the CO_2 emission should decrease 50~60% until 2050 and 80% until 2100, respectively (*1–3*). Improving the efficiency of energy utilization and increasing the use of low-carbon energy sources are considered to be the most promising ways to reduce CO_2 emission. However, it is likely that the world will continue relying on fossil fuels as the primary energy supply well during the 21st century. CO_2 capture and sequestration has been received significant attention and recognized as an important option for the reduction of CO_2 emission.

Extensive studies have been carried out in worldwide to develop the cost-effective techniques for CO_2 capture and separation (*4*). According to the DOE report of *Advances in CO_2 capture technology*, the solvent absorption, solid adsorption, membrane separation and cryogenic distillation would be the promising technologies. The costs for CO_2 capture and separation are estimated to make up about three-fourths of the total costs of ocean or geologic storage sequestration. Preliminary analysis has suggested that if the CO_2 separation and sequestration is industrialized, an economically cost less than 10 US$ per ton of CO_2 avoided from stationary sources is needed. Chemical absorption (conventional MEA aqueous solution) is today's reference process; it requires an energy cost ranging from 4.2 to 4.8 MJ.kg^{-1} CO_2 (*5*). Based on it, with existing technology, about 20 to 30% of the energy produced by a power plant would be needed to recover the CO_2 from the amine solution in absorption technology (*6*). This energy penalty makes for bad economics. Adsorption is another competitive potential technique for CO_2 separation. The recent studies on the pressure/vacuum swing adsorption (PSA/VSA) for CO_2 capture have highlighted its potential (*7–9*). Ho et al. (*9*) recently examined the economic feasibility of

PSA/VSA for recovering CO_2 from post-combustion power plant flue gas by using commercial adsorbent 13X, which has a working capacity of 2.2 mol.kg^{-1} and CO_2/N_2 selectivity of 54. Their analysis showed that the capture cost of CO_2 by using vacuum desorption can be reduced to US$51 per ton of CO_2 avoided and is comparable in cost to CO_2 capture using conventional MEA absorption of US$49 per ton of CO_2 avoided. The capture cost can be even reduced to US$30 per ton of CO_2 avoided if the adsorbent has a working capacity of 4.3 mol.kg^{-1} and a CO_2/N_2 selectivity of 150. Therefore, to realize the industrialization of the adsorption technology, the crucial is to find adsorbents with high CO_2 adsorption capacity and CO_2/N_2 selectivity, as well as to optimize the adsorption technical process. To achieve this object, computational simulation can play an important role, which can be adopted to design the structure of adsorbents at microscopic level, and to optimize the technical process at macroscopic level.

Downloaded by UNIV OF GUELPH LIBRARY on June 23, 2012 | http://pubs.acs.org
Publication Date (Web): December 3, 2010 | doi: 10.1021/bk-2010-1056.ch014

1.1. Zeolite Adsorbents

Zeolites such as 13X, 5A, 4A, are widely used as adsorbents for the removal of CO_2 (*10–16*). In the flue gas, the CO_2 concentration is about 10-15%, and the CO_2 partial pressure is relatively lower. For this reason, PSA/VSA is usually adopted due to their high efficiency and low energy consuming (*7–9*, *17*, *18*). Meanwhile, Temperature Swing Adsorption (TSA) process on zeolites has been studied as well (*19*, *20*). Clausse et al. (*19*) obtained a volumetric productivity of 37 kg.m$^{-3}{}_{ads}\cdot$h and a specific-heat consumption of 6 MJ.kg$^{-1}{}_{CO2}$ at their laboratory scale and 4.5 MJ.kg$^{-1}{}_{CO2}$ for the adiabatic estimate, which is in the same order of magnitude as those obtained industrially with the reference MEA amine process. These results are promising because their process was not optimized yet and the scale-up on an industrial version will involve a reduction in specific-heat consumption. Many researches have shown that CO_2 is more strongly adsorbed on metal modified zeolite such as M-ZSM-5 (M = Li, Na, Ca, Ba, Sr) (*21–23*), MX or MY (M = Na, Ca, Ba) (*24–26*) due to the quadrupolar moment and acidity of CO_2. Quantum chemistry calculations found that CO_2 undergoes a two-step interaction with the metallic ions. At a low equilibrium pressure linear 1:1 (CO_2 : M^{n+}) adducts are formed; upon increasing the CO_2 equilibrium pressure, the metallic cation coordinates a second CO_2 molecule, forming a 2:1 adducts (*21*).

Although the zeolite adsorbents possess relatively high CO_2 adsorption capacities in numerous cases, the sole presence of micropores also imposes significant limitations on the rapidly declining adsorption ability with increasing temperature and humid.

1.2. Mesoporous Adsorbents

The ordered mesoporous materials that are known as M41S-type mesoporous silica were first synthesized by Mobil (*27*, *28*). The uniform ordered pores and extremely high surface area attracted enormous research interesting, many other ordered mesoporous silica materials templated by various surfactant micelles have been developed, such as the families of SBA-*n* produced by Santa Barabara University (*29*, *30*), FDU-*n* produced by Fudan University (*31*), KIT-*n* produced

In Advances in CO2 Conversion and Utilization; Hu, Y.;
ACS Symposium Series; American Chemical Society: Washington, DC, 2010.

by Korea Advanced Institute of Science and Technology (*32*) and anionic surfactant templated mesoporous silica (AMS) (*33*). Compared to the zeolites, the high surface area, large pore volume and ordered pores of 2-50 nm in the mesoporous materials obviously improve the gas diffusion and transport property. Recently, there has been increasing interest in the investigation of mesoporous materials in CO_2 adsorption.

It has been demonstrated that the CO_2 adsorption over pure silica mesoporous materials is mainly physical adsorption. Although the mesoporous silica materials have large surface area, lacking of strong interactions between CO_2 and silica surfaces, the CO_2 adsorption capacity and CO_2/N_2 selectivity show a limitation. The CO_2 adsorption capacity of pure mesoporous silica MCM-41 and MCM-48 are about 0.7-0.9 $mmol.g^{-1}$, respectively (*34*). The CO_2 adsorption capacity can have obvious increment with increasing pressure, when the pressure increased to 3 MPa, the pure silica SBA-15 showed its capacity of 7 $mmol.g^{-1}$ (*35*).

The surface modification of mesoporous silica with functional groups is proved to be a reasonable approach to increase the CO_2 adsorption capacity by introducing specific interactions with CO_2 (*36*). Compared to the high steric hindrance in the microporous silica, the large pore volume and pore size of mesoporous silica materials appear to be easy for surface modification with aminosilane. In addition, the high density of silanol groups on the mesoporous silica pore walls is beneficial to the introduction of functional groups (*37*). Many investigations on aminosilane (*38–40*) or polymer-containing amino groups (*41*) modified silica have been done.

Modifications of the silica surface can be made in chemical tethering or physical adsorption. Surface coatings or pore fillings have demonstrated the highly selective uptake of CO_2 (*42–46*), however, the longevity of the physically modified mesoporous silicas is questionable because of the potential loss of amines (*46*). Among various aminosilanes, the n-propylamine modification has been particularly popular (*38–40*, *47–50*). Different types of structures of mesoporous silica support materials, such as MCM-41 (*34*, *39*, *40*), MCM-48 (*37*, *51*), SBA-15 (*49*, *52*) and mesocaged silica materials (*53*) have been employed to study the optimum modification conditions and their CO_2 adsorption capacities. Although the CO_2 adsorption capacity of the most aminosilane modified mesoporous materials is no more than 2.5 $mmol.g^{-1}{}_{ads}$, lower than that of zeolite type adsorbent (e.g. 4.7 $mmol.g^{-1}$ of 13X), the high selectivity in CO_2/N_2 separation indicates the promise of these molecularly engineered materials for adsorptive separation of CO_2.

To improve the CO_2 adsorption capacity, another important type of amino group compound, polyethylenimine (PEI), has been impregnated into the mesoporous silica (*41*, *53*, *54*). PEI has branched chains with multiple amine groups as CO_2 adsorption sites, the CO_2 adsorption capacity is significantly increased after loading PEI, almost 8-10 times as high as that of pure mesoprous silica. The increment of the CO_2 adsorption capacity comes from not only the chemical affinity between PEI and CO_2, but also the synergetic effect of the confined mesoporous environment (*41*). In addition, the adsorption of N_2 on the PEI-impregnated mesoporous materials is negligible; therefore, the selectivity of CO_2/N_2 increases obviously. A systematic comparison (*55*) of

Downloaded by UNIV OF GUELPH LIBRARY on June 23, 2012 | http://pubs.acs.org
Publication Date (Web): December 3, 2010 | doi: 10.1021/bk-2010-1056.ch014

Downloaded by UNIV OF GUELPH LIBRARY on June 23, 2012 | http://pubs.acs.org
Publication Date (Web): December 3, 2010 | doi: 10.1021/bk-2010-1056.ch014

various mesoporous silica support materials for PEI-impregnation showed that the materials possessing 3-D mesopores with large pore volume, such as KIT-6, were more effective than MCM-41, MCM-48 or SBA-15 for the CO_2 capture. The highest CO_2 adsorption capacity of PEI-KIT-6 was 3.07 $mmol.g^{-1}{}_{ads}$.

With the assistance of in situ IR spectroscopy, the chemical and the physical CO_2 adsorption mechanisms on the amine modified mesoporous materials have been revealed. Several authors have examined the type of enhanced CO_2 capacity of amine-modified materials in the presence of water (*41*, *56*, *57*). The carbamate formed during the reaction of CO_2 with the (primary or secondary) amine group can further react with CO_2 and H_2O to form a bicarbonate group. In the presence of water, one mole of amines can theoretically chemisorb one mole of CO_2. In the absence of water, this ratio is shifted to two moles of amine to one mole of CO_2. Therefore, the presence of water in the flue gas will be an assistant to the enhancement of the CO_2 adsorption on the amine modified mesoporous materials (*56*).

1.3. Computer Simulation for CO_2 Adsorption

The molecular simulation plays a crucial role in understanding, characterizing, and developing adsorption systems. Molecular simulation techniques including Monte Carlo (MC) and molecular dynamics (MD) are widely use to study the gas adsorption on porous materials and the gas diffusion process in the confined space.

Zeolites are the three-dimensional microporous materials with aluminosilicate crystalline framework. The common structure forms are based on the primary building units (PBUs) of TO_4 tetrahedra, where T is an aluminum or silicon atom; and the secondary building units (SBUs), such as four rings (4R), five rings (5R), six rings (6R), eight rings (8R), double four rings (D4R), double six rings (D6R), double eight rings (D8R). These SBUs assembled together give rise to a large variety of different zeolites (*58*). Extensive simulation works have been carried out on the adsorption and separation of gas mixtures on zeolites, including the zeolite structure prediction, the adsorbed gas molecules states, dynamics, and the function of metal species in zeolites (*59–61*). The metal impregnated zeolites have shown a great potential in gas adsorption and seperation. The CO_2/N_2 selectivity in a flue gas can be enhanced greatly on Na-ZSM-5 due to the quadrupolar moment of CO_2 (*62*). Compared with the experimental results on the pure silica MFI, the adsorption capacity of CO_2, N_2 and H_2 on dehydrated Na-4A were enhanced, and the strong selectivity of CO_2 over both N_2 and H_2 were observed (*63*).

Mesoporous materials also show great potential in CO_2 capturing. Seaton et al. (*64*) used one pore model to represent the structure of MCM-41, and found the adsorption of CO_2 is different from that of methane and ethane, which may attribute to the electrostatic interactions between CO_2 and adsorbents, Zhuo et al. (*65*) systematically studied the adsorption performance of CO_2 on MCM-41, and the selectivity of CO_2/N_2, CO_2/CH_4. Garcia-Sanchez et al. (*66*) simulated the effect of Si/Al ratio and Na_+ ion on the adsorption isotherm of CO_2.

Novel hybrid inorganic-organic porous materials have been recently developed named metal organic framework (MOF), covalent organic framework

(COF) and zeolitic imidazolate frameworks (ZIF). Composed of light elements, COFs have lower density than MOFs. CO_2 storage in various structures of 3D, 2D and 1D of COFs were simulated and the extremely high capacity of COF-105 and COF -108 was observed (*67*). Recently, Zhong et al. (*68*, *69*) systematically simulated the performance of CO_2 adsorption on MOFs of MOF-5, CuBTC; COFs of COF-8, COF-10, as well as ZIFs of ZIF-68 and ZIF-69. The simulation and experimental results were a close match; however, the selectivity of CO_2/H_2 on CuBTC deviated from the ideal adsorbed solution theory (IAST). Johnson et al. (*70*) simulated geometrical structures of ZIF-68 and ZIF-70, and found that the simulation and experimental results for the N_2 adsorption isotherms coincided with each other. In contrast, simulations over-predicted the amount of CO_2 adsorbed. Jiang et al. (*71*, *72*) compared the performance of CO_2 adsorption and the CO_2/CH_4 selectivity on MFI, C_{168}, IRMOF-1. The separation performance of mixtures of CO_2/H_2, CO_2/CH_4, and CO_2/N_2 were also simulated on the Na^+ doping rho-ZMOF. By switching on/off the charge model of framework, they found the charge of framework highly heightened the CO_2 adsorption capacity.

In this chapter, both the experimental and the computer simulation works in our laboratory are demonstrated to analyze the CO_2 adsorption behavior on porous materials. The former concentrates on the effect of mesoporous surface modification by aminosilane and metal ions, while the later mainly explores the potential adsorbents.

Downloaded by UNIV OF GUELPH LIBRARY on June 23, 2012 | http://pubs.acs.org
Publication Date (Web): December 3, 2010 | doi: 10.1021/bk-2010-1056.ch014

Synthesis of Porous Silica Adsorbents and Its Application to CO_2 Adsorption

2.1. Experimental Section

2.1.1. Synthesis of Silica MCM-41 and SBA-15

The synthesis of MCM-41 and SBA-15 were prepared by the hydrothermal method described elsewhere (*28*, *29*). In brief, the structure directing template of $C_{16}H_{33}(CH_3)_3NBr$ (CTAB) for MCM-41 (or pluronic $PEO_{20}PPO_{70}PEO_{20}$ (P123) for SBA-15) was dissolved in distilled water that was followed by addition of the pH controlling agent of ethylamine (EA) at pH = 10-11 (or hydrochloric acid (HCl) at pH = 1-1.5,). Then silica source of tetraethyl orthosilicate (TEOS) was added slowly with strong stirring. The whole slurry was then transferred into an autoclave and aged for 24-48 h at 373 K (or 393 K). The products were then calcined in ambient air at 823 K for 5 h, with a heating rate of 2 $K.min^{-1}$.

2.1.2. Amine Modification

Amine modification details were described in the reference (*40*), in brief, MCM-41 or SBA-15 was mixed with γ-(aminpropyl)-triethoxysilane (APTS) or [N-(β-aminoethyl)-γ-amino propyl] trimethoxysilane (AEAPMDS) by strong stirring in dry toluene. After refluxed at 343 K for 18 h, the products were obtained and denoted as APTS-MCM-41, AEAPMDS- MCM-41, APTS- SBA-15 and AEAPMDS- SBA-15, respectively.

2.1.3. Magnesium Modification

The Mg modified methods for the silica mesoporous materials can be divided into two types, doping and impregnating. For the former, it is usually by means of co-condensation; and for the latter, it includes dispersion, ionic exchange.

In the case of co-condensation, the synthesis procedure of Mg doping material was similar with that of pure silica mesoporous materials, except the magnesium acetate ($MgAC_2$) salt was added together with the silica precursor of TEOS.

In the Mg impregnating procedures, the pure silica mesoporous powder MCM-41 and SBA-15 was produced beforehand, respectively. In the case of dispersion, the powder of MCM-41 or SBA-15 was immersed in the $MgAC_2$ solution, and a certain amount of urea, APTS or ethyl diamine (EDA) was added to adjust the pH value of the surface microenvironment of the powder, respectively. Besides, the synergic effect of metal Al was also investigated by preparing the samples as immersing the silica mesoporous powder in the $AlCl_3$ solution (named Al-SBA-15) before $MgAC_2$.

Moreover, in the case of ionic exchange, Na/Al-MCM-41 and Na/Al-SBA-15 composites had been obtained by the co-condensation procedure beforehand, respectively. The powder of Na/Al-MCM-41 or Na/Al-SBA-15 was immersed in the $MgAC_2$ solution under ultrasonic at 313 K for 24 h.

The final products were denoted as Mg-(Al)-MCM-41(SBA-15)-X*n* or Mg-SBA-15-C*n*, respectively, where *n* is the molar ratio of n_{Si}:n_{Mg}. X represents different methods, C, co-condensation; D, dispersion; and I, ionic exchange, respectively. (Al) is just for the dual dispersion methods.

2.1.4. Characterization

The powder X-ray diffraction (XRD) patterns of MCM-41 and SBA-15 before and after modification were recorded on the D/Max2550 VB/PC spectrometer using Cu K_α radiation at both the low angle range (from 0.6 ° to 10 °) and the wide angle range (from 1° to 50 °). ^{29}Si NMR spectra were recorded on the Bruker- Avance-500 NMR spectrometer with special width of 39682Hz. The thermal gravimetric analyses (TGA) were carried out by the Perkin-Elmer-Pris thermal gravimeter, and the differential thermal gravimetric analyses (DTGA) were calculated based on its TGA curve.. The temperature range was 303 to 973 K with heating rate of 20 $K.min^{-1}$ in 60 $mL.min^{-1}$ N_2 flow. Nitrogen adsorption measurements were conducted at 77.4 K on the ASAP-2020 sorptionmeter. The sample was activated for more than 10 h at 373 K before measuring. The BET specific surface area and pore size distribution were calculated based on the BET and BJH model.

Downloaded by UNIV OF GUELPH LIBRARY on June 23, 2012 | http://pubs.acs.org
Publication Date (Web): December 3, 2010 | doi: 10.1021/bk-2010-1056.ch014

Downloaded by UNIV OF GUELPH LIBRARY on June 23, 2012 | http://pubs.acs.org
Publication Date (Web): December 3, 2010 | doi: 10.1021/bk-2010-1056.ch014

2.1.5. CO_2 Adsorption

The adsorption and desorption CO2 performance at different pressure was measured on ASAP-2020 sorptionmeter. All samples were activated at 373 K for more than 10 h before measurement.

2. 2. Result and Discussion

2.2.1. The Effect of Amine Surface Modification on CO_2 Adsorption

The XRD patterns of the samples before and after surface modification are shown in Figure 1. The pattern (a) of MCM-41 in Figure 1(A) is the typical feature of hexagonal mesoporous structure. After surface modification, the pattern (b) of APTS-MCM-41 and the pattern (c) of AEAPMDS-MCM-41 have the similar shapes; however, the peaks have a lower intensity and slightly higher 2θ. All these results indicate that the aminosilane-grafted MCM-41 still have the original hexagonal structure, but have less ordered and smaller pore size.

The XRD patterns of SBA-15 serial samples are displayed in Figure 1(B). Significant diffraction peaks in pattern (a-c) suggest that before and after modification, the SBA-15s samples have the typical hexagonal mesoporous structure. Due to the relatively large channels of SBA-15, the pattern (b) of APTS-SBA-15 and the pattern (c) of AEAPMDS-SBA-15 have little change.

The modify reaction between aminosilane and Si-OH on the channel surface is detected by the ^{29}Si-NMR spectrum, take APTS-MCM-41 for an example as shown in Figure 2. The resonances at -60ppm and -68ppm are assigned to the silicon atoms associated with the T^2 and T^3 groups, respectively (T^n = R-Si(OSi)$_n$(OH)$_{3-n}$). The resonance peaks at -100 ppm and -110 ppm are assigned to the Q^3 (isolated silanol) and Q^4 (internal siloxane) silicon environments (Q^n = Si(OSi)$_n$(OH)$_{4-n}$), respectively, which confirms the attachment of the amine group to the silica surface via Si-O-Si linkages. The higher peak of T^2 suggests the two attachment forms of R-Si(OSi)$_2$(OH) is dominated.

The results of TGA weight loss profile of modified MCM-41s and SBA-15s are shown in Figure 3. Besides the first peak in the weight loss rate curve attribute to the water release, the significant weight losses occur when samples are heated from about 333 to 633 K. For AEAPMDS modified samples, having one onset at around 500 K and another at 620 K, there are two peaks on the DTAG curves; while for APTS modified samples, it happens at about 600 K. The thermal stability of each sample in N_2 can then be determined as about 500 K. Besides, the amount of amine loading on APTS-MCM-41, AEAPMDS-MCM-41, APTS-SBA-15 and AEAPMDS- SBA-15 can be estimated as 1.5, 2.9, 1.6 and 2.8 mmol (N) per gram of sorbent, respectively.

The BET surface area, pore volume and average pore size calculated from the nitrogen adsorption isotherms are summarized in Table 1. After modification, the BET surface of APTS-MCM-41 and AEAPMEDS-MCM-41 significantly decrease, as well as the pore volumes reduce to 1/10 of unmodified MCM-41, especially for the later, there are almost no channel surface remained. It is

Downloaded by UNIV OF GUELPH LIBRARY on June 23, 2012 | http://pubs.acs.org
Publication Date (Web): December 3, 2010 | doi: 10.1021/bk-2010-1056.ch014

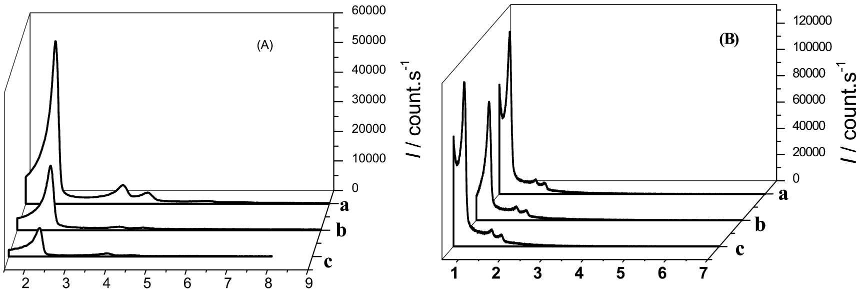

Figure 1. The XRD patterns of mesoporous materials before and after surface modification. (A) MCM-41s, in which the curves (a) MCM-41, (b) APTS-MCM-41, (c) AEAPMDS-MCM-41. (B) SBA-15s, in which the curves (a) SBA-15, (b) APTS-SBA-15, (c) AEAPMDS-SBA-15, respectively.

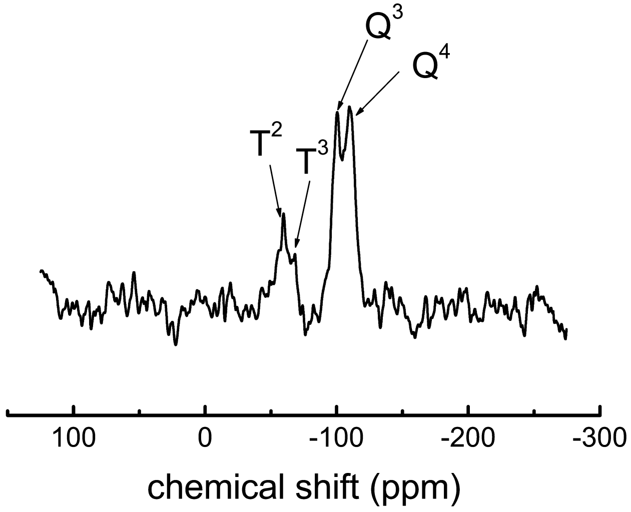

Figure 2. ^{29}Si-NMR spectra of APTS-MCM-41. (Reproduced from the Ref. (40) with permission from Acta Physico-Chimica Sinica)

obviously caused by the amine groups grafted into or even more, blocked the channels.

The BET surface area of unmodified and modified SBA-15 have similar change tendency. Since the pore diameter of SBA-15 is much larger than that of MCM-41, the decrease of surface areas of modified SBA-15 is much smaller. As for the same reason, the pore volume and diameter values of APTS-SBA-15 and AEAPMDS-SBA-15 are almost similar with each other.

Figure 4 show the CO_2 adsorption isotherms of MCM-41 and SBA-15 before and after modification. In Figure 4(A), the amount of CO_2 adsorption on MCM-41 sample as shown in isotherm (a) is 0.67 mmol·g^{-1}, and significantly increase to 1.16 mmol·g^{-1} on APTS-MCM-41 in isotherm (b) and 2.20 mmol·g^{-1} on AEAPMDS-MCM-41 in isotherm (c). In despite of much lower BET surface

Downloaded by UNIV OF GUELPH LIBRARY on June 23, 2012 | http://pubs.acs.org
Publication Date (Web): December 3, 2010 | doi: 10.1021/bk-2010-1056.ch014

area and pore volume of AEAPMDS-MCM-41, it has as twice adsorption amount as APTS-MCM-41 due to the former possessing of two amino groups per aminosilane molecule. The similar results of amine modified mesoporous materials have higher CO_2 adsorption capability also turned out for the SBA-15 samples. As shown in Figure 4(B), the amount of CO_2 adsorption increased from 0.59 $mmol \cdot g^{-1}$ of SBA-15 to 0.96 $mmol \cdot g^{-1}$ of APTS-SBA-15 and 1.27 $mmol \cdot g^{-1}$ of AEAPMDS-SBA-15, respectively.

Each of the CO_2 adsorption isotherms mentioned above has a hysteresis loop. Before modification, the hysteresis loop is caused by the capillary condensation, while after modification it is caused by both the chemisorption and the capillary condensation. Generally, significant physisorption occurs only when pressure is higher than 1 kPa. In Figures 4, the modified samples already have obvious adsorption when the pressure approach to 1 kPa, and their corresponding desorption, especially for AEAPMDS modified materials, don't occur simultaneously as the pressure decreased. Only when the pressure decreases to 20 kPa, significant desorption starts, which indicates the adsorptive CO_2 on amine modified sample are through chemisorption.

MCM-41 and SBA-15 have ordered nano-scale channels and the channels of MCM-41 are smaller than that of SBA-15. According to the Kelvin formula $p = p * e^{-2\gamma V_{\mathrm{m}} / rRT}$, the smaller the pore radius is, the further the capillary condensation occurs, which explains that the amounts of CO_2 adsorption on MCM-41 based materials are higher than that on SBA-15 based materials

2.2.2. *The Effect of Metal Modification on CO_2 Adsorption*

Figures 5 and 6 are the XRD patterns of SBA-15 and MCM-41 before and after magnesium modification by co-condensation method. In the small angle range as shown in Figures 5(A) and 6(A), the calcined Mg-SBA-15-C*n* and Mg-MCM41-C(*n*) composites still preserve three diffraction peaks of hexagonal symmetry when the amount of modified Mg is lower. However, the order of mesoporous structure decrease with increasing amount of modified Mg, finally, the ordered structure collapse. Moreover, the dispersion levels of MgO species in mesoporous channels with different amount of loading Mg are different. The wide angle range XRD patterns of Mg-SBA-15-C*n* composites in Figure 5(B) show that MgO is amorphously dispersed at lower amount of loading Mg and they gradually aggregate to form a crystal phase with increasing the amount of Mg. Since the channels of MCM-41 are narrow, we only added a small amount of Mg to modified MCM-41. From Figure 6(B), MgO amorphously disperse without obvious crystal phase in all samples except the one with *n* (Si/Mg) = 1.

The mesoporous properties such as the surface area, total pore volume and average pore size of Mg-SBA-15-C*n* and Mg-MCM-41-C*n* are demonstrated by the nitrogen adsorption measurements, and summarized in Tables 2 and 3. The introduction of Mg species into SBA-15 and MCM-41 results the decrease of the surface area and total pore volume. When the Mg loading is not too high, because of the highly dispersion of amorphous MgO species or the lattices of Mg-O-Si

Downloaded by UNIV OF GUELPH LIBRARY on June 23, 2012 | http://pubs.acs.org
Publication Date (Web): December 3, 2010 | doi: 10.1021/bk-2010-1056.ch014

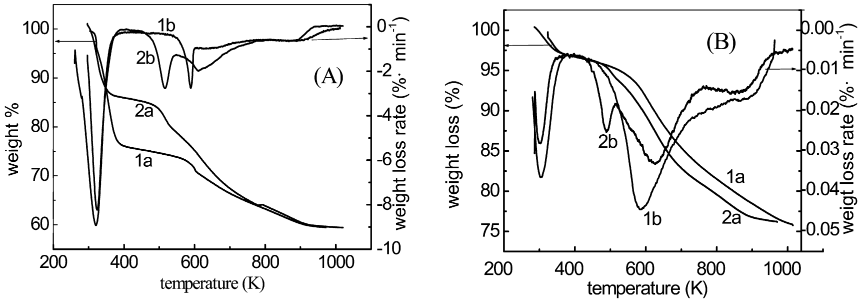

Figure 3. The TGA and DTGA patterns of modified mesoporous materials. (A) MCM-41s and (B) SBA-15s, in which "1" for APTS modified and "2" for AEAPMDS modified; "a" for TGA and "b" for DTGA, respectively.

Table 1. Physicochemical Characteristics of mesopourous materials before and after surface modification.[a] **(Reproduced from the Ref. (*40*) with permission from Acta Physico-Chimica Sinica)**

Samples	S / $m^2 \cdot g^{-1}$	V / $cm^3 \cdot g^{-1}$	D_p / nm
MCM-41	1059	0.68	2.60
APTS-MCM-41	198	0.13	4.50
AEAPMDS-MCM-41	33	0.04	5.20
SBA-15	548	0.95	7.40
APTS- SBA-15	304	0.55	6.70
AEAPMDS- SBA-15	312	0.58	6.68

[a] S: BET surface area; V : pore volume; D_p : pore size.

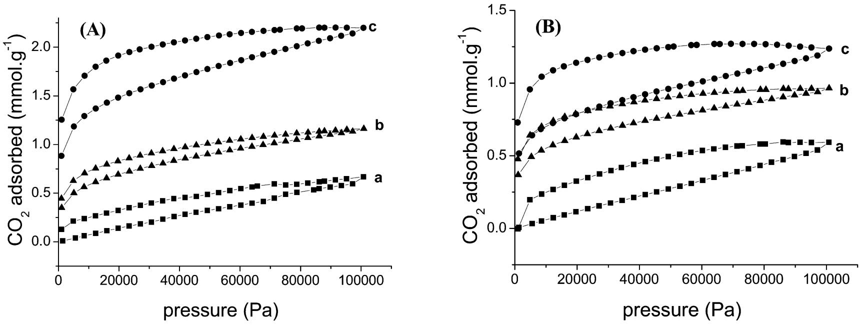

Figure 4. Adsorption and desorption isotherms of CO_2 on mesopourous materials before and after surface modification (A) MCM-41s, (B)SBA-15s, in each (a) pure silica, (b) APTS modified, (c) AEAPMDS modified.

bonding in the wall of the mesoporous materials, the pore properties only have a small reduction. The decrement is enhanced with the increase of amount of Mg loading. Combining the information of the wide angle XRD, the MgO species

Downloaded by UNIV OF GUELPH LIBRARY on June 23, 2012 | http://pubs.acs.org
Publication Date (Web): December 3, 2010 | doi: 10.1021/bk-2010-1056.ch014

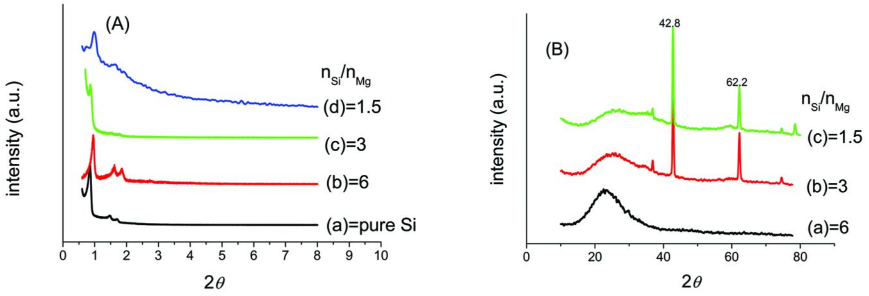

Figure 5. Low-angle (A) and wide angle (B) XRD patterns of Mg-SBA-15-C with different molar ratios.

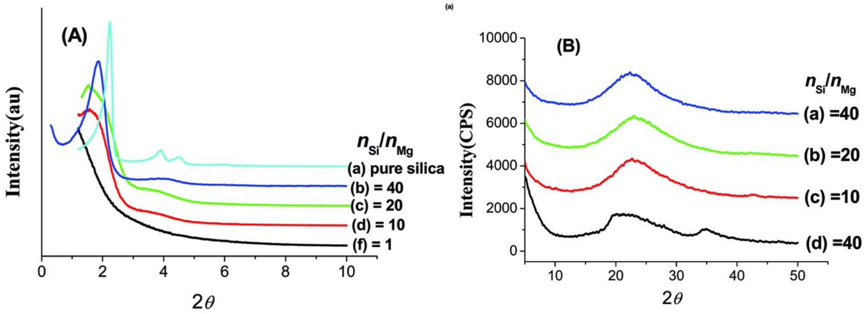

Figure 6. Low-angle (A) and wide angle (B) XRD patterns of Mg-MCM41-C with different molar ratios.

may aggregate together to form the crystals and block the channels, which result the decrease of surface area.

The phenomena of MgO block in the channels of Mg-SBA-15-C1.5 are further confirmed by TEM images. Before modification, the pure silica SBA-15 exhibited uniform parallel channel arrays as shown in Figure 7(A). After modification, unconnected bright dots like dash lines can be observed as shown in Figure7(B), this indicates that Mg-SBA-15-C1.5 still preserve the mesoporous structure of SBA-15, however, the channels have been seriously blocked up, and the diameter of the channels decreased evidently. In some area, the channels are totally obstructed.

Different from the doping modification, the impregnating modification depends much on the diffusion ability of the metal cations, and the interaction between the metal cations and the surface hydroxyls of SBA-15 or MCM-41. Usually, the microenvironment of the surface of silica channels is relative positive charged due to the surface hydroxyls, which makes Mg^{2+} cations difficult to diffuse into the channels and hence may block the entrance of the channels.

To improve the diffusion situation, urea, APTS or EDA has been adopted to modify the microenvironment of the channel surface. Take urea for an example, the effect of amino type groups on the impregnating of Mg into silica channels is shown in schema of Figure 8. Urea molecules can closely attach at the surface of

Downloaded by UNIV OF GUELPH LIBRARY on June 23, 2012 | http://pubs.acs.org
Publication Date (Web): December 3, 2010 | doi: 10.1021/bk-2010-1056.ch014

Table 2. Properties of Mg modified SBA-15 composites by various methods

	n Si / n Mg	*S* $m^2 \cdot g^{-1}$	*V* $cm^3 \cdot g^{-1}$	D_p *nm*	CO_2 $mmol \cdot g^{-1}$
SBA-15	---	773	0.85	7.8	0.42
Mg-SBA-15-C6	6:1	500	0.73	5.5	0.64
Mg-SBA-15-C3	3:1	298	0.53	5.8	0.67
Mg-SBA-15-C1.5	3:2	204	0.37	7.5	0.86
Mg- urea-SBA-15- D2	2:1	708	1.10	5.7	0.86
Mg- urea-SBA-15- D1	1:1	538	0.82	5.6	0.74
Al-SBA-15	---	505	0.76	5.9	0.72
Mg-Al-SBA-15-D1	1:1	235	0.41	5.0	1.35
Mg-Al-SBA-15-I1	1:1	626	0.96	6.7	0.83

channels of SBA-15 or MCM-41 through hydrogen bonding between $-NH_2$ groups of urea and –OH groups on silica surface, which provide a basic environment and ligands for easier diffuse of the Mg^{2+} cations. More importantly, urea can be decomposed into $NH_3 \cdot H_2O$ and CO_2 during the hydrothermal process, which can make Mg species precipitated as $Mg(OH)_2$ on the surface of channels and transformed into MgO homogeneously by later calcination.

As summarized in Table 2, Mg-urea-SBA-15-D2 has much higher surface area than that of all Mg-SBA-15-C*n*. Increasing the amount of modified Mg^{2+}, the pore properties of Mg- urea-SBA-15-D1 have a slight decrease. Anyhow, the Mg species is dispersed very well in the channels in this concentration range. From Table.3, similar results can also be observed for MCM-41 based materials.

Another effective way to improve the dispersion of Mg is to incorporate Al^{3+} into SBA-15 or MCM-41, where Al^{3+} will adopt tetra-coordinated and the unpaired electron defects can enhance Mg^{2+} grafting into the channels. As shown in the small angle XRD patterns of Figure 9(A), after modification, Mg-Al-SBA-15-D1 still held hexagonal structure. However, the surface area, the pore volume and the pore size of Al-SBA-15, Mg-Al-SBA-15-D1 and Al-MCM-41, Mg-Al-MCM-41-D10 decrease as summarized in Table 2 or Table 3, which indicate that Al and Mg species have been both introduced into the channels. The only one broad peak in the wide angle XRD patterns as the insert of Figure 9(A) suggest that the amorphous MgO have been well dispersed, the channels have not been blocked yet after modification.

The idea of ionic exchange to modify the mesoporous SBA-15 or MCM-41 is original from the strategy of the metal modified zeolite. The impregnated Na^+ cations can be easily exchanged with the Mg^{2+} cations by the dispersion method. As shown in Figure 9(B), the calcined product Mg-SBA-15-I1 still preserves ordered hexagonal structure. However, there are several week peaks appeared in the wide angle XRD pattern of the insert, suggesting most MgO oxides are in amorphous phase, while some crystals are formed. Moreover, the Mg^{2+} cations may not only graft on the surface of the channels but also diffuse

In Advances in CO2 Conversion and Utilization; Hu, Y.;
ACS Symposium Series; American Chemical Society: Washington, DC, 2010.

Downloaded by UNIV OF GUELPH LIBRARY on June 23, 2012 | http://pubs.acs.org
Publication Date (Web): December 3, 2010 | doi: 10.1021/bk-2010-1056.ch014

Table 3. Properties of Mg modified MCM-41 composites by various methods

	n Si / n Mg	*S* $m^2 \cdot g^{-1}$	*V* $cm^3 \cdot g^{-1}$	D_p *nm*	CO_2 $mmol \cdot g^{-1}$
MCM41	---	1024	0.87	3.52	0.67
Mg-MCM41-C40	40 : 1	897	0.87	4.2	0.97
Mg-MCM41-C20	20 : 1	788	1.51	8.0	0.89
Mg-MCM41-C10	10 : 1	469	0.91	8.3	0.70
Mg-MCM41-C1	1 : 1	221	0.69	12.4	0.22
Mg-MCM41-D10	10 : 1	690	0.24	2.2	0.73
Al-MCM41-D	---	321	0.42	5.6	0.68
Mg-Al- MCM41-D10	10 : 1	235	0.41	7.4	1.04
Mg-APTS-MCM41-D10	10 : 1	497	0.56	2.7	1.09
Mg-EDA-MCM41-D10	10 : 1	627	1.15	7.6	1.32

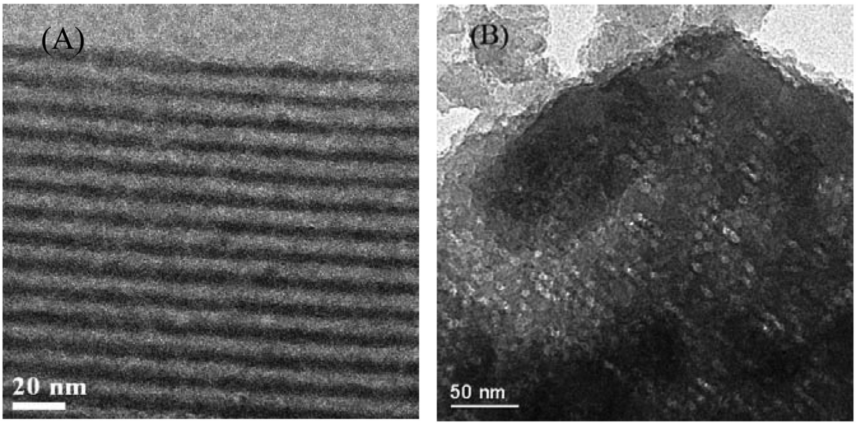

Figure 7. The TEM image of (A) pure silica SBA-15, (B) Mg-SBA-15-C1.5.

into the frameworks through the ionic exchange. Consequently, the larger size of Mg^{2+} cation results the increasing of the pore volume and pore size.

As shown in Figure 10, the CO_2 adsorption capacity increase with introducing Mg into pure silica SBA-15 and MCM-41. It is expected that acidic CO_2 molecule would interact more strongly with basic MgO, accordingly, the more basic sites, the higher the CO_2 adsorption capacity. From Table 2, the CO_2 adsorption capacity of Mg-SBA-15-C(*n*) increased with the increasing amount of doping Mg. However, the increment is not proportion to the amount of Mg, which gives evidence that the dispersion state of MgO species is an important factor for the CO_2 adsorption. For MCM-41 based adsorbents, when small amount of Mg is introduced, the CO_2 adsorption capacity increases. however, it goes in the contrary way with further increasing amount of doping Mg due to the serious block at the entrance of the narrow channels. The contrast effects of the amount

Downloaded by UNIV OF GUELPH LIBRARY on June 23, 2012 | http://pubs.acs.org
Publication Date (Web): December 3, 2010 | doi: 10.1021/bk-2010-1056.ch014

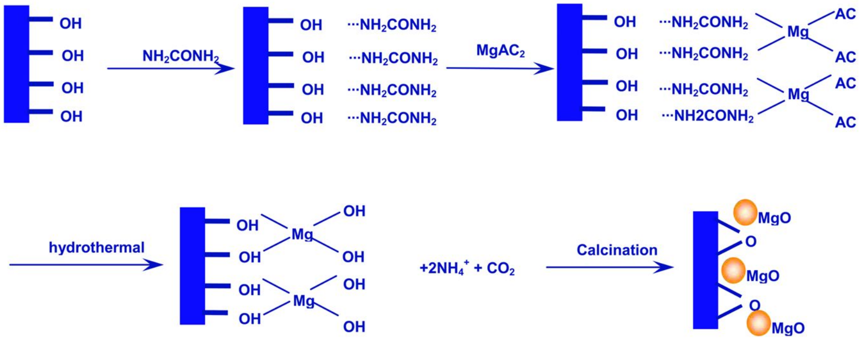
OH
OH
OH
OH
NH2CONH2
OH ···NH2CONH2
OH ···NH2CONH2
OH ···NH2CONH2
OH ···NH2CONH2
MgAC2
OH ···NH2CONH2
OH ···NH2CONH2
OH ···NH2CONH2
OH ···NH2CONH2
Mg
AC
AC
Mg
AC
AC
hydrothermal
OH
Mg
OH
OH
OH
OH
Mg
OH
OH
OH
+2NH4+ + CO2
Calcination
MgO
O
MgO
O
MgO

Figure 8. The possible schema of the coordination of Mg^{2+} cations on the mesoporous silica surface by urea.

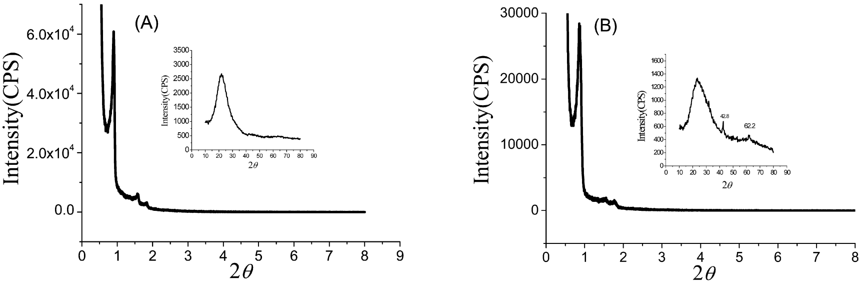

Figure 9. the XRD patterns of (A) Mg-Al-SBA-15-D1, (B) Mg-Al-SBA-15-I1, and the inserts are their corresponding wide angle XRD pattern, respectively.

of Mg doping on MCM-41 and SBA-15 gives further evidence that the highly dispersed Mg species in channels have a dominate effect on the CO_2 adsorption.

Different impregnating procedures result in different status of Mg grafting, in consequence, different increment of the CO_2 adsorption capacity. Figures 11 and 12 are the comparison of the CO_2 adsorption capacity of SBA-15s and MCM-41s by various Mg modified methods. As we can see, no matter what kinds of the modify procedures are used, all the CO_2 adsorption capacity of increase, but the increments of the CO_2 adsorption capacity are different. Among them, for the similar molar ratio of *n*(Si/Mg), the product of Mg-Al-SBA-15-D1 by the dispersion method enhanced by Al^{3+} has the best result in the SBA-15 series, the CO_2 adsorption capacity is 1.35 $mmol.g^{-1}$. For MCM-41s, the most important fact is how to obtain the highly dispersed MgO in such narrow channels. The curves (a) and (b) of the dispersion enhanced by basic agent of EDA and APTS have the best results, since the molecular size of APTS is much larger than that of EDA, EDA can diffuse into the narrow channels more efficiently, as a result, the CO_2 adsorption capacity of Mg-EDA-MCM-41-D10 has the best CO_2 adsorption capacity as 1.32 $mmol.g^{-1}$.

Downloaded by UNIV OF GUELPH LIBRARY on June 23, 2012 | http://pubs.acs.org
Publication Date (Web): December 3, 2010 | doi: 10.1021/bk-2010-1056.ch014

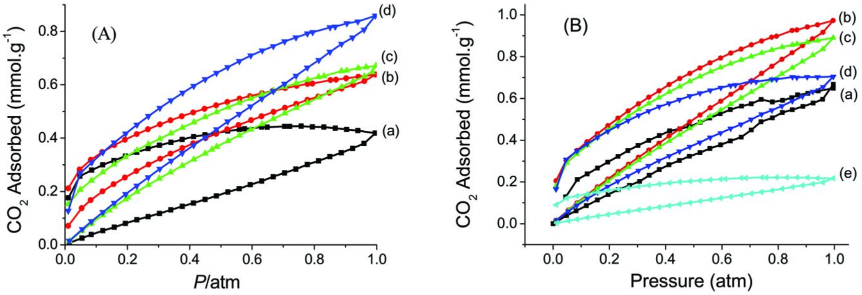

Figure 10. The CO_2 adsorption capacity of Mg modified by the co-condensation method (A) SBA-15s, in which (a) SBA-15, (b) Mg-SBA-15-C6, (c) Mg-SBA-15-C3, (d) Mg-SBA-15-C1.5. (B) MCM-41s, in which (a) MCM-41, (b) Mg-MCM41-C40, (c) Mg-MCM41-20, (d) Mg-MCM41-C10, (e) Mg-MCM41-C1, respectively.

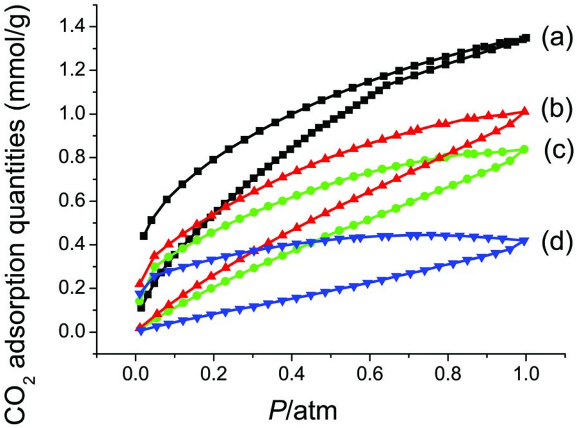

Figure 11. The comparison of the CO_2 adsorption capacity of Mg-SBA-15s modified by various methods (a) the dispersion enhanced by Al^{3+}, (b) the co-condensation, (c) the ionic exchange, (d) the pure silica SBA-15.

Molecular Simulation of CO_2 Adsorption on Porous Adsorbents

3.1. CO_2 Adsorption on Micro/Mesoporous Composite MFI/MCM-41

MCM-41 silica contains a hexagonal array of nearly uniform mesoscopic pores. It is one of the potential high performance adsorbents. A full-atom MCM-41 model has been constructed by caving cylindrical pores from an amorphous silica matrix and energetically optimized (*65*). The optimized MCM-41 maintains a hexagonal array of the mesoscopic pores as evidenced by the three characteristic peaks in the XRD pattern as shown in Figure 13. The pore surface of MCM-41 is corrugated and coated with hydroxyls and defects. The pore size exhibits a Gaussian distribution with an average radius of 14.38 Å, close to the experimental value. Microporous zeolites are also widely used as adsorbents.

Downloaded by UNIV OF GUELPH LIBRARY on June 23, 2012 | http://pubs.acs.org
Publication Date (Web): December 3, 2010 | doi: 10.1021/bk-2010-1056.ch014

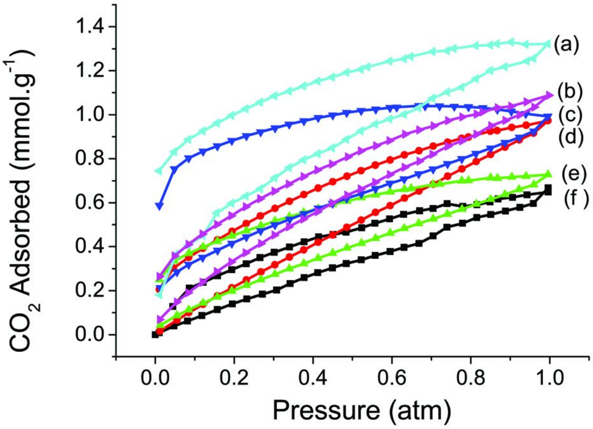

Figure 12. The comparison of the CO_2 adsorption capacity of Mg-MCM-41s modified by various methods (a) the dispersion enhanced by EDA, (b) the dispersion enhanced by APTS, (c) the dispersion enhanced by Al^{3+}, (d) the co-condensation, (e) the simple dispersion, (f) the pure silica MCM41.

Similarly, a new type of porous material, the micro/mesoporous composite of MFI/MCM-41, which possesses bimodal pore size distribution, has been investigated. The MFI zeolite, as shown in Figure 14(A), also can be acted as a matrix, by caving cylindrical pores from it and energetically optimized, the structure of MFI/MCM-41 has been constructed as shown in Figure 14(B). For MFI/MCM-41, the density is lower, while the free volume and specific surface area are greater than those of MFI due to the presence of mesopores.

The details about the simulation method can be seen in Ref. (*65*). The simulated adsorption isotherms and isosteric heats of pure CO_2, N_2 and CH_4 on MFI and MCM-41 match well with experimental data. CO_2 is preferential adsorbed than N_2 and CH_4. Thus the adsorption and isosteric heat of CO_2 are greater than that of the other two gases on both MFI and MFI/MCM-41. CO_2 is preferentially adsorbed at the active sites near the pore surface, while N_2 tends to adsorb homogeneously on the pore surface. As shown in Figure 15, at low pressures, MFI has the highest CO_2 adsorption capacity, followed by MFI/MCM-41 and finally MCM-41. At high pressures, however, the CO_2 adsorption capacity of both MFI/MCM-41 and MCM-41 exceed that on MFI and MFI/MCM-41 has the highest one. N_2 shows similar adsorption capacity of MFI, MCM-41 and MFI/MCM-41.

For the adsorption of flue gas, as shown in Figure 16(a) the CO_2/N_2 selectivity on the three adsorbents decreases in the order of MFI > MFI/MCM-41 > MCM-41. With increasing pressure, the CO_2/N_2 selectivity increases on MFI and MFI/MCM-41, but slightly decreases on MCM-41. In addition, the CO_2/N_2 selectivity increases with increasing CO_2 concentration in flue gas, but drops rapidly with increasing temperature. At temperatures above 400 K, the selectivity approaches constant and pressure has no distinct effect.

Downloaded by UNIV OF GUELPH LIBRARY on June 23, 2012 | http://pubs.acs.org
Publication Date (Web): December 3, 2010 | doi: 10.1021/bk-2010-1056.ch014

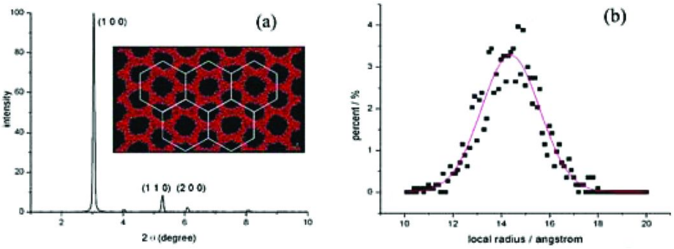

Figure 13. Characterization of MCM-41 model: (a) XRD pattern of the optimized MCM-41 model. The inset is the snapshot. Key: Si, yellow; O, red; H, white. (b) Distribution of pore radius in the MCM-41 model. The curve is a Gaussian distribution fit to the data. (Reproduced from the Ref. (65) with permission from ACS)

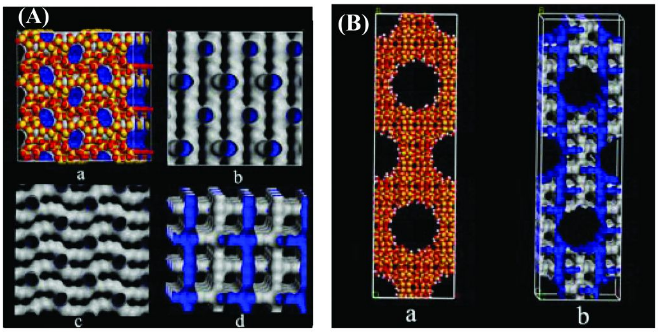

Figure 14. (A) Atomic model of MFI zeolite viewed at X, Y and Z direction, (B) Atomic model of pore network of MFI/MCM-41. Characterized by a probe with a diameter of 3.3 Å. Color code: Si, yellow; O, red; H, white. The interior of Connolly surface is in gray, while the exterior is in blue.

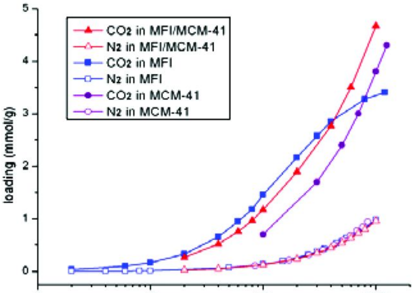

Figure 15. Isotherms of CO_2 and N_2 on MFI/MCM-41, MFI and MCM-41. (Reproduced from the Ref. (65) with permission from ACS)

Downloaded by UNIV OF GUELPH LIBRARY on June 23, 2012 | http://pubs.acs.org
Publication Date (Web): December 3, 2010 | doi: 10.1021/bk-2010-1056.ch014

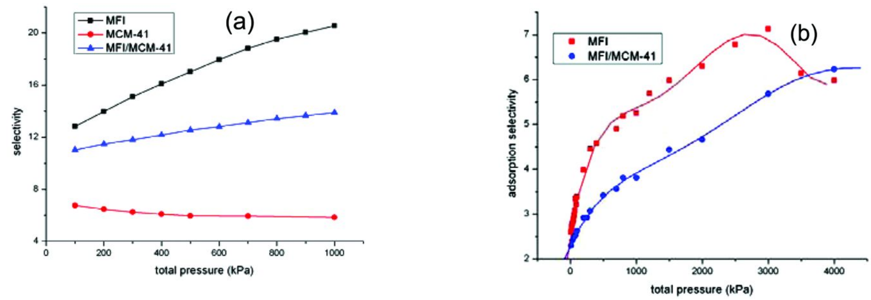

Figure 16. Adsorption selectivity of (a) CO_2/N_2, (b) CO_2/CH_4 for the adsorption of their equipmolar mixture on MFI and MFI/MCM-41.

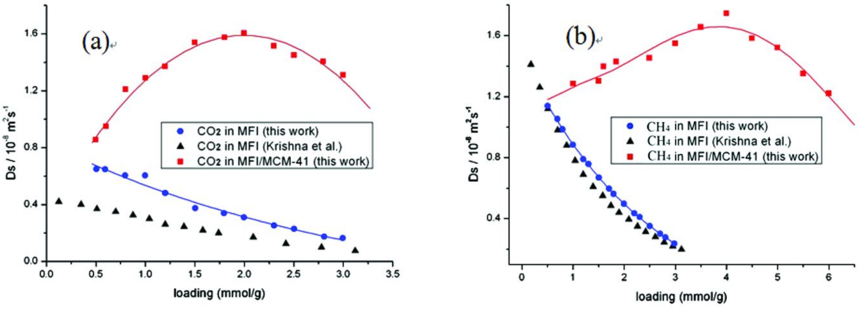

Figure 17. The self diffusivity of (a) CO_2 and (b) CH_4 on MFI and MFI/MCM-41. (Reproduced from the Ref. (65) with permission from ACS)

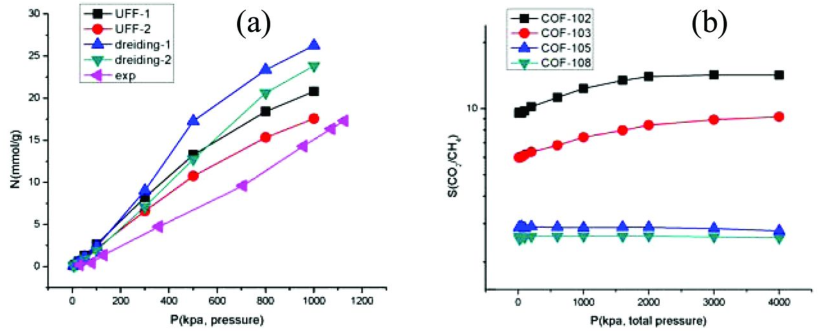

Figure 18. (a) Comparison of the CO_2 adsorption capacity between the simulation and experimental results. (b) Simulated selectivity of CO_2/CH_4 on various types of COFs by the UFF-2 combination

For the adsorption of natural gas, the adsorption capacities of CO_2 and CH_4 on MFI are higher than those on MFI/MCM-41 at low pressures. However, reverse situation occurs at high pressures. The adsorbate molecules in MFI/MCM-41 are first located in micropores and subsequently in mesopores when micropores are almost filled. Adsorption enthalpy is the dominant factor in gas adsorption

Downloaded by UNIV OF GUELPH LIBRARY on June 23, 2012 | http://pubs.acs.org
Publication Date (Web): December 3, 2010 | doi: 10.1021/bk-2010-1056.ch014

and selectivity, while size effect becomes increasingly important with the rise of amount of adsorption. As shown in Figure 16(b), the selectivity of CO_2 over CH_4 on MFI first increases with increasing pressure and then drops at higher pressures because of entropy effect. But the selectivity on MFI/MCM-41 increases monotonically up to 4 MPa. As shown in Figure 17, the self-diffusivities of CO_2 and CH_4 on MFI decrease with the increase of amount of adsorption, but exhibit a maximum on MFI/MCM-41. The diffusion of CO_2 and CH_4 is enhanced by the presence of mesopores, especially at high pressures. In conclusion, the adsorption capacity, selectivity and diffusion on MFI/MCM-41 are greater than those on MFI for the separation of high pressure natural gas. The micro/mesoporous composite is one of the excellent candidates of high performance CO_2 adsorbents.

3.2. CO_2 Adsorption on COFs

Covalent organic framework (COF) is another promising candidate for CO_2 adsorption and separation. In simulation, one of the key issues is the force field of gases and adsorbents. Two different charge models of CO_2 for its adsorption on 3D-COFs have been tested. The 3D-COFs is used as adsorbent for CO_2 capture due to its large adsorption capacity to ascertain the effect of charge models on the simulated results of CO_2 adsorption. The first charge model of CO_2 has the partial charges on C and O atoms as qC = 0.7e and qO = -0.35e, and the second has the partial charges as qC = 0.576e and qO = -0.288e. The results of the simulated CO_2 adsorption capacity by the different combinations of charge model and force field are shown in Figure 18(a). It is found that the combination of UFF force field and the second charge model (UFF-2) gives a result closely agree with experimental data. For the gas mixture, CO_2, CH_4 adsorption isotherms and the selectivity of CO_2/CH_4 on various types of COFs are also simulated by the different combinations of charge model and force field. As shown in Figure 18(b), simulated by the UFF-2 combination, the selectivity of CO_2/CH_4 on COF-102 has the best result, followed by COF-103, finally COF-105 and COF-108.

Conclusions

Possessing of high surface area and ordered pore structure, mesoporous materials, such as MCM-41 and SBA-15, are the promising candidates of high performance CO_2 adsorbents. After amine modification, the ordered structures are kept, but the BET surface area, pore volume and pore size decrease significantly. However, the amine groups become active centers of adsorption and higher amount of CO_2 adsorption are obtained through chemisorption. The amount of CO_2 adsorption on MCM-41 based materials is larger than that on SBA-15s, as well as the dual amine groups of AEAPMDS has better effect than the single amine group of APTS. The best CO_2 adsorption capacity of MCM-41-AEAPMDS is 2.20 $mmol \cdot g^{-1}$ at room temperature.

Furthermore, Mg species are successfully introduced into the mesoporous material MCM-41 and SBA-15 by the co-condensation, the dispersion (enhanced by Al^{3+} electronic defeat, and amine surface modification), the ionic exchange, and

Downloaded by UNIV OF GUELPH LIBRARY on June 23, 2012 | http://pubs.acs.org
Publication Date (Web): December 3, 2010 | doi: 10.1021/bk-2010-1056.ch014

so on. A suitable small amount of Mg^{2+} impregnated can effectively increased the CO_2 adsorption capacity, and the highly dispersed MgO state is the key factor to improve the CO_2 adsorption capacity. For the larger size channels, Mg-Al-SBA-15-D1 produced by the dual metal Al and Mg dispersion method can effective increase the CO_2 adsorption capacity as 1.35 mmol.g^{-1}. While for the smaller size channels, Mg-EDA-MCM-41-D10 produced by the EDA surface adjusting dispersion method can effectively enhance the CO_2 adsorption capacity as 1.32 mmol.g^{-1}.

The molecular simulation can give a direction for optimize the adsorbent structure. The adsorption and diffusion of CO_2, CH_4, N_2 and their mixtures on MCM-41, MFI and MFI/MCM-41 have been simulated by using GCMC and MD simulations. At low pressure, the CO_2 adsorption capacity of MFI is higher than those on MFI/MCM-41, in contrast to the situation at high pressure. Therefore, the CO_2/CH_4 selectivity on MFI/MCM-41 composite exceeds that on MFI at high pressures. Because of the presence of mesopores, diffusion on MFI/MCM-41 is enhanced compared to that on MFI. The micro/mesoporous composite shows better performances in the separation at high pressure.

The charge models can be an important factor in the simulation process of gas adsorption. Two charge models of CO_2 and two types of force field have been evaluated in the simulation of CO_2 adsorption on different COFs. When the specified CO_2 charge model such as the partial charges of qC= 0.576e and qO = -0.288e and UFF force field are combined, the simulated results closely agree with the experimental data for the pure CO_2 adsorption capacity. For the gas mixture, the selectivity of CO_2/CH_4 on COF-102 has the best simulated result.

Acknowledgments

This work is supported by the National Natural Science Foundation of China (20736002, 20776045), the National High Technology Research and Development Program of China (2008AA062302), Program for Changjiang Scholars and Innovative Research Team in University of China (IRT0721) and the 111 Project of China(B08021).

References

1. *Vision 21: Fossil Fuel Options for the Future*; National Academy Press: 2000; pp 61−84. http://www.nap.edu/catalog/9862.html.
2. *IPCC Special Report on Carbon Dioxide Capture and Storage*. http://arch.rivm.nl/env/int/ipcc/pages_media/SRCCS-final/IPCCSpecialReportonCarbondioxideCaptureandStorage.htm.
3. Idem, R.; Tontiwachwuthikul, P. *Ind. Eng. Chem. Res.* **2006**, *45*, 2413.
4. Aaron, D.; Tsouris, C. *Sep. Sci. Technol.* **2005**, *40*, 321.
5. Aroonwilas, A.; Veawab, A. Proceedings of the 8th International Conference on Greenhouse Gas Control Technologies (GHGT-8), Norway, 2006.
6. Stephen, K. R. *Chem. Eng. News* **2010**, *88* (30), 36.

7. Chue, K. T.; Kim, J. N.; Yoo, Y. J.; Cho, S. H. *Ind. Eng. Chem. Res.* **1995**, *34*, 591.
8. Park, J. H.; Beum, H. T.; Kim, J. N.; Cho, S. H. *Ind. Eng. Chem. Res.* **2002**, *41*, 4122.
9. Ho, M. T.; Allinson, G. W.; Wiley, D. E. *Ind. Eng. Chem. Res.* **2008**, *47*, 4883.
10. Bonelli, B.; Onida, B.; Fubini, B.; Arean, C. O.; Garrone, E. *Langmuir* **2000**, *16*, 4976.
11. Cavenati, S.; Grande, C. A.; Rodrigues, A. E. *J. Chem. Eng. Data* **2004**, *49*, 1095.
12. Li, G.; Xiao, P.; Webley, P.; Zhang, J.; Singh, R.; Marshall, M *Adsorption* **2008**, *14*, 415.
13. Pakseresht, S.; Kazemeini, M.; Akbarnejad, M. M. *Sep. Purif. Technol.* **2002**, *28*, 53.
14. Chaffee, A. L.; Knowles, G. P.; Liang, Z.; Zhang, J.; Xiao, P.; Webley, P. A. *Int. J. Greenhouse Gas Control* **2007**, *1*, 11.
15. Zhou, Q.; Chan, C. W.; Tontiwachiwuthikul, P.; Idem, R.; Gelowitz, D. *Int. J. Greenhouse Gas Control* **2009**, *1*, 1.
16. Siriwardane, R. V.; Shen, M. S.; Fisher, E. P.; Poston, J. A. *Energy Fuels* **2001**, *15*, 279.
17. Chou, C.; Chen, C. *Sep. Purif. Technol.* **2004**, *39*, 51.
18. Ko, D.; Siriwardane, R.; Biegler, L. T. *Ind. Eng. Chem. Res.* **2005**, *44*, 8084.
19. Merel, J.; Clausse, M.; Meunier, F. *Ind. Eng. Chem. Res.* **2008**, *47*, 209.
20. Clausse, M.; Bonjour, J.; Meunier, F. *Chem. Eng. Sci.* **2004**, *59*, 3657.
21. Bonelli, B.; Civalleri, B.; Fubini, B.; Ugliengo, P.; Aren, C. O.; Garrone, E. *J. Phys. Chem. B* **2000**, *104*, 10978.
22. Wirawan, S. K.; Creaser, D. *Sep. Purif. Technol.* **2006**, *52*, 224.
23. Wirawan, S. K.; Creaser, D. *Microporous Mesoporous Mater.* **2006**, *91*, 196.
24. Rege, S. U.; Yang, R. T. *Chem. Eng. Sci.* **2001**, *56*, 3781.
25. Plant, D. F.; Maurin, G.; Deroche, I.; Gaberova, L.; Llewellyn, P. L. *Chem. Phys. Lett.* **2006**, *426*, 387.
26. Walton, K. S.; Abney, M. B.; Le Van, M. D. *Microporous Mesoporous Mater.* **2006**, *91*, 78.
27. Kresge, C. T.; Lenowicz, M. E.; Roth, W. J.; Vartuli, J. C.; Beck, J. S. *Nature* **1992**, *359*, 710.
28. Beck, J. S.; Vartuli, J. C.; Roth, W. J.; Leonowich, M. E.; Kresge, C. T.; Schmitt, K. D.; Chu, C. T. W.; Olson, D. H.; Sheppard, E. W.; Mcculler, S. B.; Schlenker, J. B. *J. Am. Chem. Soc.* **1992**, *114*, 10834.
29. Zhao, D.; Feng, J.; Huo, Q.; Melosh, N.; Fredrickson, G. H.; Chmelka, B. F.; Stucky, G. D. *Science* **1998**, *297*, 548.
30. Zhao, D.; Huo, Q.; Feng, J.; Chmelka, B. F.; Stucky, G. D. D. *J. Am. Chem. Soc.* **1998**, *120*, 6024.
31. Yu, T.; Zhang, H.; Yan, X.; Chen, Z.; Zou, X.; Oleynikov, P. *J. Phys. Chem. B.* **2006**, *110*, 21467.
32. Kleitz, F.; Choi, S. H.; Ryoo, R. *Chem. Commun.* **2003**, 2136.
33. Yokoi, T.; Yoshitake, H.; Tatsumi, T. *Chem. Mater.* **2003**, *15*, 4536.

Downloaded by UNIV OF GUELPH LIBRARY on June 23, 2012 | http://pubs.acs.org
Publication Date (Web): December 3, 2010 | doi: 10.1021/bk-2010-1056.ch014

34. Macario, A.; Katovic, A.; Giordano, G.; Iucolano, F.; Caputo, D. *Microporous Mesoporous Mater.* **2005**, *81*, 139.
35. Sun, Y.; Liu, X.; Su, W.; Zhou, Y.; Zhou, L. *Appl. Surf. Sci.* **2007**, *253*, 5650.
36. Knofel, C.; Descarpentries, J.; Benzaouia, A.; Zelenak, V.; Mornet, S.; Lewellyn, P. L.; et al. *Microporous Mesoporous Mater.* **2007**, *99*, 79.
37. Huang, H. Y.; Yang, R. T.; Chinn, D.; Munson, C. L. *Ind. Eng. Chem. Res.* **2003**, *42*, 2427.
38. Kim, S.; Son, W.; Choi, J.; Ahn, W. S. *Microporous Mesoporous Mater.* **2008**, *115*, 497.
39. Yokoi, T.; Yoshitake, H.; Tatsumi, T. *J. Mater. Chem.* **2004**, *14*, 951.
40. Zhao, H. L.; Hu, J.; Wang, J. J.; Zhou, L. H.; Liu, H. L. *Acta Phys.-Chim. Sin.* **2007**, *23*, 801.
41. Xu, X.; Song, C.; Miller, B. G.; Scaroni, A. W. *Ind. Eng. Chem. Res.* **2005**, *44*, 8113.
42. Knowles, G. P.; Graham, J. V.; Delaney, S. W.; Chaffee, A. L. *Fuel Process. Technol.* **2005**, *86*, 1435.
43. Khatri, R. A.; Chuang, S. S. C.; Soong, Y.; Gray, M. *Ind. Eng. Chem. Res.* **2005**, *44*, 3702.
44. Franchi, R. S.; Harlick, P. J. E.; Sayari, A. *Ind. Eng. Chem. Res.* **2005**, *44*, 8007.
45. Chen, C.; Yang, S. T.; Ahn, W. S.; Ryoo, R. *Chem. Commun.* **2009**, 3627.
46. Hicks, J. C.; Drese, J. H.; Fauth, D. J.; Gray, M. L.; Qi, G.; Jones, C. W. *J. Am. Chem. Soc.* **2008**, *130*, 2902.
47. Harlick, P. J. E.; Sayari, A. *Ind. Eng. Chem. Res.* **2007**, *46*, 446.
48. Hiyoshi, N.; Yogo, K.; Yashima, T. *Microporous Mesoporous Mater.* **2005**, *84*, 357.
49. Chang, A. C. C.; Chuang, S. S. C.; Gray, M.; Soong, Y. *Energy Fuels* **2003**, *17*, 468.
50. Knowles, G. P.; Delaney, S. W.; Chaffee, A. L. *Ind. Eng. Chem. Res.* **2006**, *45*, 2626.
51. Kim, S.; Ida, J.; Guliants, V. V.; Lin, J. Y. S. *J. Phys. Chem. B* **2005**, *109*, 6287.
52. Hiyoshi, N.; Yogo, K.; Yashima, T. *Chem. Lett.* **2004**, *33*, 510.
53. Bacsik, Z.; Atluri, R.; Garcia-Bennett, A. E.; Hedin, N. *Langmuir* **2010**, *26*, 10013.
54. Chen, C.; Yang, S.; Ahn, W. S.; Ryoo, R. *Chem. Commun.* **2009**, 3627.
55. Son, W. J.; Choi, J. S.; Ahn, W. S. *Microporous Mesoporous Mater.* **2008**, *113*, 31.
56. Hiyoshi, N.; Yogo, K.; Yashima, T. *Stud. Surf. Sci. Catal.* **2004**, *153*, 417.
57. Belmabkhout, Y.; Sayari, A. *Adsorption* **2009**, *15*, 318.
58. Baerlocher, C.; McCusker, L. B. Database of Zeolite Structures, June 26, 2001. International Zeolite Association. http://www.iza-structure.org/databases/.
59. Catlow, C. R. A.; van Santen, R. A.; Smit, B. *Computer Modelling of Microporous Materials*; Elsevier Science: London, 2004.
60. Krishna, R.; Smit, B.; Calero, S. *Chem. Soc. Rev.* **2002**, *31*, 185.

Downloaded by UNIV OF GUELPH LIBRARY on June 23, 2012 | http://pubs.acs.org
Publication Date (Web): December 3, 2010 | doi: 10.1021/bk-2010-1056.ch014

61. Goj, A.; Sholl, D. S.; Atken, E. D.; Kohen, D. *J. Phys. Chem. B.* **2002**, *106*, 8367.
62. Jiang, J. W.; Sandler, S. I. *J. Am.Chem. Soc.* **2005**, *127*, 11989.
63. Akten, E. D.; Siriwardane, R.; Sholl, D. S. *Energy Fuels* **2003**, *17*, 977.
64. He, Y. F.; Seaton, N. A. *Langmuir* **2006**, *22*, 1150.
65. Zhuo, S. C.; Huang, Y. M.; Hu, J.; Liu, H. L.; Hu, Y. *J. Phys. Chem. C.* **2008**, *112*, 11295.
66. Almudena, G.; Conchi, O. A.; Jose, B. P.; David, D.; Thijs, J. H. V.; Rajamani, K.; Sofia, C. *J. Phys. Chem. C.* **2009**, *113*, 8814.
67. Garberoglio, G. *Langmuir* **2007**, *23*, 12154.
68. Yang, Q. Y.; Zhong, C. L. *J. Phys. Chem. B* **2006**, *110*, 17776.
69. Yang, Q. Y.; Zhong, C. L. *Langmuir* **2009**, *25*, 2302.
70. Rankin, R. B.; Liu, J.; Kulkarni, A. D.; Johnson, J. K. *J. Phys. Chem. C* **2009**, *113*, 16906.
71. Babarao, R.; Jiang, J. W. *J. Am. Chem. Soc.* **2009**, *131*, 11417.
72. Babarao, R.; Jiang, J. W.; Sandler, S. I. *Langmuir* **2009**, *25*, 5239.

Downloaded by UNIV OF GUELPH LIBRARY on June 23, 2012 | http://pubs.acs.org
Publication Date (Web): December 3, 2010 | doi: 10.1021/bk-2010-1056.ch014

Downloaded by DUKE UNIV on June 23, 2012 | http://pubs.acs.org
Publication Date (Web): December 3, 2010 | doi: 10.1021/bk-2010-1056.ch015

Chapter 15

Advances on Alkaline Ceramics as Possible CO_2 Captors

Heriberto Pfeiffer[*]

Instituto de Investigaciones en Materiales, Universidad Nacional Autónoma de México, Circuito exterior s/n, Ciudad Universitaria, Del. Coyoacán, CP 04510, México DF, Mexico.
[*]**pfeiffer@iim.unam.mx**

CO_2 capture is one of the most important issues in the environmental field. In that way, materials science has become an important tool, trying to solve this problem. Several materials and processes have been published as possible solution to the CO_2 trapping process, the alkaline ceramics among them. It has been found that alkaline ceramics are able to absorb CO_2 under specific conditions, showing some interesting and promising properties such as high CO_2 capture capacities, large temperature intervals in which the process occur and the possibility of their reutilization. Therefore, the aim of the present chapter is to summarize all the research work performed up to now in this field, and visualize possible future work and possible applications. Different alkaline (mainly lithium and sodium) zirconates, silicates, aluminates and cuprates have been test as possible CO_2 captors. In general, all these ceramics trap CO_2 through a chemical reaction, in other words by an absorption process. Hence, chemical and physical modifications have been performed to these ceramics in order to improve different kinetic factors. For example, some of these ceramics have been doped or mixed with other elements to produce solid solutions. On the other hand, as the limiting step of the general process seems to be diffusion, it has been analyzed the effect of particle size on the chemisorption. However, there are several specific points that have not been explained. Finally, the cyclability and possible application of these materials are presented.

In Advances in CO2 Conversion and Utilization; Hu, Y.;
ACS Symposium Series; American Chemical Society: Washington, DC, 2010.

Downloaded by DUKE UNIV on June 23, 2012 | http://pubs.acs.org
Publication Date (Web): December 3, 2010 | doi: 10.1021/bk-2010-1056.ch015

1. Introduction

Since the beginning of the industrial revolution, the use of fuels has become an essential part of the human life. Additionally, in the same period of time, the population on the earth has grown continuously in a considerably way. As a consequence of these two factors, among others, the pollution produced in our planet has increased dramatically, where one of the most important pollution types corresponds to the air pollution. In that way, most of the air pollution is produced from the fossil fuels combustion. The combustion of these materials, (coal, oil and gas, among others) has raised the carbon dioxide (CO_2) amounts in the atmosphere to levels never seen before (*1*). As a result of that, the green house effect has produced an over-warming of the earth, bringing different consequences. In order to solve this threatening problem, several proposals have been established; where a possible key means, for reducing the green house effect, is to capture, separate and concentrate CO_2 (*2–4*). The first step corresponds to the CO_2 capture, and the key for the CO_2 sequestration is to separate it from the flue gas. However, there are usually two different kinds of problems. 1) Fuels are generally burned in the presence of natural air, which provides the oxygen necessary for the combustion reaction. As a consequence of that, mixtures of N_2 and CO_2, among many other gases, are produced in the flue gas, and these two compounds have similar sizes. Therefore, its separation is not easy at all (*5*). 2) The flue gas is produced at high temperatures. Hence, in many treatments, the combustion gas has to be cooled down before the CO_2 capture can be performed (*5*, *6*).

In that intelligence, several proposals have been published in the last years. For example, the presence of N_2 can be eliminated or at least reduced by oxycombustion. In this process, the fuel is burned in the presence of pure or enriched oxygen. Then, the presence of N_2 is reduced considerably from the flue gas (*7*). Of course, many other propositions strongly suggest the use of different energy sources, from which CO_2 is not produced such as: fuel cells, solar energy and fission and fusion nuclear energies, among others (*8–12*). Of course, all these alternative technologies are already important, but there is a fact, human will continue using the fossil combustibles, until we finish with them.

2. Materials Science as a Possible Solution

A considerable variety of materials has been tested for CO_2 sequestration such as: zeolites, organic materials, minerals, polymers, oxides and ceramics, among others (*13–22*). These materials present some advantages for the CO_2 capture, but at the same time most of them present disadvantages as well. For example, zeolites are relatively stable at high temperatures, but they have very poor CO_2 sorption capacities, and in many cases, the use of high pressures is necessary. As another example, amines and polymeric membranes can capture good quantities of CO_2, although in both cases the flue gas has to be cooled down to 200°C or lower temperatures, otherwise these captor materials are decomposed. Hence, to find novel and more effective technologies for the separation and capture of CO_2, new materials must cover the following aspects (*23–25*):

1. High selectivity and sorption capacity for CO_2 at elevated temperatures.
2. Adequate sorption/desorption kinetics for CO_2.
3. Good cyclability for the sorption/desorption processes.
4. Good hydrothermal and mechanical properties.

There are some ceramics materials which seem to cover these ideal properties as CO_2 captors: The "alkaline ceramics", which could be defined as a binary-metal oxide, where at least one of the metals is an alkaline element, for example: lithium orthosilicate (Li_4SiO_4), sodium metazirconate (Na_2ZrO_3) or lithium cuprate (Li_2CuO_2). In that sense, a first obvious approximation could be the use of pure alkaline oxides and hydroxides such as lithium oxide (Li_2O), lithium hydroxide (LiOH), sodium hydroxide (NaOH), which in fact have been studied as possible CO_2 captors (*15*, *26–30*). Lithium hydroxide (LiOH) has been utilized as CO_2 absorbent into spaceships and submarines (*26*). These ceramics seems to present similar or even better reactivity than earth alkaline oxides: magnesium oxide (MgO), calcium oxide (CaO) and hydroxide ($Ca(OH)_2$) (*31–35*). Nevertheless, although they have some good specific properties, these materials do not cover all the ideal points previously mentioned. Alkaline and earth-alkaline oxides present three main problems: 1) The cyclability process is not always possible; 2) These materials are very reactive and therefore they are highly instable; and 3) Most of these materials suffer huge volume expansions during the CO_2 capture (*15*, *36*).

Downloaded by DUKE UNIV on June 23, 2012 | http://pubs.acs.org
Publication Date (Web): December 3, 2010 | doi: 10.1021/bk-2010-1056.ch015

3. Alkaline Ceramics

Based on the different issues and problems presented by the pure alkaline oxides, in 1998, Nakagawa and Ohashi demonstrated that lithium zirconate (Li_2ZrO_3) was able to absorb CO_2 at relatively high temperatures. Since then, different research groups have further studied Li_2ZrO_3 and other alkaline ceramics, as CO_2 captors. The materials that have been mainly studied are; lithium zirconates (Li_2ZrO_3 and $Li_6Zr_2O_7$) (*5*, *6*, *25*, *30*, *37–47*), lithium silicates (Li_4SiO_4 and Li_2SiO_3) (*47–64*) and sodium metazirconate (Na_2ZrO_3) (*47*, *65–67*). In a minor scale, other alkaline ceramics have been analyzed as well as CO_2 absorbents: lithium cuprate (Li_2CuO_2) (*68*, *69*), lithium ferrite ($LiFeO_2$) (*70*), lithium titanate (Li_4TiO_4) (*47*, *71*), sodium titanate (Na_2TiO_3) lithium aluminates (Li_5AlO_4 and $LiAlO_2$) (*72*) and sodium antimonite (Na_3SbO_4) (*65*).

3.1. Lithium Zirconate (Li_2ZrO_3), the First Case of Study

The first report about the CO_2 capture on any lithium ceramic was made by Nakagawa and Ohashi from Toshiba Japan, who reported a novel method to capture CO_2 at high-temperatures using lithium metazirconate (Li_2ZrO_3) (*36*). They proposed the use of lithium metazirconate (Li_2ZrO_3), a binary-metal oxide containing an alkaline element, which traps CO_2 according to the reaction 1:

$$Li_2ZrO_3 + CO_2 \leftrightarrow Li_2CO_3 + ZrO_2 \qquad (1)$$

In Advances in CO2 Conversion and Utilization; Hu, Y.;
ACS Symposium Series; American Chemical Society: Washington, DC, 2010.

Li_2ZrO_3 is able to absorb CO_2 at high temperatures (400-600°C), which is a great advantage, because the flue gas does not have been cooled down. Additionally, CO_2 can be extracted, thermally, reforming the Li_2ZrO_3. In other words, Li_2ZrO_3 is recyclable. Finally, the volume expansion (34 %) reported for this material is considerably smaller than that observed for pure oxides, for instance MgO (149 %).

After that publication, the same authors showed that CO_2 absorption process can be dramatically improved with the addition of potassium carbonate (K_2CO_3) to Li_2ZrO_3 (*37*). Later, other authors (*6*, *30*, *73*) have further studied this statement. All of them explained that CO_2 diffuses through the molten lithium-potassium carbonate at a much faster rate, covering the Li_2ZrO_3 bulk material. Lithium-potassium carbonate may melt and become a liquid layer, in which CO_2 can be transported more efficiently. Otherwise, in absence of potassium, lithium carbonate stays solid hindering the diffusion.

All the previous Li_2ZrO_3 results were obtained using the monoclinic phase. Nevertheless, Ochoa-Fernández and coworkers have published different works of CO_2 absorption on the Li_2ZrO_3 tetragonal phase (*42–46*). This phase has resulted to be more reactive to CO_2 than the monoclinic one. In fact, the tetragonal phase is able to absorb much more CO_2 than the monoclinic phase. Some of the Li_2ZrO_3 results are summarized in the Table I, in which it is easy to elucidate that CO_2 absorption is importantly increased when Li_2ZrO_3 is doped with potassium, or when the tetragonal phase is produced instead of the monoclinic one.

Downloaded by DUKE UNIV on June 23, 2012 | http://pubs.acs.org
Publication Date (Web): December 3, 2010 | doi: 10.1021/bk-2010-1056.ch015

3.2. Sodium Zirconate (Na_2ZrO_3)

Other alkaline zirconate that has been studied as possible CO_2 captor is sodium zirconate, Na_2ZrO_3. Although Na_2ZrO_3 has not been studied as extensively as Li_2ZrO_3, it seems to have much better characteristics for the CO_2 capture. The first work reporting some results of this ceramic was presented by López-Ortiz and coworkers (*65*). This paper demonstrated that Na_2ZrO_3 is able to absorb CO_2. After that, in 2007 and 2008, a few more papers have been published, showing some results about the CO_2 absorption on Na_2ZrO_3 (*66*, *67*, *74*). All these papers agree in the fact that Na_2ZrO_3 presents much better characteristics as CO_2 captor, in comparison to Li_2ZrO_3. In general, Na_2ZrO_3 is able to absorb CO_2 even at room temperature, which is a much lower temperature than Li_2ZrO_3 (≈ 400°C). In fact, in a dynamic CO_2 absorption process, the trends observed for Li_2ZrO_3 and Na_2ZrO_3 are significantly different (Figure 1). While, the so called, superficial and bulk CO_2 absorption processes are indistinguishable in Li_2ZrO_3, these two processes can be inferred on the Na_2ZrO_3. It supposes a higher reactivity for Na_2ZrO_3, which has been confirmed analyzing isothermically the CO_2 absorption processes.

The differences observed on the CO_2 absorption efficiencies of Li_2ZrO_3 and Na_2ZrO_3 may be correlated to the mobility of lithium or sodium atoms into their crystalline structures, constituted in both cases by $(ZrO_3)^{2-}$ chains. Although both zirconates have the same elemental stoichiometry, their crystalline structures are not the same. The Li_2ZrO_3 structure turns out to be more packed than the Na_2ZrO_3 structure (Figure 2) (*75*). Actually, Na_2ZrO_3 has a lamellar-like structure, where sodium atoms are located among the $(ZrO_3)^{2-}$ layers. On the contrary, lithium

Table I. CO_2 absorption efficiencies observed, into dynamic processes, for Li_2ZrO_3 pure and modified

Li_2ZrO_3	*wt% gained*	*Efficiency (%)*	*Reference*
Structure:			
Monoclinic	10	34.8	(*36*)
	6.5	22.6	(*25*)
Tetragonal	22	76.6	(*43*)
Li_2ZrO_3 doped:			
K-doped Li_2ZrO_3	21	73.1	(*37*)
	22.5	78.3	(*73*)
	20	69.6	(*6*)6

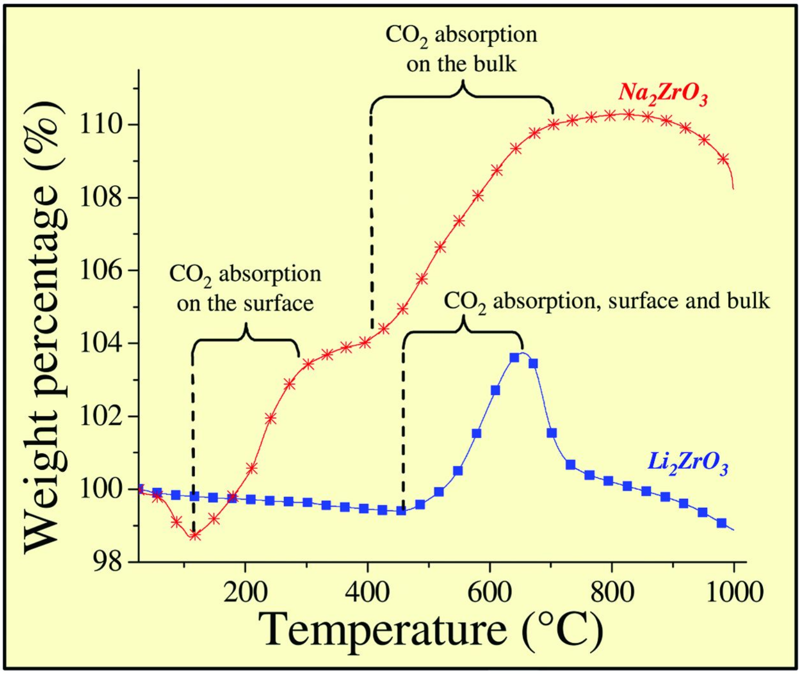

Figure 1. Thermogravimetric analyses of Li_2ZrO_3 and Na_2ZrO_3 in a CO_2 flux. While surface and bulk absorption processes are indistinguishable on Li_2ZrO_3, it is clearly marked on Na_2ZrO_3. Additionally, it is evident that CO_2 absorption temperature range of Na_2ZrO_3 is much larger than that of Li_2ZrO_3.

atoms are located into narrow channels, in a Li_2ZrO_3 dense crystalline structure. These channels do allow lithium movement, but it must be more limited that the sodium movement, which is produced over a whole layer. Therefore, the crystalline structure of the ceramic seems to be a very important issue in the CO_2 absorption process.

Downloaded by DUKE UNIV on June 23, 2012 | http://pubs.acs.org
Publication Date (Web): December 3, 2010 | doi: 10.1021/bk-2010-1056.ch015

Downloaded by DUKE UNIV on June 23, 2012 | http://pubs.acs.org
Publication Date (Web): December 3, 2010 | doi: 10.1021/bk-2010-1056.ch015

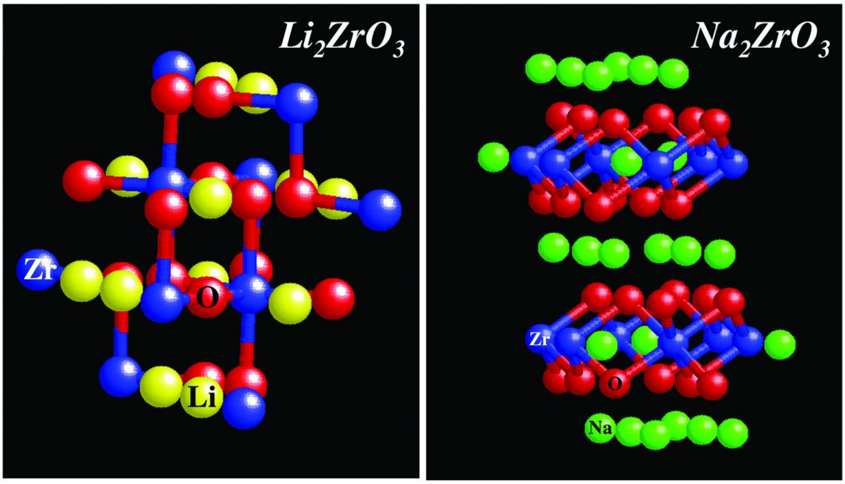

Figure 2. Snapshots of Li_2ZrO_3 and Na_2ZrO_3 structures. The spheres represent; zirconium (dark gray; blue online), oxygen (medium gray; red online) and alkaline element, lithium (light gray in left panel; yellow online) or sodium (light gray in right panel; green online), respectively.

3.3. Lithium Silicates (Li_4SiO_4 and Li_2SiO_3)

At the same time that lithium and sodium zirconates have been studied as CO_2 captors, other alkaline ceramics have been proposed and analyzed as well. Actually, so far, among all these alkaline ceramics, lithium orthosilicate (Li_4SiO_4) seems to be one of the best options to absorb CO_2. In this case, several authors have reported the CO_2 capture in this material through the following reaction (reaction 2) (*50–52*, *55*, *57–59*).

$$Li_4SiO_4 + CO_2 \leftrightarrow Li_2CO_3 + Li_2SiO_3 \qquad (2)$$

Although the CO_2 absorption mechanism proposed for Li_4SiO_4 is the same one as that proposed for lithium zirconates, it has been probed that Li_4SiO_4 absorbs CO_2 much better than Li_2ZrO_3, in different ways. For example, Nakagawa and coworkers (*51*, *52*, *55*, *57*) have performed different experiments, showing that Li_4SiO_4 absorbs up to 30 times more CO_2, its absorption rate is much faster and this ceramic is able to absorb CO_2 even at room temperature. Additionally, the same research group has done some experiments including water steam into the flue gas. They showed that H_2O improves CO_2 absorption at room temperature due to a chemical affinity between Li_4SiO_4 and H_2O. The presence of H_2O produces some kind of dissolution of the Li_2CO_3 core shell, promoting the CO_2 absorption on the particle's bulk (*50*).

Gauer and Heschel reported that CO_2 absorption on Li_4SiO_4 can be improved doping the ceramic (*59*). In this specific paper, authors produced Fe- and Al-doped Li_4SiO_4 ceramics. Under these doping conditions, CO_2 absorption was significantly improved at moderate temperatures (from room temperature to 400°C). The explanation given for this behavior was attributed to the introduction of vacancies into the crystal lattice, which of course, facilitates the cation diffusion and consequently the CO_2 absorption.

Several of these Li_4SiO_4 papers show, implicitly, that Li_2SiO_3 does not react (see reaction 2). In fact, some specific tests of CO_2 absorption on Li_2SiO_3 had been performed, and they did not report any CO_2 absorption (*50*, *54*, *58*). It was justified due to Li_2SiO_3 reactivity and kinetic factors. Nevertheless, more recent studies suggest that Li_2SiO_3 does absorb CO_2 in small quantities, under a specific condition; the synthesis of Li_2SiO_3 small particles, which implies an increment of the surface area (*48*, *53*). The general reaction proposed for the CO_2 absorption on Li_2SiO_3 is (reaction 3):

$$Li_2SiO_3 + CO_2 \leftrightarrow SiO_2 + Li_2CO_3 \qquad (3)$$

Finally, Kalinkin and coworkers (*62*, *63*) performed the CO_2 absorption on this lithium ceramic through mecanochemical interactions, getting similar results to that observed for the other authors. Additionally, several authors have done different comparisons of Li_2SiO_3 with sodium (Na_2SiO_3) and potassium (K_2SiO_3) metasilicates (*58*, *60*, *62*, *63*). They found out that CO_2 absorption increases on the alkali metasilicates as follows: $Li_2SiO_3 < Na_2SiO_3 < K_2SiO_3$. Authors used thermodynamic factors ($\Delta G_{f\text{-}M2CO3}$) to explain these differences observed in reactivity.

3.4. Other Alkaline Ceramics

Apart from the alkaline zirconates and silicates, which are the ceramics more studied into this field up to now, there have been published other works presenting the CO_2 absorption on other similar ceramics; Lithium ferrite ($LiFeO_2$), lithium cuprate (Li_2CuO_2), lithium and sodium titanates (Li_4TiO_4 and Na_2TiO_3), lithium aluminates ($LiAlO_2$ and Li_5AlO_4) and sodium antimonite (Na_3SbO_4) (*65*, *68–72*). Among the sodium ceramics mentioned (Na_2TiO_3 and Na_3SbO_4), none of them presented similar or better properties as CO_2 captor, in comparison to Na_2ZrO_3. Hence, these materials have not been further studied. However, lithium ceramics ($LiFeO_2$; Li_4TiO_4, Li_5AlO_4 and Li_2CuO_2) present different interesting properties. Although lithium ferrite did not possess high CO_2 absorption rates, it has a different and interesting thermal behavior. $LiFeO_2$ absorbs CO_2 in a lower temperature range (350-500°C) (*70*) than those observed for Li_2ZrO_3 and Li_4SiO_4 (450-650°C). Hence, if the absorption rate mechanism could be improved, this ceramic may become an option as CO_2 captor under different thermal conditions, specifically at lower temperatures.

Lithium orthotitanate (Li_4TiO_4 (*71*)) and penta-lithium aluminate (Li_5AlO_4 (*72*)) seem to have excellent properties for the CO_2 absorption. First studies, on each ceramic, show that both ceramics are able to absorb CO_2 in a wide range of temperatures (250-800°C). The excellent behaviors observed in each case have been justified in different ways. Li_4TiO_4 thermal absorption behavior was associated to the products obtained during the CO_2 capture, where oxygen plays and important role (reaction 4):

Downloaded by DUKE UNIV on June 23, 2012 | http://pubs.acs.org
Publication Date (Web): December 3, 2010 | doi: 10.1021/bk-2010-1056.ch015

$$Li_4TiO_4 + 1.5CO_2 \leftrightarrow LiTiO_x + 1.5Li_2CO_3 + {}^{(2.5-x)}/_2\, O_2 \quad \text{where } x = 2 \sim 2.5 \quad (4)$$

Li_4TiO_4 reaches very high CO_2 absorption efficiencies (95 %), even into a dynamic heating process. On the other hand, Li_5AlO_4 possesses the best theoretical CO_2 absorption capacity, due to two different facts: 1) The Li/Al molar ratio, equal to 5, and 2) aluminum is the lighter structural element used into the lithium ceramics tested as CO_2 captors. Up to now, the CO_2 absorption on Li_5AlO_4, is presented in the reaction 5, assuming a complete lithium reactivity:

$$2Li_5AlO_4 + 5CO_2 \leftrightarrow 5Li_2CO_3 + Al_2O_3 \qquad (5)$$

Finally, Li_2CuO_2 absorbs CO_2 in a very open range of temperatures, from 120°C to 690°C and it presents good CO_2 absorption rates and similar capacities than other alkaline ceramics (*68*).

4. Reaction Mechanism

In all the previous cases, the CO_2 capture occurs chemically, through an absorption process. In fact, the chemical process is an acid-base reaction; CO_2 is a very acid molecule, while alkaline elements are just the opposite, they have high basic properties. Additionally, there is an agreement, in which it has been proposed a general reaction mechanism at a micrometric scale, where the following steps have been established: Initially, using the lithium metazirconate case as example, Li_2ZrO_3 particles react with CO_2 at the surface. This reaction implies the formation of an external shell of Li_2CO_3 and ZrO_2. Nevertheless, the controversy becomes in the subsequent stage of the mechanism. Once the external shell is produced, there must be some kind of mechanism from which the CO_2 absorption can continue until end. Some authors have mentioned that lithium merely diffuses from the core to the surface through the Li_2CO_3. If that were the case, ZrO_2 might stay at the core of the particles with the lithium carbonate covering it. Of course, it cannot be so easy, as there is not any evidence of that. Therefore, there must be other factors influencing the bulk absorption.

The formation of the Li_2CO_3 external shell produces changes in volume and these changes must induce the formation of fractures over the surface. When these fractures are produced, new fresh and reactive Li_2ZrO_3 surface may become available. However, it should happen in a small proportion, as the particle size of the ceramics does not seem to change significantly after several absorption/desorption cycles. Hence, it cannot explain the CO_2 absorption by itself, so a second and more important phenomenon must take place. Lithium, or any alkaline element atoms must diffuse and this effect should be the main responsive of the absorption process after the Li_2CO_3 shell formation. This idea is, initially, supported from some theoretical data, showing that self-diffusion coefficient of lithium is considerably increased at around the same temperatures in which CO_2 absorption occurs (*25*, *76*). Nevertheless, the lithium diffusion mechanism cannot be as easy as mentioned above. Lithium diffusion may occur through vacancies on the Li_2CO_3, generated by the high temperatures. This vacancy mechanism only requires a lithium atom and a vacancy which move

Downloaded by DUKE UNIV on June 23, 2012 | http://pubs.acs.org
Publication Date (Web): December 3, 2010 | doi: 10.1021/bk-2010-1056.ch015

Downloaded by DUKE UNIV on June 23, 2012 | http://pubs.acs.org
Publication Date (Web): December 3, 2010 | doi: 10.1021/bk-2010-1056.ch015

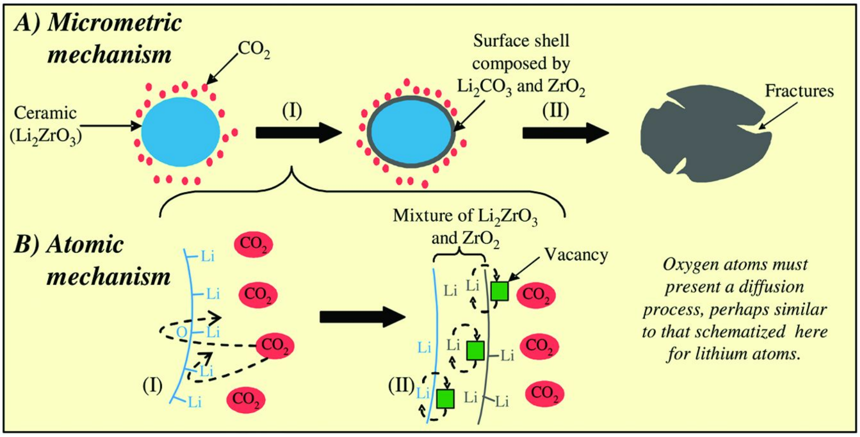
A) Micrometric mechanism
CO_2
Ceramic (Li_2ZrO_3)
(I)
Surface shell composed by Li_2CO_3 and ZrO_2
(II)
Fractures
B) Atomic mechanism
Li
CO_2
O
(I)
Mixture of Li_2ZrO_3 and ZrO_2
Vacancy
(II)
Oxygen atoms must present a diffusion process, perhaps similar to that schematized here for lithium atoms.

Figure 3. Micrometric (A) and atomic (B) mechanisms for the CO_2 absorption process on lithium ceramics. I) represents the surface reaction, which produces the Li_2CO_3 external shell, and II) shows the bulk absorption, where the volume expansion and fracture formation are schematized.

swamping positions. Then, lithium atoms may diffuse and "release" to the particle surface and continue the with the CO_2 absorption, increasing the Li_2CO_3-ZrO_2 external layer, from the surface inwards (Figure 3).

Something else has to be pointed out from the CO_2 absorption mechanism. Most of the papers published up to now have mentioned that lithium atoms must diffuse in some way to react with CO_2 and then produce Li_2CO_3. However, not only lithium atoms have to go through this process; because in order to complete the reaction $^1/_3$ of the oxygen atoms present in the Li_2ZrO_3 crystal becomes part of the Li_2CO_3. In other words, some oxygen atoms are involved on the reaction mechanism, otherwise it would not be completed.

Different experiments have been performed in order to clarify these hypotheses. Gauer and coworkers doped Li_4SiO_4 with different hetero-atoms (Al and Fe), in order to produce interstitial Li^{1+} sites, or anionic vacancies (*59*). The vacancy doped samples ($Li_{3.7}Al_{0.1}SiO_4$ and $Li_{3.7}Fe_{0.1}SiO_4$) showed much better CO_2 absorption rates than those observed for Li_4SiO_4 at low temperatures. However, Li_4SiO_4 absorbed more CO_2 at high temperatures. These results showed that the formation of vacancies improve diffusion and therefore the reactivity of alkaline ceramics (*47*, *59*).

Additionally, it has been reported some kinetic and thermodynamic data about the CO_2 absorption on alkaline ceramics. In general, there are two different kinetic and thermodynamic parameters that have been calculated; 1) the ceramic-CO_2 reaction and, 2) diffusion parameters. Table II summarizes these results for several alkaline ceramics (*48*, *66*, *69*, *72*). As can be seen, from this table, there are different factors that are consistent in all the ceramics.

First, the reaction constant values (k_{reaction}) are, at least, one order of magnitude larger than those of diffusion processes ($k_{diffusion}$). In other words, the limiting step of the whole CO_2 absorption mechanism on alkaline ceramics seems to be diffusion process. Additionally, CO_2 absorption and diffusion constant values increase as a function of the temperature. In general, both parameters are improved by one or even two orders of magnitude. Nevertheless, it has to be mentioned that in some cases, when temperature is increased a third process is activated, the CO_2 desorption, and an absorption/desorption equilibrium is reached. Finally, in order to analyze the temperature dependence of the different processes, different works have reported the activation enthalpies (ΔH), using the Eyring's model, which fits to a solid-gas system reaction. Results show that diffusion process is more dependent on temperature, in comparison to the ceramic-CO_2 reaction. In the Li_2CuO_2 case, ΔH could not be determined as kinetic constants did not linearly fitted to the Eyring's model, which implies that other thermodynamic or diffusion factors influence on the reaction.

Downloaded by DUKE UNIV on June 23, 2012 | http://pubs.acs.org
Publication Date (Web): December 3, 2010 | doi: 10.1021/bk-2010-1056.ch015

5. Physicochemical Modifications on Alkaline Ceramics To Improve the CO_2 Absorption Properties

CO_2 absorption investigations, on alkaline ceramics, have not been limited to the study of the ceramics in "standard" conditions. Several studies have shown that modifying different physical and/or chemical properties of the alkaline ceramics, the kinetic, efficiency and temperature range of CO_2 capture, among other properties, can be enhanced or adjusted (*5*, *6*, *30*, *37*, *39*, *48*, *53*, *73*, *77*).

Among the physical modifications, one of the most studied factors implies changes in particle size. For example, when, Li_2ZrO_3 is prepared with different particle sizes the CO_2 absorption is significantly improved (*5*, *39*). The efficiency, in a dynamic process, can be improved from 11 % to 48 %, decreasing the particle size from 0.5-1 μm to 10 nm, respectively (*39*). Therefore, these experiments proved that CO_2 absorption was importantly enhanced when the particle size was diminished, in other words, when the surface area was increased. It can be interpreted as follows, when there are large surface areas most of the lithium and oxygen atoms are located over the surface, being able to react with CO_2. Of course, these results are totally correlated to diffusion process, which has been established as the limiting step of the whole CO_2 absorption process, as mentioned previously on the absorption mechanism description.

Similar results have been obtained if Li_4SiO_4 and Li_2SiO_3 powders are produced with different particle sizes. For example, although several papers showed that Li_2SiO_3 does not react with CO_2, the reaction does occur in small quantities, under a specific condition; small particles, which implies large surface areas (*48*, *53*). Authors explained the CO_2 absorption on Li_2SiO_3 nanoparticles, focusing on different chemical aspects. In one hand, some authors say that lithium vapor and CO_2 pressures change into the nanoparticle system, especially at the grain boundaries and triple points (*48*). Then, the reactivity of the ceramic is highly optimized. Additionally, the presence of high surface areas must diminish the diffusion process importantly, which usually is the limiting step for the CO_2 absorption on this kind of ceramics. On the other hand, Khomane and coworkers (*53*) explained the Li_2SiO_3 activation as a function of the formation of non-stoichiometric surfaces. These authors say that there is a SiO_{2-x} tetrahedral

Table II. Kinetic and thermodynamic data from the CO_2 absorption on different alkaline ceramics (*64*, *66*, *69*, *72*)

Ceramic	*Temp (°C)*	*Kinetic data*		*Thermodynamic data*	
		$k_{reaction}$ *(seg^{-1})*	$k_{diffusion}$ *(seg^{-1})*	$\Delta H_{reaction}$ *(kJ/mol)*	$\Delta H_{diffusion}$ *(kJ/mol)*
Na_2ZrO_3					
	from 200	0.00116	$8X10^{-5}$	33.8	48.0
	to 700	0.0959	0.00695		
Li_4SiO_4					
	from 500	$3.3X10^{-4}$	$2X10^{-5}$	88.9	79.5
	to 650	$3.7X10^{-3}$	$1.9X10^{-4}$		
Li_5AlO_4					
	from 300	0.00073	$6.78X10^{-6}$	15.6	52.1
	to 675	0.00736	$6.8X10^{-4}$		
Li_2CuO_2					
	from 350	0.0016	$2.2X10^{-4}$	--	--
	to 725	0.03809	0.01965		

formation and strengthening of the $Li_2O\text{-}SiO_{2-x}$ bonds, all induced at high temperatures. Therefore, Lewis acidity is increased, making Li_2SiO_3 more reactive (*77*).

Nevertheless, although the production of small lithium ceramic particles enhances several CO_2 absorption properties, it brings an important problem as well; the thermal stability of these ceramics is highly reduced. It has been reported in the literature that lithium ceramics, and in general of alkaline ceramics, tend to sinter or to lose lithium through a sublimation process when they are exposed to high temperatures (*47*, *66*, *72*, *78*). Sintering process generates a significant decrement of the surface area, and lithium sublimation reduces the capacity of reaction, both inhibiting the CO_2 absorption.

A possible solution to this inconvenient would be the synthesis of porous materials. Usually, porous materials present a combination of good thermal and chemical stability, as well as good textural properties, for example large surface areas. In this way, template-based macro- and/or mesoporous materials have been studied as a novel method to fabricate ordered porous structures, among many other methods (*79–82*). Based on this idea, different schemes could be proposed as they are shown in Figure 4. One possible ceramic porous-type material could be the production of porous alkaline ceramics (Figure 4-A). In this case, the whole material would be composed by the alkaline ceramic. However, as it has been mentioned previously, the CO_2 absorption process implies a volume change, which could deteriorate the mechanical stability of these porous materials, propitiating their collapse and sintering. A second option could be the formation of a thermal and mechanical stable porous metal oxide, from which the alkaline

Downloaded by DUKE UNIV on June 23, 2012 | http://pubs.acs.org
Publication Date (Web): December 3, 2010 | doi: 10.1021/bk-2010-1056.ch015

Downloaded by DUKE UNIV on June 23, 2012 | http://pubs.acs.org
Publication Date (Web): December 3, 2010 | doi: 10.1021/bk-2010-1056.ch015

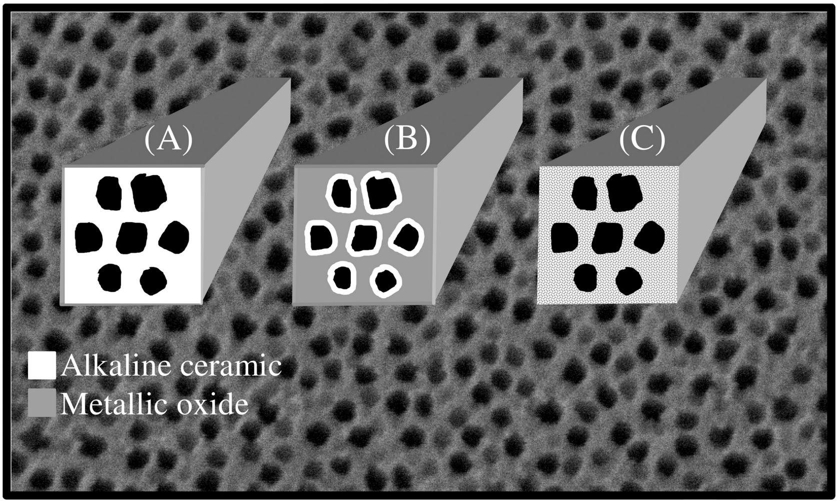

Figure 4. Representation of different porous systems for the CO_2 absorption. A) Porous alkaline ceramic; B) Porous metal oxide ceramic, where the alkaline ceramic is only deposited over the surface of the porous and; C) Metal oxide-composite porous materials.

ceramic is produced only over the surface of it. In this case, although the CO_2 reactivity could be limited to the external surface area, the porous and textural properties would be preserved (Figure 4-B). A third option could be the synthesis of a ceramic-composite porous material, from which the metal oxide gives the mechanical properties, while the alkaline ceramic absorbs CO_2 (Figure 4-C). Of course, in the last two cases, the ideal situation should be the combination of analogous metal oxides and alkaline ceramics, such as ZrO_2-Li_2ZrO_3 or SiO_2-Li_4SiO_4.

Apart from the physical modifications just mentioned above, there are another kind of variations; chemical modifications, which have shown to improve or modify the CO_2 absorption properties on alkaline ceramics. In fact, the synthesis of doped-ceramics, have been already mentioned on this text. Li_2ZrO_3 has been chemically modified through its doping mainly with potassium (*6*, *30*, *37*, *73*, *83*, *84*). This modification has showed that CO_2 absorption kinetic is enhanced. It seems that CO_2 diffuses faster through the molten lithium-potassium carbonate. Hence, as lithium-potassium carbonate is liquid at high temperatures, CO_2 can be transported more efficiently.

Other works have reported the synthesis of different solid solutions, such as $Li_{2-x}Na_xZrO_3$, $Na_{2-x}Li_xZrO_3$, $Li_{3.7}Al_{0.1}SiO_4$, $Li_{3.7}Fe_{0.1}SiO_4$ and $Li_{4-x}Na_xSiO_4$ (*59*, *64*, *74*, *75*). In general, all these solid solutions improve different properties of the CO_2 absorption reaction, such as temperature range on CO_2 absorption, some kinetic parameters and efficiency, among others; of course, all these improvements are in comparison to their respective pure alkaline ceramics. The improvements observed on the different solid solutions have been attributed to punctual modification on the crystalline structure of the ceramics or the formation of secondary phases into or over the ceramic particles. For example, $Na_{2-x}Li_xZrO_3$

Downloaded by DUKE UNIV on June 23, 2012 | http://pubs.acs.org
Publication Date (Web): December 3, 2010 | doi: 10.1021/bk-2010-1056.ch015

is a solid solution where lithium atoms are totally integrated into the Na_2ZrO_3 crystalline structure, occupying sodium positions. In this particular case, the solubility of lithium corresponds to $x \leq 0.6$. Experimental CO_2 absorption results showed that specifically $Na_{1.4}Li_{0.6}ZrO_3$ is able to absorb almost twice more CO_2 than Na_2ZrO_3 at different temperatures For example, the CO_2 absorption efficiency increased from 26 % to 47 % at 600 °C for Na_2ZrO_3 and $Na_{1.4}Li_{0.6}ZrO_3$, respectively (*74*).

A significant different behavior was observed on the $Li_{4-x}Na_xSiO_4$ system. In this case, sodium atoms did not seem to be incorporated into the Li_4SiO_4 crystalline structure; they were mostly located over the surface of the particles. However, sodium addition did increase importantly the CO_2 absorption. Therefore, sodium atoms were acting as reactive active sites for the CO_2 capture. Among these solid solutions, the sample that presented the best CO_2 absorption properties was $Li_{3.85}Na_{0.15}SiO_4$, presenting up to 93.3 % of efficiency at 600 °C, in comparison to the Li_4SiO_4, which only had efficiency equal to 58.6 % at the same temperature. However, in this system the addition of sodium atoms diminished the temperature range of absorption, as the equilibrium absorption/desorption was activated at lower temperatures (650 °C) than that for pure Li_4SiO_4 (almost 700 °C) (*64*).

Among the chemical modifications, a different option could not be the atom substitution, but its addition, generating non-stoichiometric ceramics. Li_2CuO_2 has a laminar-like structure, where lithium atoms are located into the $[CuO_4]$ layers, and it is possible to introduce lithium atoms on these layers, producing non-stoichiometric ceramics, $Li_{2+x}CuO_{2+x/2}$ (*69*). This kind of ceramics have shown that lithium excess is stabilized chemically into the laminar-like structure and these atoms are as reactive to the CO_2 absorption as the structural lithium atoms, improving the CO_2 absorption capacity of the ceramic.

Finally, it should be mentioned that all the doped and solid-solutions systems follows the same reaction mechanism as that showed above.

6. Regeneration and Reutilization Processes

The cyclability of these ceramics, which corresponds to the processes of regeneration and their consequent reutilization, is one of the most important aspects to be covered, in order to reduce the production of waste materials. In general, the cyclability processes followed by this kind of ceramics is shown on Figure 5. Initially, CO_2 is absorbed on the ceramic at a determined temperature. Then, in order to regenerate the ceramic, the flux gas is switched from CO_2 to an inert gas, N_2 for example. Additionally, at this point temperature is increased as well. These changes produced the CO_2 desorption and hypothetically the ceramic regeneration. Finally, to reuse the ceramic, CO_2 is fluxed again, and temperature is fixed at the absorption condition (Figure 5-A). During the performance of several cycles, different behaviors would be observed. In the first case, CO_2 absorption is maintained during the cycles, which means a high stability of the ceramic through the absorption/desorption processes (Figure 5-B). Other possibility implies an increment of the CO_2 absorption during the first cycles, and then its stabilization. Here, it is said that ceramic is activated during the

Downloaded by DUKE UNIV on June 23, 2012 | http://pubs.acs.org
Publication Date (Web): December 3, 2010 | doi: 10.1021/bk-2010-1056.ch015

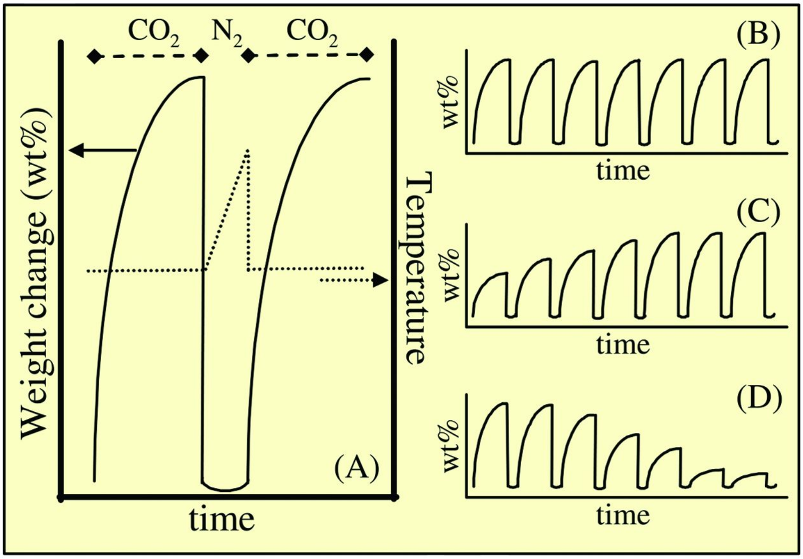

Figure 5. General illustration of the CO_2 absorption-desorption cyclability process (A) and different possible performances. B) CO_2 cyclability maintained during n number of cycles. C) CO_2 cyclability shows an increment on efficiency during the first n cycles. D) CO_2 cyclability deactivation as a function of the cycles.

first cycles. Ceramics must present some expansion-contraction during these initial cycles producing fractures, which increase the external surface area. As a consequence of these phenomena, the CO_2 absorption is increased as well (Figure 5-C). The third possibility corresponds to the CO_2 absorption deactivation, where the CO_2 absorption decreases in each cycle. The deactivation process, may be produced by thermal decomposition of the ceramic or in some cases, desorption process may not be produced (Figure 5-D).

Of course, cyclability and deactivation processes may be different in each ceramic. In this sense, alkaline ceramics do not seem to present any kind of trend, and each ceramic behaves differently. While some ceramics present high cyclability performances, others are not able to be regenerated, as they decomposed on other materials (*6*, *30*, *42*, *54*, *55*, *59*, *73*). Examples of these two different situations are Li_4SiO_4 and $Li_6Zr_2O_7$ (*25*, *30*). Li_4SiO_4 possesses high stability during the cyclability, even after eight cycles; it seems not to present any kind of degradation of the CO_2 absorption efficiency (*30*). On the other hand, $Li_6Zr_2O_7$ cannot be recycled. $Li_6Zr_2O_7$ absorbs relatively high CO_2 quantities. However, when CO_2 is desorbed, the ceramic decomposed on Li_2ZrO_3 and Li_2O, which sublimes due to temperature effects (*25*).

7. CO_2 Absorption Applications of the Alkaline Ceramic

As a consequence of the knowledge produced up to now, there have been already proposed different practical applications for the CO_2 absorption on alkaline ceramics (*30*, *43*, *47*, *56*, *61*, *85*, *86*). The two main applications proposed and tested for the alkaline ceramics are:

1. Steam reforming processes.
2. CO_2 separation with membranes.

7.1. Steam Reforming Process

Nowadays, industry widely uses steam reforming of natural gas. In fact, one of the most utilized steam reforming processes corresponds to hydrogen production through the steam methane reforming (SMR). However, during H_2 production, CO_2 is also produced. Therefore, CO_2 must be concentrated, captured, and sequestered. In that sense, different examples of reforming processes, using lithium ceramics, have been analyzed. Kato and coworkers (*56*) proposed the post-combustion CO_2 capture using Li_4SiO_4 and methane steam reforming. As Li_4SiO_4 is able to capture CO_2 at higher temperatures than 400°C, it has the advantages of enabling CO_2 separation in power plants without lowering temperature and absorbing CO_2 from the steam-methane reforming process at the same time. Additionally, as the absorption is exothermic but the steam reforming is an endothermic process, it is expected that the energy consumption would be reduced by combining these two reactions. Simultaneously, Chen and coworkers have tested the hydrogen production enhanced by steam methane reforming using either Li_2ZrO_3 or Li_4SiO_4 (*43*, *86*). Results showed that processes are capable to produce up to 95 mol% of H_2, with methane as the main side product, and only 0.2 mol% of CO.

7.2. CO_2 Separation with Membranes

The use of membranes for CO_2 separation has a great technological interest. However, one of the most importants limitations in this field is the fact that most of the reported membranes only works at low temperatures (~200 °C) (*87*). Therefore, the production of CO_2 separations membranes which are able to work at higher temperatures would be very useful. Membranes based on high temperature CO_2 absorbing materials may offer the opportunity to separate CO_2 selectively at high temperature, even from gas mixtures containing lighter molecules (*47*). Yamaguchi and coworkers (*61*) prepared Li_4SiO_4 membranes for CO_2 separation. They obtained a separation factor of 5.5 between CO_2 and N_2 gas molecules at 525°C. Something else has to be pointed out; the cyclability of Li_4SiO_4 has been analyzed, showing that it is able to perform several absorption-desorption cycles without presenting any significant decrease in the CO_2 capture efficiency (*30*). In a different work, lithium zirconate membranes for CO_2 separation were prepared and In this case, the CO_2 separation was done from a CO_2-CH_4 mixture, obtaining a separation factor of 4.9 at 600°C. This value is considerably high compared with the Knudsen diffusion limit of 0.6 (*85*). These results clearly show that CO_2 separation membranes produced from alkaline ceramics may be a suitable option for the CO_2 separation at higher temperatures than other material membranes.

Downloaded by DUKE UNIV on June 23, 2012 | http://pubs.acs.org
Publication Date (Web): December 3, 2010 | doi: 10.1021/bk-2010-1056.ch015

Downloaded by DUKE UNIV on June 23, 2012 | http://pubs.acs.org
Publication Date (Web): December 3, 2010 | doi: 10.1021/bk-2010-1056.ch015

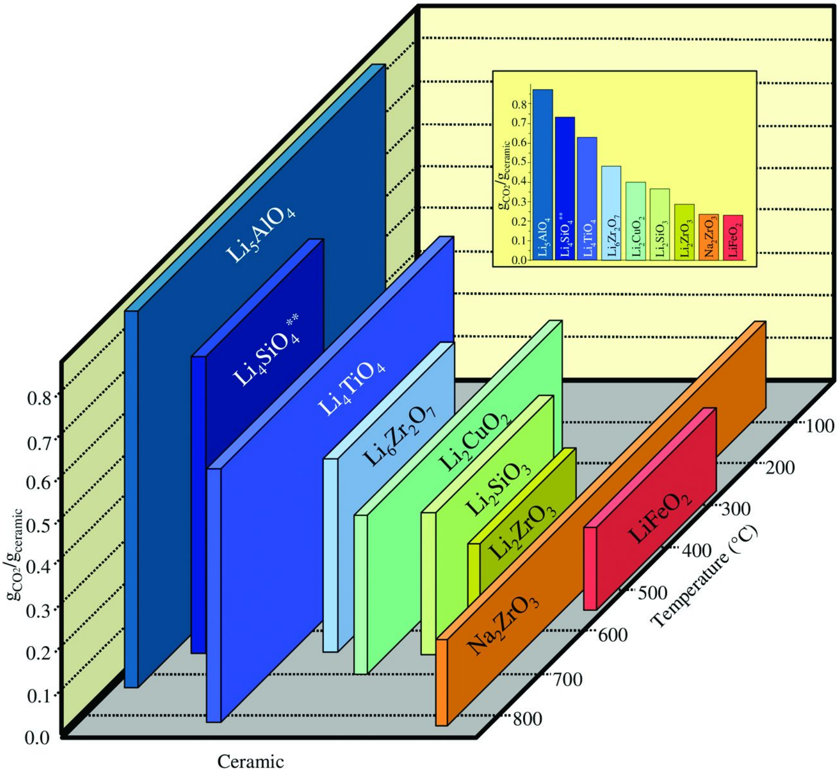

*Figure 6. Comparison of the CO_2 absorption on different alkaline ceramics as a function of the temperature and capacity per gram. While Li_4SiO_4 represents a partial lithium conversion (reaction 2), Li_4SiO_4** represents a total lithium conversion (assuming consecutive reactions 2 and 3).*

8. Conclusions

Summarizing, Figure 6 shows the CO_2 maxima absorption theoretical capacities for the most studied alkaline ceramics. As can be seen, Li_2ZrO_3, one of the ceramic most studied, and $LiFeO_2$ seems to be the ceramics with less expectatives, as they only absorb CO_2 in a small range of temperatures and their capacities are not either the best. On the other hand, although Na_2ZrO_3 presents a similar absorption capacity than that observed for Li_2ZrO_3, this ceramics presents as an advantage the large temperature ranges in which it can absorb CO_2. Li_4SiO_4 may deserve especial attention: If a total conversion from Li_4SiO_4 to Li_2CO_3 and SiO_2 is produced, this ceramic would become one the best ceramics for CO_2 absorption. Otherwise, if its conversion only corresponds to the partial decomposition, according to reaction 2, Li_4SiO_4 capacity decreases significantly. In this case, the CO_2 absorption would correspond to the Li_2SiO_3 ceramic. Finally, from the Figure 6 something very interesting comes out; Li_4TiO_4, $Li_6Zr_2O_7$ Li_5AlO_4 and Li_2CuO_2 apparently posses some of the best CO_2

Downloaded by DUKE UNIV on June 23, 2012 | http://pubs.acs.org
Publication Date (Web): December 3, 2010 | doi: 10.1021/bk-2010-1056.ch015

Table III. General comparison among some of the most representative materials used for the CO_2 capture (*20*, *45*, *88–91*)

Material	*Temp. range (°C)*	*Thermal stability*	*Efficiency (%)*	*Cyclability*	*Conditions or effects on the CO_2 capture*
Alk. ceramics	120-650	Good	Good	Possible	-----
Earthalk. oxides	120-450	Good	Good	Possible	Vol changes
Zeolites	150-400	Regular	Poor	Not possible	High pressure
Hydrotalcites	≤ 300	Poor	Regular	Possible	-----
Soda lime	150-400	Good	Excellent	Not possible	-----
Polymer memb.	≤ 200	Poor	Good	Possible	Not selective
Amines	≤ 200	Poor	Excellent	Possible	Aqueous media
Perovskites	200-550	Excellent	Poor	Not possible	-----

absorption properties: temperature ranges and CO_2 absorption capacities. These assertions may open a new window to further study these ceramics and other similar ceramics which has not been analyzed as possible CO_2 captors.

As it has been shown, the so called "alkaline ceramics" may become an alternative for the CO_2 capture. This kind of materials could be considered as promising ceramics for CO_2 absorption because they present the following advantages: These ceramics could be used for the CO_2 capture into pre-combustion and/or reforming systems; they present a great selectivity to CO_2 and the presence of steam vapor did not affect the absorption process, in fact, it seems to be enhanced; the temperature range of capture is very open, then different ceramics could be used under different thermal conditions; and some of these ceramics present good multicyclic behaviors. Table III presents a qualitative comparison among these ceramics with other materials which are used as CO_2 captors as well.

Acknowledgments

I would like to thank to Consejo Nacional de Ciencia y Tecnología (CONACYT), Instituto de Ciencia y Tecnología del Distrito Federal (ICyT-DF) and Universidad Nacional Autónoma de México (PAPIIT), for the financial support. Special thanks are given to all the students that at some moment have been part of this group.

References

1. Schrag, D. P. *Elements* **2007**, *3*, 171–178.
2. Friedmann, S. J. *Elements* **2007**, *3*, 179–184.
3. Busch, A.; Alles, S.; Gensterblum, Y.; Prinz, D.; Dewhurst, D. N.; Raven, M. D.; Stanjek, H.; Krooss, B. M. *Int. J. Greenhouse Gas Control* **2008**, *2*, 297–308.

Downloaded by DUKE UNIV on June 23, 2012 | http://pubs.acs.org
Publication Date (Web): December 3, 2010 | doi: 10.1021/bk-2010-1056.ch015

4. Leuning, R.; Etheridge, D.; Luhar, A.; Dunse, B. *Int. J. Greenhouse Gas Control* **2008**, *2*, 401–414.
5. Xiong, R.; Ida, J.; Lin, Y.S. *Chem. Eng. Sci.* **2003**, *58*, 4377–4385.
6. Ida, J.; Lin, Y. S. *Environ. Sci. Technol.* **2003**, *37*, 1999–2004.
7. Yang, Q.; Lin, Y.S. *Ind. Eng. Chem. Res.* **2007**, *46*, 6025–6031.
8. Young, S. *Nature* **2001**, *414*, 487–488.
9. Steele, B.H.; Heinzel, A. *Nature* **2001**, *414*, 345–352.
10. Dennis, C.; Davey, R.; Stein, W. *Nature* **2006**, *443*, 23–24.
11. Gur, I.; Fromer, N. A.; Geier, M.L.; Alivisatos, A. P. *Science* **2005**, *310*, 462–465.
12. Patterson, W. *Nature* **2007**, *449*, 664–664.
13. Pawlesa, J.; Zukal, A.; Cejka, J. *J. Int. Adsorp. Soc.* **2007**, *13*, 257–265.
14. Maceiras, R.; Alves, S. S.; Cancela, M. A.; Alvarez, E. *Chem. Eng. J.* **2008**, *137*, 422–427.
15. Mosqueda, H. A.; Vazquez, C.; Bosch, P.; Pfeiffer, H. *Chem. Mater.* **2006**, *18*, 2307–2310.
16. Romeo, L. M.; Bolea, I.; Escosa, J. M. *Appl. Therm. Eng.* **2008**, *28*, 1039–1046.
17. Siauciunas, R.; Rupsyté, E.; Kitrys, S.; Galeckas, V. *Colloids Surf., A* **2004**, *244*, 197–204.
18. Chen, J.; Loo, L. S.; Wang, K. *J. Chem. Eng. Data* **2008**, *53*, 2–4.
19. Bertelle, S.; Gupta, T.; Roizard, D. *Desalination* **2006**, *199*, 401–402.
20. Nomura, K.; Tokumistu, K.; Hayakawa, T.; Homonnay, Z. *J. Radioanal. Nucl. Chem.* **2000**, *246*, 69–77.
21. Park, S. W.; Cho, H. B.; Sohn, I. *J. Sep. Sci. Technol.* **2002**, *37*, 639–661.
22. Zhao, Z.; Cui, X.; Ma, J.; Li, R. *J. Greenhouse Gas Control* **2007**, *1*, 355–359.
23. Hutson, N. D.; Speakman, S. A.; Payzant, E. A. *Chem. Mater.* **2004**, *16*, 4135–4143.
24. Yong, Z.; Mata, V.; Rodriguez, A. E. *Sep. Purif. Technol.* **2002**, *26*, 195–205.
25. Pfeiffer, H.; Bosch, P. *Chem. Mater.* **2005**, *17*, 1704–1710.
26. Hrycak, M. B.; McKenna, D. B. U.S. Patent No. 60/539343, 2004.
27. Feng, B. H.; Tan, E. *Energy Fuels* **2007**, *21*, 426–434.
28. Siriwardane, R. V.; Robinson, C.; Shen, M.; Simonyi, T. *Energy Fuels* **2007**, *21*, 2088–2097.
29. Lee, S. C.; Choi, B.Y.; Lee, T. J.; Ryu, C. K.; Ahn, Y. S.; Kim, J. C. *Catal. Today* **2007**, *111*, 385–390.
30. Ida, J.; Xiong, R.; Lin, Y. S. *Sep. Purif. Technol.* **2004**, *36*, 41–51.
31. Reddy, E. P.; Smirniotis, P. G. *J. Phys. Chem. B* **2004**, *108*, 7794–7800.
32. Wu, S. F.; Li, Q. H.; Kim, J. N.; Yi, K. B. *Ind. Eng. Chem. Res.* **2008**, *47*, 180–184.
33. Stolaroff, J. K.; Keith, D. W. *Energy Convers. Manage.* **2005**, *46*, 687–699.
34. Ochs, D.; Brause, M.; Braun, B.; Maus, W.; Kempter, V. *Surf. Sci.* **1998**, *397*, 101–107.
35. Iyer, M. V.; Gupta, H.; Sakadjian, B.; Fan, L. S. *Ind. Eng. Chem. Res.* **2004**, *43*, 3939–3947.
36. Nakagawa, K.; Ohashi, T. *J. Electrochem. Soc.* **1998**, *145*, 1344–1346.
37. Nakagawa, K.; Ohashi, T. *Electrochemistry* **1999**, *67*, 618–621.

Downloaded by DUKE UNIV on June 23, 2012 | http://pubs.acs.org
Publication Date (Web): December 3, 2010 | doi: 10.1021/bk-2010-1056.ch015

38. Fauth, D. J.; Frommell, A.; Hoffman, J. S.; Reasbeck, R. P.; Pennline, H. W. *Fuel Process. Technol.* **2005**, *86*, 1503–1521.
39. Choi, K. H.; Korai, Y.; Mochida, I. *Chem. Lett.* **2003**, *32*, 924–925.
40. Hwang, K. S.; Lee, Y. H.; Hwangbo, S. *Mater. Sci.-Pol.* **2007**, *25*, 969–975.
41. Nair, B. N.; Yamaguchi, T.; Kawamura, H. *J. Am. Ceram. Soc.* **2004**, *87*, 68–74.
42. Yi, K. B.; Eriksen, D. Ø. *Sep. Sci. Technol.* **2006**, *41*, 283–296.
43. Ochoa-Fernández, E.; Rusten, H. K.; Jakobsen, H. A.; Rønning, M.; Holmen, A.; Chen, D. *Catal. Today* **2005**, *106*, 41–46.
44. Ochoa-Fernández, E.; Rønning, M.; Grande, T.; Chen, D. *Chem. Mater.* **2006**, *18*, 1383–1385.
45. Ochoa-Fernández, E.; Rønning, M.; Grande, T.; Chen, D. *Chem. Mater.* **2006**, *18*, 6037–6046.
46. Ochoa-Fernández, E.; Rønning, M.; Yu, X.; Grande, T.; Chen, D. *Ind. Eng. Chem. Res.* **2008**, *47*, 434–442.
47. Nair, B. N.; Burwood, R. P.; Goh, V. J.; Nakagawa, K.; Yamaguchi, T. *Prog. Mater. Sci.* **2009**, *54*, 511–541.
48. Venegas, M. J.; Fregoso-Israel, E.; Pfeiffer, H. *Ind. Eng. Chem. Res.* **2007**, *46*, 2407–2412.
49. Okumura, T.; Enomoto, K.; Togashi, N.; Oh-ishi, K. *J. Ceram. Soc. Jpn.* **2007**, *115*, 491–497.
50. Escobedo-Bretado, M.; Guzmán-Velderrain, V.; Lardizabal-Gutierrez, D. *Catal. Today* **2005**, *107−108*, 863–867.
51. Essaki, K.; Nakagawa, K.; Kato, M.; Uemoto, H. *J. Chem. Eng. Jpn.* **2004**, *37*, 772–777.
52. Essaki, K.; Kato, M.; Uemoto, H. *J. Mater. Sci.* **2005**, *18*, 5017–5019.
53. Khomane, R. B.; Sharma, B.; Saha, S.; Kulkarni, B. D. *Chem. Eng. Sci.* **2006**, *61*, 3415–3418.
54. Kato, M.; Nakagawa, K. *J. Ceram. Soc. Jpn.* **2001**, *109*, 911–914.
55. Kato, M.; Nakagawa, K.; Essaki, K.; Maezawa, Y.; Takeda, S.; Kogo, R.; Hagiwara, Y. *Int. J. Appl. Ceram. Technol.* **2005**, *2*, 467–475.
56. Kato, M.; Maezawa, Y.; Takeda, S.; Hagiwara, Y.; Kogo, R.; Semba, K.; Hamamura, M. *Key Eng. Mater.* **2006**, *317-318*, 81–84.
57. Kato, M.; Yoshikawa, S.; Nakagawa, K. *J. Mater. Sci. Lett.* **2002**, *21*, 485–487.
58. Tsumura, N.; Kuramoto, A.; Shimamoto, Y.; Aono, H.; Sadaoka, Y. *J. Ceram. Soc. Jpn.* **2005**, *113*, 269–274.
59. Gauer, C.; Heschel, W. *J. Mater. Sci.* **2006**, *41*, 2405–2409.
60. Rodriguez, M. T.; Pfeiffer, H. *Thermochim. Acta* **2008**, *473*, 92–95.
61. Yamaguchi, T.; Niitsuma, T.; Nair, B. N.; Nakagawa, K. *J. Membr. Sci.* **2007**, *294*, 16–21.
62. Kalinkin, A. M.; Kalinkina, E. V.; Zalkind, O. A.; Makarova, T. I. *Colloid J.* **2008**, *70*, 33–41.
63. Kalinkin, A. M.; Kalinkina, E. V.; Zalkind, O. A. *Colloid J.* **2008**, *70*, 42–47.
64. Mejía-Trejo, V. L.; Fregoso-Israel, E.; Pfeiffer, H. *Chem. Mater.* **2008**, *20*, 7171–7176.

Downloaded by DUKE UNIV on June 23, 2012 | http://pubs.acs.org
Publication Date (Web): December 3, 2010 | doi: 10.1021/bk-2010-1056.ch015

65. López-Ortiz, A.; Perez-Rivera, N. G.; Reyes, A.; Lardizabal-Gutierrez, D. *Separ. Sci. Technol.* **2004**, *39*, 3559–3572.
66. Alcérreca-Corte, I.; Fregoso-Israel, E.; Pfeiffer, H. *J. Phys. Chem. C* **2008**, *112*, 6520–6525.
67. Zhao, T.; Ochoa-Fernández, E.; Rønning, M.; Chen, D. *Chem. Mater.* **2007**, *19*, 3294–3301.
68. Palacios-Romero, L. M.; Pfeifer, H. *Chem. Lett.* **2008**, *37*, 862–863.
69. Palacios-Romero, L. M.; Lima, E.; Pfeifer, H. *J. Phys. Chem. A* **2009**, *113*, 193–198.
70. Kato, M.; Essaki, K.; Nakagawa, K.; Suyama, Y.; Terasaka, K. *J. Ceram. Soc. Jpn.* **2005**, *113*, 684–686.
71. Togashi, N.; Okumura, T.; Oh-ishi, K. *J. Ceram. Soc. Jpn.* **2007**, *115*, 324–328.
72. Ávalos-Rendón, T.; Casa-Madrid, J.; Pfeiffer, H. *J. Phys. Chem. A* **2009**, 6919–6923.
73. Pannocchia, G.; Puccini, M.; Seggiani, M.; Vitolo, S. *Ind. Eng. Chem. Res.* **2007**, *46*, 6696–6706.
74. Pfeiffer, H.; Vazquez, C.; Lara, V. H.; Bosch, P. *Chem. Mater.* **2007**, *19*, 922–926.
75. Pfeiffer, H.; Lima, E.; Bosch, P. *Chem. Mater.* **2006**, *18*, 2642–2647.
76. Pfeiffer, H.; Sánchez-Sánchez, J.; Álvarez, L. J. *J. Nucl. Mater.* **2000**, *280*, 295–303.
77. Sharma, B. K.; Sharma, M. P.; Kumar, S.; Roy, S. K.; Roy, S. K.; Badrinarayanan, S.; Sainkar, S. R.; Mandale, A. B.; Date, S. K. *Appl. Catal. A* **2001**, *211*, 203–211.
78. Cruz, D.; Bulbulian, S.; Lima, E.; Pfeiffer, H. *J. Solid State Chem.* **2006**, *179*, 909–916.
79. Stein, A. *Microporous Mesoporous Mater.* **2001**, *227*, 44–45.
80. Stein, A.; Schroden, R. C. *Curr. Opin. Solid State Mater. Sci.* **2001**, *5*, 553–561.
81. Velev, O. D.; Lenhoff, A. M. *Curr. Opin. Colloid Inteface Sci.* **2000**, *5*, 56–59.
82. Guliants, V. V.; Carreon, M. A.; Lin, Y. S. *J. Membr. Sci.* **2004**, *53*, 235–239.
83. Sandoval-Diaz, A.; Pfeiffer, H. *Rev. Mex. Fis.* **2008**, *54*, 65–68.
84. Veliz-Enriquez, M. Y.; Gonzalez, G.; Pfeiffer, H. *J. Solid State Chem.* **2007**, *180*, 2485–2492.
85. Kawamura, H.; Yamaguchi, T.; Nair, B. N.; Nakagawa, K.; Nakao, S. I. *J. Chem. Eng. Jpn.* **2005**, *38*, 322–328.
86. Rusten, H. K.; Ochoa-Fernandez, E.; Lindborg, H.; Chen, D.; Jakobsen, H. A. *Ind. Eng. Chem. Res.* **2007**, *46*, 8729–8737.
87. Bredesen, R.; Jordal, K.; Bolland, A. *Chem. Eng. Proc.* **2004**, *43*, 1129–1158.
88. Wirawan, S. K.; Creaser, D. *Microporous Mesoporous Mater.* **2006**, *91*, 196–205.
89. Macario, A.; Katovic, A.; Giordano, G.; Iucolano, F.; Caputo, D. *Microporous Mesoporous Mater.* **2005**, *81*, 139–147.
90. Yong, Z.; Rodrigues, A. E. *Energy Convers. Manage.* **2002**, *43*, 1865–1876.

91. Pfeiffer, H.; Knowles, K. M. *J. Eur. Ceram. Soc.* **2004**, *24*, 2433–2443.

Downloaded by DUKE UNIV on June 23, 2012 | http://pubs.acs.org
Publication Date (Web): December 3, 2010 | doi: 10.1021/bk-2010-1056.ch015

Downloaded by OHIO STATE UNIV LIBRARIES on June 23, 2012 | http://pubs.acs.org
Publication Date (Web): December 3, 2010 | doi: 10.1021/bk-2010-1056.ch016

Chapter 16

Characteristics of a Chemical Lung for Carbon Dioxide Conversion to Oxygen

Jin Ho Kim,[1] Tae-Hoon Jurng,[2] YoonKook Park,*,[1] and Soon Kwan Jeong[3]

[1]Department of Biological and Chemical Engineering, Hongik University, Jochiwon, S. Korea
[2]J. C. Technology, Cheil Bd., 4th Floor, 275-16 Sungsoo-3-dong, Seongdong-gu, Seoul, S. Korea
[3]Korea Institute of Energy Research, 71-2 Jang-dong, Yuseong-gu, Daejeon, S. Korea
***Corresponding author: parky@hongik.ac.kr**

This study demonstrates the feasibility of a chemical lung, consisting of potassium superoxide and a silicone polymer, for conversion of CO_2 in air to oxygen. In the first type of chemical lung, the extremely high reactivity of potassium superoxide was reduced by its combination with polysiloxane. The second type of chemical lung used a mixture of potassium superoxide and calcium hydroxide to further reduce the reactivity of potassium superoxide, and the mixture was dispersed in a silicone polymer matrix that also served as a water repellant. In general, the amount of converted CO_2 is proportional to potassium superoxide in the chemical lung. The small surface area of the chemical lung and the rapid reaction rate indicate that CO_2 conversion in the presence of potassium superoxide is controlled by reaction between CO_2 and the chemical lung.

Introduction

The greenhouse gases produced by burning fossil fuels have been recognized as a primary cause of global warming, which increases the average temperature on Earth, and will ultimately result in the melting icebergs in the polar regions. Achieving a consensus on how to deal with global warming is complicated on

In Advances in CO2 Conversion and Utilization; Hu, Y.;
ACS Symposium Series; American Chemical Society: Washington, DC, 2010.

Downloaded by OHIO STATE UNIV LIBRARIES on June 23, 2012 | http://pubs.acs.org
Publication Date (Web): December 3, 2010 | doi: 10.1021/bk-2010-1056.ch016

many fronts, including technological and economic, so it is extremely difficult to find a reasonable solution satisfying all countries. Because CO_2 is one of the main contributors to global warming, CO_2 capture and conversion are necessary.

Great progresses have been made in removing CO_2 via absorption (*1*), adsorption (*2*–*5*), and other techniques (*6*). Table 1 shows the advantages and disadvantages for each process for treating CO_2. Absorption and adsorption processes can be used at much lower temperature than those used for reaction-based CO_2 capture. However, the CO_2 capacities per unit mass sorbent for absorption and adsorption processes are almost an order of magnitude lower than those of reaction-based processes. Although activated carbon and zeolites rapidly adsorb large quantities of toxic compounds, these mesoporous materials quickly become saturated, and then begin to release the pollutants slowly back into the atmosphere because they rely on reversible adsorption principles. Furthermore, these mesoporous materials are not able to generate oxygen.

Because of its exceptional oxygen generating properties, potassium superoxide is used in spacecraft life-support systems. However, its high reactivity and hygroscopic properties severely limit the use of potassium superoxide due to safety considerations.

Several attempts have been made to construct a more commercially viable filter by mixing a strongly alkaline air purification material with a polymer resin (*7*). Potassium superoxide is a strong candidate for use in such air revitalization materials because it not only efficiently captures CO_2 in the atmosphere, but also generates oxygen:

$$4\ KO_2 + 2\ CO_2 \rightarrow 2\ K_2CO_3 + 3\ O_2 \qquad (1)$$

However, owing to its extremely high reactivity, spontaneous ignition is likely to occur when the potassium superoxide is blended with a molten polymer. In order to solve this issue, Rho and Jurng (*7*) suggested the use of silicone as the polymer resin because silicone has a much higher gas permeability than any other polymer resin, which allows harmful gases to escape rapidly and easily. Since silicone is highly water repellent, the superoxide will not readily react with water, even when in direct contact with it. In addition, as silicone is cured at room temperature, there is little danger of spontaneous ignition when the superoxide and the silicone are blended.

In this study, two types of chemical lung for CO_2 capture and oxygen generation were synthesized. In the first type, potassium superoxide, organopolysiloxane, and a curing agent were used. In the second type, in order to further decrease the reactivity of potassium superoxide in the chemical lung, the potassium superoxide is mixed with calcium hydroxide before it was used to convert CO_2 to oxygen. The effects of the amount of potassium superoxide on CO_2 conversion in the chemical lungs was investigated at room temperature and at various CO_2 initial concentrations. Fourier-transform infrared (FT-IR) analysis, Brunauer-Emmett-Teller (BET) analysis, and thermogravimetric analysis (TGA) were carried out to characterize the properties of the chemical lungs.

Downloaded by OHIO STATE UNIV LIBRARIES on June 23, 2012 | http://pubs.acs.org
Publication Date (Web): December 3, 2010 | doi: 10.1021/bk-2010-1056.ch016

Table 1. Capacity and disadvantages of CO_2 sorbents (*13*)

Category	*Candidates*	*Capacity g CO_2/g sorbent*	*Regeneration Temp. (°C)*	*Use*	*Disadvantages*
reaction	LiOH $2LiOH+CO_2=Li_2CO_3+H_2O$	0.920	1310	-Extravehicular mobility unit life support back pack	-High regen. T. -Short duration -One time use
	Dolomite $CaO+CO_2=CaCO_3$	0.786	600-900	-coal mines -IGCC plants	-Kinetically slow at low temp. -High regen. T
	KO_2 $2KO_2 + CO_2 = K_2CO_3 + 1.5O_2$	0.31 Plus 1.5 mol O_2 generated	>2000	-Air Regeneration systems (Drager®)	-High regen. T -One time use
	K_2CO_3 $K_2CO_3+CO_2+H_2O =2KHCO_3$	0.318	180-250	-Ammonia and syngas production	-Liquid phase absorption -Large space required -Not readily amendable to random orientation
absorption	Amine absorption	0.088 (PEI: (*2*))	150	-shuttle extended duration orbiter	-Excess moisture increases ΔP and reduces capacity
adsorption	Molecular Sieves (adsorption)	0.066 (MS 5A: (*4*))	250-350	-skylab mission (*5*)	-Protective bed is needed to remove H_2O -Easy to degrade

Downloaded by OHIO STATE UNIV LIBRARIES on June 23, 2012 | http://pubs.acs.org
Publication Date (Web): December 3, 2010 | doi: 10.1021/bk-2010-1056.ch016

Table 2. Chemical lung composition (basis: 5g sample)[a]

No.	*ratio*[b]	*Silicon polymer*			*KO_2*	*KO_2 in $Ca(OH)_2$*[c]
		Dimethyl polysiloxane	*Methyltriacetoxy silane*	*Dibutyl superoxide*		
S3K7	3:7	1.366	0.143	0.002	3.5	-
S5K5	5:5	2.273	0.227	0.005	2.5	-
S7K3	7:3	3.182	0.318	0.007	1.5	-
S3KC7	3:7	1.366	0.143	0.003	-	3.5
S4KC6	4:6	1.812	0.196	0.005	-	3.0
S5KC5	5:5	2.273	0.227	0.007	-	2.5
S6KC4	6:4	2.737	0.303	0.008	-	2.0
S7KC3	7:3	3.185	0.317	0.009	-	1.5

[a] initial carbon dioxide concentration is 0.2 % with nitrogen balance. [b] mass ratio between silicon polymer and KO_2. [c] mass ratio between KO_2 and $Ca(OH)_2$ is 3:7.

Experimental

Materials and Sample Preparation

Potassium superoxide (KO_2, CAS No.: 12030-88-5, Cat. No.: 278904), methyltriacetoxysilane (CAS No.: 4253-34-3372358, Cat. No.: 372358), and dibutyltin dilaurate (CAS No.: 77-58-7291234, Cat. No.: 291234) were purchased from Aldrich. Dimethylpolysiloxane (CAS No.: 9016-00-6) with hydroxyl blocking groups at both ends of the molecular chain, and a room temperature viscosity of 1,000 cSt, was purchased from Sigma. The SFC grade CO_2 supplied by a local gas company (Sebotech Inc., S. Korea) had a reported purity of 99.999%. All chemicals were used as received without further purification. The chemical lungs were prepared immediately before each experiment was performed by mixing dimethylpolysiloxane, methyltriacetoxysilane, dibutyltin dilaurate, and potassium superoxide in different ratios, and curing (Table 2). Detailed physical properties of the polysiloxanes can be found in the literature (*8*).

Experimental Setup and Method

A container (L × W × H = 32 cm × 32 cm × 42 cm) made of acrylic plate was used as a reaction chamber (see Figure 1); the container was sealed using a commercially available glue gun to obtain a reliable seal. A fan was placed inside the container in order to mix the gas in the container efficiently. USB–6008 Multifunction DAQ (12-bit 10-kS(Sample)/s, National Instruments, Seoul, S. Korea) was used for data acquisition (DAQ). A CO_2 sensor (Telaire 6004 CO_2 module, GE Sensing, Billerica, MA) and oxygen sensor (AO3 CiTiceL, City Technology Ltd., Portsmouth, UK) were placed inside the container to monitor the CO_2 and oxygen concentrations over time. Before any experimental data

Downloaded by OHIO STATE UNIV LIBRARIES on June 23, 2012 | http://pubs.acs.org
Publication Date (Web): December 3, 2010 | doi: 10.1021/bk-2010-1056.ch016

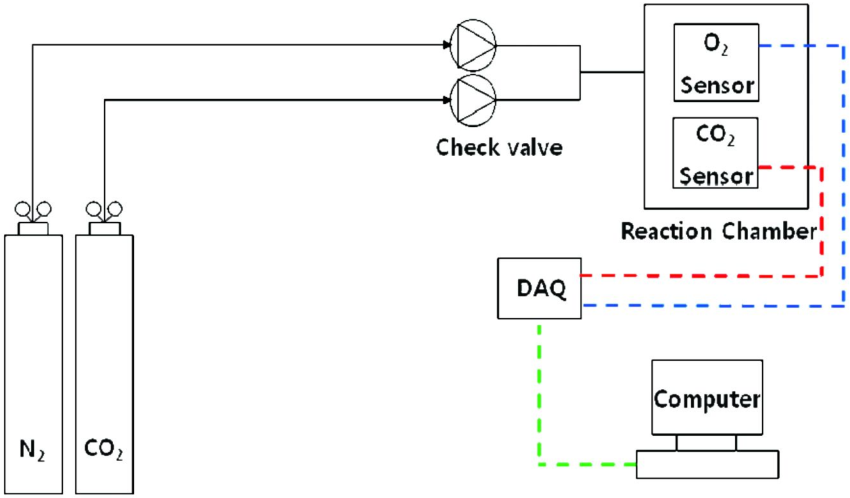

Figure 1. Experimental setup

were collected, a blank test without the chemical lung was carried out to ensure that the sensors were functioning correctly and were capable of monitoring the changes in CO_2 and oxygen concentrations. As soon as the chemical lung had been synthesized, it was loaded onto the glass plate and placed at the center of the container. The initial CO_2 concentration inside the container was controlled by using mass flow controllers for CO_2 and nitrogen. CO_2 and nitrogen were supplied via a 1/8" stainless steel tube connected to the back of the container. In order to investigate the effect of CO_2 concentration, initial CO_2 concentrations of 0.2%, 0.3%, and 0.4% were used. The temperature and moisture level in the container were in the ranges 24 ± 2 °C and 20 ± 5 %, respectively.

Analytical Methods

After each experiment, analysis of the chemical lung was performed by FT-IR spectroscopy using IRPrestige-21 spectrometer (Shimadzu, Kyoto, Japan) with an attached ATR cell (MIRacle™, PIKE Technologies, Madison, WI, USA). TGA was carried out to analyze the thermal properties of the chemical lung by using Q500IR-TGA (TA Instrument Inc. DE, USA). A BET surface analyzer (BELSORP-max, BEL-Japan, Inc., Osaka, Japan) was used to determine the texture properties of the chemical lung.

Results and Discussion

CO_2 Conversion to Oxygen in the Presence of a Chemical Lung

Figure 2 shows that CO_2 is converted into oxygen in the presence of a high ratio of potassium superoxide (silicon:KO_2 = 3:7) for an initial CO_2 concentration of 0.2%. Almost all of the CO_2 was converted into oxygen within 3 h; the conversion rate could be controlled by varying the amount of potassium

Downloaded by OHIO STATE UNIV LIBRARIES on June 23, 2012 | http://pubs.acs.org
Publication Date (Web): December 3, 2010 | doi: 10.1021/bk-2010-1056.ch016

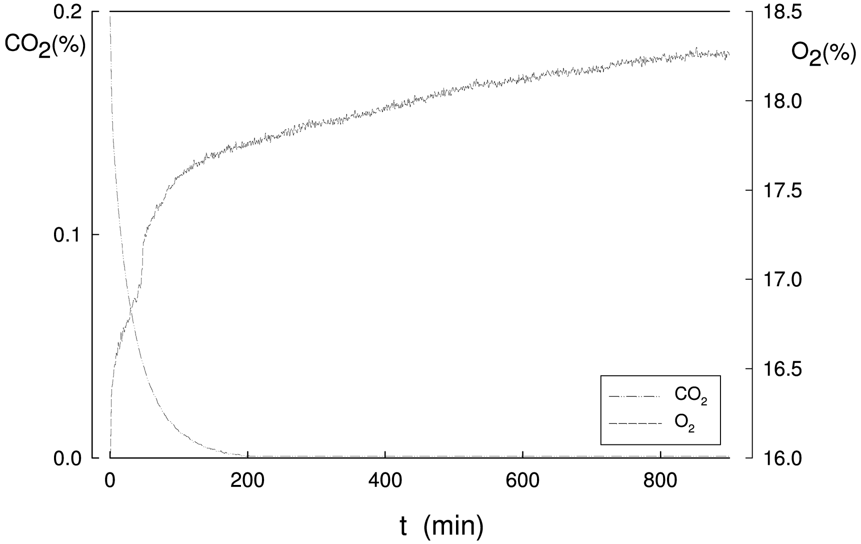

Figure 2. Conversion of CO_2 to O_2 in the presence of chemical lung composed of silicon:KO_2 = 3:7

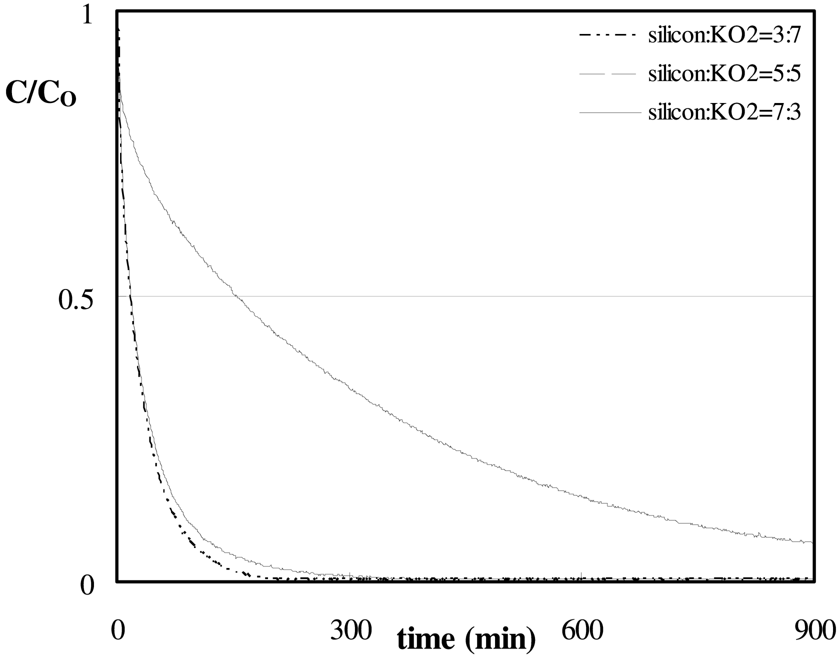

Figure 3. Conversion of CO_2 in the presence of different amounts of potassium superoxide at 0.2 % of CO_2 initial concentration.

superoxide in the chemical lung. The effects of initial CO_2 concentration and the amount of superoxide in the chemical lung on CO_2 conversion are shown in Figures 3−5. In the absence of the chemical lung, the concentration of CO_2 remained relatively constant (*9*), although a small decrease (< 2 %) in the CO_2 concentration was observed after 10 h. This was probably due to diffusion of CO_2 out of the container through the seals.

As shown in Figure 3, when a low ratio of potassium superoxide was used (3:7, S7K3) with a CO_2 concentration of 0.2%, CO_2 conversion greater than 90% was achieved after 15 h. Increasing the mass ratio of potassium superoxide to 50% (5:5, S5K5) markedly improved CO_2 conversion. For the highest ratio of 70% (7:3, S3K7), almost all of the CO_2 was converted to oxygen. Similar results were obtained when initial CO_2 concentrations were 0.3% and 0.4%, respectively (Figures 4 and 5). From the stoichiometry in Eq. (1), one can expect an increase in the amount of converted CO_2 with increasing the potassium superoxide content from 30% to 70%.

In terms of CO_2 conversion rate, the most rapid conversion of CO_2 to oxygen occurred at the highest mass ratio of potassium superoxide (S3K7) in the chemical lung. However, it should be noted that as the potassium superoxide content increases, safety becomes an issue, which great care needs must be taken to avoid triggering a fire.

Downloaded by OHIO STATE UNIV LIBRARIES on June 23, 2012 | http://pubs.acs.org
Publication Date (Web): December 3, 2010 | doi: 10.1021/bk-2010-1056.ch016

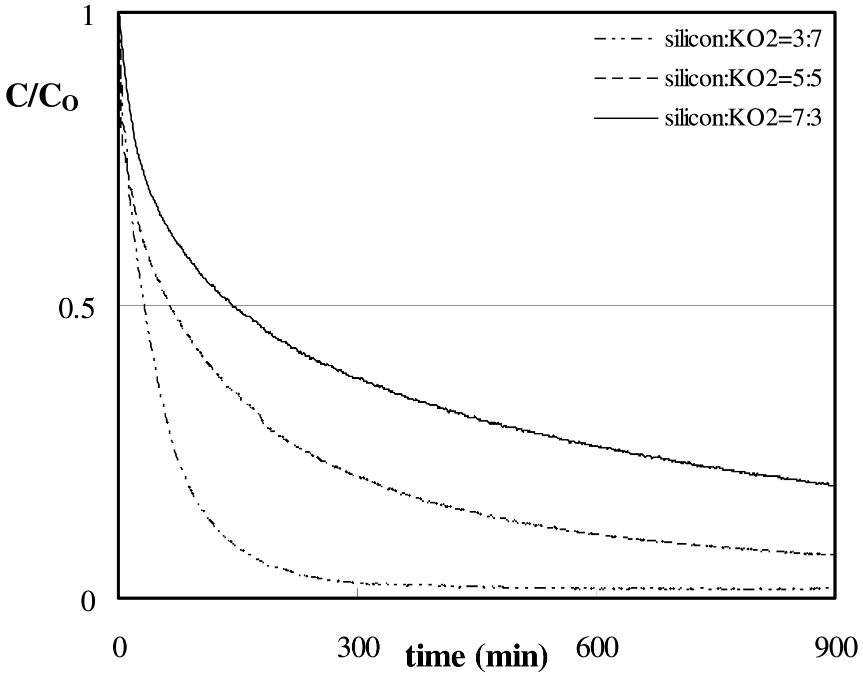

Figure 4. Conversion of CO_2 in the presence of different amounts of potassium superoxide at 0.3 % of CO_2 initial concentration.

Downloaded by OHIO STATE UNIV LIBRARIES on June 23, 2012 | http://pubs.acs.org
Publication Date (Web): December 3, 2010 | doi: 10.1021/bk-2010-1056.ch016

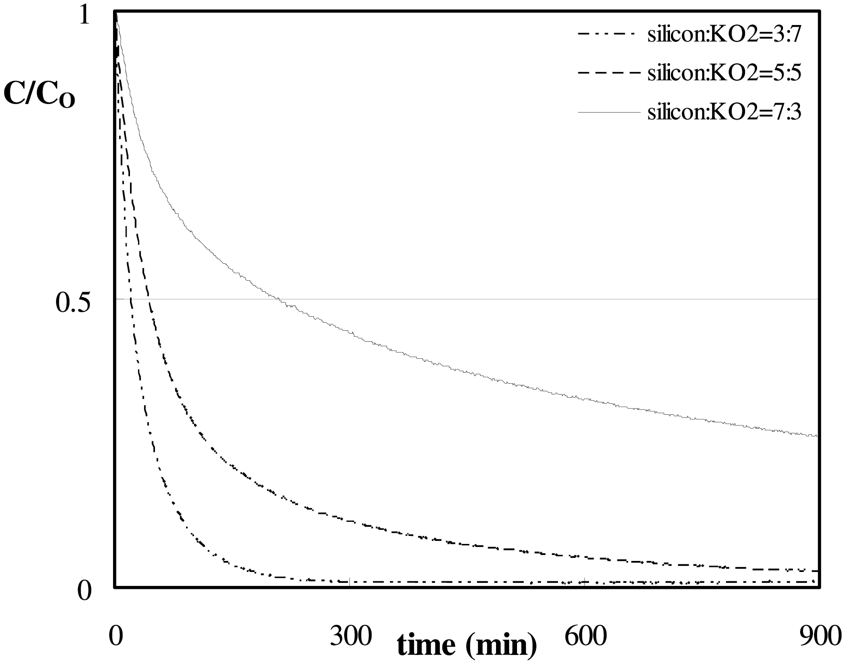

Figure 5. Conversion of CO_2 in the presence of different amounts of potassium superoxide at 0.4 % of CO_2 initial concentration.

When the first type of chemical lung was replaced by the second type, which contained calcium hydroxide to control the reactivity of the chemical lung, similar experimental results were obtained. As shown in Figure 6, with increasing the amount of potassium superoxide, a much faster CO_2 conversion reaction was observed. For example, almost all of the CO_2 was converted to oxygen within 4 h with the chemical lung containing 30% silicone (S3KC7).

It is a reasonable assumption that CO_2 serves as a limiting reagent in Eq. (1). If the reaction is assumed to be an irreversible third-order reaction with respect to CO_2 (denoted by A), the following equation can be derived:

$$\frac{1}{2}\left(\frac{1}{p_A^2}-\frac{1}{p_{A0}^2}\right)=\frac{k}{R^2T^2}t \qquad (2)$$

where p_{A0} and p_A are the initial partial pressure of CO_2 and the partial pressure at time t, R is the gas constant, and T is the absolute temperature. The rate constant k can be determined by plotting the values of the left-hand side of the equation against time. Table 3 shows that the reaction rate constants increased with the amount of potassium superoxide used.

Downloaded by OHIO STATE UNIV LIBRARIES on June 23, 2012 | http://pubs.acs.org
Publication Date (Web): December 3, 2010 | doi: 10.1021/bk-2010-1056.ch016

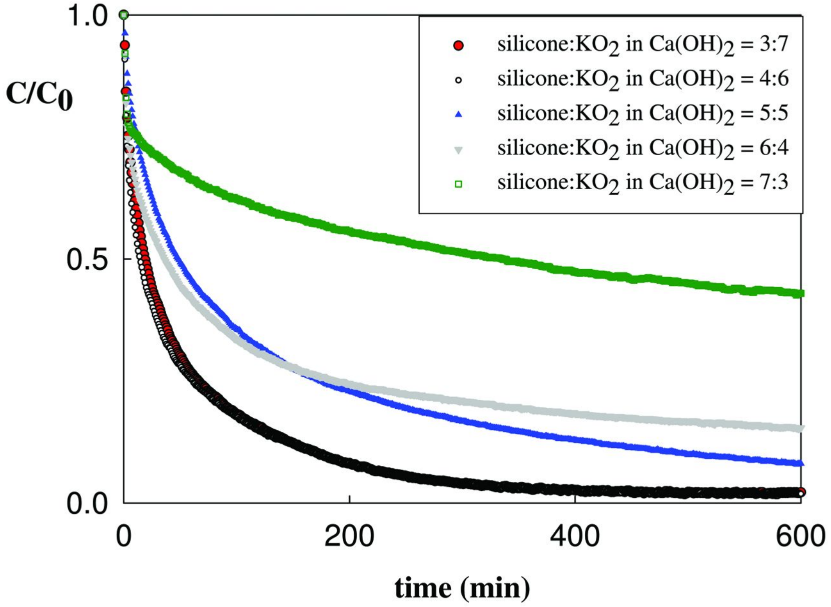

Figure 6. Conversion of CO_2 in the presence of different amounts of potassium superoxide in calcium hydroxide at 0.2% of CO_2 initial concentration.

Table 3. Experimental results

No.	*ratio*	*amount of CO_2 converted*[a]	$k\left(\frac{L^2}{mol \cdot \min}\right)$
S3K7	3:7	7.144	2111
S5K5	5:5	5.927	695
S7K3	7:3	2.940	228
S3KC7	3:7	6.377	1549
S4KC6	4:6	6.261	850
S5KC5	5:5	5.241	607
S6KC4	6:4	4.119	451
S7KC3	7:3	2.314	214

[a] reaction time over 1 hr (mg of CO_2/g of chemical lung) at 0.2% CO_2 initial concentration with N_2 balance.

Downloaded by OHIO STATE UNIV LIBRARIES on June 23, 2012 | http://pubs.acs.org
Publication Date (Web): December 3, 2010 | doi: 10.1021/bk-2010-1056.ch016

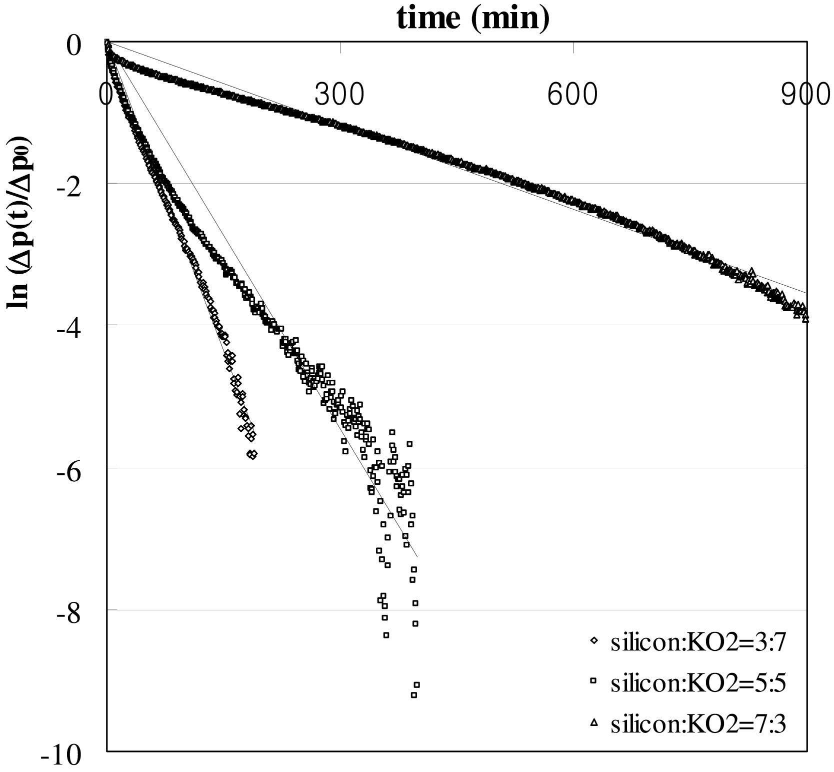

Figure 7. Determination of diffusion coefficient (D) using Eq. (5) at 0.2 % of CO_2 concentration.

Estimation of Diffusion Coefficients

Under these experimental conditions, CO_2 conversion in a chemical lung is expected as a diffusion-controlled process. The diffusion of CO_2 into the block geometry (about L × W × H = 3 cm × 2 cm × 1 cm) of the chemical lung can be described by Fick's law of diffusion (*10*):

$$\frac{c_{A,t} - c_{A,\infty}}{c_{A,0} - c_{A,\infty}} = E_a E_b E_c \tag{3}$$

where $c_{A,t}$, $c_{A,\infty}$, and $c_{A,0}$ are the concentrations of CO_2 at time t, $t \rightarrow \infty$, and t =0, respectively. E_a, E_b, and E_c are expressed by.

$$E_a = \frac{8}{\pi^2} \sum_{m=0}^{\infty} \frac{1}{(2m+1)^2} e^{-\frac{(2m+1)^2 \pi^2 D t}{4a^2}} \tag{4-1}$$

$$E_b = \frac{8}{\pi^2}\sum_{m=0}^{\infty}\frac{1}{(2m+1)^2}e^{-\frac{(2m+1)^2\pi^2 Dt}{4b^2}} \tag{4-2}$$

$$E_c = \frac{8}{\pi^2}\sum_{m=0}^{\infty}\frac{1}{(2m+1)^2}e^{-\frac{(2m+1)^2\pi^2 Dt}{4c^2}} \tag{4-3}$$

where D is the diffusion coefficient, and a, b, and c are height, width, and length of the bar geometry, respectively. Because a decrease in pressure corresponds to a decrease in CO_2 concentration in the chemical lung, $c_{A,t}$ and $c_{A,0}$ are proportional to $p(t) - p_\infty$ and $p_\infty - p_\infty$, respectively. This gives the following equation:

$$\frac{p(t) - p_\infty}{p_0 - p_\infty} = \frac{\Delta p(t)}{\Delta p_0} = E_a E_b E_c \tag{5}$$

We assume that the first term in Eqs. (4-1) to (4-3) is good enough approximation for the solution of this type of problem, which gives the following equation:

$$\frac{\Delta p(t)}{\Delta p_0} = \frac{8}{\pi^2}\left(e^{-\frac{\pi^2 D}{4a^2}t} + e^{-\frac{\pi^2 D}{4b^2}t} + e^{-\frac{\pi^2 D}{4c^2}t}\right) \tag{6}$$

Eq. (6) enables us to plot $\ln(\Delta p(t)/\ \Delta p_0)$ against t, obtaining the diffusion coefficient D. As shown in Figure 7, the plot of $\ln(\Delta p(t)/\ \Delta p_0)$ vs. t at a CO_2 concentration of 0.2 % forms a straight line; similar results were obtained at the other CO_2 concentrations of 0.3 and 0.4 %. In all cases, the value of p_∞ in Eq. (6) was close to 0. Table 4 shows the diffusion coefficients estimated under various conditions. In general, as the potassium superoxide mass ratio increased, the diffusion coefficient decreased. For example, for an initial CO_2 concentration of 0.4%, the diffusion coefficient was 1.677×10^{-3} and 0.313×10^{-3} cm^2/s for 30 and 70 % potassium superoxide, respectively.

Table 4. The diffusion coefficient, D ($10^3 \times cm^2/s$) , at 297 K

No.	*Initial CO_2 concentration (%)*		
	0.2	*0.3*	*0.4*
S3K7	0.291	0.276	0.313
S5K5	1.356	0.373	0.469
S7K3	2.161	1.222	1.677

Downloaded by OHIO STATE UNIV LIBRARIES on June 23, 2012 | http://pubs.acs.org
Publication Date (Web): December 3, 2010 | doi: 10.1021/bk-2010-1056.ch016

Downloaded by OHIO STATE UNIV LIBRARIES on June 23, 2012 | http://pubs.acs.org
Publication Date (Web): December 3, 2010 | doi: 10.1021/bk-2010-1056.ch016

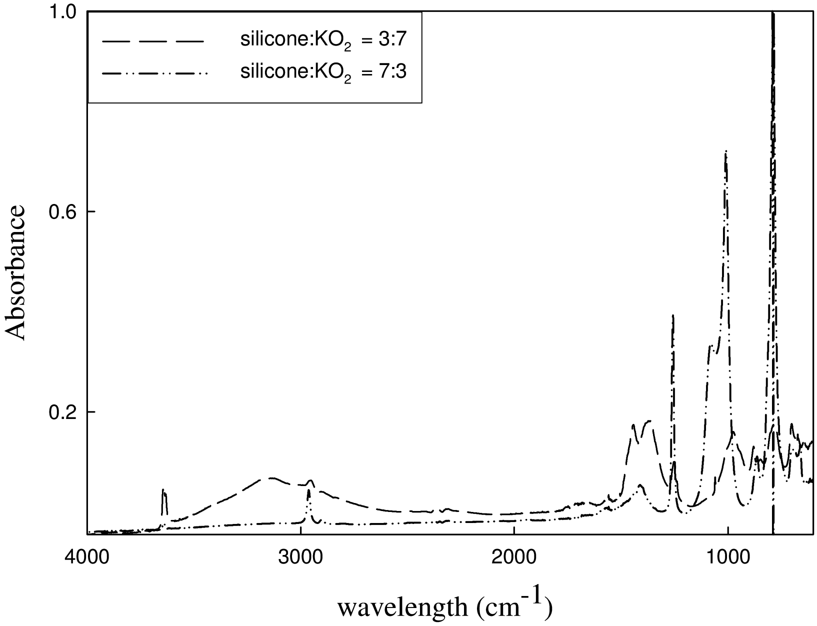

Figure 8. FTIR spectra of the chemical lung obtained after the conversion reaction.

At various CO_2 concentrations, one can see an inconsistency in the diffusion coefficients. This inconsistency may be attributed to the fact that the diffusivity was assumed to be direction-insensitive, and only the first term in Eqs. (4-1) to (4-3) was considered.

Texture Properties of the Chemical Lung

The BET specific surface area and pore volume of the chemical lung were determined using a BET surface area analyzer. The specific surface areas (< 30 cm^2/g) of the chemical lungs were extremely small compared to those of most sorbents. The pore volumes were almost zero. The small BET surface areas indicate that CO_2 conversion to oxygen is predominantly due to reaction (*1*).

FT-IR Spectroscopy

Figure 8 shows the FTIR spectra after the reaction of the first type of chemical lung. The stretching Si-C bond can be observed at 790 cm^{-1}, and its intensity increases with increasing polymer content from 30% (S3K7) to 70 % (S7K3). The peaks near 1000 cm^{-1} and 1250 cm^{-1} correspond to the CH_2 bonds in $SiCH_2$ and $Si\text{-}CH_3$, respectively (*11*). The Si-O bond (*12*), which is a repeating unit in the organopolysiloxane, appears at 1050 cm^{-1} and the intensity of this peak for samples with high silicone content (S7K3) is much larger than that for samples containing less silicone (S3K7).

Downloaded by OHIO STATE UNIV LIBRARIES on June 23, 2012 | http://pubs.acs.org
Publication Date (Web): December 3, 2010 | doi: 10.1021/bk-2010-1056.ch016

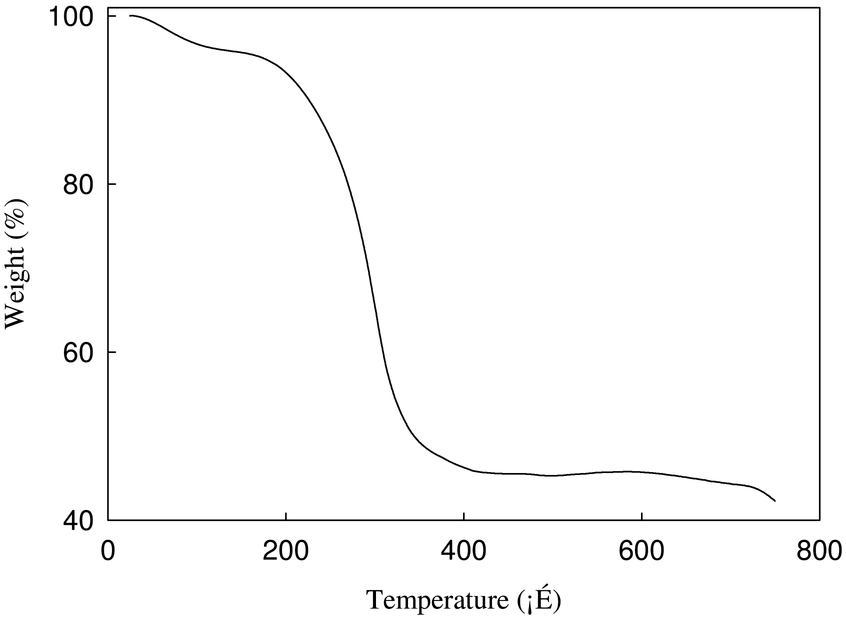

Figure 9. TGA results of chemical lung of S5KC5.

TGA Analysis

The thermogravimetric analysis results for the second type of chemical lung (S5KC5) after the conversion reaction is shown in Figure 9. The mass losses below 100 °C and 250 °C are attributed to moisture and silicone polymer, respectively. The loss after 700 °C is probably due to potassium carbonate.

Conclusions

A chemical lung consisting of potassium superoxide, methyltriacetoxysilane, dibutyltin dilaurate, and dimethylpolysiloxane gives excellent results for the conversion of CO_2 in air to oxygen. The higher the content of potassium superoxide in the chemical lung, the higher the CO_2 conversion rate is. The amount of potassium superoxide in the chemical lung is a critical factor in controlling the CO_2 conversion reaction rate. The small BET surface area indicates that CO_2 adsorption on the chemical lung was much less important than the CO_2 conversion reaction.

Potassium superoxide, potassium peroxide, calcium peroxide, lithium peroxide, and sodium superoxide can also be used to convert CO_2 in air to oxygen. The chemical lung composition tested here may extend the application of potassium superoxide as a capture agent to safely and effectively remove acidic gases, such as sulfur oxides and nitrogen oxides, from air.

Downloaded by OHIO STATE UNIV LIBRARIES on June 23, 2012 | http://pubs.acs.org
Publication Date (Web): December 3, 2010 | doi: 10.1021/bk-2010-1056.ch016

References

1. Puxty, G.; Rowland, R.; Allport, A.; Yang, Q.; Bown, M.; Burns, R.; Maeder, M.; Attalla, M. *Env. Sci. Technol.* **2009**, *43*, 6427–6433.
2. Xu, X.; Song, C.; Miller, B. G.; Scaroni, A. W. *Fuel Process. Technol.* **2005**, *86*, 1457–1472.
3. Jang, H. T.; Park, Y.; Ko, Y. S.; Lee, J. Y.; Margandan, B. *Int. J. Greenhouse Gas Control* **2009**, *3*, 545–549.
4. Defu, L.; Jinqu, W. *Adsorpt. Sci. Technol.* **2002**, *20*, 83–90.
5. Barker, R. S.; Russel, M. R.; Whitmer, L. R. SAE Technical Paper Series No. 911470, 21st International Conference on Environmental Systems, San Francisco, CA, July 15−18, 1991.
6. Muldoon, M. J.; Aki, S. N. V. K.; Anderson, J. L.; Dixon, J. K.; Brennecke, J. F. *J. Phys. Chem. B* **2007**, *111*, 9001–9009.
7. Rho, M.; Jurng, T. PCT WO 085708, 2006.
8. Mark, H. F. *Encyclopedia of Polymer Science and Engineering*, Vol. 15; Wiley-Interscience: New York, 1989; pp 204−308.
9. Kim, J. M.S. Thesis, Hongik University, Seoul, Korea, 2009.
10. Treybal, R. E. *Mass-Transfer Operations*, 3rd ed.; McGraw Hill, Inc.: New York, 1981.
11. Kaneko, T.; Nemoto, D.; Horiguchi, A.; Miyakawa, N. *J. Crystal Growth* **2005**, *275*, e1097–e1101.
12. Galeener, F. L. *Phys. Rev. B.* **1979**, *19*, 4292.
13. Sathitsuksanoh, N.; Tatarchuk, B. J. Paper 333e, AIChE National Meeting, San Francisco, CA, November 15, 2006.

Subject Index

A

- Acid-base equilibrium
  - **2** (X = H_2O), 146*f*
  - hydroxyl and oxyanion forms, 145*f*
- AEAPMDS. *See* N-(β-aminoethyl)-γ-amino propyl] trimethoxysilane
- Alcohols, aerobic oxidation, 94*s*
- Alkaline ceramics, 235
  - and CO_2 absorption
    - applications, 246
    - capacity per gram, 248*f*
    - kinetic and thermodynamic data, 243*t*
    - physicochemical modifications, 242
    - regeneration and reutilization processes, 245
    - separation with membranes, 247
    - steam reforming process, 247
    - temperature, 248*f*
  - CO_2 captors, 233
  - lithium zirconate, 235
  - other types, 239
  - reaction mechanism, 240
  - sodium zirconate, 236
- Al_2O_3
  - glow discharge plasma treatment, 178*f*
  - and MWCNT, 130*t*
- γ-Al_2O_3
  - CO_2 adsorption and activation, 197
  - and Fe_3Zn and Fe_4 clusters, 197
  - FT-IR spectra, 113, 114*f*
  - XRD patterns, 112, 113*f*
- γ-Al_2O_3(110)
  - adsorbed cluster, 203*f*
  - CO_2 adsorption configurations, 204*f*
  - and Fe_4 and Fe_3Zn, 203*f*
- Aminobenzonitrile, 88
- γ-(Aminpropyl)-triethoxysilane, 217*f*
  - MCM-41, 217*f*
  - SBA-15, 217*f*, 219*f*
- Anderson-Schulz-Flory distribution, 131*f*
- APTS. *See* γ-(Aminpropyl)-triethoxysilane
- Arynes, 91*s*
- Aziridines, 85

B

- Biomass and CO_2 hydrothermal reduction, 35*s*, 38
- Bu_2SnO. *See* Dibutyltin oxide

C

- Carbide catalyst
  - dry reforming of methane, 181
  - and nickel, 184
- Carbon cloth GDM electrode, 72*f*
- Carbon cycle, global
  - improvement, 31
  - pathways, 33*f*
- Carbon dioxide
  - absorption
    - lithium zirconate, 237*t*, 241*f*
    - metal oxide-composite porous materials, 244*f*
    - porous alkaline ceramic, 244*f*
    - porous metal oxide ceramic, 244*f*
  - adsorption
    - amine surface modification, 216
    - computer simulation, 213
    - mesoporous materials, 219*f*
    - MFI/MCM-41, 224
    - Mg-MCM-41, 225*f*
    - Mg-SBA-15, 224*f*
    - molecular simulation, 224
    - porous adsorbents, 224
    - porous materials, 209
    - porous silica adsorbents, 214
    - SBA-15, 224*f*
  - adsorption and activation
    - γ-Al_2O_3, 197
    - catalysts, 197
    - computational details, 199
    - Fe_3Zn and Fe_4 clusters, 197
    - synergetic effect, 204
  - alkaline ceramics, 233
  - arynes, 91*s*
  - captors, 233
  - capture, materials, 249*t*
  - catalytic conversion, 77
  - chemical lung, 255
  - chemistry, 77
  - and cyclic carbonates synthesis, 78
  - diacetylene, cyclic polymerization, 91*s*
  - dimethyl carbonate synthesis, 90
  - and diynes, 91*s*
  - DMC production, 91*s*
  - electrocatalytic reduction, 55
  - epoxide/propargyl amine carboxylation, 89*s*
  - and epoxides
    - cyclic carbonates synthesis, 78
    - cycloaddition reaction, 81*s*

Downloaded by 89.163.34.136 on June 23, 2012 | http://pubs.acs.org
Publication Date (Web): December 3, 2010 | doi: 10.1021/bk-2010-1056.ix002

Downloaded by 89.163.34.136 on June 23, 2012 | http://pubs.acs.org
Publication Date (Web): December 3, 2010 | doi: 10.1021/bk-2010-1056.ix002

ethane, oxidative dehydrogenation, 103
and formic acid, 43*f*, 151*f*
H_2O_2-tunable reaction, 84*s*
hydrogen
  formation, 48*t*
  storage material, 141
hydrogenation, 125, 141
  catalyst, 143, 144*s*, 145, 149
  continuously stirred tank reactor set-up, 129
  formic acid decomposition, 144*f*
  homogeneous catalytic process, 143*f*
  iridium-DHBP catalyst, 148*t*
  jet fuel synthesis, 125
  MWCNT, 125
  powder X-ray diffraction, 129
  preparation, 127
  prototype catalyst, 144*f*
  scanning electron microscope, 130
  testing and characterization, 128
  X-ray photoelectron spectroscopy, 130
hydrothermal reduction
  biomass, 38
  EPDM, 37
  Fe and Ni, 47
  formic acid yield, 47
  hydrogen production, 46
  metals, 45
  organic wastes, 34, 35*s*
  PE, 35
  value-added products, 31
  water, 36*f*
lactone synthesis, 89, 91*s*
Nankai group, 77
O_2, conversion
  chemical lung, 259, 260*f*, 263*t*, 264*f*, 265*t*
  K/Mn/Fe catalysts, 130*t*
  potassium superoxide, 260*f*, 261*f*, 262*f*, 263*f*
  silicon:KO_2, 260*f*
and oil, 39*f*
PEG radical chemistry, 95
photocatalytic reduction, 15, 23
  CO evolutions, 23*f*
  H_2, 23*f*
and quinazoline synthesis, 88
reduction, gas phase
  aqueous, 68
  carbon cloth GDM electrode, 72*f*
  Fe encapsulated in CNT, 72*f*
  formic acid, 40, 42
  gas diffusion electrode, 68
  GDE and SPE, 68
    See also Gas diffusion electrode and Solid polymer electrolyte
    glucose, 39
    nafion 117 cation exchange membrane, 72*f*
  reduction and metals electrodes, 61*t*, 62*f*
  soluble catalyst, 82*f*
  sorbents, 257*t*
  splitting
    cycles, 3*f*
    solar energy, 1
    solar thermochemical cycle, 25, 27*f*
    thermochemical, 1
    thermodynamics and kinetic analyses, 26
    ZnO/Zn redox reactions, 25, 27*f*
  urea derivatives synthesis, 92
Carbon dioxide reforming of methane
  catalysts, 155, 158
    Ni/γ-Al_2O_3, 160, 161*f*
    Ni/CaO, 160, 161*f*
    Ni/La_2O_3, 160, 161*f*, 162*f*
    plasma treatments, 168
    promoting effects, 163
    solid solution formation, 164
    strategies, 159
    supports, role, 159
  CH_4 conversion, 166*f*
  CO_2 conversion, 166*f*
  CO yield, 166*f*
  equilibrium gas composition, 158*f*
  H_2 yield, 166*f*
  Ni catalysts, 175
  NiO/alkaline earth metal oxides, 166*f*
  NiO/MgO catalyst, 167*f*
  thermodynamic consideration, 157
Carbon monoxide
  CO_2 photoreduction, 23*f*
  β-Ga_2O_3, 22*f*
  photoirradiation, 22*f*, 23*f*
  reduction and metal electrodes, 66*t*
Carboxylation and epoxide/propargyl amine, 89*s*
Catalysts
  carbide, 181
  cerium-based oxide, 106
  CO_2
    adsorption and activation, 197
    conversion, 77
    reforming of methane, 155, 158, 175
  Cr-based, 104
  free process, 88*s*
  gallium-based oxide, 105
  glow discharge plasma treatment, 176
  iridium complex catalysts, 141
  metal, 55

Downloaded by 89.163.34.136 on June 23, 2012 | http://pubs.acs.org
Publication Date (Web): December 3, 2010 | doi: 10.1021/bk-2010-1056.ix002

  - Mn-based oxide, 104
  - Mo_2C, 185*f*, 186*f*
  - nickel, 175
  - photocatalysts, 15
  - value-added chemicals, 77
- Catalytic oxidation–reduction cycle, 194*s*
- C_2H_4. *See* Ethylene
- Chemical lung
  - characteristics, 255
  - CO_2 conversion to O_2, 255, 259, 260*f*
    - diffusion coefficient, 264*f*, 265*t*
    - FTIR spectra, 266*f*
  - composition, 258*t*
  - potassium superoxide, 260*f*
  - silicon:KO_2, 260*f*
  - S5KC5, 267*f*
  - texture properties, 266
  - TGA analysis, 267*f*
- Chloramine-T, 94*s*
- 7-Chloroquinazoline-2, 4(1H, 3H)-dione, 89*s*
- CH_4-TPR, 183
- CO. *See* Carbon monoxide
- CO_2. *See* Carbon dioxide
- $CO_2^{\delta-}$ adsorbed on metals, 62*f*
- COF. *See* Covalent organic framework and Co_2 adsorption
- Coke resistant Ni catalysts, 175
- Continuously stirred tank reactor set-up, 129
- CoO_x species, 103
- $CoO_x/MgAl_2O_4$ catalyst, 117, 120
- 5-$CoO_x/MgAl_2O_4$-CP catalyst, 118*t*
  - H_2-TPR plots, 117*f*
  - TEM characterization, 116*f*
  - XRD patterns, 112, 113*f*
- 1-$CoO_x/MgAl_2O_4$-HT catalyst, 117*f*
- $CoO_x/MgAl_2O_4$-HT catalyst, 120*f*
  - Co-loading, 118*t*
  - H_2-TPR plots, 118*t*
- 3-$CoO_x/MgAl_2O_4$-HT catalyst, 117*f*
- 5-$CoO_x/MgAl_2O_4$-HT catalyst, 112, 112*f*, 113*f*
  - H_2-TPR plots, 117*f*
  - TEM characterization, 116*f*
- 8-$CoO_x/MgAl_2O_4$-HT catalyst, 117*f*
- 10-$CoO_x/MgAl_2O_4$-HT catalyst, 112, 113*f*, 117*f*
- Copper
  - electrocatalysts, 64
  - electrode and partial current data, 59*f*
- CO_2-TPO. *See* Temperature-programmed oxidation using CO_2
- Covalent organic framework and CO_2 adsorption, 227*f*, 228
- Cr-based oxide catalysts, 104
- CSTR. *See* Continuously stirred tank reactor set-up
- Cu(100) crystal and C_2H_4 formation, 104
- Cyclic carbonates
  - routes, 81*s*
  - synthesis
    - alkenes and CO_2, 84*s*
    - 1,2-diols and CO_2, 83
    - epoxides and CO_2, 78
    - functionalized-PEG, 82*s*
    - halohydrin and CO_2, 87*s*
    - olefins and CO_2, 82
    - supported catalyst, 82*s*
    - vicinal halohydrin and CO_2, 84
- Cyclic polymerization of diacetylene and CO_2, 91*s*
- Cycloaddition reaction
  - chiral Co-salen, 82*s*
  - CO_2 and epoxides, 81*s*

D

- Density functional theory, 197
- DFT. *See* Density functional theory
- DHBP. *See* 4,4’-Dihydroxy-2,2’-bipyridine
- Diacetylene, cyclic polymerization, 91*s*
- Dibutyltin oxide, 84*s*
- 4,4’-Dihydroxy-2,2’-bipyridine
  - complex **2**, 148*f*, 148*t*
- Dimethyl carbonate synthesis
  - and CO_2, 90, 91*s*
  - EC transesterification, 93*s*
  - Lewis basic ionic liquids-catalyzed, 93*s*
- 1,2-Diols and CO_2, 83
- Diynes, 91*s*
- DMC. *See* Dimethyl carbonate synthesis
- DRM. *See* Dry reforming of methane
- Dry reforming of methane, 181
  - carbide catalyst, 181
    - characterization, 182
    - evaluation, 183
    - preparation, 182
  - Mo_2C catalyst, 185*f*, 186*f*, 187*f*, 188*f*
  - Ni and Mo_2C generation, 191
  - Ni-Mo_2C catalyst, 185*f*, 186*f*, 187*f*, 188*f*

E

- EBS. *See* Electron backscattered image
- EDS. *See* Energy-dispersive spectroscopy
- Electrocatalytic metals, 58
- Electrocatalytic reduction of CO_2
  - challenges, 57

Downloaded by 89.163.34.136 on June 23, 2012 | http://pubs.acs.org
Publication Date (Web): December 3, 2010 | doi: 10.1021/bk-2010-1056.ix002

  - Cu-based electrocatalysts, 64
    - CO_{ads} to hydrocarbons, 64, 66*f*
    - Cu alloy electrocatalysts, 67
    - surface treatment, 67
  - metal catalysts, 55
  - organic molecule fuels, 55
  - pH, 59*f*
  - reaction mechanisms
    - adsorbed $CO_2^{\cdot -}$ formation, 62, 63
    - $CO_2^{\cdot -}$ formation, 60
    - $HCOO^-$, 62
    - hydrogen evolution reaction, 64
    - rate-determining step, 60

- Electrolysis cell and synthesis gas, 70*f*
- Electron backscattered image, 6*f*
- Energy-dispersive spectroscopy, 6*f*
- EPDM. *See* Ethylene-propylene-dieneterpolymer
- Epoxide/propargyl amine, carboxylation, 89*s*
- Epoxides and carbon dioxide
  - cyclic carbonates synthesis, 78
  - cycloaddition reaction, 81*s*
- Ethane, oxidative dehydrogenation, 103
- Ethylene
  - Cu(100) crystal, formation, 68*f*
  - ethane, oxidative dehydrogenation, 103
- Ethylene-propylene-dieneterpolymer
  - CO_2 hydrothermal reduction, 37
  - structure, 35*f*

F

- Fe_4
  - and γ-Al_2O_3 system
    - atomic charges, 203*t*, 206*t*
    - CO_2 adsorbed, 204*t*, 206*t*
  - binding energy, 206*f*
  - isolated, 201*f*
  - structure, 203*f*
- Feedstock chemicals and CO_2 hydrogenation, 125
- Fe_2O_3:YSZ. *See* Iron oxide:yttria-stabilized zirconia
- Ferrite materials, 1
- Fe_3Zn
  - and γ-Al_2O_3 system
    - atomic charges, 203*t*, 206*t*
    - CO_2 adsorbed, 204*t*, 206*t*
  - binding energy, 206*f*
  - structure, 203*f*
- Fe_3Zn and Fe_4 clusters
  - adsorption, 200
  - binding energy, 201*t*
  - CO_2 adsorption, 202
    - and activation, 197
  - isolated, 201*f*
  - relative energy, 201*t*
- FK 366. *See* Zenarestat®
- Formic acid
  - CO_2 hydrothermal reduction, 40, 42, 47
  - decomposition, 141, 149, 150*t*
    - CO_2, 151*f*
    - iridium catalyst, 151*f*
  - formation and CO_2, 43*f*
  - and glucose, 40*f*, 44*f*
  - NaOH, 40*f*
  - pH, 44*f*
  - yield
    - Fe/$NaHCO_3$ and Fe/Ni, 48*t*
    - temperature and time, 49*t*

G

- Ga-based oxide catalysts, 105
- Ga_2O_3, 21, 22*f*
- Gas diffusion electrode, 68*f*
  - C_1-C_2 fuels, 69
  - CO and H_2, 69, 70*f*
  - fuel precursors, 69
  - long-chain carbon fuels, 71
- GDE. *See* Gas diffusion electrode
- Glow discharge plasma treatment, 175, 177*f*
  - Al_2O_3 and Ni nitrate, 178*f*
  - catalyst, 176, 177*f*
  - SiO_2 powder and Ni nitrate, 178*f*
  - supporting material, 178
- Glucose
  - CO_2 reduction, 39*f*
  - formic acid, 40*f*
    - molar ratio, 44*f*
  - $NaHCO_3$, 40*f*
  - NaOH, 41*f*
- Guanidines, 90*s*

H

- H_2. *See* Hydrogen
- Hammett plot, 147*f*, 151*f*
- Helium and Fe_2O_3:8YSZ, 10*f*
- Homogeneous catalyst recycling, 82*f*
- Hot-wall aerosol flow reactor, 29*f*
- Hydrogen
  - CO_2, photocatalytic reduction, 15, 23*f*
  - formation, 48*t*
  - storage system, 141, 142*f*

Downloaded by 89.163.34.136 on June 23, 2012 | http://pubs.acs.org
Publication Date (Web): December 3, 2010 | doi: 10.1021/bk-2010-1056.ix002

- Hydrogen evolution reaction, 64
- Hydrogenation of carbon dioxide, 141
- Hydrothermal reduction of CO_2
  - biomass, 38
  - glucose, 39
  - metals, 45
  - organic wastes, 34, 35*s*
    - EPDM, 37
    - PE, 35
  - value-added products, 31
- 2-Hydroxyethyl methyl carbonate formation, 93*s*

I

- Iridium complex catalysts, 141, 151*f*
- Iridium-DHBP catalyst **2**, 148*t*
- Iridium-DHPT catalyst **3**, 148*t*
- Iron and CO_2 hydrothermal reduction, 47
- Iron oxide:yttria-stabilized zirconia
  - Ar, reduction, 8*f*
  - as-synthesized, 8*f*, 9*f*
  - CO_2 and H_2O splitting cycles, 3*f*, 5*f*
  - EBS-SEM image, 6*f*
  - Fe-EDS map, 6*f*
  - and helium, 10*f*
  - HT-XRD intensity, 10*f*
  - redox cycle, 7*f*
  - SEM/EDS, 9*f*
  - TGA redox cycle, 7*f*, 9*f*

J

- Jet fuel synthesis and CO_2 hydrogenation, 125

K

- KF31327, 89*s*
- $KHCO_3$ and CO reduction, 66*t*
- K/Mn/Fe catalysts, 134*t*
  - Al_2O_3 and MWCNT supports, 130*t*
  - CO_2 conversion, 130*t*
  - MWCNT, 131*f*
- KO_2. *See* Potassium superoxide and CO_2 conversion

L

- Lactone synthesis, 91*s*
  - arynes, 91*s*
  - CO_2, 89, 91*s*
  - diynes, 91*s*
- Lewis basic ionic liquids-catalyzed synthesis, 93*s*
- Li_4SiO_4. *See* Lithium orthosilicate
- Lithium orthosilicate, 248*f*
- Lithium zirconate, 235
  - CO_2 absorption, 237*f*, 237*t*, 241*f*
  - structure, 238*f*
- Li_2ZrO_3. *See* Lithium zirconate

M

- Materials science, 234
- MCM-41
  - AEAPMDS, 217*f*, 219*f*
  - APTS, 217*f*, 219*f*
  - CO_2
    - adsorption, 219*f*, 224*f*
    - and N_2, isotherms, 226*f*
  - metal modification, 218
  - Mg modified, 222*t*
  - model, 226*f*
  - and SBA-15
    - amine modification, 214, 216
    - characterization, 215
    - CO_2 adsorption, 216
    - magnesium modification, 215
    - silica, 214
- Mesoporous adsorbents, 211
  - CO_2 adsorption and desorption isotherms, 219*f*
  - DTGA, 219*f*
  - modification, 217*f*
  - physicochemical characteristics, 219*t*
  - TGA, 219*f*
- Mesoporous silica surface
  - Mg^{2+} cation, 223*f*
  - urea, 223*f*
- Metal catalysts and electrocatalytic reduction of CO_2, 55
- Metal electrodes
  - CO reduction, 66*t*
  - CO_2 reduction, 61*t*, 62*f*
- Metal oxide-composite porous materials, 244*f*
- Metals
  - CO_2 hydrothermal reduction, 45
  - $CO_2^{\delta-}$ adsorbed, 62*f*
  - oxides, 168*t*

Downloaded by 89.163.34.136 on June 23, 2012 | http://pubs.acs.org
Publication Date (Web): December 3, 2010 | doi: 10.1021/bk-2010-1056.ix002

Methane, 137*f*, 179*f*
Methane temperature-programmed reduction, 189*f*
MFI zeolite, atomic model, 226*f*
MFI/MCM-41
  CH_4 self diffusivity, 227*f*
  CO_2 and N_2, isotherms, 226*f*
  CO_2 self diffusivity, 227*f*
  CO_2/CH_4 adsorption selectivity, 227*f*
  CO_2/N_2 adsorption selectivity, 227*f*
  pore network, 226*f*
Mg^{2+} cations and mesoporous silica surface, 223*f*
Mg modified
  MCM-41 composites, 222*t*
  SBA-15 composites, 221*t*
$MgAl_2O_4$, 103, 107
$MgAl_2O_4$-CP
  FT-IR spectra, 113, 114*f*
  TEM characterization, 116*f*
  XRD patterns, 112, 113*f*
$MgAl_2O_4$-HT
  FT-IR spectra, 113, 114*f*
  TEM characterization, 116*f*
Mg-Al-SBA-15-D1, 223*f*
Mg-Al-SBA-15-I1, 223*f*
Mg-MCM-41, 225*f*
Mg-MCM41-20, 224*f*
Mg-MCM41-C, 220*f*
Mg-MCM41-C1, 224*f*
Mg-MCM41-C10, 224*f*
Mg-MCM41-C40, 224*f*
MgO, 19
  bidentate species, 19*c*
  CO_2, 19*c*, 22*f*
  phosphorescence excitation spectra, 22*f*
Mg-SBA-15-C, 220*f*
Mg-SBA-15-C1.5, 222*f*, 224*f*
Mg-SBA-15-C3, 224*f*
Mg-SBA-15-C6, 224*f*
Mg-SBA-15s, 224*f*
Mn-based oxide catalysts, 104
Mo_2C catalyst, 185*f*, 186*f*
  CH_4 and CO_2, surface reactions, 186
  CH_4/CO_2 dry reforming, 187*f*
  CH_4-TPR profiles, 189*f*
  CO_2-TPO profiles, 190*f*
  oxidation–reduction cycle, 194*s*
Multi-walled carbon nanotubes, 125
  Al_2O_3, 130*t*
  catalyst dispersed, 133*f*
  HNO_3, 129*f*
  K/Mn/Fe catalyst, 130*t*, 132*f*
  metal impregnation, 128
  pre-treatment, 127, 127*f*
  SEM image, 128*f*, 129*f*
  XRD, 132*f*
MWCNT. *See* Multi-walled carbon nanotubes

N

Nafion 117 cation exchange membrane, 72*f*
$NaHCO_3$, 41*f*
N-(β-aminoethyl)-γ-amino propyl] trimethoxysilane, 217*f*, 219*f*
Nankai group and carbon dioxide chemistry, 77
$NaNO_2$/[Imim-TEMPO][Cl]/CO_2/H_2O, 94*s*
NaOH
  formic acid formation, 40*f*
  glucose, 40*f*, 41*f*
Na_2ZrO_3. *See* Sodium zirconate
Nickel
  γ-Al_2O_3 catalyst, 161*f*
  CaO catalyst, 161*f*
  carbide formation, 184
  catalysts and CO_2 reforming of methane, 175
  CO_2 hydrothermal reduction, 47
  La_2O_3 catalyst, 161*f*, 162*f*
  MCM-41 catalysts, 179*f*
  Mo_2C catalyst, 185*f*, 186*f*
    CH_4 and CO_2, surface reactions, 186
    CH_4-TPR profiles, 189*f*
    CO_2-TPO profiles, 190*f*
    lifetime study, 187*f*
$NiMoO_x$, in situ carburization, 191*f*
NiO/alkaline earth metal oxides
  CO_2 reforming of methane, 166*f*

O

ODE. *See* Oxidative dehydrogenation of ethane
Oil and CO_2, 39*f*
Olefin, 137*f*
  cyclic carbonates synthesis, 82
  oxazolidinone one-pot synthesis, 93
One-pot synthesis
  oxazolidinone, 93
  5-phenyl-2-oxazolidinone, 94*s*
Organic molecule fuels, 55
Organic reactions and PEG radical, 96*s*
Organic wastes and hydrothermal reduction of CO_2, 34, 35*s*
Oxazolidinones, 93
  synthesis
    aziridines and CO_2, 85

Downloaded by 89.163.34.136 on June 23, 2012 | http://pubs.acs.org
Publication Date (Web): December 3, 2010 | doi: 10.1021/bk-2010-1056.ix002

        catalyst-free process, 88*s*
        CO_2, 87*s*
        propargylamines and CO_2, 86
Oxidative dehydrogenation of ethane, 103
    catalysts characterization
        FT-IR, 112
        H_2-TPR, 115, 117*f*
        N_2 isothermal adsorption-desorption, 114
        surface area and pore volume, 115*t*
        TEM, 114, 116*f*
        XRD, 112
    catalysts performance, 110*t*
        CO_2, 112*f*
        Co-loading, 110*t*
        5-$CoO_x/MgAl_2O_4$-HT, 112*f*
        $MgAl_2O_4$, 111
        reaction temperature, 111
    $CoO_x/MgAl_2O_4$-HT, 120*f*
Oxide catalysts
    Ce, 106
    Cr, 104
    Ga, 105
    Mn, 104
Oxygen and chemical lung, 255

P

Paraffins, 137*f*
PEC. *See* Photoelectrochemical device and CO_2 reduction
PEG
    PEG/CO_2 biphasic system and oxidation reaction, 95
    radical chemistry and dense CO_2, 95
    thermal oxidative degradation, 96*s*
5-Phenyl-2-oxazolidinone, 94*s*
Photocatalytic reduction of CO_2, 15, 23
Photoelectrochemical device and CO_2 reduction, 70*f*
Photoreduction of CO_2
    carbon monoxide, 23*f*
    H_2, 23*f*
Porous adsorbents, 209
Porous alkaline ceramic, 244*f*
Porous metal oxide ceramic, 244*f*
Porous silica adsorbents, 214
Potassium superoxide and CO_2 conversion, 259, 260*f*, 261*f*, 262*f*, 263*f*
Propargylamines, 86

Q

Quinazoline synthesis, 88, 90*s*

R

Rh/TiO_2, 18

S

SBA-15
    AEAPMDS, 217*f*, 219*f*
    APTS, 217*f*, 219*f*
    CO_2 adsorption, 219*f*, 224*f*
    metal modification, 218
    Mg modified, 221*t*
    silica, 222*f*
Self-neutralizing *in situ* acidic CO_2/H_2O system, 94
Silica MCM-41 and SBA-15, 214
SiO_2 and glow discharge plasma treatment, 178*f*
Sodium zirconate, 236
    CO_2 flux, 237*f*
    structure, 238*f*
Solar energy and CO_2 splitting, 1
Solar reactor, 28, 28*f*
Solar thermochemical cycle
    CO_2 splitting, 1, 25, 27*f*
    Zn/ZnO redox reactions, 25, 27*f*
Solid base photocatalysts, 15
Solid polymer electrolyte, 68*f*
    C_1-C_2 fuels, 69
    CO and H_2, 69, 70*f*
    fuel precursors, 69
    long-chain carbon fuels, 71
SPE. *See* Solid polymer electrolyte
Steam reforming process, 247
Styrene, 94*s*

T

Temperature-programmed oxidation, 179*f*
    using CO_2, 190*f*
TGA. *See* Thermogravimetric analysis
Thermochemical CO_2 splitting, 1
Thermogravimetric analysis
    Fe_2O_3:8YSZ, redox cycle, 7*f*, 8*f*, 9*f*
TPO. *See* Temperature-programmed oxidation

U

UFF-2 combination and COF, 227*f*
Urea
  derivatives synthesis
    amine, 94*s*
    CO_2, 92
    KOH/PEG-catalyzed, 94*s*
  and mesoporous silica surface, 223*f*

V

Vicinal halohydrin and cyclic carbonates, 84

W

Water and CO_2 hydrothermal reduction, 36*f*

X

XPS. *See* X-ray photoelectron spectroscopy
X-ray diffraction, 129
  Fe_2O_3:8YSZ, 5*f*, 8*f*
  MWCNT, 132*f*
X-ray photoelectron spectroscopy, 130
XRD. *See* X-ray diffraction

Y

YSZ. *See* Yttria-stabilized zirconia and Fe_2O_3
Yttria-stabilized zirconia and Fe_2O_3, 3*f*, 5*f*

Z

Zenarestat®, 89*s*
Zeolite adsorbents, 211
ZnO/Zn redox reactions, 25, 27*f*
ZrO_2, 17

Downloaded by 89.163.34.136 on June 23, 2012 | http://pubs.acs.org
Publication Date (Web): December 3, 2010 | doi: 10.1021/bk-2010-1056.ix002